9-1-2008

Technical Support in Engineering Construction Phase of Craney Island Eastward Expansion

Mac Sisson
Virginia Institute of Marine Science

Harry V. Wang
Virginia Institute of Marine Science

Yuepeng Li
Virginia Insitute of Marine Science

Jian Shen
Virginia Institute of Marine Science

Albert Y. Kuo
Virginia Institute of Marine Science

See next page for additional authors

Recommended Citation

Sisson, M., Wang, H. V., Li, Y., Shen, J., Kuo, A. Y., & Gong, W. (2008) Technical Support in Engineering Construction Phase of Craney Island Eastward Expansion. Special Reports in Applied Marine Science and Ocean Engineering (SRAMSOE) No. 400. Virginia Institute of Marine Science, William & Mary. https://doi.org/10.21220/V54Q98

Technical Support in Engineering Construction Phase of Craney Island Eastward Expansion

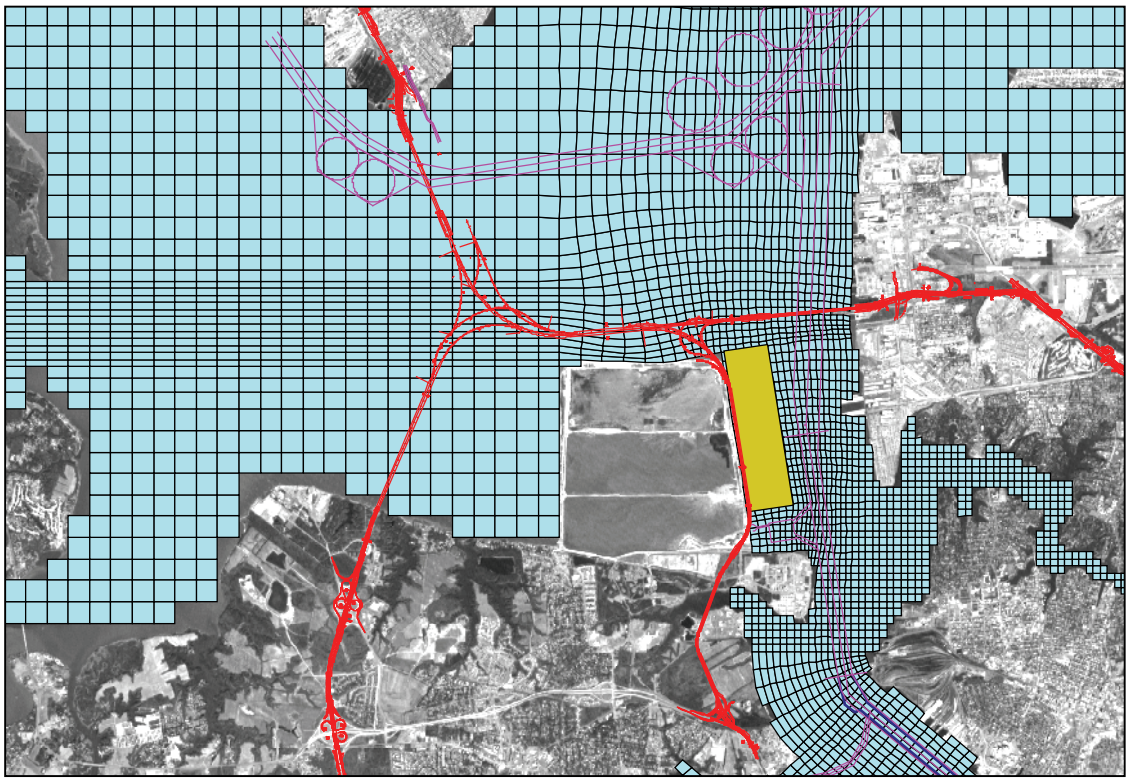

Mac Sisson, Harry Wang, Yuepeng Li,
Jian Shen, Albert Kuo, and Wenping Gong

Final Report to the
Craney Island Design Partners
via
The Virginia Port Authority

Special Report No. 400
In Applied Marine Science and Ocean Engineering

Virginia Institute of Marine Science
Department of Physical Sciences
Gloucester Point, Virginia 23062

September 2008

EXECUTIVE SUMMARY

"Technical Support in Engineering Construction Phase of Craney Island Eastward Expansion"

1. The three primary concerns for the Craney Island Eastward Expansion project in the engineering phase are: (a) the flushing and far-field impacts on tidal flow due to cross-sectional changes incurred by the construction of the cell and dredging of the access channels and berthing areas, (b) the sediment plume generated during the construction and dredging of the access channels and berthing areas, and (c) the water quality impact, particularly on the bottom dissolved oxygen, due to Eastward Expansion.

2. Analysis of historical long-term water quality data collected by the Virginia Department of Environmental Quality as well as the EPA Chesapeake Bay monitoring program indicate that bottom dissolved oxygen seldom falls below 5.0 mg/l in either Hampton Roads or the Elizabeth River. Without a major phytoplankton bloom in the spring and summer, the observed chlorophyll-a levels remain below 40 μg/l. The historical DO levels in the region around the CIEE have benefited from strong gravitational circulation in the James River, which provides sufficient and adequate flushing for the system.

3. A coupled hydrodynamic/water quality model HEM3D was developed to assess the potential impact of the Craney Island Eastward Expansion in the Elizabeth River. The model domain contains the entire tidal James River, the Elizabeth River, and a portion of the Chesapeake Bay at the downstream end of James River as the boundary condition. Based on the revised Craney Island expansion configuration, the Elizabeth River portion was re-segmented into a higher resolution orthogonal grid with a 90-120 m scale in the horizontal plane and 6 layers in the vertical plane. Twenty-four state variables are incorporated in the water quality analysis, including salinity, temperature, total suspended solids, and various forms of phytoplankton, nutrients, carbon, and silica. A separate benthic sediment sub-model is dynamically coupled with the water column water quality model for addressing benthic and pelagic interaction.

4. The periods selected for water quality analysis were 1999, 2000, and 2001, for which the fall line and the non-point source loadings for the entire James River basin are available from the EPA Chesapeake Bay Program HSPF Phase V watershed model. In addition, the point source loadings from inside Elizabeth River are available and included. The mean annual load of total nitrogen (16 million kg) and total phosphorus (2 million kg) could probably support a background phytoplankton level comparable to the historical levels of 20 to 30 μg of chlorophyll-a. The modeling framework was calibrated for all three years in terms of major variables. Comparisons were made of the observed and computed values of the relevant variables, including water elevation, velocity, and salinity for the hydrodynamic model, and dissolved oxygen, chlorophyll-a, total nitrogen, total phosphorus, ammonium, nitrite and nitrate, and dissolved phosphate for the water quality model. The analysis indicated that the model reproduces major hydrodynamic features and compared well with the intensive measurements. In addition, the principal components of the oxygen budget, the interaction between phytoplankton, photosynthesis, and respiration, COD and NOD, SOD, atmospheric reaeration, and vertical mixing were incorporated and the model produces

reasonably well the observed spatial and temporal distributions for all three calibration years. The differences associated with the comparison of model prediction and observed data are well within the range of natural variation in a given season of measurements of water quality parameters.

5. The calibrated hydrodynamic/water quality model are thus suitable for use (a) as a management tool for assessing the impact of various construction phases, (b) as a basis for providing the hydrodynamic flow field as an input to a high-resolution suspended sediment fate (SSFATE) model, and (c) to gain insight and understanding of the transport, kinetic, and transfer processes in the James and Elizabeth estuaries, which affect the distribution of water quality constituents, and in particular, oxygen levels. Hydrodynamic and water quality model state variable differences between the scenario and base case results were used throughout this study to provide the metric for impact assessment (differences provided are scenario results minus base case results).

6. Hydrodynamic analysis indicates that the flushing capabilities of the Elizabeth River system, and thus, the cross-sectional impacts near Craney Island, would not be adversely affected by the full expansion. An analysis of the cross-section at the mouth of the river shows that the reduction in the surface area, causing a slight reduction in tidal prism (4%), is completely compensated for by a more significant increase in the non-tidal residual flow (26% on average) both in and out of the system. By adding the slight decrease in tidal prism and significant increase in non-tidal residual volume, it translates to a net increase of total flushing capability by 2% on average due to the full expansion. For the intermediate plan of the south cell expansion without full scale dredging, the overall flushing capability has a slight reduction of 1-2%.

7. The results using the SSFATE modeling of the sediment plume generated during the construction and dredging of the access channels and berthing areas will be provided in a separate report (CHT, 2008). The full reference is: Computation Hydraulics and Transport (2008): “Modeling Suspended Sediment Plumes Created by Dredging Operation for the Craney Island Eastward Expansion Project.” Billy Johnson of CHT, Edwards, MS.

The water quality impact due to the Eastward Expansion is described as follows:

8. Water quality analysis for the south cell expansion

(a) The temporal variability

The impact of the construction of the south cell was analyzed by examining differences in predicted values of key water quality variables (dissolved oxygen, chlorophyll-a, total phosphorus, total nitrogen, ammonium, nitrate-nitrite, and dissolved phosphate) on a 30-day-average basis over the 3-year record. Differences were derived at Station LE5.6 adjacent to the project site, Station ELI2 just to the south to the project site, and a reference Station LE5.5 in the James River. Differences were extracted for surface and bottom model layers as well as for vertical averages of all 6 layers. For all parameters other than dissolved oxygen and chlorophyll-a, the differences were less than any instrument detection limits (on the order of 0.001 mg/l). For oxygen, the difference ranged from -0.02 mg/l to 0.02 mg/l and for chlorophyll-a, the differences ranged between 0.0 and 0.5 μg/l. Both of these were less than or equal to their respective detection limits of 0.1 mg/l and 0.5 μg/l.

(b) The spatial variability

Spatial plots of the differences in dissolved oxygen (DO) were constructed to assess the location and extent of the impact of the south cell expansion on DO levels. The domain of these plots included Hampton Roads and the entire Elizabeth River. These plots showed 30-day averages at both surface and bottom model layers, as well as a vertical average of all 6 layers, for the potentially critical months of June, July, August, and September in the summer and fall. Throughout all of these plots, only the small dredged region just east of Craney Island showed differences between - 0.3 mg/l and - 0.6 mg/l for the bottom dissolved oxygen. However, these differences are due to the artifact of comparison between the unequal depth layers between the pre-dredged shallow bottom layer (for the base case) versus the post-dredging deeper bottom layer (for the scenario). When the comparison was made at the same depth, the difference of dissolved oxygen becomes negligibly small (on the order of one one-hundredth mg/l). In conclusion, the impact to DO levels due to the south cell expansion is minimal and well within the range of variation within a given season.

9. Water quality analysis for the full expansion

(a) The temporal variability

The impact of the construction of the full expansion was analyzed by examining differences in predicted values of key water quality variables on a 30-day average basis over the 3-year record. Differences were derived at Station LE5.6 adjacent to the project site, Station ELI2 just to the south to the project site, and a reference Station LE5.5 in the James River. Differences were extracted for surface and bottom model layers as well as for vertical averages of all 6 layers. As in the results for the south cell expansion analysis, for all parameters other than dissolved oxygen and chlorophyll-a, the differences were less than instrument detection limits (on the order of 0.001 mg/l). For oxygen, the differences ranged from 0.03 -0.05 mg/l, and for chlorophyll-a, the differences ranged between 0.0 and 0.5 μg/l. These differences are within their respective detection limits as well. The bottom dissolved oxygen actually showed a slight increase after the scenario run for full-scale expansion and dredging.

(b) The spatial variability

Spatial plots of the differences in dissolved oxygen (DO) were constructed to assess the location and extent of the impact of the full cell expansion on DO levels. The domain of these plots included Hampton Roads and the entire Elizabeth River. These plots showed monthly averages at both surface and bottom model layers, as well as a vertical average of all 6 layers, for the potentially critical months of June, July, August, and September of 1999, 2000, and 2001 in the summer and fall. Throughout all of these plots, only the small dredged region just east of Craney Island showed differences between - 0.3 mg/l and – 0.6 mg/l for the bottom dissolved oxygen. However, these differences are due to the artifact of comparison between the unequal depth layers between the pre-dredged shallow bottom layer (for the base case) versus the post-dredging bottom layer (for eastward expansion scenario). When the comparison was made at the same depth, the difference of dissolved oxygen again becomes negligibly small, on the order of one one-hundredth mg/l difference. In conclusion, the impacts to DO levels due to the full expansion are minimal and are well within the range of variation in a given season.

10. The overall assessment of dissolved oxygen comparison

Given the relatively strong physical circulation in the Lower James and mouth region of the Elizabeth River, the existing dissolved oxygen budget in the bottom waters off the Craney Island expansion site are controlled by the combination effect of reaeration (corresponding to vertical mixing), the bottom DO flux from the James River, as well as biological and chemical water column DO demand, and sediment oxygen demand.

As a result of the Craney Island Eastward Expansion, both the vertical mixing and the non-tidal residual transport actually increase. These are the positive factors that benefit the bottom DO in the post-expansion condition. There are, however, negative factors that reduce the shallow oxygen-rich region in exchange of deeper dredging area that is prone to oxygen deficiency. As computed by the model, the positive benefit from the expansion outweighs the negative aspect of the dredging, which results in overall negligible impacts, if there are any. In other words, in terms of DO changes (caused by the Craney Island expansion) the increase of advective DO flux from the James River and local vertical mixing overcome the increase of low DO volumes. Overall, the impacts to DO levels due to both the south cell and the full expansion are minimal and are well within the range of the detection limit.

There are regions that are dredged adjacent to the berthing area just east of Craney Island that show some impact. However, these differences are due to the effect of comparison between the unequal depth layers between the pre-dredged shallow bottom layer (for the base case) versus the post-dredging deeper bottom layer (for the scenario). When the comparison was made at the same depth, the difference of dissolved oxygen again becomes negligibly small. It should be kept in mind that the healthy water quality condition in the Lower James River is the premium asset and a key factor that plays an important role in minimizing the impact from the Craney Island Eastward Expansion.

11. Uncertainty of the model results was assessed by conducting a sensitivity analysis by varying the most sensitive parameters that affect the water quality results. These parameters include: watershed loading partitioning, phytoplankton growth rate, and vertical mixing parameters. These additional results gave the calibration a proper constraint in terms of their upper and lower bounds. In the case of dissolved oxygen, which is the water quality parameter of highest concern for this study, the calculation showed that it is relatively resilient to the variation of these parameters.

TABLE OF CONTENTS

LIST OF TABLES

LIST OF FIGURES

LIST OF APPENDICES

Appendix E. CIEE South Cell Expansion Scenario
Water Quality Model Analysis
Differences from Base Case (scenario minus base)
For 1999, 2000, and 2001 at CBP Stations LE5.5, LE5.6, and ELI2

Appendix I. CIEE Full Expansion Scenario
Water Quality Model Analysis
Differences from Base Case (scenario minus base) for 1999, 2000, 2001 at CBP Stations LE5.5, LE5.6, and ELI2

Appendix J. CIEE Full Expansion Scenario
Water Quality Model Scenario Analysis:
30-Day Average Differences from Base Case (scenario minus base case)
- Plots of surface and bottom layer differences and vertical average differences
- Tables of vertical average differences
For 1999, 2000, 2001 at CBP Stations LE5.5, LE5.6, and ELI2

Appendix K1. Spatial Plots of DO Differences
(between CIEE full expansion and Base Case)
for 30-day Averages in June, July, August, and September of 1999, 2000, and 2001
Comparison at Present Bottom Depth (pre-construction depth)

Figure L.36. Differences of model predictions for ammonium, nitrate-nitrite, and dissolved inorganic phosphorus at CBP Station ELI2 (surface and bottom layers) for 1999 due to a decrease in the background eddy diffusivity from 10^{-6} m^2/s to 10^{-7} m^2/s (ST-6).

CHAPTER I. BACKGROUND

The Craney Island Dredged Material Management Area (CIDMMA) is a federally owned and operated facility located in Hampton Roads adjacent to the city of Portsmouth, Virginia (Figure I.1). The proposed expansion of the CIDMMA addresses a Federal interest in increasing the capacity of the CIDMMA and extending its useful life beyond the year 2050. In addition, the expansion would serve a further interest in obtaining logistical and tactical areas for the deployment of national defense forces. It simultaneously addresses the interest of the Commonwealth in future expansion of its commercial, deep-water port facilities.

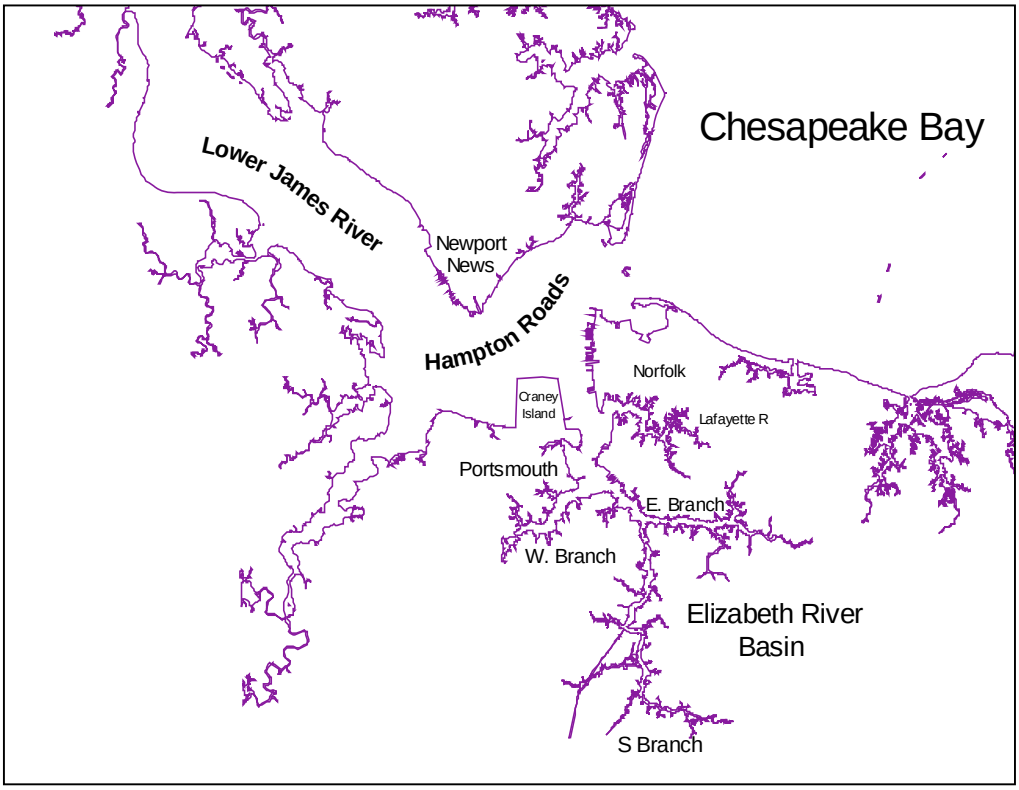

Figure I.1. Hampton Roads and the Elizabeth River Basin.

The agencies in charge of the present development efforts are the Norfolk District, U.S. Army Corps of Engineers (ACE) representing the federal government, and the Virginia Port Authority (VPA) representing the Commonwealth of Virginia. Following a successful *Reconnaissance Study* by ACE that determined the required federal interest, both ACE and VPA signed a feasibility cost-sharing agreement and adopted a *Project Study Plan* (PSP) to determine suitable and acceptable means for designing and implementing the expansion. The PSP required, among other items, the development and evaluation of preliminary designs for added material placement areas and new port facilities, including a marine terminal, to be incorporated in the expansion. More specifically, in order to determine the possible impact that any of these designs might

have on the estuarine environment in Hampton Roads and adjacent areas, the PSP recommended for hydrodynamic modeling studies to be conducted.

VIMS has developed the hydrodynamic model called HEM-3D (Hydrodynamic Eutrophication Model in 3 Dimensions) (Hamrick,1992; Park et al., 1995). The HEM-3D model solves the three-dimensional primitive variable vertically hydrostatic equations of motion for turbulent flow over a coordinate system that is curvilinear and orthogonal. It describes the hydrodynamic behavior of the estuary by predicting time-varying surface elevation, horizontal and vertical water movement (including both tidal and non-tidal currents), and 3D distributions of conservative water properties such as salinity. It also determines bed shear stress throughout its bottom layer that, in turn, allows for the prediction of sedimentation potential. The model domain for the James River spans from its mouth to the limit of tide (i.e., Richmond, Virginia). A coarse grid cell of 370 meters was used for the James River to accommodate the length of the river. A higher resolution is used in the Elizabeth River, and a cell size there of 123 m was selected. A model grid with a dual scale resolution, as shown in Figure I.2, was developed for use in the initial and additional studies of the Craney Island Expansion.

The VIMS numerical modeling group has conducted two projects that have specifically evaluated the Craney Island Eastward Expansion impact of construction combined with the other construction projects.

(1) The hydrodynamic modeling study, "Three Dimensional Hydrodynamic Modeling Study of Craney Island Eastward Expansion" (Wang et al., 2001) was conducted by the Virginia Institute of Marine Science (VIMS) for the purpose of evaluating the Craney Island land expansion options under consideration until that time. In this study, impacts of land expansion options for Craney Island were assessed. The HEM-3D model was used to compare expansion options of Craney Island to the east, west, north, northeast, and east/west. Model simulations of one to several months were made for each expansion option, as well as two channel depths being considered at the time. Physical changes to the estuarine environment (i.e., tidal range and phase, strength and direction of tidal and tidally-averaged currents, salinity and its distribution, circulation and flushing ability, and sedimentation potential) were evaluated and ranked according to impact. Additionally, specific features important to the well-being of estuarine processes (e.g., flushing capability, the Newport News Pt. frontal system, tidal prism, etc.) were examined extensively. The conclusions of the study were that the Eastward Expansion of Craney Island had the least impact, the east/west and westward expansions had the next least impact, and the expansions to the north and northeast had the most impact.

(2) A subsequent modeling study, "Additional Assessments of the Craney Island Eastward Expansion in the Elizabeth River and Hampton Roads - Hydrodynamic Model Study" (Sisson et al., 2005), was conducted in order to assess the cumulative impacts of the dredging of the Maersk (APM) Terminal area south of Craney Island and the berthing of ships at both the APM and Craney Island Eastward Expansion. The conclusions were that both the Maersk Terminal dredging and the berthing of ships at both port facilities had minimal impact on either the surface elevation or the sedimentation potential. The

berthing of ships at CIEE, if considered permanent, was shown to exhibit a small localized effect on both the salinity distribution and the velocity distribution. In late 2006, the final Environmental Impact Statement (EIS) for the Craney Island Expansion, drafted by the Norfolk District of the U.S. Army Corps of Engineers, was approved.

In addition, there have been several important construction projects proposed in the Elizabeth River region. These include the construction of (1) the deepening of the Norfolk Harbor Channel by the Navy and (2) the construction of the 3rd Crossing of Hampton Roads by the Virginia Department of Transportation, which is still under consideration.

Whereas brief descriptions of these studies are provided above, the reader is referred to the website **http://www.vims.edu/craney** for more explanation or to download full reports of these studies.

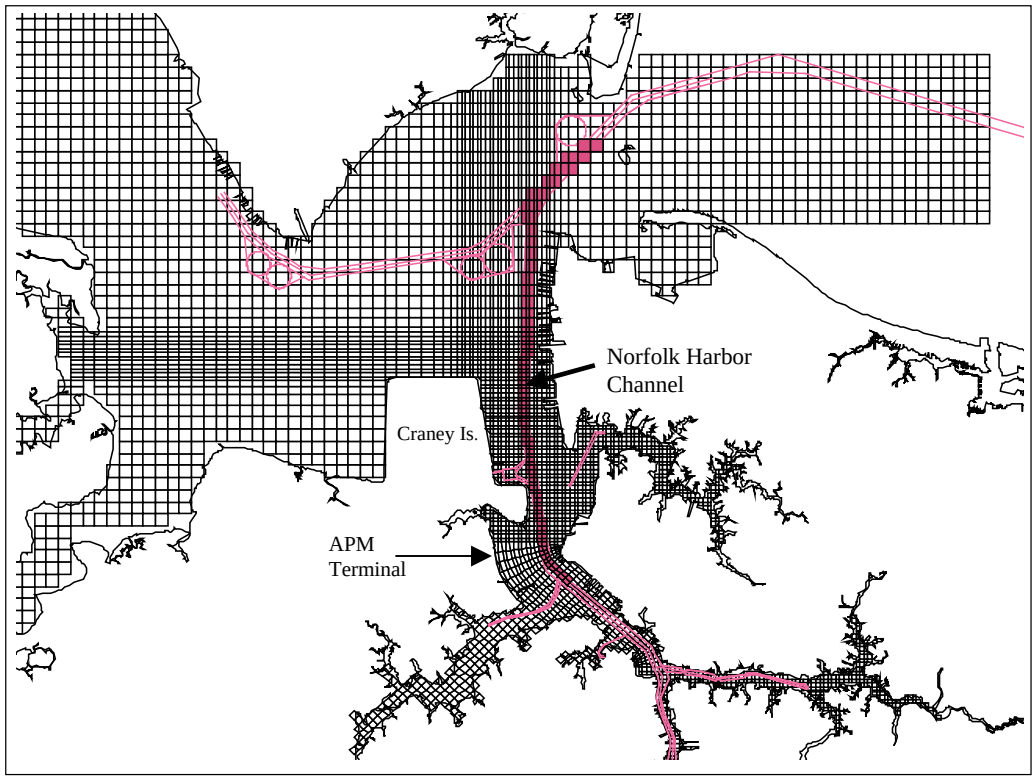

Figure I.2. Dual-scale model grid and Norfolk Harbor Channel.

CHAPTER II. INTRODUCTION

The Craney Island Dredged Material Management Area or CIDMMA extends over an area of 2,500 acres along the south bank of the James River in Portsmouth, Virginia, as shown in Figure II.1. For the last 50 years, the site has served as a long-term disposal area for material dredged from the channels and ports of Hampton Roads. In 1997 the U.S. House of Representatives Committee on Transportation and Infrastructure authorized USACE to prepare a Feasibility Study to determine the viability of expanding Craney Island, and to consider rapid filling of the new dredge material site to provide an area for a new marine terminal.

The Feasibility Study determined that the existing CIDMMA would reach capacity in 2025 and the VPA would run out of cargo handling capacity in 2011. Among 4 design plans that were evaluated in the original modeling study (Wang et al., 2001), the eastward expansion was found to be the design of least impact for the long-term disposal displacement and provision of an area for a new terminal. In this phase, the Virginia Port Authority and the US Army Corps of Engineers are partnering to construct the Eastward Expansion of Craney Island**.** The project has two purposes: (1) to effectively extend the life of Craney Island as a dredged material placement area and (2) to provide land for the construction of a new marine terminal. In accordance with the National Environmental Policy Act (NEPA), federal and state agencies are required to integrate environmental

Figure II.1. Aerial view of CIDMMA, located along James River south bank in Portsmouth, VA

values into their decision-making processes by considering the environmental impacts. To meet this requirement, an Environmental Impact Statement (EIS) is needed for the EPA's reviews and comments before the project can proceed. It is the purpose of this study to provide an analysis framework for determining various potential impacts and reasonable alternatives. The primary scope of this study is to determine:

(a) the flushing and far-field impacts on tidal flow due to cross-sectional changes by the construction of the cell and dredging of the access channels and berthing areas,

(b) the sediment plume generated during the construction and dredging of the access channels and berthing areas, and

(c) the water quality impact, particularly on the bottom dissolved oxygen, due to Eastward Expansion.

II-1. Overview of "Engineering construction phase" for the Craney Island Project

The Craney Island Eastward Expansion, as shown in Figure II.2, consists of north and south cells. These cells have east-west dimensions of approximately 2400 feet, with the wharf positioned at a distance of 1000 feet from the western toe of the Norfolk Harbor Channel (NHC). The north-south dimension is approximately 9240 feet, which is divided between the length of the north cell (6200 feet) and that of the south cell (3040 feet). The total expansion area is approximately 500 acres, which was scaled back from the original plan for 539 acres.

During the engineering construction phase of the Craney Island Eastward Expansion, a 2.1-km dike will be constructed, as shown in Figure II.3, running longitudinally along the eastern side of the 500-acre area of the CIEE. This construction will require a foundation dredging to an elevation of -100 feet MLLW. Once dredged, the dike would then be built in lifts with quarry-run rock and sand fill. The quarry-run rock will have a maximum 12-inch size, and a d50 of 5 inches. The d50 is defined as the median stone diameter for which 50% of the fill material is smaller. Rock and sand may be placed with the use of a mechanism with a telescopic arm designed to deliver sediment directly to its destination. While most of the dredged material released or lifted will be deposited on the disposal site, some portion may be transported away from the originally intended designated area. This can happen in two ways: 1) fine dredged sediments may be carried by currents as well as waves while they are still in the water column, and 2) these sediments may be deposited at the bottom of the sea floor and resuspended into the water column by the occasionally high current and wave conditions.

The actual construction sequence is divided into at the least two phases: Phase I and II, as shown in Figures II.4 and II.5, and the final stage, as shown in Figure II.6.

Figure II.2. Craney Island Eastward Expansion with its north and south cells

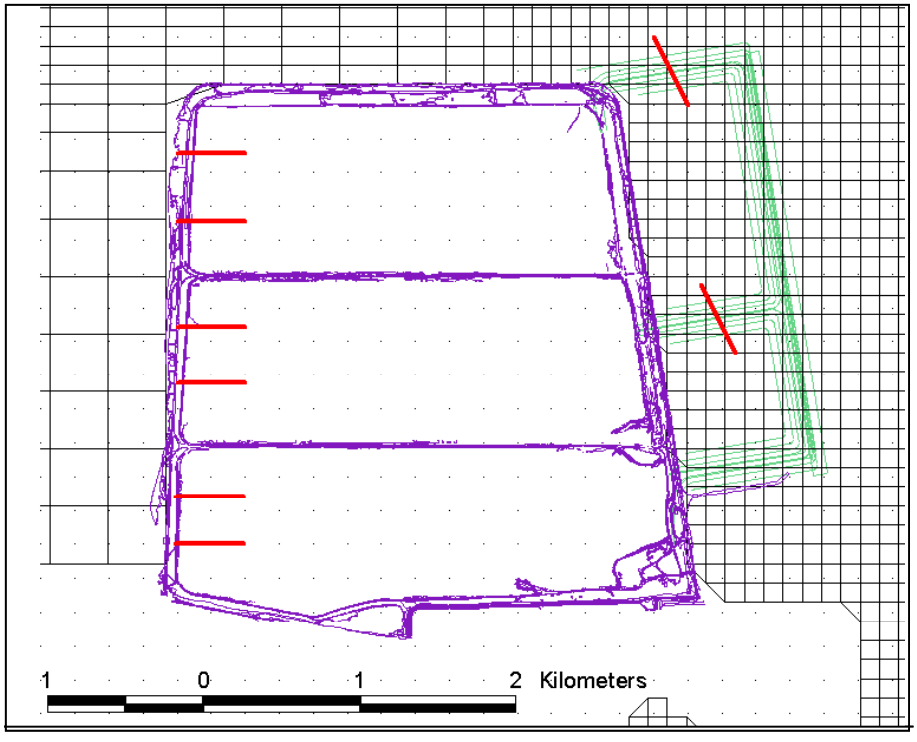

Figure II.3. The HEM-3D model grid with existing disposal site (purple), the expansion dike locations (green), and the effluent discharge site (red)

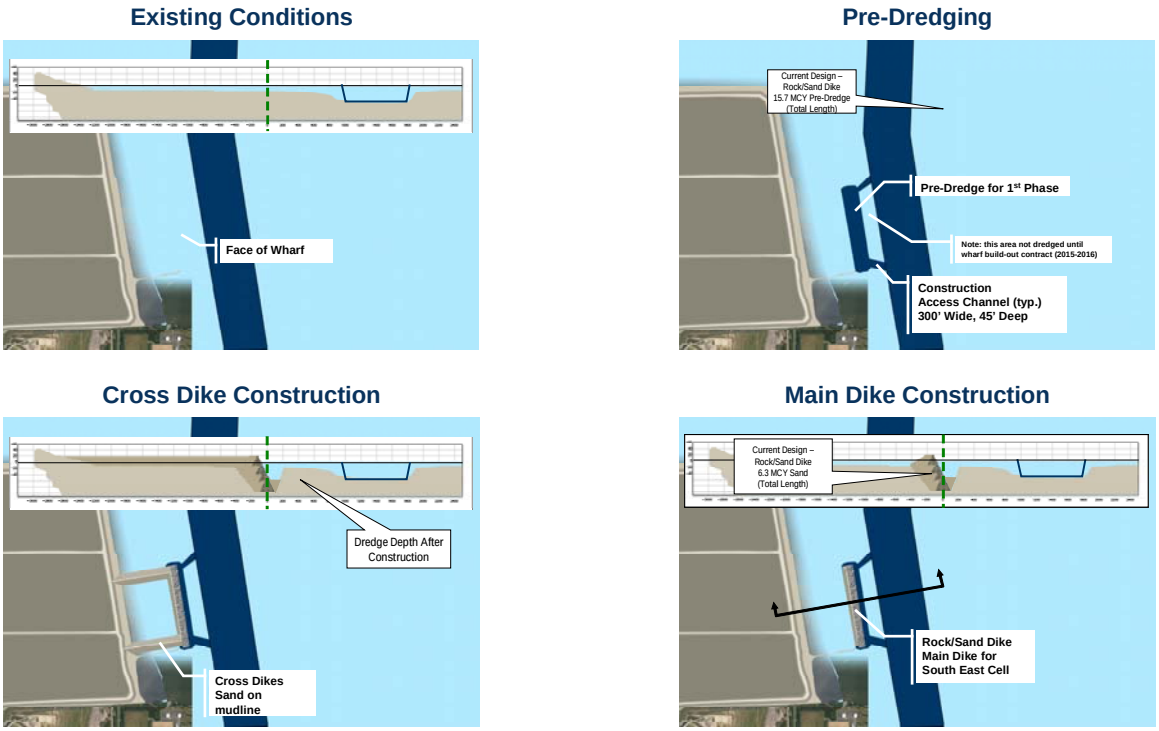

Figure II.4. Phase I construction sequence (starting clockwise with the existing conditions)

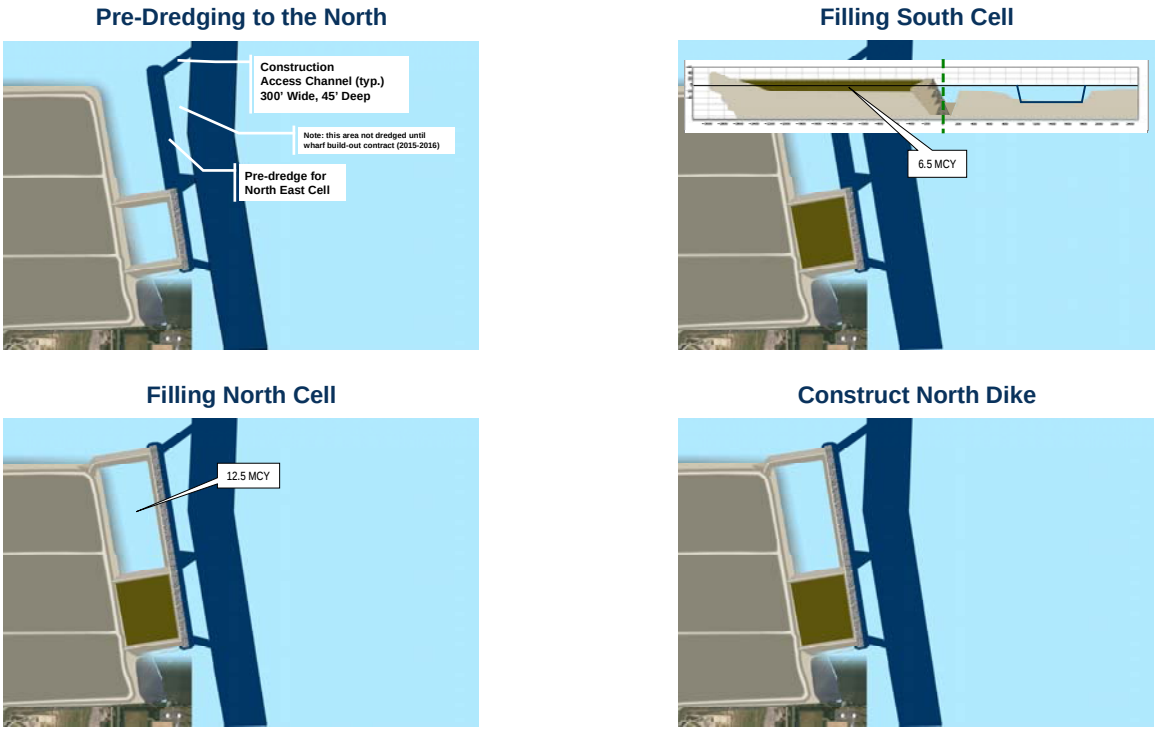

Figure II.5. Phase II construction sequence (starting clockwise with pre-dredging to the north)

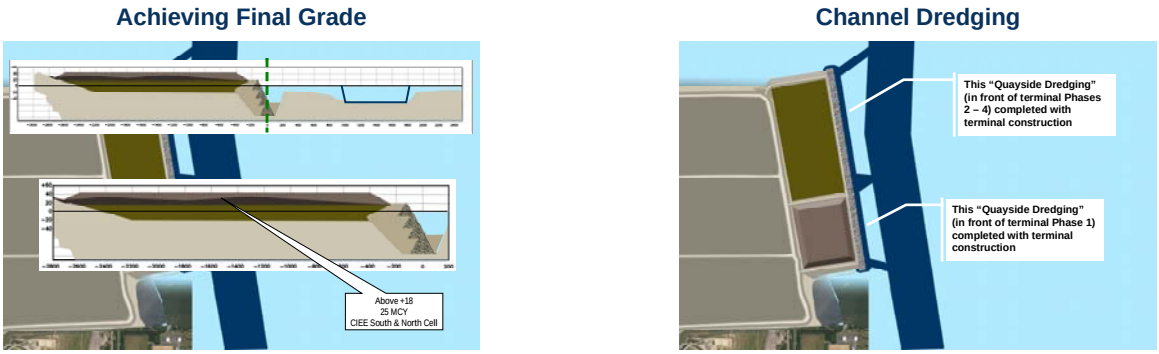

Figure II.6. Final phase (sequence follows from left to right) (courtesy VPA)

Two expansion options will be investigated in this study. The full eastward expansion and the expansion of the south cell only, referred to as the "Phase I" expansion, are described as follows:

A. Expansion of South Cell Only ("Phase 1" expansion)

The expansion for this option is a rectangular area to be added to the eastern side of Craney Island, as shown in Figure II.7. The footprint shown has a total perimeter, all four sides included, of 3,689 yd (3,373 m) and a horizontal area of 173 acres (0.70 km^2).

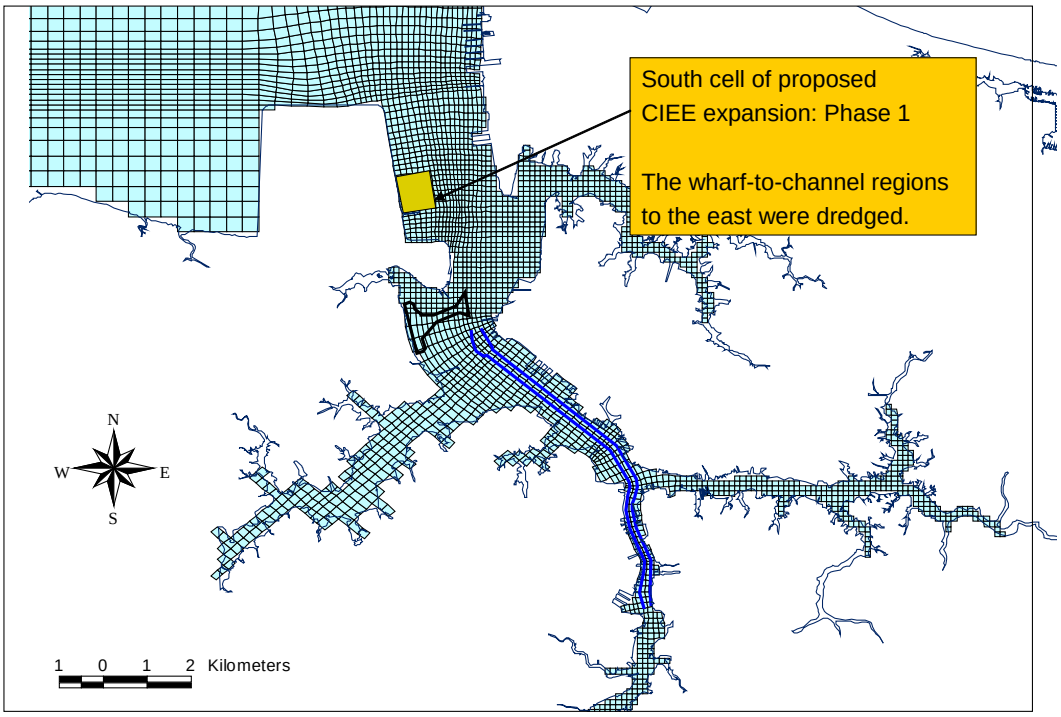

Figure II.7 The design for the south cell expansion

B. Full CIEE Expansion ("final phase") - This option includes a rectangular expansion added to the east side of Craney Island, as shown in Figure II.8. The expansion footprint has a total perimeter of 7,822 yd (7,152 m) and an area of 501.3 acres (2.03 km^2).

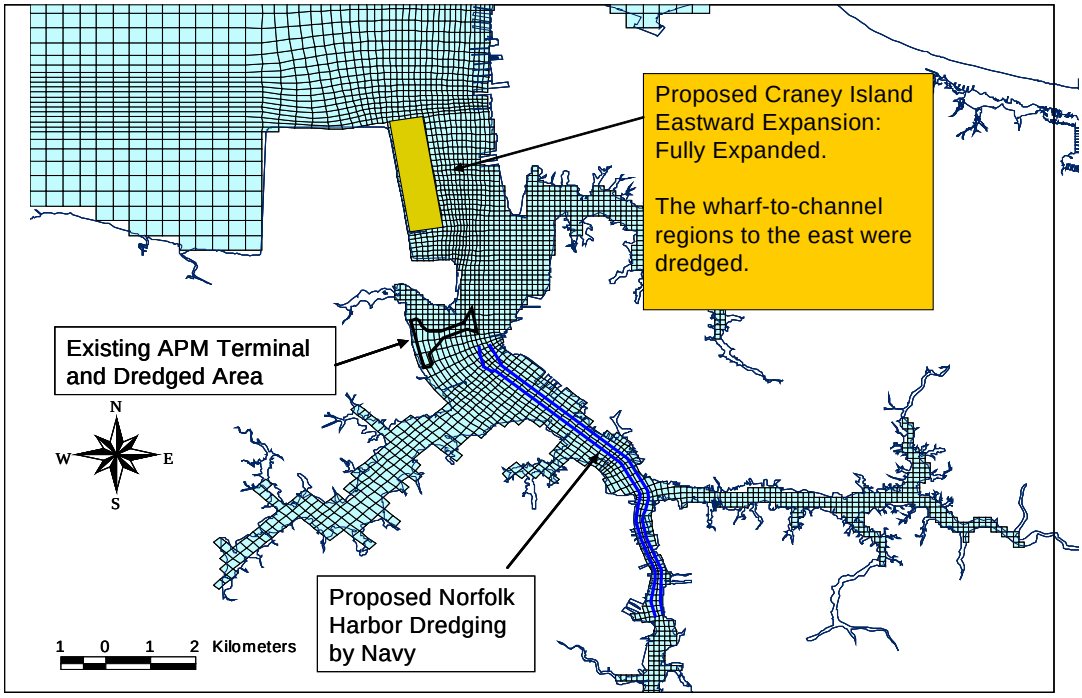

Figure II.8. The new design for the full expansion of Craney Island

II-2. CIEE design change and HEM-3D model grid modification

The CIEE design provided for the original hydrodynamic study of Craney Island (Wang et al., 2001) specified a 500-foot clearance from the face of the wharf to the western toe of the Norfolk Harbor Channel (NHC). However, the design was modified to become a 1000-foot clearance between the wharf face and the NHC western toe at the recommendation of a mooring study that was concluded in August 2007. This westward shift of the wharf face decreased the overall area of the expansion from 539 acres to approximately 500 acres, as shown in Figures II.9, II.10, and II.11.

Due to the 2007 change of the CIEE design, VIMS needed to realign the model grid over the CIEE vicinity, revise the model setups, and re-assess the impacts caused by the cross-sectional increase and surface area decrease incurred by the new design. Results of these assessments are reported in Chapter V (Section V-1).

Figure II.9. Schematic drawing of the new CIEE design (courtesy VPA)

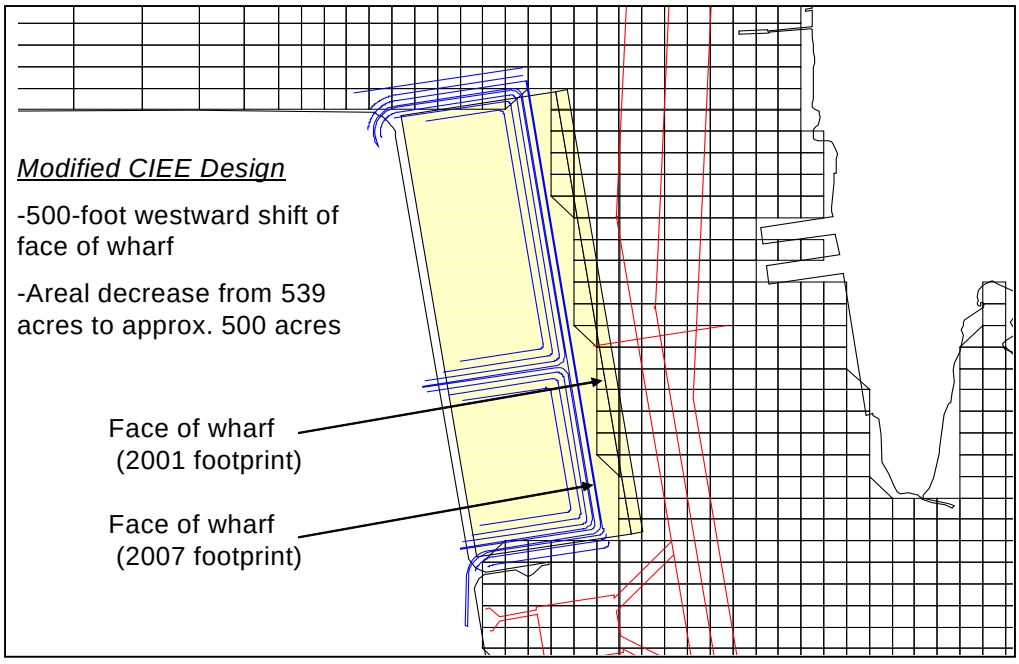

Figure II.10. A plan view of the 500-foot westward shift of the face of the wharf incorporated into the CIEE design

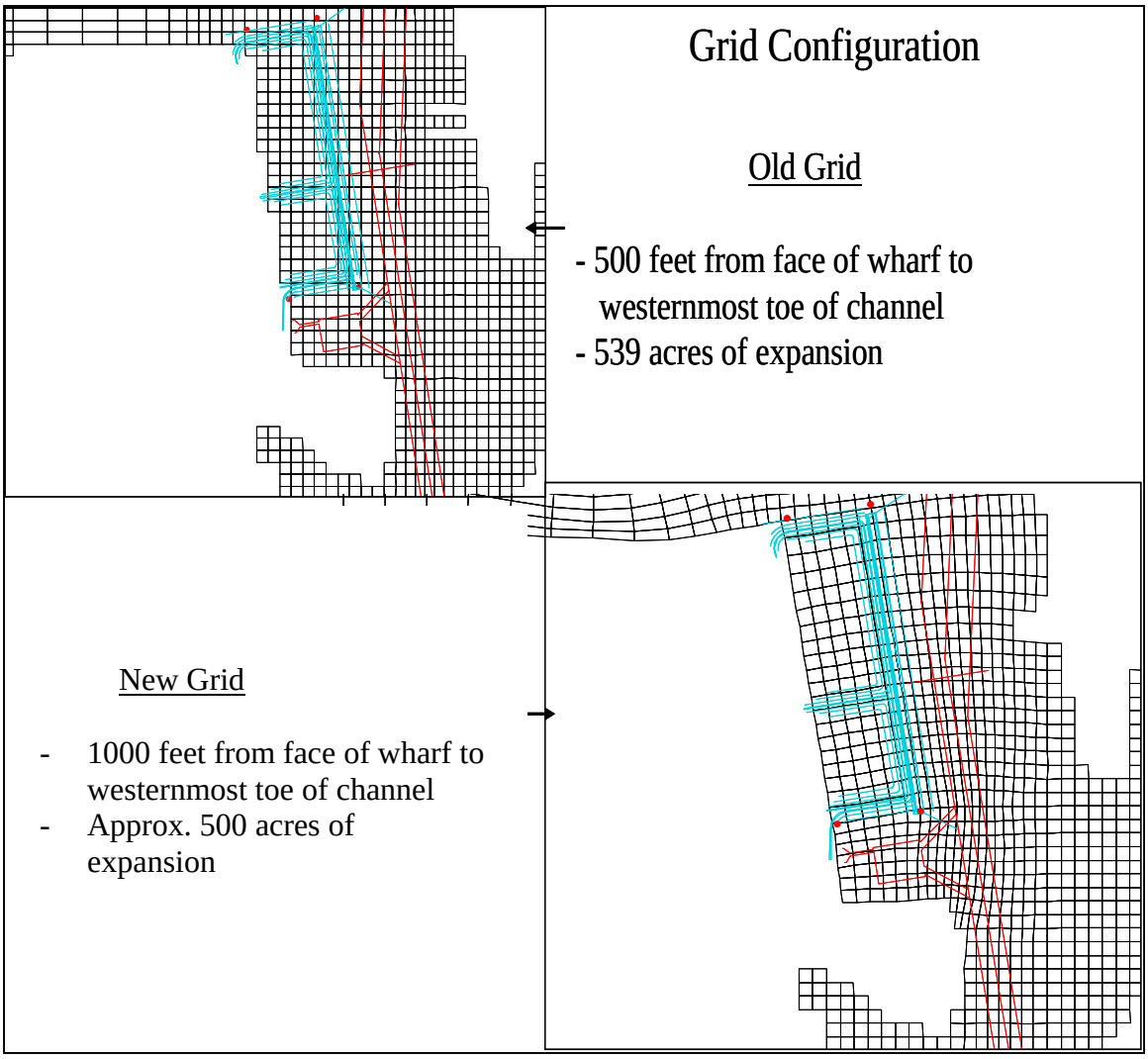

Figure II.11. Plan views showing the modification of the HEM-3D grid in the vicinity of the eastward expansion

II-3. Far-field Impact Assessment (HEM-3D)

One vital element in the modeling effort is to ensure that no significant impacts to hydrodynamics due to dredging in either the access channel or the ship berthing area, or constructing the new cell, have occurred (USACE EIS, page IV-8). The original CIEE study (Wang et al., 2001a) concluded little change, with "no significant effects to water circulation, sedimentation, salinity, currents, and tidal flushing from the Elizabeth River with an eastward expansion of the CIDMMA" (EIS, page IV-2).

Another feature of key importance is the volume of water that enters and leaves the Elizabeth River during a tidal cycle. The magnitude of the tidal prism and residual current are indicators of the flushing ability of the Elizabeth River Basin, a system that includes not only the tidal waterways of the river stem and its four main branches but also

adjacent watershed areas that deliver land-based runoff to the system as well. One of the main purposes of the present study is to determine whether any of the expansion designs would cause the combined effect of tidal prism and residual circulation, and in turn the flushing ability of the Elizabeth River Basin, to decrease.

For the far-field assessment of the Craney Island Eastward Expansion, the HEM-3D model has been used. A full description of the HEM-3D model is provided in Chapter III. The hydrodynamic portion of HEM-3D has been fully calibrated and validated for tidal elevation, velocity, and salinity. The model was previously calibrated for these parameters in the mainstem James River in a previous study (Boon et al., 1999). Calibration in the Elizabeth River consisted of simulating the prototype conditions for the period April 24 to June 8, 2000, during which time high-frequency observations of tides, velocities (surface, mid-depth, and bottom), and salinities (surface, mid-depth, and bottom) were available. Additionally, monthly comparisons of predicted versus observed salinity throughout the water column at multiple locations throughout the Elizabeth mainstem and the Southern Branch showed the model's ability to accurately simulate the observed stratification. The model was further validated with respect to surface elevation induced by both astronomical and meteorological tides, current velocities (tidal and residual), and salinity distributions. As part of that study, VIMS developed a global analysis methodology to determine the far-field, long-term effects of each expansion option on each of several hydrodynamic state variables (i.e., water elevation, current velocity, salinity, and sedimentation potential). A complete description of model calibration and validation for the Elizabeth and James River model is presented in Wang et al. (2001), Chapter IV.

II-4. Sediment plume impact assessment

For the sediment plume assessment of the Craney Island Eastward Expansion, a near-field study is conducted. The near-field study consists of three major components that involve coupling between SSFATE and HEM-3D:

A. Modeling sediment plumes caused by dredging and placement operations (SSFATE)
B. Modeling of localized impacts to dissolved oxygen levels (HEM-3D)
C. Assessment of cross-sectional area and impacts (HEM-3D)

The results of the SSFATE modeling of sediment plumes caused by dredging and placement operations are provided in a separate report for this project (CHT, 2008). However, a brief description of its application in this project is herein provided for reference.

The Corps of Engineers' SSFATE model has been used to simulate conditions during the dredging operation both with clamshell dredging or hydraulic dredging. SSFATE computes the suspended sediment distribution resulting from dredging operations. The processes modeled are the fate of suspended sediment in which the ocean transport and turbulence associated with ambient currents dominate. The transport and dispersion of

suspended material from a sediment source are computed using a particle-based model. Particle advection is based on the simple relationship that a particle moves linearly with a local velocity, obtained from the hydrodynamic input, for a specified model time step. Particle diffusion is assumed to follow simple random walk processes. A diffusion distance defined as the square root of the product of an input diffusion coefficient and the time step is decomposed into x and y displacements via a random direction function. The z diffusion distance is scaled by a random positive or negative direction.

The transport, dispersion, and eventual fate of dredged or fill materials released into the marine environment depend upon both the physical characteristics of the dredged material and the dynamics in the water column. Ocean currents affect the transport and the dispersion of sediment particles. The vertical density structure and intensity of the turbulence field can determine the length of time the sediment particles remain in the water column. The modeling framework used is the combination of a high-resolution HEM-3D model application and the Suspended Sediment Fate (SSFATE) model application. HEM-3D was used in a larger area around the Lower James and Elizabeth River proper while SSFATE was set up in the vicinity of the engineering operation with a higher resolution, but driven by the boundary condition provided by HEM-3D.

The particle model allows the user to predict the transport and fate of classes of settling particles (e.g., sands, silts, and clays). The fate of multi-component mixtures of suspended sediments is predicted by linear superposition. The particle-based approach is extremely robust and independent of the grid system. Thus, the method is not subjected to artificial diffusion near sharp concentration gradients, and is easily interfaced with all types of sediment sources.

In addition to transport and dispersion, sediment particles also settle at some rate from the water column. Settling of mixtures of particles, some of which may be cohesive in nature, is a complicated process with the different size classes interacting (i.e., the settling of one particle type is not independent of that of the other types). In SSFATE, particle settling is handled in the following manner. At the end of each time step, the concentration of each sediment class, as well as the total concentration, is computed. Material database properties for input include specifying up to five components which are elements of the released material with a single bulk density. The settling velocity of each particle size class is computed along with a deposition probability based on shear stress. Finally, the deposition of sediment from each size class from each bottom cell during the current time step is computed, and the calculation cycle begins anew. Additional details concerning SSFATE can be found in Johnson et al. (2000). The sediment plume from the spill box discharges will also be simulated. The sediment concentration in the water column and its final deposition will be evaluated.

II-5. Modeling Impacts of Dissolved Oxygen Levels

To simulate DO accurately, the model must be capable of simulating nutrients and carbon cycles, algae dynamics, benthic fluxes of nutrients, sediment oxygen demands, and DO

dynamics. For the current project, the main concern has been how the project influences the existing DO conditions. It was known from the inception of the project that, since little nutrient or organic matter sources are expected to be added to the estuary due to the project, the main influence on DO could result from the change of dynamic conditions locally. It was important to investigate the new construction as to how it may cause changes in the flow field and result in a change of stratification or trapping of organic matters locally. Therefore, a water quality eutrophication model was used for assessing the influence of the project on DO. Our objective has been to assess the change of DO locally and as well as for the entire Lower James and Elizabeth Rivers that result from the change of geometry and dynamic conditions under different hydrological conditions and construction phases.

The VIMS HEM-3D is to be used to simulate nutrients, algae, and DO dynamics in the river. Extensive computer resources have been acquired, since the water quality model simulates 21 state variables in the water column and 23 state variables in the sediment together with the velocity field, suspended sediments, and temperature. VIMS has collected point source information in the Elizabeth River and determined the nutrient and organic material loads from point sources. We have also used the EPA Chesapeake Bay Phase V watershed model results to estimate nonpoint source nutrient loads and benthic nutrient and SOD fluxes. The water quality model has been set up using these loads for selected calibration and validation years. The model has been calibrated and validated against the Chesapeake Bay Program (CBP) monthly monitoring data for the years 1999, 2000, and 2001, which covers different hydrological conditions. We have used the calibrated model together with DEQ's monitoring data to establish current DO conditions in the estuary, which will be used as baseline DO distributions representative of different hydrological conditions. The DO baseline condition is created to identify the critical period that can trigger DO problems in the estuary and to establish a foundation for developing scenarios to assess the impact of the project on DO under different hydrological and dynamic conditions. We have focused on the calibration of the model to be capable of representing some typical DO conditions (e.g., the summer low DO condition). By comparing the change of DO due to expansion with respect to these baseline conditions, one can assess the change of DO in the estuary resulting from the project.

Scenarios have been developed to focus on the south cell and full expansion cases, with respect to the changes of bathymetry and shoreline. The model results with respect to the existing and changed conditions have been analyzed to assess the influence of the project on the local DO conditions.

CHAPTER III. METHODOLOGY

In order to provide technical support and evaluation of the environment impacts of the Engineering Construction Phase of the Craney Island Eastward Expansion, a combination of data analysis and hydrodynamic and water quality modeling was conducted. The credibility of model calculations is evaluated, to a large extent, by their agreement with observed data. For a successful hydrodynamic and water quality modeling application, it is essential to analyze the data from the monitoring programs. In this section, historical dissolved oxygen data and watershed loading characteristics are first presented using the EPA Chesapeake Bay Program database.

This information is then followed by the description of the formulation for the hydrodynamic and water quality models in HEM-3D. Specifically, the hydrodynamic numerical solution, the dissolved oxygen process, and the phytoplankton kinetics are highlighted. In order to perform the skill assessment, a global analysis technique was described.

III-1. Analysis of Historical Dissolved Oxygen Data

The dissolved oxygen (DO) concentration is the primary water quality indicator of a water body. The Virginia Institute of Marine Science (VIMS) conducted monthly slackwater surveys in all three major tributaries (James, York, and Rappahannock) of the Chesapeake Bay from 1971 to 1986. Dissolved oxygen, temperature, and salinity were the principal parameters measured in these surveys. Kuo and Neilson (1987) summarized the findings from the analyses of these data. They concluded that the DO conditions in the lower reach of the James River were much better than those in the lower York River, which, in turn, were better than those in the lower Rappahannock River. The bottom water DO in the lower James River seldom fell below 5.0 mg/l in summer months. Of a total of 39 summer surveys, the DO of less than 5.0 mg/l was observed in only 2 surveys. Kuo and Neilson (1987) attributed the better DO conditions in the lower James to the much stronger non-tidal residual circulation there, i.e., the lower James is a much stronger estuary. Based on the analyses of salinity data, USGS freshwater discharge records, and tidal information, they concluded that all three Virginia tributaries of the Bay are partially-mixed estuaries with classical two-layered estuarine circulation. They estimated that the non-tidal, residual current in the lower James averages about 16 cm/s, twice the strength of those in the York River, and more than twice that in the Rappahannock River. The lower James River is such a strong estuary that the two-layered estuarine (non-tidal residual) circulation was observed 90 % of the time.

With the support of the USEPA Chesapeake Bay Program, the Virginia Department of Environmental Quality (DEQ) has conducted water quality surveys in the Virginia major tributaries of the Chesapeake Bay since late 1980s. These surveys were conducted semi-monthly in the summer, and monthly during the remainder of the year. The DEQ survey stations in the James and the Elizabeth Rivers are shown in Figure III.1. The DO data in

the lower James and in the lower Elizabeth Rivers show the similar general characteristics to the original VIMS data. Figure III.2 presents the DO data in time series. These time series plots show a conspicuous annual cycle in DO concentrations at all stations. The DO was lowest in the summer months, and occasionally dipped below 5.0 mg/l in the bottom waters. There is no apparent long-term trend in DO concentrations at any station.

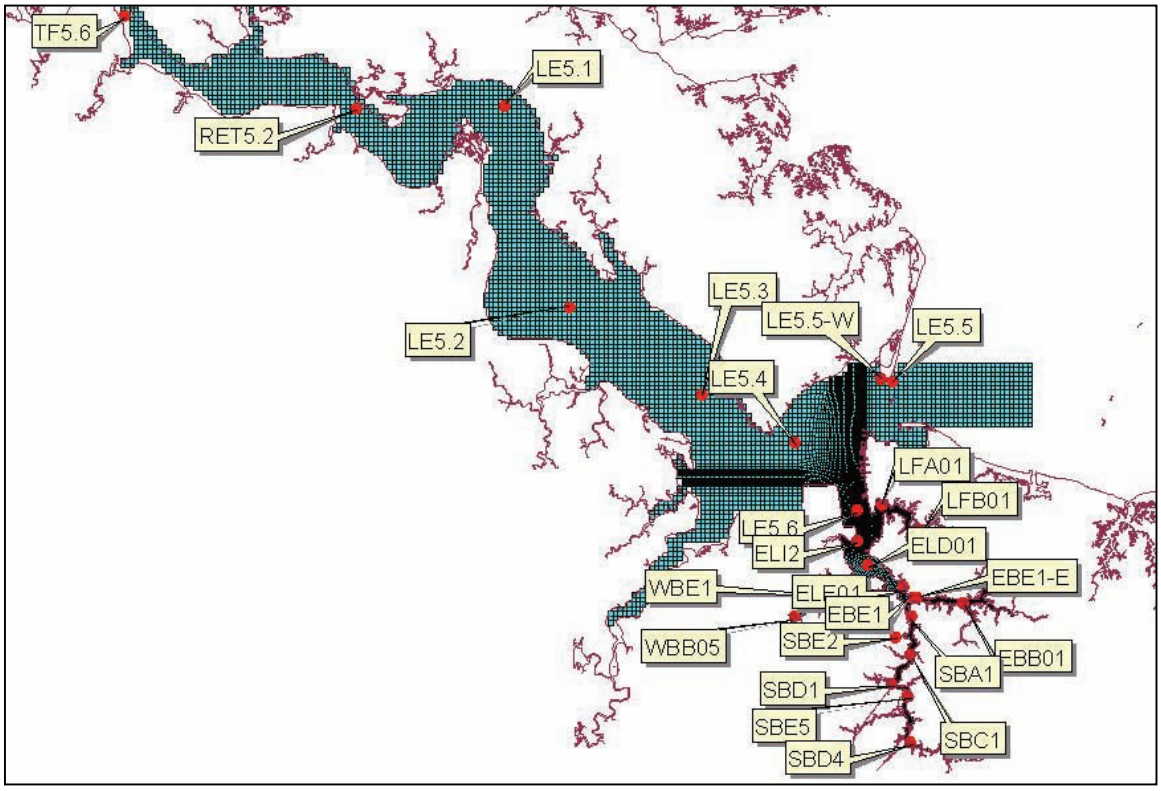

Figure III.1. The Chesapeake Bay Program monitoring stations in the James and the Elizabeth Rivers.

In order to examine the vertical variability, portions of the data at station LE5.5 (near the James River mouth), and station ELI2 (in the lower Elizabeth River) are presented with an expanded time scale in Figures III.3 and III.4, respectively. The vertically averaged DO (Figures III.3 (b) and III.4 (b)) almost repeated itself year after year. However, the difference between the surface and bottom DO (Figures III.3 (a) and III.4 (a)) varied from time to time. Figure III.4 ((a) shows that the bottom DO at station ELI2 fell significantly below 5.0 mg/l when there was a large difference between surface and bottom DO. Furthermore, there was a general tendency that, when the bottom DO dipped below the general trend, the surface DO increased, thus maintaining the same vertically averaged values from year to year. This occasional DO stratification may be attributed to the variation of the mixing process in partially-mixed estuaries. When the vertical mixing is weak, both the salinity and DO will be stratified. Figure III.5 demonstrates the close relationship between vertical differences in water density and DO computed from the

summer data at Stations LE 5.5 and ELI2, respectively. The density gradient in estuarine water is primarily controlled by salinity; salinity stratification represents density stratification, which suppresses vertical mixing and results in DO stratification. Besides the random mixing events induced by meteorological forcing, the tidal mixing varies regularly over the fortnightly spring-neap cycle. Therefore, high frequency measurements, much higher than semi-monthly, are required to monitor the occasional dips in bottom DO in the lower James and Elizabeth Rivers.

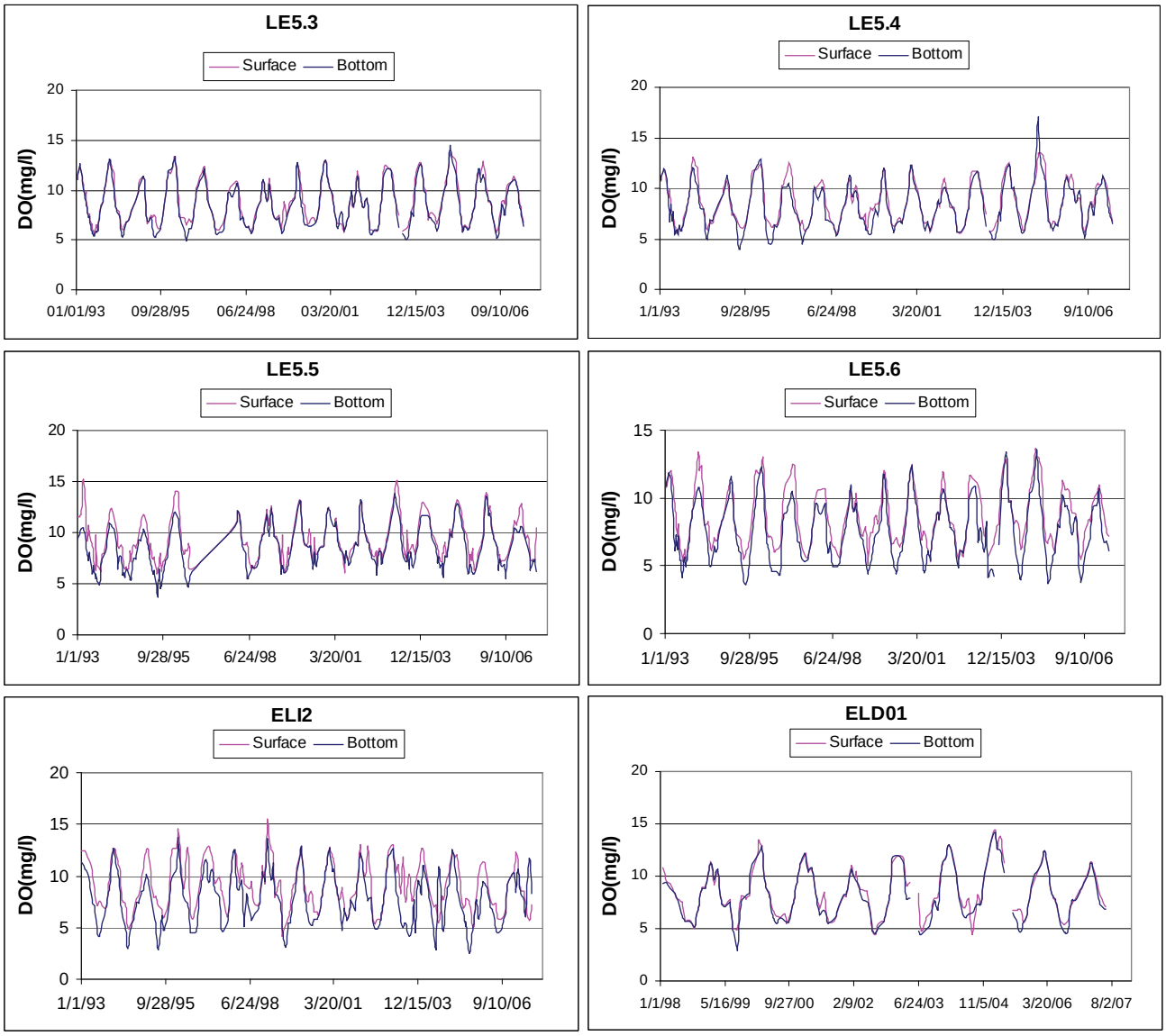

Figure III.2. The long-term DO variations in the lower James and lower Elizabeth Rivers, at stations (a) LE5.3, (b) LE5.4, (c) LE5.5. (d) LE5.6, (e) ELI2, and (f) ELD01.

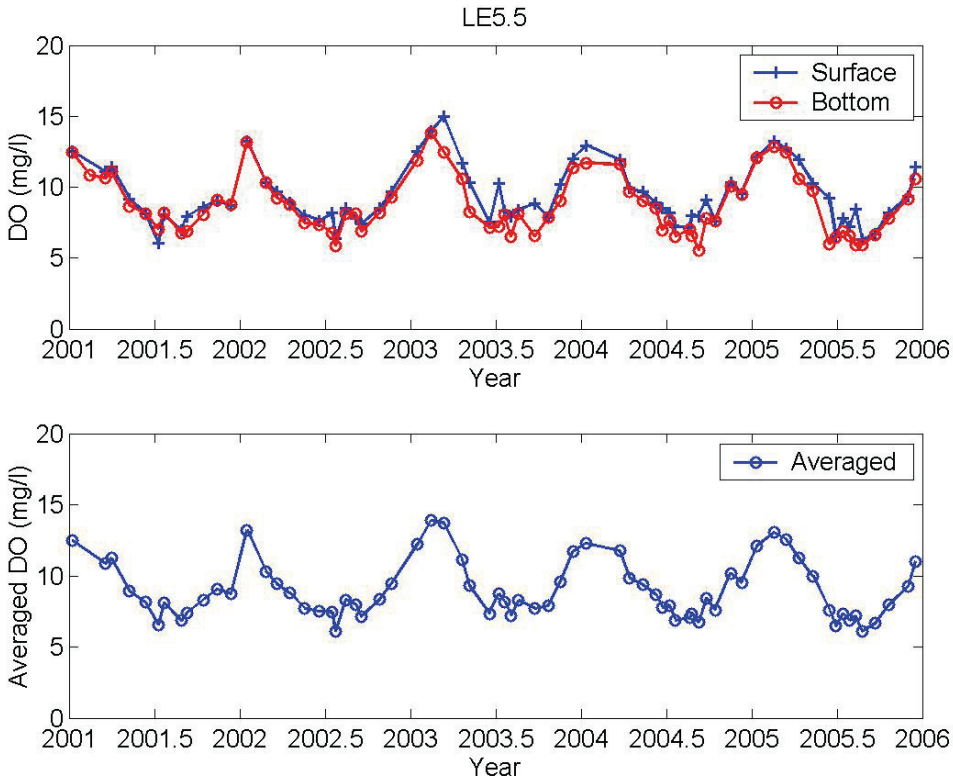

Figure III.3. The DO conditions at station LE5.5 near the James River mouth, (a) surface and bottom DO, and (b) vertically averaged DO.

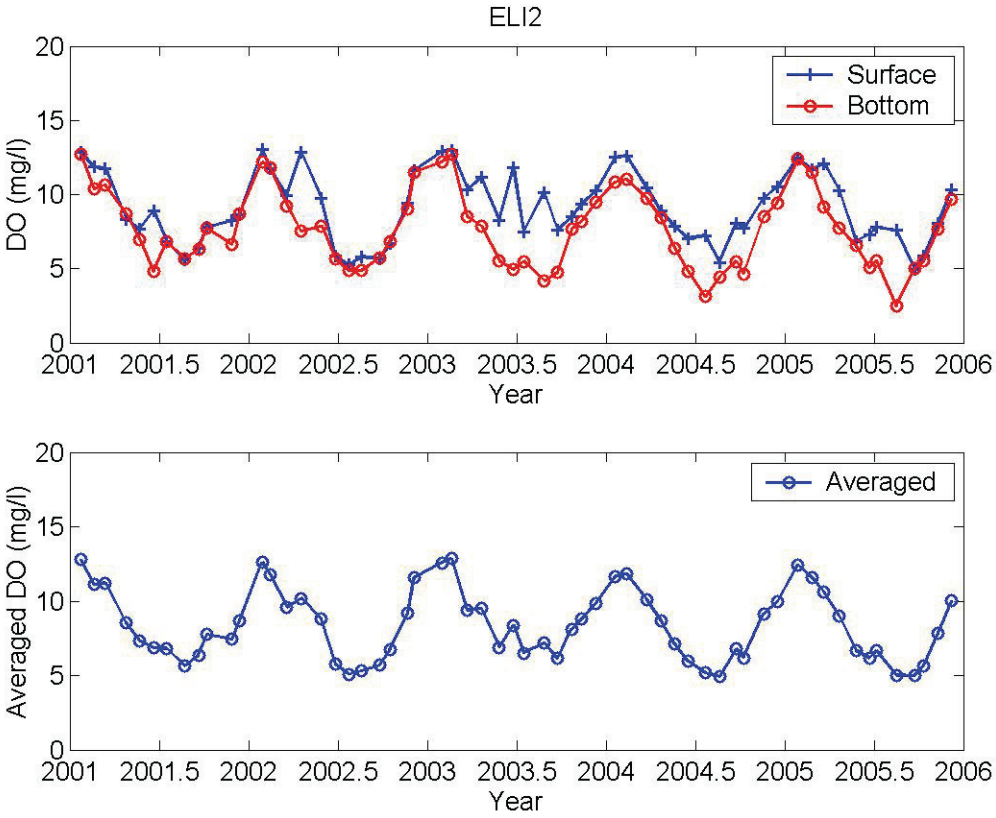

Figure III.4. The DO conditions at station ELI2 in the lower Elizabeth River, (a) surface and bottom DO, and (b) vertically averaged DO.

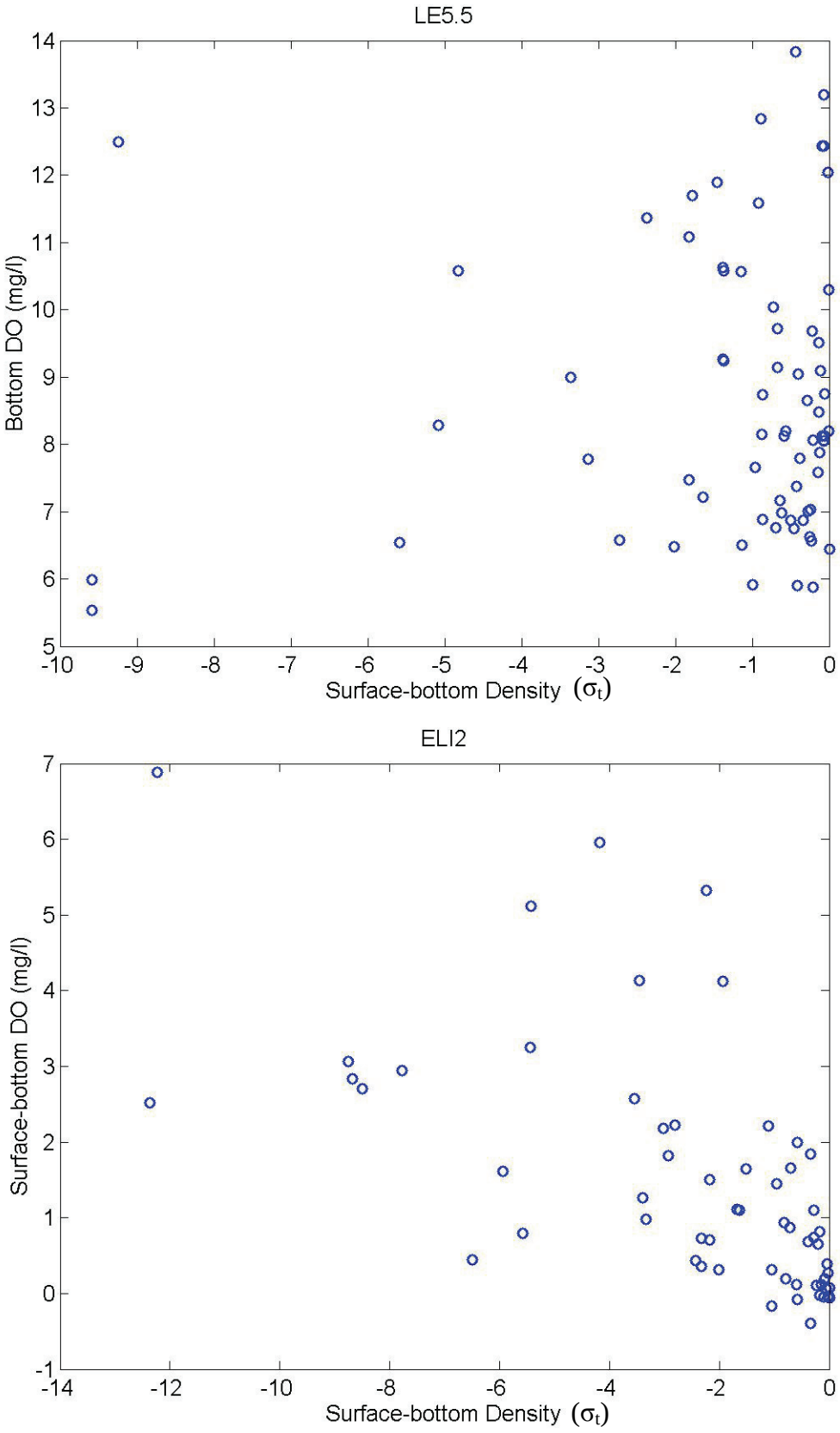

Figure III.5. Vertical difference in DO vs. difference in water density at stations (a) LE5.5 and (b) ELI2.

III-2. Characteristics of Watershed Loads

The non-point nutrient loadings from the watershed discharged to the James and Elizabeth Rivers were obtained from the Chesapeake Bay Program's Watershed Phase V Model. The Chesapeake Bay Program's Watershed Model was initiated by the US Environmental Protection Agency (EPA) for the development of the Chesapeake Bay water quality model and for the development of dissolved oxygen TMDLs of the Bay (http://www.chesapeakebay.net/model_phase5.aspx?menuitem=26169). The watershed model covers the entire Chesapeake Bay drainage basin (Figure III.6). For the Phase V version, a number of improvements were made from the previous version of the model, Phase 4.3, especially the improvement of the scale. A fine scale of watershed delineation has been implemented in the Phase V version that is consistent with the scale needed for the development of TMDLs. The improvements include: refined and updated rainfall, fertilizer, Best Management Practice (BMP), and landscape processes data. All data have been updated to 2002, allowing an 18-year simulation period from 1984 to 2002. Some areas have been updated to 2004. Refined segmentation of land segments and river reaches include the simulation of all major reservoirs in the watershed. There are approximately 20 Phase V land uses, a two-fold increase from the number of land uses in Phase 4.3. Phase V land use includes 12 different crop types, and several new BMP types are directly simulated.

The Elizabeth River watershed is an urbanized watershed. Large portions of the watershed are classified as low to high-density residential areas and commercial areas (Figure III.7). Nutrient loads discharging into the Elizabeth River are from both point and non-point sources directly from the drainage area of the Elizabeth River. Because of the connection between the Elizabeth and James Rivers, nutrients in the James River can be transported to the Elizabeth River. In order to accurately estimate the nutrient loadings, the water quality model uses watershed model simulation results together with point source data. Watershed segmentations of the James and Elizabeth River watersheds are shown in Figures III.8 and III.9, respectively.

The model used to simulate non-point sources is the Hydrological Simulation Program FORTRAN (HSPF) with substantial improvements during the period of model development. The model driven by hourly precipitation simulates the freshwater and nutrients. The sub-watersheds were used as modeling units for the simulation of flow and nutrient loads based on meteorology, land use, crop types, nutrient application, atmospheric deposition, as well as point source located in the watersheds. Model results of daily discharge including flow, total nitrogen and phosphorus, ammonium, nitrate, and phosphate can be used directly to link to the three-dimensional water quality model. In order to have a better spatial resolution of the Elizabeth River watershed, the sub-watershed of the Chesapeake Bay Program was further segmented into small sub-watersheds like tributaries and small creeks. The daily flow and nutrient loads from each sub-watershed were fed into the adjacent water quality model segments. The flow and loads for each sub-watershed were partitioned from original Phase V model results based on the ratio of sub-watershed area and land use to the Phase V model segment.

•Source of Elizabeth River watershed loading:

EPA Chesapeake Bay Program, Phase V

watershed model

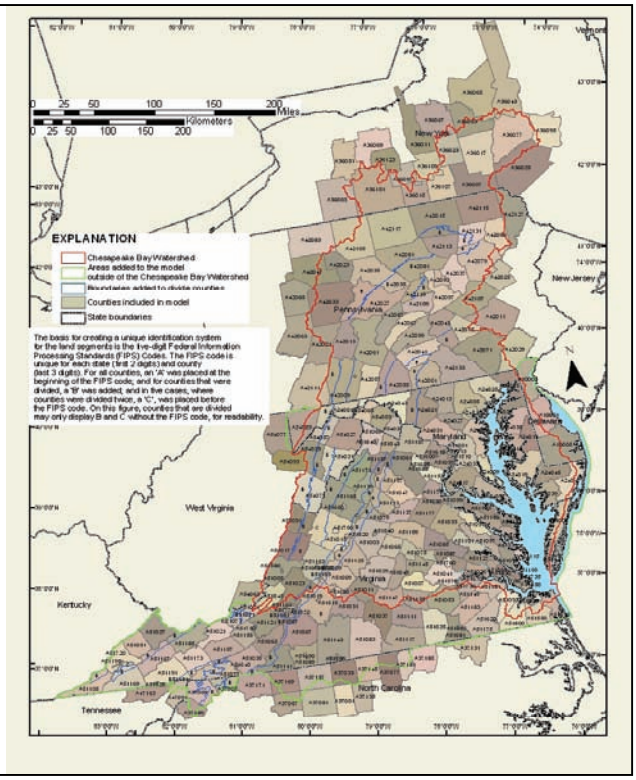

Figure III.6. Regions covered by the Chesapeake Bay Program Phase V watershed model.

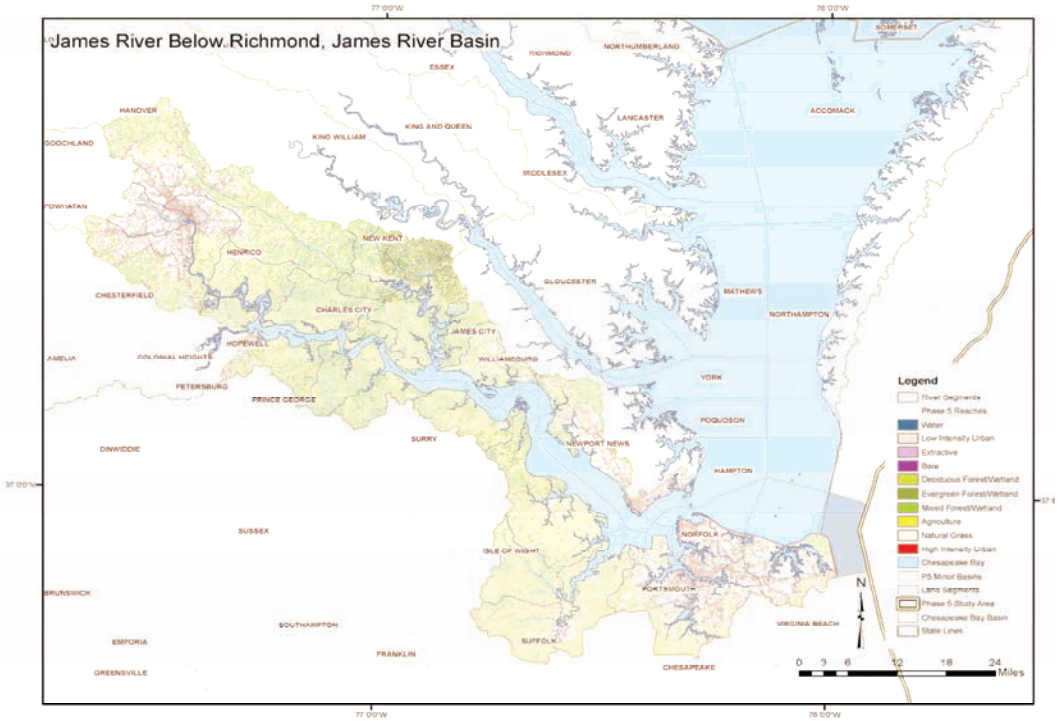

Figure III.7. James River basin land use utilized by the Chesapeake Bay Program Phase V watershed model.

The annual loading of nutrients distribution from 1985 to 2005 is shown in Figure III.10. It can be seen that TKN ranges from 1×10^7-2.1×10^7 kg per year, TP ranges from 1×10^6-4×10^6 kg per year, NH_4 ranges 2×10^6-8×10^6 kg per year, NO_3 ranges from 3×10^6-8×10^6 kg per year, and PO_4 ranges from 5×10^5-15×10^5 kg per year.

There are more than 70 permitted point sources and 306 outfalls located in areas adjacent to the Elizabeth River. Among them, approximately 90 outfalls have measured flow or nutrient data, which discharged directly into the Elizabeth River or into large creeks adjacent to the Elizabeth River. Nutrients discharged to the Elizabeth River include ammonium (NH_4), nitrate (NO3), organic nitrogen (ON), and total phosphorus (TP), and phosphate (PO_4). Figure III.11 shows the location of these point sources and Table III.1 lists selected major point source facility names and locations in the Elizabeth River.

The watershed model has included all the point sources in the watershed except those point sources discharged to the Elizabeth River. For this reason, the point source data of monthly monitoring data obtained from VADEQ were processed and included in the model. The monitoring data reported include either monthly averaged concentration or maximum concentration, or both. Because maximum concentrations are often reported by the point source facilities, the averaged maximum concentrations and mean flows from 1999 to 2004 were used for estimating mean nutrients loading. There are only 6 major point sources discharging nutrients to the Elizabeth River. The total annual loading from point sources for NH_4, NO_3, TP are approximately 4×10^5 kg, 4×10^4 kg, and 3.3×10^5 kg, respectively.

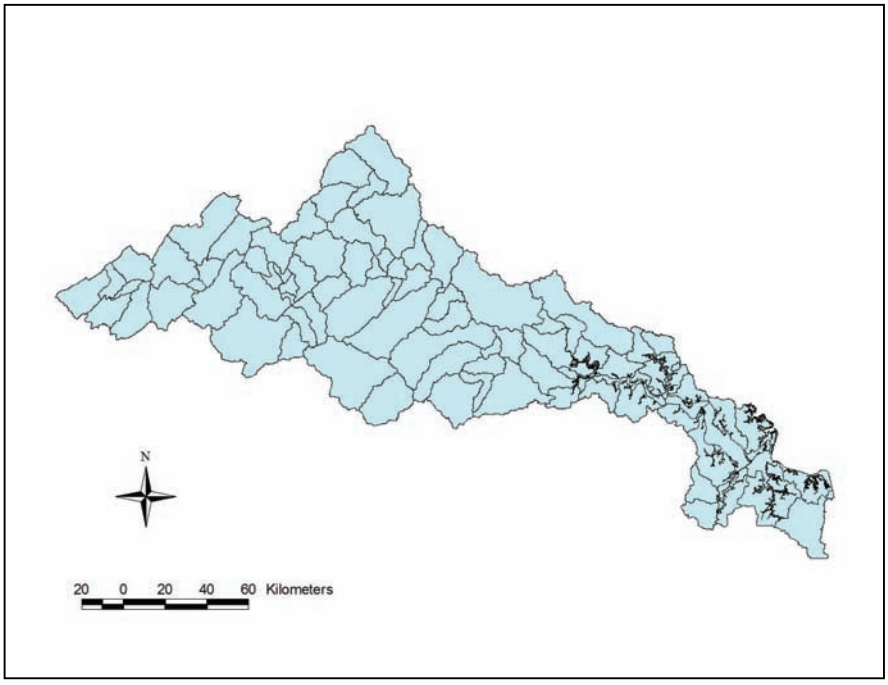

Figure III.8. Watershed segmentation of the Phase V model of the James River watershed

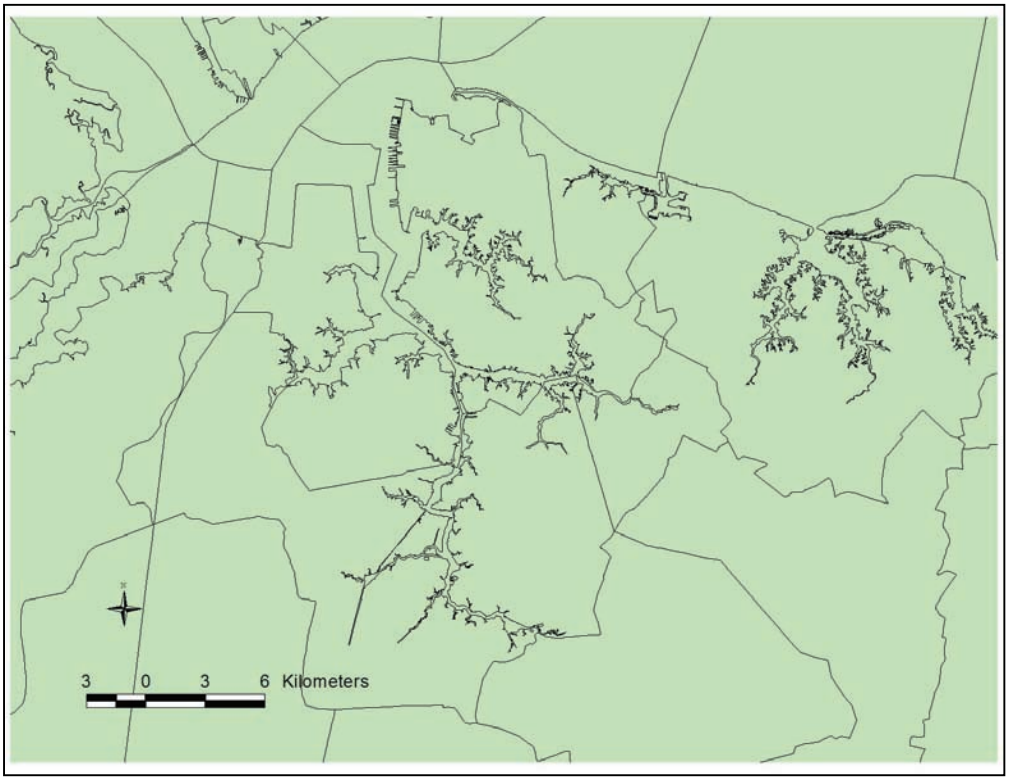

Figure III.9. Watershed segmentation of the Elizabeth River watershed

Table III.1. Selected point source facility names and locations in the Elizabeth River

Facility Name	Permit Number	Location
U. S. Navy – Norfolk Naval Shipyard	VA0005215	Southern Branch
VDOT – Downtown ER Tunnel	VA0005851	Southern Branch
Chesapeake City – Northwest River WTP	VA0088404	Upper Elizabeth R.
VDOT – I-564 Tunnel	VA0005835	Willoughby Bay
Cogentrix Virginia Leasing Corporation	VA0074781	Lake Kingman, ER
JH Miles and Company Incorporated	VA0003263	ER River Mile 6
Transmantaigne Product Services	VA0091561	Southern Branch
Kinder Morgan Southeast Terminals	VA0053911	Chesapeake
Bayshore Concrete Products Corp.	VA0064645	Southern Branch
VDOT – Hampton Roads District – Bridge Tunnel	VA0005657	Hampton Roads

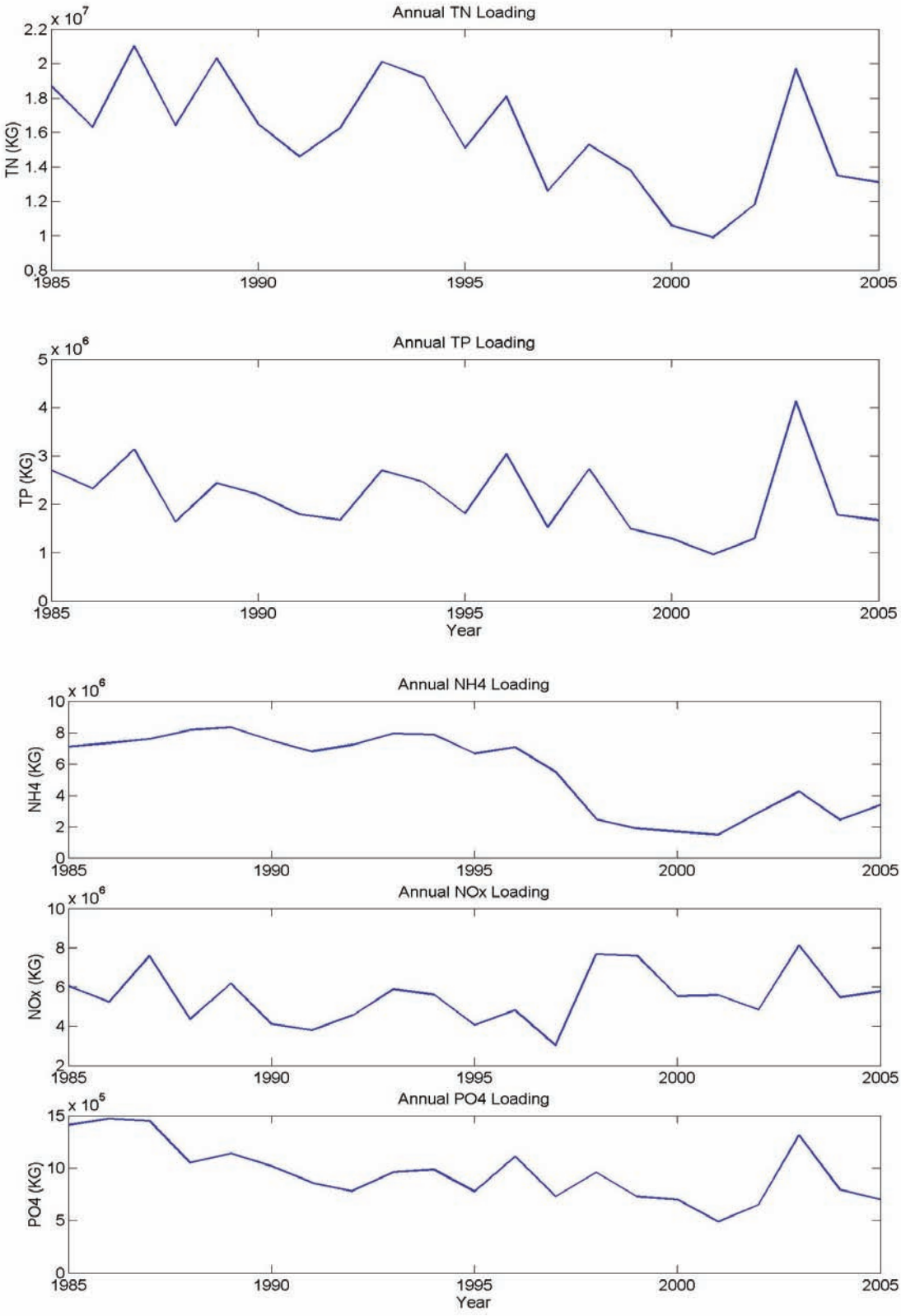

Figure III.10. Annual nutrient loadings discharged to the Elizabeth River

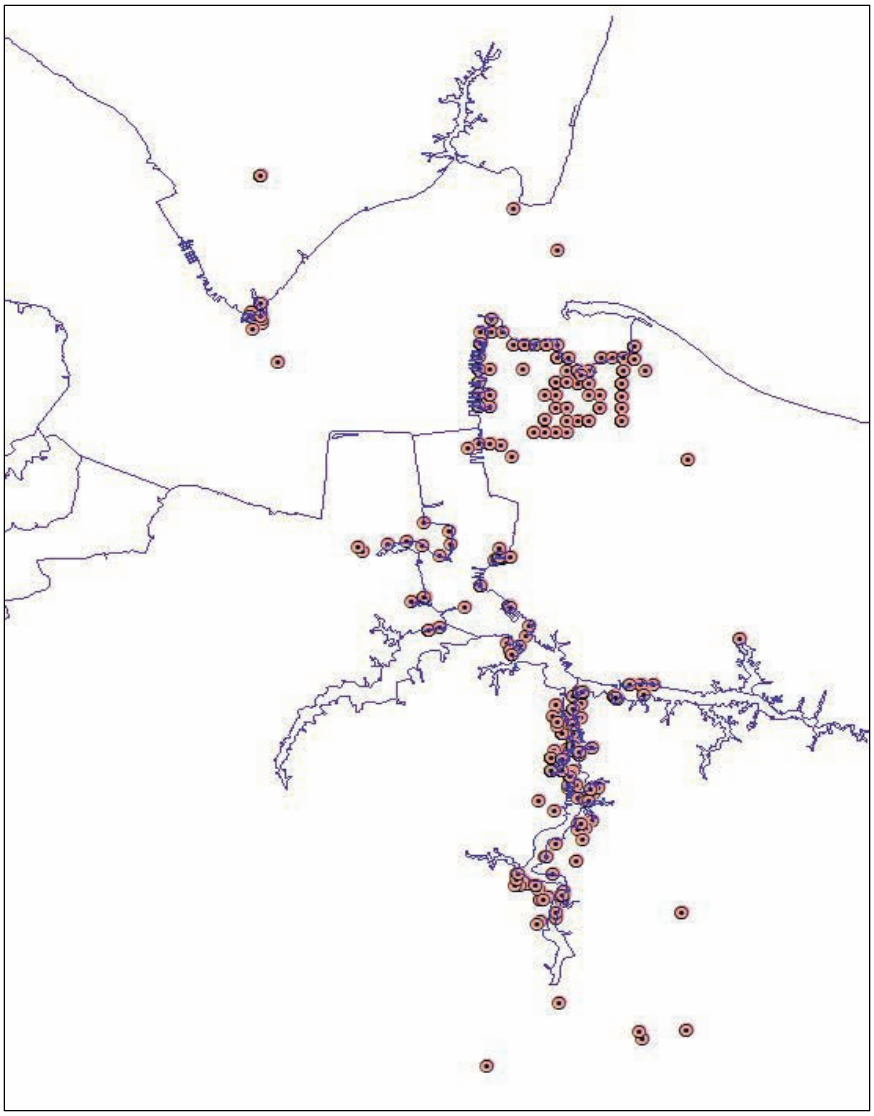

Figure III.11. Locations of major point sources in the Elizabeth River

III-3. Description of Numerical Modeling Framework

The VIMS HEM-3D involves an integrated modeling approach, as shown in Figure III.12, in which the water quality model is shown to be the central processing mechanism and interacts with:

1) the hydrodynamic model for mass and volume transport
2) the watershed model for both freshwater discharge and nutrient loadings, and
3) the sediment model for sediment flux information.

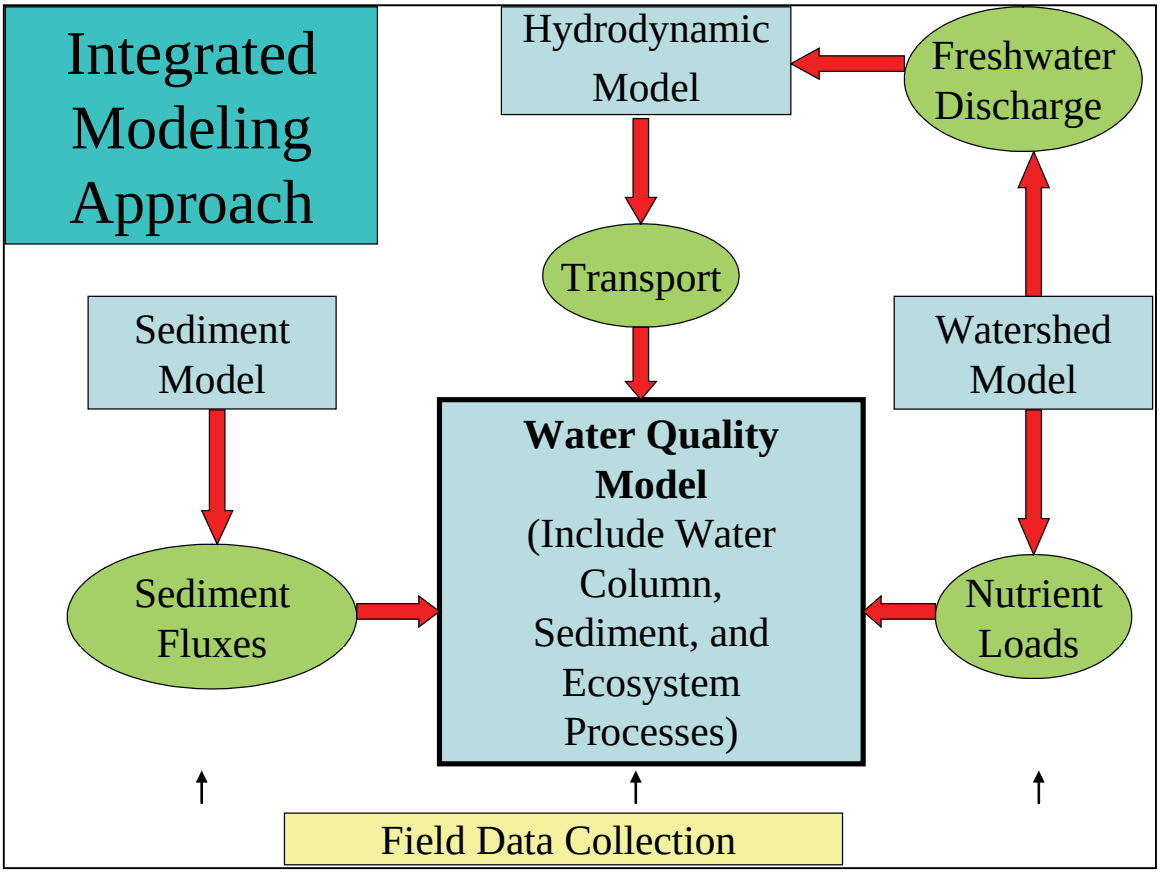

Figure III.12. The integrated modeling approach used for the VIMS HEM-3D model

III-3-1. Hydrodynamic model

The Virginia Institute of Marine Science (VIMS) has worked with the Army Corps of Engineers and the Craney Island Design Partners personnel to utilize the calibrated Hydrodynamic Eutrophication Model in 3 dimensions (HEM-3D) of the Elizabeth and James Rivers for the environmental assessment. The original HEM-3D model was developed and refined at VIMS over the period 1988-1995 (Hamrick, 1992; Park et al., 1995). It is a multi-parameter finite difference model representing estuarine flow and material transport in three dimensions. Wind stress and momentum transfer can also be represented as input at the air-water interface with salinity and freshwater discharge handled as input at the appropriate longitudinal boundary. Tidal input can be represented at the downstream open boundary by either a specific time history of water level or a simulated tide based on one or a combination of multiple tidal constituents of known amplitude and phase. The code is written in standard FORTRAN 77 and is highly portable to UNIX or DOS platforms. It is computationally efficient due to the programmer's avoidance of logical operators, and it economizes on required storage by

maintaining only active water cell variables in memory. This code was written to be highly vectorizable, anticipating upcoming developments in parallel processing. Due to a well-designed user interface, the internal source code remains the same from application to application. The HEM-3D model can be quickly converted to a 2D model either horizontally or vertically for preliminary testing. The model's most unique features include the mass conservative scheme that it uses for drying and wetting in shallow areas. It also incorporates vegetation resistance formulations (Hamrick, 1994). The most valuable feature is the model's ability to couple with both water quality and sediment transport models. The model uses a stretched (i.e., "sigma") vertical coordinate system and a curvilinear-orthogonal horizontal coordinate system to solve vertically hydrostatic, free surface, variable density, and turbulent-averaged equations of motion. This solution is coupled with a solution of the transport equations for turbulent kinetic energy, solving the equations of motion. Integration over time involves an internal-external mode splitting procedure separating "the internal shear or baroclinic mode" from the external turbulent length scale, salinity, and temperature. A staggered grid provides the framework for the spatial finite differencing (second order accurate) used by the numerical scheme to "free surface gravity wave or barotropic mode" (Hamrick, 1995).

A. Formulation of the governing equations

The formulation of the governing equations for ambient environmental flows characterized by horizontal length scales, which are orders of magnitude greater than their vertical length scales, begins with the vertically hydrostatic, boundary layer form of the turbulent equations of motion for an incompressible, variable density fluid. To accommodate realistic horizontal boundaries, it is convenient to formulate the equations such that the horizontal coordinates, x and y, are curvilinear and orthogonal. To provide uniform resolution in the vertical direction, aligned with the gravitational vector and bounded by bottom topography and a free surface permitting long wave motion, a time variable mapping or stretching transformation is desirable. The mapping or stretching is given by:

$$z = (z^* + h) / (\zeta + h) \qquad \text{(III-1)}$$

where * denotes the original physical vertical coordinates and -h and ζ are the physical vertical coordinates of the bottom topography and the free surface respectively, see Figure III.13.

Details of the transformation may be found in Vinokur (1974), Blumberg and Mellor (1987), or Hamrick (1986). Transforming the vertically hydrostatic boundary layer form of the turbulent equations of motion and utilizing the Boussinesq approximation for variable density results in the momentum and continuity equations and the transport

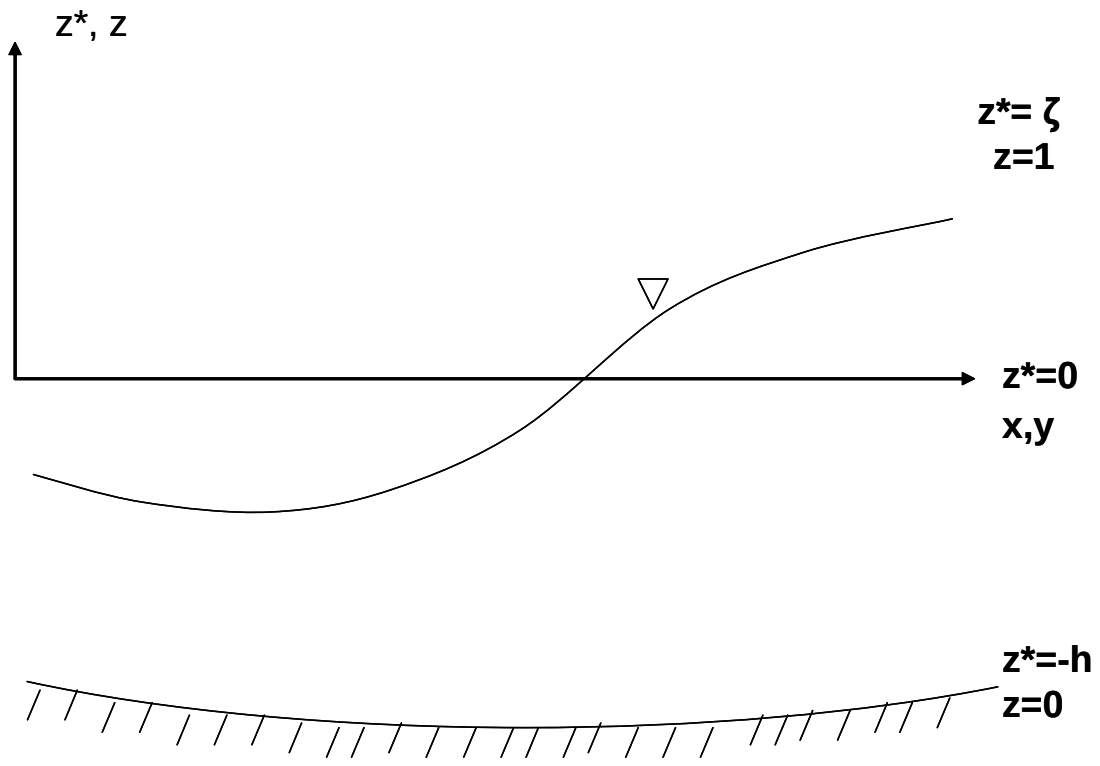

Figure III.13. The stretched vertical coordinate system

equations for salinity and temperature to take on the following form:

$$\partial_t(mHu) + \partial_x(m_y Huu) + \partial_y(m_x Hvu) + \partial_z(mwu) - (mf + v\partial_x m_y - u\partial_y m_x)Hv$$
$$= -m_y H\partial_x(g\zeta + p) - m_y(\partial_x h - z\partial_x H)\partial_z p + \partial_z(mH^{-1}A_v\partial_z u) + Q_u \qquad \text{(III-2)}$$

$$\partial_t(mHv) + \partial_x(m_y Huv) + \partial_y(m_x Hvv) + \partial_z(mwv) + (mf + v\partial_x m_y - u\partial_y m_x)Hu$$
$$= -m_x H\partial_y(g\zeta + p) - m_x(\partial_y h - z\partial_y H)\partial_z p + \partial_z(mH^{-1}A_v\partial_z v) + Q_v \qquad \text{(III-3)}$$

$$\partial_z p = -gH(\rho - \rho_o)\rho_o^{-1} = -gHb \qquad \text{(III-4)}$$

$$\partial_t(m\zeta) + \partial_x(m_y Hu) + \partial_y(m_x Hv) + \partial_z(mw) = 0 \qquad \text{(III-5)}$$

$$\partial_t(m\zeta) + \partial_x(m_y H\int_0^1 u dz) + \partial_y(m_x H\int_0^1 v dz) = 0 \qquad \text{(III-6)}$$

$$\rho = \rho(p, S, T) \tag{III-7}$$

$$\partial_t(mHS) + \partial_x(m_y HuS) + \partial_y(m_x HvS) + \partial_z(mwS) = \partial_z(mH^{-1}A_b\partial_z S) + Q_S \tag{III-8}$$

$$\partial_t(mHT) + \partial_x(m_y HuT) + \partial_y(m_x HvT) + \partial_z(mwT) = \partial_z(mH^{-1}A_b\partial_z T) + Q_T \,. \tag{III-9}$$

In these equations, u and v are the horizontal velocity components in the curvilinear, orthogonal coordinates x and y; m_x and m_y are the square roots of the diagonal components of the metric tensor; $m = m_x m_y$ is the Jacobian or square root of the metric tensor determinant. The vertical velocity, with physical units, in the stretched, dimensionless vertical coordinate z is w, and is related to the physical vertical velocity w* by:

$$w = w^* - z(\partial_t\zeta + um_x^{-1}\partial_x\zeta + vm_y^{-1}\partial_y\zeta) + (1-z)(um_x^{-1}\partial_x h + vm_y^{-1}\partial_y h) \,. \tag{III-10}$$

The total depth, $H = h + \zeta$, is the sum of the depth below and the free surface displacement relative to the undisturbed physical vertical coordinate origin, $z^* = 0$. The pressure p is the physical pressure in excess of the reference density hydrostatic pressure, $\rho_o gH(1 - z)$, divided by the reference density, ρ_o. In the momentum equations (III-2,III-3) f is the Coriolis parameter, A_v is the vertical turbulent or eddy viscosity, and Q_u and Q_v are momentum source-sink terms that will be later modeled as subgrid scale horizontal diffusion. The density, ρ, is in general a function of temperature, T, and salinity or water vapor, S, in hydrospheric and atmospheric flows respectively and can be a weak function of pressure, consistent with the incompressible continuity equation under the anelastic approximation (Mellor, 1991; Clark and Hall, 1991). The buoyancy, b, is defined in equation (III-4) as the normalized deviation of density from the reference value. The continuity equation (III-5) has been integrated with respect to z over the interval (0,1) to produce the depth integrated continuity equation (III-6) using the vertical boundary conditions, w = 0, at z = (0,1), which follows from the kinematic conditions and equation (III-10). In the transport equations for salinity and temperature (III-8, III-9) the source and sink terms, Q_S and Q_T include subgrid scale horizontal diffusion and thermal sources and sinks, while A_b is the vertical turbulent diffusivity. It is noted that constraining the free surface displacement to be time independent and spatially constant yields the equivalent of the rigid lid ocean circulation equations employed by Smetner (1974) and equations similar to the terrain following equations used by Clark (1977) to model mesoscale atmospheric flow.

The system of eight equations (III-2 to III-9) provides a closed system for the variables u, v, w, p, ζ, ρ, S, and T, provided that the vertical turbulent viscosity and diffusivity and the source and sink terms are specified. To provide the vertical turbulent viscosity and diffusivity, the second moment turbulence closure model developed by Mellor and Yamada (1982) and modified by Galperin *et al.* (1988) was used. The model relates the

vertical turbulent viscosity and diffusivity to the turbulent intensity, qq, a turbulent length scale, l, and a Richardson number R_q by:

$$A_v = \phi_v q l = 0.4(1+36R_q)^{-1}(1+6R_q)^{-1}(1+8R_q)ql \tag{III-11}$$

$$A_b = \phi_b q l = 0.5(1+36R_q)^{-1} ql \tag{III-12}$$

$$R_q = \frac{gH\partial_z b}{q^2}\frac{l^2}{H^2}. \tag{III-13}$$

where the so-called stability functions ϕ_v and ϕ_b account for reduced and enhanced vertical mixing or transport in stable and unstable vertically density-stratified environments, respectively. The turbulence intensity and the turbulence length scale are determined by a pair of transport equations:

$$\partial_t(mHq^2) + \partial_x(m_y Huq^2) + \partial_y(m_x Hvq^2) + \partial_z(mwq^2) = \partial_z(mH^{-1}A_q\partial_z q^2) + Q_q$$
$$+2mH^{-1}A_v\left((\partial_z u)^2 + (\partial_z v)^2\right) + 2mgA_b\partial_z b - 2mH(B_1 l)^{-1}q^3 \tag{III-14}$$

$$\partial_t(mHq^2 l) + \partial_x(m_y Huq^2 l) + \partial_y(m_x Hvq^2 l) + \partial_z(mwq^2 l) = \partial_z(mH^{-1}A_q\partial_z q^2 l) + Q_l$$
$$+mH^{-1}E_1 l A_v\left((\partial_z u)^2 + (\partial_z v)^2\right) + mgE_1E_3 l A_b\partial_z b - mHB_1^{-1}q^3\left(1 + E_2(\kappa L)^{-2}l^2\right) \tag{III-15}$$

$$L^{-1} = H^{-1}\left(z^{-1} + (1-z)^{-1}\right), \tag{III-16}$$

where B_1, E_1, E_2, and E_3 are empirical constants and Q_q and Q_l are additional source-sink term such as subgrid scale horizontal diffusion. The vertical diffusivity, A_q, is in general taken equal to the vertical turbulent viscosity, A_v.

B. Numerical solution techniques for the equations of motion

The equations of motion (III-2 to III-6) are solved in a region subdivided into six faced cells. The projection of the vertical cell boundaries to a horizontal plane forms a curvilinear, orthogonal grid in the orthogonal coordinate system (x,y). In a vertical (x,z) or (y,z) plane, the cells bounded by the same constant z surfaces will be referred to as cell layers or layers. The equations will be solved using a combination of finite volume and finite difference techniques, with the variable locations shown in Figure III.14.

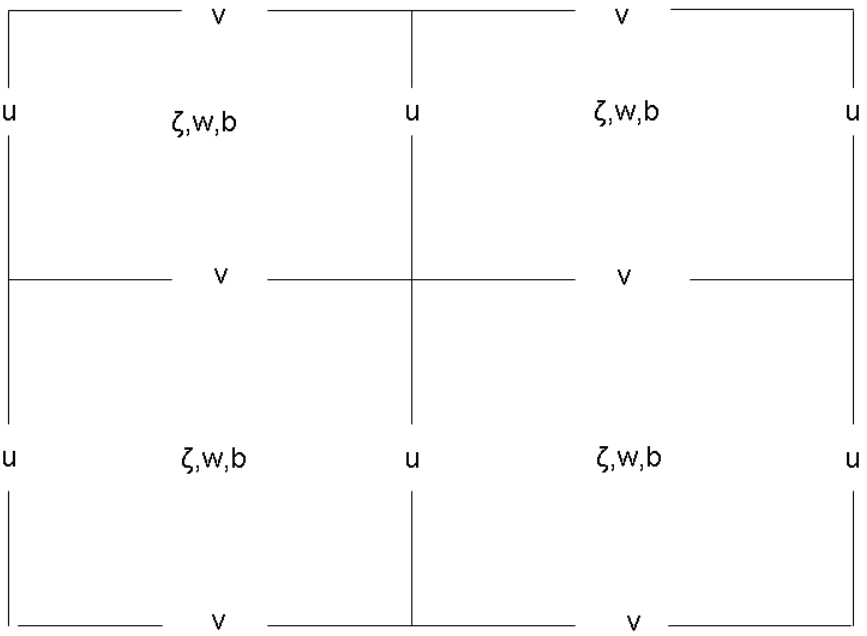

Figure III.14. Free surface displacement centered horizontal grid.

The staggered grid location of variables is often referred to as the C grid (Arakawa and Lamb, 1977) or the MAC grid (Peyret and Taylor, 1983). To proceed, it is convenient to modify equations (III-2, III-3) by eliminating the vertical pressure gradients using equation (III-4). After some manipulation, the horizontal momentum equations become:

$$\begin{aligned}
&\partial_t(mHu) + \partial_x(m_y Huu) + \partial_y(m_x Hvu) + \partial_z(mwu) - (mf + v\partial_x m_y - u\partial_y m_x)Hv \\
&= -m_y H\partial_x p - m_y Hg\partial_x\zeta + m_y Hgb\partial_x h - m_y Hgbz\partial_x H + \partial_z(mH^{-1}A_v\partial_z u) + Q_u \qquad \text{(III-17)} \\
&\partial_t(mHv) + \partial_x(m_y Huv) + \partial_y(m_x Hvv) + \partial_z(mwv) + (mf + v\partial_x m_y - u\partial_y m_x)Hu \\
&= -m_x H\partial_y p - m_x Hg\partial_y\zeta + m_x Hgb\partial_y h - m_x Hgbz\partial_y H + \partial_z(mH^{-1}A_v\partial_z v) + Q_v \qquad \text{(III-18)}
\end{aligned}$$

The vertical discretization of Equations (III-17, III-18) is considered first. The equations are integrated with respect to z over a cell layer assuming that variables defined vertically at the cell or layer centers are constant and that variables defined vertically at the cell layer interfaces or boundaries vary linearly over the cell, to give:

$$\partial_t(mH\Delta_k u_k) + \partial_x(m_y H\Delta_k u_k u_k) + \partial_y(m_x H\Delta_k v_k u_k) + (mwu)_k - (mwu)_{k-1}$$
$$-(mf + v_k\partial_x m_y - u_k\partial_y m_x)\Delta_k H v_k = -0.5m_y H\Delta_k\partial_x(p_k + p_{k-1}) - m_y H\Delta_k g\partial_x\zeta$$
$$+m_y H\Delta_k gb_k\partial_x h - 0.5m_y H\Delta_k gb_k(z_k + z_{k-1})\partial_x H + m(\tau_{xz})_k - m(\tau_{xz})_{k-1} + (\Delta Q_u)_k \qquad \text{(III-19)}$$

$$\partial_t(mH\Delta_k v_k)_k + \partial_x(m_y H\Delta_k u_k v_k) + \partial_y(m_x H\Delta_k v_k v_k) + (mwv)_k - (mwv)_{k-1}$$
$$+(mf + v_k\partial_x m_y - u_k\partial_y m_x)\Delta_k H u_k = -0.5m_x H\Delta_k\partial_y(p_k + p_{k-1}) - m_x H\Delta_k g\partial_y\zeta$$
$$+m_x H\Delta_k gb_k\partial_y h - 0.5m_x H\Delta_k gb_k(z_k + z_{k-1})\partial_y H + m(\tau_{yz})_k - m(\tau_{yz})_{k-1} + (\Delta Q_v)_k \qquad \text{(III-20)}$$

where Δ_k is the vertical cell or layer thickness and the turbulent shear stresses at the cell layer interfaces are defined by:

$$(\tau_{xz})_k = 2H^{-1}(A_v)_k(\Delta_{k+1} + \Delta_k)^{-1}(u_{k+1} - u_k) \qquad \text{(III-21)}$$
$$(\tau_{yz})_k = 2H^{-1}(A_v)_k(\Delta_{k+1} + \Delta_k)^{-1}(v_{k+1} - v_k). \qquad \text{(III-22)}$$

If there are K cells in the z direction, the hydrostatic equation can be integrated from a cell layer interface to the surface to give:

$$p_k = gH\left(\sum_{j=k}^{K}\Delta_j b_j - \Delta_k b_k\right) + p_s, \qquad \text{(III-23)}$$

where p_s is the physical pressure at the free surface or under the rigid lid divided by the reference density. The continuity equation (III-5) is also integrated with respect to z over a cell or layer to give:

$$\partial_t(m\Delta_k\zeta) + \partial_x(m_y H\Delta_k u_k) + \partial_y(m_x H\Delta_k v_k) + m(w_k - w_{k-1}) = 0 \qquad \text{(III-24)}$$

The numerical solution of the vertically discrete momentum equations (III-19, III-20) now proceeds by splitting the external depth integrated mode associated with external long surface gravity waves from the internal mode associated with vertical current structure.

The external mode equations are obtained by summing equations (III-19, III-20) over K cells or layers in the vertical utilizing equation (III-23), and are given by:

$$\partial_t(mH\bar{u}) + \sum_{k=1}^{K}\left(\partial_x(m_y H\Delta_k u_k u_k) + \partial_y(m_x H\Delta_k v_k u_k) - H(mf + v_k\partial_x m_y - u_k\partial_y m_x)\Delta_k v_k\right)$$
$$= -m_y Hg\partial_x\zeta - m_y H\partial_x p_s + m_y Hg\bar{b}\partial_x h - m_y Hg\left(\sum_{k=1}^{K}(\Delta_k\beta_k + 0.5\Delta_k(z_k + z_{k-1})b_k)\right)\partial_x H$$
$$-0.5m_y H^2\partial_x\left(\sum_{k=1}^{K}\Delta_k\beta_k\right) + m(\tau_{xz})_K - m(\tau_{xz})_0 + \bar{Q}_u$$

(III-25)

$$\partial_t(mH\bar{v}) + \sum_{k=1}^{K}\left(\partial_x(m_y H\Delta_k u_k v_k) + \partial_y(m_x H\Delta_k v_k v_k) + H(mf + v_k\partial_x m_y - u_k\partial_y m_x)\Delta_k u_k\right)$$
$$= -m_x Hg\partial_y\zeta - m_x H\partial_y p_s + m_x Hg\bar{b}\partial_y h - m_x Hg\left(\sum_{k=1}^{K}(\Delta_k\beta_k + 0.5\Delta_k(z_k + z_{k-1})b_k)\right)\partial_y H$$
$$-0.5m_x H^2\partial_y\left(\sum_{k=1}^{K}\Delta_k\beta_k\right) + m(\tau_{yz})_K - m(\tau_{yz})_0 + \bar{Q}_v$$

(III-26)

$$\partial_t(m\zeta) + \partial_x(m_y H\bar{u}) + \partial_y(m_x H\bar{v}) = 0$$

(III-27)

$$\beta_k = \sum_{j=k}^{K}\Delta_j b_j - 0.5\Delta_k b_k$$

(III-28)

where the over bar indicates an average over the depth. The depth integrated continuity equation (III-27) follows from equation (III-6) and provides the continuity constraint for the external mode. Consistent with the form of equation (III-27), the external mode variables will be chosen to be the free surface displacement, ζ, and the volumetric transports $m_y Hu$ and $m_x Hv$.

A number of formulations are possible for the internal mode equations. Equations (III-19, III-20) have K degrees of freedom for each of the horizontal velocity components. However, the summation of these equations over K cells or layers in the vertical to form the external mode equations (III-25, III-26) effectively removes a degree of freedom since the constraints:

$$\sum_{k=1}^{K}\Delta_k u_k = \bar{u}$$

(III-29)

$$\sum_{k=1}^{K}\Delta_k v_k = \bar{v}$$

(III-30)

must be satisfied. One approach to the internal mode is to solve equations (III-19, III-20) using the free surface slopes, or the surface pressure gradients in the rigid lid case, from the external solution and distribute the error such that equations (III-29, III-30) are satisfied. A second approach is to form equations for the deviations of the velocity components from their vertical means by subtracting the external equations (III-25, III-26) from the layer integrated equations (III-19, III-20). However, it will still be necessary to satisfy the constraints (III-29, III-30). The approach used herein is to reduce the systems of K layer averaged equations (III-19, III-20) to systems of K-1 equations and use equations (III-29, III-30) to provide the Kth equation consistent with the actual degrees of freedom.

The internal mode equations are formed by dividing equations (III-19, III-20) by the cell layer thickness, Δ_k, subtracting the equations for cell layer k from the equations for cell layer k+1, and then dividing the results by the average thickness of the two cell layers to give:

$$
\begin{aligned}
&\partial_t\left(mH\Delta^{-1}_{k+1,k}(u_{k+1}-u_k)\right)+\partial_x\left(m_yH\Delta^{-1}_{k+1,k}(u_{k+1}u_{k+1}-u_ku_k)\right)+\partial_y\left(m_xH\Delta^{-1}_{k+1,k}(v_{k+1}u_{k+1}-v_ku_k)\right)\\
&+m\Delta^{-1}_{k+1,k}\left(\Delta^{-1}_{k+1}((wu)_{k+1}-(wu)_k)-\Delta^{-1}_k((wu)_k-(wu)_{k-1})\right)\\
&-\Delta^{-1}_{k+1,k}\left((mf+v_{k+1}\partial_x m_y-u_{k+1}\partial_y m_x)Hv_{k+1}-(mf+v_k\partial_x m_y-u_k\partial_y m_x)Hv_k\right)\\
&=m_yH\Delta^{-1}_{k+1,k}g(b_{k+1}-b_k)(\partial_x h-z_k\partial_x H)-0.5m_yH^2\Delta^{-1}_{k+1,k}g(\Delta_{k+1}\partial_x b_{k+1}+\Delta_k\partial_x b_k)\\
&+m\Delta^{-1}_{k+1,k}\left(\Delta^{-1}_{k+1}((\tau_{xz})_{k+1}-(\tau_{xz})_k)-\Delta^{-1}_k((\tau_{xz})_k-(\tau_{xz})_{k-1})\right)+\Delta^{-1}_{k+1,k}((Q_u)_{k+1}-(Q_u)_k)
\end{aligned}
\qquad \text{(III-31)}
$$

$$
\begin{aligned}
&\partial_t\left(mH\Delta^{-1}_{k+1,k}(v_{k+1}-v_k)\right)+\partial_x\left(m_yH\Delta^{-1}_{k+1,k}(u_{k+1}v_{k+1}-u_kv_k)\right)+\partial_y\left(m_xH\Delta^{-1}_{k+1,k}(v_{k+1}v_{k+1}-v_kv_k)\right)\\
&+m\Delta^{-1}_{k+1,k}\left(\Delta^{-1}_{k+1}((wv)_{k+1}-(wv)_k)-\Delta^{-1}_k((wv)_k-(wv)_{k-1})\right)\\
&+\Delta^{-1}_{k+1,k}\left((mf+v_{k+1}\partial_x m_y-u_{k+1}\partial_y m_x)Hu_{k+1}-(mf+v_k\partial_x m_y-u_k\partial_y m_x)Hu_k\right)\\
&=m_xH\Delta^{-1}_{k+1,k}g(b_{k+1}-b_k)(\partial_y h-z_k\partial_y H)-0.5m_xH^2\Delta^{-1}_{k+1,k}g(\Delta_{k+1}\partial_y b_{k+1}+\Delta_k\partial_y b_k)\\
&+m\Delta^{-1}_{k+1,k}\left(\Delta^{-1}_{k+1}((\tau_{yz})_{k+1}-(\tau_{yz})_k)-\Delta^{-1}_k((\tau_{yz})_k-(\tau_{yz})_{k-1})\right)+\Delta^{-1}_{k+1,k}((Q_v)_{k+1}-(Q_v)_k)
\end{aligned}
\qquad \text{(III-32)}
$$

$$
\Delta_{k+1,k}=0.5(\Delta_{k+1}+\Delta_k)\ . \qquad \text{(III-33)}
$$

Inspection of equations (III-31, III-32) reveals that they could have also been obtained by differentiating the horizontal momentum equations (III-17, III-18) with respect to z and introducing a finite difference discretion in z. Using equations (III-21, III-22) to relate the shear stresses to the velocity differences across the interior interfaces suggest that equations (III-31, III-32) be interpreted as a system of K-1 equations for either the K-1 interfacial velocity differences or the K-1 interior interfacial shear stresses.

The solution of the vertical velocity, w, employs the continuity equations. Dividing equation (III-24) by Δ_k, and subtracting equation (III-27) gives:

$$w_k = w_{k-1} - m^{-1}\Delta_k\left(\partial_x\left(m_y H(u_k - \bar{u})\right) + \partial_y\left(m_x H(v_k - \bar{v})\right)\right). \qquad \text{(III-34)}$$

Since $w_o = 0$, the solution proceeds from the first cell layer to the surface. Provided the constraints (III-29, III-30) are satisfied, the surface velocity at k = K will be zero and satisfy the boundary condition.

C. Numerical solution techniques for the transport equations

In this section, solution techniques for the transport equations for salinity, temperature, turbulence intensity and turbulence length scale are presented. Stability and accuracy aspects of the advection schemes common to the transport equations and the external and internal horizontal momentum equations are also discussed. The salinity transport equation (III-8) is used as a generic example and the location of variables is shown in Figure III.15.

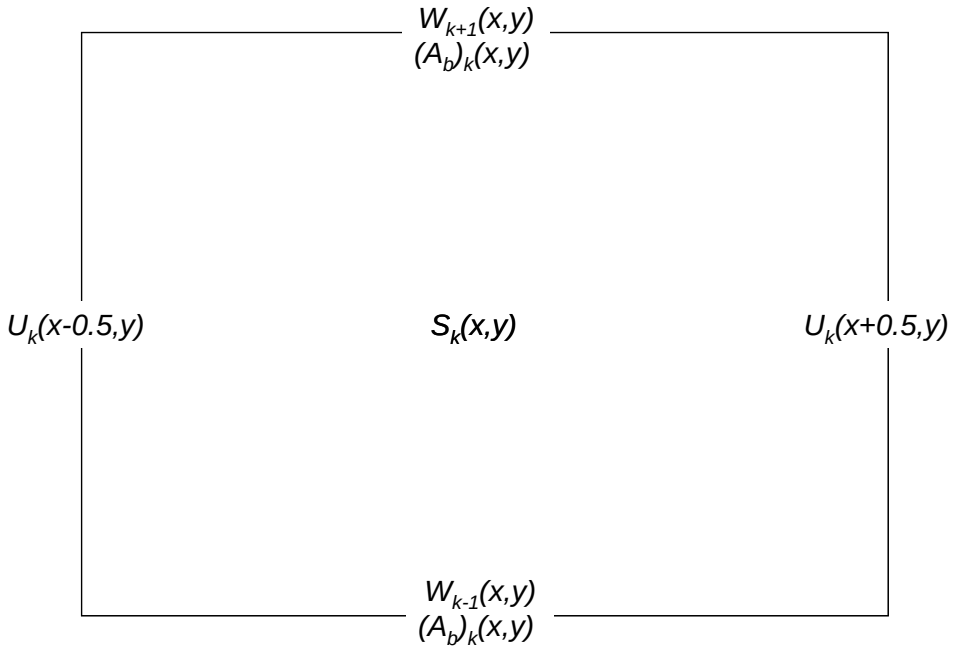

Figure III.15. S-centered grid in the vertical (x,z) plane.

The salinity transport equation (III-8) is integrated over a cell layer to give:

$$\partial_t(mHS_k) + \partial_x(U_k S_k) + \partial_y(V_k S_k) + \Delta_k^{-1}((WS)_k + (WS)_{k-1})$$
$$-\Delta_k^{-1} m((H^{-1}A_b\partial_z S)_k - (H^{-1}A_b\partial_z S)_{k-1}) - (Q_S)_k = 0 \qquad \text{(III-35)}$$

The source, sink, advection, and vertical diffusion portions of equation (112) are treated in separate fractional steps. The three time level fractional step sequence is given by:

$$S_k^* = S_k^{n-1} + 2\theta(mH^{n-1})^{-1}(Q_S)_k^{n-1} \qquad \text{(III-36)}$$

$$(mH)^{n+1} S_k^{**} = (mH)^{n-1} S_k^* - 2\theta\left(\delta_x^\zeta(U_k S_k) + \delta_y^\zeta(V_k S_k) + \Delta_k^{-1}((WS)_k - (WS)_{k-1})\right) \qquad \text{(III-37)}$$

$$(HS_k)^{n+1} - 2\theta\left(\left(\frac{(H^{-1}A_b)_k^n (S_{k+1} - S_k)^{n+1}}{\Delta_k \Delta_{k+1,k}}\right) - \left(\frac{(H^{-1}A_b)_{k-1}^n (S_k - S_{k-1})^{n+1}}{\Delta_k \Delta_{k,k-1}}\right)\right) = H^{n+1} S_k^{**} \qquad \text{(III-38)}$$

The source, sink step, equation (III-36), is explicit and involves no changes in cell volumes. When the source, sink term represents horizontal turbulent diffusion, it is evaluated at time level n-1, for stability (Fletcher, 1988). The advection step, equation (III-37), is explicit and involves changes in cell volumes. The vertical diffusion step, equation (III-38), which involves no changes in cell volumes, is fully implicit and unconditionally stable (Fletcher, 1988).

Rearranging equation (III-38), the vertical diffusion step, gives:

$$-\frac{2\theta}{\Delta_k \Delta_{k,k-1}}\left(\frac{A_b}{H}\right)_{k-1}^n S_{k-1}^{n+1} + \left(\frac{2\theta}{\Delta_k \Delta_{k,k-1}}\left(\frac{A_b}{H}\right)_{k-1}^n + H^{n+1} + \frac{2\theta}{\Delta_k \Delta_{k+1,k}}\left(\frac{A_b}{H}\right)_k^n\right) S_k^{n+1}$$
$$-\frac{2\theta}{\Delta_k \Delta_{k+1,k}}\left(\frac{A_b}{H}\right)_k^n S_{k+1}^{n+1} = H^{n+1} S_k^{**} \qquad \text{(III-39)}$$

For salinity, temperature, and suspended sediment concentration, the generic variable S is defined vertically at cell layer centers, and the diffusivity is defined at cell layer interfaces. Equation (III-39) then represents a system of K equations and the boundary conditions are generally of the specified flux type. Specified surface and bottom flux boundary conditions are most conveniently incorporated in the surface and bottom cell layer source and sink terms allowing A_b at the bottom boundary, k = 0, and the surface boundary, k = K+1, to be set to zero making equation (III-39) tridiagonal. For turbulence intensity and turbulence length scale, equations (III-14, III-15), the generic variable S is defined vertically at cell layer interfaces and the diffusivity is defined at cell layer centers. Equation (III-39) then represents a system of K-1 equations for the variables at internal interfaces with the variable values at the free surface and bottom being provided as boundary conditions. For the turbulence intensity and length scale, the boundary conditions are:

$$q_0^2 = B_1^{2/3}|\tau_0|$$
$$q_K^2 = B_1^{2/3}|\tau_K|$$
$$l_0 = 0$$
$$l_K = 0$$

where τ_0 and τ_K are the bottom and surface stress vectors respectively. Insertion of these boundary conditions results in equation (III-39) representing tridiagonal systems of K-1 equations for the turbulence intensity and length scale.

Without loss of generality, the notation used in analyzing the three time level advection step, equation (114), is simplified by replacing the double and single asterisk intermediate time level indicators by n+1 and n-1, respectively to give:

$$(mHS_k)^{n+1} = (mHS_k)^{n-1} - 2\theta\big(U_k(x+0.5)S_k(x+0.5) - U_k(x-0.5)S_k(x-0.5)$$
$$+V_k(y+0.5)S_k(y+0.5) - V_k(y-0.5)S_k(y-0.5) + \Delta_k^{-1}\big((WS)_k - (WS)_{k-1}\big)\big) \qquad \text{(III-40)}$$

where the horizontal central difference operators have been expanded about the cell volume centroid (x,y).

For the centered in time and space form, equation (III-40) becomes:

$$(mHS_k)^{n+1} = (mHS_k)^{n-1} - \theta\big(\tilde{U}_k(x+0.5)\big(S_k(x+1)+S_k(x)\big) - \tilde{U}_k(x-0.5)\big(S_k(x)+S_k(x-1)\big)\big)$$
$$+\tilde{V}_k(y+0.5)\big(S_k(y+1)+S_k(y)\big) - \tilde{V}_k(y-0.5)\big(S_k(y)+S_k(y-1)\big)\big)$$
$$+\Delta_k^{-1}\tilde{W}_k(S_{k+1}+S_k) - \Delta_k^{-1}\tilde{W}_{k-1}(S_k+S_{k-1})\big) \qquad \text{(III-41)}$$

The transports in equation (III-41) are evaluated at the centered time level when used in the external and internal momentum equations, and are averaged to the centered time level using:

$$\tilde{U}_k = 0.5\big(U_k^{n+1} + U_k^{n-1}\big) \qquad \text{(III-42)}$$

when used in the transport equations for scalar variables.

To investigate the stability and accuracy of the centered in time and space scheme, the Fourier representation:

$$S_k = S_0 \exp\big(i\,\omega n\theta + ik_x m_x x + ik_y m_y x + ik_z H\Delta z\big) \qquad \text{(III-43)}$$

is introduced into equation (III-41) giving the characteristic polynomial

$$\lambda^2 + 2i\psi\lambda - 1 = 0 \qquad \text{(III-44)}$$

$$\psi = \frac{u\theta}{m_x}\sin(k_x m_x) + \frac{v\theta}{m_x}\sin(k_y m_y) + \frac{w\theta}{H\Delta}\sin(k_z H\Delta) \qquad \text{(III-45)}$$

for a steady and spatially uniform velocity field. The roots of equation (III-44) are:

$$\lambda = \left(\sqrt{1-\psi^2} - i\psi\right), -\left(\sqrt{1-\psi^2} + i\psi\right) \qquad \text{(III-46)}$$

and the scheme is neutrally stable if the absolute value of ψ is less than or equal to one. The most restrictive stability condition is then:

$$\frac{|u|\theta}{m_x} + \frac{|v|\theta}{m_x} + \frac{|w|\theta}{H\Delta} \le 1 \quad . \qquad \text{(III-47)}$$

which requires the sum of the directional Courant Numbers to be less than or equal to unity. Since the centered in time and space scheme is neutrally stable when equation (III-47) is satisfied, the numerical scheme, like the continuous equations, has no dissipation. Since the scheme involves three time levels, a spurious solution mode corresponding the second eigenvalue in equation (III-46) is introduced. The dispersion relation for the physical mode of the numerical scheme is:

$$\sin(\omega\theta) = -\frac{u\theta}{m_x}\sin(k_x m_x) - \frac{v\theta}{m_x}\sin(k_y m_y) - \frac{w\theta}{H\Delta}\sin(k_z H\Delta) \quad . \qquad \text{(III-48)}$$

The dispersion relation for the equivalent continuous equation is:

$$\omega\theta = -\frac{u\theta}{m_x}(k_x m_x) - \frac{v\theta}{m_x}(k_y m_y) - \frac{w\theta}{H\Delta}(k_z H\Delta) \quad . \qquad \text{(III-49)}$$

Comparison of the dispersion relations shows that errors in the phase and propagation speed of the centered in time and space numerical scheme are smallest for directional Courant numbers near unity in magnitude and for small values of the wave number component, grid spacing products (Fletcher, 1988). Figure III.16 shows equations (III-48, III-49) for a two-dimensional flow with directional Courant Numbers of 0.5.

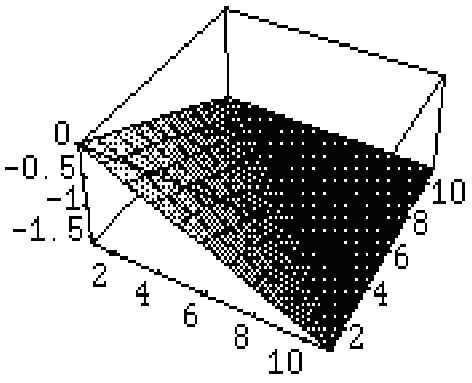

(a) Continuous equation (values less than -1.5 shown as -1.5)

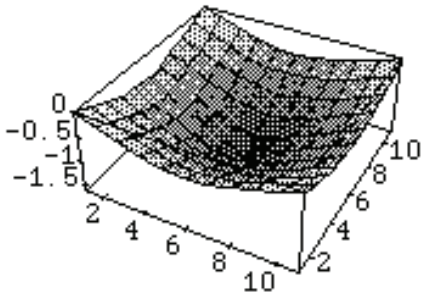

(b) Three time level centered in time and space

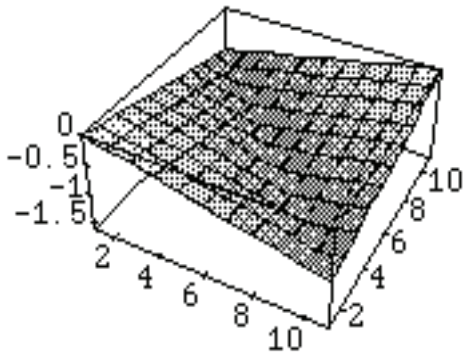

(c) Three time level forward in time and upwind in space

Figure III.16. Dispersion relations: $\omega\theta$ (vertical axis) versus $k_x m_x$ and $k_y m_y$ (horizontal axes) for advection scheme under Courant Numbers = 0.5

Although the centered in time and space scheme is desirable because it has no dissipation, its phase errors at high wave numbers are undesirable. For the transport of the horizontal momentum components in regions having large velocity gradients due to topographic variations, the centered in time and space scheme generates high wave number spatial oscillations that can corrupt the solution for the velocity field, (Smith and Cheng, 1987). The addition of horizontal diffusion to smooth the local oscillations can result in unrealistic damping of the surface wave propagation in other regions of the solution domain. When used for the transport of positive scalar fields, particularly in regions having high gradients or frontal discontinuities, the dispersive character of the centered in time and space scheme at high wave numbers is undesirable since it can lead to high wave number oscillations and unrealistic negative values of strictly positive scalar field variables.

An ideal advective transport scheme for scalar variables should retain the positive definite character of the forward in time and upwind in space scheme, but control the dissipation of the scheme. A high-order upwind scheme developed by Smolarkiewicz (Smolarkiewicz, 1984; Smolarkiewicz and Clark, 1986; Smolarkiewicz and Grabowski, 1990), which is referred to as the multi-dimensional positive definite advective transport algorithm, has all these properties and has a sound transparent theoretical basis. Therefore, this high-order positive definite advective transport scheme is used for scalar advective transport in the EFDC model. For a detailed description of the scheme, readers are referred to the above references and Hamrick (1992).

The Elizabeth and James River HEM-3D model was developed in 2000-2001 by VIMS under contract with the Norfolk District of the Army Corps of Engineers (ACE) and the Virginia Port Authority (VPA) to apply its 3D hydrodynamic model to assess the environmental impacts of various expansion options for Craney Island (Wang et al., 2001). The model covers the entire James River and the Elizabeth River including the Lafayette River, Western Branch, Eastern Branch, Deep Creek, and the Southern Branch up to Great Bridge. The model was calibrated for these parameters in the mainstem James River in a previous study (Boon et al., 1999). Calibration in the Elizabeth River consisted of simulating the prototype condition for the period April 24 to June 8, 2000, during which period high-frequency observations of tides, velocities (surface, mid-depth, and bottom), and salinities (surface, mid-depth, and bottom) were available. Additionally, monthly comparisons of observed versus predicted salinity throughout the water column at multiple locations throughout the Elizabeth mainstem and the Southern Branch showed the model's ability to accurately simulate the observed stratification. The model was further validated with respect to surface elevation induced by both astronomical and meteorological tides, current velocities (tidal and residual), and salinity distributions. As part of that study, VIMS developed a global analysis methodology to determine the far-field long-term effects of each expansion option on each of several hydrodynamic state variables (i.e., water elevation, current velocity, salinity, and sedimentation potential). A complete description of model calibration and validation for the Elizabeth and James River model is presented in Wang et al. (2001), Chapter IV.

D. Incorporation of the ECOM-SED sediment transport module

In order to address the need for sediment transport modeling in this project, the ECOM-SED model module was incorporated into HEM-3D. ECOM-SED is a full-blown 3D sediment model that simulates resuspension, transport, and deposition of both cohesive and non-cohesive sediments. The settling of cohesive sediments is modeled as a function of aggregation and settling. Figure III.17 illustrates the 7-layer sediment bed beneath the sediment-water interface that is used to track the history of accumulation based on shear stress within each layer for the ECOM-SED model. Calibration results of the ECOM-SED model are presented in Section IV-1 of Chapter IV.

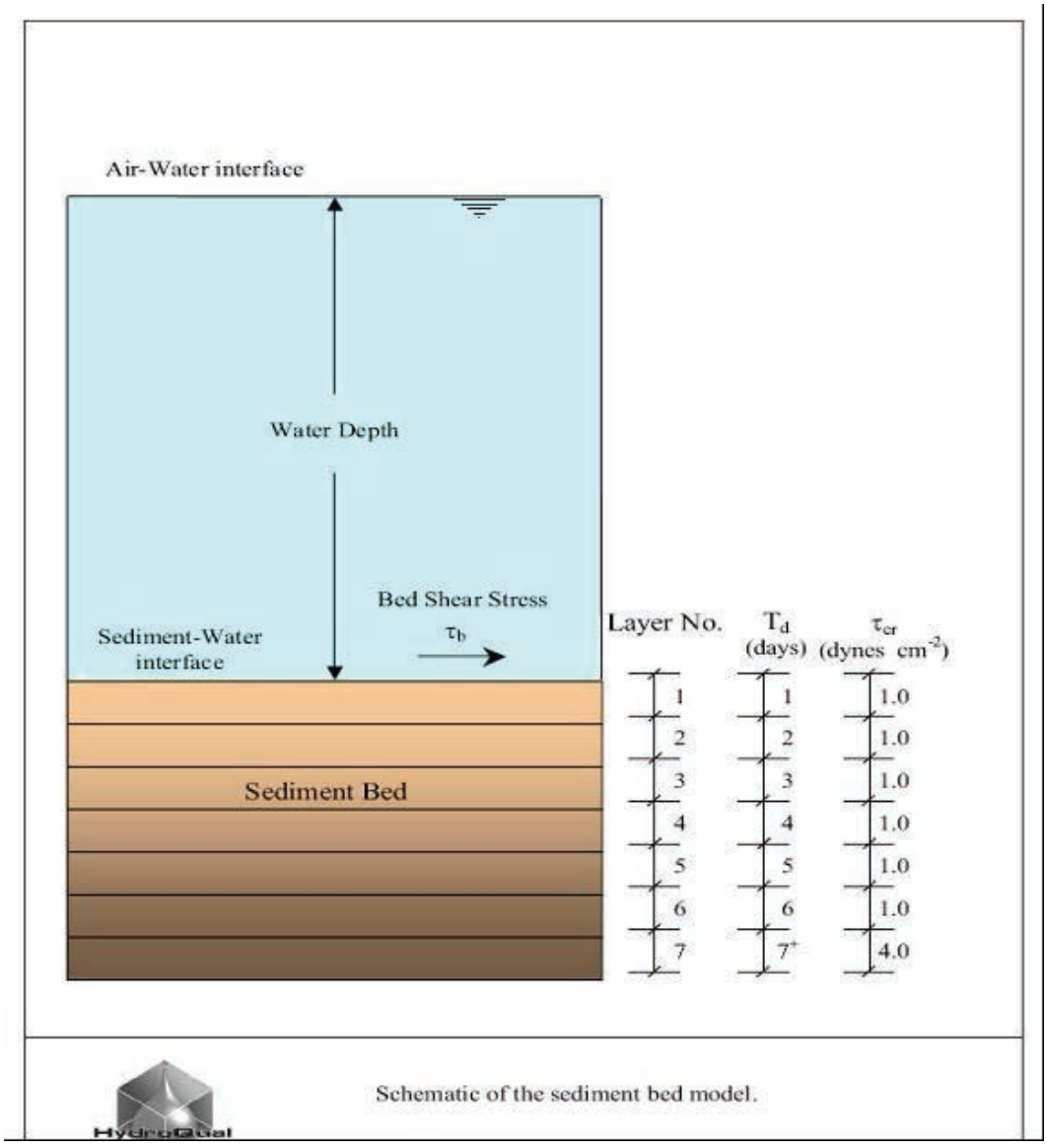

Figure III.17. Illustration of ECOM-SED model layers.

III-3-2 Water Quality Model

A water quality model with twenty-one state variables has been developed and integrated with the hydrodynamic model to form the three-dimensional VIMS Hydrodynamic-Eutrophication Model (HEM-3D) (Park et al., 1995). The information of physical transport processes, both advective and diffusive, simulated by the hydrodynamic model described in Section III-2.A are used to account for the transport of passive substances including non-conservative water quality parameters. The model, upon receiving the physical transport from the hydrodynamic model, simulates the spatial and temporal distributions of water quality parameters including dissolved oxygen, suspended algae (3 groups), various components of carbon, nitrogen, phosphorus, and silica cycles, and fecal coliform bacteria.

The VIMS HEM-3D was used to simulate nutrients, algae, and DO dynamics in the river. The model was calibrated and validated against the DEQ's monthly monitoring data for selected years. We used DEQ's monitoring data to estimate DO conditions in the estuary and create a range of baseline DO distributions (including the worst case and average conditions), in order to bracket some existing DO conditions. The creation of the existing DO baseline condition allowed us to identify the critical period that can trigger DO problems in the estuary and establish a foundation for developing scenarios to assess the impact of the project on DO under different hydrological and dynamic conditions. We calibrated the model to be capable of representing some typical DO conditions (e.g., worst case and average conditions) through existing scenarios. We identified the critical period in terms of temperature and flow that may likely cause the worst case condition in the estuary. We then collected all the point source information in the estuary and estimate the nutrient and organic material loads from point sources. By using the EPA Chesapeake Bay Phase V watershed model results to estimate nonpoint source nutrient loads and benthic nutrient and SOD fluxes, the water quality model was set up using these estimated loads for selected calibration and validation years. Once the model was calibrated and validated, the model was set up to represent the identified baseline condition. A series of scenarios were developed with the consultation of the project managers and the evaluation team. The model was used to run scenarios with respect to the changes of bathymetry and shoreline. The model results with respect to the existing and changed conditions were fully analyzed to assess the influence of the project on the local DO conditions.

Effluent from the filling of the containment cells were modeled as point sources. The model includes a simulation of effluent discharge of suspended sediment for the 6 existing spillboxes (two per cell, in the corners) located along the Craney Island west dike, as well as proposed spillboxes for the expansion cell. Current plans would call for a spillbox for the South CIEE Cell, and one for the North CIEE Cell. The water quality model simulates 21 state variables in the water column and 23 state variables in the sediment together with the velocity field, suspended sediments, and temperature. Therefore, extensive computer resources are required. Numerous model simulations were made during the model calibration and validation periods, especially using the inverse method to calibrate the model in order to reduce the uncertainty in loading

estimation. Multiple scenarios were simulated under different dynamic conditions for a better assessment of the DO conditions in the river. The sediment concentration in the water column and its final deposition was evaluated. We have made extensive use of computer resources. In order to increase the speed of the model simulations to complete the project within the specified period, we used a 25-node computing cluster for this project. Additionally, two construction alternatives were accounted for throughout the modeling effort. The first was the construction of all the dikes prior to any filling, and the second was an initial construction of the south cell only, followed by filling of the south cell prior to building out of the remaining dikes.

A. Dissolved oxygen process

(1) Effects of algae in water column on dissolved oxygen

Algae produce oxygen during photosynthesis and consume oxygen through respiration. The quantity produced during photosynthesis depends on the form of nitrogen taken up. Since oxygen is released in the reduction of nitrate (NO_3), more oxygen is produced, per unit of carbon fixed, when NO_3 is the algal nitrogen source than when ammonia NH_4 is the source. When NH_4 is the nitrogen source, one mole of oxygen is produced per mole carbon dioxide fixed. When NO_3 is the nitrogen source, 1.3 moles oxygen are produced per mole carbon dioxide fixed. The equation that describes the effect of algae photosynthesis on DO in the model is:

$$\frac{\delta DO}{\delta t} = \sum_x \left(\left(1.3 - 0.3 PN_x\right) P_x \right) AOCR \cdot B_x \qquad \text{(III-50)}$$

where:

PN_x = algal group x preference for ammonium in which

P_x = production rate of algal group x (day^{-1})

AOCR = DO-to-carbon ratio in respiration (2.67 g O_2 per g C)

B_x = algal biomass (g C m^{-3})

As employed here, basal metabolism is the sum of all internal processes that decrease algal biomass. A portion of the metabolism is respiration and may be viewed as a reversal of production. In respiration, carbon and nutrients are returned to the environment accompanied by the consumption of DO. Respiration cannot proceed in the absence of DO. Basal metabolism cannot decrease in proportion to oxygen availability.

Formulation of this process is described as:

$$\frac{\delta DO}{\delta t} = \sum_x \left(-\frac{DO}{KHR_x + DO} BM_x \right) AOCR \cdot B_x \quad \text{(III-51)}$$

where:

KHR_x = half-saturation constant of DO for algal DOC exudation (g O_2 m^{-3})

BM_x = basal metabolism rates for algal group x (day^{-1})

(2) Effects of nitrification on dissolved oxygen

Nitrification is a process mediated by specialized groups of autotrophic bacteria that obtain energy through the oxidation of ammonia to nitrite and oxidation of nitrite to nitrate. A simplified expression for complete nitrification is:

$$NH_4^+ + 2O_2 \rightarrow NO_3^- + H_2O + 2H^{2+} \quad \text{(III-52)}$$

The equation indicates that two moles of oxygen are required to nitrify one mole of ammonia into nitrate. The simplified equation is not strictly true, however. Cell synthesis by nitrifying bacteria is accomplished by the fixation of carbon dioxide so that less than two moles of oxygen are consumed per mole ammonium utilized (Wezernak and Gannon, 1968). In this study, nitrification is modeled as a function of available ammonium, dissolved oxygen, and temperature:

$$NT = \frac{DO}{KHONT + DO} \frac{NH_4}{KHNNT + NH_4} f(T) \cdot NTM \quad \text{(III-53)}$$

where:

NT = nitrification rate (gm N m^{-3} day^{-1})

NTM = maximum nitrification rate at optimal temperature (gm N m^{-3} day^{-1})

KHONT = half-saturation constant of DO required for nitrification (gm DO m^{-3})

KHNNT = half-saturation constant of NH_4 required for nitrification (gm N m^{-3})

Therefore, the effect of nitrification on DO is described as follows:

$$\frac{\delta DO}{\delta t} = -AONT \cdot NT \quad \text{(III-54)}$$

where:

AONT = mass DO consumed per mass ammonia nitrified (4.33 gm DO gm^{-1} N)

(3) Effects of surface reaeration on dissolved oxygen

Reaeration occurs only in the model surface cells. The effect of reaeration is:

$$\frac{\delta DO}{\delta t} = \frac{K_R}{\Delta z_s}(DO_S - DO) \tag{III-55}$$

where:

K_R = reaeration coefficient (m day^{-1})

Δz_s = model layer thickness (m)

DO_S = dissolved oxygen saturation concentration (gm DO m^{-3})

Saturation dissolved oxygen concentration DO_S is computed (Genet et al., 1974):

$$\begin{aligned} DO_S &= 14.5532 - 0.38217 \cdot T + 0.0054258 \cdot T^2 \\ &\quad - \frac{S}{1.80655}\left(0.1665 - 5.866 \cdot 10^{-3} \cdot T + 9.796 \cdot 10^{-5} \cdot T^2\right) \end{aligned} \tag{III-56}$$

where:

S = salinity (ppt)

(4) Effects of Chemical Oxygen Demand on dissolved oxygen

In the present model, chemical oxygen demand represents the reduced materials that can be oxidized through inorganic means. The kinetic equation showing the effect of chemical oxygen demand (bottom cells only) is:

$$\frac{\delta DO}{\delta t} = - \frac{DO}{KHO_{COD} + DO} K_{COD} \cdot COD \tag{III-57}$$

where:

COD = chemical oxygen demand concentrations (g O_2-equivalents m^{-3})

KHO_{COD} = half-saturation constant of DO for oxidation of COD (g O_2 m^{-3})

K_{COD} = oxidation rate of COD (day^{-1})

BF_{COD} = sediment flux of COD (g O_2-equivalents m^{-2} day^{-1}).

$$K_{COD} = K_{CD} \cdot \exp\left(KT_{COD}[T - TR_{COD}]\right) \quad \text{(III-58)}$$

where:

K_{CD} = oxidation rate of COD at reference temperature TR_{COD} (day^{-1})

KT_{COD} = effect of temperature on oxidation of COD ($°C^{-1}$)

TR_{COD} = reference temperature for oxidation of COD (°C).

Overall, the internal sources and sinks of dissolved oxygen include algal photosynthesis and respiration, atmospheric reaeration (surface cells only), heterotrophic respiration, nitrification, and oxidation of COD. The complete kinetic equation showing sediment oxygen demand (bottom cells only) is:

$$\begin{aligned}\frac{\delta DO}{\delta t} = & \sum_x \left((1.3 - 0.3 \cdot PN_x) P_x - \frac{DO}{KHR_x + DO} BM_x \right) AOCR \cdot B_x \\ & + \lambda_1 \frac{K_R}{\Delta z_S} (DO_S - DO) - \frac{DO}{KHO_{DOC} + DO} AOCR \cdot K_{DOC} \cdot DOC \\ & - AONT \cdot NIT - \frac{DO}{KHO_{COD} + DO} K_{COD} \cdot COD + \lambda_2 \frac{SOD}{\Delta z}\end{aligned} \quad \text{(III-59)}$$

B. Model Phytoplankton Kinetics

There are three functional groups for algae: cyanobacteria, diatoms, and green algae. This grouping is based upon the distinctive characteristics of each class and upon the significant roles these characteristics play in the ecosystem. Cyanobacteria are characterized by their bloom-forming characteristics in fresh water. They are characterized as having small settling velocity and are subject to low predation pressure. Diatoms are large phytoplankton that usually produce the spring bloom in the saline water. Settling velocity of diatoms is relatively large, so the diatoms settling into sediment may be a significant source of carbon for sediment oxygen demand. Diatoms are also distinguished by their requirement of silica as a nutrient. The green algae represent the mixture that characterizes blooming in saline waters during summer and autumn, and are subject to relatively high grazing pressure.

Equations governing the three algal groups are similar. Differences among groups are expressed through the magnitudes of parameters in the equations. Generic equations are presented below, except when group-specific relationships are required. Algal sources and sinks in the conservation equation include production, metabolism, predation, and

settling. In the following equations, a subscript, **x**, is used to denote three algal groups: **c** for cyanobacteria, **d** for diatoms, and **g** for green algae. The internal sources and sinks included are growth (production), basal metabolism (respiration and exudation), predation, and settling. The following kinetic equations for algae are:

$$\frac{\delta B_x}{\delta t} = \left(P_x - BM_x - PR_x\right)B_x - WS_x \frac{\delta B_x}{\delta z} \qquad \text{(III-60)}$$

where:

B_x = algal biomass, expressed as carbon (g C m^{-3})

P_x = growth (production) of algae (day^{-1})

BM_x = basal metabolism of algae (day^{-1})

PR_x = predation rates of algae (day^{-1})

WS_x = algal settling velocity (m day^{-1})

z = vertical coordinate

(1) Growth (Production)

Algal growth depends on nutrient availability, ambient light, and temperature. The effects of these processes are considered to be multiplicative as follows:

$$P_x = PM_x \cdot f(N) \cdot f(I) \cdot f(T) \qquad \text{(III-61)}$$

where:

PM_x = maximum production rate under optimal conditions (day^{-1})

f(N) = effect of sub-optimal nutrient

f(I) = effect of light intensity

f(T) = effect of temperature

(2) Effect of nutrient on growth

Liebig's "law of the minimum" (Odum, 1971) is used, so that nutrient limitation is determined by the single most limiting nutrient:

$$f(N) = \text{minimium}\left\{\frac{NH_4 + NO_3}{KHN_x + NH_4 + NO_3}, \frac{PO_{4d}}{KHP_x + PO_{4d}}, \frac{SAd}{KHS_d + SAd}\right\} \quad \text{(III-62)}$$

where:

NH_4, NO_3 = ammonium and nitrate nitrogen concentrations, respectively (g N m^{-3})

PO_4d = dissolved phosphate concentration (g P m^{-3})

SAd = dissolved silica concentration (g Si m^{-3})

KHN_x = half-saturation constant for algal nitrogen uptake (g N m^{-3})

KHP_x = half-saturation constant for algal phosphorus uptake (g P m^{-3})

KHS_d = half-saturation constant for silica uptake by diatoms (g Si m^{-3})

(3) Effects of light on growth

The influence of light on phytoplankton production is represented by a chlorophyll-specific production equation (Jassby and Platt, 1976):

$$P^B = P^Bm \frac{I}{\sqrt{I^2 + IK^2}} \quad \text{(III-63)}$$

where:

P^B = photosynthetic rate (g C g^{-1} Chl d^{-1})

P^Bm = maximum photosynthetic rate (g C g^{-1} Chl d^{-1})

I = irradiance (E m^{-2} d^{-1})

Parameter Ik is defined as the irradiance at which the initial slope of the production vs. irradiance relationship intersects the value of P^Bm:

$$IK = \frac{P^Bm}{\alpha} \quad \text{(III-64)}$$

where:

α = initial slope of production vs. irradiance relationship (g C g^{-1} Chl (E m^{-2})$^{-1}$)

Chlorophyll-specific production rate is readily converted to carbon specific growth rate, through division by the carbon-to-chlorophyll ratio:

$$G = \frac{P^B}{CChl} \qquad \text{(III-65)}$$

where:

CChl = carbon-to-chlorophyll ratio (g C g^{-1} chlorophyll-a)

(4) Effect of temperature on growth

The effect of temperature on algal production is represented by a function similar to a

Gaussian probability curve:

$$\begin{aligned} f(T) &= \exp\left(-KTG1_x\,[T - TM_x]^2\right) \quad \text{when } T \le TM_x \\ &= \exp\left(-KTG2_x\,[TM_x - T]^2\right) \quad \text{when } T > TM_x \end{aligned} \qquad \text{(III-66)}$$

where:

TM_x = optimal temperature for algal growth (°C)

$KTG1_x$ = effect of temperature below TM_x on algal growth ($°C^{-2}$)

$KTG2_x$ = effect of temperature above TM_x on algal growth ($°C^{-2}$)

(5) Constructing the photosynthesis vs. irradiance curve

A production versus irradiance relationship is constructed for each model cell at each time step. First, the maximum photosynthetic rate under ambient temperature and nutrient concentrations is determined:

$$P^Bm(N,T) = P^Bm * f(T) * f(N) \qquad \text{(III-67)}$$

where:

$P^Bm(N,T)$ = maximum photosynthetic rate under ambient temperature and nutrient concentrations (g C g^{-1} Chl d^{-1})

The single most limiting nutrient is employed in determining the nutrient limitation. Next, parameter Ik is derived from Equation III-64. Finally, the production vs. irradiance relationship is constructed using $P^B m$ (N,T) and Ik.

(6) Water surface irradiance

Irradiance at the water surface is evaluated at each model time step. Instantaneous irradiance is computed by fitting a sine function to daily total irradiance:

$$I_o = \frac{I_T}{FD}\frac{\pi}{2}\sin\left(\pi\frac{DSSR}{FD}\right) \quad \text{(III-68)}$$

where:

I_o = irradiance at water surface (E m^{-2} d^{-1})

IT = daily total irradiance (E m-1)

FD = fractional daylength (0 < FD < 1)

DSSR = time since sunrise (d)

I_o is evaluated only during the interval:

$$\frac{1-FD}{2} \le DSM \le \frac{1+FD}{2} \quad \text{(III-69)}$$

where:

DSM = time since midnight (d)

Outside the specified interval, I_o is set to zero.

Irradiance declines exponentially with depth below the surface. The diffuse attenuation coefficient, K_e, is computed as a function of background extinction and concentrations of chlorophyll-a and total suspended solids.

(7) The light attenuation model

The water quality model requires daily solar radiation intensity except fractional day length, in order to simulate the algal growth. The light attenuation model also requires input of the light attenuation coefficient. It is assumed that the light extinction coefficient consists of three parts: background extinction, the light extinction due to suspended solids, and light extinction due to algae:

$$Ke = a_1 + a_2 * TSS + a_3 * CHL \qquad \text{(III-70)}$$

where:

a_1 = background attenuation (m^{-1})

a_2 = attenuation by inorganic suspended solids ($m^2\,g^{-1}$)

a_3 = attenuation by organic suspended solids ($m^2\,gm^{-1}$ CHL)

TSS = total suspended solids concentration ($g\,m^{-3}$)

CHL = chlorophyll-a concentration (mg CHL m^{-3})

The "background" attenuation term included attenuation from both water and dissolved organic matter. Individual parameters were determined from Park et al. (1995b). The value for a_1 used in the model is 0.735 m^{-1}, a_2 is 0.018 $m^2\,g^{-1}$, and a_3 is 0.06 $m^2\,mg^{-1}$ CHL.

(8) Basal metabolism

Basal metabolism is commonly considered to be an exponentially increasing function of temperature:

$$BM_x = BMR_x * \exp\left(KTB_x\,[T - TR_x]\right) \qquad \text{(III-71)}$$

where:

BMR_x = metabolic rate at reference temperature TR_x (day^{-1})

KTB_x = effect of temperature on metabolism ($C^{\circ -1}$)

TR_x = reference temperature for metabolism (C°)

(9) Predation

The predation formulation is identical to basal metabolism. The difference in predation and basal metabolism lies in the distribution of the end products of these processes.

$$PR_x = BPR_x \exp (KTB_x (T - TR_x)) \quad \text{(III-72)}$$

where:

BPR_x = predation rate at TR_x (day $^{-1}$)

KTB_x = effect of temperature on predation ($C^{\circ -1}$)

TR_x = reference temperature for predation (C°)

(10) Settling velocity

The algal settling rate employed in the model represents the total effect of all physiological and behavioral processes that result in the downward transport of phytoplankton. The settling rate employed, from 0.1 m d^{-1} to 0.2 m d^{-1}, was used in the model to optimize the agreement between predicted and observed algae.

(11) Effect of algae on phosphorus

Model phosphorus state variables include total phosphate (dissolved, sorbed, and algal), dissolved organic phosphorus, labile particulate organic phosphorus, and refractory particulate organic phosphorus. The amount of phosphorus incorporated in algal biomass is quantified through a stoichiometric ratio. Thus, total phosphorus in the model is expressed:

$$TotP = PO_4d + PO_4p + Apc*Bx + DOP + LPOP + RPOP \quad \text{(III-73)}$$

where:

TotP = total phosphorus (g P m^{-3})

PO_4d = dissolved phosphate (g P m^{-3})

PO_4p = particulate inorganic phosphate (g P m^{-3})

Apc = algal phosphorus-to-carbon ratio (g P g^{-1} C)

DOP = dissolved organic phosphorus (g P m^{-3})

LPOP = labile particulate organic phosphorus (g P m^{-3})

RPOP = refractory particulate organic phosphorus (g P m^{-3})

Algae take up dissolved phosphate during production and release dissolved phosphate and organic phosphorus through respiration. The fate of phosphorus released by respiration is determined by empirical distribution coefficients. The fate of algal phosphorus incorporated by zooplankton and lost through zooplankton mortality is determined by a second set of distribution parameters.

(12) Effect of algae on nitrogen

Model nitrogen state variables include ammonium, nitrate, dissolved organic nitrogen, labile particulate organic nitrogen, and refractory particulate organic nitrogen. The amount of nitrogen incorporated in algal biomass is quantified through a stoichiometric ratio. Thus, total nitrogen in the model is expressed:

$$TotN = NH_4 + NO_3 + Anc*Bx + DON + LPON + RPON \quad \text{(III-74)}$$

where:

TotN = total nitrogen (g N m^{-3})

NH_4 = ammonium (g N m^{-3})

NO_3 = nitrate (g N m^{-3})

Anc = algal nitrogen-to-carbon ratio (g N g^{-1} C)

DON = dissolved organic nitrogen (g N m^{-3})

LPON = labile particulate organic nitrogen (g N m^{-3})

RPON = refractory particulate organic nitrogen (g N m^{-3})

Algae take up ammonium and nitrate + nitrite during production and release ammonium and organic nitrogen through respiration. Nitrate + nitrite is internally reduced to ammonium before synthesis into biomass occurs (Parsons et al., 1984). Trace concentrations of ammonium inhibit nitrate reduction so that, in the presence of multiple nitrogenous nutrients, ammonium is utilized first. The “preference” of algae for ammonium is expressed by an empirical function (Thomann and Fitzpatrick, 1982):

$$PN = NH_4 * \frac{NO_x}{(KHn + NH_4) * (KHn + NO_x)} + NH_4 * \frac{KHn}{(NH_4 + NO_x) * (KHn + NO_x)} \quad \text{(III-75)}$$

where:

PN = algal preference for ammonium uptake (0 < Pn < 1)

KHn = half saturation concentration for algal nitrogen uptake (g N m^{-3})

When nitrate + nitrite is absent, the preference for ammonium is unity. When ammonium is absent, the preference is zero.

(13) Effect of algae on silica

The model incorporates two siliceous state variables: dissolved silica and particulate biogenic silica. The amount of silica incorporated in algal biomass is quantified through a stoichiometric ratio. Thus, total silica in the model is expressed:

TotSi = Dsil + Asc * Bx + PBS (III-76)

where:

TotSi = total silica (g Si m^{-3})

Dsil = dissolved silica (g Si m^{-3})

Asc = algal silica-to-carbon ratio (g Si g^{-1} C)

PBS = particulate biogenic silica (g Si m^{-3})

As with the other nutrients, the fate of algal silica released by metabolism and predation is represented by distribution coefficients.

C. Benthic sediment process

Additionally, a benthic sediment process model developed by DiToro and Fitzpatrick (1993) was incorporated and coupled with HEM-3D for the present model application. The model state variables, and resulting fluxes, include dissolved oxygen, ammonium, nitrate-nitrite, and phosphate and the parameters used in this sediment flux model are listed in the Table IV.10 of Chapter IV.

The sediments in this model are represented by two layers: the upper aerobic layer (Layer 1) and the lower anoxic layer (Layer 2). The sediment process model is coupled with the water column eutrophication model through depositional and sediment fluxes. First, the sediment model is driven by net settling of particulate organic matter from the overlying water column to the sediments (depositional flux). Then, the mineralization of particulate organic matter in the lower anoxic sediment layer produces soluble intermediates, which are quantified as diagenesis fluxes. The intermediates react in the upper oxic and lower anoxic layers, and portions are returned to the overlying water column as sediment fluxes. Computation of sediment fluxes requires mass-balance equations for ammonium, nitrate, phosphate, sulfide/methane, and available silica. Mass-balance equations are solved for these variables for both the upper and lower layers. Complete model documentation of the sediment flux model can be found in DiToro and Fitzpatrick (1993).

III-4 A Global Analysis Technique for impact analysis

The global analysis methodology can be described as a series of steps involved in the post-processing of results of both the base case and the expansion case:

1) Determine differences in time series between the base case and the expansion case for all locations in the three-dimensional domain.
2) Generate spatial plots of these differences.
3) Plot frequency distributions of these differences as an areal percentage.
4) Compare the cumulative percentages of the frequency plots as a metric for impact assessment.

In order to determine the long-term, time-averaged impacts, a controlled execution of the model (i.e., the single variable run) was performed in which the model input is restricted by allowing only a single variable, tidal range, to vary between astronomical extremes during the course of a run. A three-constituent harmonic model is used including the M_2, S_2, and N_2 tidal constituents with phasing adjusted to produce tides of maximum (perigean-spring), mean, and minimum (apogean-neap) range during a single run of 34 days. The generated time series, used as the boundary condition at the James River mouth in single variable runs, is shown in Figure III.18. This is a semi-monthly progression between the extremes in tidal range for the month.

The purpose of the simple design of the single variable run is to isolate the long-term average impacts caused by the expansion option. Here, the term “global” is used to refer to the entire spatial domain for Hampton Roads. Global analysis comprises an attempt to determine any and all far-field effects caused by the expansion and related dredging.

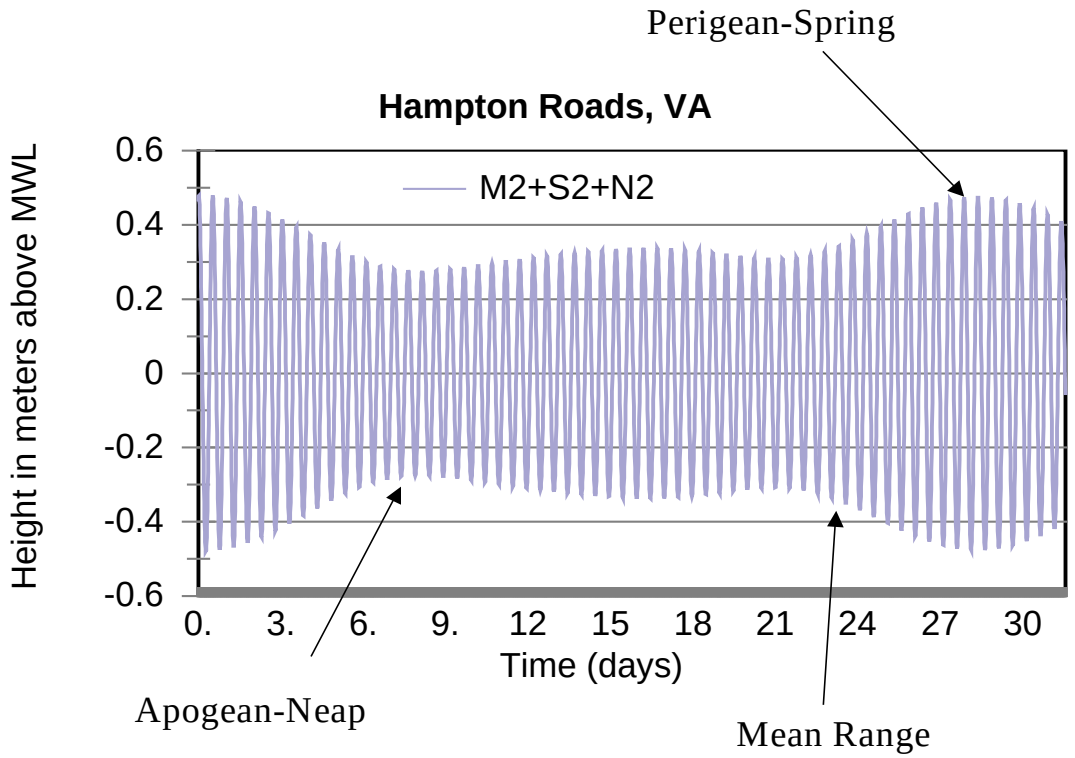

Figure III.18. Tide curve generated using M_2, S_2, and N_2 constituent amplitudes for Hampton Roads, Virginia.

The motivation for the use of the global technique is to examine both the magnitude of changes and the spatial distribution of these changes for those parameters that can have a critical impact on the circulation in the Elizabeth River. These parameters include the surface elevation, surface and bottom salinity, surface and bottom velocity, surface and bottom residual velocity, and sedimentation potential**.**

A time series of 74 tidal cycles was designed and used to provide the combination of essential tidal components including spring, neap, perigean-spring and apogean-neap tides. The semi-monthly progression between the extremes in tidal range for the model is shown in Figure II.6. The duration of each single variable scenario run was 134 tidal cycles and the model results were saved every half-hour throughout the entire modeling domain after the model spin-up period of 60 tidal cycles.

In order to assess the impacts exerted on the James/Elizabeth River system, the differences between the expansion cases and the base Case were obtained and analyzed. From the numerical modeling point of view, what these Test Cases introduce into the system are perturbations from the change in the modeling domain itself (the impact of an expansion). In measuring the effect of these perturbations, we first conduct a global analysis using 4 key variables: tidal elevation, current velocity, salinity, and sedimentation potential.

The global technique described in this section involves the generation of a plotted spatial distribution of a long-term (i.e., 74 tidal cycles) time average comparison of parameters

predicted by the model for the base case (i.e., pre-expansion existing condition) and the project case (i.e., expansion plus dredging specifications). The comparison is made possible by virtue of the fact that all model output for the 6-layer, 7500-cell domain of the VIMS James/Elizabeth River HEM-3D model version is saved 24 times per tidal cycle (i.e., approximately every half hour). This allows one to compare, for each location in the model domain, time series of the base case versus the project case and to characterize the difference as either an RMS (root mean square) difference or a simple average difference:

$$\text{RMS\_DIFFERENCE} = \sqrt{\sum_{i=1}^{n} (\text{MP}_{\text{test,i}} - \text{MP}_{\text{base,i}})^2 / \text{n}}$$

for tidal elevation and velocity magnitude

$$AVERAGE\_DIFFERENCE = \sum_{i=1}^{n} (MP_{test,i} - MP_{base,i}) / n$$

for salinity, sedimentation potential, and residual velocity

where: n is number of data points, (1776 for 74 tidal cycles)
MP_{test} is model prediction for the project case
MP_{base} is model prediction for the base case

For this project, 8 spatial plots representing the project case - base case comparisons (i.e., post-expansion minus pre-expansion differences), are presented as follows:

1) RMS difference of tidal elevation
2) average difference of surface salinity
3) average difference of bottom salinity
4) RMS difference of surface velocity magnitude
5) RMS difference of bottom velocity magnitude
6) average difference of surface residual velocity magnitude
7) average difference of bottom residual velocity magnitude
8) sedimentation potential difference between Test Case and Base Case

In this fashion, one is able to obtain, for each state variable, a simple difference between the predicted value of the project case and that of the base case for each cell and layer of the model domain. It is not only useful to know the relative size of the differences described above, but also their spatial distributions. Use of ArcView Avenue scripts allows for the mapping of the derived differences into the exact cell areas of this curvilinear, variable cell size grid. Differences are derived for the entire Hampton Roads portion of the modeling domain and shown individually for each state variable using spatial plots spanning Hampton Roads.

IV. MODEL CALIBRATION

The hydrodynamic and water quality model of the coupled James and Elizabeth Rivers system was developed using the framework outlined in Chapter III. The hydrodynamic model was calibrated using intensive data collected in year 2000 and the water quality model was applied for the years 1999, 2000, and 2001, during which period the non-point source loading data was provided by the HSPF watershed model obtained from the EPA Chesapeake Bay Program.

IV-1 Calibration of the Hydrodynamic Model

Calibration in the Elizabeth River consisted of simulating the prototype condition for the period April 24 to June 8, 2000, during which period high-frequency observations of tides, velocities (surface, mid-depth, and bottom), and salinities (surface, mid-depth, and bottom) were available.

IV-1-1 Calibration for tidal elevation

The astronomical tide accounts for about 80 % of the energy of water surface fluctuations in Hampton Roads and the Elizabeth River. Therefore an accurate reproduction of the tidal wave propagation in the Elizabeth River is of the utmost importance. Furthermore, once the model is calibrated with respect to astronomical tide, a minimum of additional adjustment is required for calculations of surface elevation and current velocity. Tidal propagation in an estuary is controlled by river geometry and frictional dissipation of energy. With river geometry and tidal range at the open boundary given, we used the distribution of tidal range as a function of distance along the Elizabeth River to calibrate against the roughness height, the model parameter for bottom friction. Shown in Figure IV.1 are locations of stations measuring water surface elevations at 6-minute intervals for several months in 2000. During the process of roughness height adjustment, minor refinements of the geometric representation by the model were performed from time to time. Figure IV.2 shows the slightly increasing tidal range as the Elizabeth River tide propagates upriver from the Sewells Pt. station near its mouth. Figure IV.3 shows the small longitudinal differences in tidal phase for both high and low tide.

River inflow from the USGS gages available upstream at Richmond, the mouth of the Chickahominy River, and at Appomattox were used as inputs for this model calibration run. A long-term mean of 234 cms was specified at the upriver boundary of the model domain. A single tidal constituent, M2, was specified as the boundary condition at the open boundary out of the James River mouth. Since there is no tidal record at the open boundary, an inverse approach was adopted. The tidal amplitude at the open boundary was adjusted until the model produced a tidal amplitude at Sewells Point exactly half the average tidal range measured by NOAA over a 19-year tidal epoch, 75.5 cm.

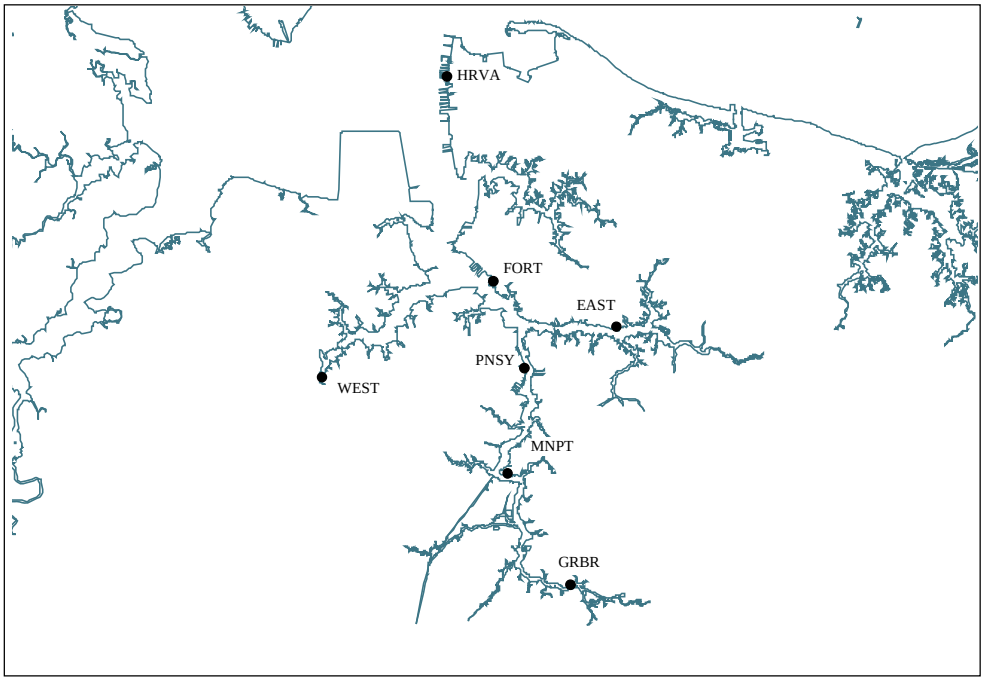

Figure IV.1. Location of Elizabeth River Tide Stations.

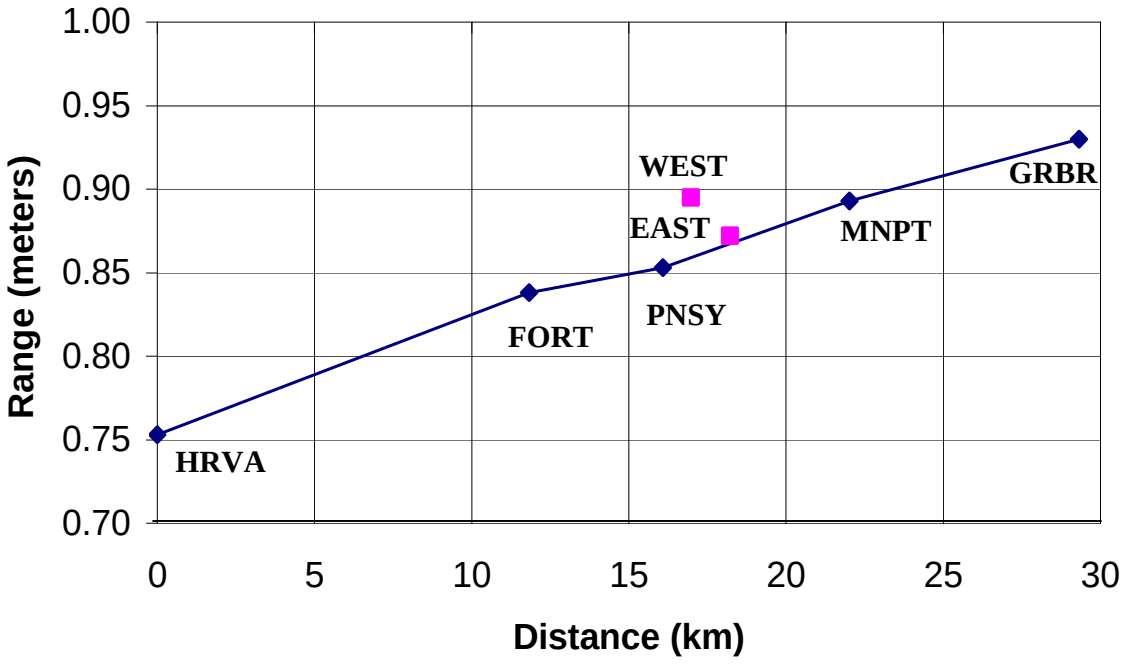

Figure IV.2. Mean Tidal Range (1960-1978 Tidal Epoch), Elizabeth River

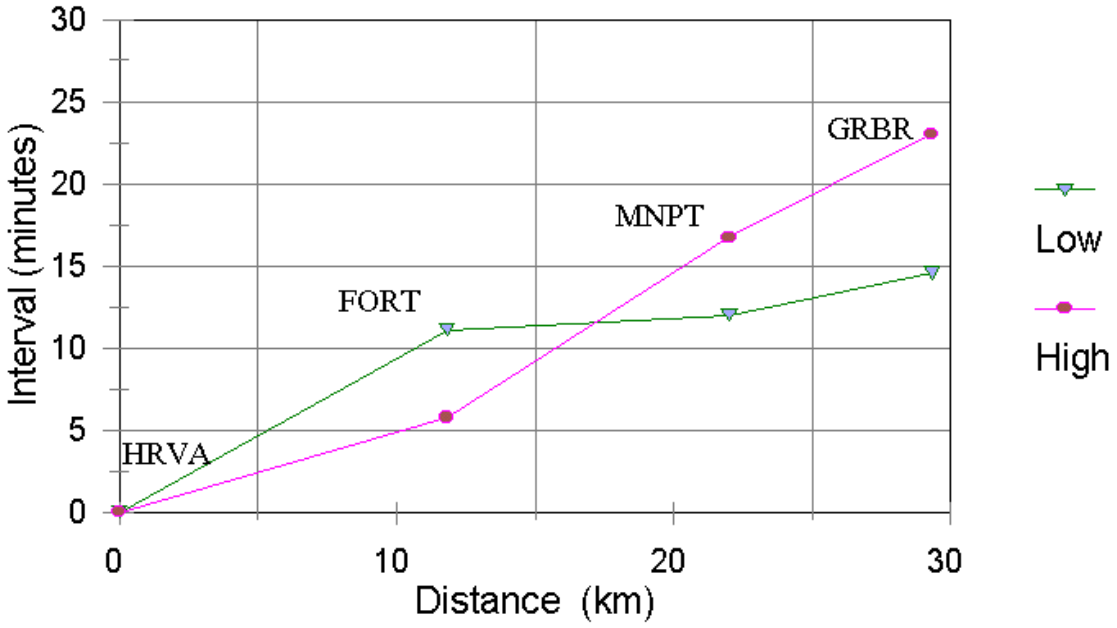

Figure IV.3. Mean High and Low Water Intervals, Elizabeth River.

Figure IV.4 compares the calibrated model results of the tidal ranges with those derived from field data. The field data at some stations cover only a duration of the order of one month. The tidal ranges derived from these short-term records have been adjusted to long-term mean by simultaneous comparison with data at Sewells Point. The figure shows a generally increasing trend as the tide propagates upriver. The root-mean-square difference between model simulation and field observation is 2.03 cm, or less than 3 % of the observed tidal range. The longitudinal variation of observed versus predicted phase lags is shown below in Figure IV.5.

The calibration also included the comparison of observed surface elevation time-series data with model predictions. For this model simulation, the water surface elevation for the open boundary condition was derived from data measured at the CBBT (Chesapeake Bay Bridge Tunnel). The measured time series data were delayed for half an hour to account for the time lag between CBBT and the model boundary. No adjustment on surface elevation was made. The surface elevation at CBBT and Sewells Point can have significant variations due to the transient meteorological and hydrological events that are routinely observed in the lower Chesapeake Bay, as shown in the synoptic time series of two NOAA/NOS records shown in Figure IV.6

The model-predicted time series water surface elevation was compared with observed data at Sewells Point, Fort Norfolk, Money Point, Great Bridge, Eastern Branch and Western Branch over the periods when data were available.

All comparisons are characteristically the same; Figures IV.7 and IV.8 show two examples of the comparisons. The top panel of each figure compares the real-time predicted and observed data. They consist of both the astronomical tide and those induced by meteorological and hydrological forcing. To isolate the non-tidal signal, both the predicted and observed time series data were passed through a low-pass filter with a 36-hour cutoff period. The low frequency time series signals were compared in the middle panel of each figure. It is noted that the model reproduced the meteorological event accurately (note the set-up around Julian Day 151). The lower panels of the figures plot the difference between the predicted and observed real-time data.

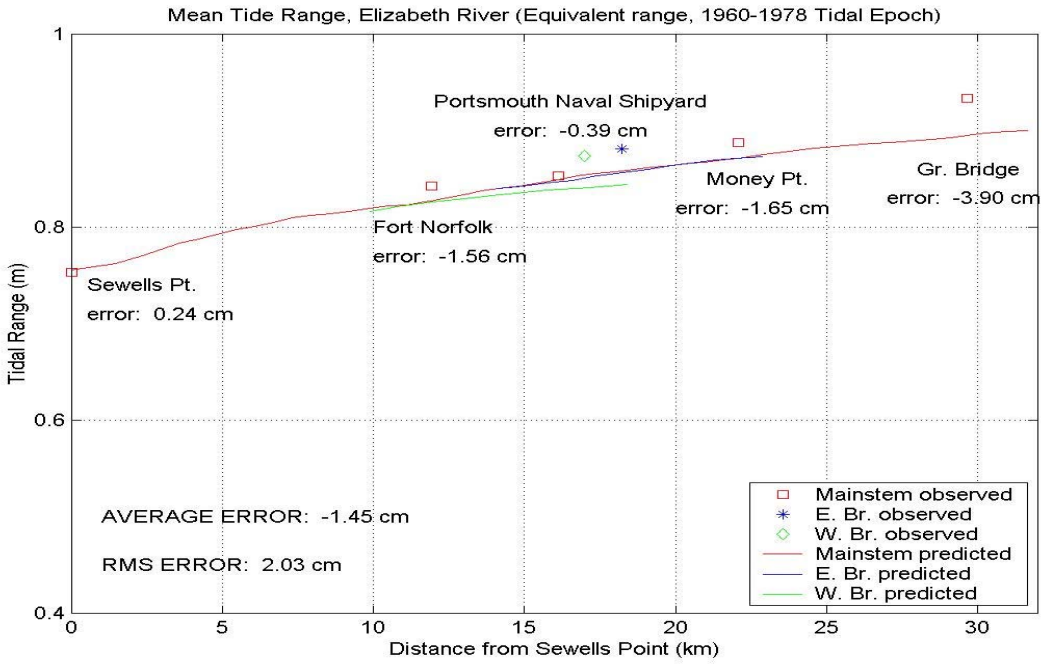

Figure IV.4. Mean Tide Range Calibration for the Elizabeth River.

It is noted that the model reproduced the astronomical tide as well as the meteorological event accurately. Notice that there is a set-up event around Julian Day 151, which was captured by the model. Figure IV.8 shows the prediction for Money Point, which is located inside the Elizabeth River and thus particularly relevant to this study.

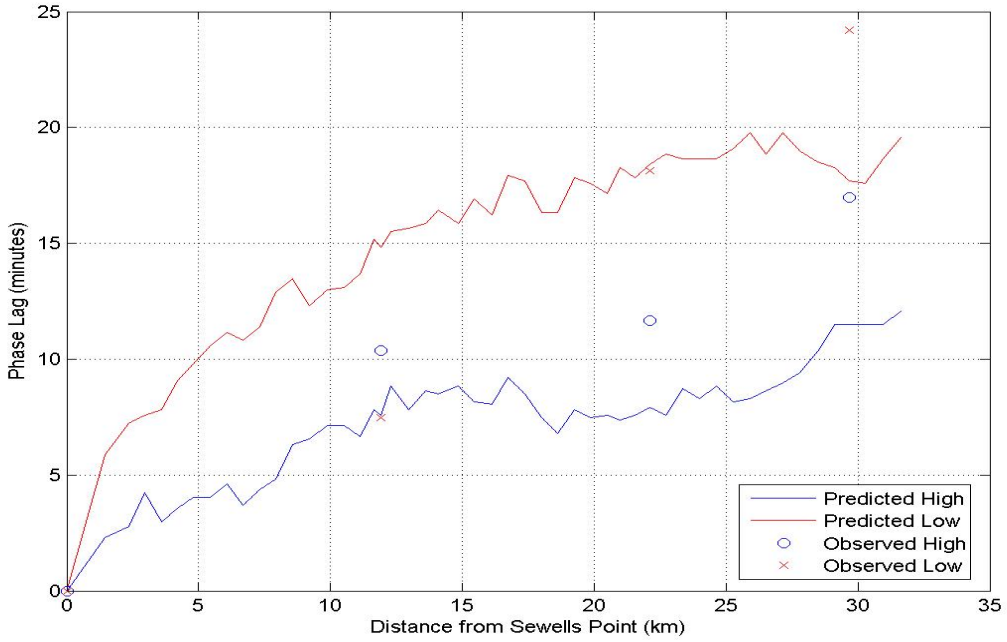

Figure IV.5. Comparison of predicted and observed high and low tide phases

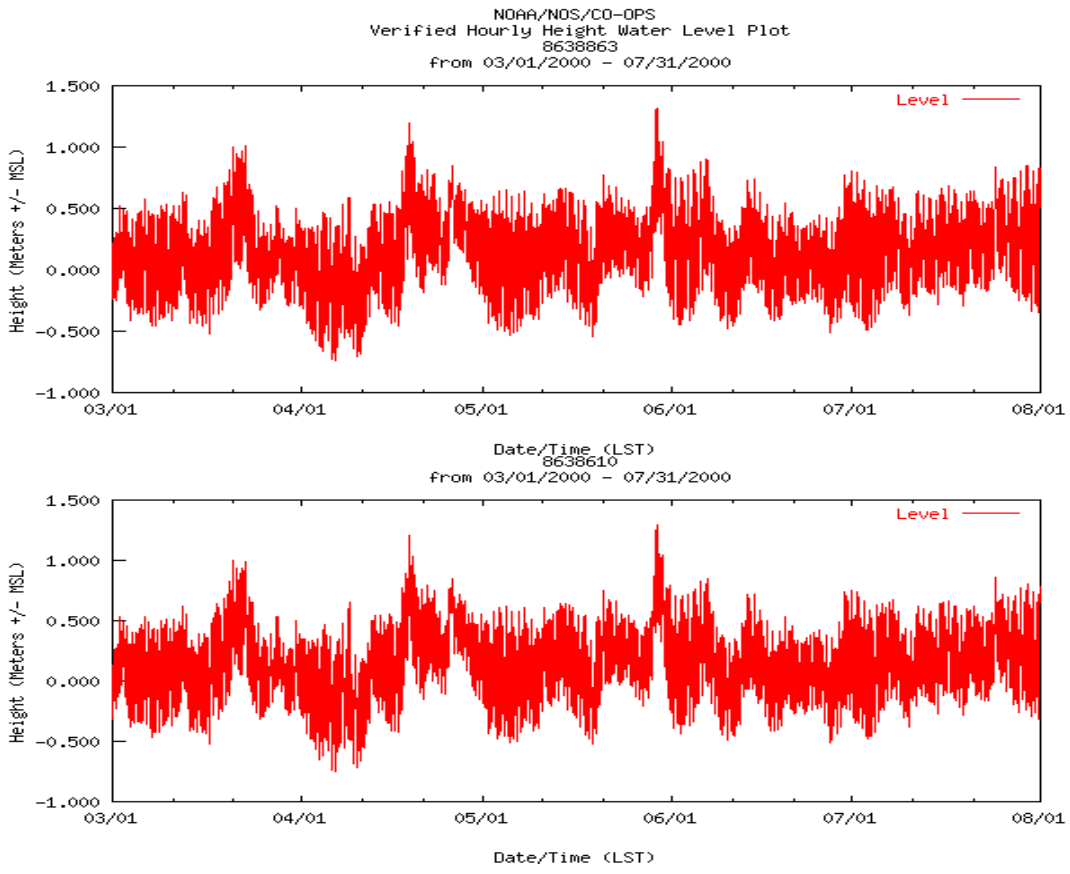

Figure IV.6. Water levels at Chesapeake Bay Bridge Tunnel (upper panel) and Sewells Point, VA (lower panel) from March 1 to August 1, 2000

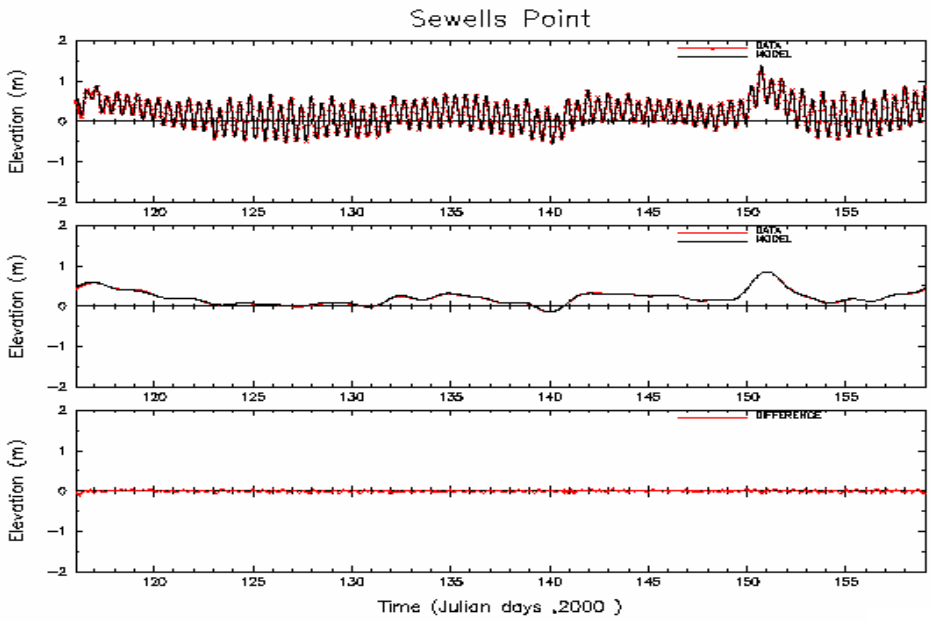

Figure IV.7. Simulated water level variation at Sewells Point.

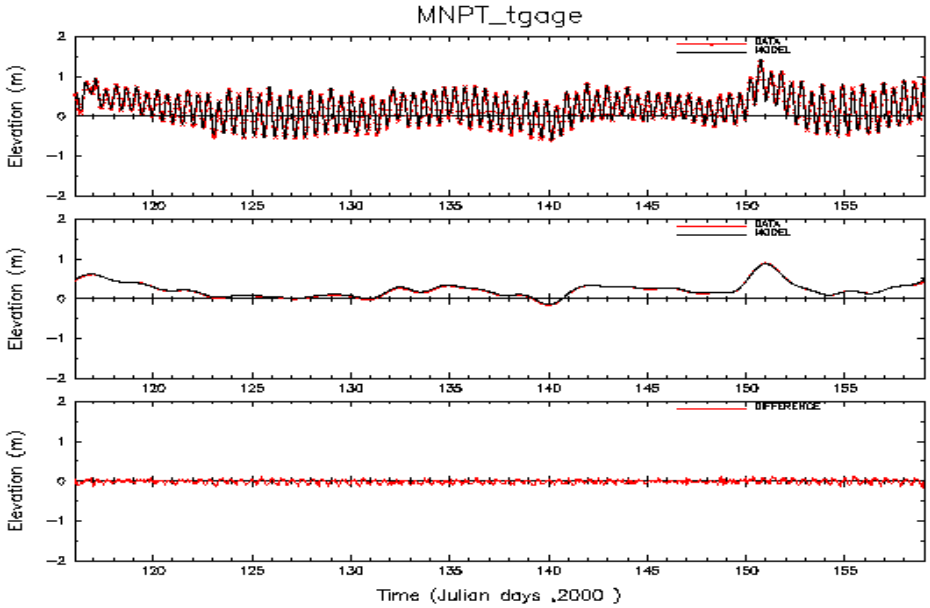

Figure IV.8. Simulated water level variation at Money Point.

IV-1-2 Calibration with the velocity measurements

Predicted versus *Measured* principal axis current curves can be compared within the same time period to check amplitude, phase, and mean value agreement. However, rather than visually comparing one curve with another plotted on a common set of axes (speed versus time), a quantitative comparison is made possible by plotting predicted speed against measured speed on a point-by-point basis herein termed a *P-M plot*. To provide insight into the error involved in tidal current predictions, we first consider the comparison of two simple sine waves, each with a period of 12.42 hours. These sine waves represent two hypothetical time series of predicted and measured current speed oscillating around a mean of zero. If the curves are identical (i.e., have the same amplitude, phase, and mean value), the points from the curves will plot along a straight line with 1:1 slope.

Error Estimation - P-M plots formed with actual current data typically show a scatter of points that fall within the ellipse outline, suggesting linear regression as a means for deriving model error estimates. Statistical error estimates are made using linear regression models of predicted (Y) versus observed (X) current values from a given time series. Error is defined as the difference $(Y_i - Y_{ir})$ where Y_i is the i^{th} model predicted current value and Y_{ir} is the i^{th} value obtained from regression of Y on X. Assuming sinusoidal variation and no measurement error, $Y_{ir} = mX_i + b$ is the least squares regressor for differences due to phase error. Differences in this case appear as deviations from a line of best fit to the data. Regression estimates for differences due to total error (phase, amplitude and mean) use $Y_{ir} = X_i$ (m=1, b=0). Differences in this case appear as deviations from the 1:1 line of perfect prediction. Standard error is the root-mean-square (RMS) value of either difference for a sample of size n (i=1...n).

James River Bridge – Certain current calibration data previously reported for the James River HEM-3D model (Boon et al., 1999) are included in this report for completeness. Two examples prepared with model calibration data collected near the James River Bridge's main channel are shown in Figures IV.9 and IV.10. Using the regression methods described above, RMS error estimates of 6.66 cm/s and 4.25 cm/s were determined at surface and bottom, respectively, which are attributed solely to P-M phase differences. Utilizing deviations from the 1:1 line of perfect prediction, additional RMS error estimates of 9.86 cm/s and 5.07 cm/s at surface and bottom were made that are attributed to amplitude and phase differences combined. P-M means were not significantly different from zero in these examples.

The plot of the James River Bridge surface current data (Figure IV.9) reveals a slight counter-clockwise rotation of the best-fit axis relative to the 1:1 axis. The resulting greater spread of points over the predicted current axis indicates that the model slightly over-predicts the surface current in this region. The best-fit axis in Figure IV.10 does not show evidence of any rotation, suggesting that the model neither over-predicts nor under-predicts the bottom current at this location.

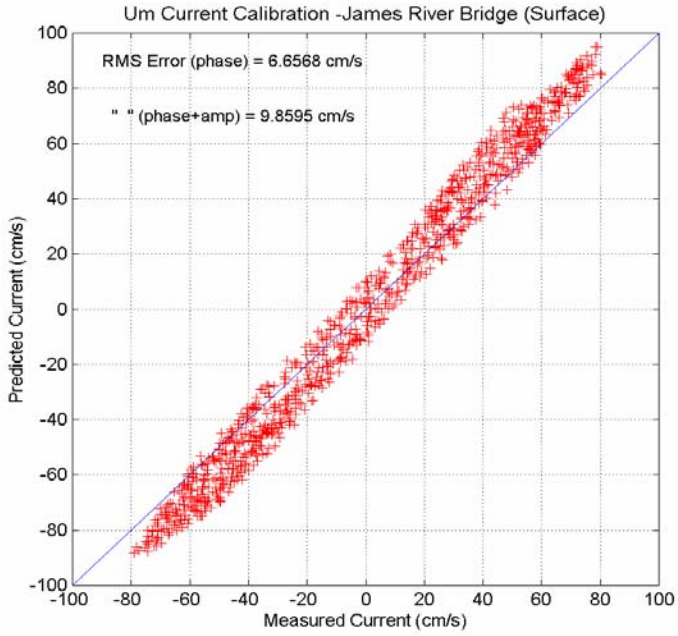

Figure IV.9. Predicted versus measured surface current, James River Bridge

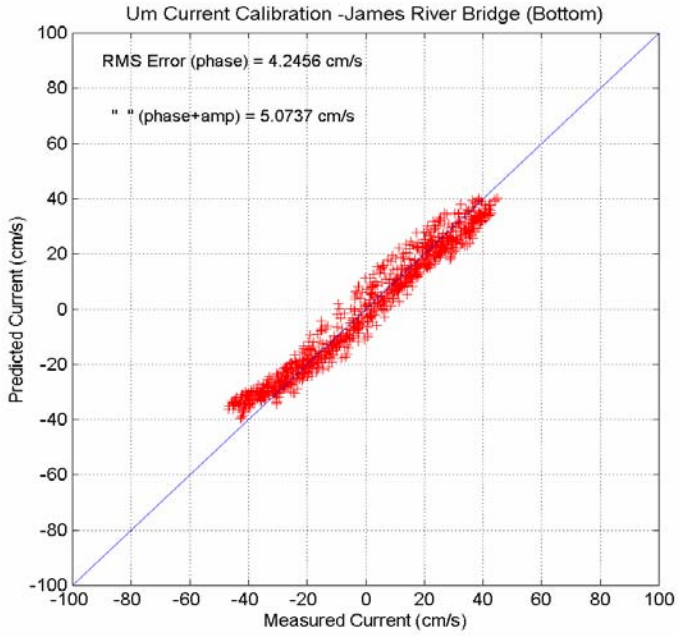

Figure IV.10. Predicted versus measured bottom current, James River Bridge

Craney Island Reach - The ADP current data obtained from the Craney Island Reach in the previous study is shown first as a time series of the surface current in Figure IV.11. As noted in this figure, the model in general tends to under-predict the measured surface current with the greatest difference appearing in the ebb extremes. Figure IV.12a contains a P-M plot showing a clockwise rotation of the ellipse axis as well as an ebb-directed leftward shift in the data centroid (blue circle intersected by dashed best-fit line). The former indicates a slight under-prediction of surface tidal current. Concerning the latter, a centroid shift (negative measured current mean of approximately 6 cm/s combined with a near-zero predicted current mean) suggests that a small non-tidal surface current is present at this location that the model does not account for. The *total* RMS error attributable to both effects (11.20 cm/s) is more than the total RMS error found at the James River Bridge site (9.86 cm/s) but the RMS phase error (6.19 cm/s) is slightly less than that at the James River Bridge site (6.66 cm/s).

Because the ADP current sensor could only be installed at the eastern margin rather than within the main shipping channel, the lowest level obtainable for current measurement corresponds to the middle depth (model layer 4) in the Craney Island Reach. The resulting P-M plot is shown in Figure IV.12b with an RMS phase error of 6.42 cm/s and a total RMS error of 9.53 cm/s. The orientation of the ellipse axis is similar to that of the surface plot and shows that the model also under-predicts the current at the middle depth position. In contrast to the surface plot, both the predicted and measured current means are approximately zero at middle depth. The RMS errors obtained at James River Bridge, Craney Island Reach, and Hospital point are summarized in Table IV.1.

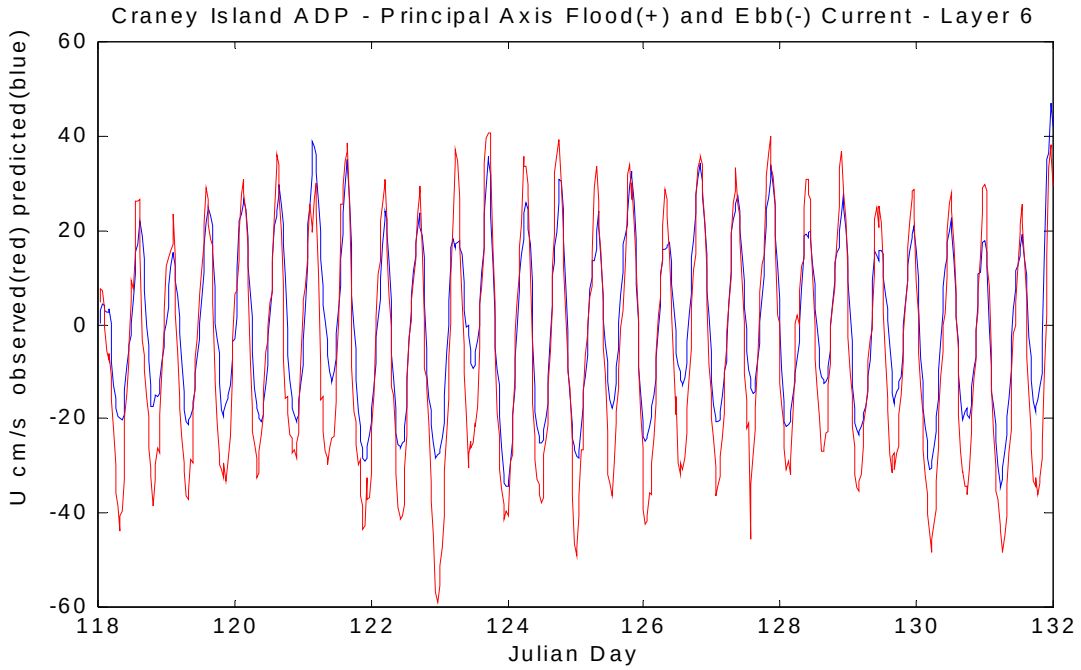

Figure IV.11. Craney Island Reach ADP station - time series of principal axis current in the surface layer (model layer 6), predicted (blue) and measured (red).

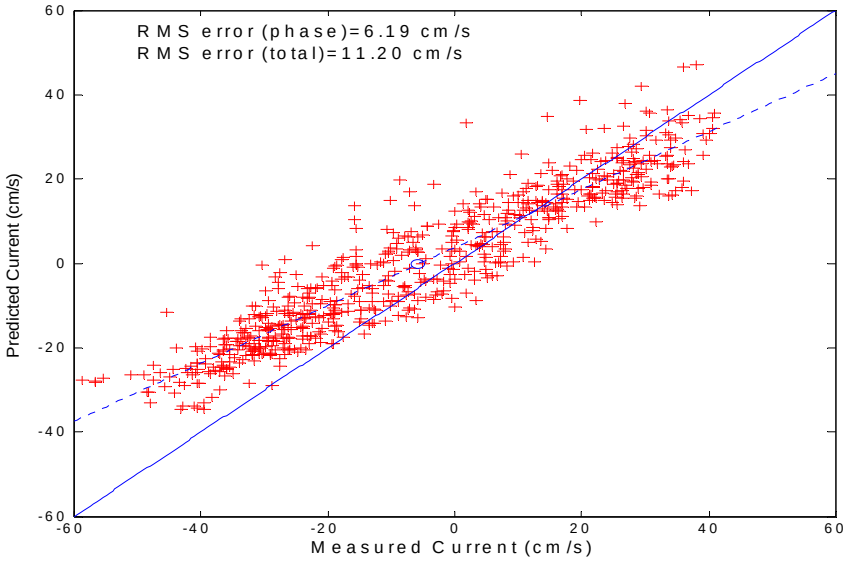

Figure IV.12a. Craney Island Reach ADP station - predicted versus measured current, surface layer (model layer 6).

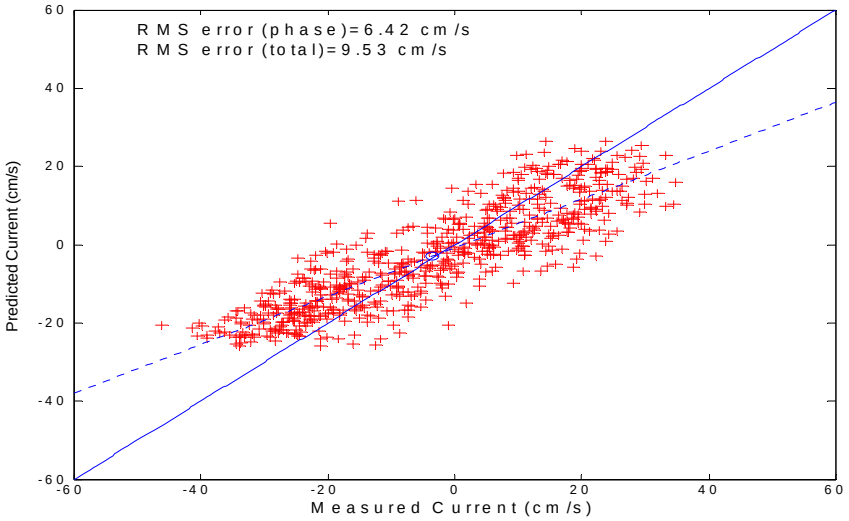

Figure IV.12b. Craney Island Reach ADP station - predicted versus measured current, middle layer (model layer 4).

Table IV.1 – Summary of RMS Error for Predicted Principal Axis Currents at Fixed Locations

Location	RMS Error (Phase)	RMS Error (Total)
James River Bridge (surface)	6.66 cm/s	9.86 cm/s
James River Bridge (bottom)	4.25 cm/s	5.07 cm/s
Craney Island Reach (surface)	6.19 cm/s	11.20 cm/s
Craney Island Reach (middle)	6.42 cm/s	9.53 cm/s
Hospital Point (surface layer)	8.54 cm/s	12.17 cm/s
Hospital Point (middle layer)	4.67 cm/s	10.49 cm/s

Assessment of current verification in the Elizabeth River – The RMS errors presented in Table IV.1 apply to an individual sample of the modeled current randomly drawn from the total population of current values (i.e., the series of principal axis current values predicted at half-hour intervals for approximately 67 tidal cycles). These error estimates are therefore the appropriate ones to consider in model evaluations that utilize the complete series of current values (e.g., volume transport calculations within the Elizabeth River). We note that the Total RMS error increases proceeding into the Elizabeth River.

In addition to the above, there is sometimes a need to examine a certain current phase such as slack water or the peak value of the current (e.g., ship navigation). A visual inspection of the P-M current series shown in Figure IV.11 (Craney Island Reach) raises concern that the modeled current extremes frequently under-predict the measured current extremes at these locations. Pre- and post-deployment calibration data for our current meters were carefully checked and ruled out instrument error as the source of this discrepancy. Yet, as noted above, NOAA current table predictions for maximum flood and ebb current agreed closely with the modeled current extremes. Since NOAA current table predictions are based on the astronomical tide wherein all variation occurs at known tidal frequencies, we concluded that the discrepancies noted must occur primarily at non-tidal frequencies. Least squares harmonic analysis was then applied to the measured current data to examine both tidal and non-tidal current components in more detail.

Harmonic analysis of measured current – Tidal harmonic analysis involves the least squares (LS) fitting of tidal harmonic constituents to a time series of water level or components of current velocity such as the principal axis component. A predicted series based on these constituents is referred to as the *astronomical* tide or current. To fit the principal axis current at Craney Island Reach, we chose 14.5-day current series recorded at 0.5-hour intervals beginning April 25, 2000 (Julian Day 116) and fitted them with nine tidal constituents (M_2, S_2, N_2, K_1, O_1, M_4, S_4, MS_4, M_6). The resulting astronomical current series are presented in Figures IV.13 and IV.14. Figure IV.13 shows the complete measured and fitted series for the Craney Island Reach. At Craney Island Reach the fitted series accounted for 88.2 percent of the measured series variance compared to 74.9 percent at Hospital Point. Adding other tidal constituents such as M_8 to the analysis did not significantly lower the proportion of variance unaccounted for in independent series. To observe the variations in greater detail, a 3-day window beginning on Julian Day 122 is shown for these stations in Figures IV.14. The 3-day segments contain residual curves (difference between measured and fitted curves) that are considered to be estimates of the non-tidal current at Craney Island Reach.

Examining tidal and non-tidal currents at Craney Island Reach, it is apparent that large- and small-scale meteorological and hydrological "events" exert their influence, but without much consistency and amid considerable local variability. This point is illustrated by an event appearing near the end of Julian Day 122 in Figures IV.14. At this time the measured ebb current briefly increased by approximately 10 cm/s relative to the peak ebb of the fitted current at both stations, also previously noted at Hospital Point. However, comparing the non-tidal (residual) current at both stations, it is difficult to recognize a common event amid the numerous oscillations present at relatively high

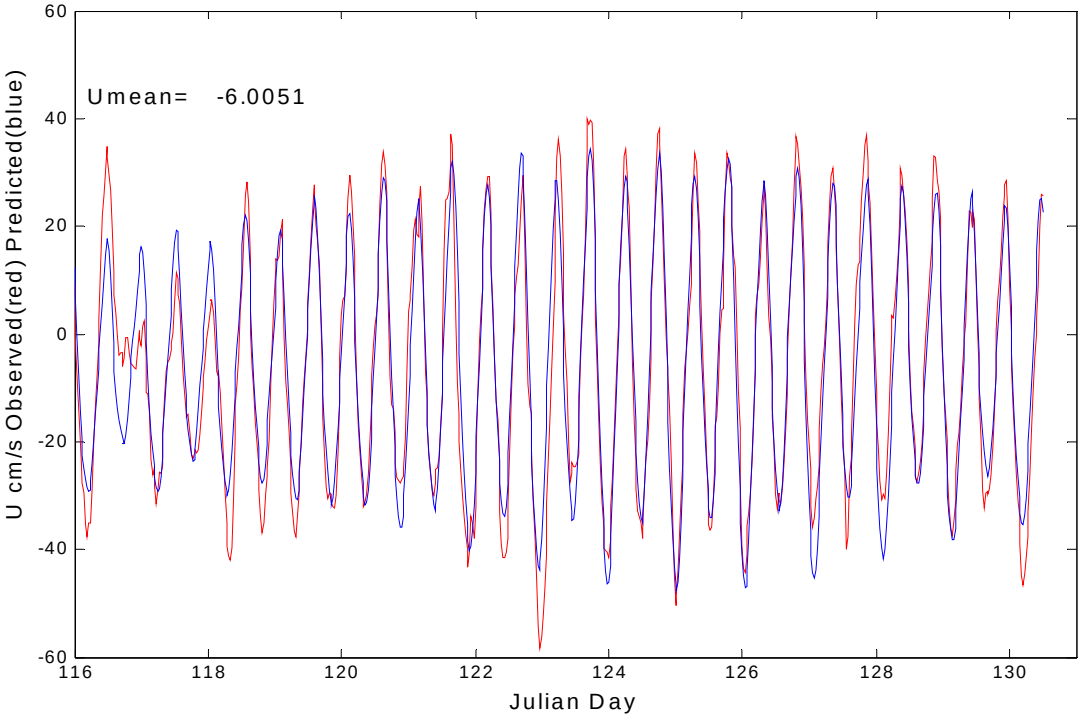

Figure IV.13. Measured (red) and LS-fitted (blue) surface current, Craney Island Reach

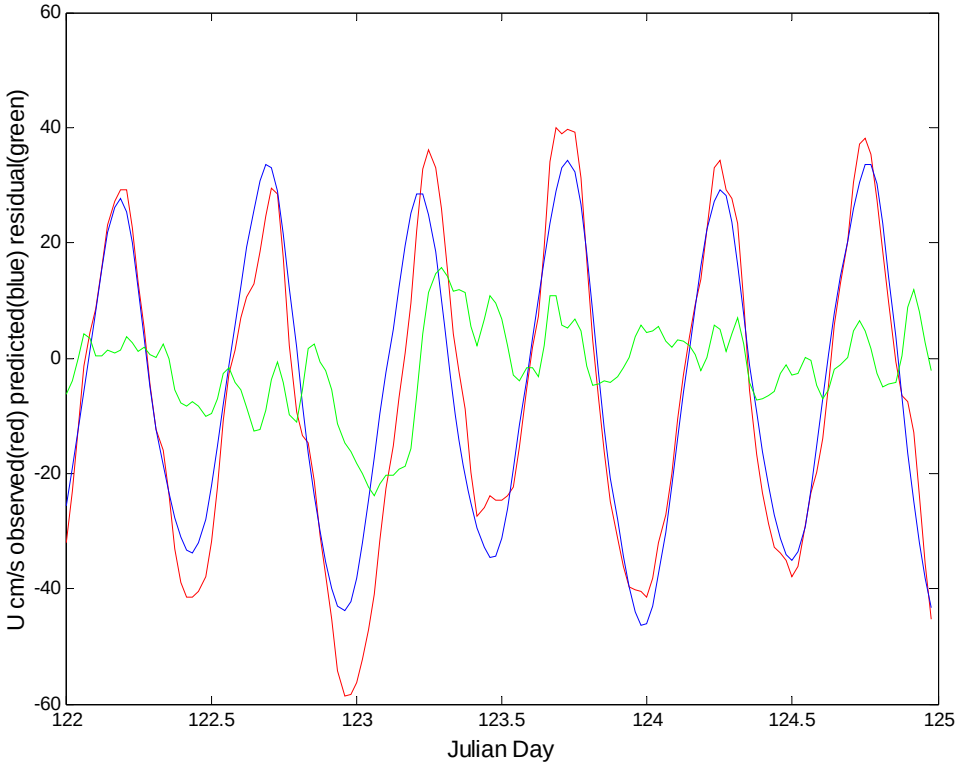

Figure IV.14. Measured (red), LS-fitted (blue), and residual (green) surface current, Craney Island Reach.

frequencies (periods of less than 3 hours with no apparent phase coherence). Finally, analysis shows that model-predicted currents agree very well with astronomical currents independently predicted using nine tidal harmonic constituents obtained from LS-fitting of our observed current series.

The conclusion drawn from the above analysis is that a minor but still significant portion of the variation in current speed observed within the Elizabeth River occurs at supra-tidal frequencies where it exhibits a behavior more random than deterministic. Accordingly, the ability of hydrodynamic or similar types of deterministic models to fully replicate this particular behavior is limited.

IV-1-3 Calibration for salinity

In an estuary, fresh water originating from inland river sources encounters the salt water coming from the ocean to produce the longitudinal salinity gradient. The baroclinic pressure gradient generated from the fresh water at the upstream of the estuary and the salt water at the downstream then serves as the major driving force for the gravitational circulation, in which the fresh water flows seaward while the salt water flows landward. When fresh water overlays salt water, the vertical profile of salinity exhibits stratification as a result of the density difference from surface to bottom. The turbulent mixing induced by forces such as tide, wind, surface waves, internal waves and internal current shear, on the other hand, tends to homogenize property gradients in the water column both in the vertical and the horizontal direction. This turbulent activity thus counter-acts the stratification produced by the buoyancy forces.

Each estuary has its own shoreline, topography, hydrology, freshwater inputs, and turbulent mixing pattern; the salinity distributions are thus different from one another. By carefully examining the salinity pattern, the characteristics of the estuary can be revealed and classified. Salinity is also an excellent natural tracer due to its conservative property. All in all, salinity is an important parameter for estuarine hydrodynamics and thus is selected to assess the performance of the estuarine hydrodynamic model. In this study, salinity time series and spatial distributions are presented from prototype measurement and compared with the model simulation results.

During the months of April – October, 2000, VIMS conducted a total of 12 slack water surveys in the Elizabeth River. Among them, there are 5 consecutive weekly surveys during the months of May and early June, 2000, in which both good data coverage and data quality were obtained. These surveys were conducted on May 1 (Julian day 122), May 8 (Julian day 129), May 15 (Julian day 136), May 22 (Julian day 143), and June 7 (Julian day 159). We have chosen to use the salinity data measured during this intensive period to compare with the modeled results in detail. In each of these surveys, data from 31 stations were collected; 20 in the main-stem and 11 in the tributaries (see Wang et al., 2001). Since the Elizabeth River has a relatively short length (the propagation of tidal phase from the mouth to the head only takes about 25 minutes), the survey vessel was unable to catch the same tidal phase all the time when measuring the salinity. For this

reason, caution needs to be taken when interpreting the survey data. Nevertheless, the data exhibit rich information and reveal key phenomena characterizing the Elizabeth. Several important points are summarized as follows:

(1) Both the spatial and time series plots in the Elizabeth River show an alternately stratified and de-stratified salinity pattern over the course of this 5-week period. During stratified conditions, the salinity difference from the surface to the bottom can reach as much as 10 ppt whereas, during de-stratified conditions, the salinity difference could be reduced to as low as 1-2 ppt. It appears that the de-stratified condition generally coincides with large tidal ranges (> 2.5 feet) while the stratified condition coincides with smaller tidal ranges (< 2.5 feet). For example, May 8 and June 7, both exhibit de-stratified conditions, and both of their tidal ranges are well over 2.5 feet, nearing 3.0 feet. In contrast, May 1, 15, and 22 exhibit stratified conditions, which coincide with small tidal ranges below 2.5 feet. In other cases, we also found that wind forcings, particularly those from the northwest direction, can significantly reduce the stratification in the lower James and Elizabeth Rivers.

(2) Somewhat counter-intuitively, a reverse surface salinity gradient was observed several times in the mouth region of the Elizabeth during the intensive survey period. By “reverse surface salinity gradient”, we mean that the observed surface salinity at the mouth of the Elizabeth is actually lower than the salinity inside the Elizabeth River. This reverse salinity gradient phenomenon, when it occurs, penetrates to about 5-10 km inside the Elizabeth and ends near Lamberts Point. Together with the reverse salinity, there is a relative homogeneous surface salinity zone just upstream of the salinity reverse region. The reverse salinity phenomena in the Elizabeth has not been reported in the literature, but it was documented in Baltimore Harbor where fresh water that originated from the Susquehanna River to the north can intrude into the Harbor and generate the three-layered circulation. In the James/Elizabeth River system, we suspect that during the freshet period in March - May the James River may have provided excess fresh water from upstream that was carried into the Elizabeth mouth, thus producing a reversed salinity gradient. However, the reverse salinity pattern appears to be transient in nature, rather than as a steady phenomena.

The salinity calibration effort benefited greatly from extensive field measurements in the Elizabeth River in year 2000. Figures IV.15 and IV.16 illustrate the model’s capability in reproducing the periodic stratification occurring in the Elizabeth River. These comparisons of observed versus predicted salinity throughout the water column at multiple locations throughout the Elizabeth mainstem and the Southern Branch showed the model's ability to accurately simulate the observed stratification.

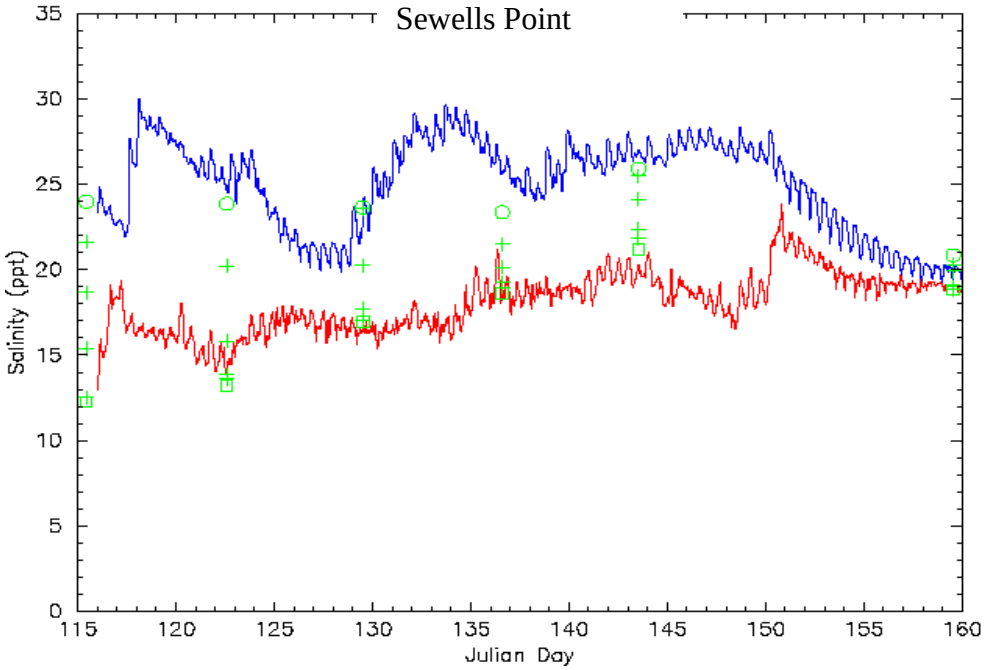

Figure IV.15. Modeled salinity time series at Sewells Point (surface-red, bottom-blue) and measured salinity (surface-squares, middle depth-crosses, bottom-circles).

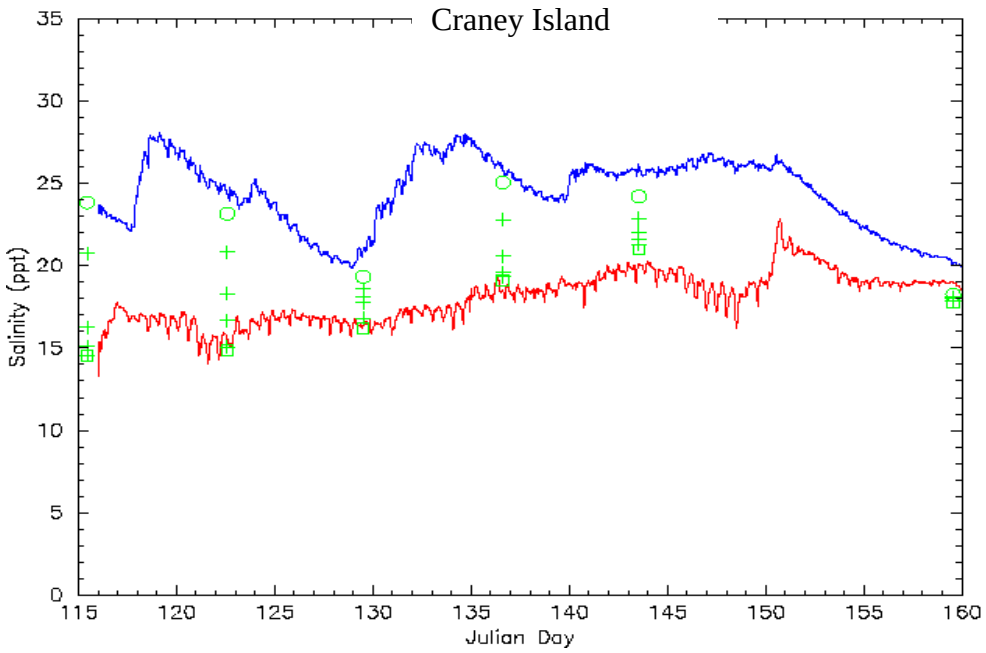

Figure IV.16. Modeled salinity time series at Craney Island (surface-red, bottom-blue) and measured salinity (surface-squares, middle depth-crosses, bottom-circles).

IV-1-4 Calibration for suspended sediments

In the latest HEM-3D model, the ECOM-SED sediment transport module was incorporated into the EFDC hydrodynamic model. ECOM-SED can predict: (1) the suspended sediment concentration, (2) sediment bed elevation changes, (3) flux at the sediment-water column interface, and (4) the change in sediment bed composition. The sediment types used for model simulation are cohesive (< 75 μm) and non-cohesive (75-500 μm) sediments. The Van Rijn procedure is used for non-cohesive sediment suspension and the bed armoring procedure is used to address particle-size heterogeneity. To compute the rate of erosion/resuspension, an erosion formulation as a function of shear stress is utilized:

$$E = M\left(\frac{\tau_b(t)}{\tau_c} - 1\right) \qquad if\ (\tau_b > \tau_c)$$

$$E = 0 \qquad if\ (\tau_b \le \tau_c) \qquad \text{(IV-1)}$$

Where τ_c is the instantaneous critical shear stress, τ_b is the bottom stress, and M is an erosion rate parameter, which was calibrated for this study to be 0.0004 g/m^2/s.

In this study, extensive comparisons of TSS model predictions with CBP measurements were conducted. Time series showing model predictions, with and without the expansion, against CBP measurements at 21 stations spanning the Lower James and Elizabeth Rivers are shown in Appendix B, Figures B1 through B12. These figures show that, overall, model predictions match the observed data well. It should be noted that peaks in the TSS model predictions are difficult to compare since the monitoring surveys are generally conducted during calm weather when lower TSS levels are observed. The close agreement of model predictions for TSS with and without the expansion suggests the minimal impact that the CIEE construction can have on TSS levels, both in the near-field and far-field.

In the early stages of the present study, the model grid was modified in the region around Craney Island in order to align model grid cells with the exact outline of the eastward expansion adapted in August 2007 by the Craney Island Design Partners after they received results from ship mooring studies for the CIEE design (see Chapter I). The new grid, previously Cartesian in the CIEE vicinity, was modified to orthogonally curvilinear. It was then necessary to confirm that the model maintained calibration through this grid modification process. This verification was done by comparing model predictions of total suspended solids (TSS) and salinity from both the old and new grids extensively. Predictions using the old and new grids were compared at the CBP stations shown in Figure IV.17 for the period March 2001 to June 2001 and the comparison for the CBP Station just east of Craney Island (i.e., LE5.6) is shown in Figure IV.18. Time series comparisons for all stations shown in Figure IV.17 are shown in Appendix A, Figures A1 to A22. Inspection of the time series at these 22 CBP stations shows that model predictions of both salinity and TSS levels using the new grid were in close agreement with model predictions using the old grid throughout the Hampton Roads and Elizabeth River regions.

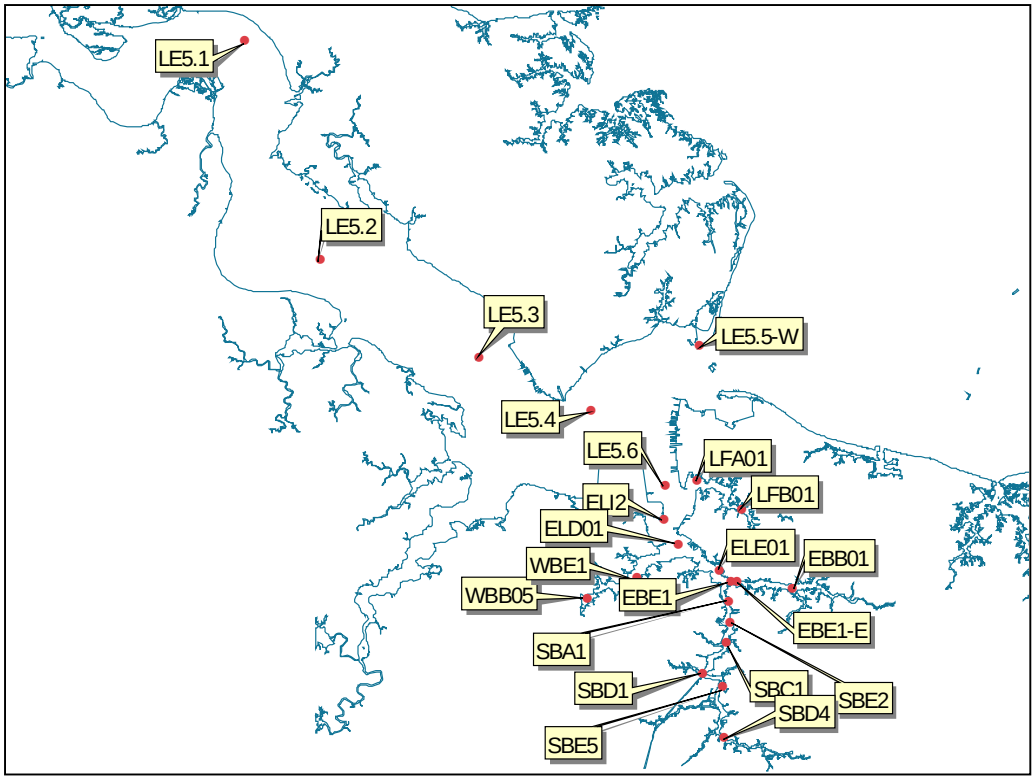

Figure IV.17. CBP stations in lower James and Elizabeth Rivers at which old grid model results were compared to new grid model results

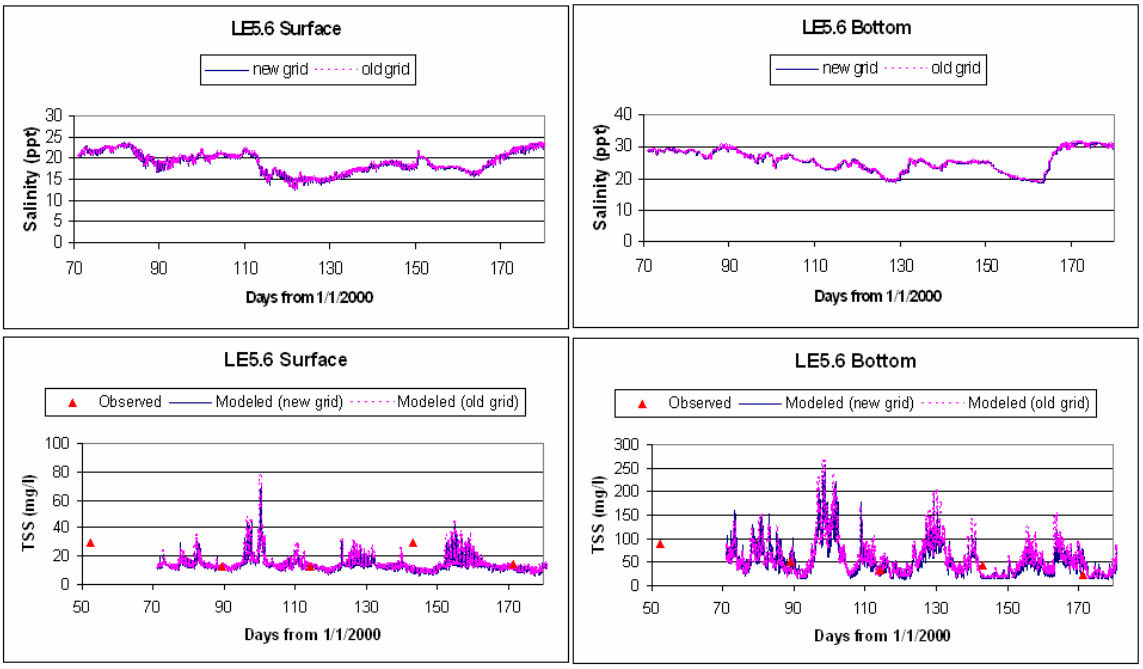

Figure IV.18. Comparison of prediction from old grid and new grid surface and bottom salinity and TSS at CBP station LE5.6

IV-2 Calibration of Water Quality Model

The overall objective of the model validation procedure is to calibrate the water quality model to the observed data utilizing a set of model coefficients and parameters that are consistent with field measurements and are within the general ranges of values accepted by the modeling community as reported in the literature.

The main steps involved in the calibration of the water quality model are: the appropriate boundary condition has to be chosen, the verified external nutrient loads have to be included, the correct initial condition has to be specified, and the suitable parameter values have to be estimated.

IV-2-1 Boundary condition

As was done for the salinity calibration, the water quality monitoring data from Station CB8.1 of the Chesapeake Bay Program (CBP) were used for the water quality open boundary condition (Figure IV.19). The monthly water quality parameters at both the surface and bottom are available from 1984 to present. Table IV.11 shows the parameters measured. The same parameters presented at CB8.1 also applied to all other stations in the Chesapeake Bay measured by CBP.

For the boundary condition, the CBP Station 8.1 data is available semi-monthly during the period from spring to fall and monthly during the winter at both the surface and bottom. The middle layers were specified from the linear interpolation between the layers which were measured. The daily values were interpolated between the measured period either semi-monthly or monthly. The present water quality model is configured such that the freshwater discharge and nutrient loadings input are specified as lateral input. The open boundary condition for the hydrodynamic model was forced by the averaged measured tide of the NOAA tidal station at Sewells Pt. and at the Chesapeake Bay Bridge Tunnel.

IV-2-2 External loading

The non-point nutrient loadings from the watershed discharged to the James and Elizabeth Rivers were obtained from the Chesapeake Bay Program's Watershed Phase V Model. Nonpoint source loads enter the water quality model through specification of the loading at model grid cells adjacent to the land. The procedure involved mapping of the hydrodynamic model grid with the watershed segment. The point source inputs for the Elizabeth River were provided by the Tidewater Regional Office of DEQ, as shown in Figure III.11 and Table II.1. These point source inputs are specified at the surface of the model cell at the location where it discharged. The external nutrient loads also include the atmospheric loads that are generated by the HSPF watershed PhaseV model and are specified at each surface cell of the model. The time increment input value of loading was derived through the interpolation of point source and non-point source daily loads.

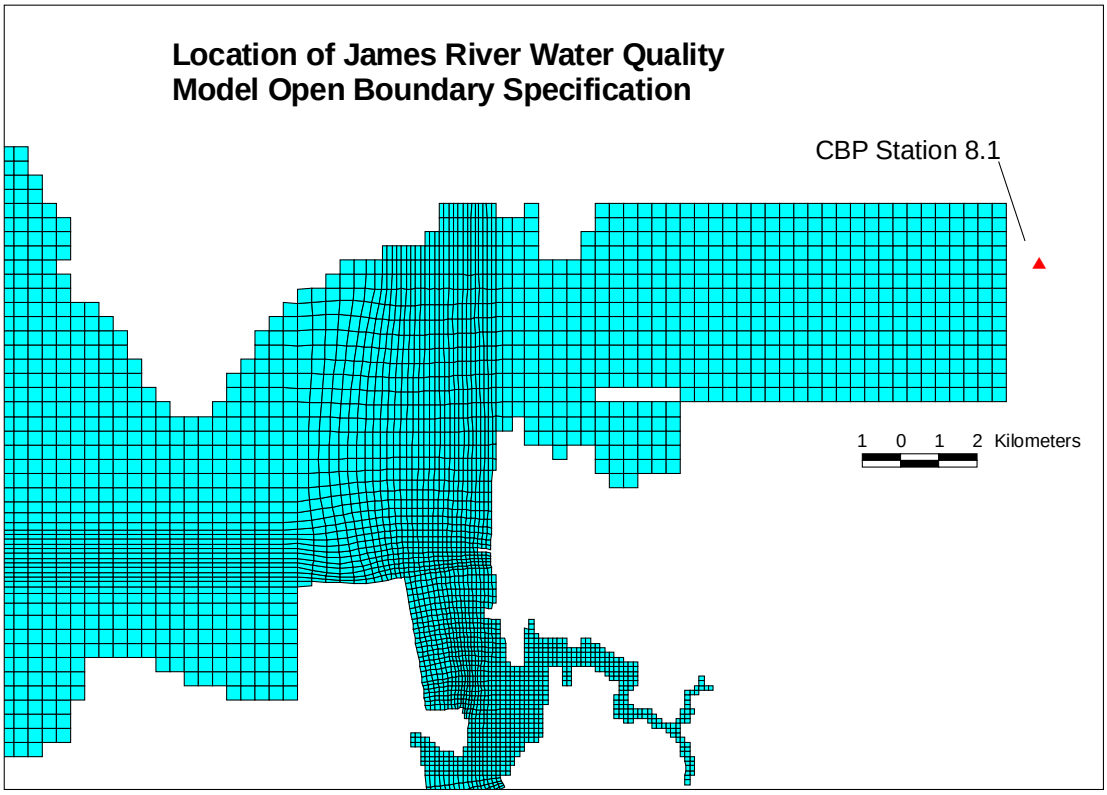

Figure IV.19. Location of CBP Station 8.1 along eastern portion of model domain.

IV-2-3 Initial condition

The initial condition was specified using the long-term averaged data measured by CBP for the first simulation. Within the Elizabeth, the initial condition for each cell was specified through linear interpolation between two adjacent CBP stations. Whenever only surface water data were available, the same value was specified for each layer vertically for those cells. Outside of the Elizabeth, the initial condition was specified based on the linear interpolation between CBP Stations LE5.5-W and CB8.1. The values of all computed model cell output from prior model results were used to specify a suitable initial condition.

IV-2-4 Estimation of parameters

Most of the parameters in the HEM-3D water quality model were adopted from the default parameters for the Chesapeake Bay (Cerco and Cole, 1994). The parameters used in the water column of this study are listed in Tables IV.4 to IV.9. The modification of parameters depended on the comparison with measured data or unique features of the Elizabeth. The remaining parameters used in the sediment flux are listed in Table IV.10.

Table IV.2. Model state variables in the eutrophication water quality model

Parameter	symbol
Temperature	T
Salinity	S
Total Suspended Solids	TSS
Cyanobacteria	B_c
Diatoms	B_d
Green Algae	B_g
Refractory Particulate Organic Carbon	RPOC
Labile Particulate Organic Carbon	LPOC
Dissolved Organic Carbon	DOC
Refractory Particulate Organic Nitrogen	RPON
Labile Particulate Organic Nitrogen	LPON
Dissolved Organic Nitrogen	DON
Ammonium Nitrogen	NH_4
Nitrate+nitrite Nitrogen	NO_3
Refractory Particulate Organic Phosphorus	RPOP
Labile Particulate Organic Phosphorus	LPOP
Dissolved Organic Phosphorus	DOP
Total Phosphate	PO_4t
Particulate Biogenic Silica	SU
Available Silica	SA
Chemical Oxygen Demand	COD
Dissolved Oxygen	DO

Table IV.3. Model state variables and fluxes in the benthic sediment flux model

Parameters
particulate organic carbon in Layer 2 (G_1, G_2 and G_3 classes)
particulate organic nitrogen in Layer 2 (G_1, G_2 and G_3 classes)
particulate organic phosphorus in Layer 2 (G_1, G_2 and G_3 classes)
particulate biogenic silica in Layer 2
sulfide (salt water) or methane (fresh water) in Layers 1 and 2
ammonium nitrogen in Layers 1 and 2
nitrate nitrogen in Layers 1 and 2
phosphate phosphorus in Layers 1 and 2
available silica in Layers 1 and 2
ammonium nitrogen flux
nitrate nitrogen flux
phosphate flux
silica flux
sediment oxygen demand
release of chemical oxygen demand
sediment temperature
benthic microalgae

Table IV.4. Parameters related to algae in the water column

parameter	description	value	unit
PM_c	maximum growth rate of algae group 1	250	g C g^{-1} Chl d^{-1}
PM_d	maximum growth rate of algae group 2	300	g C g^{-1} Chl d^{-1}
PM_g	maximum growth rate of algae group 3	300	g C g^{-1} Chl d^{-1}
KHN_x	half-saturation constant of N uptake by algae	0.01	g N m^{-3}
KHP_x	half-saturation constant of P uptake by algae	0.001	g P m^{-3}
KHS	half-saturation constant of Si uptake by diatoms	0.05	g Si m^{-3}
KHRx	half-saturation constant of DO for algal excretion of DOC	0.5	g O_2 m^{-3}
α_c	initial slope of production vs. irradiance relationship for algal group 1	8	g C g^{-1} Chl (E m^{-2})$^{-1}$
α_d	initial slope of production vs. irradiance relationship for algal group 2	8	g C g^{-1} Chl (E m^{-2})$^{-1}$
α_g	initial slope of production vs. irradiance relationship for algal group 3	8	g C g^{-1} Chl (E m^{-2})$^{-1}$
a_1	background light attenuation coefficient	0.735	m^{-1}
a_2	light attenuation coefficient due to total suspended solid	0.018	m^2 per g TSS
a_3	light attenuation coefficient due to algae	0.06	m^2 per mg CHL
$CCHL_x$	C-to-CHL ratio in algae	60.0	g C per g CHL
TM_c	optimum T for algal group 1 growth	29.0	°C
TM_d	optimum T for algal group 2 growth	16.0	°C
TM_g	optimum T for algal group 3 growth	25.0	°C
$KTG1_c$	effect of T below optimum T on algal Group 1 growth	0.006	$°C^{-2}$
$KTG2_c$	effect of T above optimum T on algal Group 1 growth	0.006	$°C^{-2}$
$KTG1_d$	effect of T below optimum T on algal Group 2 growth	0.004	$°C^{-2}$
$KTG2_d$	effect of T above optimum T on algal Group 2 growth	0.006	$°C^{-2}$
$KTG1_g$	effect of T below optimum T on algal Group 3 growth	0.012	$°C^{-2}$
$KTG2_g$	effect of T above optimum T on algal Group 3 growth	0.007	$°C^{-2}$
BMR_c	basal metabolism rate of algae group 1 at reference T	0.02	day^{-1}
BMR_d	basal metabolism rate of algae group 2 at reference T	0.04	day^{-1}
BMR_g	basal metabolism rate of algae group 3 at reference T	0.02	day^{-1}
PRR_c	predation rate of algae group 1 at reference T	0.02	day^{-1}
PRR_d	predation rate of algae group 2 at reference T	0.15	day^{-1}
PRR_g	predation rate of algae group 3 at reference T	0.25	day^{-1}
KTB_x	effect of T on basal metabolism of algae	0.069	$°C^{-1}$
TR_x	reference T for basal metabolism of algae	20.0	°C
WS_c	settling velocity for algal group 1	0.1	m day^{-1}

Table IV.4 (cont'd)

WS_d	settling velocity for algal group 2	0.2	m day^{-1}
WS_g	settling velocity for algal group 3	0.1	m day^{-1}

Table IV.5. Parameters related to organic carbon in the water column

Parameters	description	value	units
FCRP	fraction of predated algal C produced as RPOC	0.20	none
FCLP	fraction of predated algal C produced as LPOC	0.65	none
FCDP	fraction of predated algal C produced as DOC	0.15	none
FCD_x	fraction of metabolized C by algae produced as DOC	0.0	none
KHR_x	half-saturation constant of DO for algal excretion of DOC	0.5	g O_2 m^{-3}
KHO_{DOC}	half-saturation constant of DO for oxic respiration of DOC	0.5	g O_2 m^{-3}
K_{RC}	minimum respiration rate of RPOC	0.005	day^{-1}
K_{LC}	minimum respiration rate of LPOC	0.075	day^{-1}
K_{DC}	minimum respiration rate of DOC	0.020	day^{-1}
K_{Rcalg}	constant relating respiration of RPOC to algal biomass	0.0	day^{-1} per g C m^{-3}
K_{Lcalg}	constant relating respiration of LPOC to algal biomass	0.0	day^{-1} per g C m^{-3}
K_{Dcalg}	constant relating respiration of DOC to algal biomass	0.0	day^{-1} per g C m^{-3}
KT_{HDR}	effect of T on hydrolysis/ mineralization of POM/DOM	0.069	$°C^{-1}$
KT_{MNL}	effect of T on hydrolysis/ mineralization of POM/DOM	0.069	$°C^{-1}$
TR_{HDR}	reference T for hydrolysis of POM	20.0	°C
TR_{MNL}	reference T for mineralization of DOM	20.0	°C
$KHNDN_N$	half-saturation constant of NO_{23} for denitrification	0.1	g N m^{-3}
AANOX	ratio of denitrification to oxic DOC respiration rate	0.5	none

Table IV.6. Parameters related to nitrogen in the water column

Parameters	description	value	units
FNRP	fraction of predated algal N produced as RPON	0.15	none
FNLP	fraction of predated algal N produced as LPON	0.25	none
FNDP	fraction of predated algal N produced as DON	0.20	none
FNIP	fraction of predated algal N produced as NH_4	0.40	none
FNR	fraction of metabolized algal N produced as RPON	0.05	none
FNL	fraction of metabolized algal N produced as LPON	0.20	none
FND	fraction of metabolized algal N produced as DON	0.20	none
FNI	fraction of metabolized algal N produced as NH_4	0.55	none
ANC_{min}	minimum N-to-C ratio in algae	0.135	g N per g C
ANC_{max}	maximum N-to-C ratio in algae	0.20	g N per g C
ANDC	mass of NO_{23}-N consumed per mass DOC oxidized	0.933	g N per g C
K_{RN}	minimum hydrolysis/mineralization rate of RPON	0.005	day^{-1}
K_{LN}	minimum hydrolysis/mineralization rate of LPON	0.075	day^{-1}
K_{DN}	minimum hydrolysis/mineralization rate of DON	0.015	day^{-1}
K_{Rnalg}	constant relating hydrolysis/mineralization of RPON to algal biomass	0.0	day^{-1} per g N m^{-3}
K_{Lnalg}	constant relating hydrolysis/mineralization of LPON to algal biomass	0.0	day^{-1} per g N m^{-3}
K_{Dnalg}	constant relating hydrolysis/mineralization of DON to algal biomass	0.0	day^{-1} per g N m^{-3}
$KHDO_{NIT}$	half-saturation constant of DO for nitrification	1.0	g O_2 m^{-3}
KHN_{NIT}	half-saturation constant of NH_4 for nitrification	1.0	g N m^{-3}
NT_M	maximum nitrification at optimum T	0.007	day^{-1}
KT_{NT1}	effect of T below optimum T on nitrification rate	0.0045	$°C^{-2}$
KT_{NT1}	effect of T above optimum T on nitrification rate	0.0045	$°C^{-2}$
TM_{NT}	optimum T for nitrification rate	27.0	°C

Table IV.7. Parameters related to phosphorus in the water column

Parameter	description	value	units
FPRP	fraction of predated algal P produced as RPOP	0.03	none
FPLP	fraction of predated algal P produced as LPOP	0.07	none
FPDP	fraction of predated algal P produced as DOP	0.40	none
FPIP	fraction of predated algal P produced as DIP	0.50	none
FPR_x	fraction of metabolized P by algae produced as RPOP	0.0	none
FPL_x	fraction of metabolized P by algae produced as LPOP	0.0	none
FPD_x	fraction of metabolized P by algae produced DOP	0.25	none
FPI_x	fraction of metabolized P by algae produced DOP	0.75	none
APCMIN	minimum P-to-C ratio in algae	0.0125	g P per g C
APCMAX	maximum P-to-C ratio in algae	0.0175	g P per g C
PO4DMAX	maximum PO4d beyond which APC = APCMAX	0.01	g P m^{-3}
K_{RP}	minimum hydrolysis/mineralization rate of RPOP	0.005	day^{-1}
K_{LP}	minimum hydrolysis/mineralization rate of LPOP	0.075	day^{-1}
K_{DP}	minimum hydrolysis/mineralization rate of DOP	0.1	day^{-1}
K_{Rpalg}	constant relating hydrolysis/ mineralization of RPOP to algal biomass	0.0	day^{-1} per g P m^{-3}
K_{Lpalg}	constant relating hydrolysis/ mineralization of LPOP to algal biomass	0.0	day^{-1} per g P m^{-3}
K_{Dpalg}	constant relating hydrolysis/ mineralization of DOP to algal biomass	0.0	day^{-1} per g P m^{-3}

Table IV.8. Parameters related to silica in the water column

Parameter	description	value	units
FSA	fraction of predated diatom Si as SA	0.0	none
ASC_d	Si-to-C ratio in diatoms	0.5	g Si per g C
K_{SU}	dissolution rate of SU at reference T	0.025	day^{-1}
KT_{SUA}	effect of T on dissolution of SU	0.092	$°C^{-1}$
TR_{SUA}	reference T for dissolution of SU	20.0	°C

Table IV.9. Parameters related to chemical oxygen demand and dissolved oxygen in the water column

Parameters	description	value	units
KHO_{COD}	half-saturation constant of DO for oxidation of COD	1.5	g O_2 m^{-3}
K_{CD}	oxidation rate of COD at reference temperature	20.0	day^{-1}
KT_{COD}	effect of T on oxidation of COD	0.041	$°C^{-1}$
TR_{COD}	reference T for oxidation of COD	20.0	°C
K_{RDO}	reaeration coefficient	2.4	m day^{-1}
AOCR	mass DO consumed per mass C respired by algae	2.67	g O_2 per g C
AONT	mass DO consumed per mass NH_4-N nitrified	4.33	g O_2 per g N

Table IV.10. Parameters used in the sediment flux model

parameter	description	value	units
HSEDALL	depth of sediment	10	cm
DIFFT	heat diffusion coefficient between water column and sediment	0.0018	cm^2 sec^{-1}
SALTSW	salinity for dividing fresh and saltwater for SOD kinetics (sulfide in saltwater or methane in freshwater) and for PO_4 sorption coefficients	1.0	ppt
SALTND	salinity for dividing fresh or saltwater for nitrification/denitrification rates (larger values for freshwater)	1.0	ppt
FRPPH1(1)	fraction of POP in algal group No. 1 routed into G_1 class	0.65	none
FRPPH1(2)	fraction of POP in algal group No. 1 routed into G_2 class	0.255	none
FRPPH1(3)	fraction of POP in algal group No. 1 routed into G_3 class	0.095	none
FRPPH2(1)	fraction of POP in algal group No. 2 routed into G_1 class	0.65	none
FRPPH2(2)	fraction of POP in algal group No. 2 routed into G_2 class	0.255	none
FRPPH2(3)	fraction of POP in algal group No. 2 routed into G_3 class	0.095	none
FRPPH3(1)	fraction of POP in algal group No. 3 routed into G_1 class	0.65	none

Table IV.10 (cont'd)

FRPPH3(2)	fraction of POP in algal group No. 3 routed into G_2 class	0.255	none
FRPPH3(3)	fraction of POP in algal group No. 3 routed into G_3 class	0.095	none
FRNPH1(1)	fraction of PON in algal group No. 1 routed into G_1 class	0.65	none
FRNPH1(2)	fraction of PON in algal group No. 1 routed into G_2 class	0.28	none
FRNPH1(3)	fraction of PON in algal group No. 1 routed into G_3 class	0.07	none
FRNPH2(1)	fraction of PON in algal group No. 2 routed into G_1 class	0.65	none
FRNPH2(2)	fraction of PON in algal group No. 2 routed into G_2 class	0.28	none
FRNPH2(3)	fraction of PON in algal group No. 2 routed into G_3 class	0.07	none
FRNPH3(1)	fraction of PON in algal group No. 3 routed into G_1 class	0.65	none
FRNPH3(2)	fraction of PON in algal group No. 3 routed into G_2 class	0.28	none
FRNPH3(3)	fraction of PON in algal group No. 3 routed into G_3 class	0.07	none
FRCPH1(1)	fraction of POC in algal group No. 1 routed into G_1 class	0.65	none
FRCPH1(2)	fraction of POC in algal group No. 1 routed into G_2 class	0.255	none
FRCPH1(3)	fraction of POC in algal group No. 1 routed into G_3 class	0.095	none
FRCPH2(1)	fraction of POC in algal group No. 2 routed into G_1 class	0.65	none
FRCPH2(2)	fraction of POC in algal group No. 2 routed into G_2 class	0.255	none
FRCPH2(3)	fraction of POC in algal group No. 2 routed into G_3 class	0.095	none
FRCPH3(1)	fraction of POC in algal group No. 3 routed into G_1 class	0.65	none
FRCPH3(2)	fraction of POC in algal group No. 3 routed into G_2 class	0.255	none
FRCPH3(3)	fraction of POC in algal group No. 3 routed into G_3 class	0.095	none
KPDIAG(1)	reaction (decay) rates for G_1 class POP at 20°C	0.035	day^{-1}
KPDIAG(2)	reaction (decay) rates for G_2 class POP at 20°C	0.0018	day^{-1}
KPDIAG(3)	reaction (decay) rates for G_3 class POP at 20°C	0.0	day^{-1}
DPTHTA(1)	constant for T adjustment for G_1 class POP decay	1.10	none
DPTHTA(2)	constant for T adjustment for G_2		

Table IV.10 (cont'd)

	class POP decay	1.15	none
KNDIAG(1)	reaction (decay) rates for G_1 class PON at 20°C	0.035	day^{-1}
KNDIAG(2)	reaction (decay) rates for G_2 class PON at 20°C	0.0018	day^{-1}
KNDIAG(3)	reaction (decay) rates for G_3 class PON at 20°C	0.0	day^{-1}
DNTHTA(1)	constant for T adjustment for G_1 class PON decay	1.10	none
DNTHTA(2)	constant for T adjustment for G_2 class PON decay	1.15	none
KCDIAG(1)	reaction (decay) rates for G_1 class POC at 20°C	0.035	(day^{-1})
KCDIAG(2)	reaction (decay) rates for G_2 class POC at 20°C	0.0018	(day^{-1})
KCDIAG(3)	reaction (decay) rates for G_3 class POC at 20°C	0.0	(day^{-1})
DCTHTA(1)	constant for T adjustment for G_1 class POC decay	1.10	none
DCTHTA(2)	constant for T adjustment for G_2 class POC decay	1.15	none
KSI	1^{st}-order reaction (dissolution) rate of PSi at 20°C	0.5	day^{-1}
THTASI	constant for T adjustment for PSi dissolution	1.1	none
M1	solid concentrations in Layer 1	0.5	$kg\ l^{-1}$
M2	solid concentrations in Layer 2	0.5	$kg\ l^{-1}$
THTADP	constant for T adjustment for diffusion coefficient for particle mixing	1.117	none
THTADD	constant for T adjustment for diffusion coefficient for dissolved phase	1.08	none
KAPPNH4F	optimum reaction velocity for nitrification in Layer 1 for freshwater	0.20	$m\ day^{-1}$
KAPPNH4S	optimum reaction velocity for nitrification in Layer 1 for saltwater	0.14	$m\ day^{-1}$
THTANH4	constant for T adjustment for nitrification	1.08	none
KMNH4	half-saturation constant of NH_4 for nitrification	1500.0	$mg\ N\ m^{-3}$
KMNH4O2	half-saturation constant of DO for nitrification	1.0	$g\ O_2\ m^{-3}$
PIENH4	partition coefficient for NH_4 in both layers	1.0	$per\ kg\ l^{-1}$
KAPPNO3F	reaction velocity for denitrification in Layer 1 at 20°C for freshwater	0.3	$m\ day^{-1}$
KAPPNO3S	reaction velocity for denitrification		

Table IV.10 (cont'd)

	in Layer 1 at 20°C for saltwater	0.125	m day^{-1}
K2NO3	reaction velocity for denitrification in Layer 2 at 20°C	0.25	m day^{-1}
THTANO3	constant for T adjustment for denitrification	1.08	none
KAPPD1	reaction velocity for dissolved H_2S oxidation in Layer 1 at 20°C	0.2	m day^{-1}
KAPPP1	reaction velocity for particulate H_2S oxidation in Layer 1 at 20°C	0.4	m day^{-1}
PIE1S	partition coefficient for H_2S in Layer 1	100.0	per kg l^{-1}
PIE2S	partition coefficient for H_2S in Layer 2	100.0	per kg l^{-1}
THTAPD1	constant for T adjustment for both dissolved & particulate H_2S oxidation	1.08	none
KMHSO2	constant to normalize H_2S oxidation rate for oxygen	4.0	g O_2 m^{-3}
CSISAT	saturation concentration of Si in the pore water	40000.0	mg Si m^{-3}
DPIE1SI	incremental partition coefficient for Si in Layer 1	10.0	per kg l^{-1}
PIE2SI 2	partition coefficient for Si in Layer 2	100.0	per kg l^{-1}
O2CRITSI	critical DO concentration for Layer 1 incremental Si sorption	1.0	g O_2 m^{-3}
KMPSI	half-saturation constant of PSi for Si dissolution	5×10^7	mg Si m^{-3}
JSIDETR	detrital flux of PSi to account for PSi settling to the sediment that is not associated with algal flux of PSi	100.0	mg Si m^{-2} day^{-1}
DPIE1PO4F*	incremental partition coefficient for PO_4 in Layer 1 for freshwater	3000.0	per kg l^{-1}
DPIE1PO4S*	incremental partition coefficient for PO_4 in Layer 1 for saltwater	300.0	per kg l^{-1}
PIE2PO4*	partition coefficient for PO_4 in Layer 2	100.0	per kg l^{-1}
O2CRIT	critical DO concentration for Layer 1 incremental PO_4 sorption	2.0	g O_2 m^{-3}
KMO2DP	half-saturation constant of DO for particle mixing	4.0	g O_2 m^{-3}
TEMPBEN	temperature at which benthic stress accumulation is reset to zero	10.0	°C
KBENSTR	1^{st}-order decay rate for benthic stress	0.03	day^{-1}
KLBNTH	ratio of bio-irrigation to bioturbation	0.0	none
DPMIN	minimum diffusion coefficient for particle mixing	3×10^{-6}	m^2 day^{-1}
KAPPCH4	reaction velocity for dissolved CH_4 oxidation in Layer 1 at 20°C	0.2	m day^{-1}

Table IV.10 (con't)

THTACH4	constant for T adjustment for dissolved CH_4 oxidation	1.08	none
VSED	net burial (sedimentation) rate	0.25	cm yr^{-1}
VPMIX	diffusion coefficient for particle mixing	1.2×10^{-4}	m^2 day^{-1}
VDMIX	diffusion coefficient in pore water	0.001	m^2 day^{-1}
WSCNET	net settling velocity for algal group 1	0.1	m day^{-1}
WSDNET	net settling velocity for algal group 2	0.3	m day^{-1}
WSGNET	net settling velocity for algal group 3	0.1	m day^{-1}

Table IV.11. Water quality parameters in CBP monitoring data

Parameters	**symbol**	**units**
temperature	T	degrees C
salinity	S	ppt
dissolved oxygen	DO	mg/l
chlorophyll-a	CHL	μg/l
total suspended solids	TSS	mg/l
secchi depth		m
particulate carbon	PC	mg/l
dissolved organic carbon	DOC	mg/l
particulate nitrogen	PN	mg/l
total dissolved nitrogen	TDN	mg/l
ammonium nitrogen	NH_4	mg/l
nitrate+nitrite nitrogen	NO_3	mg/l
particulate phosphorus	PP	mg/l
total dissolved phosphorus	TDP	mg/l
dissolved phosphate	PO_4d	mg/l
particulate inorganic phosphorus	PIP	mg/l
particulate biogenic silica	SU	mg/l
dissolved silica	SA	mg/l

IV-2-5 Model Calibration Results

Calibration of the water quality model took place by comparison of time series plots of selected water quality parameters with CBP observations at 3 key CBP stations spanning the CIEE region. These stations are LE5.5 in the eastern portion of Lower James River, LE5.6 just east of Craney Island inside the Elizabeth River, and ELI2 to the south of Craney Island, further upstream into the Elizabeth River. The locations of the stations are shown in Figure IV.20 below.

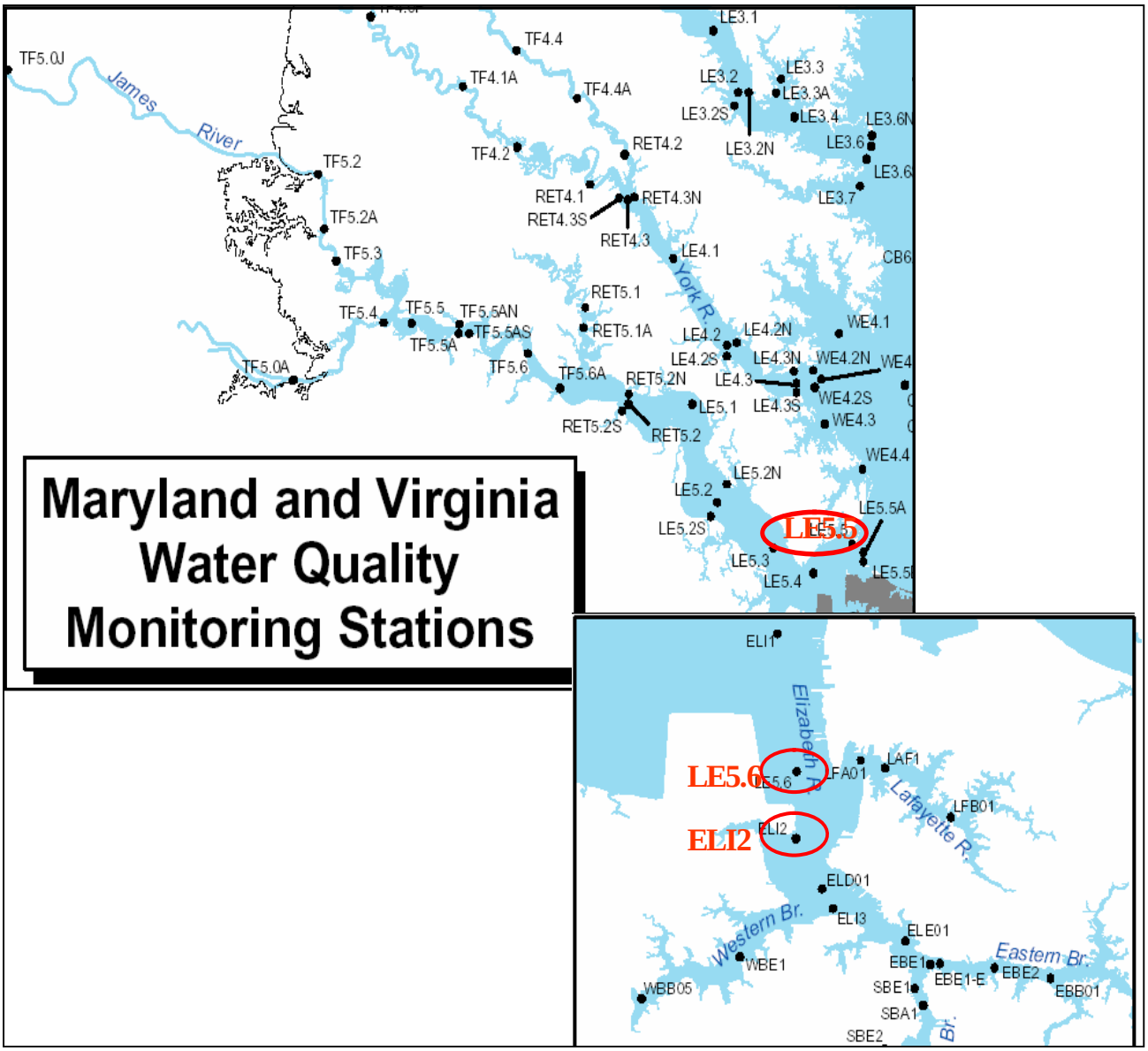

Figure IV.20. Location of CBP stations used in HEM-3D water quality model calibration.

Comparisons at each station were made for full calendar years 1999, 2000, and 2001. These comparisons included the primary parameters of dissolved oxygen, chlorophyll-a, total phosphorus, and total nitrogen, and the additional parameters of ammonia, nitrate-nitrite, and dissolved inorganic phosphorus (DIP).

Station LE5.5, located at the mouth of the James River, represents the mainstem James River condition. Station LE5.6, in the shipping channel located on the eastern side of Craney Island, represents the Craney Island condition. Station ELI2, located to the south of Craney Island, represents the Elizabeth River upstream condition. The time series comparisons for all three years were conducted, and the quantification of the model's ability to reproduce the observed data in each of the above stations, as measured by statistical analysis, is presented in Section IV-2-6.

A. James River Station Results

As illustrated in Chapter III, Kuo and Neilson (1987) indicated that the bottom water DO in the lower James River seldom fell below 4.0 mg/l, and only occasionally fell below 5.0 mg/l in summer months. They attributed the better DO conditions in the lower James to the much stronger non-tidal residual circulation, which accounts for 90% of the velocity variability.

Water quality model calibration results for CBP Station LE5.5 for 1999, 2000, and 2001 are shown, respectively, in Figures IV.21 to IV.22, Figures IV.23 to IV.24, and IV.25 to IV.26. Results for dissolved oxygen are shown in Figures IV.21, IV.23, and IV.25. As illustrated, the model reproduces the observed temporal and surface-to-bottom spatial distribution of dissolved oxygen reasonably well. Both surface and bottom values of dissolved oxygen are above 5 mg/l, with winter values slightly higher than those of summer, showing seasonal variation. Figures IV.21, IV.23, and IV.25 also present the model calculation for chlorophyll-a and for the major inorganic nutrients (i.e., total phosphorus and total nitrogen). Whereas chlorophyll-a and total phosphorus were not measured, the total nitrogen comparison was quite satisfactory. In the fall of 1999, around Julian Days 270-290, the total nitrogen and phosphorus levels were higher than those of 2000 and 2001 due to the passage of Hurricane Floyd through the Chesapeake Bay region. During this period, the ammonia, nitrate and nitrite, and dissolved phosphorus (Figures IV.22, IV.24, and IV.26) showed elevated concentrations. Correspondingly, a phytoplankton bloom was triggered in the fall of 1999, which was not found in 2000 and 2001.

Model predicted sediment fluxes at CBP Station LE5.5 for 1999, 2000, and 2001 are shown in Figures IV.27, IV.28, and IV.29, respectively. Figure IV.27 shows that the fluxes of DO at LE5.5 during 1999 are from the water column into the sediment and attains a rate of approximately 1 gram/m^2/day during the warmer months of the year, which is consistent with the study by Cerco and Cole (1994). The fluxes of NH_4, NO_x, and PO_4 are from the sediment into the water column and attain rates of approximately 0.01, 0.03, and 0.005 grams/m^2/day during the warmer months. The slightly larger than normal nitrate flux from the sediment to the water column is due to the fact that the nitrate and nitrate concentrations in the overlying water are typically less than 0.05 mg/l in the summer. Figures IV.28 shows the sediment flux model predictions at LE5.5 during 2000 as being very similar to those of 1999, whereas Figure IV.29 shows some reductions in magnitude during 2001 for these fluxes at Station LE5.5.

B. Craney Island Station Results

The calibration process was continued from the James River mainstem into its tributary, the Elizabeth River. Initially, it was uncertain whether the model calibration coefficients and parameters would be the same in the Elizabeth River as in the James River mainstem because different algae growth rates, respiration rates, cell nutrient composition, and sediment characteristics exist in the Elizabeth River. The model results were

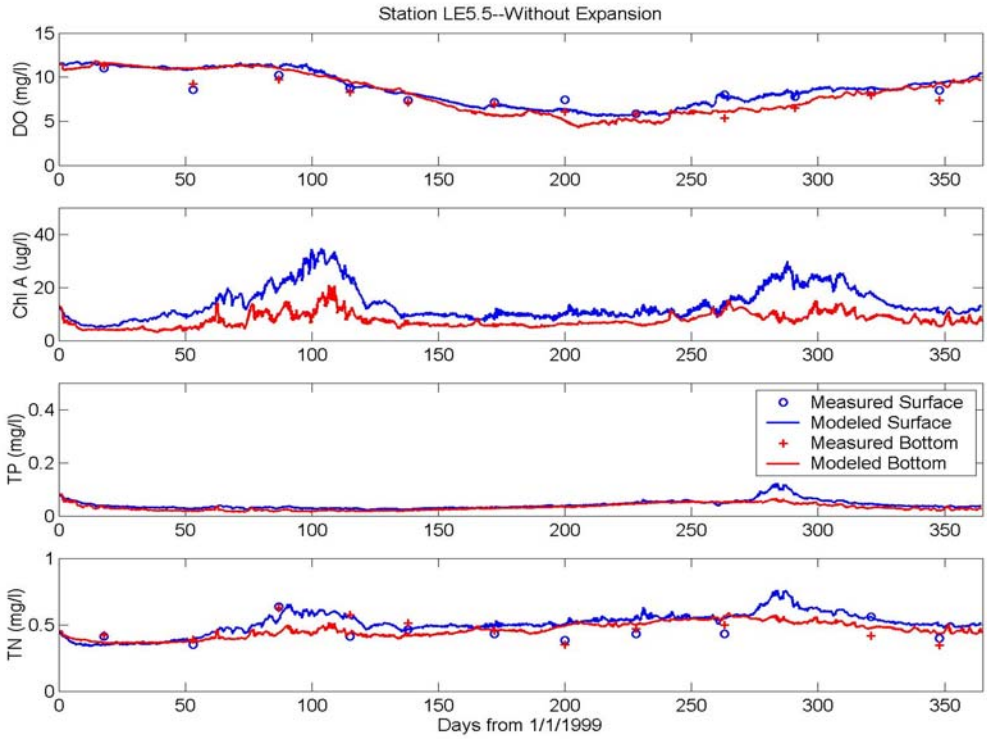

Figure IV.21. Predicted vs. observed DO, Chl-a, TP, and TN at Station LE5.5 for 1999.

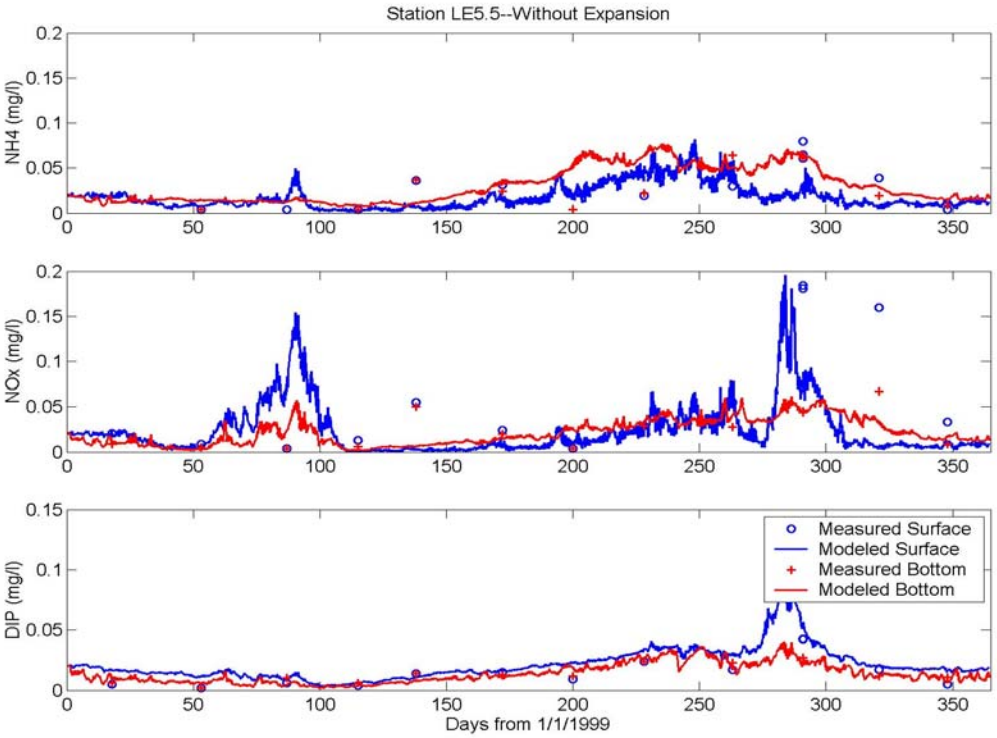

Figure IV.22. Predicted vs. observed NH_4, NO_X, and DIP at Station LE5.5 for 1999.

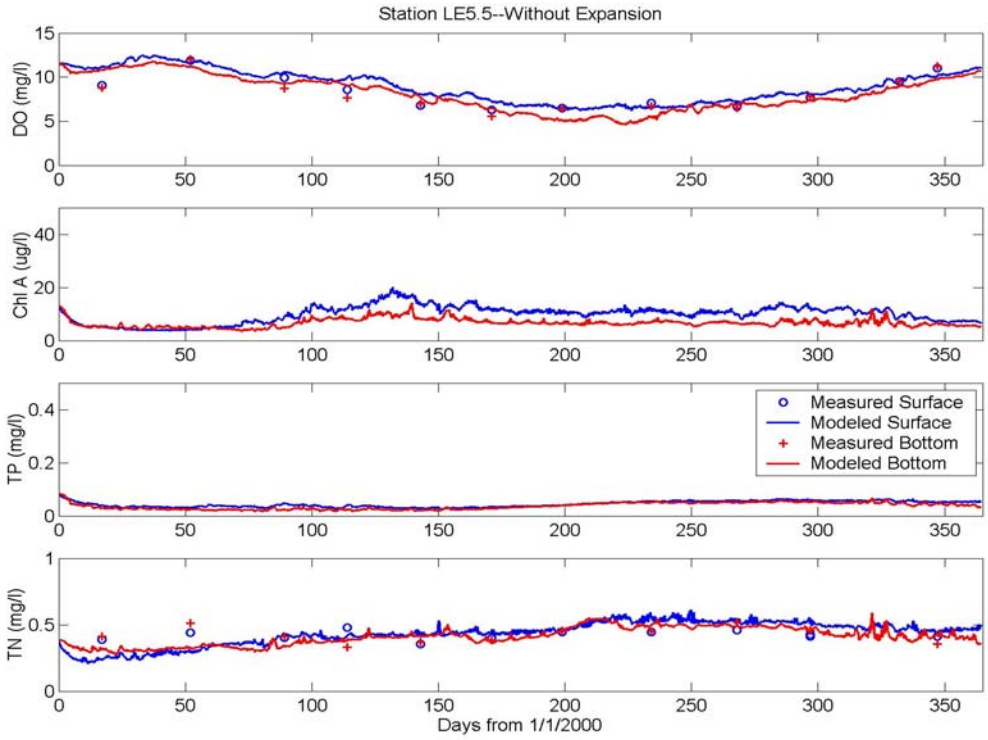

Figure IV.23. Predicted vs. observed DO, Chl-a, TP, and TN at Station LE5.5 for 2000.

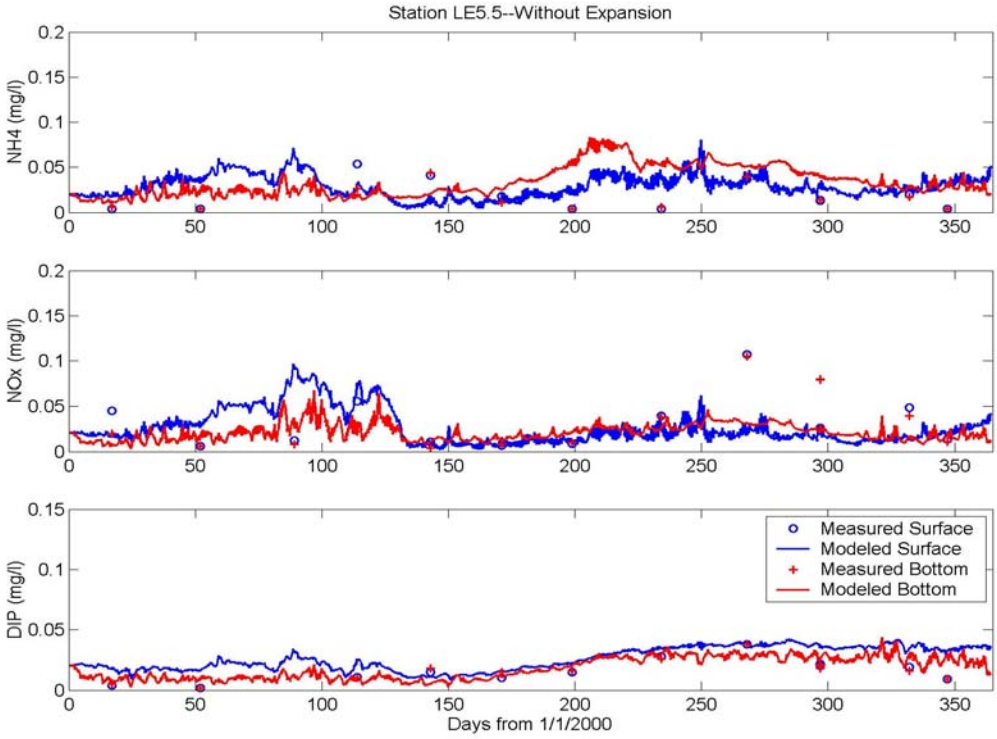

Figure IV.24. Predicted vs. observed NH_4, NO_X, and DIP at Station LE5.5 for 2000.

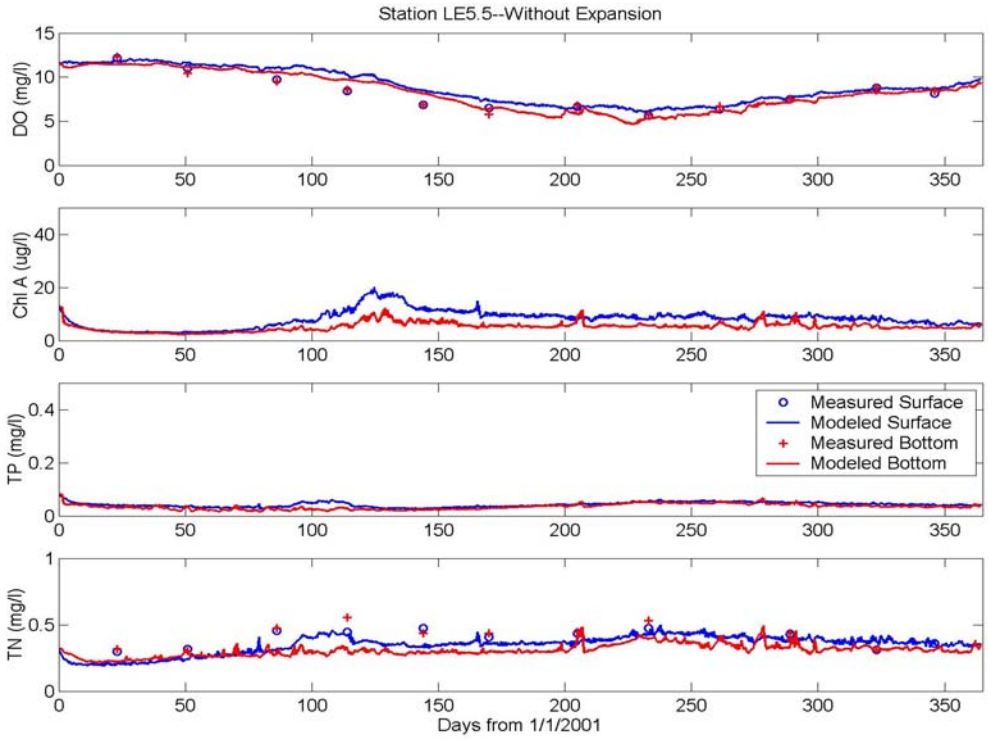

Figure IV.25. Predicted vs. observed DO, Chl-a, TP, and TN at Station LE5.5 for 2001.

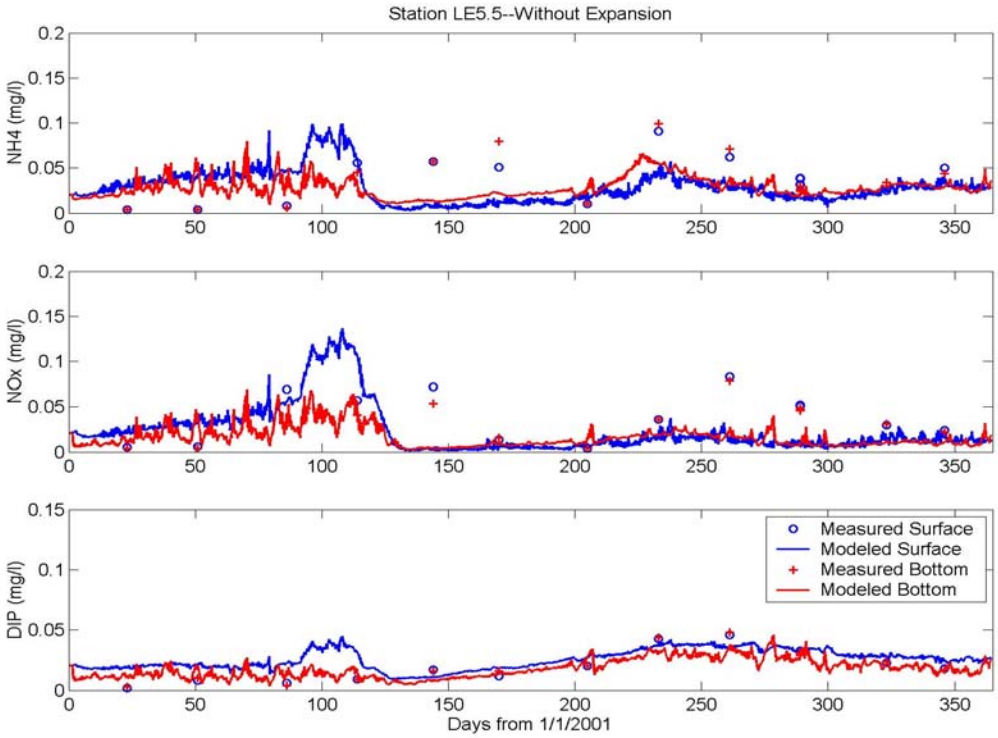

Figure IV.26. Predicted vs. observed NH_4, NO_X, and DIP at Station LE5.5 for 2001.

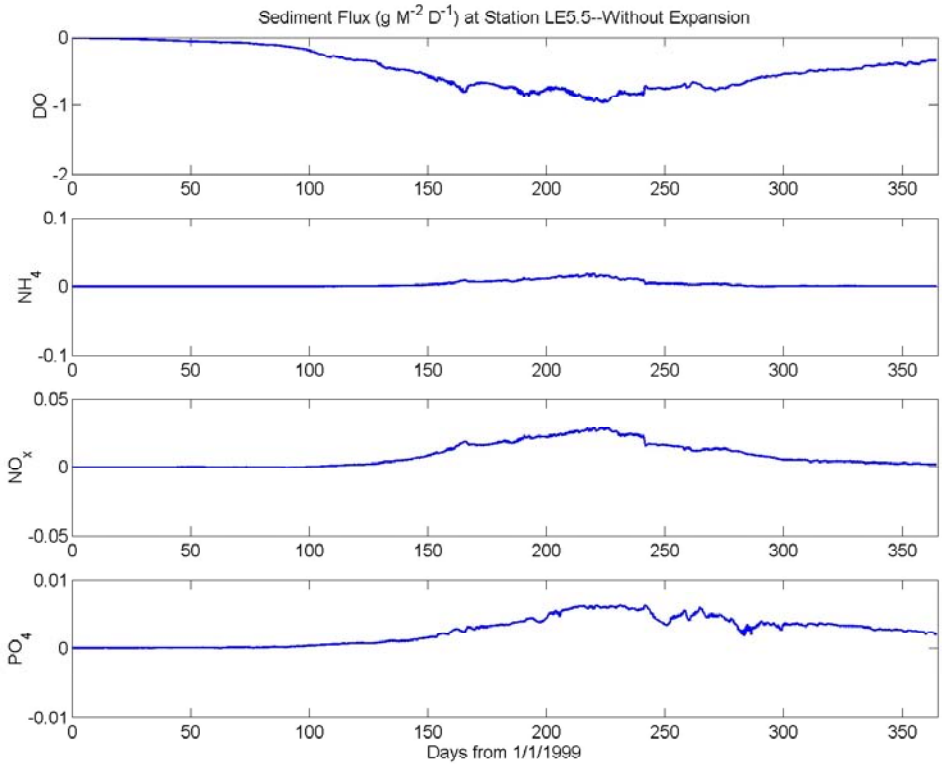

Figure IV.27. Sediment fluxes of DO, NH_4, NO_X, and PO_4 at Station LE5.5 in 1999.

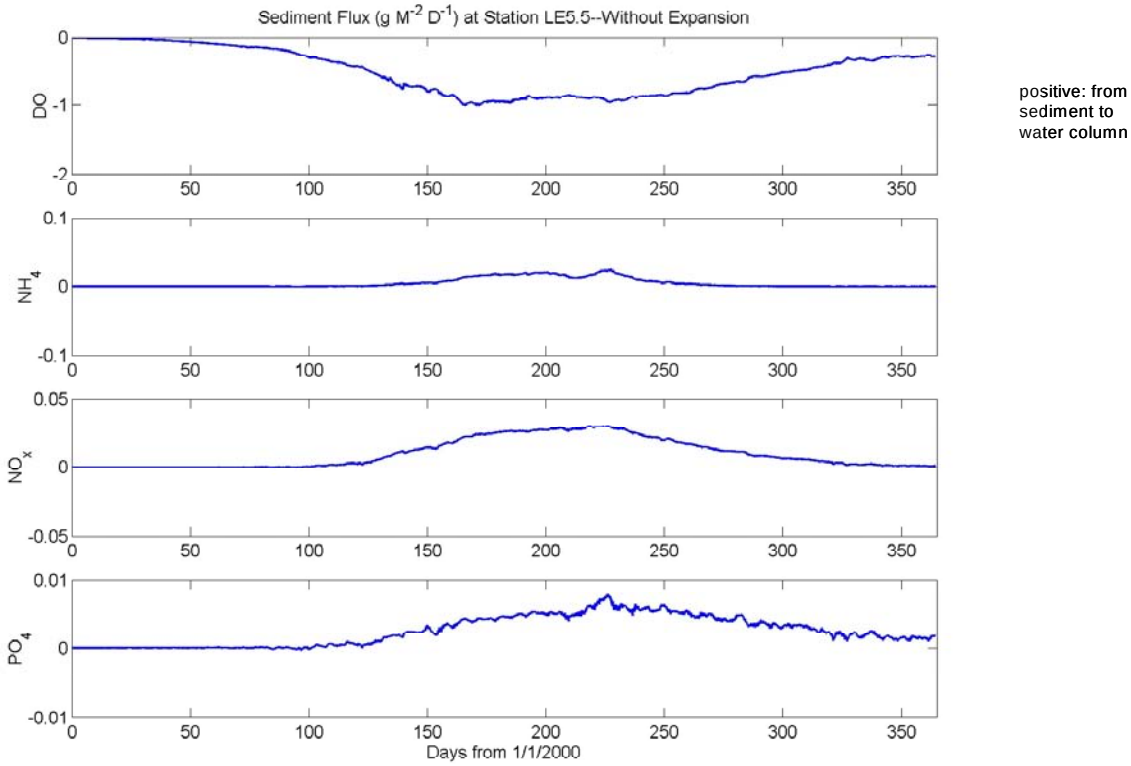

Figure IV.28. Sediment fluxes of DO, NH_4, NO_X, and PO_4 at Station LE5.5 in 2000.

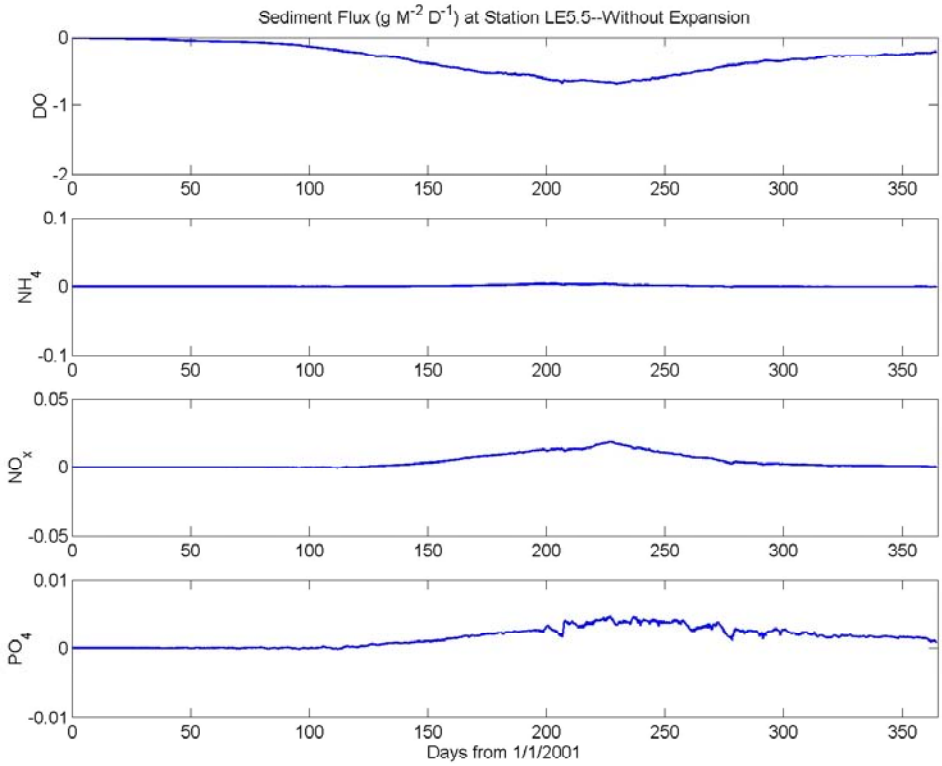

Figure IV.29. Sediment fluxes of DO, NH_4, NO_X, and PO_4 at Station LE5.5 in 2001.

encouraging. It became apparent after a series of runs comparing between model results and observed data that it was not necessary to assign a different set of calibration coefficients and parameters.

Water quality model calibration results for CBP Station LE5.6 for 1999, 2000, and 2001 are shown, respectively, in Figures IV.30 to IV.31, Figures IV.32 to IV.33, and IV.34 to IV.35. The modeled dissolved oxygen results are presented in Figures IV.30, IV.32, and IV.34. The model results are quite good for both surface and bottom DO, with the DO nearing 5 mg/l in the summer and 10 mg/l in the winter. Although this station is inside the Elizabeth River, we did not see a major degradation of oxygen as compared to that of the James River station.

The phytoplankton biomass has measurements (in terms of chlorophyll-a) at this station. The three-year record showed that the chlorophyll-a concentration is generally between 15-20 μg/l and does not have a strong seasonal variation as does that of the Chesapeake Bay mainstem, where the bloom typically occurs in the springtime fueled by the spring runoff.

The total nitrogen concentration occasionally exceeded 0.5 mg/l, slightly higher than that of the James River station and the model correctly captured this trend. Figures IV.31, IV.33, and IV.35 provide comparisons between modeled and measured data for ammonia, nitrate and nitrite, and dissolved phosphorus. It appears that ammonia, nitrate and nitrite, and dissolved phosphorus in the water column are all higher in the summer and fall at Station LE5.6 as compared to LE5.5. This trend makes the ammonia, nitrate

and nitrite, and phosphorus flux less, as shown in Figures IV.32, IV.34, and IV.36. The reduced nitrate and nitrite sediment flux, on the order of 5-10 mg m^{-2} d^{-1}, is consistent with values reported in DiToro (1993).

To model the phosphorus sediment flux correctly, an assumption was made that the oxic-anoxic boundary layer intruded into the bottom of the water column in the summer due to the elevated diagenesis process in the sediment. This process allows the release of phosphorus from the sediment to the water column and greatly improves the model and observed data comparison.

Model predicted sediment fluxes at CBP Station LE5.6 for 1999, 2000, and 2001 are shown in Figures IV.36, IV.37, and IV.38, respectively. Figure IV.36 shows that the fluxes of DO at LE5.6 during 1999 are from the water column into the sediment and attains a rate of approximately 0.8 gram/m^2/day during the warmer months of the year. The fluxes of NH_4, NO_x, and PO_4 are from the sediment into the water column and attain rates of approximately 0.005, 0.01, and 0.005 grams/m^2/day during the warmer months. Figures IV.37 shows the sediment flux model predictions at LE5.6 during 2000 as being very similar to those of 1999, whereas Figure IV.38 shows some reductions in magnitude during 2001 for these fluxes at Station LE5.6.

C. Elizabeth River Upstream Station Results

Water quality model calibration results for CBP Station ELI2 for 1999, 2000, and 2001 are shown, respectively, in Figures IV.39 to IV.40, Figures IV.41 to IV.42, and IV.43 to IV.44.

Figure IV.39 shows a reasonable agreement between predicted and observed dissolved oxygen and good overall agreements between predicted and observed chlorophyll-a, total phosphorus, and total nitrogen for the 1999 calibration. Figure IV.40 shows some under-prediction by the model in comparisons between predicted and observed ammonia (top panel) and nitrate-nitrite (middle panel), but better agreement between predicted and observed dissolved inorganic phosphate (bottom panel).

Given that the Elizabeth River watershed is an urbanized watershed, a significant portion of the loading comes from the point source loading inside the river (see Table III.1 and Figure III.11 in Chapter III.). Both model predictions and observation data indicate that the point source contributions inside the Elizabeth River augment the concentration levels of both nitrogen and phosphorus.

Figure IV.41 shows predicted and observed dissolved oxygen, chlorophyll-a, total phosphorus, and total nitrogen are in good overall agreement for the 2000 calibration. Figure IV.42 shows some discrepancy by the model in comparing predicted and observed ammonia (top panel) in the middle part of 2000. However, comparisons of the nitrate-nitrite (middle panel) and dissolved inorganic phosphate (bottom panel) show reasonably good agreement between predicted and observed values.

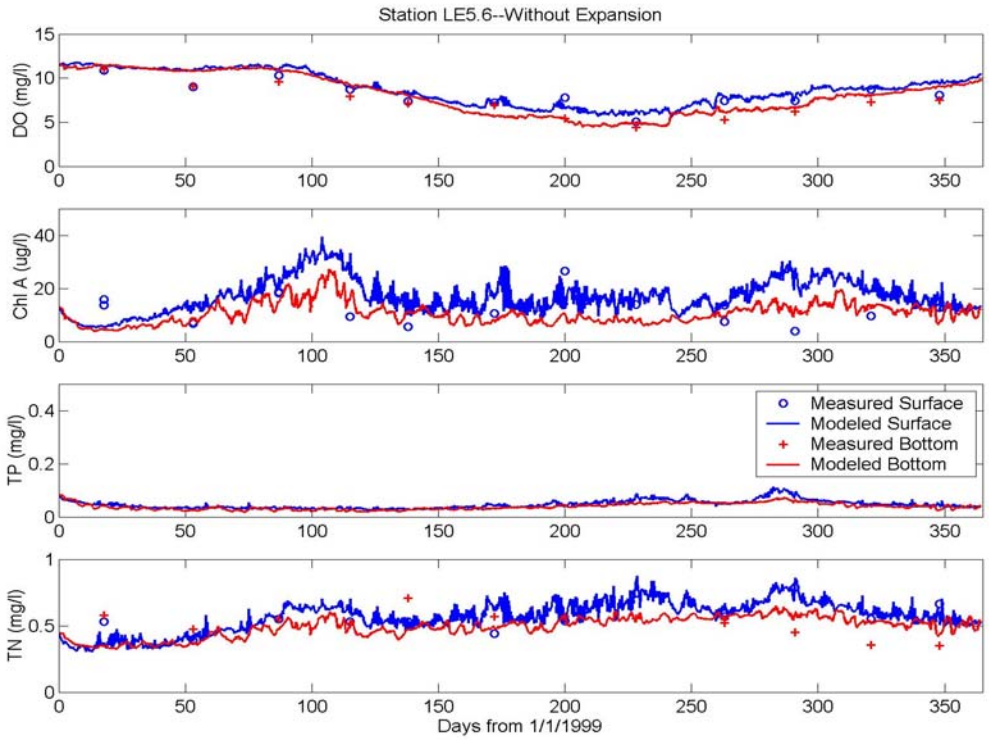

Figure IV.30. Predicted vs. observed DO, Chl-a, TP, and TN at Station LE5.6 for 1999.

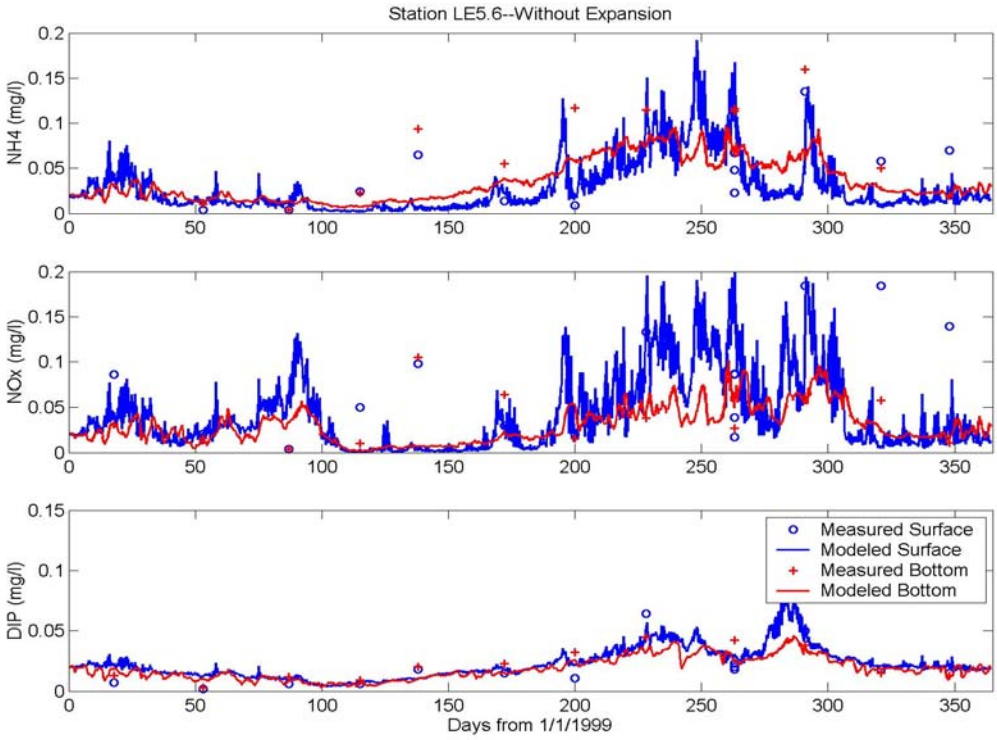

Figure IV.31. Predicted vs. observed NH_4, NO_X, and DIP at Station LE5.6 for 1999.

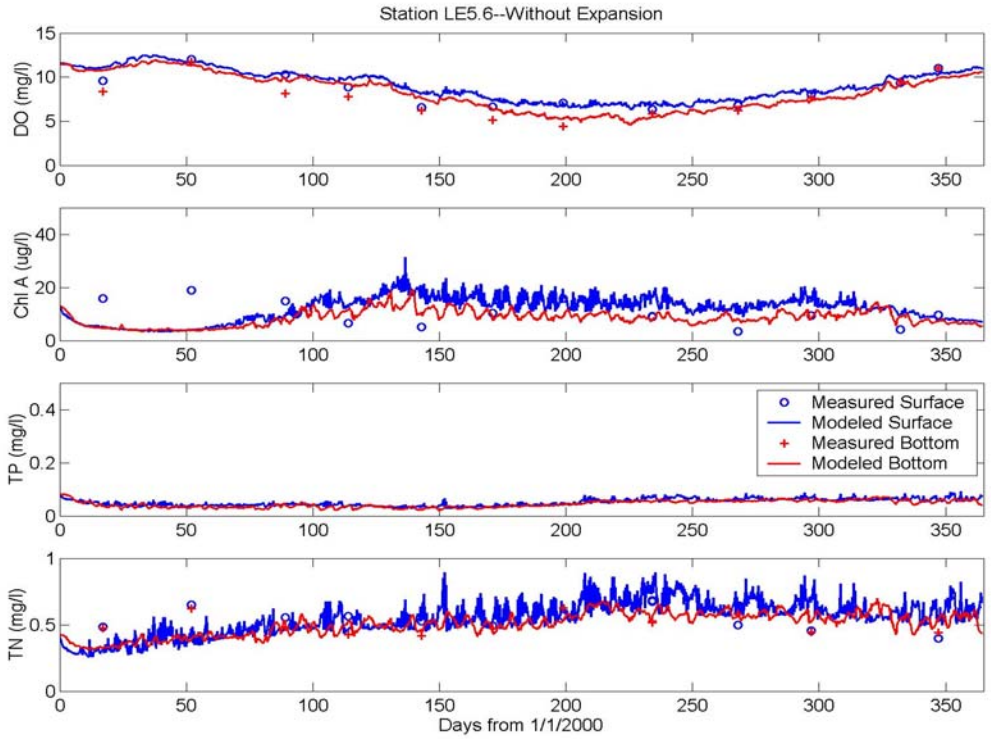

Figure IV.32. Predicted vs. observed DO, Chl-a, TP, and TN at Station LE5.6 for 2000.

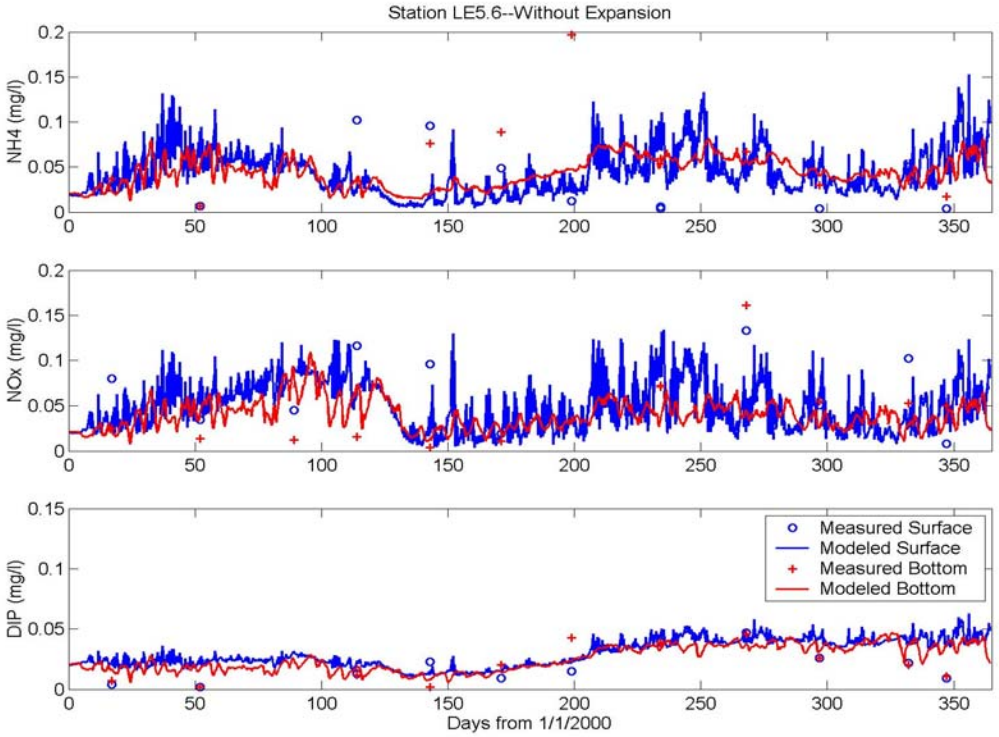

Figure IV.33. Predicted vs. observed NH_4, NO_X, and DIP at Station LE5.6 for 2000.

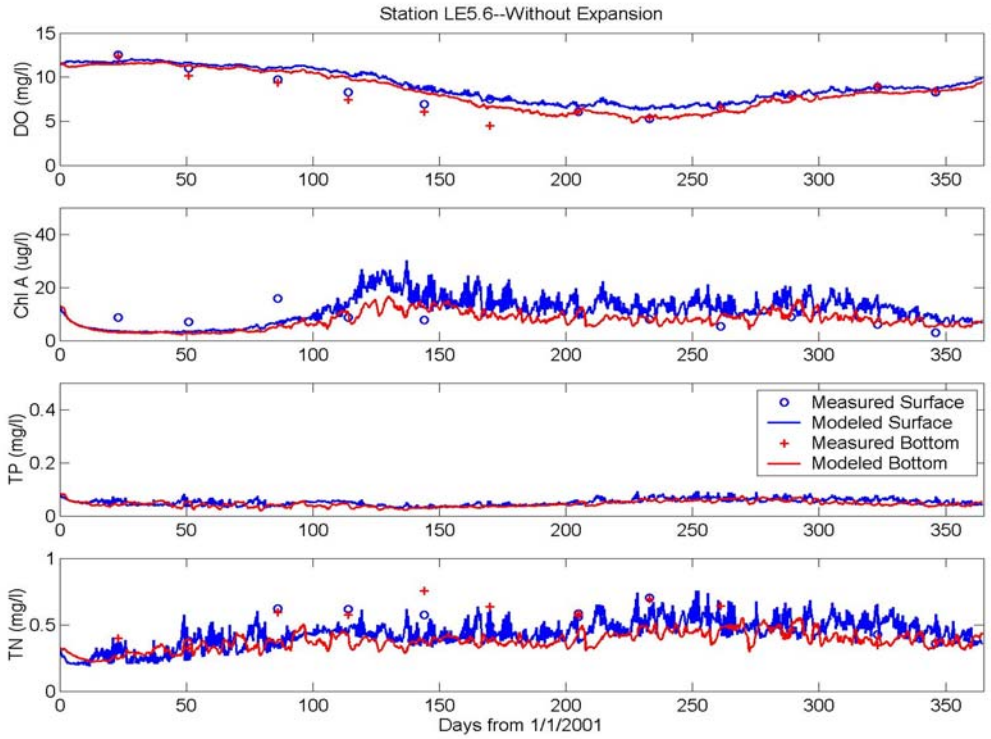

Figure IV.34. Predicted vs. observed DO, Chl-a, TP, and TN at Station LE5.6 for 2001.

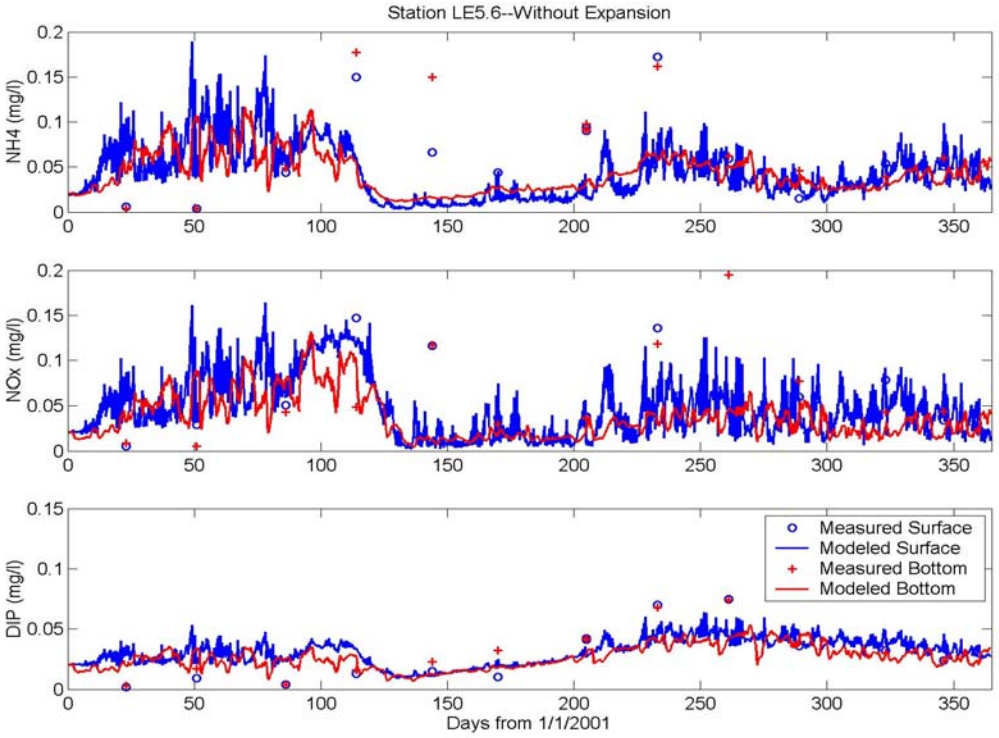

Figure IV.35. Predicted vs. observed NH_4, NO_X, and DIP at Station LE5.6 for 2001.

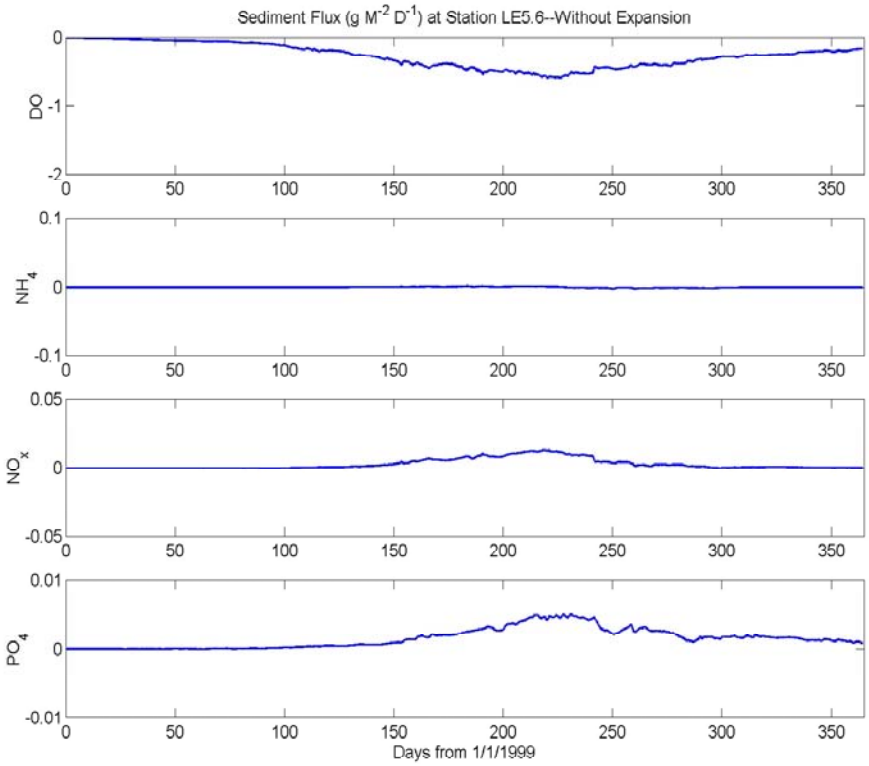

Figure IV.36. Sediment fluxes of DO, NH_4, NO_X, and PO_4 at Station LE5.6 in 1999.

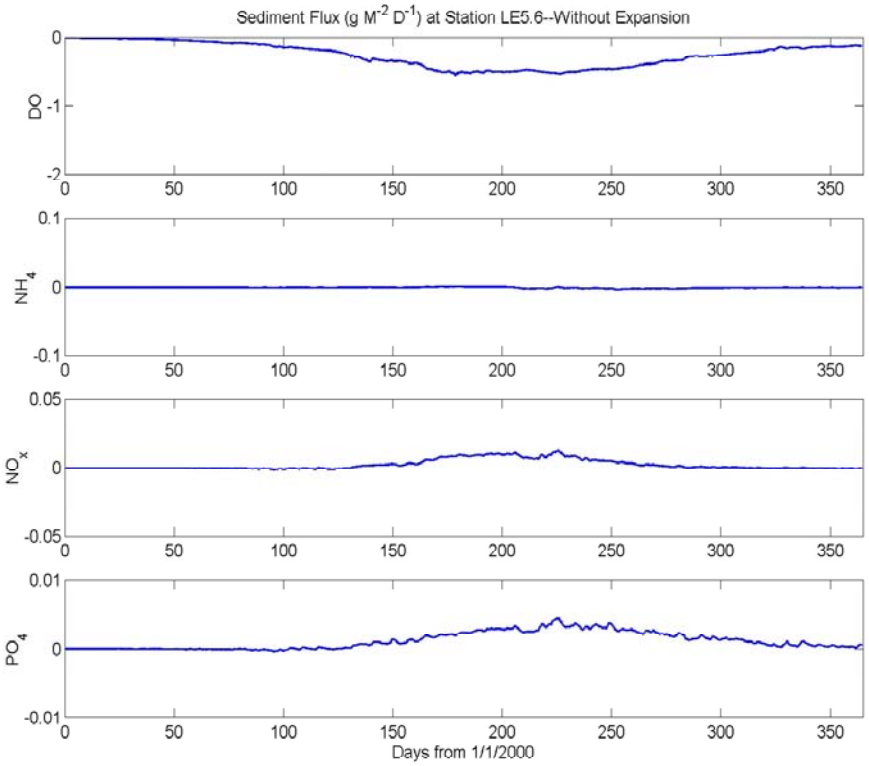

Figure IV.37. Sediment fluxes of DO, NH_4, NO_X, and PO_4 at Station LE5.6 in 2000.

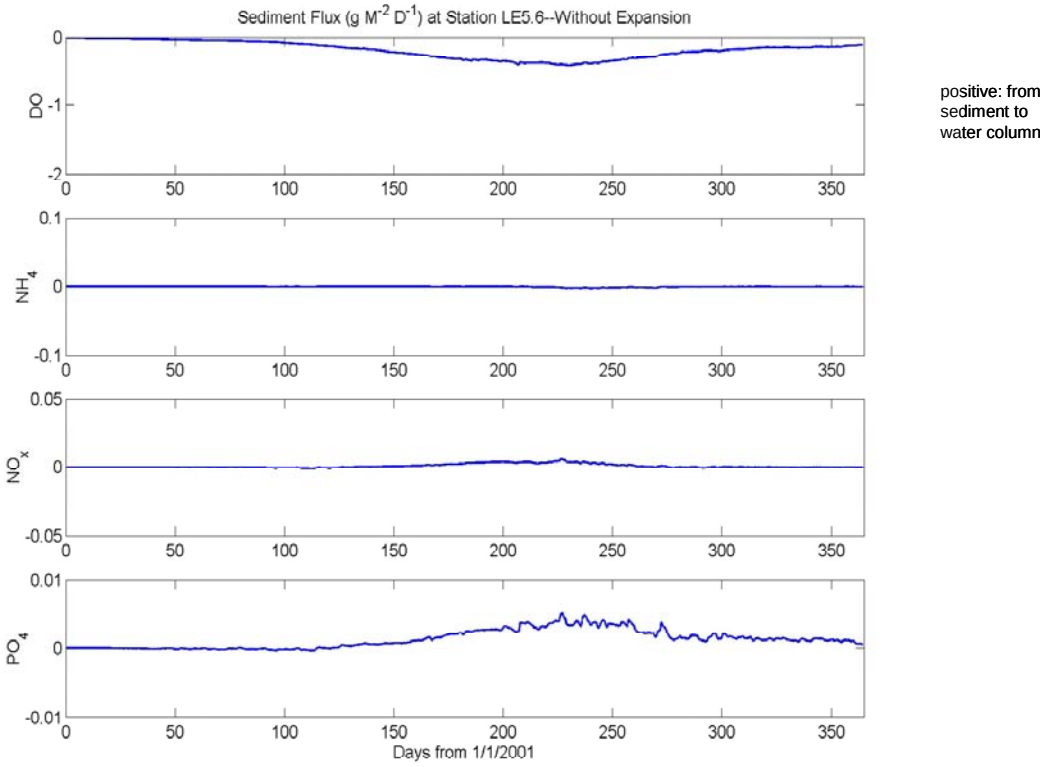

Figure IV.38. Sediment fluxes of DO, NH_4, NO_X, and PO_4 at Station LE5.6 in 2001.

Figure IV.43 again shows a good agreement between predicted and observed dissolved oxygen and a good overall agreements between predicted and observed chlorophyll-a, total phosphorus, and total nitrogen for the 2001 calibration. Figure IV.44 shows, in the comparison of predicted and observed ammonia (top panel), that the model over-predicts ammonia before Julian Day 90 of 2001 and later under-predicts ammonia (approximately Julian days 110, 140, and 170 of 2001). However, comparisons of the nitrate-nitrite (middle panel) and dissolved inorganic phosphate (bottom panel) show reasonably good agreement between predicted and observed values.

Model predicted sediment fluxes at CBP Station ELI2 for 1999, 2000, and 2001 are shown in Figures IV.45, IV.46, and IV.47, respectively.

Figure IV.45 shows that the fluxes of DO at ELI2 during 1999 are from the water column into the sediment and attains a rate of approximately 0.8 gram/m^2/day during the warmer months of the year. The fluxes of NH_4, NO_x, and PO_4 are from the sediment into the water column and attain rates of approximately 0.01, 0.03, and 0.005 grams/m^2/day during the warmer months. Figures IV.46 shows the sediment flux model predictions at ELI2 during 2000 as being very similar to those of 1999, whereas Figure IV.47 shows some reductions in magnitude during 2001 for these fluxes at Station ELI2.

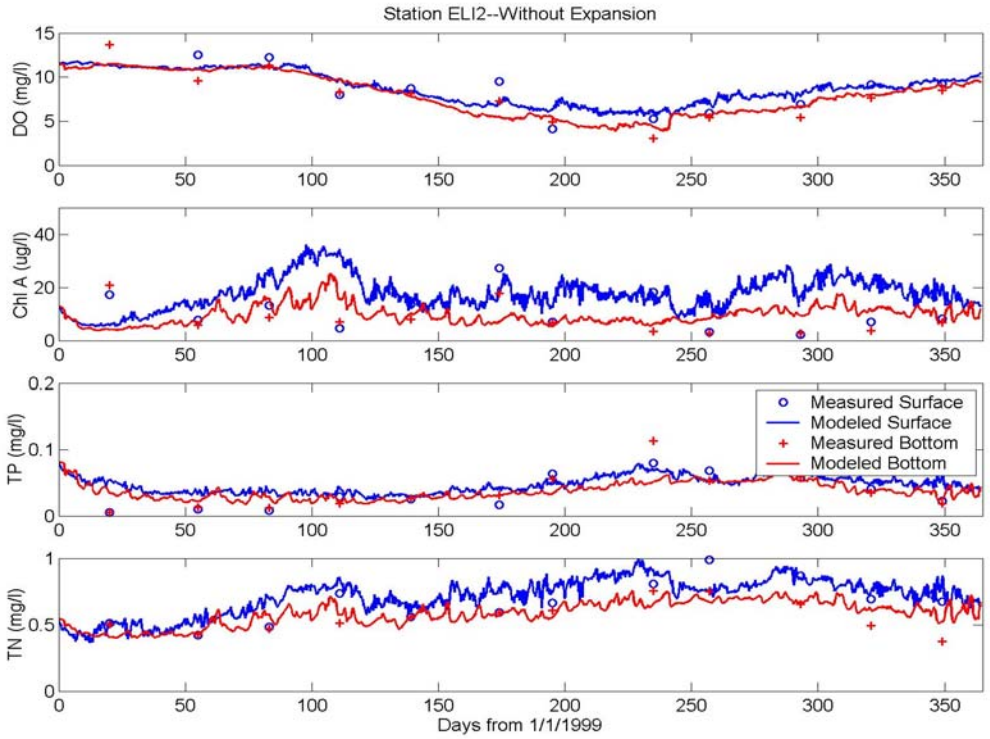

Figure IV.39. Predicted vs. observed DO, Chl-a, TP, and TN at Station ELI2 for 1999.

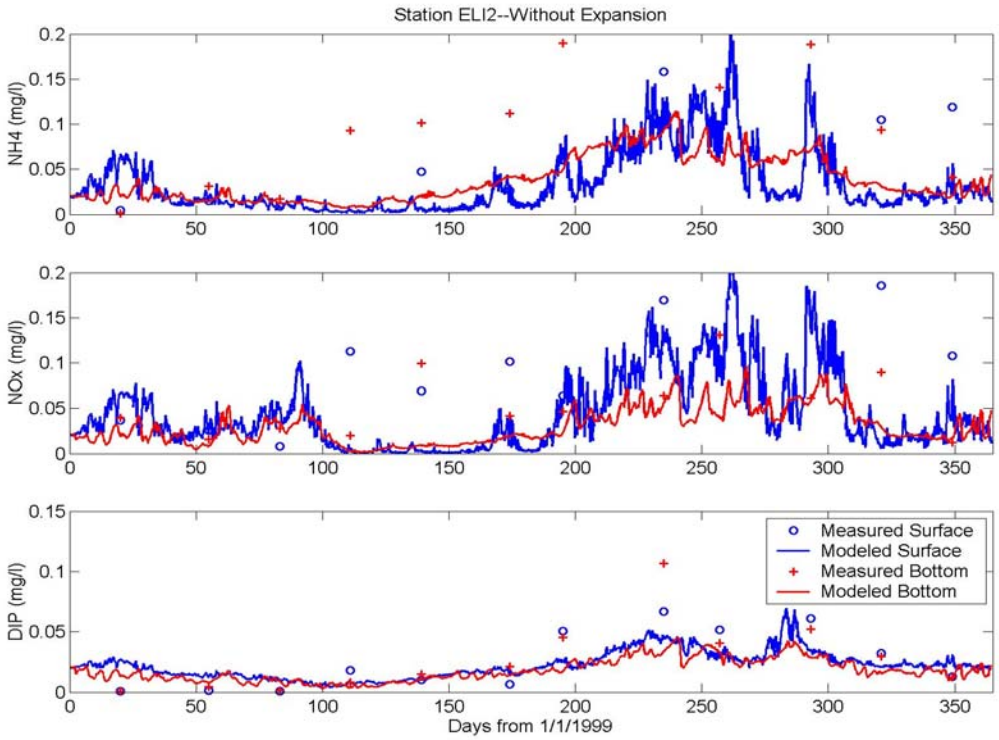

Figure IV.40. Predicted vs. observed NH_4, NO_X, and DIP at Station ELI2 for 1999.

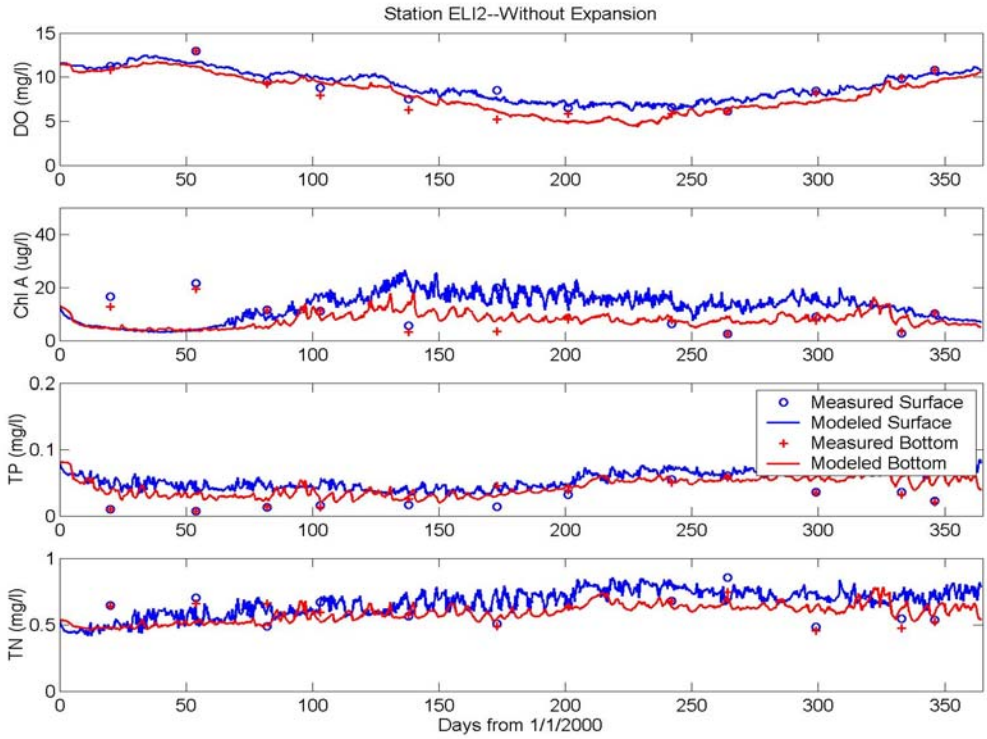

Figure IV.41. Predicted vs. observed DO, Chl-a, TP, and TN at Station ELI2 for 2000.

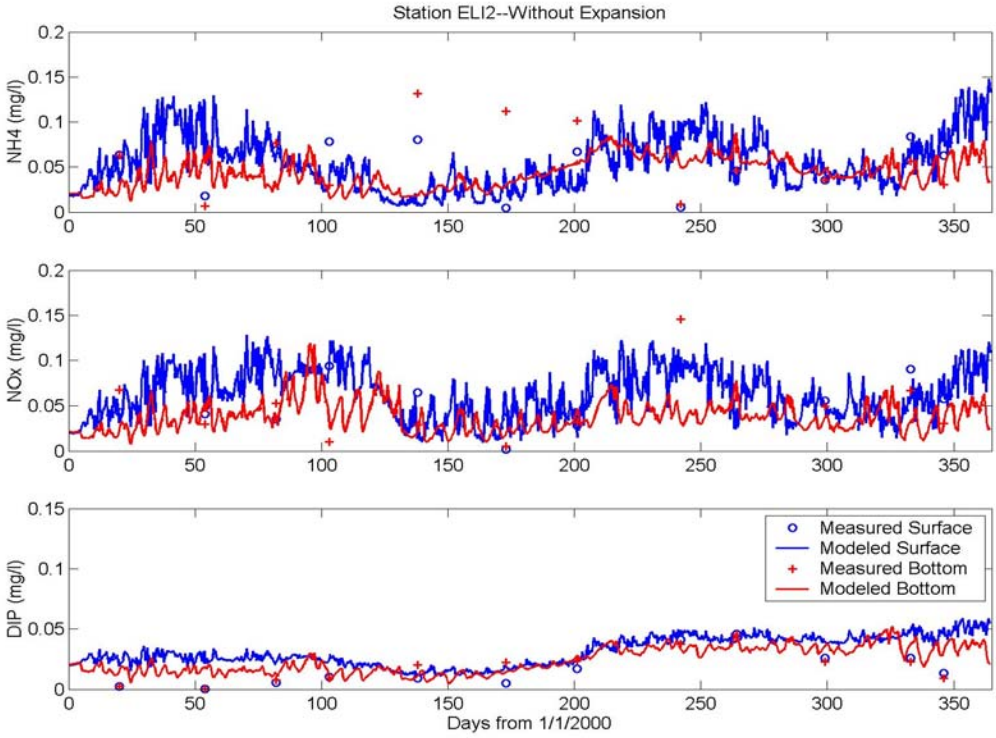

Figure IV.42. Predicted vs. observed NH_4, NO_X, and DIP at Station ELI2 for 2000.

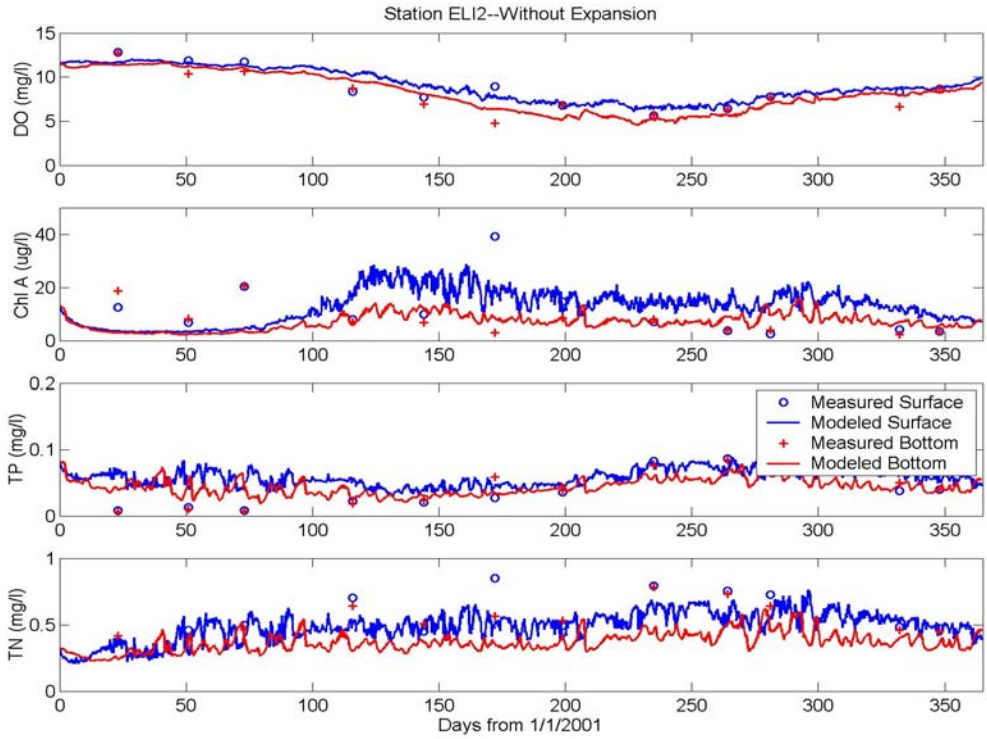

Figure IV.43. Predicted vs. observed DO, Chl-a, TP, and TN at Station ELI2 for 2001.

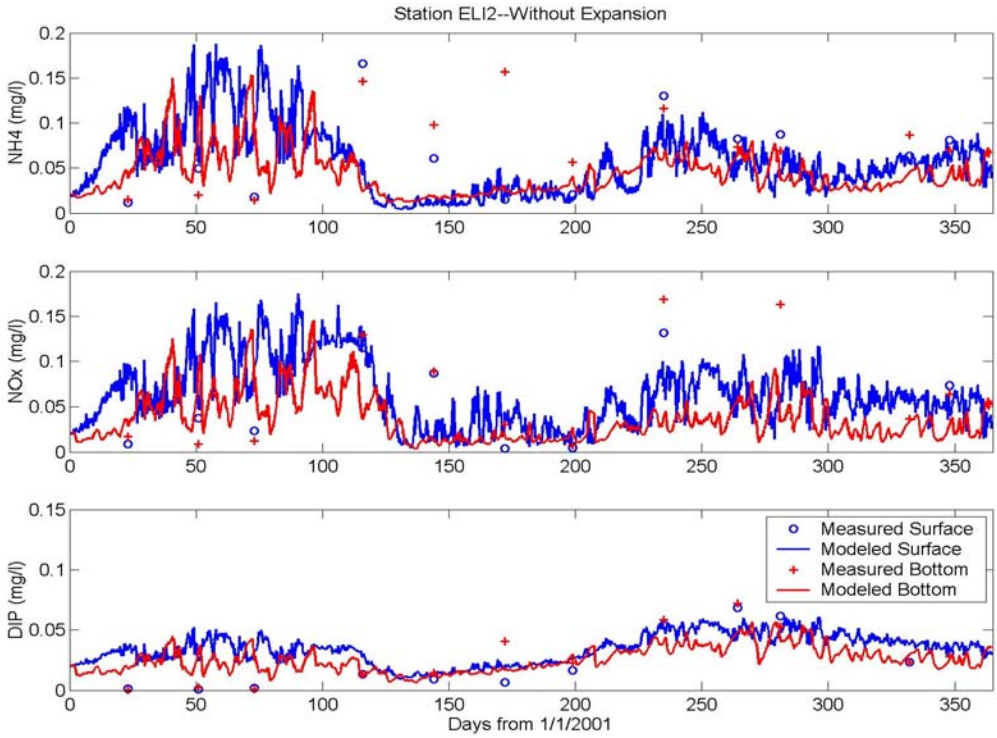

Figure IV.44. Predicted vs. observed NH_4, NO_X, and DIP at Station ELI2 for 2001.

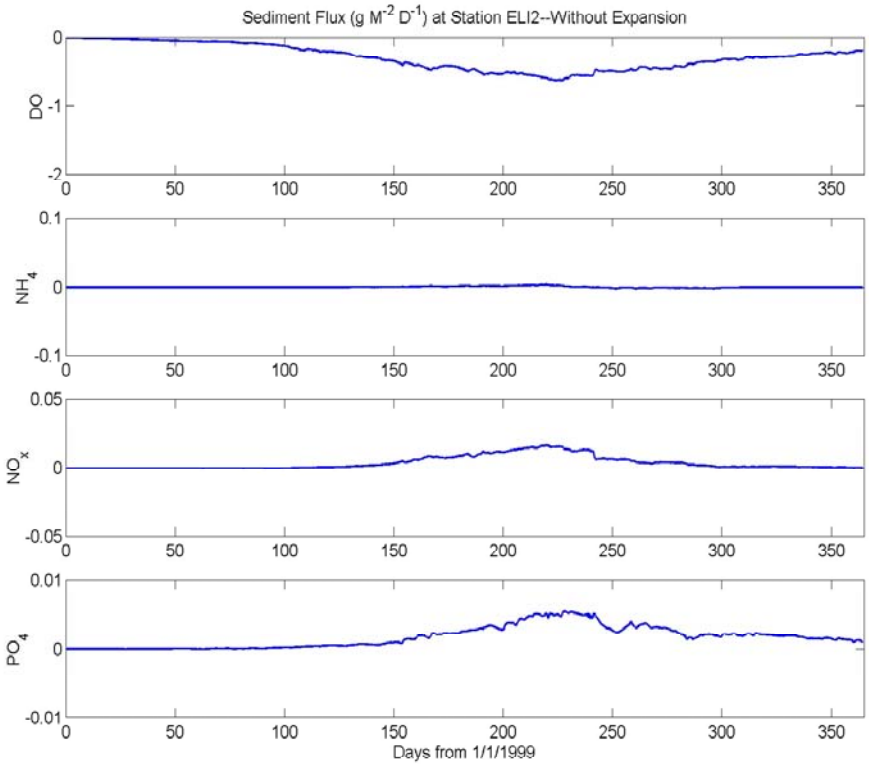

positive: from sediment to water column

Figure IV.45. Sediment fluxes of DO, NH_4, NO_X, and PO_4 at Station ELI2 in 1999.

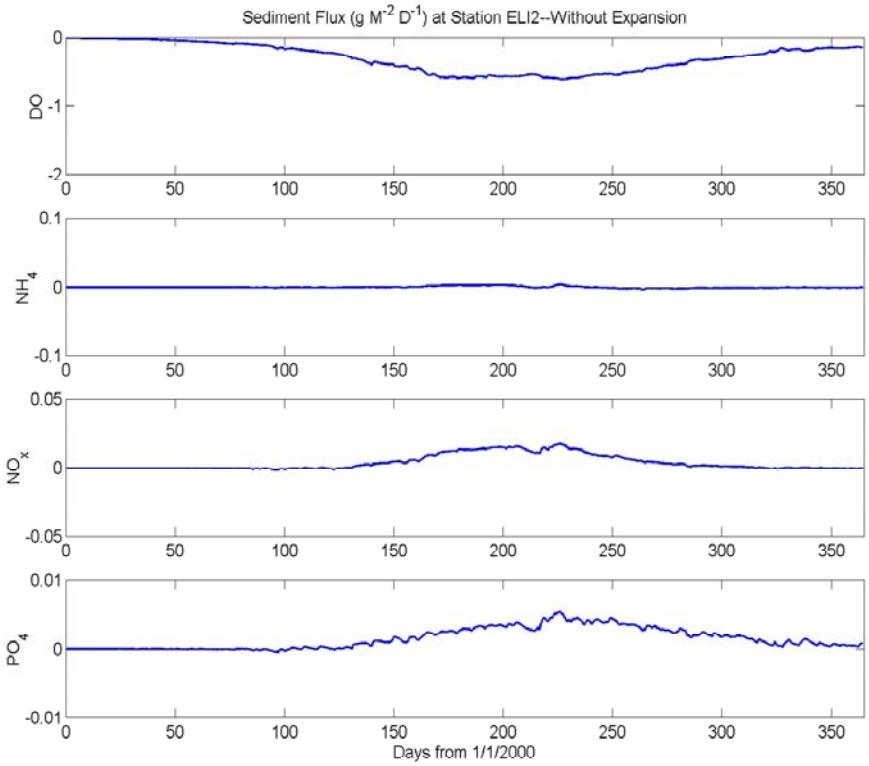

positive: from sediment to water column

Figure IV.46. Sediment fluxes of DO, NH_4, NO_X, and PO_4 at Station ELI2 in 2000.

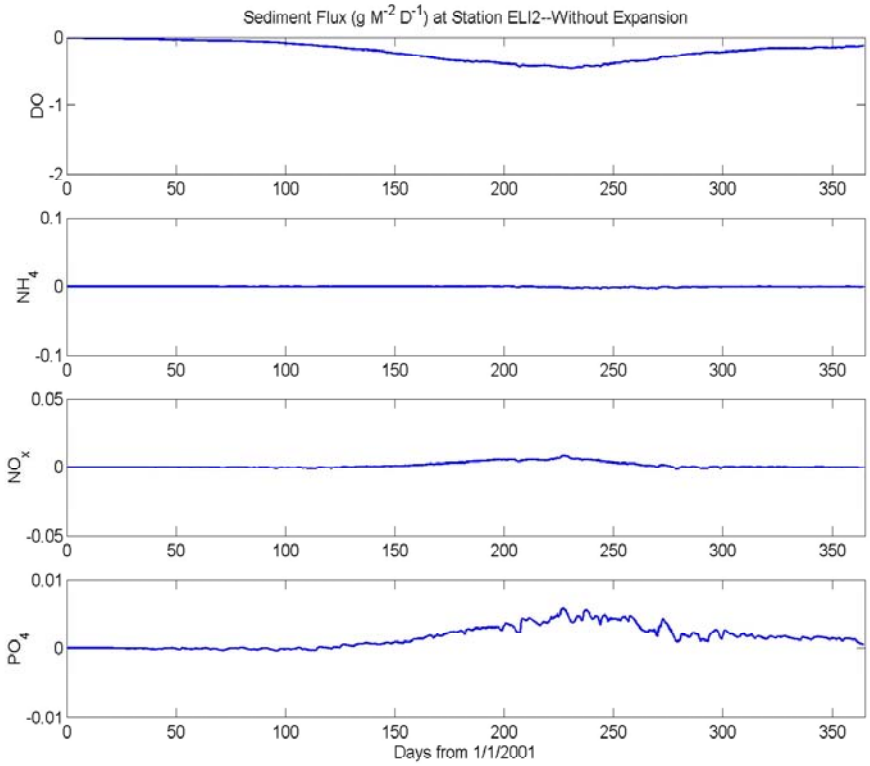

Figure IV.47. Sediment fluxes of DO, NH_4, NO_X, and PO_4 at Station ELI2 in 2001.

IV-2-6 Summary Statistics of Water Quality Model Calibration Results

In the previous portion of this section, qualitative comparisons between model results and observed values were presented. Although the comparisons indicate that HEM-3D can reproduce the physical, chemical, and biological processes that affect the eutrophication process in the James and Elizabeth Rivers, a more specific measure of the model performance is desirable.

In order to provide a more quantifiable measure of the performance of the water quality model, a statistical analysis was applied to the predicted and observed data of the water quality calibration results.

For model predictions vs. observations of the water quality parameters compared at surface and bottom layers throughout the period 1999 – 2001, various error measurements serve to quantify the performance of the water quality model. Error measurements determined include:

1) **Mean error** – The mean error statistic is defined as:

$$ME = \frac{\sum (O - P)}{n}$$

where: ME = mean error, O = observation, P = model predicted result, and *n* = number of observations. The mean error is a summary of the model tendency to overestimate or underestimate the data.

2) **Absolute Mean error** –The absolute mean error statistic is defined as:

$$AME = \frac{\sum |O - P|}{n}$$

where: AME = absolute mean error. The absolute mean error is a measure of the average discrepancy between observations and model results.

3) **Root Mean Square Error** – The root mean square error statistic is defined as:

$$RME = \sqrt{\frac{\sum (O - P)^2}{n}}$$

where: *RME* = root mean square error. The root mean square error is an alternate quantification of the average discrepancy between observations and model results.

4) **Relative Error** – The relative error statistic is defined as:

$$RE = \frac{\sum |O - P|}{\sum O}$$

where: *RE* = relative error. The relative error statistic normalizes absolute mean error by the magnitude of the observations.

Additionally, 1:1 plots of predicted results vs. observations show visually how well the model predictions compare with observations and whether the model shows a bias towards either over-prediction or under-prediction.

A. Statistical Analysis of Dissolved Oxygen Results

Due to the importance of dissolved oxygen in this project, predicted vs. observed comparisons of DO were performed at the surface and bottom individually for each of the 3 CBP stations. The monthly CBP measurements taken over the 1999-2001 period thus provided sample sizes of 36 for each of the surface and bottom comparisons at Stations LE5.5, LE5.6 and ELI2. The error measures for these 6 comparisons of predicted vs. observed DO are shown in Table IV.12 below and the 1:1 plots are shown in Figure IV.48. Overall, predicted and observed DO values compare well. The median value for mean error is about 0.3 mg/l while the absolute mean error is in the range between 0.8 and 0.9 mg/l. The root-mean-square error for both surface and bottom DO is about 1 mg/l, whereas the relative error is around 10%. These statistics are comparable to other

eutrophication model studies such as the Three-dimensional Eutrophication Model Study of the Chesapeake Bay (Cerco and Cole, 1994).

The small negative values for mean error at Stations LE5.5 and LE5.6 indicate a slight tendency for the model to over-predict DO at these locations. To demonstrate the DO variability, and thus the uncertainty of observed values, the model predicted DO range over the day of observation is also indicated in the figures as a vertical bar.

Given the low DO concentration at the bottom water is of particularly important for the project, we examined in detail the predicted versus observed comparison of lower DO and found that errors are random in nature, which are not subject to any systematic bias. It was also worthwhile to point out that the absolute mean error and root-mean-square error of water quality parameters shown in Table IV.12 are well within the range of natural variation in a given season of measurements when compared with available observations, for example, Figures III.3-III.5, IV.21-IV.26, IV.30-IV.35, and IV.39-IV.44.

Table IV.12. Statistical summary of errors derived by comparing predicted vs. observed values of dissolved oxygen.

Surface Comparisons of Predicted vs. Observed Dissolved Oxygen				
	CBP Station			
	LE5.5	LE5.6	ELI2	All 3 Stations
Sample size	36	36	36	108
Mean Error	-0.45	-0.56	-0.01	-0.34
Absolute Mean Error	0.69	0.76	0.91	0.78
RMS Error	0.89	0.94	1.23	1.03
Relative Error	0.08	0.09	0.10	0.09
Corr. Coeff. (r)	0.95	0.95	0.94	0.94

Bottom Comparisons of Predicted vs. Observed Dissolved Oxygen				
	CBP Station			
	LE5.5	LE5.6	ELI2	All 3 Stations
Sample size	36	36	36	108
Mean Error	-0.18	-0.60	-0.02	-0.27
Absolute Mean Error	0.90	0.95	0.91	0.92
RMS Error	1.03	1.16	1.06	1.08
Relative Error	0.11	0.13	0.11	0.12
Corr. Coeff. (r)	0.94	0.94	0.95	0.94

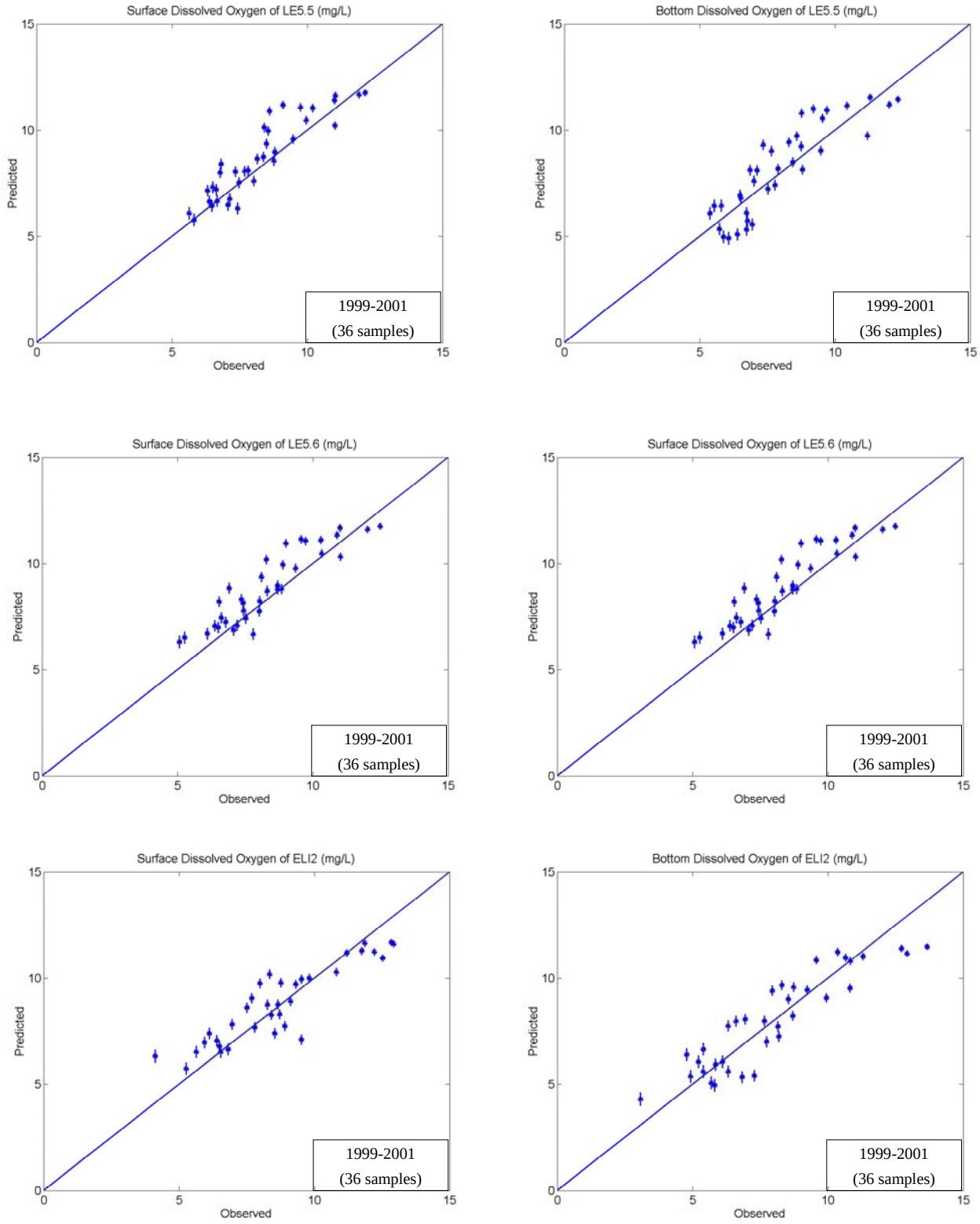

Figure IV.48. Plots of 1:1 predicted vs. observed dissolved oxygen.

B. Statistical Analysis of Total Phosphorus, Total Nitrogen, Ammonia, Nitrate-Nitrite, and Dissolved Inorganic Phosphate

To quantify the comparison between predicted and observed values TP, TN, NH_4, NO_x, and DIP, determination of statistical errors and construction of 1:1 plots were performed for these parameters as well. It is noted that chlorophyll-a was not included in the analysis due to insufficient data. Table IV.13 below shows error values of each parameter for predicted vs. observed comparisons at both the surface and bottom of all three stations.

The nitrogen and phosphorus are major nutrients that can be used for photosynthesis. In particular, NH_4, NO_x, and dissolved phosphorus are species that can be uptaken directly by the phytoplankton. Therefore, they are important indicator for the environmental quality. Nitrogen's concentration is usually higher than phosphorus. The 1:1 plots of predicted vs. observed comparisons of TP and TN at both the surface and bottom are shown in Figure IV.49 and those for NH_4, NO_x, and DIP are shown in Figure IV.50. The summary is shown in Table IV13. The absolute mean error and root mean square error of these water quality parameters show the difference between model and observation are within the range of natural variation in a given season of measurements when compared with available observation, for example, Figures IV21-IV26, IV30-IV35, and IV39-IV44.

Table IV.13. Statistical summary of errors derived by comparing predicted vs. observed values of TP, TN, NH_4, NO_X, and DIP.

Surface Comparisons of Predicted vs. Observed						
Parameter:	Chl-a	TP	TN	NH_4	NO_X	DIP
Mean Error	*	-0.02	-0.02	0.01	0.03	-0.01
Absolute Mean Error		0.02	0.09	0.04	0.05	0.01
RMS Error		0.03	0.11	0.06	0.07	0.01
Relative Error		0.70	0.17	0.75	0.65	0.53
Corr. Coeff. (r)		0.79	0.84	0.57	0.68	0.85

Bottom Comparisons of Predicted vs. Observed						
Parameter:	Chl-a	TP	TN	NH_4	NO_X	DIP
Mean Error	*	-0.02	0.03	0.02	0.02	0.00
Absolute Mean Error		0.02	0.09	0.04	0.02	0.01
RMS Error		0.03	0.11	0.06	0.05	0.01
Relative Error		0.70	0.17	0.69	0.67	0.41
Corr. Coeff. (r)		0.76	0.69	0.48	0.48	0.82

* Insufficient sample size for comparison of chlorophyll-a

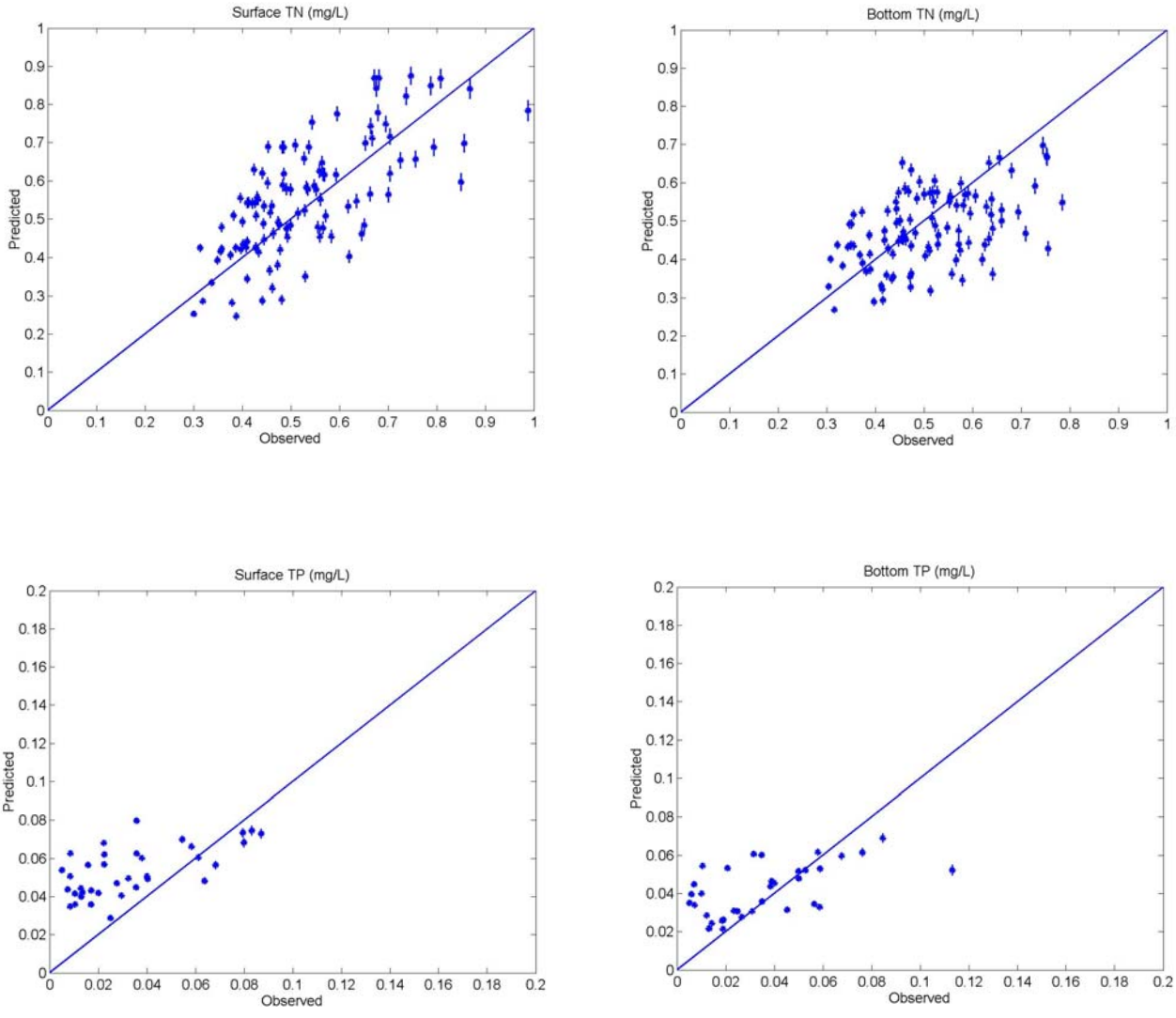

Figure IV.49. Plots of 1:1 predicted vs. observed TN and TP.

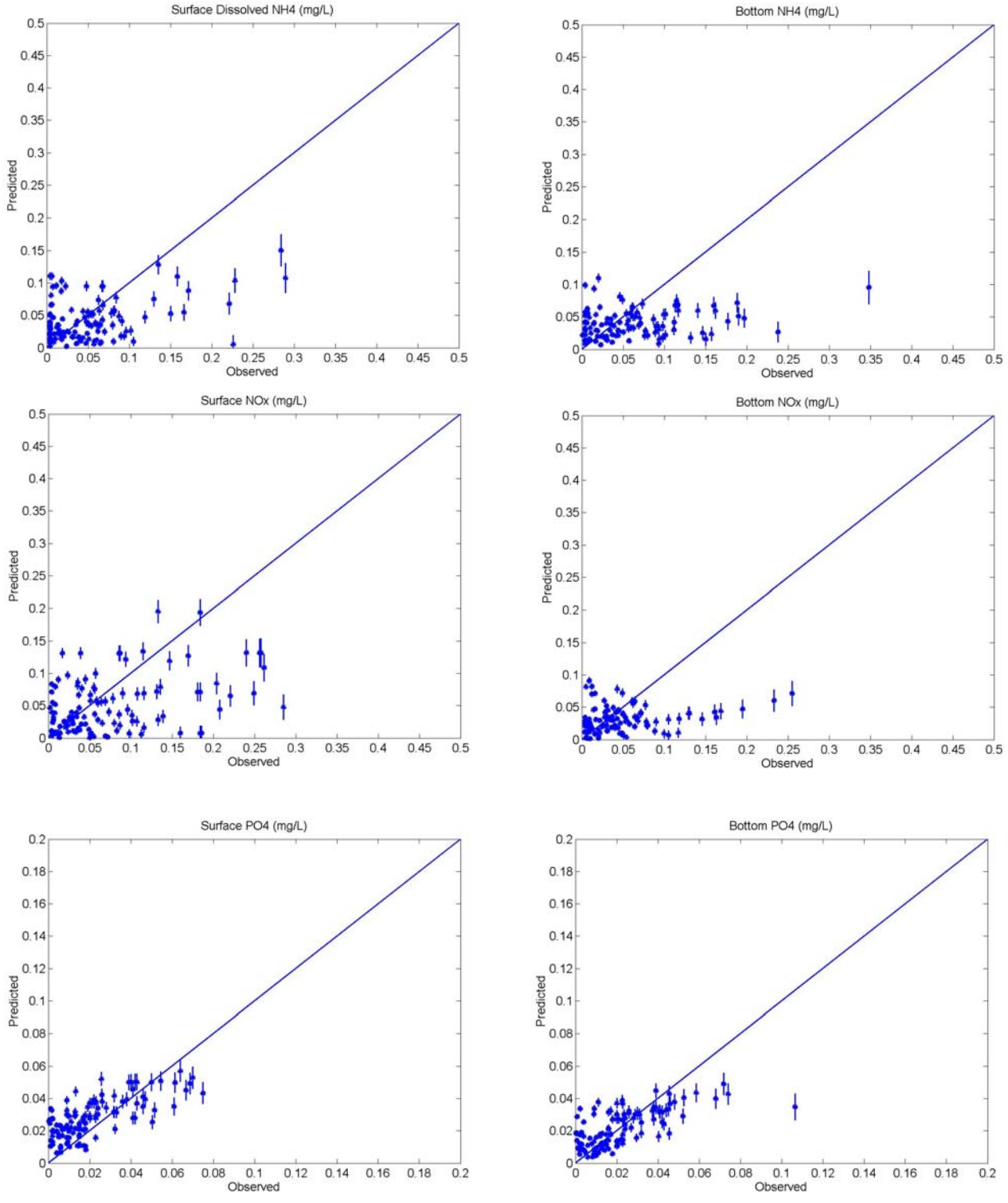

Figure IV.50. Plots of 1:1 predicted vs. observed NH_4, NO_x, and DIP.

CHAPTER V. SCENARIO RUNS AND ANALYSIS

V-1. Hydrodynamic Impact from the Construction of the Expansion and Dredging of the Access Channels and Berthing Area

V-1-1. Cross-sectional analysis of expansion impact

The Craney Island eastward expansion reduces the surface area at the mouth of the Elizabeth River. At the same time, due to the dredging of deep channels for the access channels and the berthing area, the vertical cross-section area actually increases. The focal question of this section is whether these changes will alter the characteristics of the hydrodynamic and transport properties, and pose any adverse impact on the system's flushing capability.

One of the important features is the tidal prism or volume of water that enters and leaves the Elizabeth River during a tidal cycle. The magnitude of the tidal prism is an indicator of the flushing ability of the Elizabeth River Basin, a system that includes not only the tidal waterways of the river stem and its four main branches but the adjacent watershed areas that deliver land-based runoff to the system as well. In an estuarine system such as the Elizabeth River, the water exchange through a cross-section also has a non-tidal component. Flushing is the cumulative effect of these two modes of transport in an estuarine system. The tidal prism, defined as the volume of water transported back and forth through a cross-section during a tidal cycle, quantifies the tidal flushing. The flood tide brings in the tidal prism volume of water, mixes it with the water in the system, and then removes the same volume of water during ebb tide. The non-tidal residual circulation brings in the water from one part of the cross-section, displaces the water in the system and pushes it out through another part of the cross-section. The non-tidal transport is driven by freshwater inflow at the landward end of an estuary, balanced by saltwater inflow at the seaward end of the estuary. Thus, the calculation of volume flux through a cross-section is separated into two parts, tidal and non-tidal (or residual).

The original CIEE study (Wang et al., 2001) concluded little change, with "no significant effects to water circulation, sedimentation, salinity, currents, and tidal flushing from the Elizabeth River with an eastward expansion of the CIDMMA" (EIS, page IV-2). One of the main purposes of the present study was to ensure no adverse condition changes at the cross section that could cause the flushing ability of the Elizabeth River Basin to decrease with the revised expansion plan.

The existing cross-sectional area at the Elizabeth River entrance is 16,275 m^2, based on the NGVD vertical datum and the original eastward expansion design was 16,395 m^2, as shown in Figure V.1a. The 2007 revised CIEE design, moving the face of the wharf to the west by 500 feet, is shown by the green line outlining the cross-sectional area in Figure V.1b. Possible cross-sectional impacts were investigated at length in the study by Wang et al. (2001) and it was concluded that an increase in cross-sectional area caused an increase in the non-tidal residual velocity, successfully offsetting a smaller decrease in tidal prism caused by a small decrease in surface area. However, revisions of CIEE

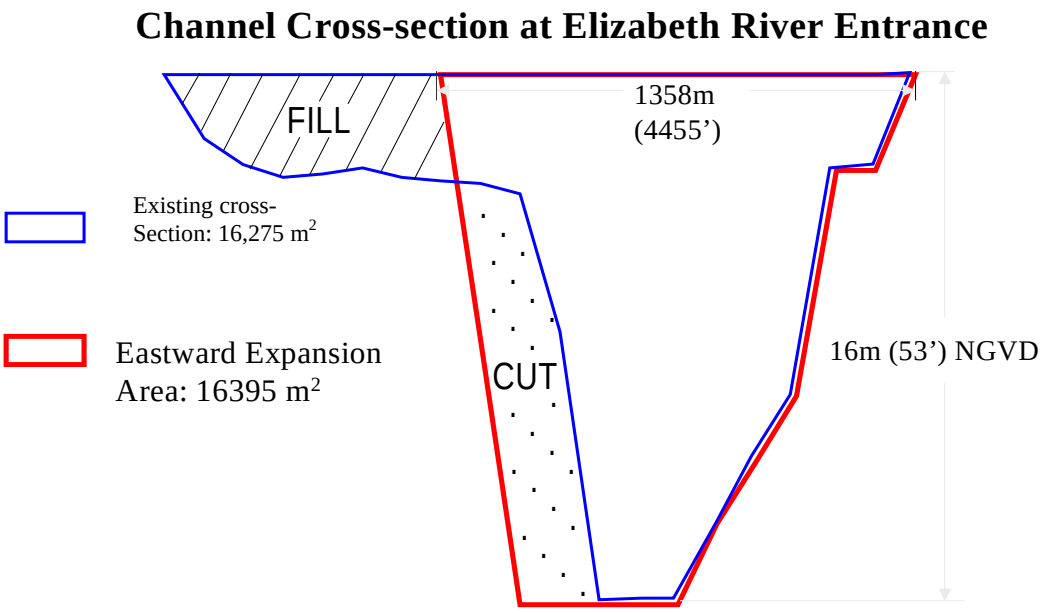

Figure V.1a. The existing cross-section and the 2001 eastward expansion design area for the channel cross-section at Elizabeth River entrance

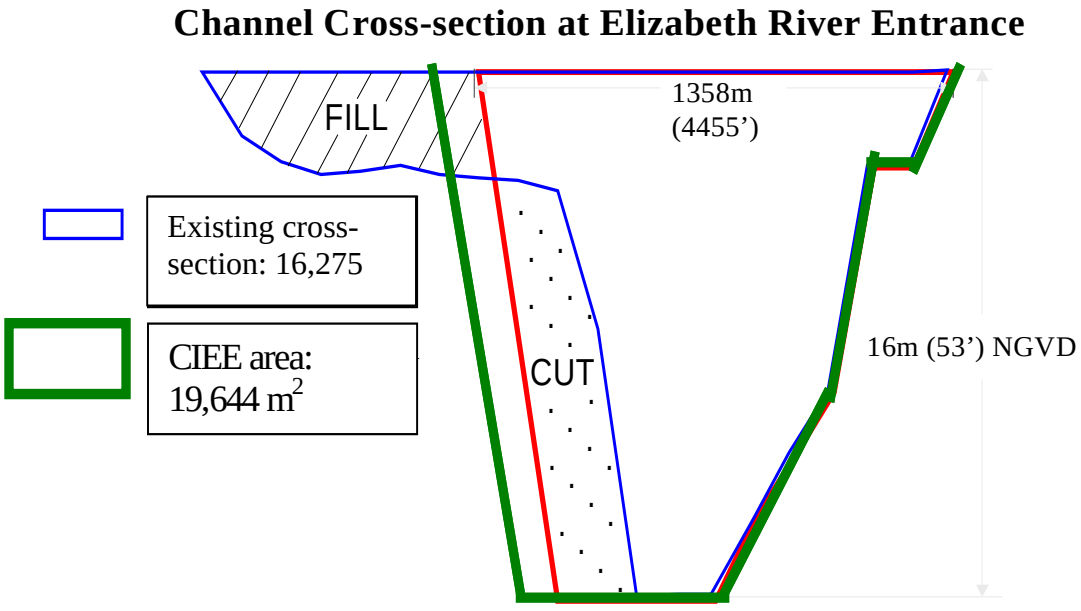

Figure V.1b. The existing cross-section and the 2007 eastward expansion design area for the channel cross-section at Elizabeth River entrance

design in 2007 made it important to request VIMS to re-assess for any impacts caused by the cross-sectional and surface areas of the new design.

In a three-dimensional hydrodynamic model with a sigma vertical grid, the east-west cross-section in the x-z plane can be divided into an array of computational cells, as shown in Figure V.2. Let the *j*-index vary along the *x*-axis in the horizontal direction and the *k*-index vary along the *z*-axis in the vertical direction. Also, let *n* be the number of columns with constant width, Δx, in the *x*-direction, with 6 cells of variable thickness, Δz, in the *z*-direction. The volume transport, q_{ijk}, over the time interval Δt at time *i* is then calculated as $q_{ijk} = \Delta x \cdot \Delta z \cdot \Delta t \cdot v_{ijk}$ where Δt is the time step and v_{ijk} is the velocity normal to the cross-section . If *nrec* is the number of time steps in a tidal cycle, then, the total residual (non-tidal) volume transport through the *j-k* cell during the tidal cycle is $qr_{jk} = \sum_{i=1}^{nrec} q_{ijk}$, and the mean residual transport for each tidal cycle becomes $\overline{qr_{jk}} = qr_{jk} / nrec$. The residual volume transports through the cross-section in the flood direction, QR_{flood}, and in the ebb direction, QR_{ebb}, are defined as

$$QR_{flood} = \sum_{j=1}^{n}\sum_{k=1}^{6} qr_{jk} \; if \; qr_{jk} \le 0$$

$$QR_{ebb} = \sum_{j=1}^{n}\sum_{k=1}^{6} qr_{jk} \; if \; qr_{jk} \ge 0$$

The net residual volume transport becomes the difference between the ebb and flood residuals and this should be the same as the freshwater inflow to the system, $Q_{freshwater}$

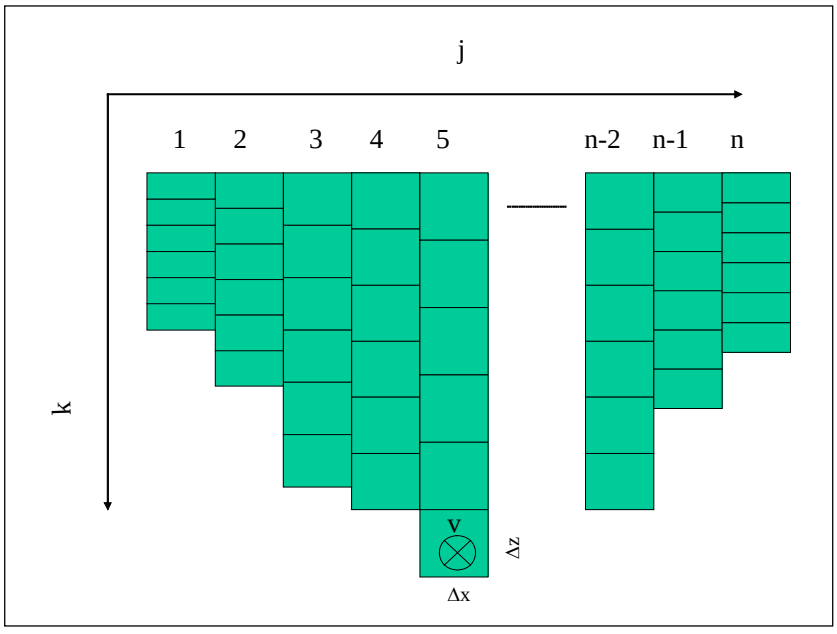

Figure V.2. Definition sketch for flux calculation.

$$QR_{net} = QR_{ebb} - QR_{flood} \approx Q_{freshwater}$$

The tidal volume transport through each cell is defined as the difference between the instantaneous volume transport and the mean residual transport:

$$qt_{ijk} = q_{ijk} - \overline{qr_{jk}}$$

Then the volume transports induced by flood and ebb tides are defined for a tidal cycle as

$$QT_{flood} = \sum_{i=1}^{nrec}\sum_{j=1}^{n}\sum_{k=1}^{6} qt_{ijk} \; if \; qt_{ijk} \le 0$$

$$QT_{ebb} = \sum_{i=1}^{nrec}\sum_{j=1}^{n}\sum_{k=1}^{6} qt_{ijk} \; if \; qt_{ijk} \ge 0$$

For the current study, this same methodology was applied and further expanded by mapping the residual velocities calculated by the sigma-grid in the vertical to a fine-resolution (i.e., 0.25 m) z-grid for calculation of fluxes. As before, the total flux was calculated by a summation in time and space and the ebb and flood components of residual velocity and tidal prism were segregated. The base case and the 2007 CIEE design were calculated for (1) ebb tidal prism, (2) flood tidal prism, (3) non-tidal ebb residual, (4) non-tidal flood residual, (5) non-tidal ebb residual plus ebb tidal prism, and (6) non-tidal flood residual plus flood tidal prism. For the full expansion, a section drawn from the northern edge of the expansion across the river mouth was used for the calculation and the results are presented in Table V.1.

Table V.1 shows that, although there is a slight reduction in the tidal prism (-4.4%), this reduction is more than compensated by a more significant increase in the non-tidal residual flow (32.1%) out of the system. This translates to a net increase in the total flushing capability of at least 3% due to the full expansion.

Table V.1. Tidal Prism and Residual Flushing Volumes for CIEE Full Expansion and Base Case

Derived Parameter	**CIEE (2007 design) (m^3)**	**Base Case (m^3)**	**Percentage Change**
Non-tidal ebb residual	13,399,912	10,143,818	32.1%
Non-tidal flood residual	12,232,397	10,136,644	20.7%
Ebb tidal prism	36,019,087	37,680,229	-4.4%
Flood tidal prism	36,019,083	37,680,212	-4.4%
Non-tidal ebb residual plus ebb tidal prism	49,418,999	47,824,047	3.3%
Non-tidal flood residual plus flood tidal prism	48,251,480	47,816,856	0.9%

For the south cell expansion, a section drawn from the northern edge of the south cell expansion across the river was used for the calculation and the results are presented in Table V.2. This intermediate stage of the expansion has a -1.3% reduction of the tidal prism due to the reduction of the surface area. The non-tidal residual, contrasted to that of the full expansion, does not increase enough to offset the reduction by the tidal prism. In the end, the total non-tidal ebb residual plus ebb tidal prism pose a -0.6% reduction and non-tidal flood residual plus flood tidal prism pose a -2.3% reduction.

Table V.2. Tidal Prism and Residual Flushing Volumes for CIEE South Cell Expansion and Base Case

Derived Parameter	**CIEE South Cell (m^3)**	**Base Case (m^3)**	**Percentage Change**
Non-tidal ebb residual	7,328,479	7,176,112	2.1%
Non-tidal flood residual	6,245,219	6,693,760	-6.7%
Ebb tidal prism	27,609,646	27,967,895	-1.3%
Flood tidal prism	27,609,648	27,967,900	-1.3%
Non-tidal ebb residual plus ebb tidal prism	34,938,125	35,144,007	-0.6%
Non-tidal flood residual plus flood tidal prism	33,854,867	34,661,660	-2.3%

The flushing characteristics for other cross-sections further upstream of the Elizabeth River, readers are referred to Wang et al. (2001, Chapter V). In that study, total of 7 cross-sections were evaluated and it was concluded that the impacts beyond ELI2 were order of magnitude less and therefore is omitted in this study.

V-1-2. Assessment of long-term far-field impacts to hydrodynamics

Upon completion of the calibration and verification of the hydrodynamic portion of HEM-3D (see Chapter IV, Section IV-1), the model was used to determine the long-term far-field impacts to the circulation caused by the construction of the expansion. In this section, the global analysis methodology (Chapter III, Section III-4) was applied to assess quantitatively the impacts to surface elevation, surface and bottom salinity, surface and bottom velocity, surface and bottom residual velocity, and sedimentation potential of both the south cell expansion and the full expansion.

One of the advantages of applying the global methodology is that it reveals locations, extents, and magnitudes of the impacts by the south cell and full expansion scenarios to the physical variables of the system. The cumulative percentages of the frequency plots can then be used as a metric for impact assessment. For example, Figure V.3 shows the small regions just to the north and east of Craney Island where the long-term average

bottom residual current of the expansion case differs from that of the base case. Based on the spatial plots of these differences, the cumulative frequency distributions of these differences derived on an areal basis occupied only 5% of the total area (or not exceed over 95%). The complete set of spatial plots for both expansion options is shown in Figures C1 - C16 of Appendix C.

For the 5% area, the values of changes for both the south cell expansion and the full expansion are shown in Table 3. The parameters examined and used as the benchmark include (1) surface elevation (2) surface and bottom current (3) surface and bottom salinity and (4) sedimentation potential. The changed are 0.08 cm, 2.6 cm/s, 2.1 cm/s, 0.03 ppt, 0.13 ppt and 0.50%, respectively, for the south expansion and are 0.18 cm, 2.7 cm/s, 2.2 cm/s, 0.04 ppt, 0.15 ppt and 0.70%, respectively, for the full expansion. Given the background values of the parameters are: 100 cm for surface elevation, 50 cm/sec for surface and bottom current, 25 ppt for surface and bottom salinity. The changes are all very small with less 1%, except for the surface and bottom currents. It appears that the local currents are sensitive to the expansion with increasing magnitude in the northern portion of the expansion while decreasing in the southern portion of the expansion. However, since the area of the change is extremely small, the cumulative impact of the currents variation should not be expected to be significant. This conclusion is independently verified by the flushing calculation in the previous section.

Table V.3. The 95th Percentile Values for the south cell and full expansions versus the base case.

Global Change – 95th Percentile (5% of area contains change greater than value listed)			
Average Long-term Impacts of CIEE Cases			
Change in:	**2001: Original CIEE Design (Case 3)**	**2008: Phase I South Cell Only**	**2008: Full Expansion**
Surface Elevation	0.22 cm	0.08 cm	0.18 cm
Surface Current	2.6 cm/s	2.6 cm/s	2.7 cm/s
Bottom Current	1.7 cm/s	2.1 cm/s	2.2 cm/s
Surface Salinity	0.03 ppt	0.03 ppt	0.04 ppt
Bottom Salinity	0.04 ppt	0.13 ppt	0.15 ppt
Sedimentation Potential	0.80 %	0.50 %	0.70 %

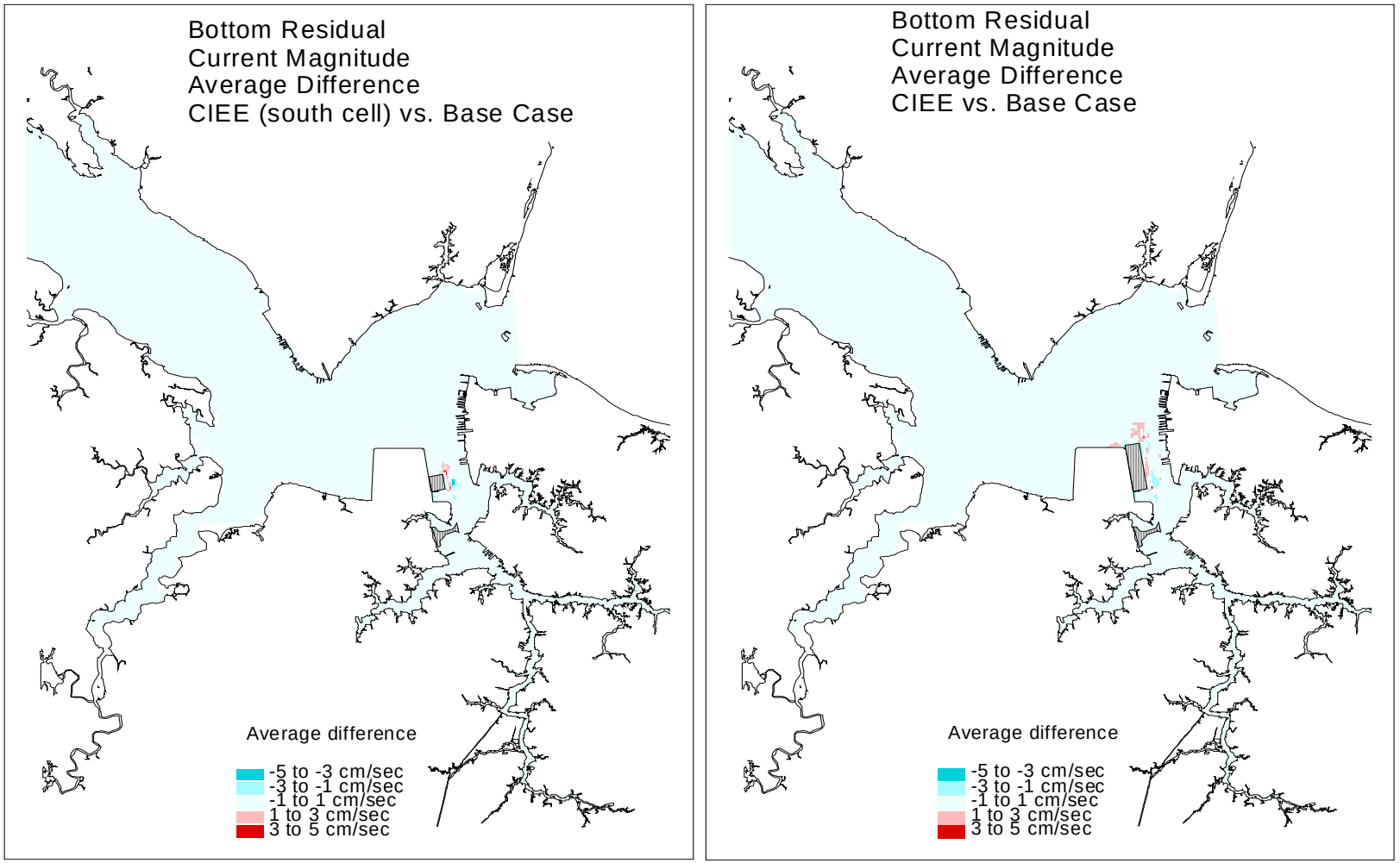

Figure V.3. Bottom residual current magnitude average difference from the base case for the south cell expansion (left panel) and the full expansion (right panel).

V-2. Water Quality Impacts from the South Cell Expansion

V-2-1 Results of the south cell expansion scenario

The south cell expansion, as shown in Figure II.4, is the first phase of construction which will have southern portion of cross dike built along with its access channel (of 55 feet) to the existing ship channel. The hydrodynamic and water model grid representing the southern cell expansion is shown in Figure II.7. Assessment of the long-term water quality impact due to the south cell expansion was initiated by running the combined modeling framework of hydrodynamic and water quality models with the built-out conditions of the south cell land expansion along with the dredging specifications in the access channels and berthing areas.

The analysis involved examination of year-long time series of 4 major water quality parameters (dissolved oxygen, chlorophyll-a, total phosphorus, and total nitrogen) as well as 3 important nutrient species (ammonium, nitrate-nitrite, and dissolved inorganic phosphorus). The locations of CBP Stations LE5.5, LE5.6, and ELI2 (shown earlier in Figure IV.20) were selected for the display of the year-long time series of surface and bottom layer concentration values of these water quality variables in each of the three calibration years 1999, 2000, and 2001. These series are shown at all 3 stations from 1999 through 2001 in Appendix D. The assessments are conducted based on:

1) Long-term time series with hourly time interval
2) Temporal variations of 30-day averaged oxygen
3) Spatial contours of monthly-averaged dissolved oxygen in the summer months

Examples of the 1999 scenario results are also shown below in Figures V.4 and V.5. Comparing Figures V.4 and V.5 with the base condition shown in Figures IV.27 and IV.28, it is readily seen that the surface and bottom trends of the major water quality parameters are very similar, as their seasonal trends are preserved. In order to unravel the impacts more closely, the differences of water quality model predictions (south cell scenario minus base case condition) were derived and plotted for all 3 stations for 1999, 2000, and 2001, as shown in Appendix E. Samples of these differences for the results of the 1999 south cell scenario at Station LE5.6 minus the 1999 base case calibration results at Station LE5.6 are shown below in Figures V.6 and V.7.

The expanded vertical scales of Figures V.6 and V.7 should be noted. The differences in water quality model variable values due to the south cell expansion are variable over time, but are bounded within very small ranges for dissolved oxygen, total phosphorus, total nitrogen, and the nutrient species shown in Figure V.7. Chlorophyll-a differences show a variation ranging approximately from - 0.5 μg/l to +0.5 μg/l. An examination of Figure V.6 reveals that the small differences in dissolved oxygen levels in the surface layer may be slightly reduced, whereas those in the bottom layer are primarily either not changed or are slightly increased. This difference is presumably due to the enhancement of local mixing and increase of non-tidal circulation which allows better exchange with

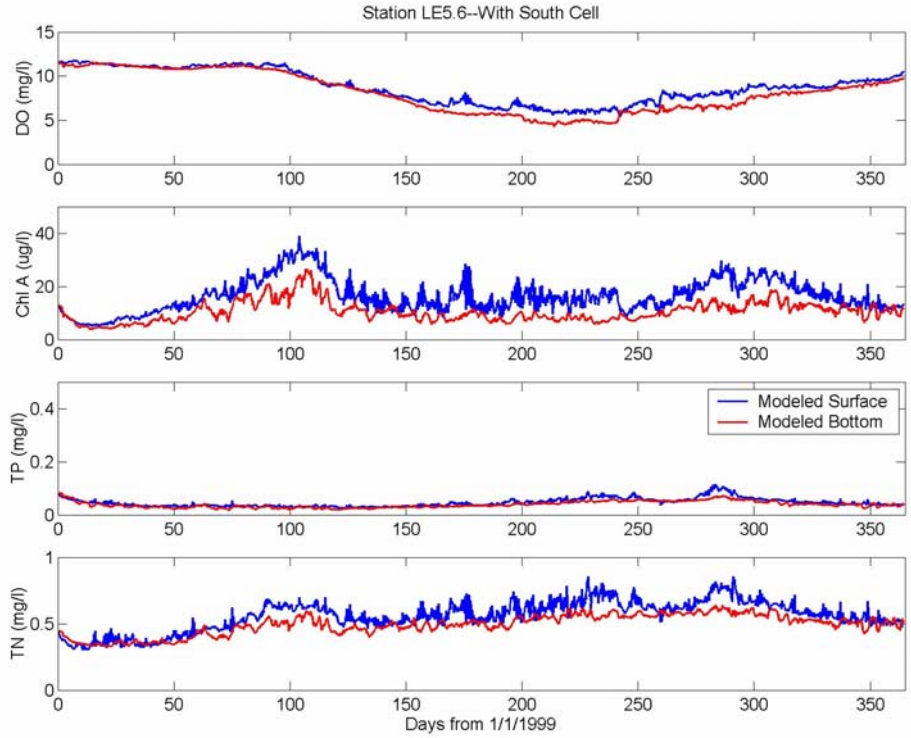

Figure V.4. CIEE south cell expansion scenario model predictions for dissolved oxygen, chlorophyll-a, total phosphorus, and total nitrogen at CBP Station LE5.6 (surface and bottom layers) for 1999.

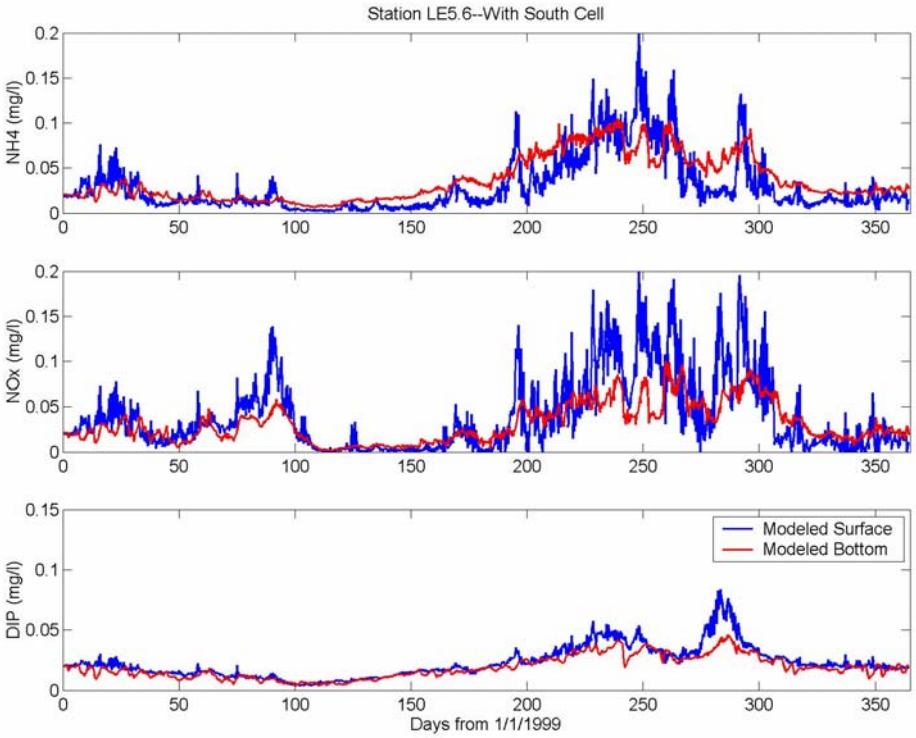

Figure V.5. CIEE south cell expansion scenario model predictions for ammonium, nitrate-nitrite, and dissolved inorganic phosphorus at CBP Station LE5.6 (surface and bottom layers) for 1999.

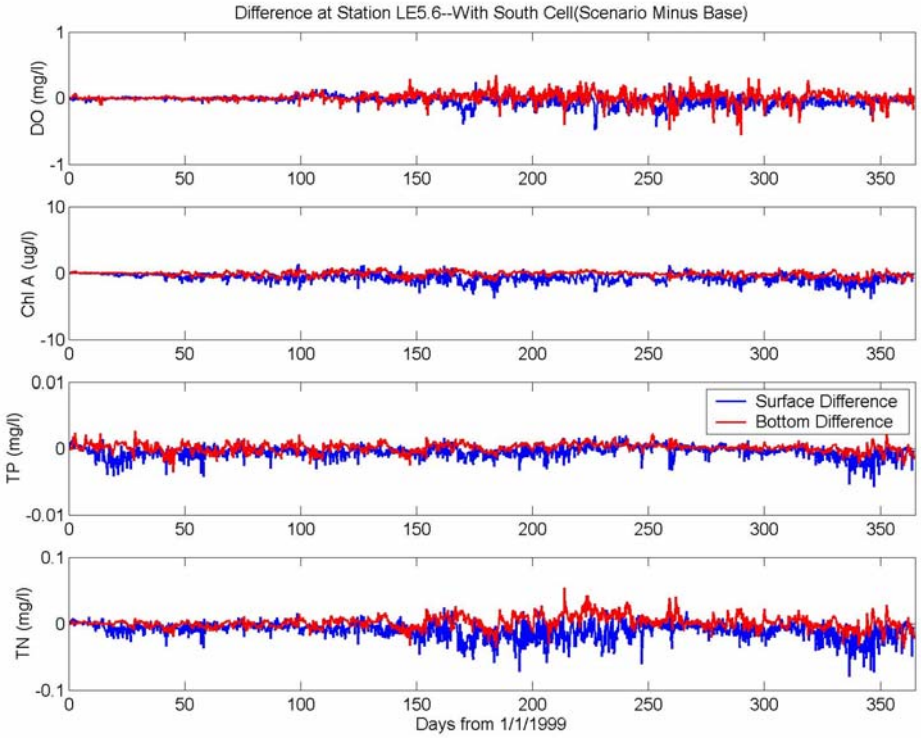

Figure V.6. CIEE south cell expansion scenario minus base case differences of dissolved oxygen, chlorophyll-a, total phosphorus, and total nitrogen at CBP Station LE5.6 (surface and bottom layers) for 1999.

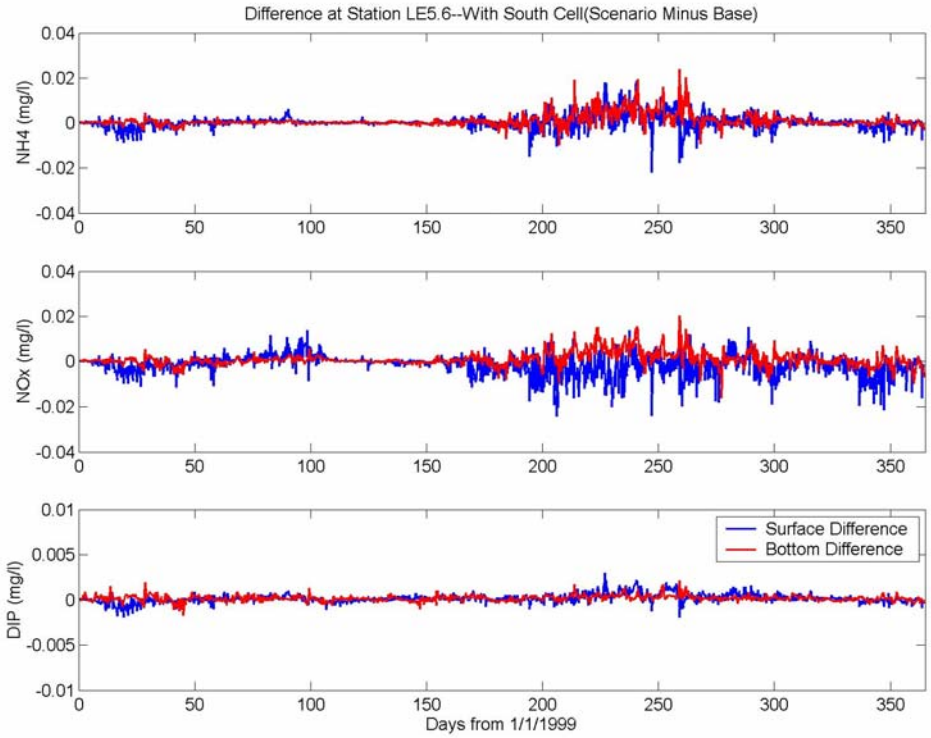

Figure V.7. CIEE south cell expansion scenario minus base case differences of ammonium, nitrate-nitrite, and dissolved inorganic phosphorus at CBP Station LE5.6 (surface and bottom layers) for 1999.

healthy waters of the nearby Hampton Roads region of the James River.

V-2-2 Temporal variation of 30-day averaged dissolved oxygen

The reason that the additional 30-day average time series is analyzed is because one of the important criteria for assessing dissolved oxygen level variation in the Virginia water quality guidelines is the variation of DO measured over a 30-day averaging period not fall below 5 mg/l. For that reason, the long-term temporal variation of 30-day averaged dissolved oxygen due to both the south cell expansion and the full expansion are investigated.

Working again with the aforementioned differences (south cell scenario predictions minus base case predictions), this analysis involved comparing these differences extracted as 30-day averages for the entire period of record for surface and bottom layers and for a vertically averaged value as well. Appendix F shows these average differences plotted at CBP Stations LE5.5, LE5.6, and ELI2 for the years 1999, 2000, and 2001, as well as a tabulation of the vertically averaged differences for all 7 water quality parameters involved in the calibration. Examples of these plots and tables are shown below in Figure V.8 (differences at surface and bottom layers) and in Figures V.9 and Table V.4 (vertically averaged differences) for those differences in the 1999 simulation predictions for CBP Station LE5.6. the fact that the change of DO is negative at the surface and positive at the bottom plus the fact that differences is smaller for the vertically averaged DO indicate that vertical mixing plays a role in mitigating the impact.

The differences due to the expansion impacts are shown to range from 0.00-0.05 mg/l (dissolved oxygen), 0.1-0.8 μg/l (chlorophyll-a), 0.0000-0.0008 mg/l (total phosphorus), 0.001-0.013 mg/l (total nitrogen), 0.000-0.004 mg/l (ammonia), 0.0001-0.0025 mg/l (nitrate-nitrite), and 0.0000-0.0005 mg/l (dissolved inorganic phosphorus). The full set of these differences (south cell expansion) for each month of 1999, 2000, and 2001 at CBP Stations LE5.5, LE5.6, and ELI2 is provided in Tables F.1, F.2, and F.3 of Appendix F. Detection limits furnished by the Chesapeake Bay program that are relevant to this study are 0.1 mg/l for dissolved oxygen, 0.5 μg/l for chlorophyll-a, 0.003 mg/l for total phosphorus, 0.01 mg/l for total nitrogen, 0.005, mg/l for ammonia, 0.001 mg/l for nitrate-nitrite, and 0.0015 mg/l for dissolved inorganic phosphorus. These limits are shown in Table V.4 for the south cell expansion along with the 30-day average differences (scenario minus base case) for each month of 1999 at CBP Station LE5.6. It is readily seen that the differences due to the south cell expansion are at most on the same order of magnitude, and in general much smaller, than these detection limits.

V-2-3 Spatial contours of summer dissolved oxygen

As part of the assessment of long-term impacts to dissolved oxygen due to the south cell construction, it is important to know the spatial extent and magnitude of any change to dissolved oxygen at either the surface or bottom layers or for the vertical average. For this reason, the model results were processed to determine the differences in dissolved

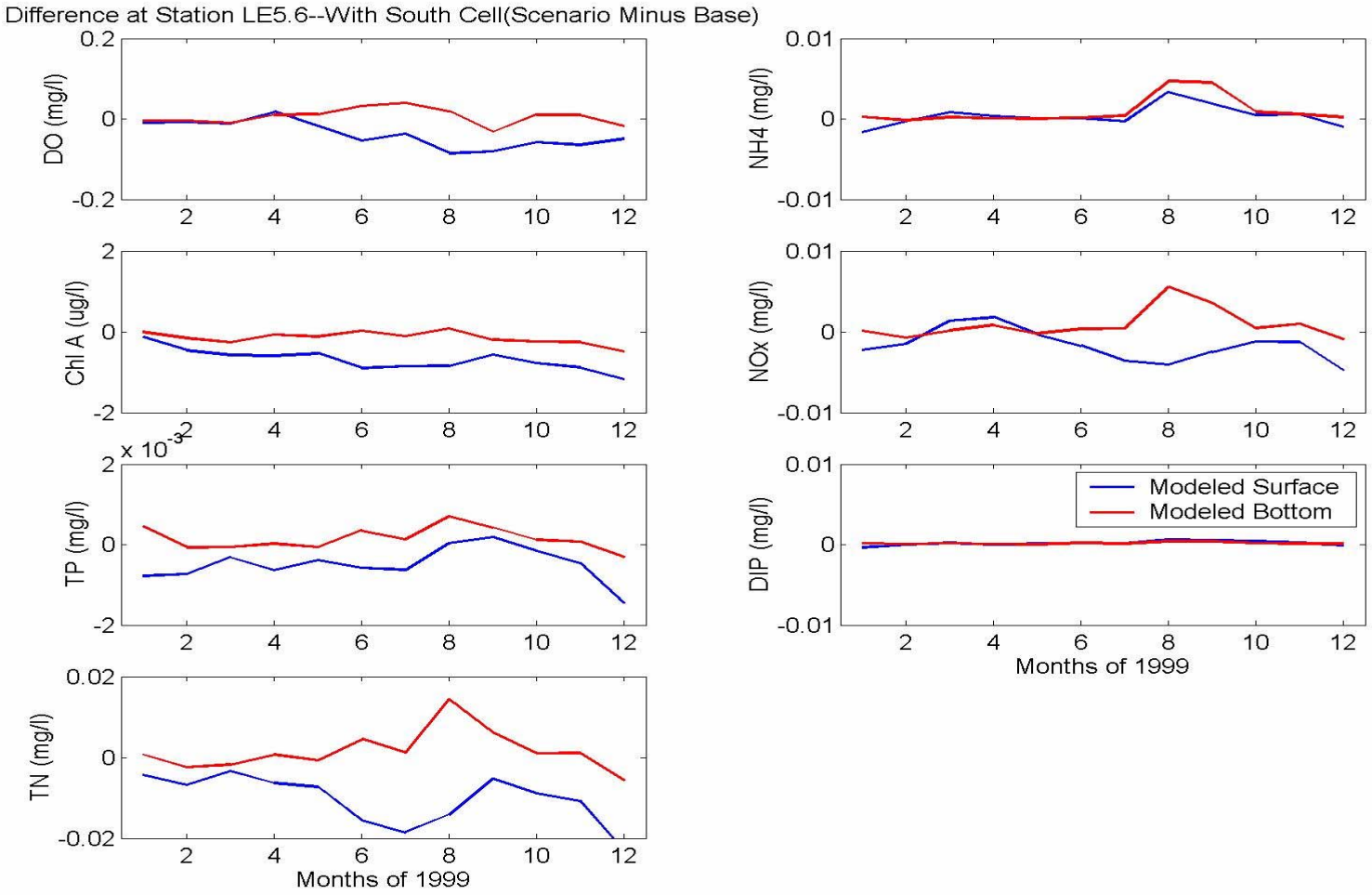

Figure V.8. South cell scenario vs. base case 30-day average differences for predictions of dissolved oxygen, chlorophyll-a, total phosphorus, total nitrogen, ammonium, nitrate-nitrite, and dissolved inorganic phosphorus at CBP Station LE5.6 (surface and bottom layers) for 1999.

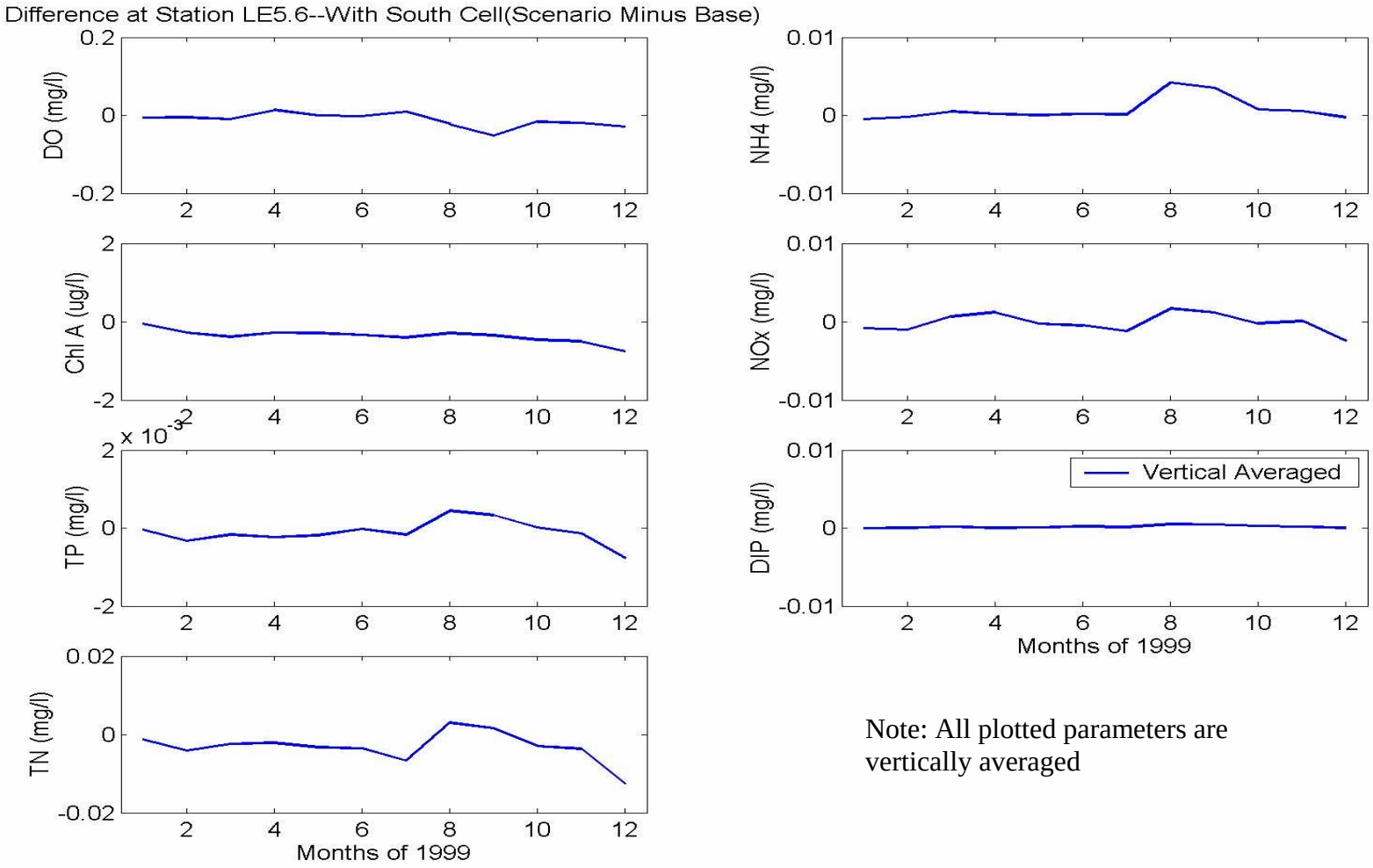

Note: All plotted parameters are vertically averaged

Figure V.9. South cell scenario vs. base case 30-day average differences for predictions of dissolved oxygen, chlorophyll-a, total phosphorus, total nitrogen, ammonium, nitrate-nitrite, and dissolved inorganic phosphorus at CBP Station LE5.6 (vertically averaged) for 1999.

	Month	DO	Chl	TP	TN	NH_4	NO_X	DIP
		mg/l	µg/l	mg/l	mg/l	Mg/l	mg/l	mg/l
Station LE5.6 (1999)	Jan.	-0.01	-0.1	0.0000	-0.001	-0.001	-0.0008	0.0000
	Feb.	-0.01	-0.3	-0.0003	-0.004	-0.000	-0.0010	0.0000
	Mar.	-0.00	-0.4	-0.0002	-0.002	0.001	0.0007	0.0002
	Apr.	0.00	-0.3	-0.0002	-0.002	0.000	0.0012	0.0000
	May	0.00	-0.3	-0.0002	-0.003	0.000	-0.0002	0.0001
	Jun.	-0.00	-0.3	0.0000	-0.004	0.000	-0.0005	0.0002
	Jul.	0.01	-0.4	-0.0002	-0.007	0.000	-0.0012	0.0001
	Aug.	-0.02	-0.3	0.0004	0.003	0.004	0.0017	0.0005
	Sep.	-0.05	-0.3	0.0003	0.002	0.004	0.0011	0.0005
	Oct.	-0.02	-0.5	0.0000	-0.003	0.001	-0.0002	0.0003
	Nov.	-0.02	-0.5	-0.0001	-0.004	0.001	0.0001	0.0002
	Dec.	-0.03	-0.8	-0.0008	-0.013	-0.000	-0.0025	0.0000
Detection limits:		**0.1**	**0.5**	**0.003**	**0.01**	**0.005**	**0.001**	**0.0015**

Table V.4. South cell expansion scenario 30-day average differences (scenario minus base) for predictions of dissolved oxygen, chlorophyll-a, total phosphorus, total nitrogen, ammonium, nitrate-nitrite, and dissolved inorganic phosphorus at CBP Station LE5.6 (vertically averaged) for 1999 (values plotted in Figure V.9)

oxygen (south cell scenario minus base case) for the 30-day average DO differences over those months of the year that low oxygen values are likely to occur.

Differences were determined globally (at each cell location and at each of the 6 cell layers) and then used to create spatial plots of DO differences for a 6-layer vertical average as well as for the surface and bottom layers. These differences were 30-day averages within each of the months of concern (June, July, August, and September) for the years 1999, 2000, and 2001. In this fashion, a total of 36 spatial plots (3 depth conditions by 4 months by 3 simulation years) of the 30-day average DO differences were generated, providing opportunity for close scrutiny of any significant impact to DO levels caused by the south cell expansion construction.

The spatial plots of DO differences are shown in Figures G1 through G12, G13 through G24, and G25 through G36, respectively, for the years 1999, 2000, and 2001 of Appendix G. Additionally, Figure V.10 is provided below as an example of these spatial plots for discussion. These spatial plots of DO differences consistently show that the difference caused by the south cell construction are less than 0.3 mg/l at all locations, with the exception of the bottom layer and vertically averaged comparisons in the very localized areas that are directly northeast, east, and, southeast of the south cell. In these small limited areas, differences are approximately 1.0 mg/l.

An inspection of Figure V.10 shows that the average differences of DO levels for the bottom layer due to the south cell expansion are slightly negative (denoted by blue) due east of the south cell. This means that there is a slightly negative impact. On the other hand, these differences are slightly positive at cell locations towards both the northeast and southeast (denoted by red).

It is important to note that the comparison of bottom layer DO between the south cell expansion scenario and the base case shows a difference to the east of Craney Island that is partially due to the depth increase. In the blown-up representation shown in Figure V.11, a comparison made at the same depth, at the existing bottom depth, shows that DO levels were actually increased due to the south cell expansion.

V-2-4 Summary of the impact assessment for the south cell expansion

The combination of temporal and spatial comparisons of differences between the south cell scenario and the base case allows the long-term impacts to water quality to be quantitatively examined. Table V.4 summarizes the impact to water quality caused by the south cell expansion. These low differences (computed over a 30-day averaging basis and ranging on the order of 0.01 – 0.001 mg/l) apply to dissolved oxygen, total phosphorus, total nitrogen, and the nutrient species NH_4, NO_x, and PO_4, and the differences in chlorophyll-a are somewhat higher (0.0 to 0.5 μg/l) are all well within the detection limit of measurement in the current technology.

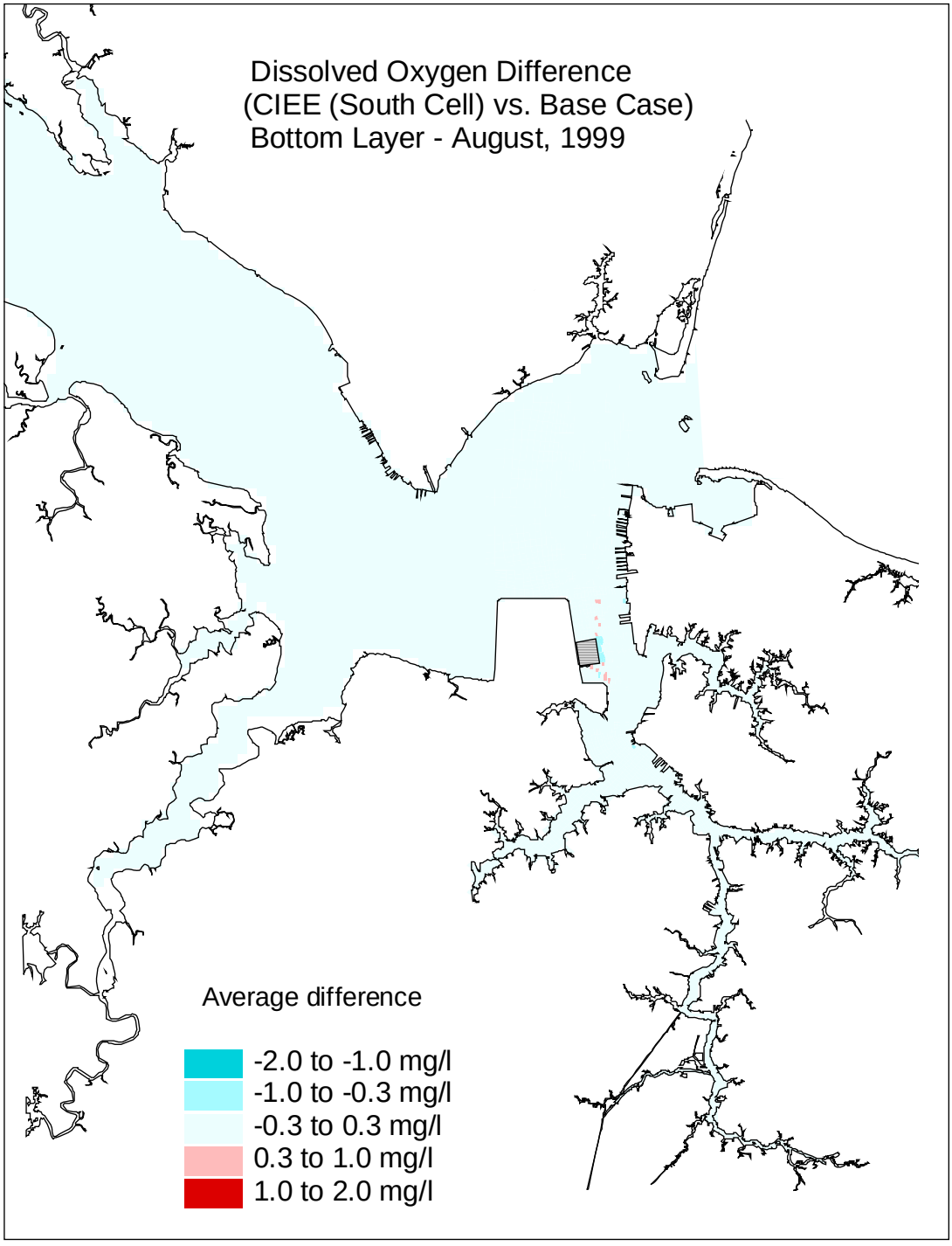

Figure V.10. Dissolved oxygen difference between the CIEE (south cell) and the base case at bottom layer for August, 1999.

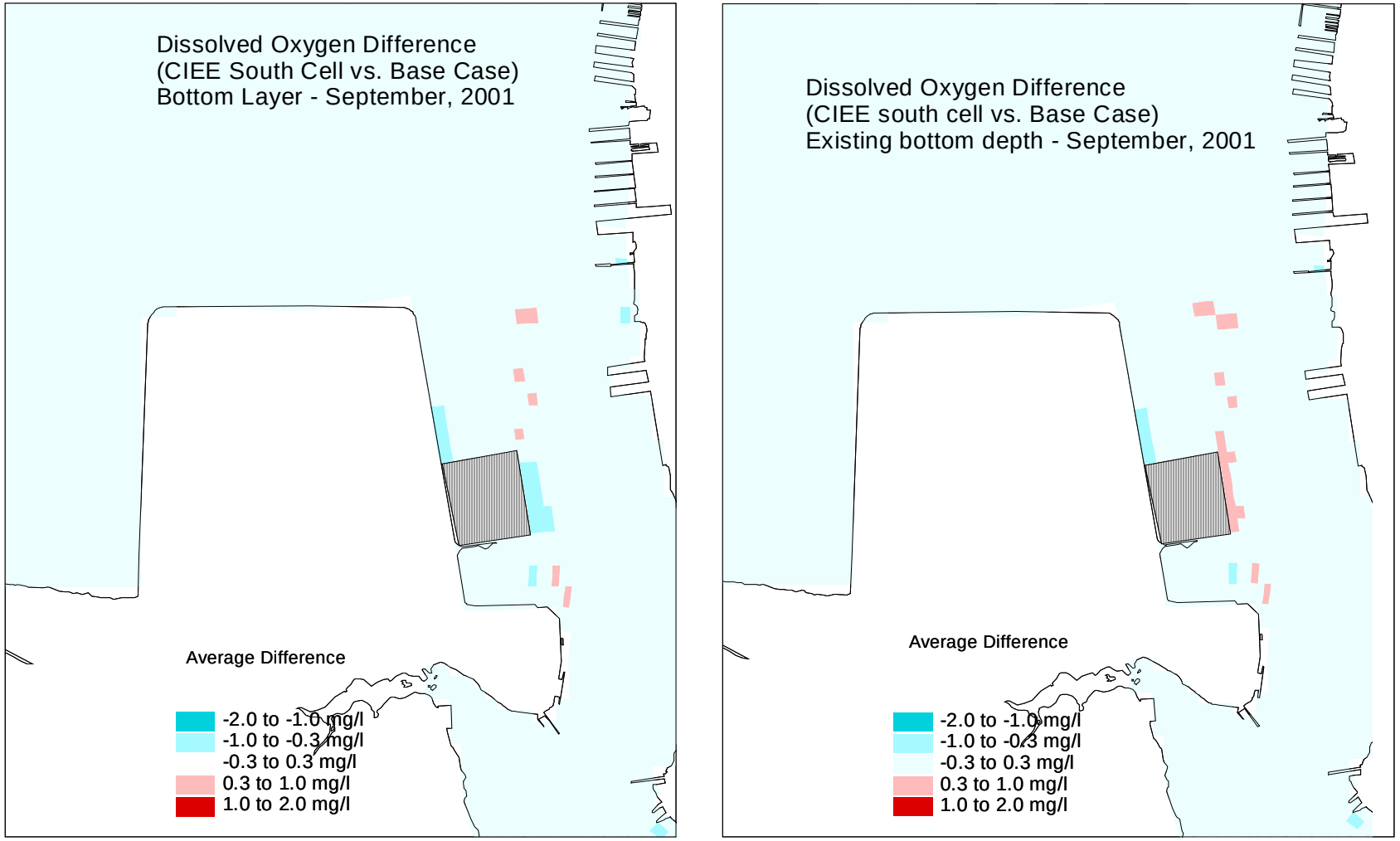

Figure V.11. Dissolved oxygen difference (30-day average) between the CIEE (south cell) and the base case at a) the bottom layer and b) the existing bottom depth for September, 2001.

V-3. Water Quality Impacts from the Full Expansion

V-3-1 Results of the full expansion scenario

The Craney Island full expansion, as shown in Figure II.6, is the final phase of construction which will have both northern and southern cell dike in place, and the completion of quayside dredging in front of terminal. The hydrodynamic and water quality model grid represented the full expansion is shown in Figure II.8. Assessment of the long-term water quality impact due to the full expansion was initiated by running the combined modeling framework of hydrodynamic and water quality models with the fully built-out conditions of the full expansion along with the dredging specifications in the access channels and berthing areas.

The analysis involved examination of year-long time series of 4 major water quality parameters (dissolved oxygen, chlorophyll-a, total phosphorus, and total nitrogen) as well as 3 important nutrient species (ammonium, nitrate-nitrite, and dissolved inorganic phosphorus). The locations of CBP Stations LE5.5, LE5.6, and ELI2 (shown earlier in Figure IV.20) were selected for the display of the year-long time series of surface and bottom layer concentration values of these water quality variables in each of the three calibration years 1999, 2000, and 2001. These series are shown at all 3 stations from 1999 through 2001 in Appendix H. Again, the assessments are conducted based on:

1) Long-term time series with hourly time interval
2) Temporal variations of 30-day averaged oxygen
3) Spatial contours of monthly-averaged dissolved oxygen in the summer months

Examples of he 1999 scenario results are also shown below in Figures V.12 and V.13. Comparing Figures V.12 and V.13 with Figures IV.30 and IV.31, it is readily seen that the surface and bottom variations of the major water quality parameters are similar, including the seasonal trend for the two 1999 simulations. The differences of water quality model predictions (full expansion scenario minus base case condition) were derived and plotted for all 3 stations for 1999, 2000, and 2001, as shown in Appendix I. Samples of these differences for the results of the 1999 full expansion scenario at Station LE5.6 minus the 1999 base case calibration results at Station LE5.6 are shown below in Figures V.14 and V.15.

The differences in water quality model variable values due to the full expansion are variable over time, but are again bounded within very small ranges for dissolved oxygen, total phosphorus, total nitrogen, and the nutrient species shown in Figure V.15. The expanded vertical scales of Figures V.14 and V.15 should be noted. An examination of Figure V.14 reveals that whereas the small differences in dissolved oxygen levels in the surface layer is slightly reduced, those in the bottom layer actually move more towards to the positive values. In addition, the chlorophyll concentration also reduced slightly as

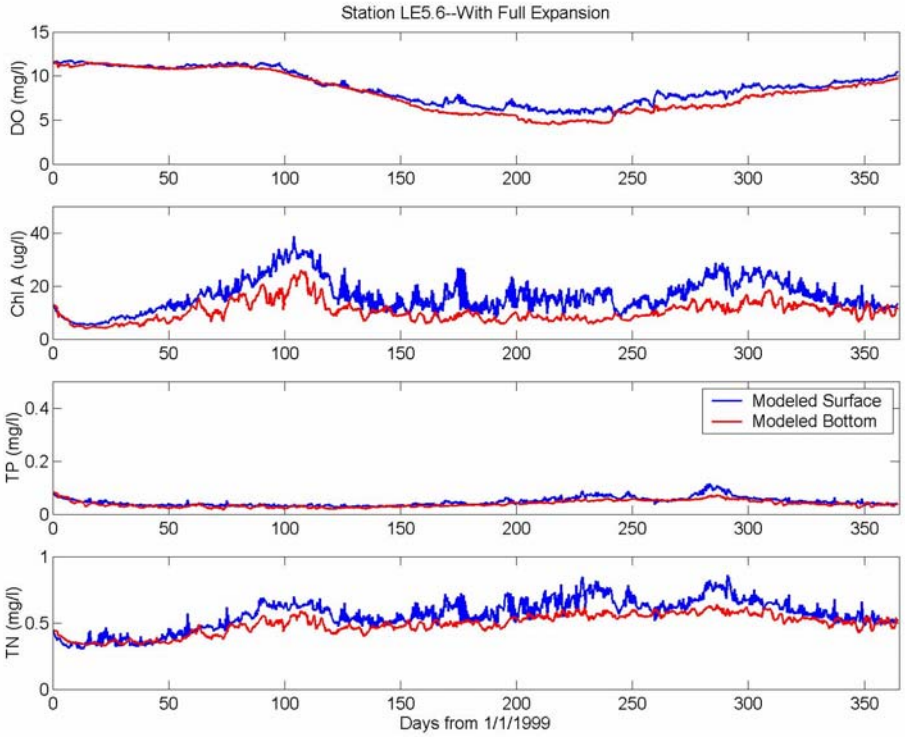

Figure V.12. CIEE full expansion scenario model predictions for dissolved oxygen, chlorophyll-a, total phosphorus, and total nitrogen at CBP Station LE5.6 (surface and bottom layers) for 1999.

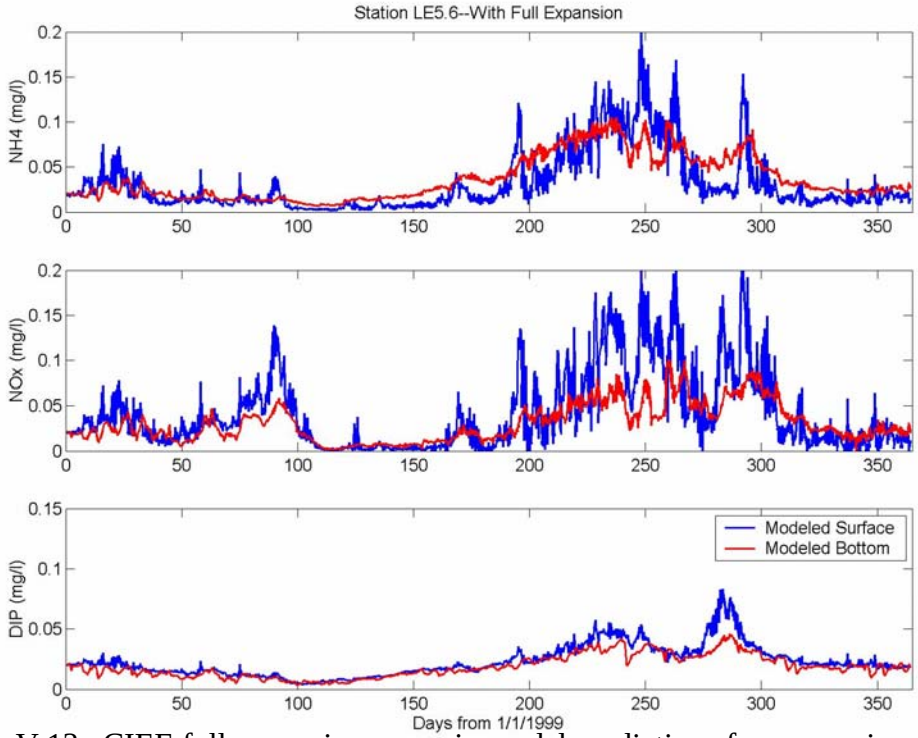

Figure V.13. CIEE full expansion scenario model predictions for ammonium, nitrate-nitrite, and dissolved inorganic phosphorus at CBP Station LE5.6 (surface and bottom layers) for 1999.

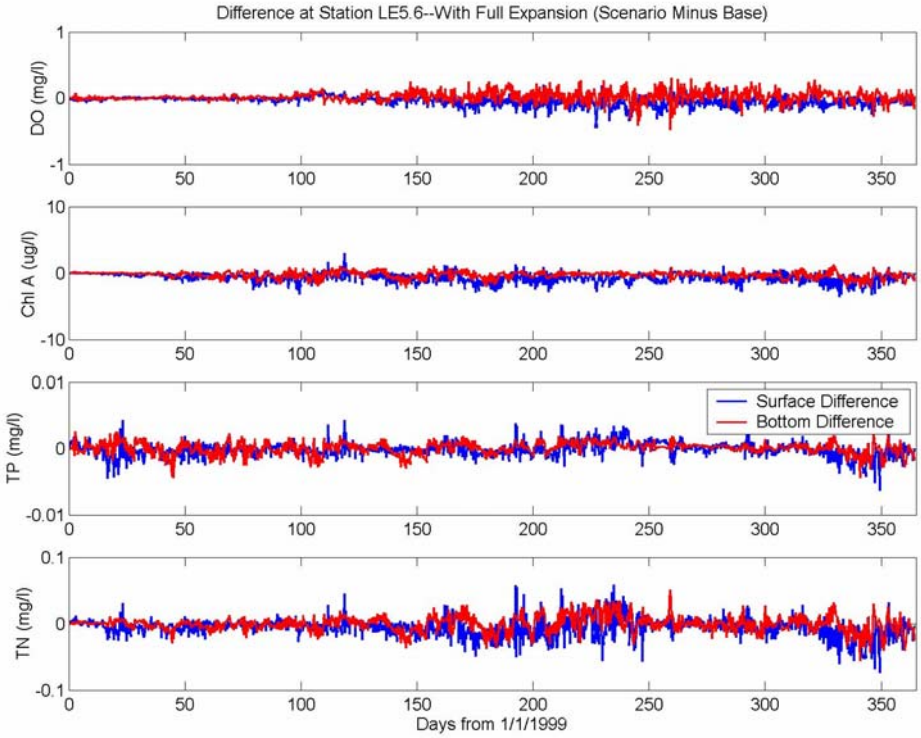

Figure V.14. CIEE full expansion scenario minus base case differences of dissolved oxygen, chlorophyll-a, total phosphorus, and total nitrogen at CBP Station LE5.6 (surface and bottom layers) for 1999.

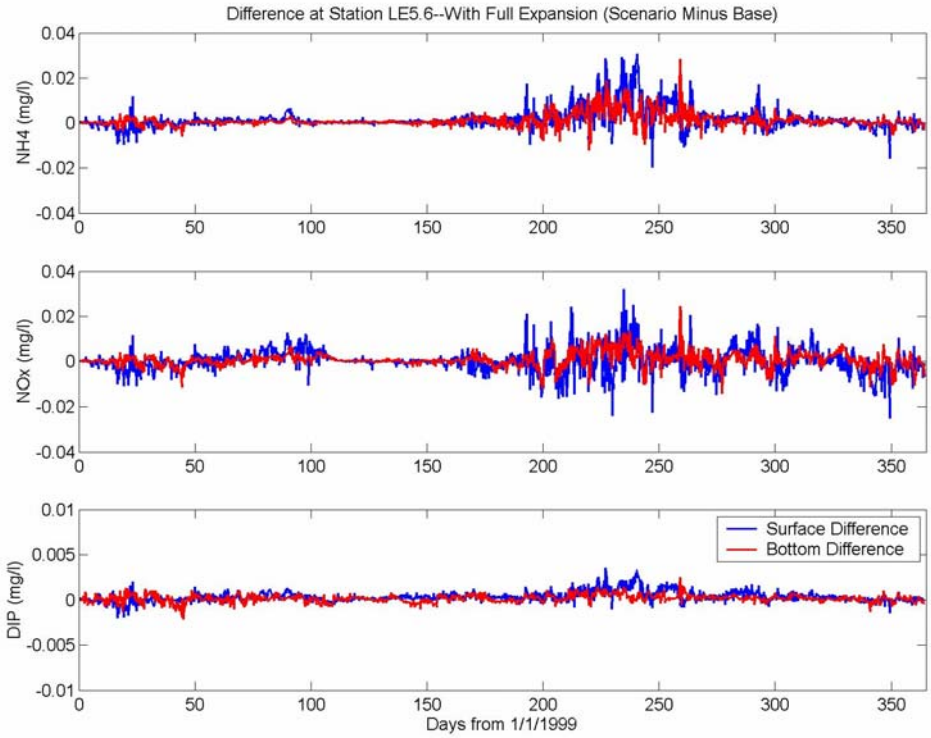

Figure V.15. CIEE full expansion scenario minus base case differences of ammonium, nitrate-nitrite, and dissolved inorganic phosphorus at CBP Station LE5.6 (surface and bottom layers) for 1999.

compared to the south expansion scenario. The reason these positive impacts were brought about in the full expansion was due in part to the fact that the total flushing capability for the full expansion is larger than that of the south cell expansion, as shown in Tables V.1. and V.2.. That means an increase of non-tidal circulation allows better exchange of water with the healthy waters of the nearby Hampton Roads region of the James River and that minimize the impacts.

V-3-2 Temporal variation of 30-day averaged dissolved oxygen

The reason the additional 30-day average time series is analyzed is because one of the important criteria for assessing dissolved oxygen level variation in the Virginia water quality guidelines is the variation of DO measured over a 30-day averaging not fall below 5 mg/l. Working again with the aforementioned differences (full expansion scenario predictions minus base case predictions), this analysis involved comparing these differences extracted as 30-day averages for the entire period of record for surface and bottom layers and for a vertically averaged value as well. Appendix J shows these average differences plotted at CBP Stations LE5.5, LE5.6, and ELI2 for the years 1999, 2000, and 2001, as well as a tabulation of the vertically averaged differences for all 7 water quality parameters involved in the calibration. Examples of these plots and tables are shown below in Figure V.16 (differences at surface and bottom layers) and in Figures V.17 and Table V.5 (vertically averaged differences) for those differences in the 1999 simulation predictions for CBP Station LE5.6.

The differences due to the expansion impact are shown to range from 0.00-0.03 mg/l (dissolved oxygen), 0.1-0.9 μg/l (chlorophyll-a), 0.0000-0.0009 mg/l (total phosphorus), 0.001-0.014 mg/l (total nitrogen), 0.000-0.007 mg/l (ammonia), 0.0001-0.0037 mg/l (nitrate-nitrite), and 0.0000-0.0008 mg/l (dissolved inorganic phosphorus). The full set of these differences (full expansion) for each month of 1999, 2000, and 2001 at CBP Stations LE5.5, LE5.6, and ELI2 is provided in Tables J.1, J.2, and J.3 of Appendix J. Detection limits furnished by the Chesapeake Bay program that are relevant to this study are 0.1 mg/l for dissolved oxygen, 0.5 μg/l for chlorophyll-a, 0.003 mg/l for total phosphorus, 0.01 mg/l for total nitrogen, 0.005, mg/l for ammonia, 0.001 mg/l for nitrate-nitrite, and 0.0015 mg/l for dissolved inorganic phosphorus. These limits are shown in Table V.5 for the full cell expansion along with the 30-day average differences (scenario minus base case) for each month of 1999 at CBP Station LE5.6. It is readily seen that the differences are at most on the same order of magnitude, and in general much smaller, than these detection limits.

V-3-3 Spatial contours of summer dissolved oxygen

As part of the assessment of long-term impacts to dissolved oxygen due to the full expansion construction, it is important to know the spatial extent and magnitude of any change to dissolved oxygen at either the surface or bottom layers or for the vertical average. For this reason, the model results were processed to determine the differences in dissolved oxygen (full expansion scenario minus base case) for the 30-day average DO differences over those months of the year that low oxygen values are likely to occur.

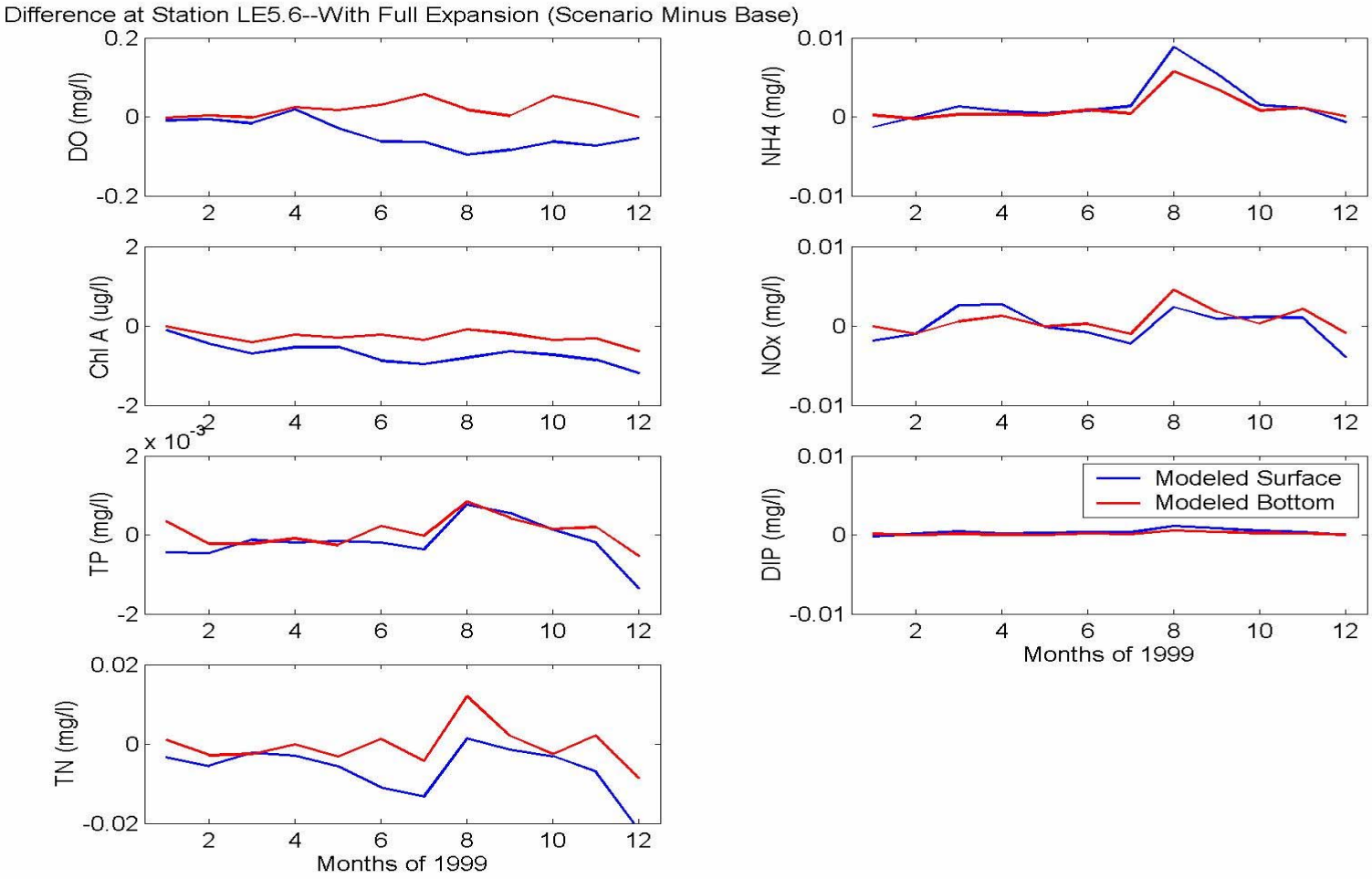

Figure V.16. Full expansion scenario vs. base case 30-day average differences for predictions of dissolved oxygen, chlorophyll-a, total phosphorus, total nitrogen, ammonium, nitrate-nitrite, and dissolved inorganic phosphorus at CBP Station LE5.6 (surface and bottom layers) for 1999.

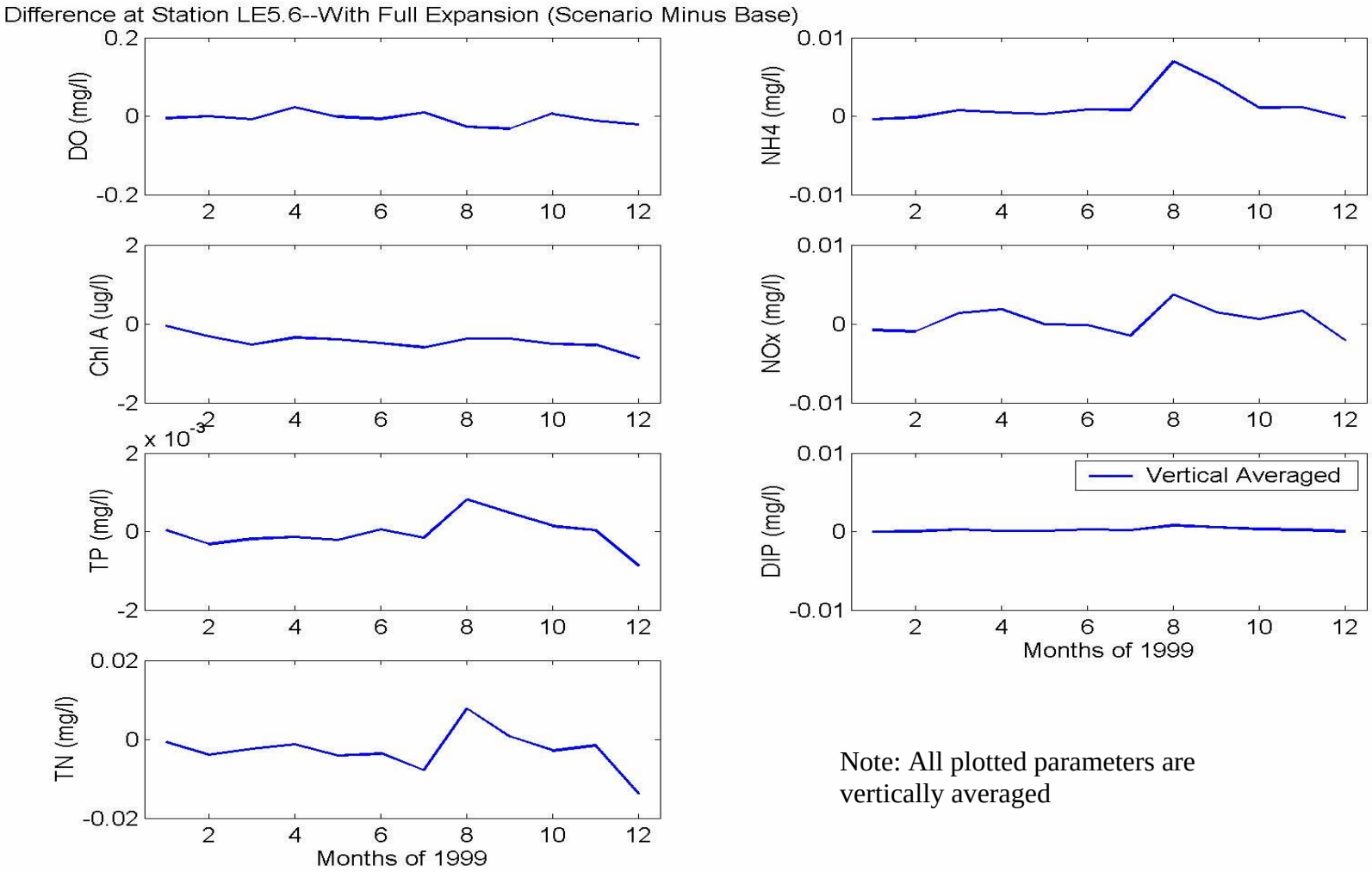

Figure V.17. Full expansion scenario vs. base case 30-day average differences for predictions of dissolved oxygen, chlorophyll-a, total phosphorus, total nitrogen, ammonium, nitrate-nitrite, and dissolved inorganic phosphorus at CBP Station LE5.6 (vertically averaged) for 1999.

	Month	DO	Chl	TP	TN	NH_4	NO_X	DIP
		mg/l	µg/l	mg/l	mg/l	mg/l	mg/l	mg/l
Station LE5.6	Jan.	-0.01	-0.1	0.0000	-0.001	-0.000	-0.0008	0.0000
	Feb.	-0.00	-0.3	-0.0003	-0.004	-0.000	-0.0010	0.0000
	Mar.	-0.01	-0.5	-0.0002	-0.002	0.001	0.0014	0.0002
	Apr.	0.02	-0.4	-0.0001	-0.001	0.001	0.0018	0.0001
	May	-0.00	-0.4	-0.0002	-0.004	0.000	-0.0001	0.0001
	Jun.	-0.01	-0.5	0.0001	-0.004	0.001	-0.0002	0.0003
	Jul.	0.01	-0.6	-0.0002	-0.008	0.001	-0.0015	0.0002
	Aug.	-0.03	-0.4	0.0008	0.008	0.007	0.0037	0.0008
	Sep.	-0.03	-0.4	0.0005	0.001	0.004	0.0014	0.0006
	Oct.	0.01	-0.5	0.0001	-0.003	0.001	0.0006	0.0003
	Nov.	-0.01	-0.5	0.0000	-0.002	0.001	0.0017	0.0002
	Dec.	-0.02	-0.9	-0.0009	-0.014	-0.000	-0.0021	0.0000
Detection limits:		**0.1**	**0.5**	**0.003**	**0.01**	**0.005**	**0.001**	**0.0015**

Table V.5 Full expansion scenario vs. base case 30-day average differences (scenario minus base) for predictions of dissolved oxygen, chlorophyll-a, total phosphorus, total nitrogen, ammonium, nitrate-nitrite, and dissolved inorganic phosphorus at CBP Station LE5.6 (vertically averaged) for 1999 (values plotted in Figure V.17).

Differences were determined globally (at each cell location and at each of the 6 cell layers) and then used to create spatial plots of DO differences for a 6-layer vertical average as well as at the surface and bottom layers. These differences were 30-day averages within each of the months of concern (June, July, August, and September) for the years 1999, 2000, and 2001. In this fashion, a total of 36 spatial plots (3 depth conditions by 4 months by 3 simulation years) of the 30-day average DO differences were generated, providing opportunity for close scrutiny of any significant impact to DO levels caused by the full expansion construction.

The spatial plots of DO differences are shown in Figures K1 through K12, K13 through K24, and K25 through K36, respectively, for the years 1999, 2000, and 2001 of Appendix K. Additionally, Figure V.18 is provided below as an example of these spatial plots for discussion. These spatial plots of DO differences consistently show that the difference caused by the full expansion construction are less than 0.3 mg/l at all locations, with the exception of the bottom layer and vertically averaged comparisons in the very localized areas that are directly northeast, east, and, southeast of the expansion. In these small limited areas, differences are 1.0 mg/l.

An inspection of Figure V.18 shows that the average differences of DO levels for the bottom layer due to the full expansion are slightly negative (denoted by blue) due east of the expansion. This means that there is a slightly negative impact. On the other hand, these differences are slightly positive at cell locations towards the southeast (denoted by red). It is important to note that the comparison of bottom layer DO between the full expansion scenario and the base case shows a difference to the east of Craney Island that is partially due to the depth increase. In the blown-up representation shown in Figure V.19, a comparison made at the same depth, at the existing bottom depth, shows that DO levels were actually increased due to the full expansion.

V-3-4 Summary of the impact assessment for the full expansion

The combination of temporal and spatial comparisons of differences between the full expansion scenario and the base case allows the long-term impacts to water quality to be quantitatively examined. Table V.5 summarizes the impact to water quality caused by the full expansion. These low differences (computed over a 30-day averaging basis and ranging on the order of 0.01 – 0.001 mg/l) apply to dissolved oxygen, total phosphorus, total nitrogen, and the nutrient species NH_4, NO_x, and PO_4. Differences in chlorophyll-a are somewhat higher (0.0 to 0.5 μg/l).

Despite there are slight differences in terms of their temporal and spatial distribution of impacts between south cell expansion and full expansion, the overall magnitude are very small and are within the same order of magnitude of measurement detection limit. From dynamical point of view, It should be kept in mind that the healthy water quality condition in the Lower James River is the premium asset and key factor that plays an important role in minimizing the impact from the Craney Island Eastward Expansion.

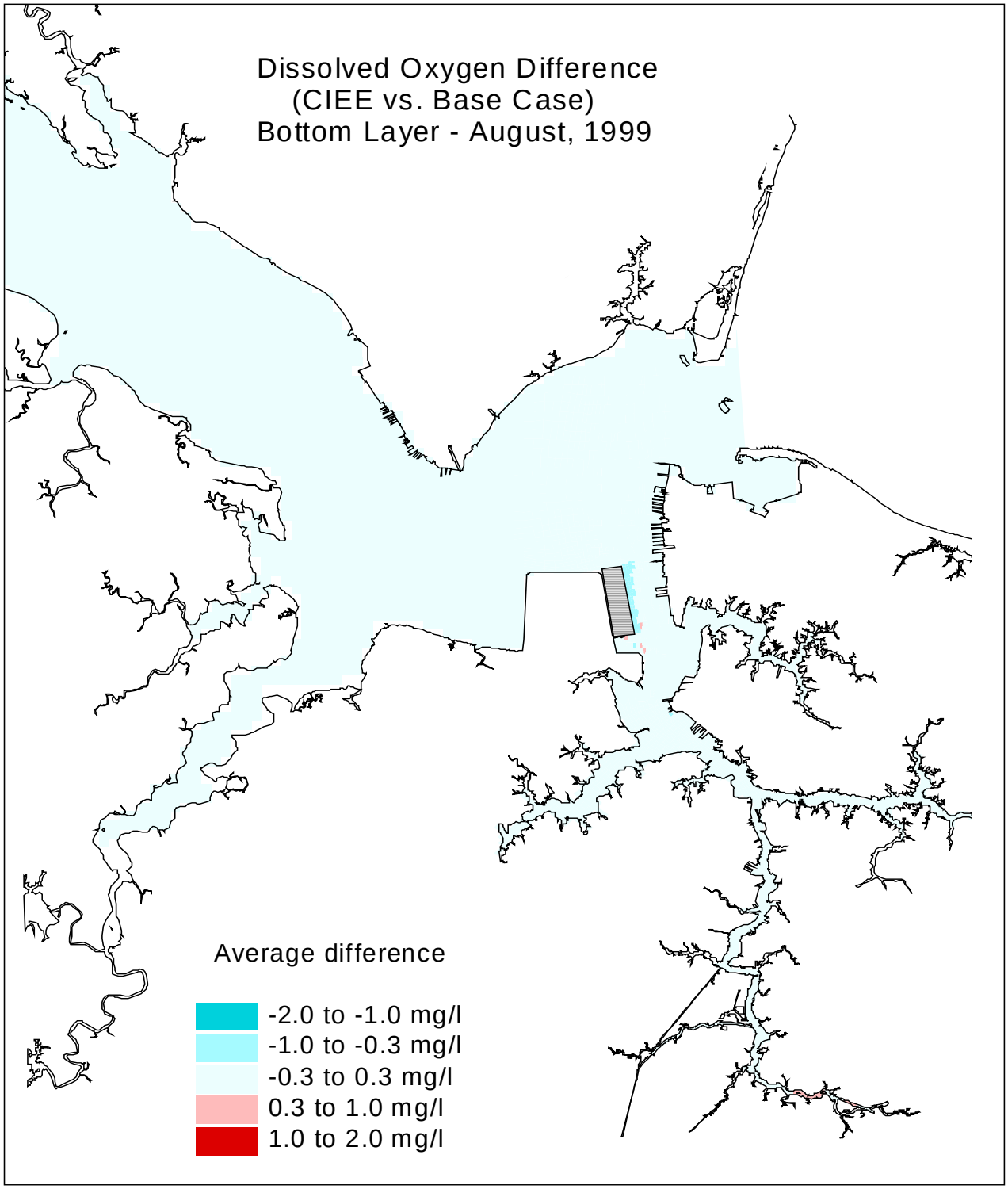

Figure V.18. Dissolved oxygen difference between the CIEE (full expansion) and the Base Case at the bottom layer for August, 1999.

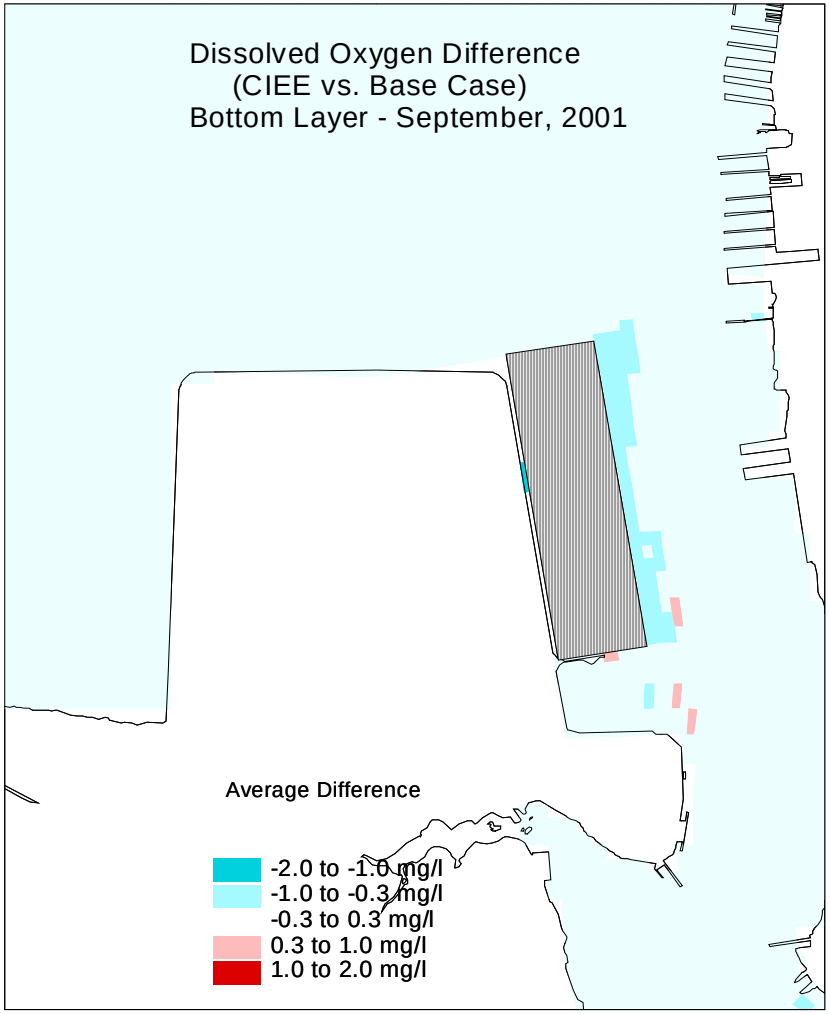

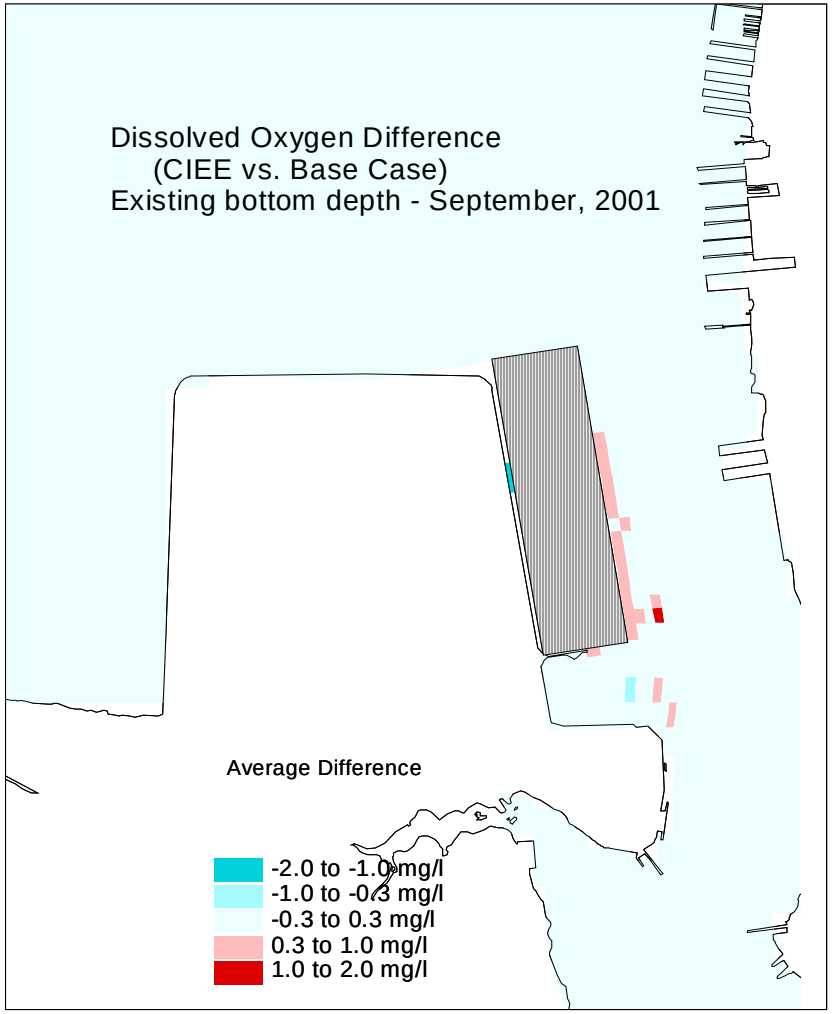

Figure V.19. Dissolved oxygen difference (30-day average) between the CIEE (full expansion) and the Base Case at a) the bottom layer and b) the existing bottom depth for September, 2001

CHAPTER VI. SENSITIVITY ANALYSIS

The model assigned parameters and coefficients have ranges. In some cases, their values are not the same for different regions of application, or during different periods of the simulation. For example, many coefficients used in the Chesapeake Bay main stem are different from those used in the tributaries, simply because the hydrodynamic and ecosystem dynamics are quite different. The HEM3D parameters and coefficients used in the calibration and in the scenario runs of this investigation are kept the same. In addition, the ones used require no change between the James and Elizabeth Rivers, nor between the individual calibration years. Among many different parameters and coefficients, our experience indicated that major uncertainties that exist during the calibration process are the response of the system to watershed loading, the maximum growth rate for phytoplankton, and the vertical mixing and stratification. This is consistent with other studies in the Chesapeake Bay, for example, eutrophication study in the Chesapeake Bay (Cero, and Cole, 1994).

The currently used watershed loadings are derived from the HSPF model results furnished by the EPA Chesapeake Bay program. Their parameters are standardized. The maximum growth rate used for phytoplankton species of diatom is 2.0/day, which is within the median range of values reported in the literature. The background vertical eddy diffusivity used from the second-order turbulence scheme is 10^{-6} m^2 /sec. These are typical values used in many estuarine modeling, but the question being raised is how sensitive is the model computation results to the variation of these values.

For this reason, it was decided to conduct sensitivity tests to examine the effects of 1) increasing and decreasing watershed nonpoint source loading, 2) incurring change to the phytoplankton dynamics by increasing and decreasing the maximum growth rates used, and 3) incurring change to the vertical stratification and mixing by increasing and decreasing the background eddy diffusivity parameter that controls the mixing. A plus and minus 10% change of watershed non-point source, plus and minus 12.5% of the maximum phytoplankton growth rate, and one order of magnitude difference of vertical eddy diffusivity have been applied for the test of model's sensitivities.

These tests were performed by running full one-year simulations (i.e., using 1999). As was done for the scenario impact assessment, the examination of the differences in the predicted values for each of 7 water quality state variables was used to illustrate the sensitivity. Differences for all key water quality variables (dissolved oxygen, chlorophyll-a, total phosphorus, total nitrogen, ammonia, nitrate-nitrate, and dissolved inorganic phosphorus) were plotted at CBP stations LE5.5, LE5.6, and ELI2 and are shown in their entirety in Appendix L. For purposes of discussion, the present chapter shows the model prediction differences at Station LE5.6 only.

Table VI.1 below lists the 6 sensitivity tests (ST) designed to test 3 model features with both an increase and a decrease to the relevant input data or model parameter.

Table VI.1. Sensitivity tests used in water quality model evaluation

Test Number	Model Feature Tested	Sensitivity Test Method	Plots of Differences
ST-1	Watershed Loading	Increase nonpoint watershed loadings by 10%	Fig. VI.10-VI.11
ST-2		Decrease nonpoint watershed loadings by 10%	Fig. VI.12-VI.13
ST-3	Phytoplankton Maximum Growth Rate	Increase maximum growth rate from 2.0/day to 2.25/day	Fig. VI.14-VI.15
ST-4		Decrease maximum growth rate from 2.0/day to 1.75/day	Fig. VI.16-VI.17
ST-5	Vertical stratification and mixing	Increase background eddy diffusivity from 10^{-6} to 10^{-5} m^2/s	Fig. VI.18-VI.19
ST-6		Decrease background eddy diffusivity from 10^{-6} to 10^{-7} m^2/s	Fig. VI.20-VI.21

VI-1 Sensitivity to the watershed loading

Sensitivity analysis of watershed loading was performed by first increasing the nonpoint loadings throughout the James and Elizabeth Rivers by 10% and then decreasing these loadings by 10%. This percentage was chosen to mimic the uncertainty associated with the flow rate and the associated nutrient load estimation. The fall-line inputs of chlorophyll-a, CBOD, and different nutrient forms of loading from both the James and Elizabeth Rivers are thereby altered.

The differences in the prediction of dissolved oxygen, chlorophyll-a, total phosphorus, and total nitrogen that are incurred by increasing the loadings are shown in Figure VI.1 and the differences in the prediction of ammonium, nitrate-nitrite, and dissolved inorganic phosphate incurred are shown in Figure VI.2. Differences for these same state variables incurred by a 10% decrease are shown in Figures VI.3 and VI.4, respectively.

Under the 1999 flow condition, the model indicates that whereas surface DO shows a slight change, the bottom DO does not show sensitive to the change of watershed loading. In terms of nutrients and phytoplankton, when the watershed loading is increased, both the surface and bottom nitrogen and chlorophyll-a increase. Conversely, when the watershed loading is decreased, both surface and bottom nitrogen and chlorophyll-a decrease. The amount of change for chlorophyll-a can be up to plus or minus 5 μg/l. This should be interpreted carefully since some portion of the loading may be deposited to the sediment bed and become available for release and uptake.

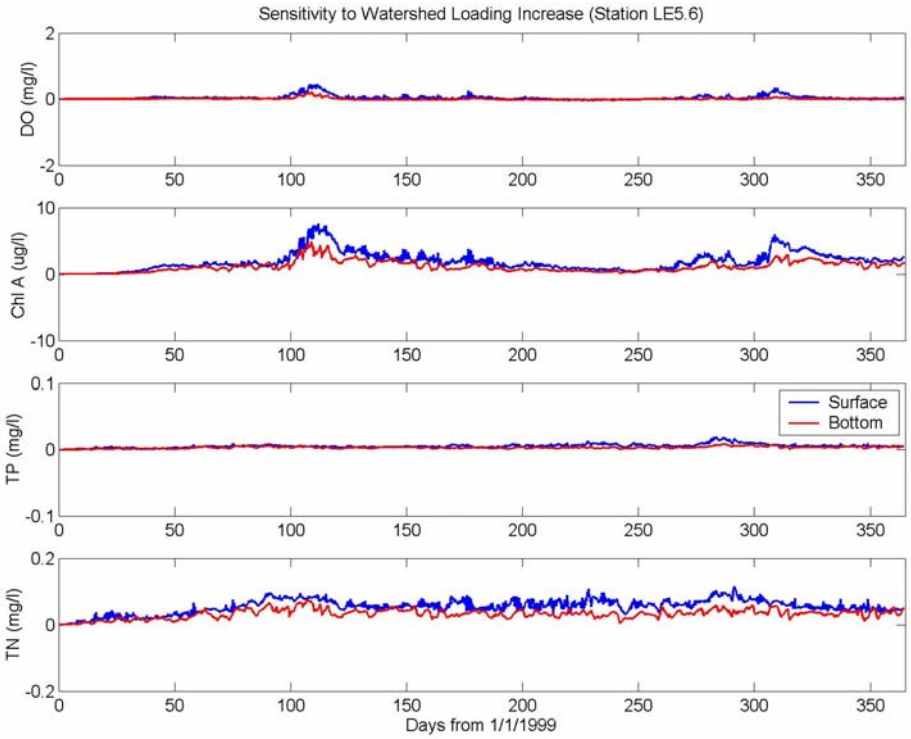

Figure VI.1. Differences of model predictions for dissolved oxygen, chlorophyll-a, total phosphorus, and total nitrogen at CBP Station LE5.6 (surface and bottom layers) for 1999 due to an increase in all watershed nonpoint loadings by 10% (ST-1).

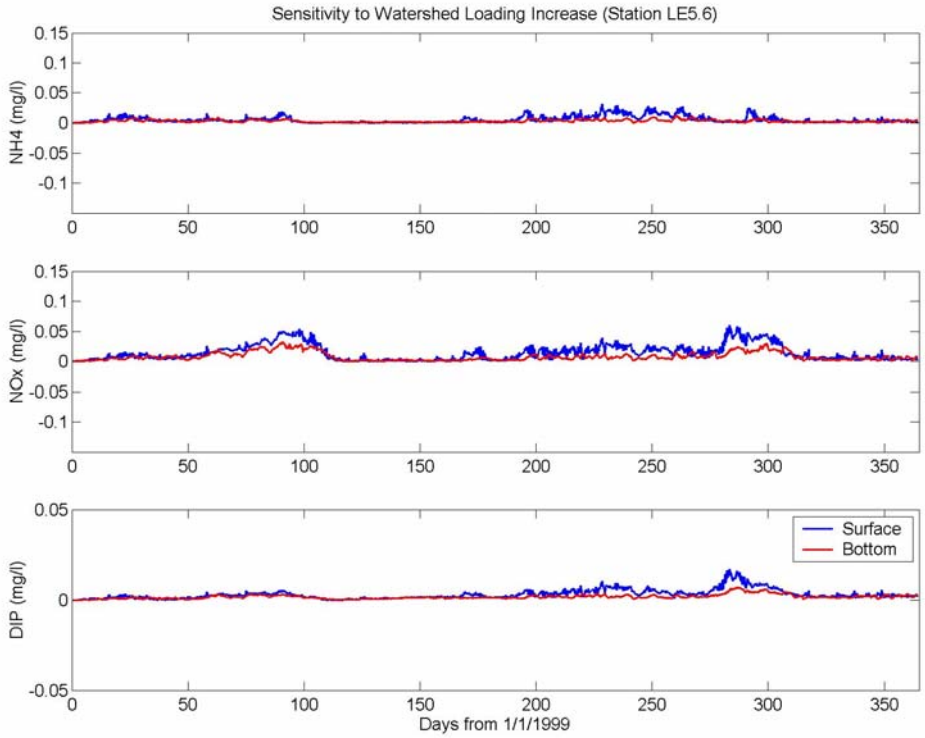

Figure VI.2. Differences of model predictions for ammonium, nitrate-nitrite, and dissolved inorganic phosphorus at CBP Station LE5.6 (surface and bottom layers) for 1999 due to an increase in all watershed nonpoint loadings by 10% (ST-1).

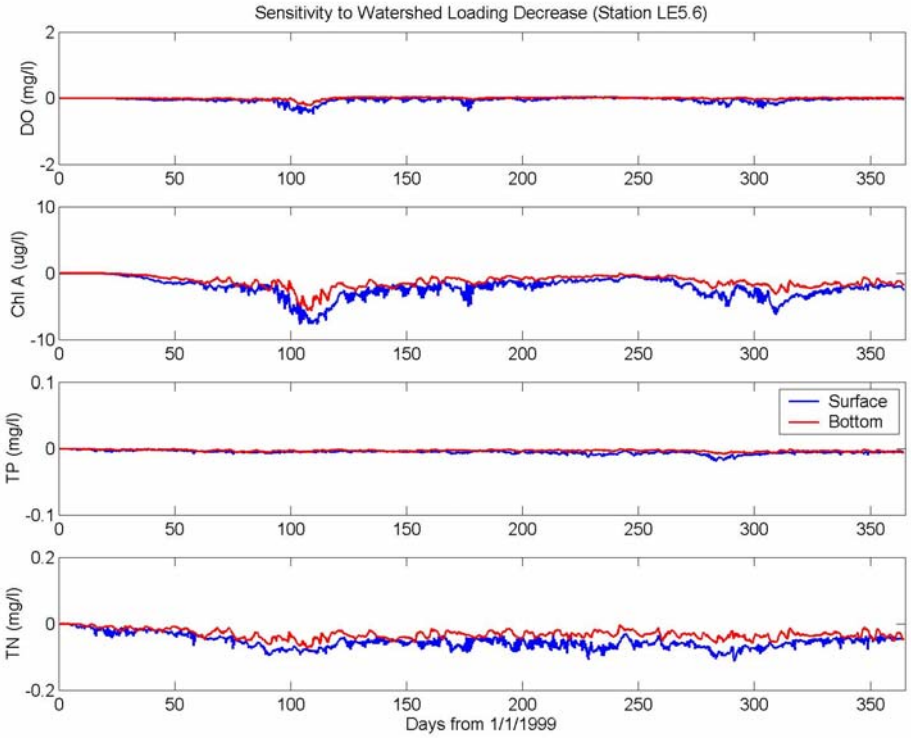

Figure VI.3. Differences of model predictions for dissolved oxygen, chlorophyll-a, total phosphorus, and total nitrogen at CBP Station LE5.6 (surface and bottom layers) for 1999 due to a decrease in all watershed nonpoint loadings by 10% (ST-2).

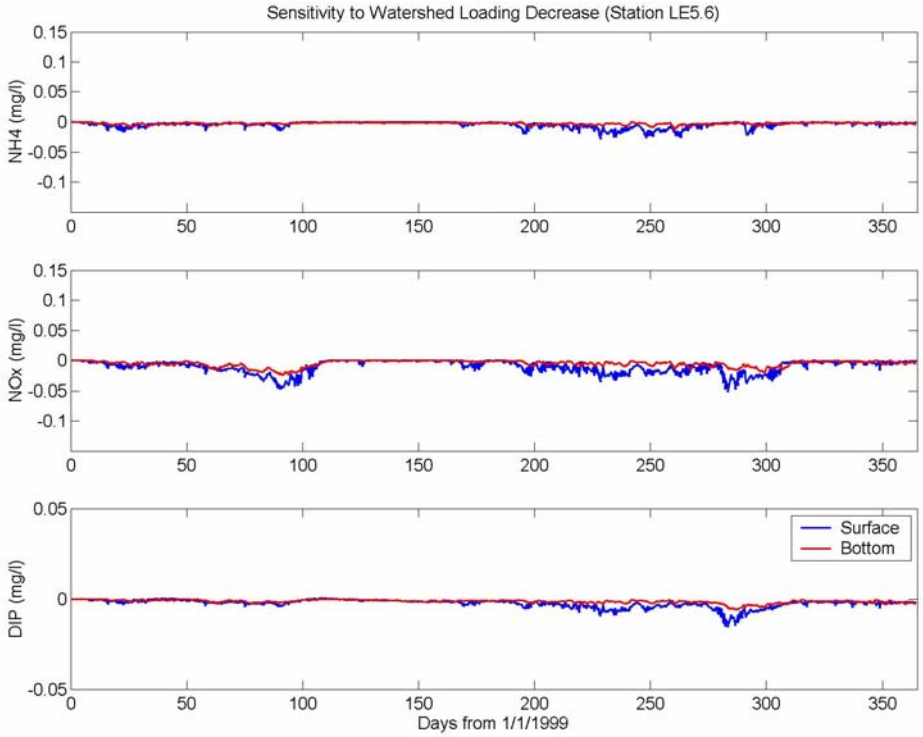

Figure VI.4. Differences of model predictions for ammonium, nitrate-nitrite, and dissolved inorganic phosphorus at CBP Station LE5.6 (surface and bottom layers) for 1999 due to a decrease in all watershed nonpoint loadings by 10% (ST-2).

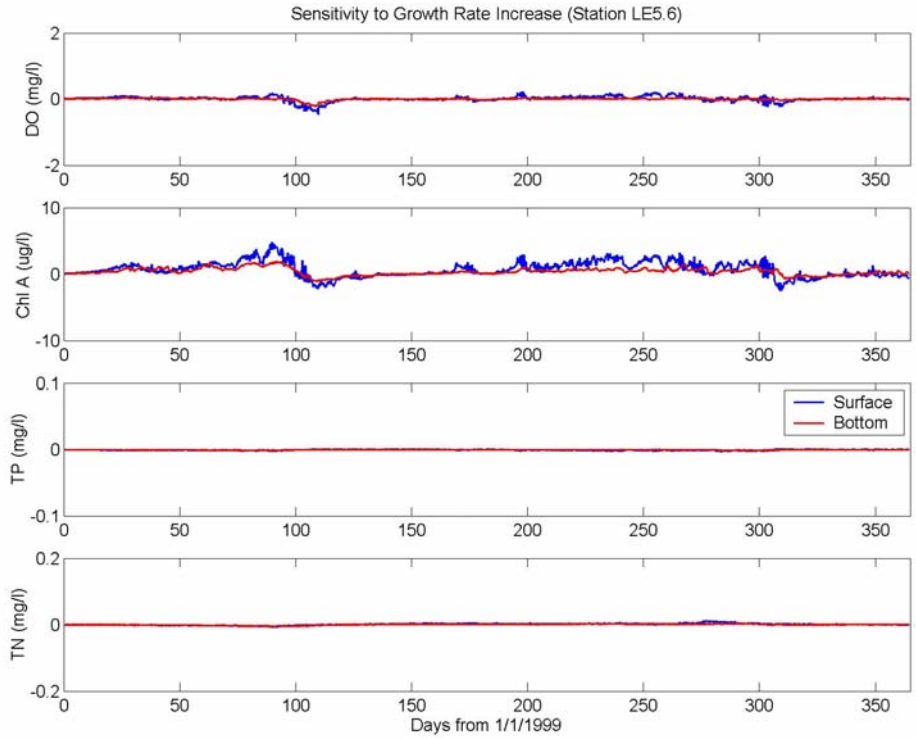

Figure VI.5. Differences of model predictions for dissolved oxygen, chlorophyll-a, total phosphorus, and total nitrogen at CBP Station LE5.6 (surface and bottom layers) for 1999 due to a increase in the maximum growth rate from 2.0/day to 2.25/day (ST-3).

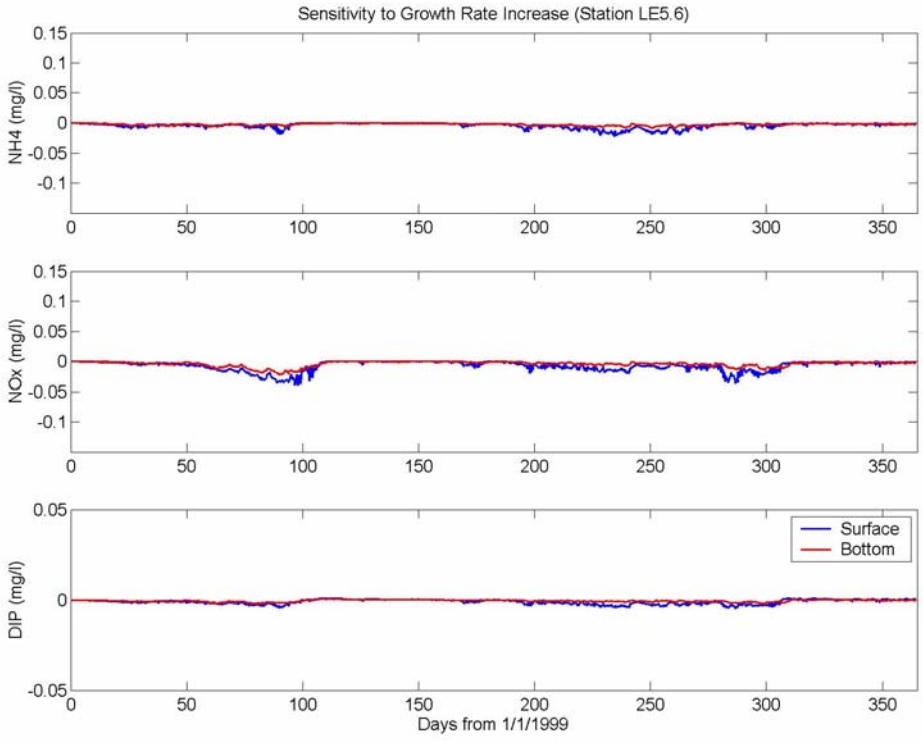

Figure VI.6. Differences of model predictions for ammonium, nitrate-nitrite, and dissolved inorganic phosphorus at CBP Station LE5.6 (surface and bottom layers) for 1999 due to a increase in the maximum growth rate from 2.0/day to 2.25/day (ST-3).

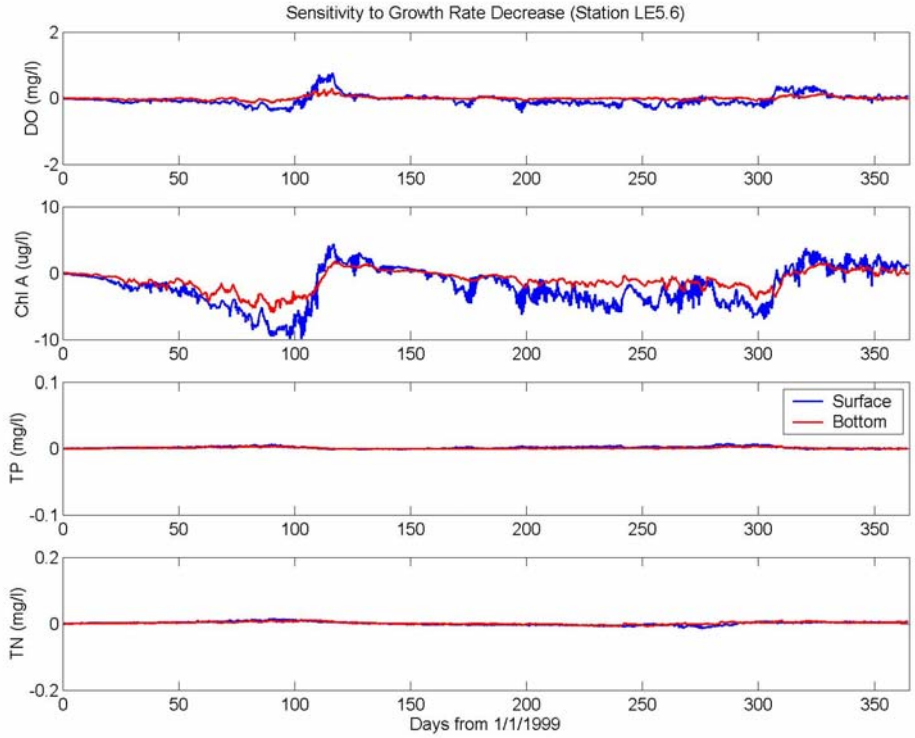

Figure VI.7. Differences of model predictions for dissolved oxygen, chlorophyll-a, total phosphorus, and total nitrogen at CBP Station LE5.6 (surface and bottom layers) for 1999 due to a decrease in the maximum growth rate from 2.0/day to 1.75/day (ST-4).

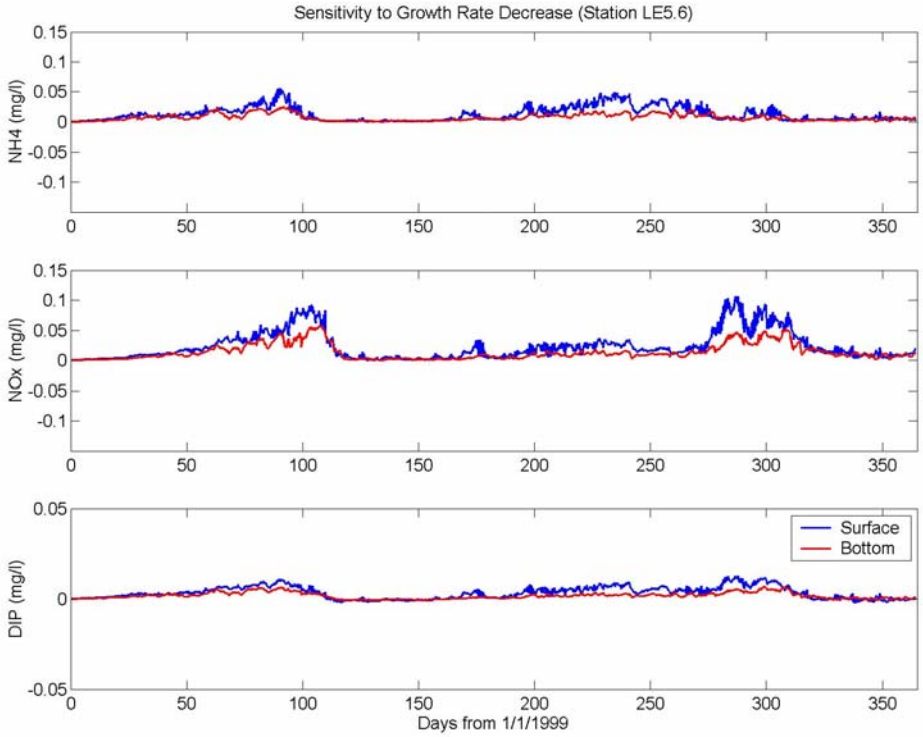

Figure VI.8. Differences of model predictions for ammonium, nitrate-nitrite, and dissolved inorganic phosphorus at CBP Station LE5.6 (surface and bottom layers) for 1999 due to a decrease in the maximum growth rate from 2.0/day to 1.75/day (ST-4).

VI-2-2. Sensitivity to phytoplankton maximum growth rate

Sensitivity analysis of phytoplankton dynamics was performed by first increasing the maximum growth rate from 2.0/day to 2.25/day (ST-3 in Table VI.1.) and then decreasing this growth rate from 2.0/day to 1.75/day (ST-4 in Table VI.1.). The differences in the prediction of DO, chl-a, TP, and TN that are incurred by increasing the growth rate are shown in Figure VI.5 and those differences in the prediction of NH_4, NO_x, and DIP incurred are shown in Figure VI.6. Differences for these same state variables incurred by the decrease of the growth rate from 2.0/day to 1.75/day are shown in Figures VI.7 and VI.8.

This sensitivity run provides some interesting insights into what is controlling algal growth presently in the model. The model appears to be most sensitive to a reduction in maximum growth rate. Reduction in the growth rate results in approximately a 10 μg/l reduction in chlorophyll-a. Accompanying this reduction in chlorophyll-a is an increase in ammonia, nitrate and nitrite, and DIP. It is interesting to note that once DIN and DIP are made available, phytoplankton biomass increases following its earlier reduction. In terms of dissolved oxygen, the surface DO is slightly reduced, but the bottom DO changes very little, as shown in Figure VI.7. Lastly, as for the increase in growth rate, the effect is less since sufficient quantities of nutrients for growth are not available and, thus, increasing the maximum growth rate has very little effect.

VI-2-3. Sensitivity to vertical stratification and mixing

The vertical mixing can affect the quantity of nutrients that can be brought up to the euphotic zone and thus made available to the photosynthesis process. It can also affect how much oxygen-rich surface water can be mixed into the bottom water. Thus, it is an important process that can affect both oxygen concentration and the eutrophication process.

Sensitivity analysis of vertical stratification and mixing was performed by first increasing the background eddy diffusivity by an order of magnitude (from 10^{-6} m^2/s to 10^{-5} m^2/s) (ST-5) and then decreasing this parameter by an order of magnitude (from 10^{-6} m^2/s to 10^{-7} m^2/s) (ST-6). The differences in the prediction of DO, chl-a, TP, and TN that are incurred by increasing the background eddy diffusivity are shown in Figure VI.9 and those differences in the prediction of NH_4, NO_x, and DIP incurred are shown in Figure VI.10. Differences caused by the order-of-magnitude decrease in the background eddy diffusivity are shown in Figures VI.11 and VI.12.

In terms of surface and bottom DO, the increase of eddy diffusivity resulted in a 0.5 mg/l increase of the bottom DO and a decrease by a similar amount to the surface DO. The decrease of eddy diffusivity does not create a discernible change in DO. In terms of nutrients, the increase of eddy diffusivity results in an increase of surface nitrogen, which in turn generates additional phytoplankton biomass by approximately 5 μg/l chlorophyll-a. Again, the decrease of diffusivity causes little change to the nutrient and

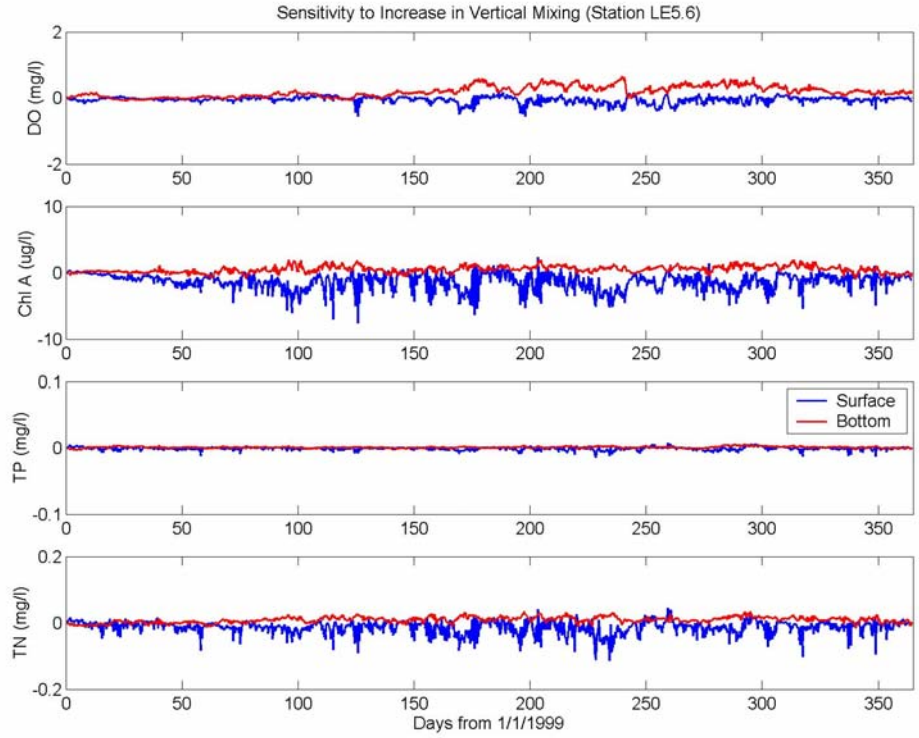

Figure VI.9. Differences of model predictions for dissolved oxygen, chlorophyll-a, total phosphorus, and total nitrogen at CBP Station LE5.6 (surface and bottom layers) for 1999 due to an increase in the background eddy diffusivity from 10^{-6} m^2/s to 10^{-5} m^2/s (ST-5).

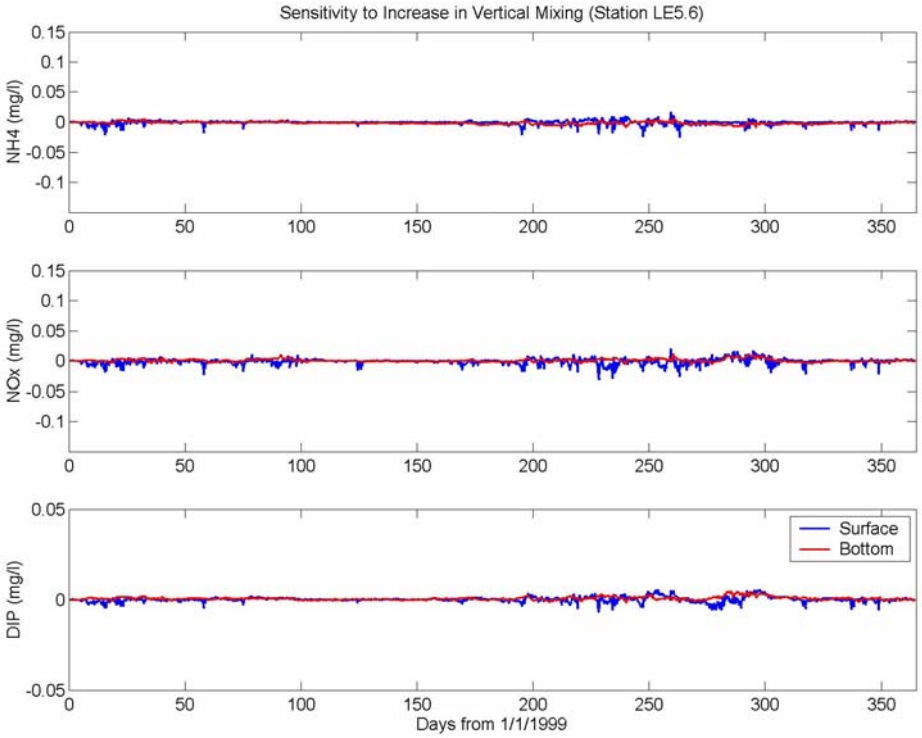

Figure VI.10. Differences of model predictions for ammonium, nitrate-nitrite, and dissolved inorganic phosphorus at CBP Station LE5.6 (surface and bottom layers) for 1999 due to an increase in the background eddy diffusivity from 10^{-6} m^2/s to 10^{-5} m^2/s (ST-5).

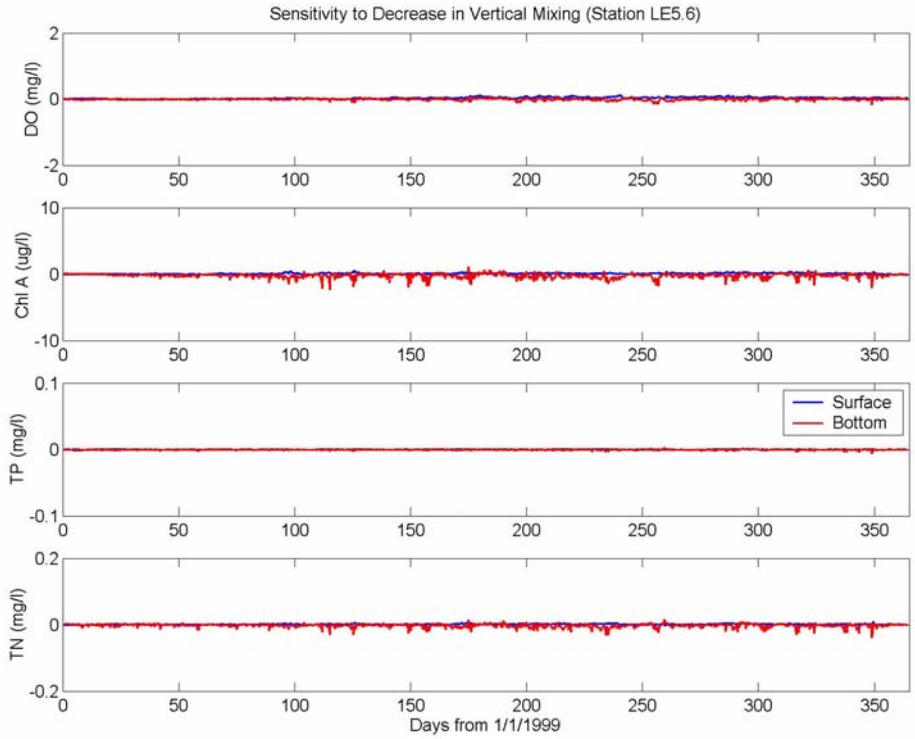

Figure VI.11. Differences of model predictions for dissolved oxygen, chlorophyll-a, total phosphorus, and total nitrogen at CBP Station LE5.6 (surface and bottom layers) for 1999 due to a decrease in the background eddy diffusivity from 10^{-6} m^2/s to 10^{-7} m^2/s (ST-6).

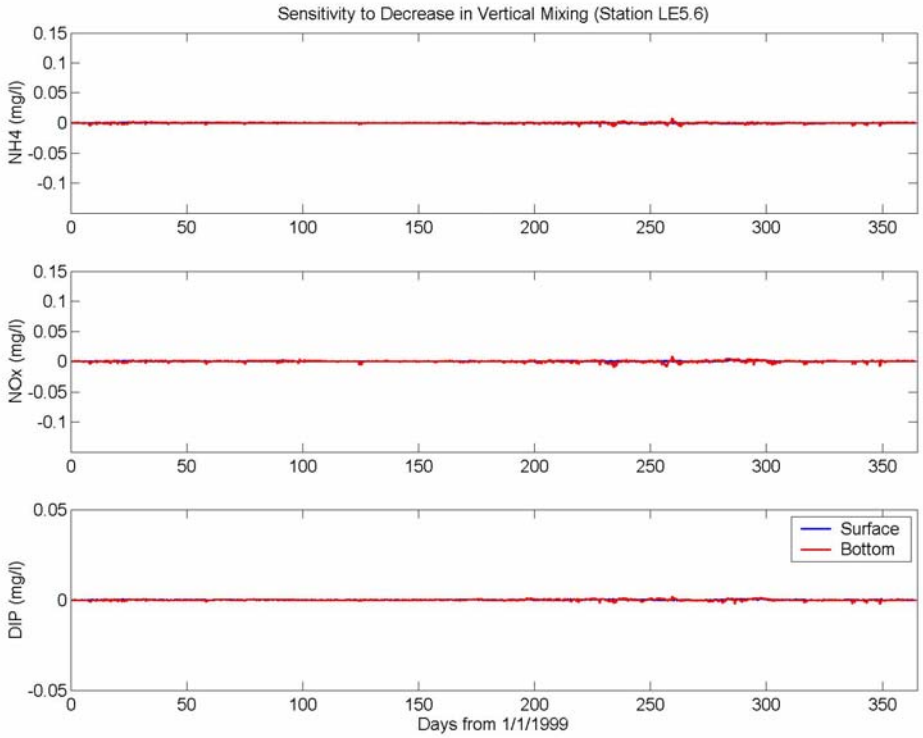

Figure VI.12. Differences of model predictions for ammonium, nitrate-nitrite, and dissolved inorganic phosphorus at CBP Station LE5.6 (surface and bottom layers) for 1999 due to a decrease in the background eddy diffusivity from 10^{-6} m^2/s to 10^{-7} m^2/s (ST-6).

phytoplankton concentrations. Generally speaking, differences in dissolved oxygen caused by changing the vertical mixing coefficient are higher that those of the other sensitivity tests performed, but these differences are still well below the predicted vs. observed RMS errors for DO.

CHAPTER VII. DISCUSSION AND ASSESSMENT OF OVERALL IMPACT TO CRANEY ISLAND EASTWARD EXPANSION, ENGINEERING PHASE

The proposed expansion of the Craney Island Dredged Material Management Area addresses a federal interest in increasing its capacity and extending its useful life beyond the year 2050. In addition, the expansion would serve a further interest in obtaining logistical and tactical areas for the deployment of national defense forces. It simultaneously addresses the interest of the Commonwealth of Virginia in future expansion of its commercial, deep-water port facilities.

The VIMS numerical modeling group has conducted "Three Dimensional Hydrodynamic Modeling Study of Craney Island Eastward Expansion" (Wang et al., 2001) as the feasibility study for the purpose of evaluating the Craney Island land expansion options under consideration until that time. The engineering phase of Craney Island Eastward Expansion project has three principal concerns. They are: (a) the flushing and far-field impacts on tidal flow due to cross-sectional changes by the construction of the cell and dredging of the access channels and berthing areas, (b) the sediment plume generated during the construction and dredging of the access channels and berthing areas, and (c) the water quality impact, particularly on the bottom dissolved oxygen, due to Eastward Expansion.

Analysis of historical long-term water quality data collected by the Virginia Department of Environmental Quality as well as the EPA Chesapeake Bay monitoring program revealed that bottom dissolved oxygen seldom falls below 5 mg/l in either Hampton Roads or the Elizabeth River. Without a major phytoplankton bloom in the spring and summer, the observed chlorophyll-a levels remain below 40 μg/l. The previous study indicates that relatively strong gravitational circulation in the James River has provided sufficient flushing and thus adequate DO for the system in the region east of Craney Island.

VIMS has developed the coupled hydrodynamic/water quality model HEM3D to assess the initial phase of the Craney Island Eastward Expansion in the Elizabeth River. The model domain contains the entire tidal James River, the Elizabeth River, and a portion of the Chesapeake Bay at the downstream end as the boundary condition. Based on the revised Craney Island expansion configuration, the Elizabeth River portion was re-segmented into a higher resolution orthogonal grid with a 90-120 m scale in the horizontal plane and 6 layers in the vertical plane. Twenty-four state variables are incorporated in the water quality analysis, including salinity, temperature, total suspended solid, and various forms of phytoplankton, nutrients, carbon, and silica. A separate benthic sediment sub-model is dynamically coupled with the water column water quality model for addressing benthic and pelagic interaction.

The hydrodynamic model of the coupled James and Elizabeth Rivers system was calibrated using intensive data collected in year 2000 and the water quality model was applied for the years 1999, 2000, and 2001, during which period the non-point source

loading data was provided by the HSPF watershed model obtained from the EPA Chesapeake Bay Program. In addition, the point source loadings from inside Elizabeth River are available and included. The mean annual load of total nitrogen (16 million kg) and total phosphorus (2 million kg) could probably support a background phytoplankton level comparable to the historical levels of 20 to 30 μg of chlorophyll-a. The modeling framework was calibrated for all three years in terms of major variables. Comparisons were made of the observed and computed values of the relevant variables, including water elevation, velocity, and salinity for the hydrodynamic model, and dissolved oxygen, chlorophyll-a, total nitrogen, total phosphorus, ammonium, nitrite and nitrate, and dissolved phosphate for the water quality model. The analysis indicated that the model reproduces major hydrodynamic features and compared well with the intensive measurements. In addition, the principal components of the oxygen budget, the interaction between phytoplankton, photosynthesis, and respiration, COD and NOD, SOD, atmospheric reaeration, and vertical mixing were incorporated and the model produces reasonably well the observed spatial and temporal distributions for all three calibration years. The differences associated with the comparison of model prediction and observed data are well within the range of natural variation in a given season of measurements of water quality parameters.

Once they are calibrated, the hydrodynamic and water quality models are used as management tools for assessing the impact of various construction phases. The hydrodynamic model was also used as a basis for providing the hydrodynamic flow field as an input to a high-resolution suspended sediment fate (SSFATE) model, and to understand the transport, kinetic, and transfer dynamics in the James and Elizabeth River estuaries, which affect the distribution of water quality constituents, and in particular, oxygen levels. The hydrodynamic and water quality impacts due to south cell expansion and full expansion are presented in the following sections with all measures for impacts is based on the difference between the values obtained from scenario run minus that obtained from the base case; namely, the metric of impact = (scenario result - base case result).

Hydrodynamic analysis indicates that the flushing capabilities of the Elizabeth River system, and thus, the cross-sectional impacts near Craney Island, would not be adversely affected by the full expansion. An analysis of the cross-section at the mouth of the river shows that the reduction in the surface area, causing a slight reduction in tidal prism (4%), is completely compensated for by a more significant increase in the non-tidal residual flow (26% on average) both in and out of the system. By adding the slight decrease in tidal prism and significant increase in non-tidal residual volume, this translates to a net increase of total flushing capability by 2% on average due to the full expansion. For the intermediate plan of the south cell expansion without full scale dredging, the overall flushing capability has a slight reduction of 1-2%.

The water quality impacts due to the Eastward Expansion are described as follows:

(1) Water quality analysis for the south cell expansion

(a) The temporal variability: The impact of the construction of the south cell was analyzed by examining differences in predicted values of key water quality variables (dissolved oxygen, chlorophyll-a, total phosphorus, total nitrogen, ammonium, nitrate-nitrite, and dissolved phosphate) on a 30-day-average basis over the 3-year record. Differences were derived at Station LE5.6 adjacent to the project site, Station ELI2 just to the south to the project site, and a reference Station LE5.5 in the James River. Differences were extracted for surface and bottom model layers as well as for vertical averages of all 6 layers. For all parameters other than dissolved oxygen and chlorophyll-a, the differences were less than instrument detection limits (on the order of 0.001 mg/l). For oxygen, the difference ranged from -0.02 mg/l to 0.02 mg/l and for chlorophyll-a, the differences ranged between 0.0 and 0.5 μg/l. Both of these were less than or equal to their respective detection limits of 0.1 mg/l and 0.5 μg/l.

(b) The spatial variability: Spatial plots of the differences in dissolved oxygen (DO) were constructed to assess the location and extent of the impact of the south cell expansion on DO levels. The domain of these plots included Hampton Roads and the entire Elizabeth River. These plots showed 30-day averages at both surface and bottom model layers, as well as a vertical average of all 6 layers, for the potentially critical months of June, July, August, and September in the summer and fall. Throughout all of these plots, only the small dredged region just east of Craney Island showed differences between - 0.3 mg/l and - 0.6 mg/l for the bottom dissolved oxygen. However, these differences are due to the artifact of comparison between the unequal depth layers between the pre-dredged shallow bottom layer (for the base case) versus the post-dredging deeper bottom layer (for the scenario). When the comparison was made at the same depth, the difference of dissolved oxygen becomes negligibly small (on the order of one one-hundredth mg/l). In conclusion, the impact to DO levels due to the south cell expansion is minimal and well within the range of variation within a given season.

(2) Water quality analysis for the full expansion

(a) The temporal variability: The impact of the construction of the full expansion was analyzed by examining differences in predicted values of key water quality variables on a 30-day-average basis over the 3-year record. Differences were derived at Station LE5.6 adjacent to the project site, Station ELI2 just to the south to the project site, and a reference Station LE5.5 in the James River. Differences were extracted for surface and bottom model layers as well as for vertical averages of all 6 layers. As in the results for the south cell expansion analysis, for all parameters other than dissolved oxygen and chlorophyll-a, the differences were less than instrument detection limits (on the order of 0.001 mg/l). For oxygen, the differences ranged from 0.03 -0.05 mg/l, and for chlorophyll-a, the differences ranged between 0.0 and 0.5 μg/l. These differences are within their respective detection limits as well. The bottom dissolved oxygen actually showed a slight increase after the scenario run for full-scale expansion and dredging.

(b) The spatial variability: Spatial plots of the differences in dissolved oxygen (DO) were constructed to assess the location and extent of the impact of the full cell expansion on DO levels. The domain of these plots included Hampton Roads and the entire Elizabeth

River. These plots showed monthly averages at both surface and bottom model layers, as well as a vertical average of all 6 layers, for the potentially critical months of June, July, August, and September of 1999, 2000, and 2001 in the summer and fall. Throughout all of these plots, only the small dredged region just east of Craney Island showed differences between - 0.3 mg/l and – 0.6 mg/l for the bottom dissolved oxygen. However, these differences are due to the artifact of comparison between the unequal depth layers between the pre-dredged shallow bottom layer (for the base case) versus the post-dredging bottom layer (for eastward expansion scenario). When the comparison was made at the same depth, the difference of dissolved oxygen again becomes negligibly small, on the order of one one-hundredth mg/l difference. The impacts to DO levels due to the full expansion are thus minimal and are well within the range of variation in a given season.

Given the relatively strong physical circulation in the Lower James and mouth region of the Elizabeth River, the existing dissolved oxygen budget in the bottom waters off the Craney Island expansion site are controlled by the combined effects of reaeration (corresponding to vertical mixing), the bottom DO flux from the James River, as well as biological and chemical water column DO demand, and sediment oxygen demand. As a result of the Craney Island Eastward Expansion, both the vertical mixing and the non-tidal residual transport actually increase. These are the positive factors that benefit the bottom DO in the post-expansion condition. There are, however, negative factors that reduce the shallow oxygen-rich region in exchange of deeper dredging area that is prone to oxygen deficiency. As computed by the model, the positive benefit from the expansion outweighs the negative aspect of the dredging, which results in overall negligible impacts, if there are any. In other words, in terms of DO changes (caused by the Craney Island expansion) the increase of advective DO flux from the James River and local vertical mixing overcome the increase of low DO volumes. Overall, the impacts to DO levels due to both the south cell and the full expansion are minimal and are well within the range of the detection limit. There are regions that are dredged adjacent to the berthing area just east of Craney Island that show some impact. However, these differences are due to the effect of comparison between the unequal depth layers between the pre-dredged shallow bottom layer (for the base case) versus the post-dredging deeper bottom layer (for the scenario). When the comparison was made at the same depth, the difference of dissolved oxygen again becomes negligibly small. It should be kept in mind that the healthy water quality condition in the Lower James River is the premium asset and a key factor that plays an important role in minimizing the impact from the Craney Island Eastward Expansion.

Lastly, the uncertainty of the model results was assessed by conducting a sensitivity analysis by varying the most sensitive parameters that affect the water quality results. These parameters include: watershed loading partitioning, phytoplankton growth rate, and vertical mixing parameters. These additional results gave the calibration a proper constraint in terms of their upper and lower bounds. In the case of dissolved oxygen, which is the water quality parameter of highest concern for this study, the sensitivity testing showed that DO is relatively resilient to the variation of these parameters.

VIII. REFERENCES

Arakawa, A., and V. R. Lamb (1977): Computational design of the basic dynamical processes of the UCLA general circulation model. Methods in Computational Physics, 17: 174-265.

Blumberg, A. F., B. Galperin, and D. J. O'Connor (1992): Modeling vertical structure of open channel flows. Journal of Hydraulic Engineering, 118: 1119-1134.

Blumberg, A. F. and G. L. Mellor (1987): A description of a three-dimensional coastal ocean circulation model. In N Heaps (ed), Three-dimensional Coastal Ocean Models, American Geophysical Union, Washington, D. C., 4: 1-16.

Boon, J. D., A. Y. Kuo, H. V. Wang, and J. M. Brubaker (1999): Proposed third crossing of Hampton Roads, James River, Virginia: feature-based criteria for evaluation of model study results. In M. L. Spaulding and H. L. Butler (eds.), ASCE 6th International Conference on Estuarine and Coastal Modeling, New Orleans, LA, 223-237.

Boon, J. D., H. V. Wang, S. C. Kim, A. Y. Kuo, and G. M. Sisson (1999): Three dimensional hydrodynamic-sedimentation modeling study, Hampton Roads Crossing, Lower James River, Virginia: Report to the Virginia Department of Transportation. Special Report No. 354 in Applied Science and Ocean Engineering, Virginia Institute of Marine Science, Gloucester Point, Virginia, 36 pp. and 3 Appendices.

Casulli, V. and R. T. Cheng (1993): Semi-implicit finite difference methods for three-dimensional shallow water flow. International Journal for Numerical Methods in Fluids, 15: 629-648.

CH2MHILL (2002): Elizabeth River hydrodynamic and water quality modeling: flushing Analysis for APM terminals Marine Container Terminal, Portsmouth, Virginia. Final Report prepared for the Williamsburg Environmental Group, 43 pp. and Appendices.

Cerco, Carl and Thomas M. Cole (1994): Three-dimensional Eutrophication Model of Chesapeake Bay. Volume I: Main Report, U.S. Army Corps of Engineers Waterways Experiment Station Technical Report EL-94-4, Vicksburg, MS.

Clark, T. L. (1977): A small-scale dynamics model using a terrain-following coordinate transformation. Journal of Computational Physics, 24, 186-215.

Clark, T. L., and W. D. Hall (1991): Multi-domain simulations of the time dependent Navier-Stokes equations: benchmark error analysis of some nesting procedures. Journal of Computational Physics, 92: 456-481.

Computation Hydraulics and Transport (Billy Johnson and Allen Teeter). (2008): Modeling Suspended Sediment Plumes Created by Dredging Operations for the Craney Island Eastward Expansion Project." CHT, Edwards, MS.

DiToro, D. M., and Fitzpatrick, J. J. (1993). Chesapeake Bay sediment flux model, Contract Report EL-93-2, U. S. Army Engineer Waterways Experiment Station, Vicksburg, MS.

Fang, C. S., B. J. Neilson, A. Y. Kuo, R. J. Byrne, and C. S. Welch (1972): Physical and geological studies of the proposed bridge-tunnel crossing of Hampton Roads near Craney Island. Special Report in Applied Marine Science and Ocean Engineering No. 24, Virginia Institute of Marine Science, Gloucester Point, VA, 199-241.

Fletcher, C. J. A. (1988): Computational techniques for fluid dynamics 1 & 2, Springer-Verlag, 409 & 484.

Galperin, B., L. H. Kantha, D. Hassid, and A. Rosati (1988): A quasi-equilibrium turbulent energy model for geophysical flow. Journal of Atmospheric Science, 45: 55-62.

Genet, L., Smith, D., and Sonnen, M. (1974). Computer program documentation for the dynamic estuary model. U.S. Environmental Protection Agency, Systems Development Branch, Washington, DC.

Hamrick, J. M. (1986): Long-term dispersion in unsteady skewed free surface flow. Estuarine Coastal Shelf Science, 23: 807-845.

Hamrick, J. M. (1994): Linking hydrodynamic and biogeochemical transport model s for estuarine and coastal waters. Estuarine and Coastal Modeling, Proceedings of the 3rd International Conference, M. L. Spaulding et al., Eds., American Society of Civil Engineers, New York, 591-608.

Hamrick, J. M. (1992): A three-dimensional environmental fluid dynamics computer code: theoretical and computational aspects. Special Report in Applied Marine Science and Ocean Engineering (SRAMSOE) # 317, Virginia Institute of Marine Science, Gloucester Pt., VA. 63 pp.

Hamrick, J. M. and Z. Yang (1995): Lagrangian mean descriptions of long-term estuarine mass transport. Proceedings of the 1994 International Conference on the Physics of Estuaries and Bays. D. Aubrey, ED., American Geophysical Union.

Hamrick, J. M. (1996): User's manual for the environmental fluid dynamics computer code. Special report in Applied Marine Science and Ocean Engineering No. 331, Virginia Institute of Marine Science, Gloucester Point, VA, 223 pp.

Jassby, A., and Platt, T. (1976): Mathematical formulation of the relationship between photosynthesis and light for phytoplankton. Limnology and Oceanography, 21: 540–547.

Johnson, B. H., K. W. Kim, R. E. Heath, B. B. Hsieh, and H. L. Butler (1993): Validation of a three-dimensional hydrodynamic model of Chesapeake Bay. Journal of Hydraulic Engineering, 119: 2-20.

Kuo, A. Y. and B. J. Neilson. (1987). Hypoxia and salinity in Virginia Estuaries. Estuaries, 10(4), 277-283.

Kuo, A. Y., R. J. Byrne, J. M. Brubaker, and J. H. Posenau (1988): Vertical transport across an estuary front. In J. Dronkers and W. van Leussen (eds.), Physical Processes in Estuaries, Springer-Verlag, Berlin, 93-109.

Kuo, A. Y., R. J. Byrne, P. V. Hyer, E. P. Ruzecki, and J. M. Brubaker (1990): Practical Application of Theory for Tidal-Intrusion Fronts. Journal of Waterway, Port, Coastal, and Ocean Engineering, 116(3): 341-361.

Li, Y. (2006): Development of an Unstructured Grid, Finite Volume Eutrophication Model for the Shallow Water Coastal Bay: Application in the Lynnhaven River Inlet System. Ph.D. dissertation. Virginia Institute of Marine Science, College of William and Mary, 305 pp.

Maa, J. P-Y, C. H. Lee, F. J. Chen (1995): VIMS sea carousel: bed shear stress measurements. Marine Geology, 129: 129-136.

Mellor, G. L. (1991): An equation of state for numerical models of oceans and estuaries. Journal of Atmospheric and Oceanic Technology, 8: 609-611.

Mellor, G. L., and T. Yamada (1982): Development of a turbulence closure model for geophysical fluid problems. Reviews of Geophysics and Space Physics, 20: 851-875.

Miller, J. L. and A. Valle-Levinson (1996): The effect of bridge piles on stratification in the lower Chesapeake Bay. Estuaries, 19(3): 526-539.

Neilson, B. J. (1975): A water quality study of the Elizabeth River: the effect of the Army Base and Lambert Point STP effluent. Special Report No. 75 in Applied Marine Science and Ocean Engineering, Virginia Institute of Marine Science, Gloucester Point, Virginia. 133 pp.

Nichols, M.M. (1977): Response and recovery of an estuary following a river flood. Journal of Sediment Petrology, 47: 1171-1186.

Odum, E. (1971): Fundamentals of Ecology, 3rd ed. W. B. Saunders. Philadelphia, Pennsylvania.

Oey, L. –Y., G. Mellor, and R. Hires (1985): Three-dimensional simulation of the Hudson-Raritan estuary. Part III: salt flux analyses. Journal of Physical Oceanography 14: 629-645.

Park, K., Kuo, A.Y., and Butt, A. (1995a): Field studies in the Lynnhaven River for calibration of a tidal prism water quality model. Special Report in Applied Marine Science and Ocean Engineering (SRAMSOE) # 325, Virginia Institute of Marine Science, Gloucester Pt., VA, 61 pp. and Appendices.

Park, K., Kuo, A.Y., Shen, J., and J. M. Hamrick. (1995b): A three-dimensional hydrodynamic-eutrophication model (HEM-3D): Description of water quality and sediment process sub-models. Special Report in Applied Marine Science and Ocean Engineering (SRAMSOE) # 327, Virginia Institute of Marine Science, Gloucester Pt., VA, 102 pp. and Appendices.

Park, K., Kuo, A.Y., and Butt, A. (1995c): Application of a tidal prism water quality model to the Lynnhaven River. Special Report in Applied Marine Science and Ocean Engineering (SRAMSOE) # 329, Virginia Institute of Marine Science, Gloucester Pt., VA.

Parsons, T., Takahashi, M., and B. Hargrave (1984). Biological oceanography processes, 3rd edition, Permagon Press, Oxford.

Peyret, R., and T. D. Taylor (1983): Computational methods for fluid flow, Springer-Verlag, 358 pp.

Ruzecki, E. P., and W. J. Hargis, Jr. (1988): Interaction between circulation of the estuary of the James River and transport of oyster larvae. In B. J. Neilson, A. Y. Kuo and J. M. Brubaker (eds.), Estuarine Circulation, 255-278.

Semtner, A. J. (1974): An oceanic general circulation model with bottom topography. Department of Meteorology, University of California, Los Angeles, Technical Report. 9: 41.

Shen, J., J. D. Boon, and A. Y. Kuo (1999): A modeling study of a tidal intrusion front and its impact on larval dispersion in the James River estuary, Virginia. Estuaries 22(3a): 681-692.

Shen, J., and A. Y. Kuo (1999): Numerical investigation of an estuarine front and its associated eddy. Journal of Waterway, Port, Coastal, and Ocean Engineering 125(3):127-135.

Sisson, G. M., J. D. Boon, and K. L. Farnsworth (1999): The use of GIS in 3D hydrodynamic model pre- and post-processing for feature-specific applications. In M. L. Spaulding and H. L. Butler (eds.), ASCE 6th International Conference on Estuarine and Coastal Modeling, New Orleans, LA, 538-548.

Smith, L. H., and R. T. Cheng (1987): Tidal and tidally averaged circulation characteristics of Suisun Bay, California. Water Resources Research, 23: 143-155.

Smolarkiewicz, P. K. (1984): A fully multidimensional positive definite advection transport algorithm with small implicit diffusion. *J. Comp. Phys.*, **54**, 325-362.

Smolarkiewicz, P. K., and T. L. Clark (1986): The multidimensional positive definite advection transport algorithm: further development and applications. *J. Comp. Phys.*, **67**, 396-438.

Smolarkiewicz, P. K., and W. W. Grabowski (1990): The multidimensional positive definite advection transport algorithm: nonoscillatory option. *J. Comp. Phys.*, **86**, 355-375.

Stigebrandt, A. (1992): Bridge-induced flow reduction in sea straits with reference to effects of a planned bridge across Öresund, Ambio 21:130-134.

Thomann, R., and Fitzpatrick, J. (1982): Calibration and verification of a mathematical model of the eutrophication of the Potomac Estuary. HydroQual Inc., Mahwah, NJ.

Vinokur, M. (1974): Conservation equations of gas dynamics in curvilinear coordinate systems. Journal of Computational Physics, 50: 71-100.

Wang, H. V. and S.-C. Kim (2000): Simulation of tunnel island and bridge piling effects in a tidal estuary. In M. L. Spaulding and H. L. Butler (eds.), ASCE 6th International Conference on Estuarine and Coastal Modeling, New Orleans, LA, 250-269.

Wang, H. V., S. C. Kim, J. D. Boon, A. Y. Kuo, G. M. Sisson, J. M. Brubaker, and J. P-Y. Maa (2001): Three dimensional hydrodynamic modeling study, Craney Island Eastward Expansion, Lower James River and Elizabeth River, Virginia. Final Report to the U.S. Army Corps of Engineers, Norfolk District and the Virginia Port Authority. Special Report No. 372 in Applied Marine Science and Ocean Engineering, Virginia Institute of Marine Science. 158 pp. and Appendices.

Wezernak, C. T., and Gannon, J. J. (1968): Evaluation of nitrification in streams. Journal of the Sanitary Engineering Division, ASCE, 94(SA5): 883-895.

APPENDIX A

Comparisons of Model Predicted Salinity and Total Suspended Solids (Surface and Bottom) using Old Model Grid and New Model Grid

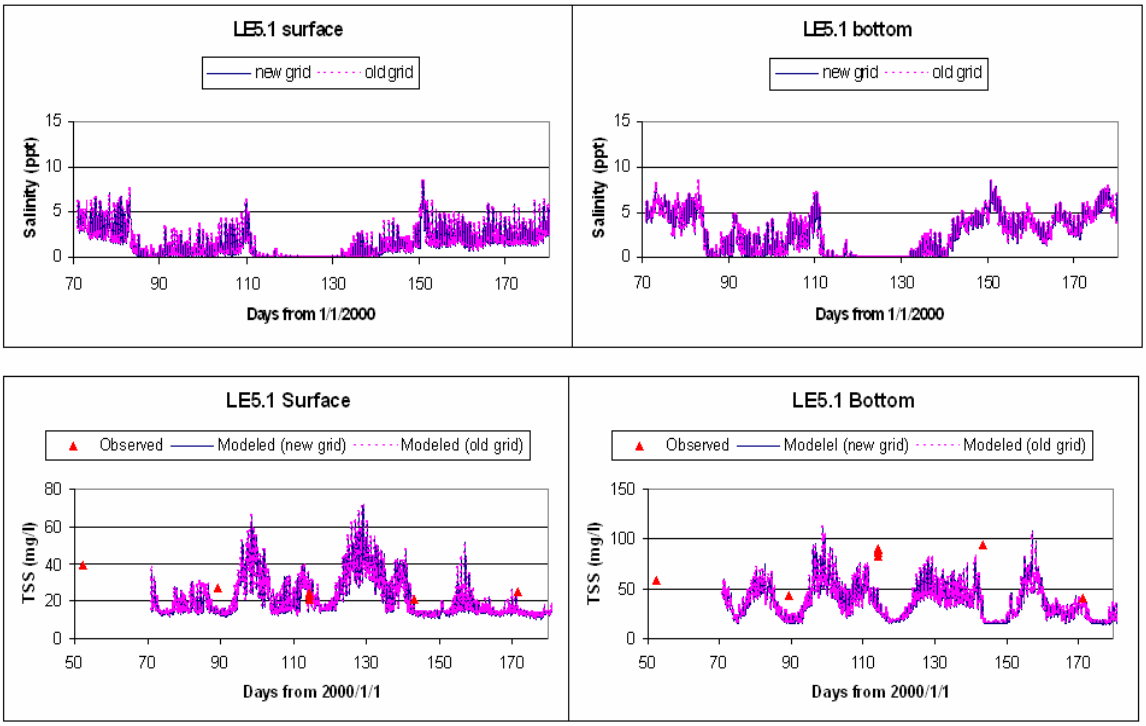

Figure A1. Comparison of model predicted salinity and total suspended solids (surface and bottom layers) at CBP Station LE5.1 from March 2000 to June 2000 using the old and new model grids.

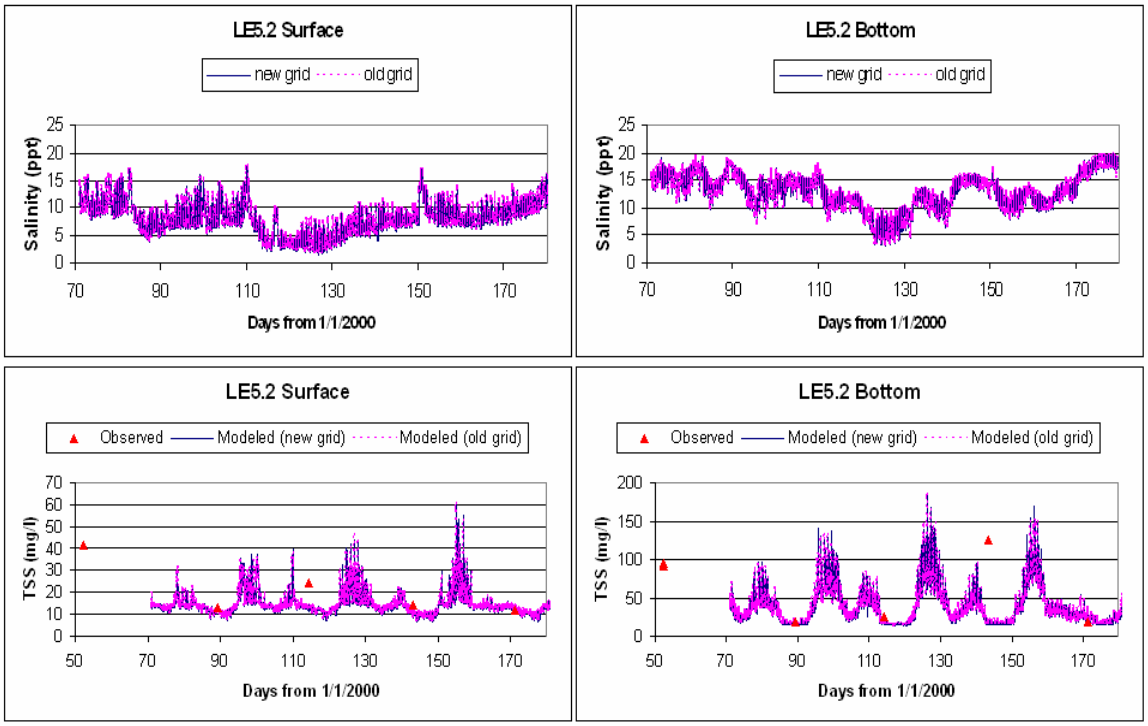

Figure A2. Comparison of model predicted salinity and total suspended solids (surface and bottom layers) at CBP Station LE5.2 from March 2000 to June 2000 using the old and new model grids.

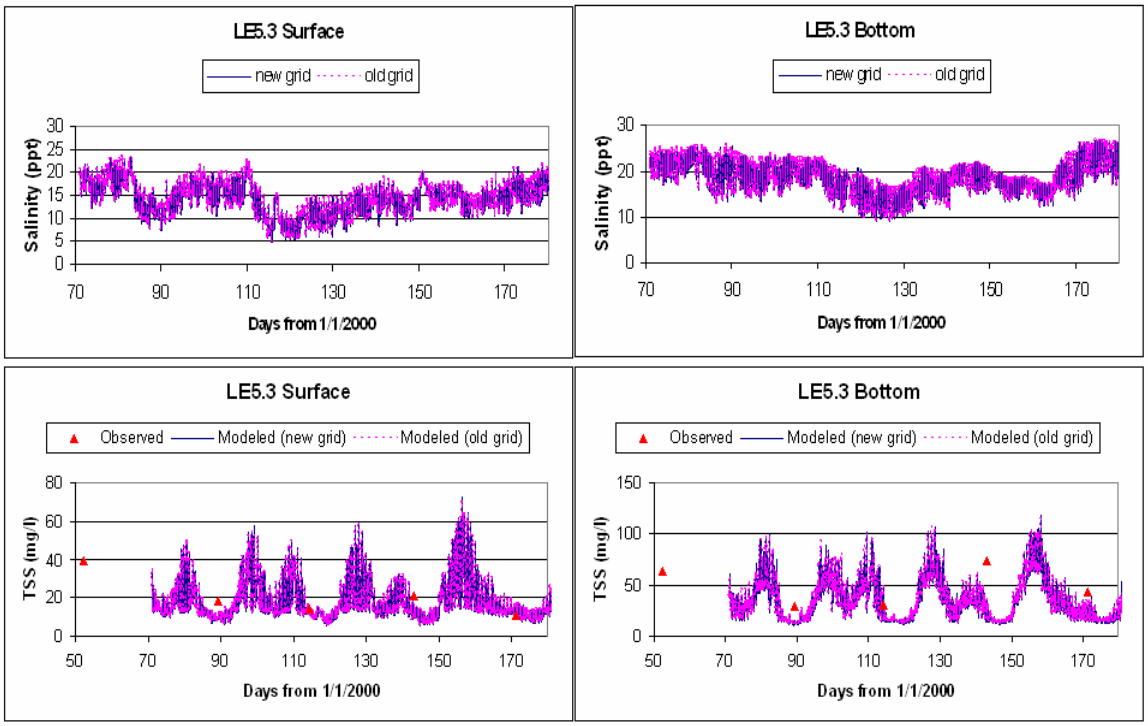

Figure A3. Comparison of model predicted salinity and total suspended solids (surface and bottom layers) at CBP Station LE5.3 from March 2000 to June 2000 using the old and new model grids.

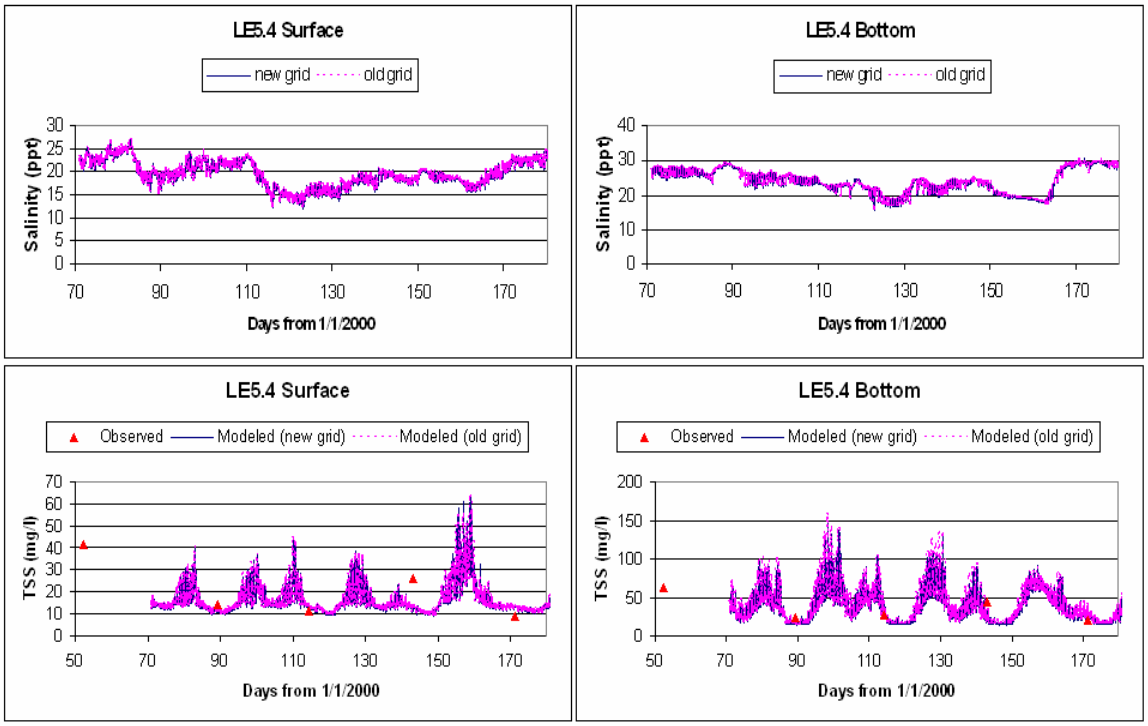

Figure A4. Comparison of model predicted salinity and total suspended solids (surface and bottom layers) at CBP Station LE5.4 from March 2000 to June 2000 using the old and new model grids.

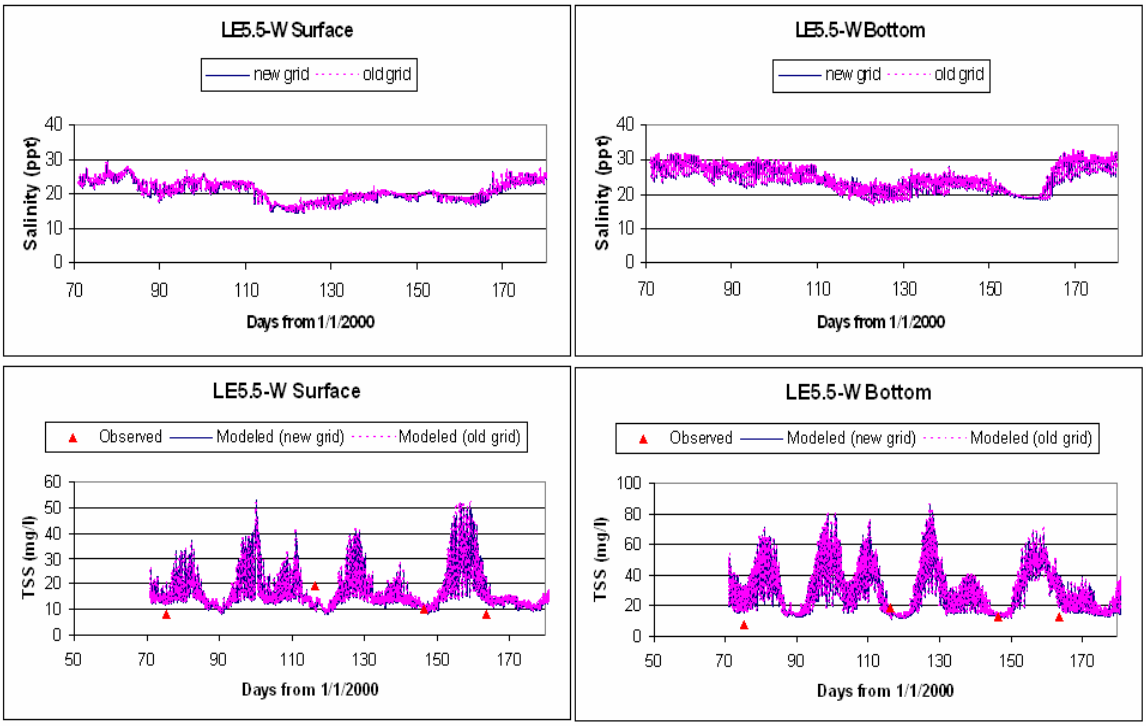

Figure A5. Comparison of model predicted salinity and total suspended solids (surface and bottom layers) at CBP Station LE5.5-W from March 2000 to June 2000 using the old and new model grids.

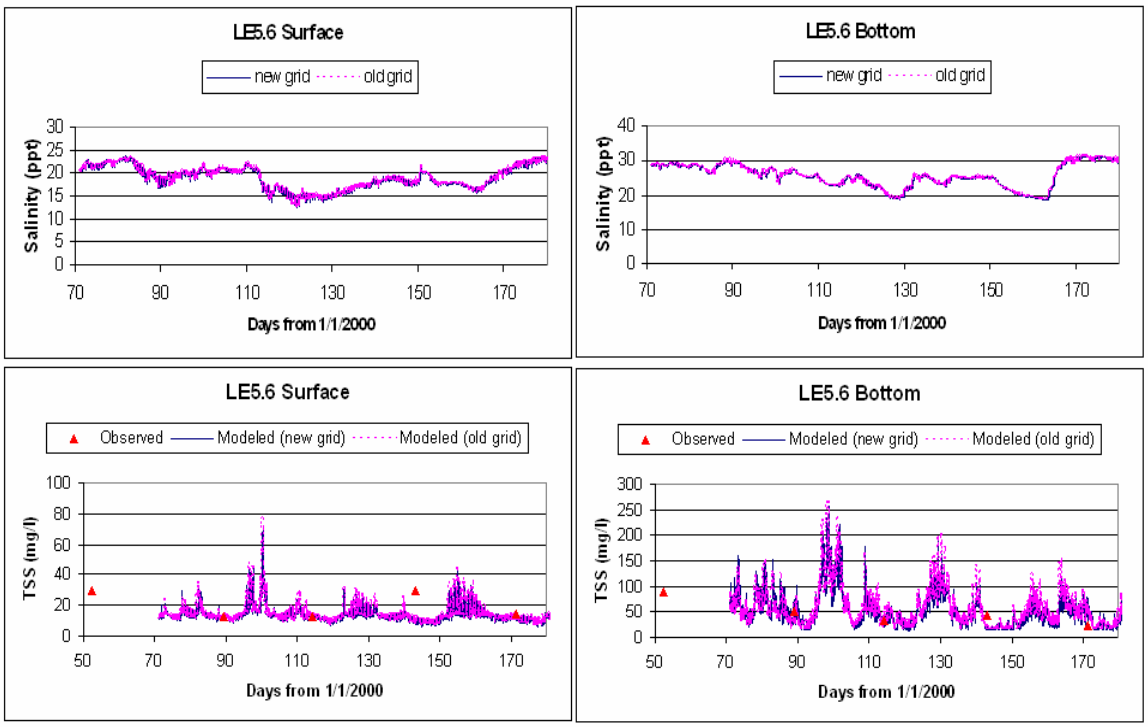

Figure A6. Comparison of model predicted salinity and total suspended solids (surface and bottom layers) at CBP Station LE5.6 from March 2000 to June 2000 using the old and new model grids.

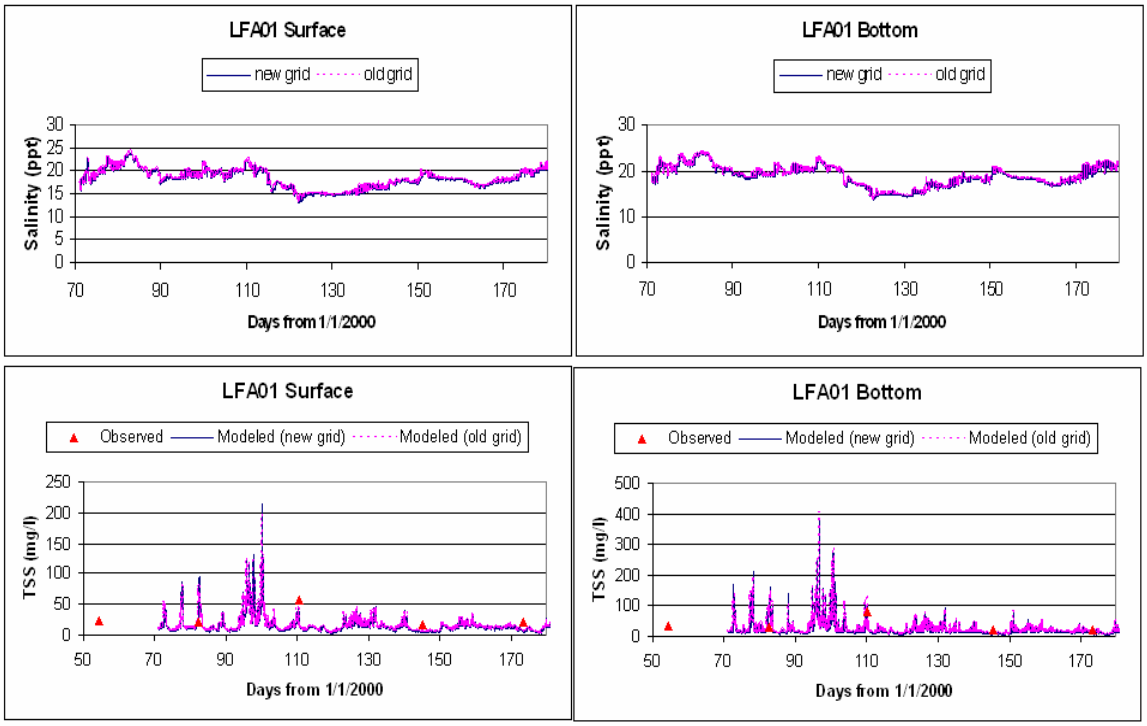

Figure A7. Comparison of model predicted salinity and total suspended solids (surface and bottom layers) at CBP Station LFA01 from March 2000 to June 2000 using the old and new model grids.

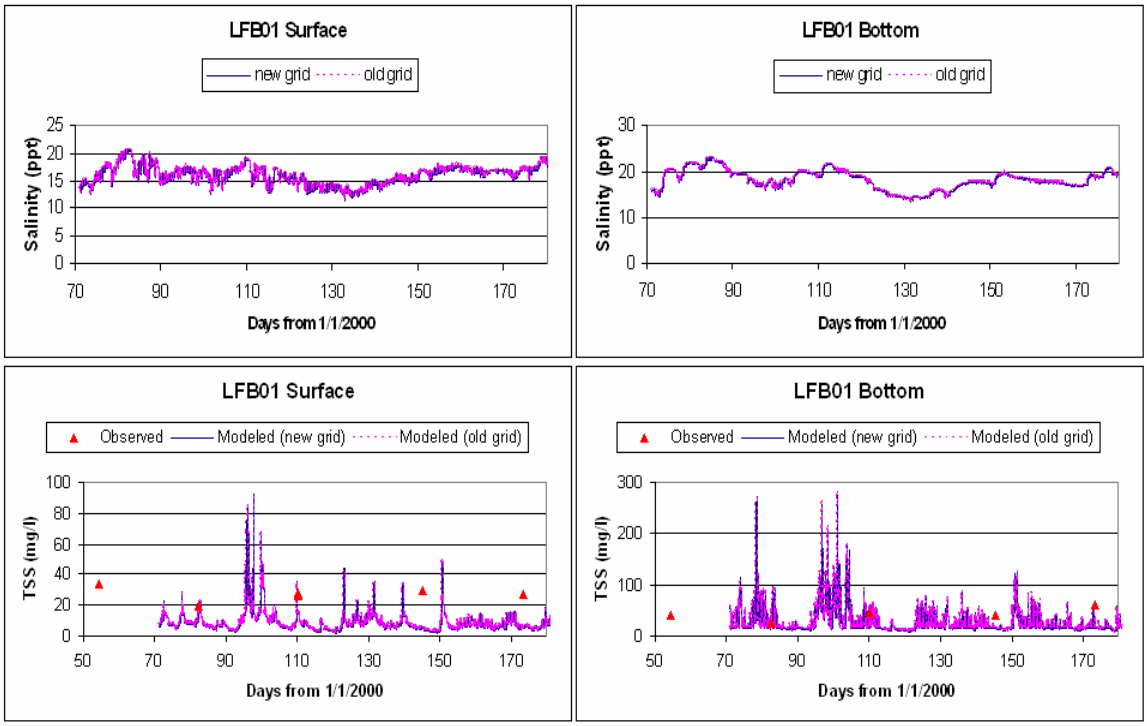

Figure A8. Comparison of model predicted salinity and total suspended solids (surface and bottom layers) at CBP Station LFB01 from March 2000 to June 2000 using the old and new model grids.

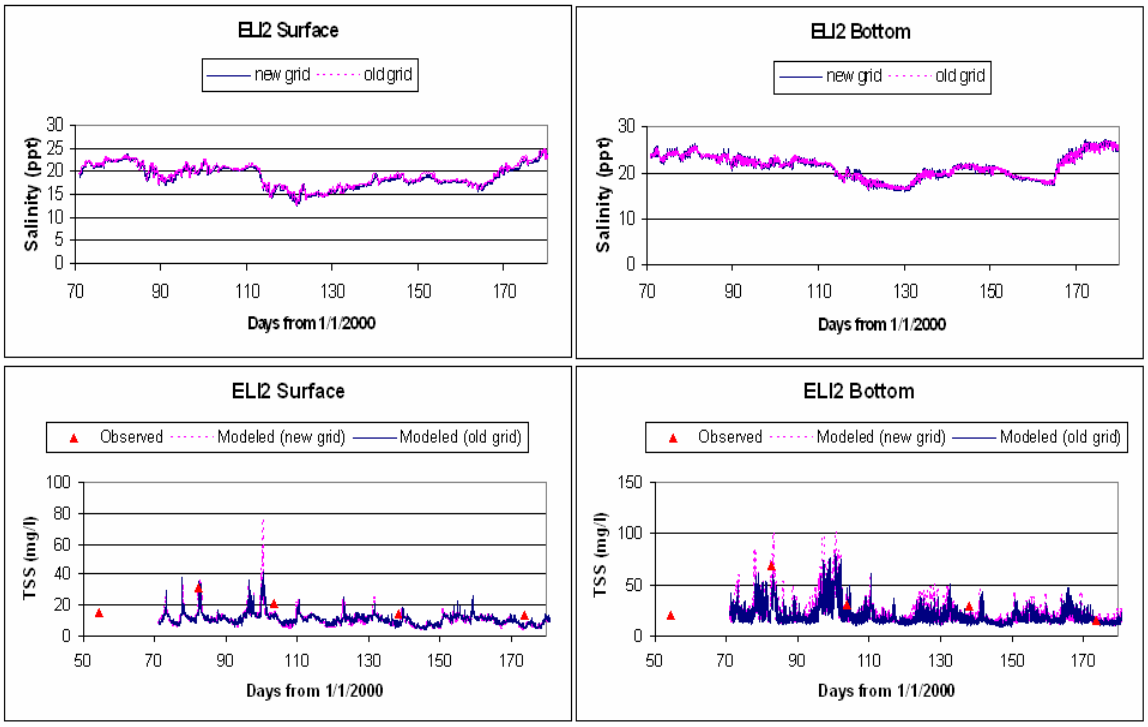

Figure A9. Comparison of model predicted salinity and total suspended solids (surface and bottom layers) at CBP Station ELI2 from March 2000 to June 2000 using the old and new model grids.

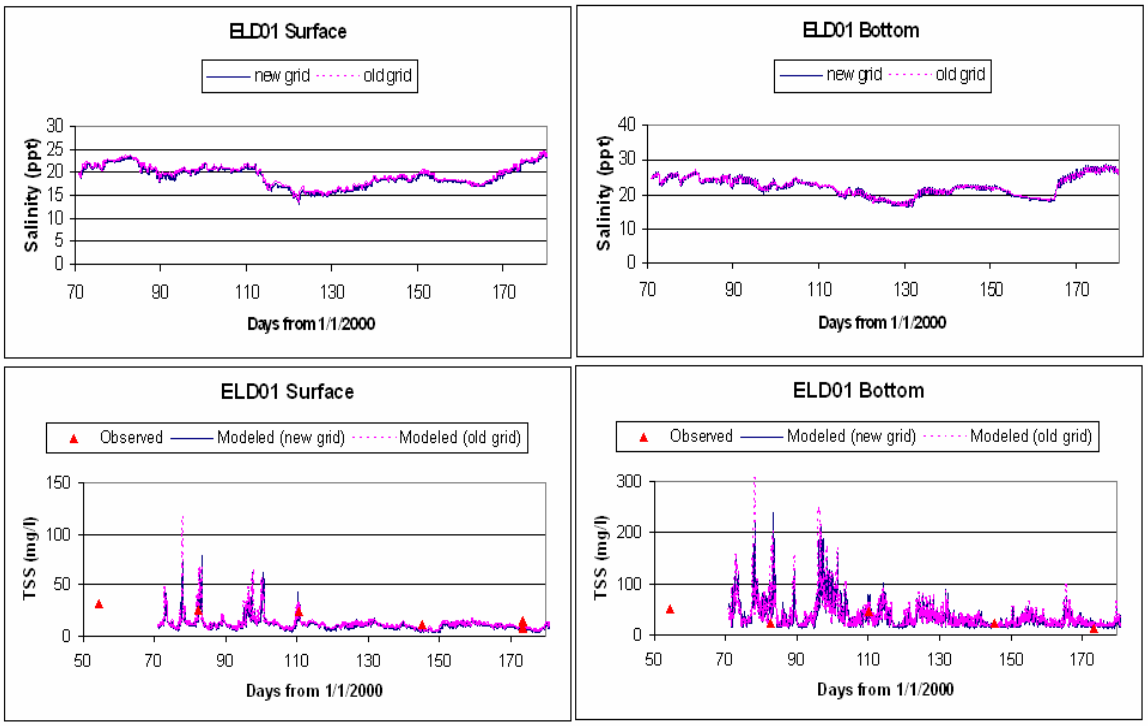

Figure A10. Comparison of model predicted salinity and total suspended solids (surface and bottom layers) at CBP Station ELD01 from March 2000 to June 2000 using the old and new model grids.

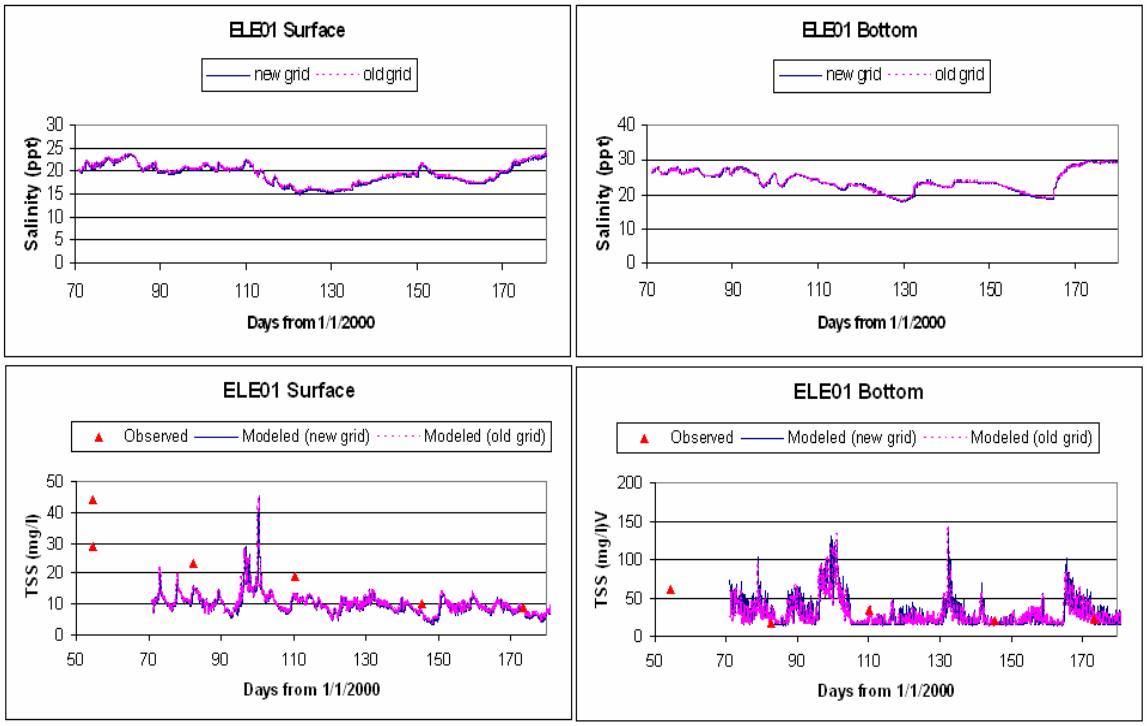

Figure A11. Comparison of model predicted salinity and total suspended solids (surface and bottom layers) at CBP Station ELE01 from March 2000 to June 2000 using the old and new model grids.

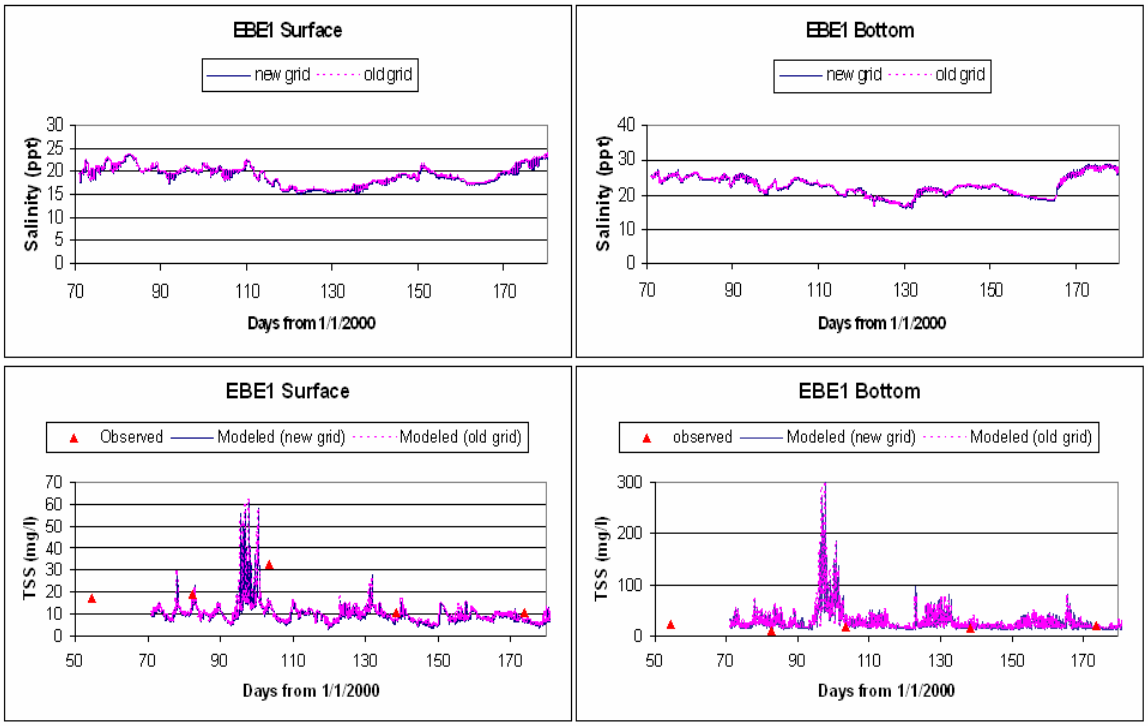

Figure A12. Comparison of model predicted salinity and total suspended solids (surface and bottom layers) at CBP Station EBE1 from March 2000 to June 2000 using the old and new model grids.

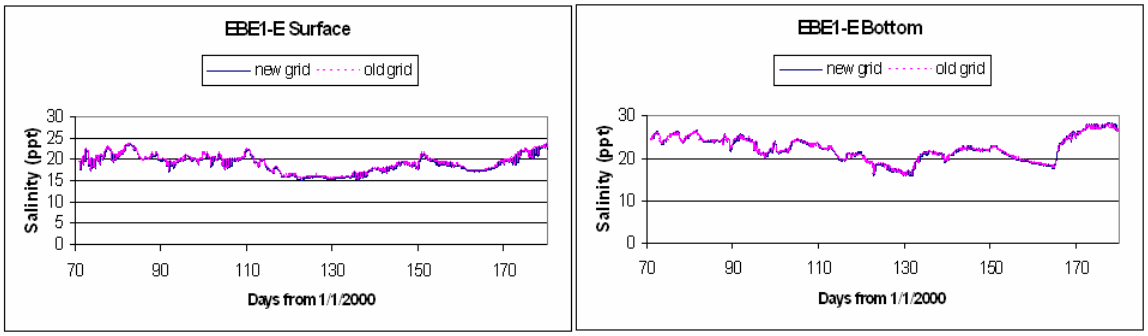

No sediment measurements available for this station

Figure A13. Comparison of model predicted salinity (surface and bottom layers) at CBP Station EBE1-E from March 2000 to June 2000 using the old and new model grids.

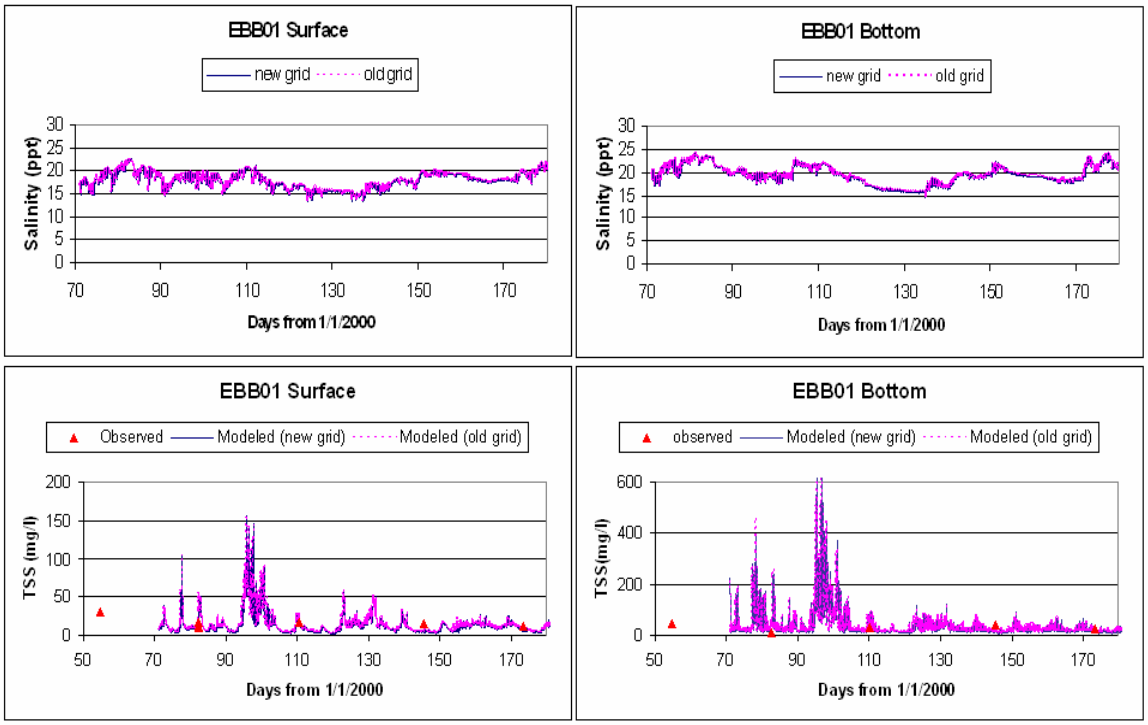

Figure A14. Comparison of model predicted salinity and total suspended solids (surface and bottom layers) at CBP Station EBB01 from March 2000 to June 2000 using the old and new model grids.

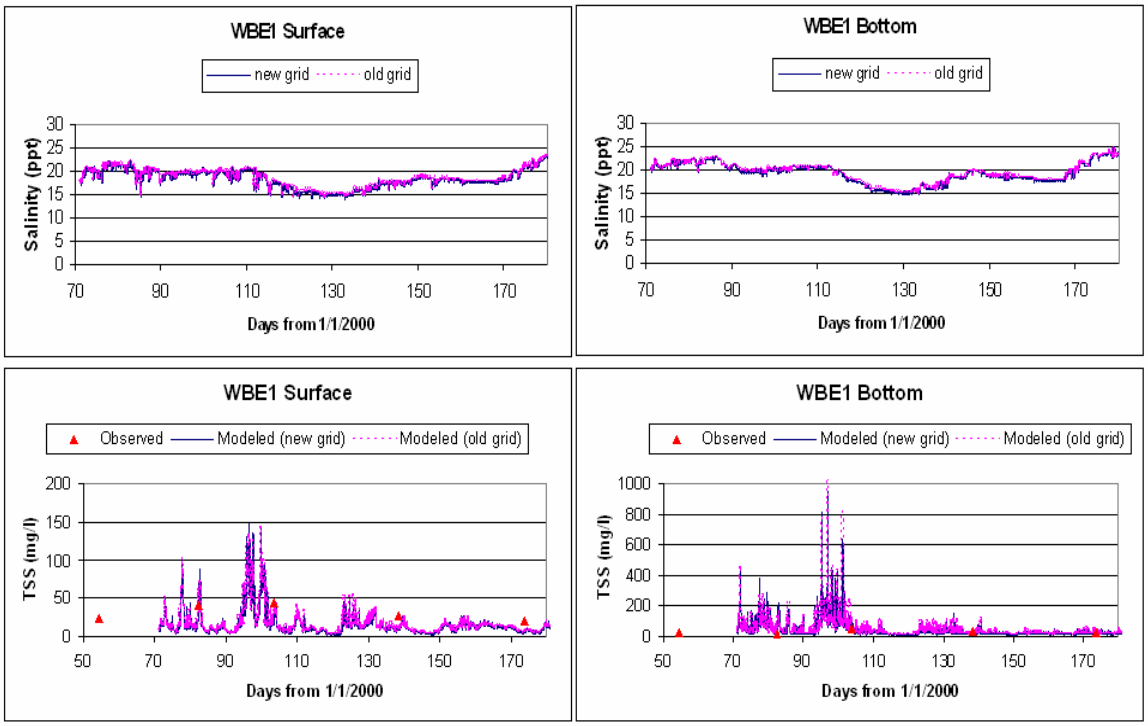

Figure A15. Comparison of model predicted salinity and total suspended solids (surface and bottom layers) at CBP Station WBE1 from March 2000 to June 2000 using the old and new model grids.

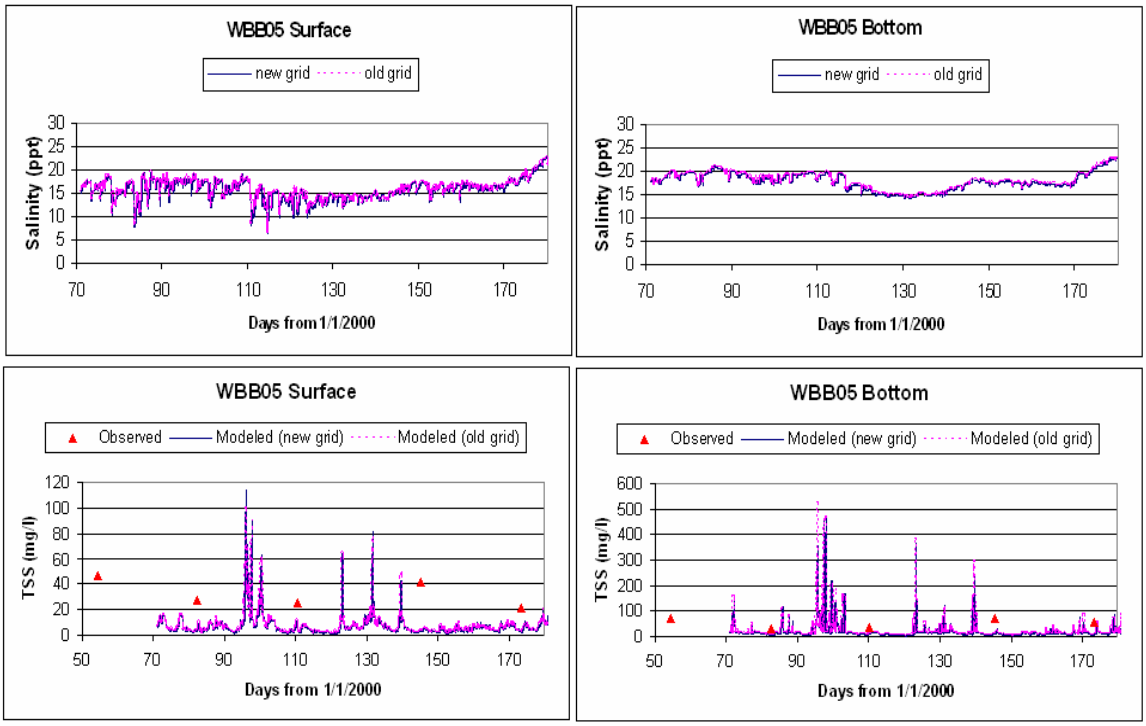

Figure A16. Comparison of model predicted salinity and total suspended solids (surface and bottom layers) at CBP Station WBB05 from March 2000 to June 2000 using the old and new model grids.

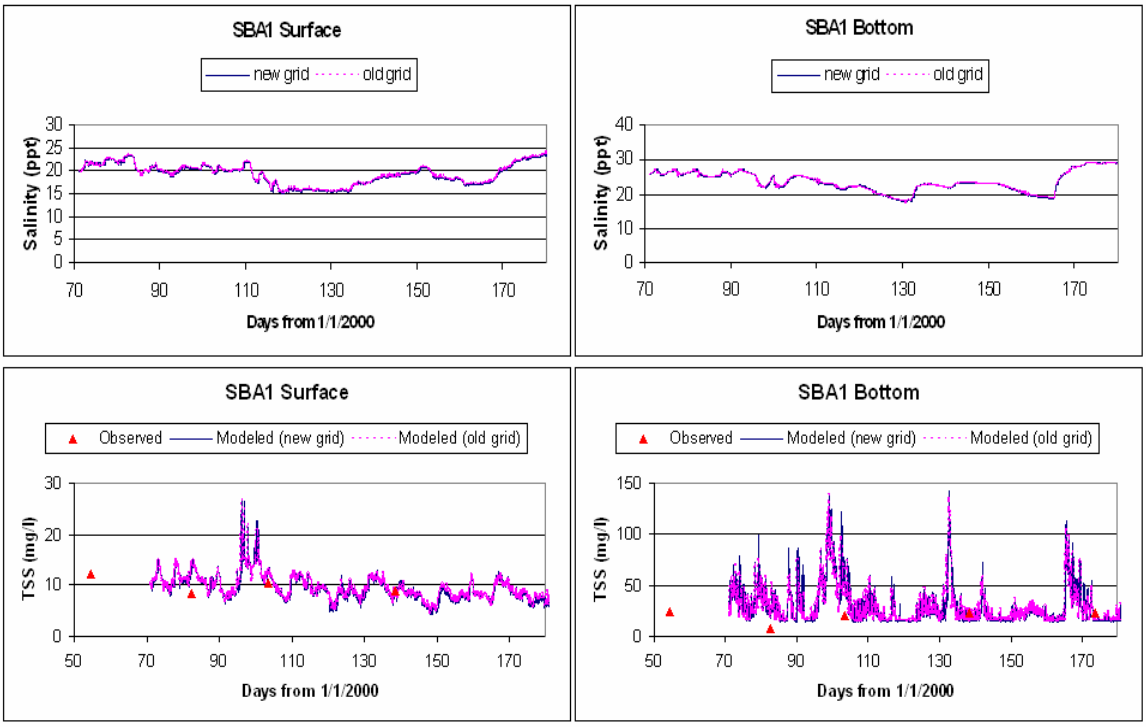

Figure A17. Comparison of model predicted salinity and total suspended solids (surface and bottom layers) at CBP Station SBA1 from March 2000 to June 2000 using the old and new model grids.

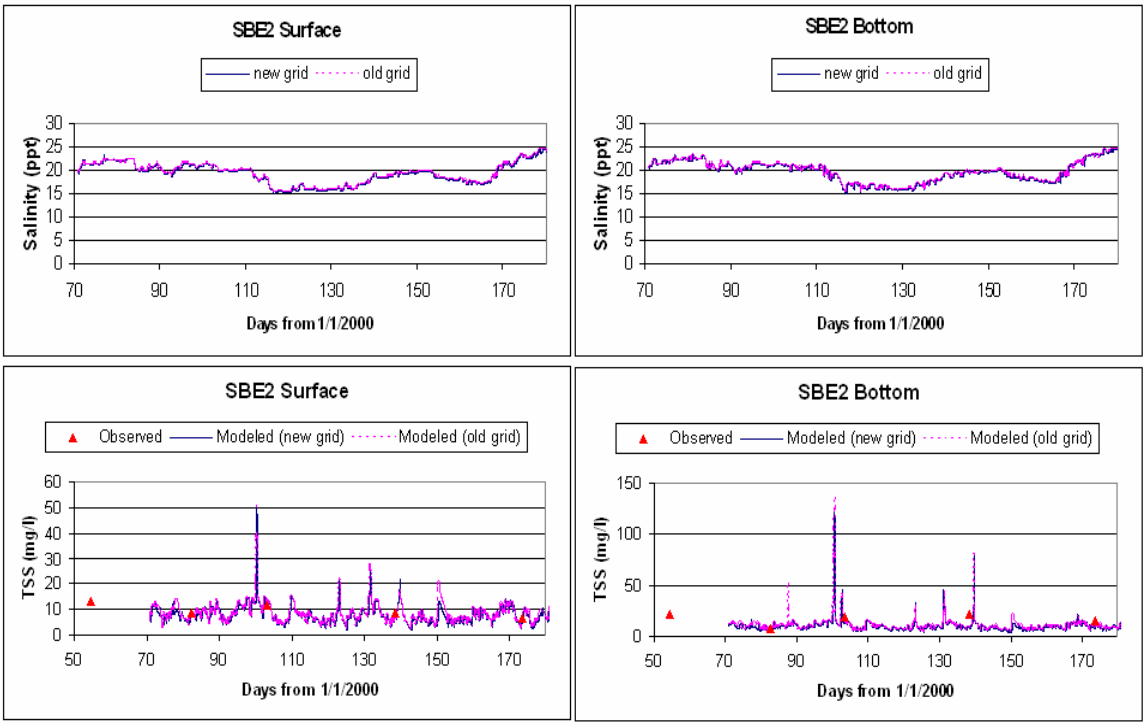

Figure A18. Comparison of model predicted salinity and total suspended solids (surface and bottom layers) at CBP Station SBE2 from March 2000 to June 2000 using the old and new model grids.

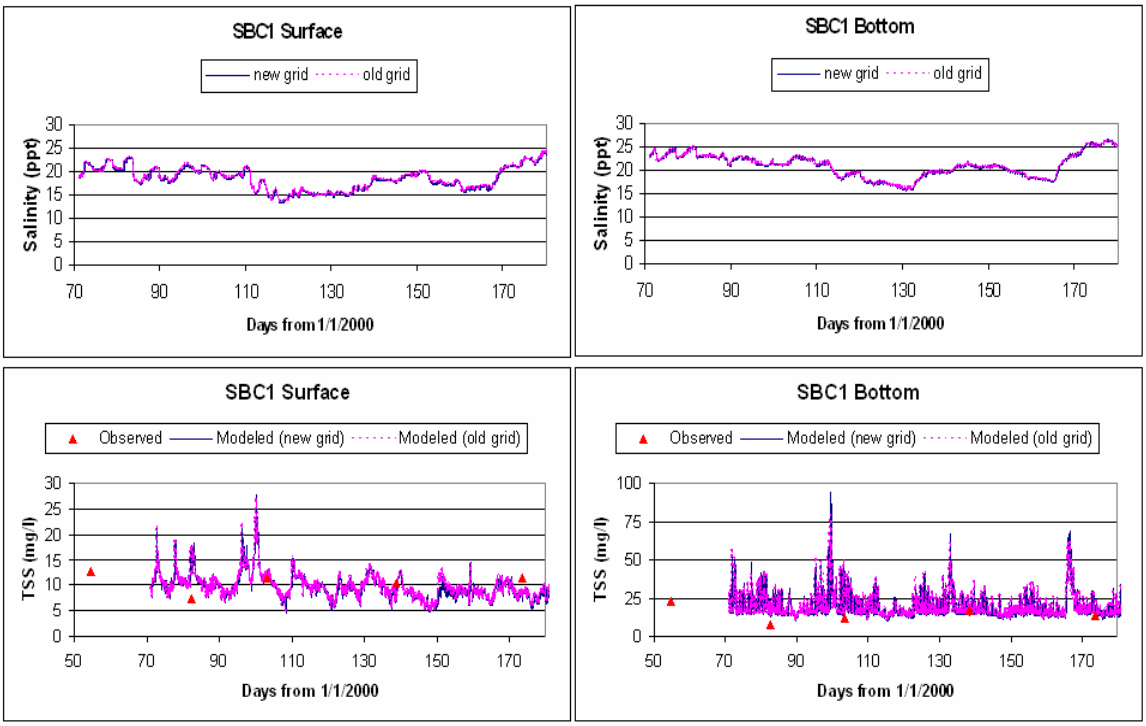

Figure A19. Comparison of model predicted salinity and total suspended solids (surface and bottom layers) at CBP Station SBC1 from March 2000 to June 2000 using the old and new model grids.

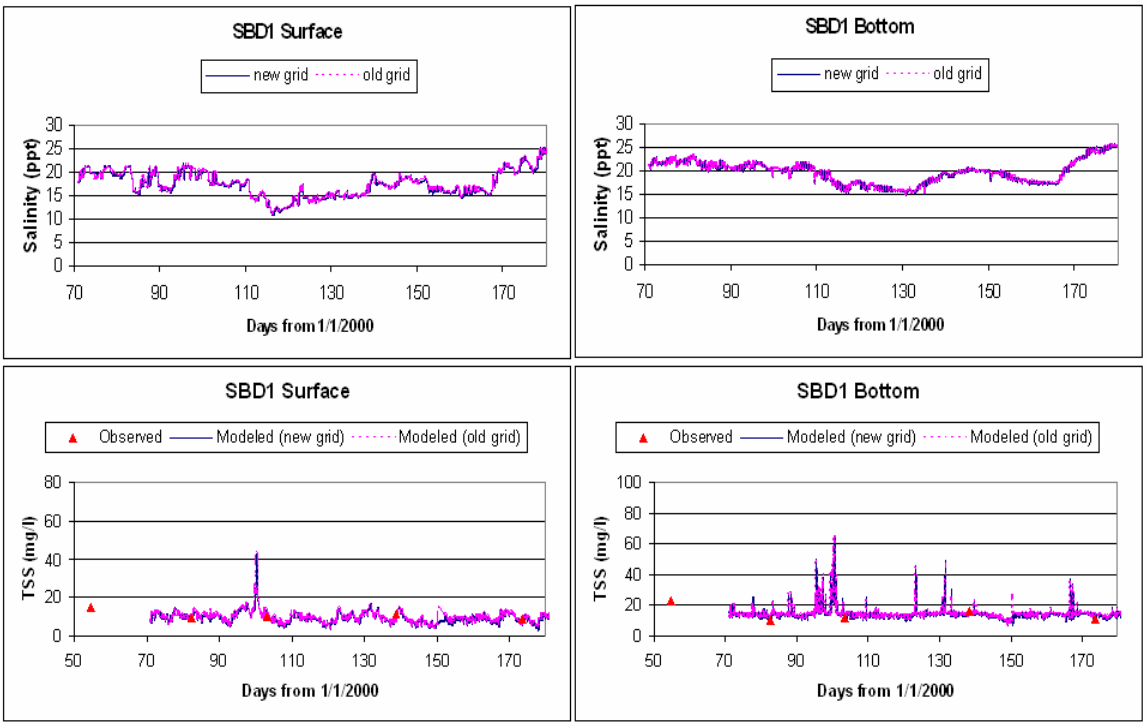

Figure A20. Comparison of model predicted salinity and total suspended solids (surface and bottom layers) at CBP Station SBD1 from March 2000 to June 2000 using the old and new model grids.

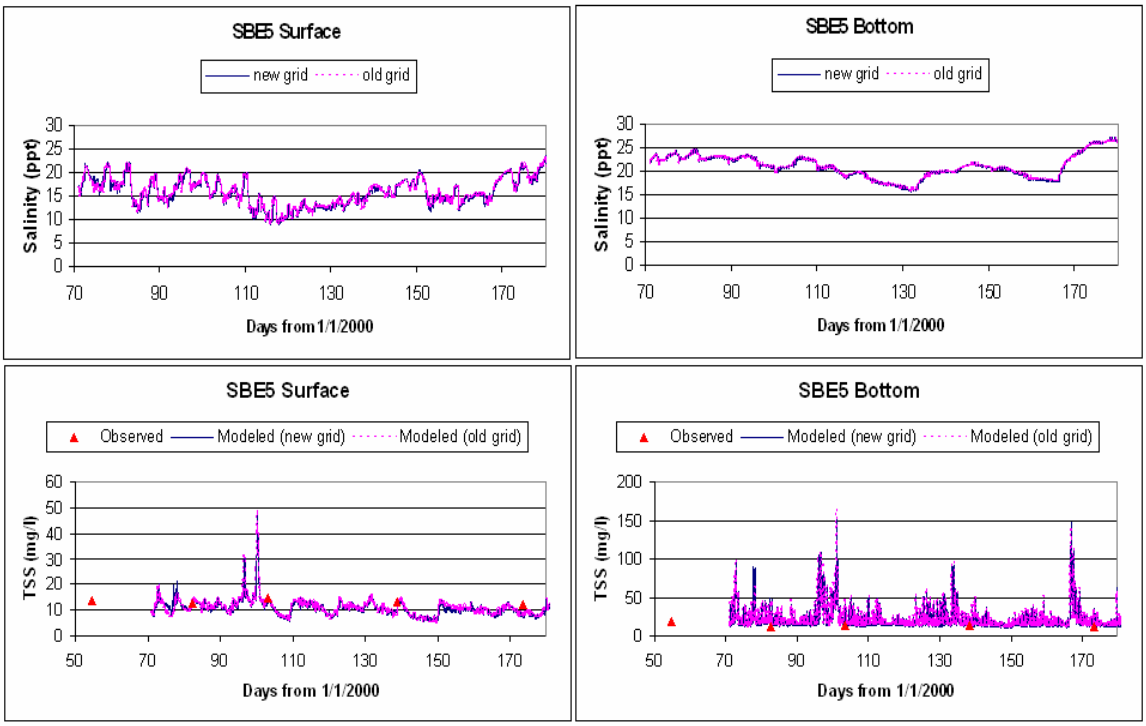

Figure A21. Comparison of model predicted salinity and total suspended solids (surface and bottom layers) at CBP Station SBE5 from March 2000 to June 2000 using the old and new model grids.

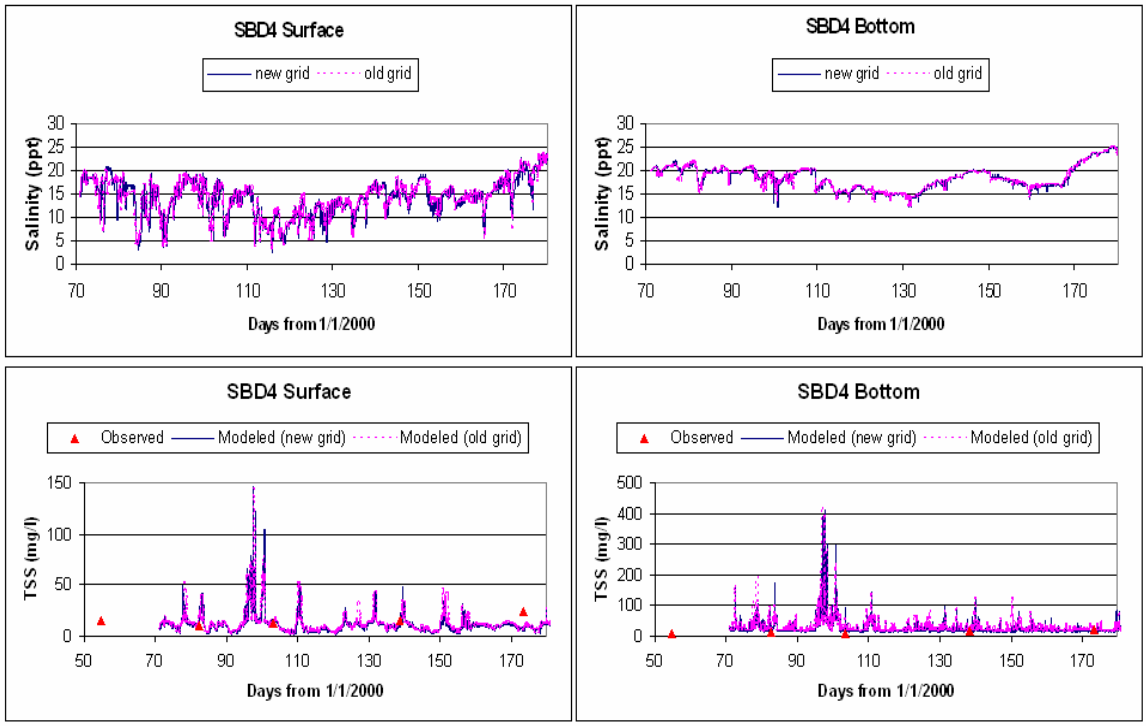

Figure A22. Comparison of model predicted salinity and total suspended solids (surface and bottom layers) at CBP Station SBD4 from March 2000 to June 2000 using the old and new model grids.

APPENDIX B

ECOM-SED Sediment Transport Module Calibration

Comparisons of Model Predicted Total Suspended Solids (Base Case and CIEE full expansion scenario) and CBP Observation Data from March 2000 to June 2000

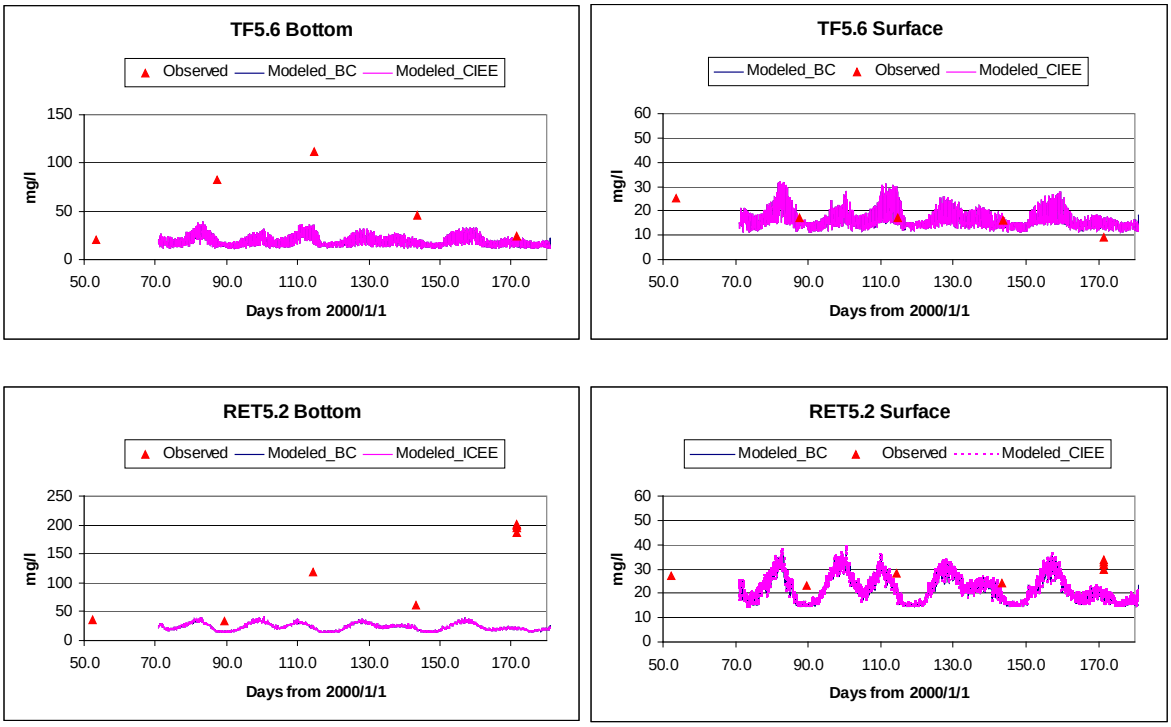

Figure B1. ECOM-SED surface and bottom layer model predictions of TSS (base case and full expansion scenario) versus observation data at CBP Stations TF5.6 and RET5.2 from March to June 2000.

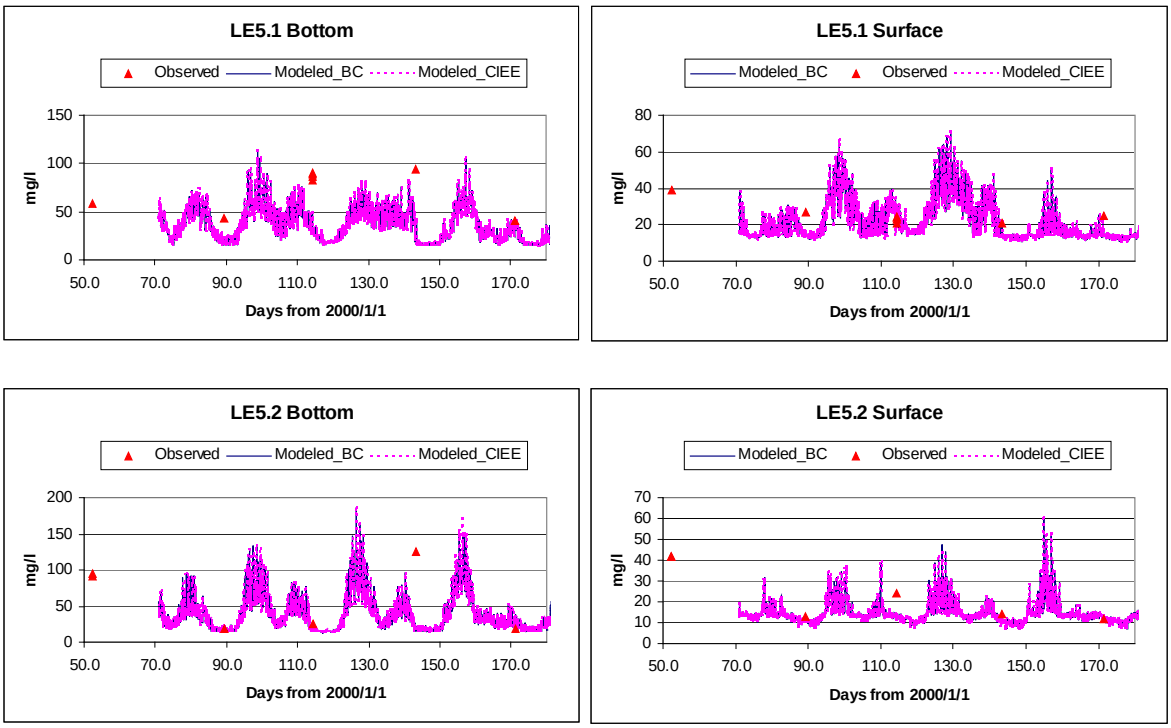

Figure B2. ECOM-SED surface and bottom layer model predictions of TSS (base case and full expansion scenario) versus observation data at CBP Stations LE5.1 and LE5.2 from March to June 2000.

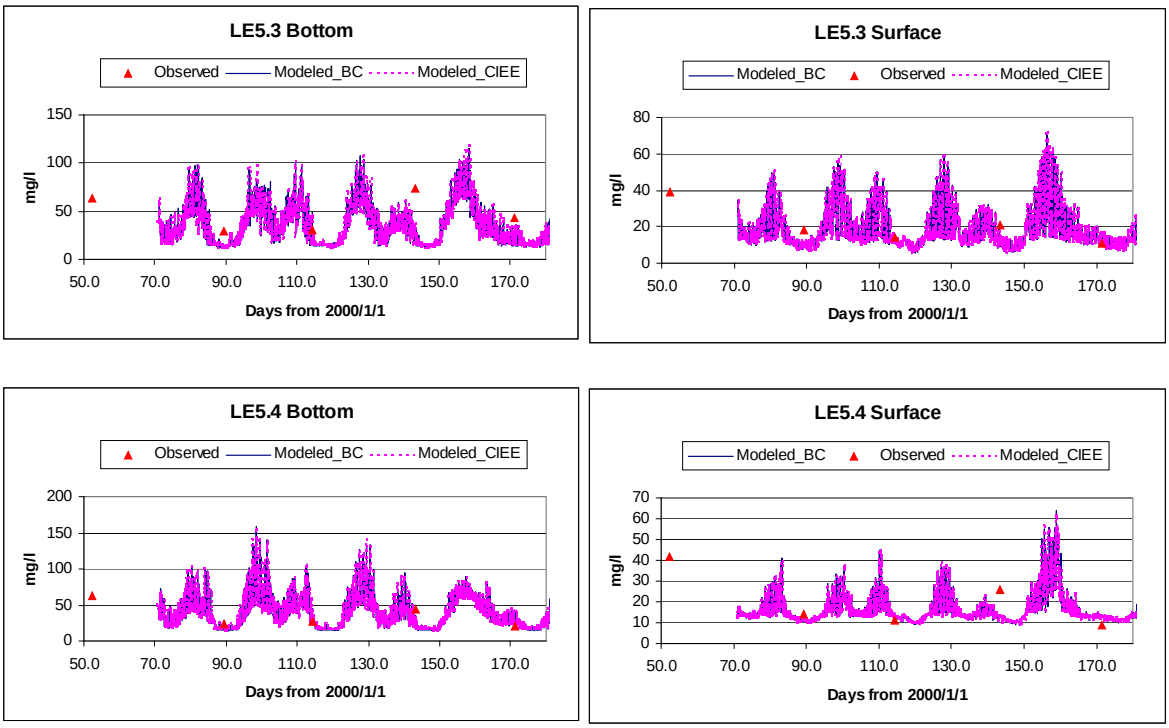

Figure B3. ECOM-SED surface and bottom layer model predictions of TSS (base case and full expansion scenario) versus observation data at CBP Stations LE5.3 and LE5.4 from March to June 2000.

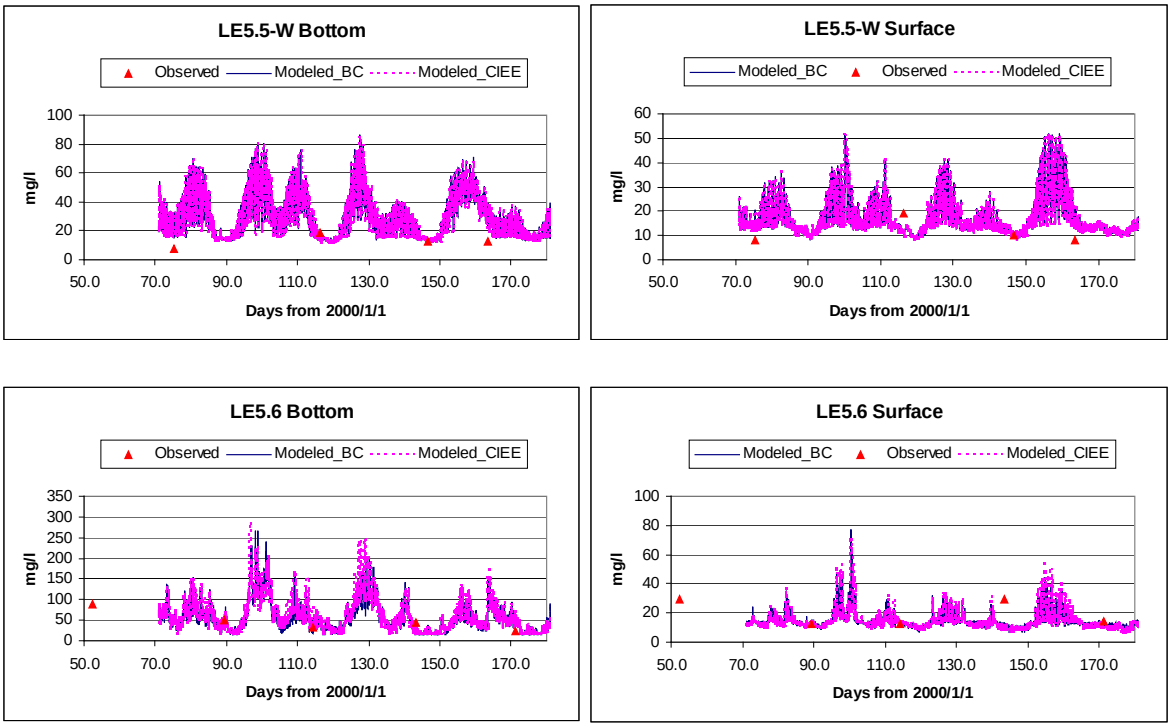

Figure B4. ECOM-SED surface and bottom layer model predictions of TSS (base case and full expansion scenario) versus observation data at CBP Stations LE5.5-W and LE5.6 from March to June 2000.

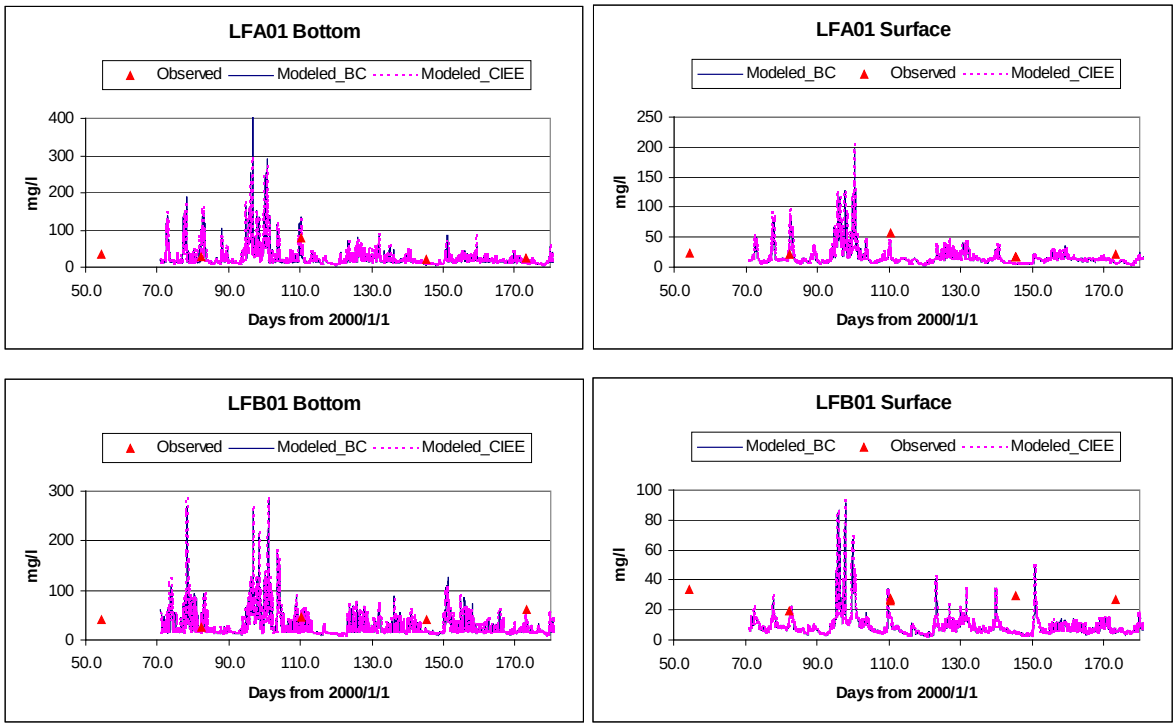

Figure B5. ECOM-SED surface and bottom layer model predictions of TSS (base case and full expansion scenario) versus observation data at CBP Stations LFA01 and LFB01 from March to June 2000.

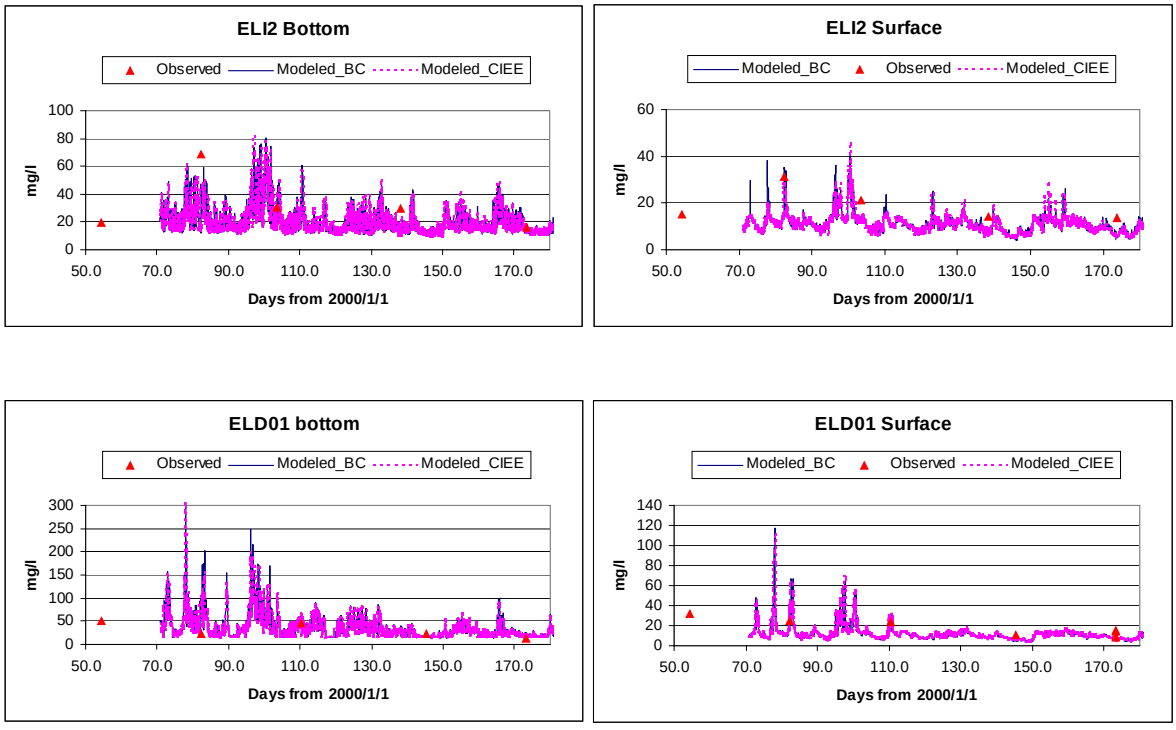

Figure B6. ECOM-SED surface and bottom layer model predictions of TSS (base case and full expansion scenario) versus observation data at CBP Stations ELI2 and ELD01 from March to June 2000.

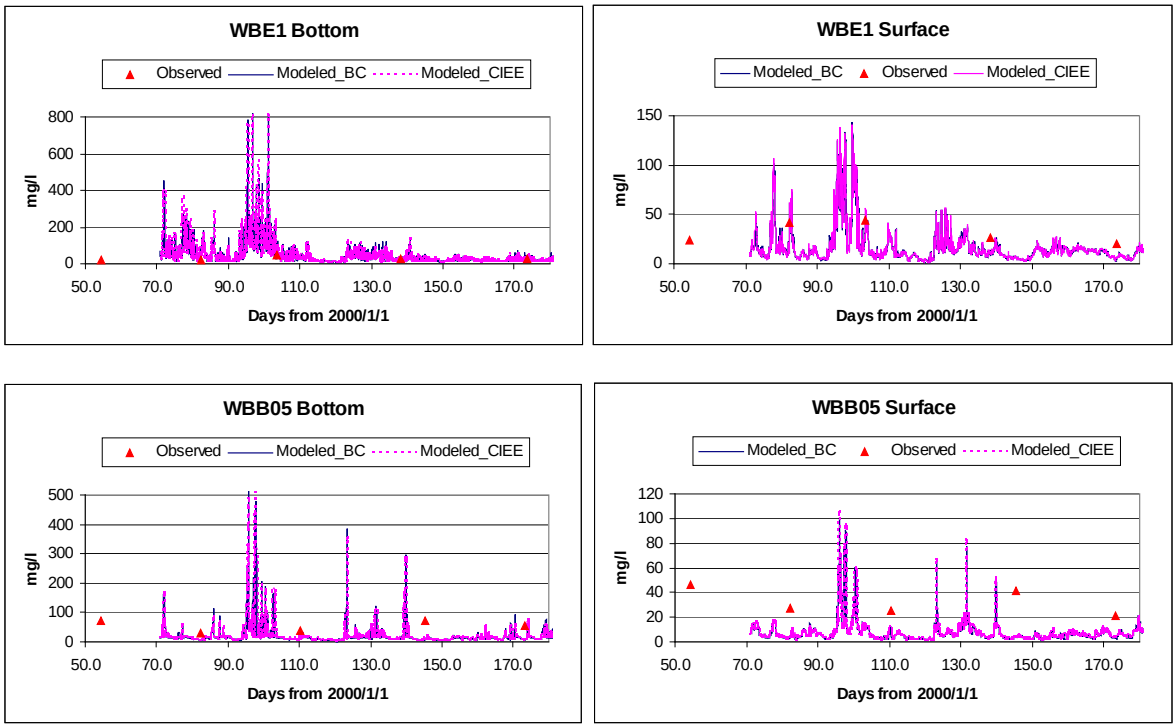

Figure B7. ECOM-SED surface and bottom layer model predictions of TSS (base case and full expansion scenario) versus observation data at CBP Stations WBE1 and WBB05 from March to June 2000.

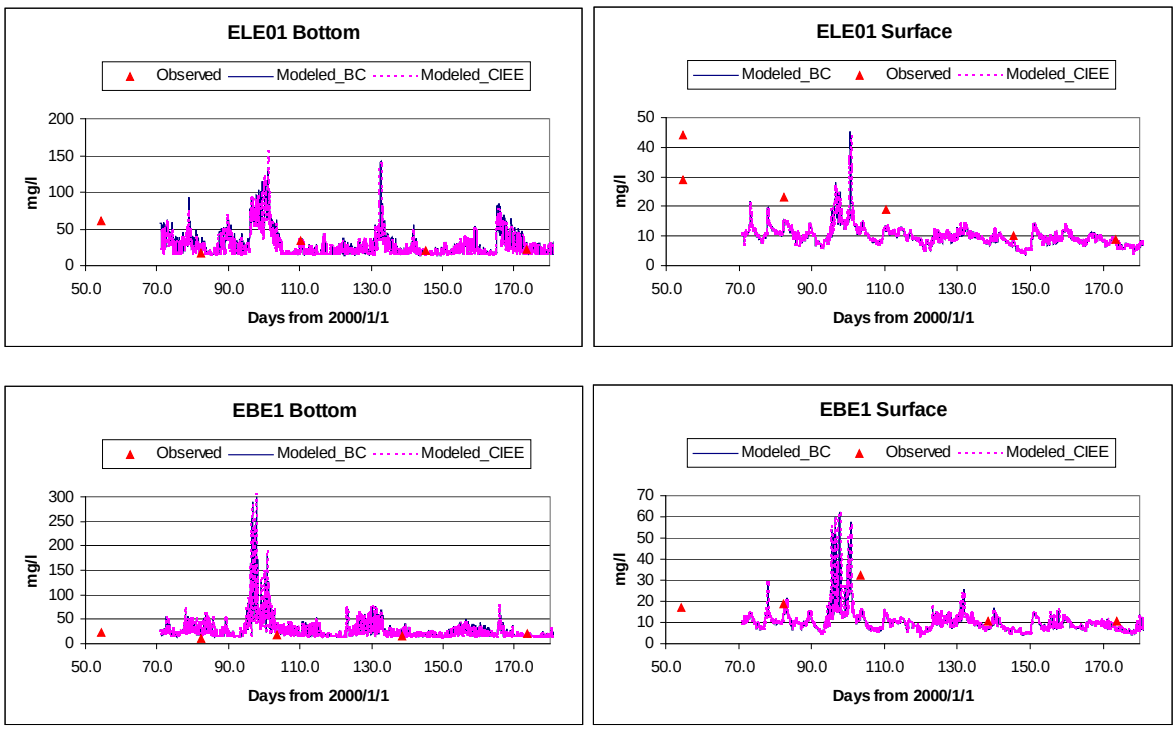

Figure B8. ECOM-SED surface and bottom layer model predictions of TSS (base case and full expansion scenario) versus observation data at CBP Stations ELE01 and EBE1 from March to June 2000.

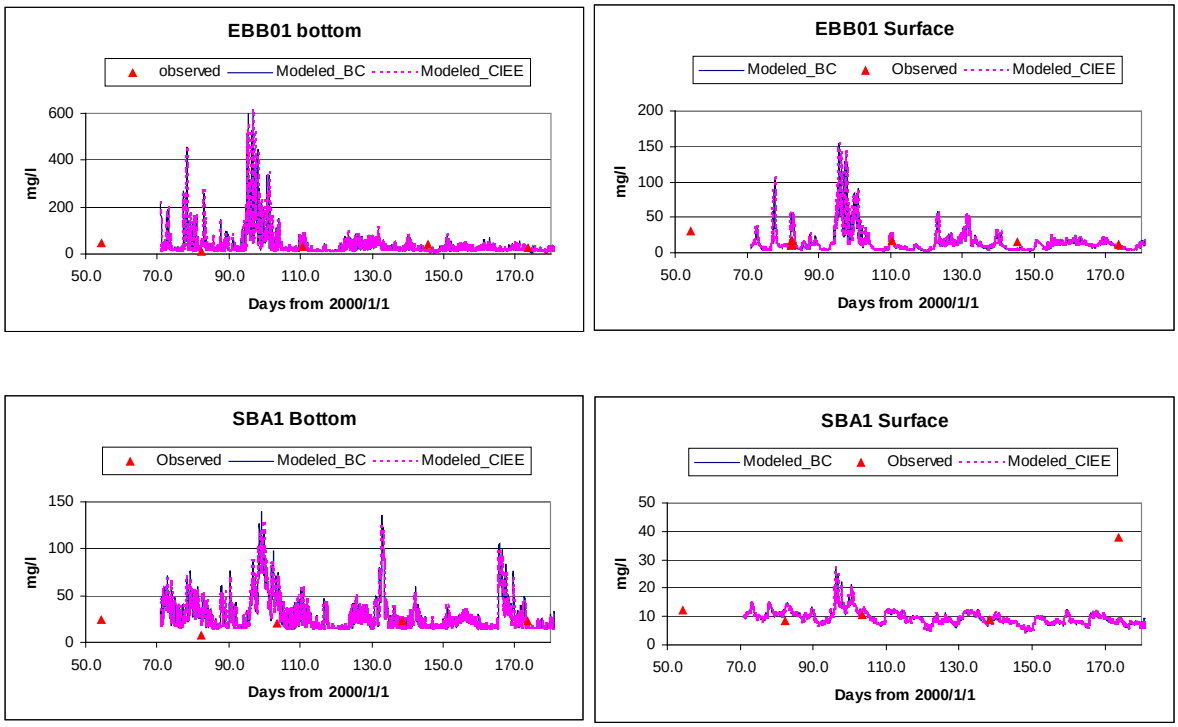

Figure B9. ECOM-SED surface and bottom layer model predictions of TSS (base case and full expansion scenario) versus observation data at CBP Stations EBB01 and SBA1 from March to June 2000.

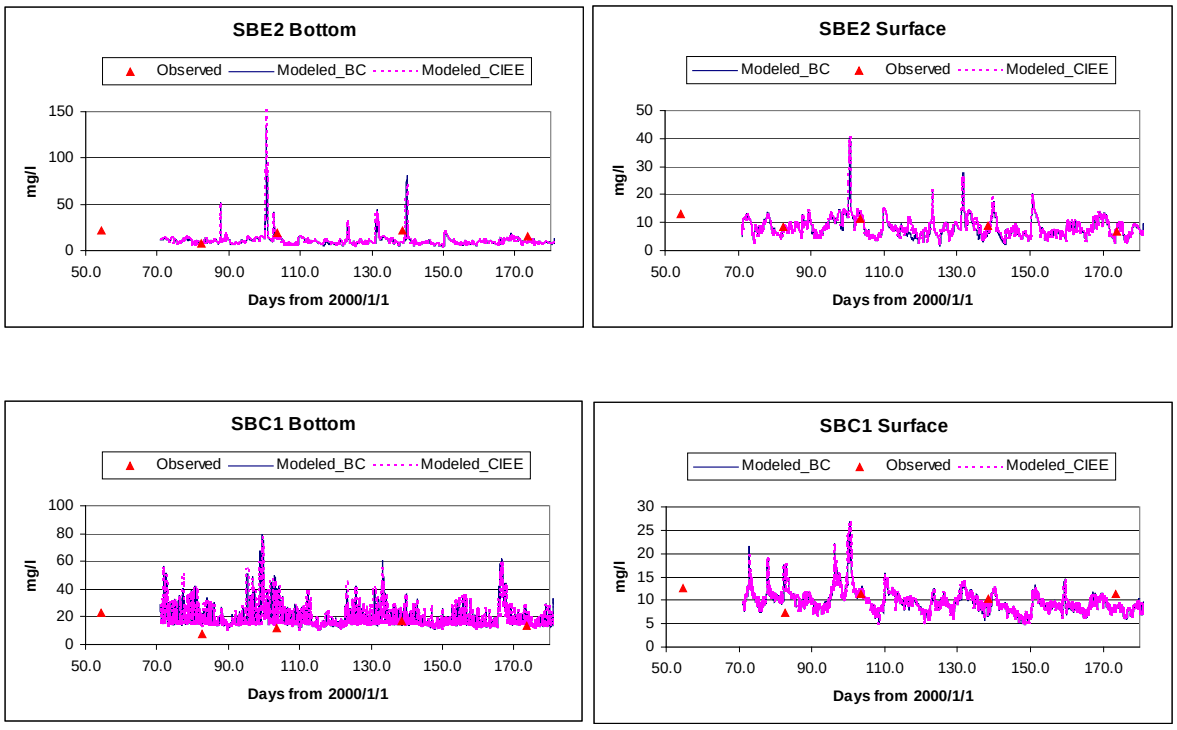

Figure B10. ECOM-SED surface and bottom layer model predictions of TSS (base case and full expansion scenario) versus observation data at CBP Stations SBE2 and SBC1 from March to June 2000.

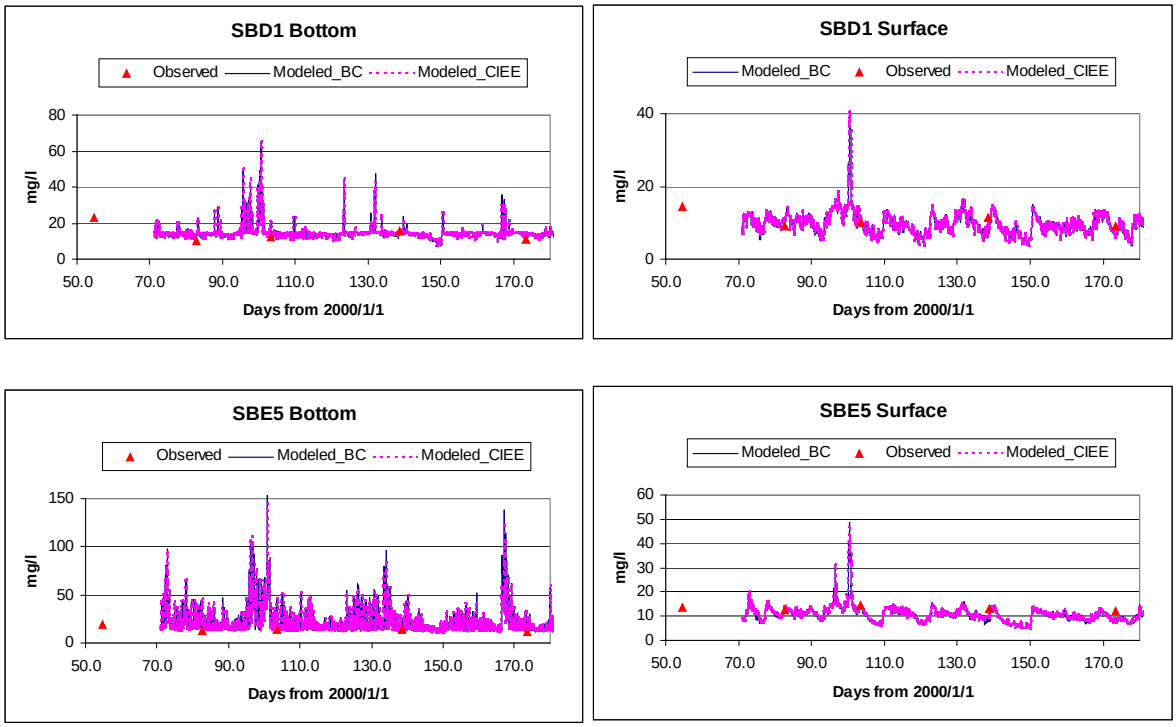

Figure B11. ECOM-SED surface and bottom layer model predictions of TSS (base case and full expansion scenario) versus observation data at CBP Stations SBD1 and SBE5 from March to June 2000.

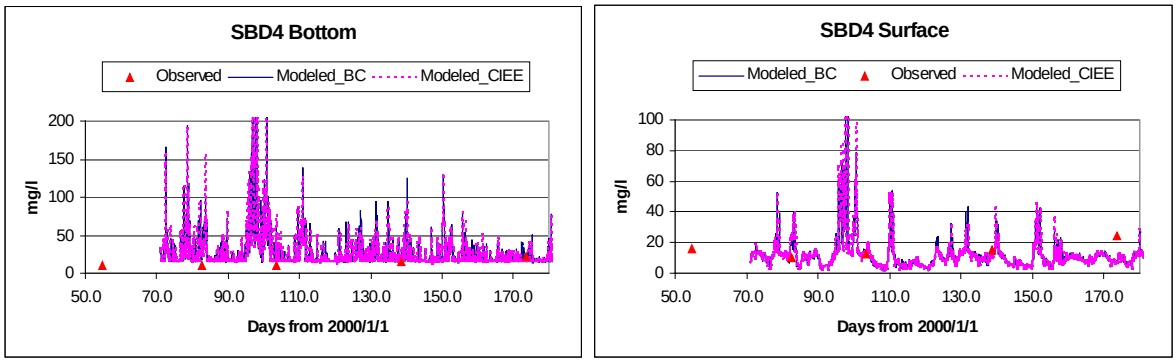

Figure B12. ECOM-SED surface and bottom layer model predictions of TSS (base case and full expansion scenario) versus observation data at CBP Station SBD4 from March to June 2000.

APPENDIX C

Global Comparisons of Single Variable Runs

1) CIEE South Cell Expansion
2) CIEE Full Expansion

Spatial Distributions

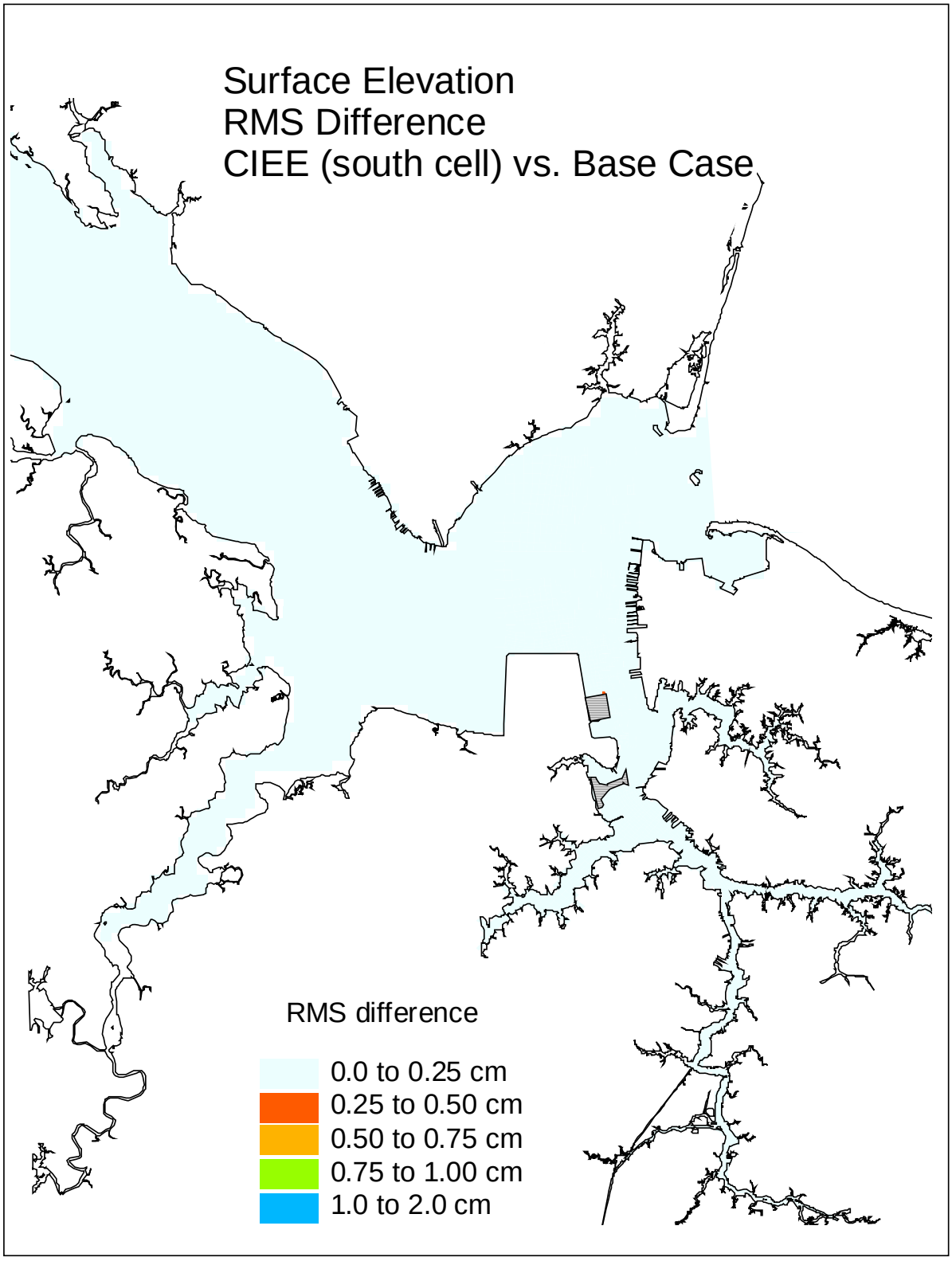

Figure C1. Single variable simulation comparison of surface elevation RMS difference for the proposed Craney Island Eastward Expansion (south cell) versus the the Base Case.

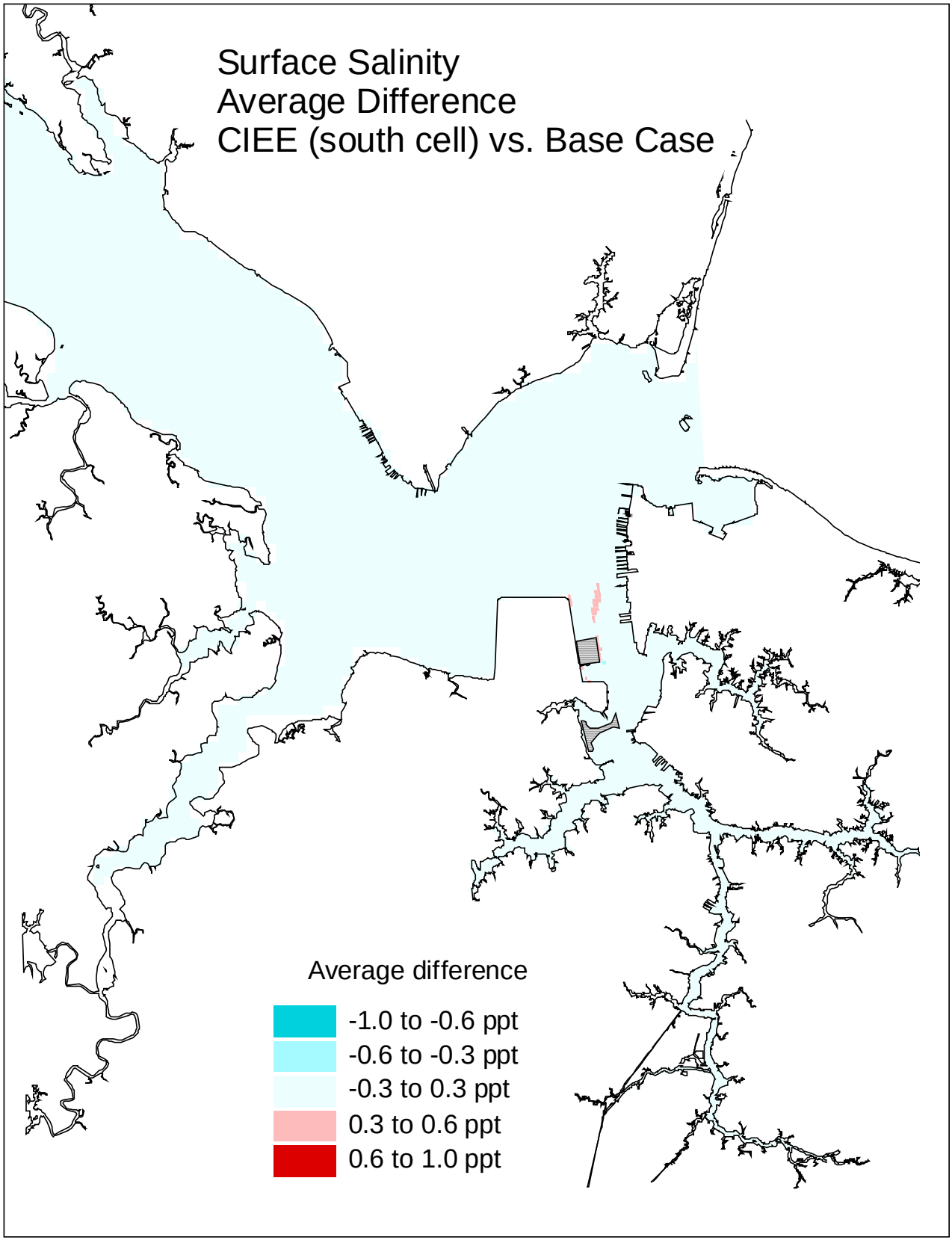

Figure C2. Single variable simulation comparison of the surface salinity average difference for the proposed Craney Island Eastward Expansion (south cell) versus the Base Case.

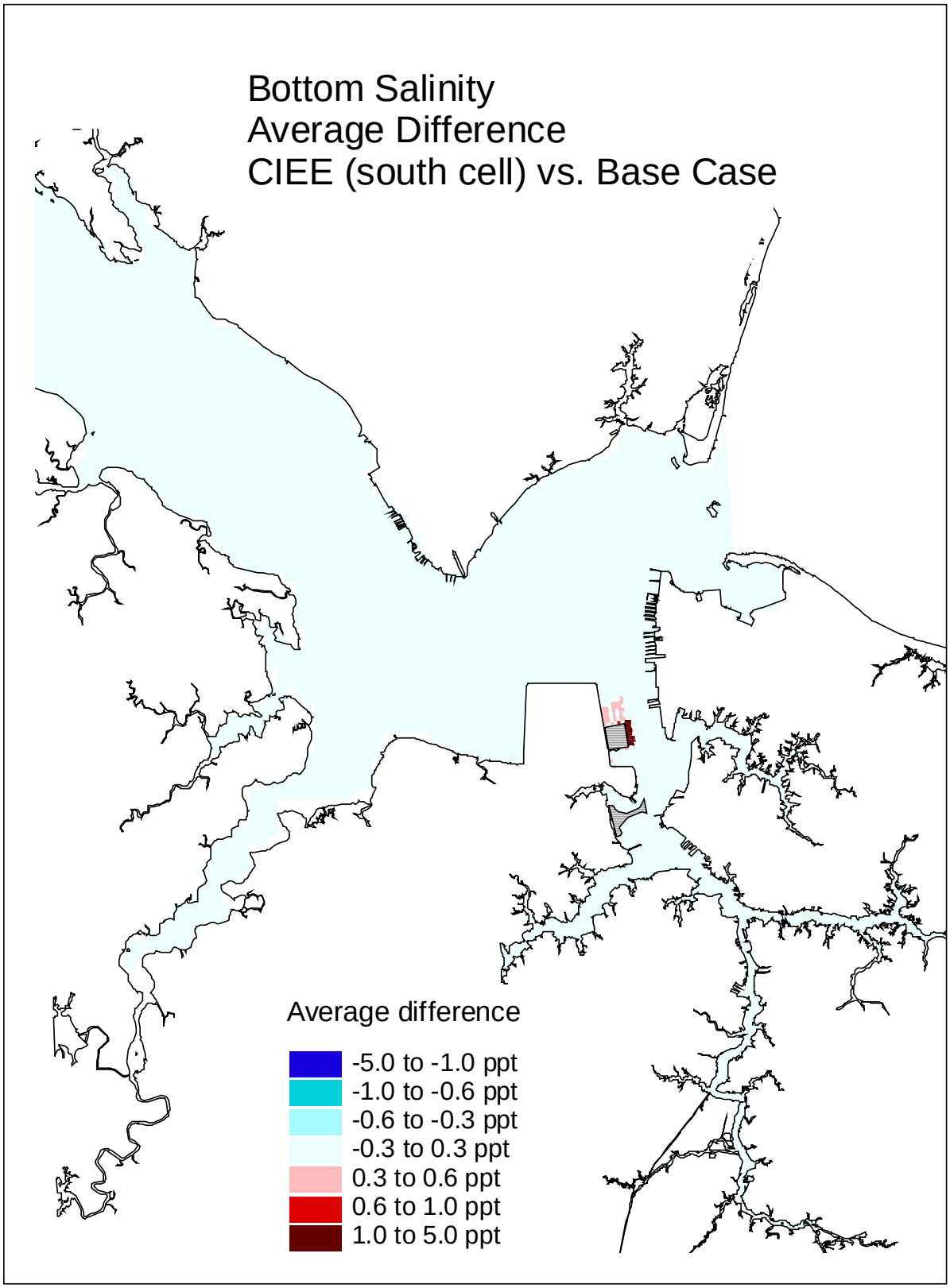

Figure C3. Single variable simulation comparison of bottom salinity average difference for the proposed Craney Island Eastward Expansion (south cell) versus the Base Case.

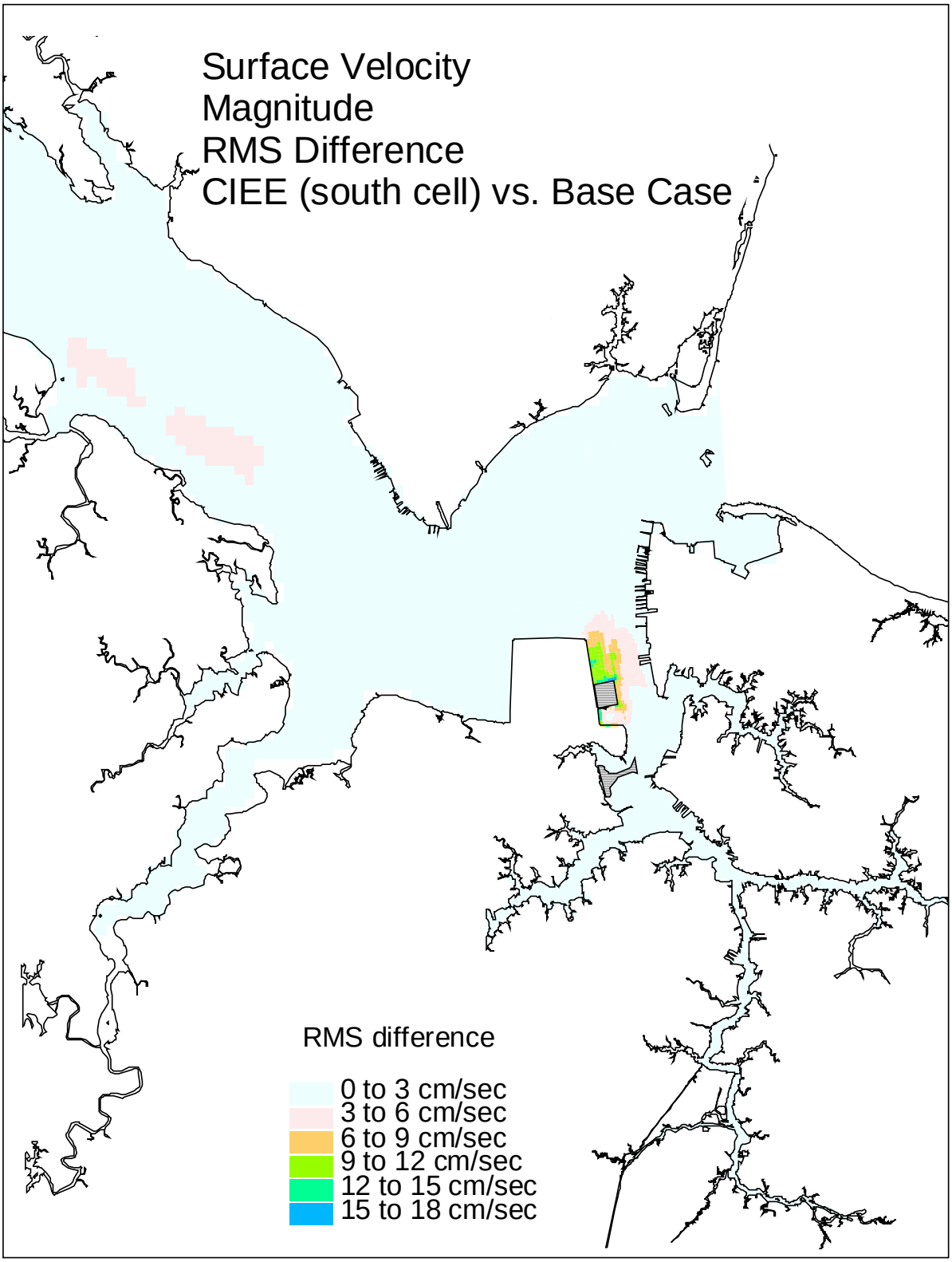

Figure C4. Single variable simulation comparison of surface velocity RMS difference for the proposed Craney Island Eastward Expansion (south cell) versus the Base Case.

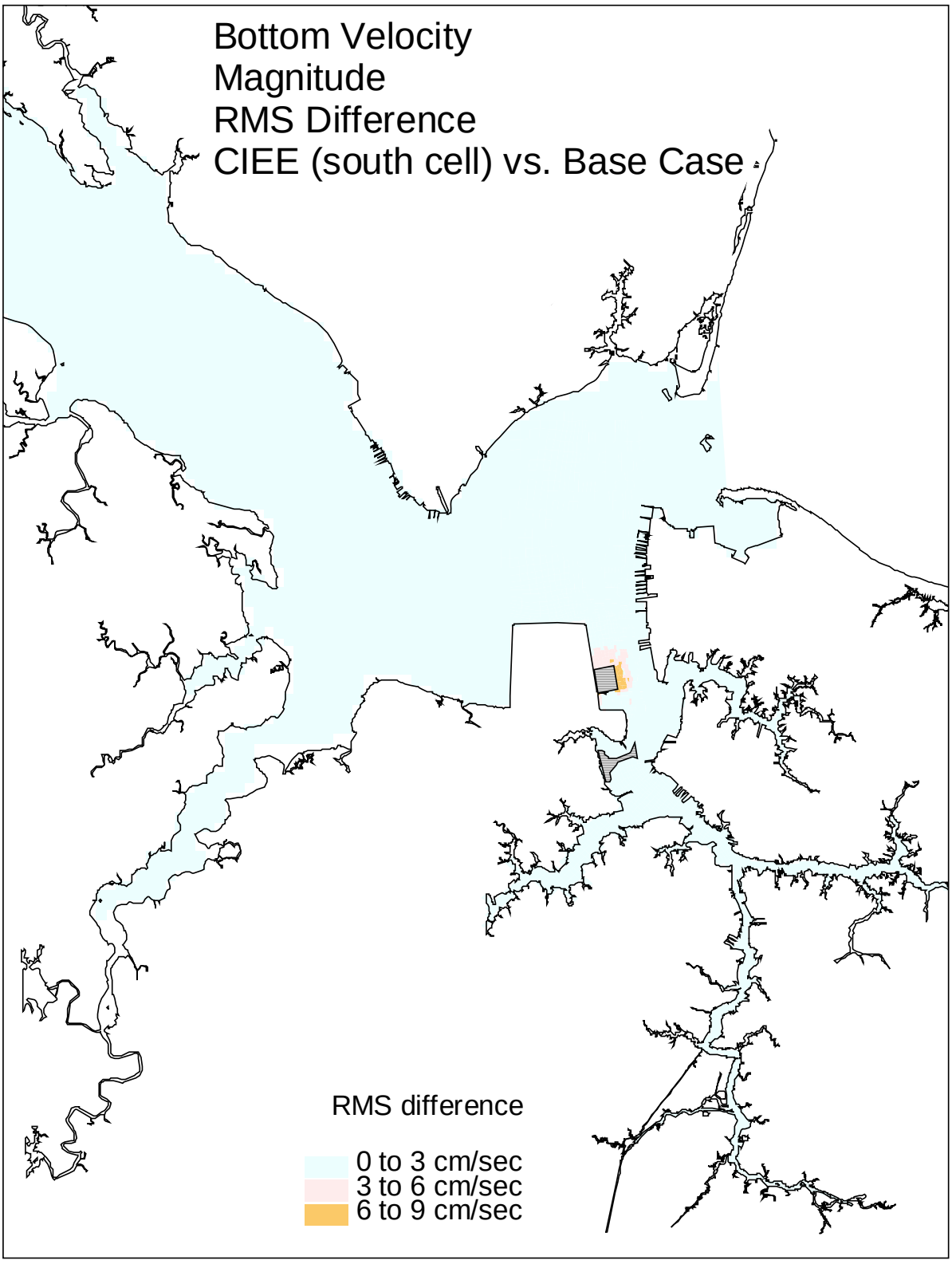

Figure C5. Single variable simulation comparison of the bottom velocity RMS difference for the proposed Craney Island Eastward Expansion (south cell) versus the Base Case.

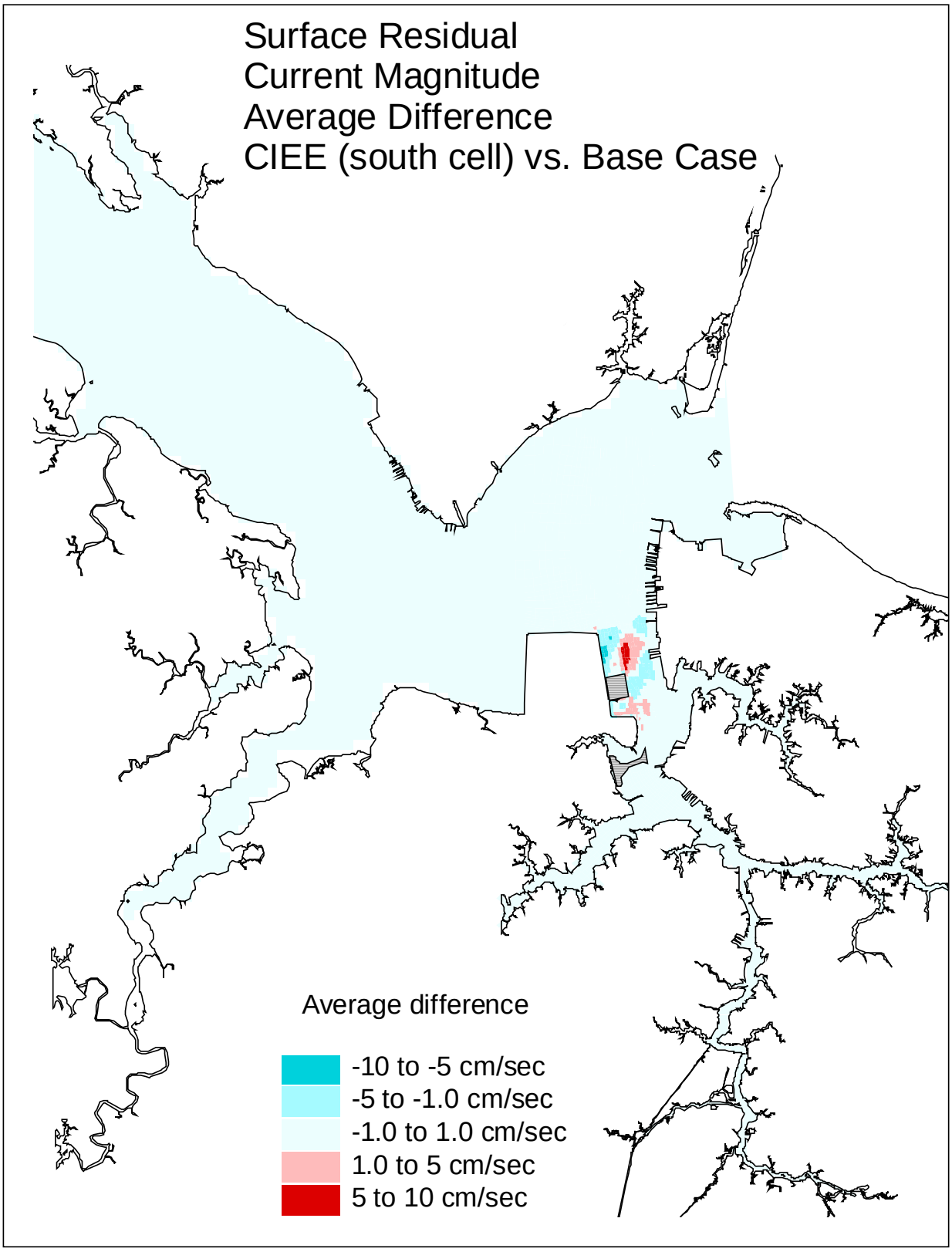

Figure C6. Single variable simulation comparison of the surface residual velocity average difference for the proposed Craney Island Eastward Expansion (south cell) versus the Base Case.

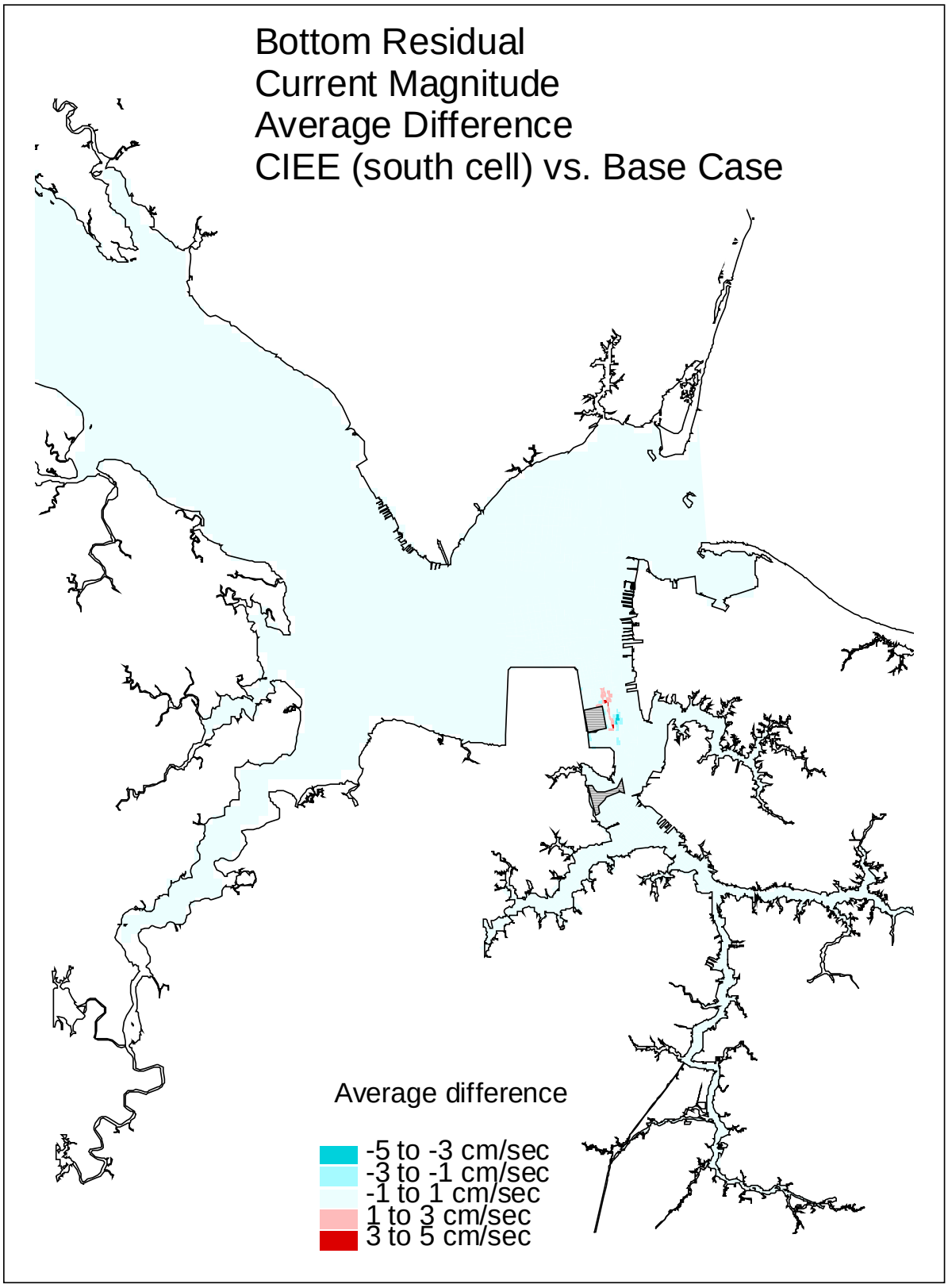

Figure C7. Single variable simulation comparison of the bottom residual velocity average difference for the proposed Craney Island Eastward Expansion (south cell) versus the Base Case.

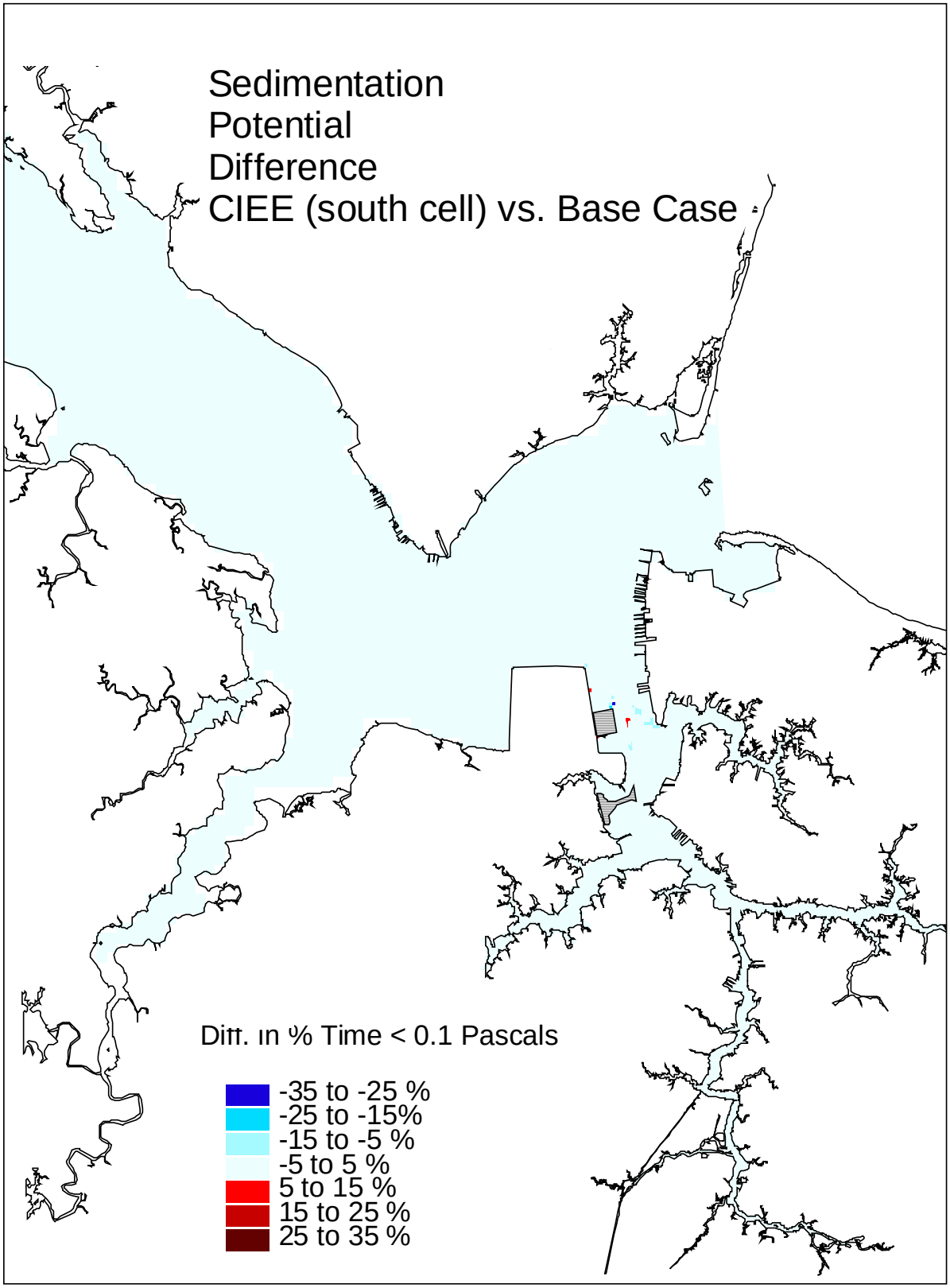

Figure C8. Single variable simulation comparison of the sedimentation potential difference for the proposed Craney Island Eastward Expansion (south cell) versus the Base Case.

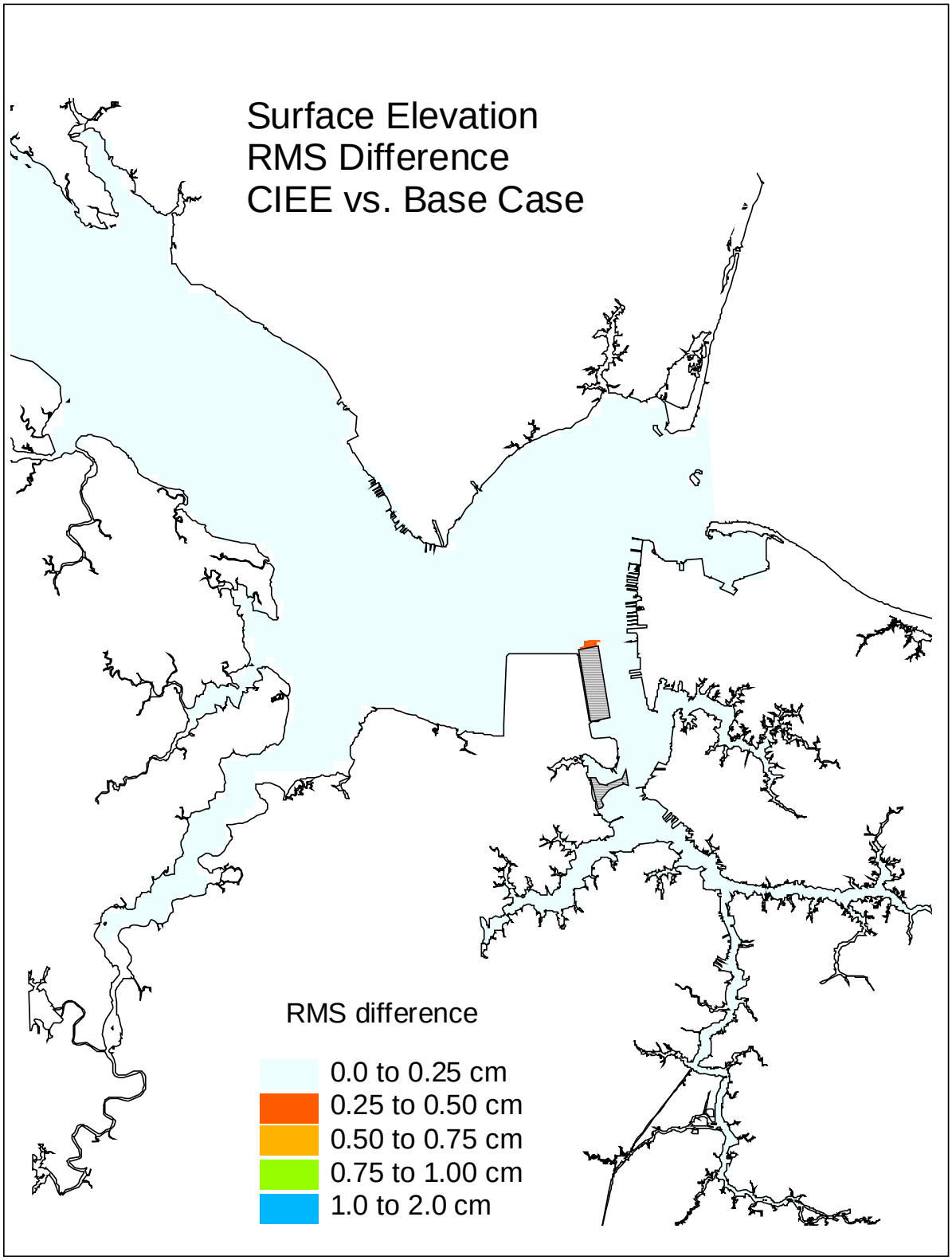

Figure C9. Single variable simulation comparison of surface elevation RMS difference for the proposed Craney Island Eastward Expansion versus the Base Case.

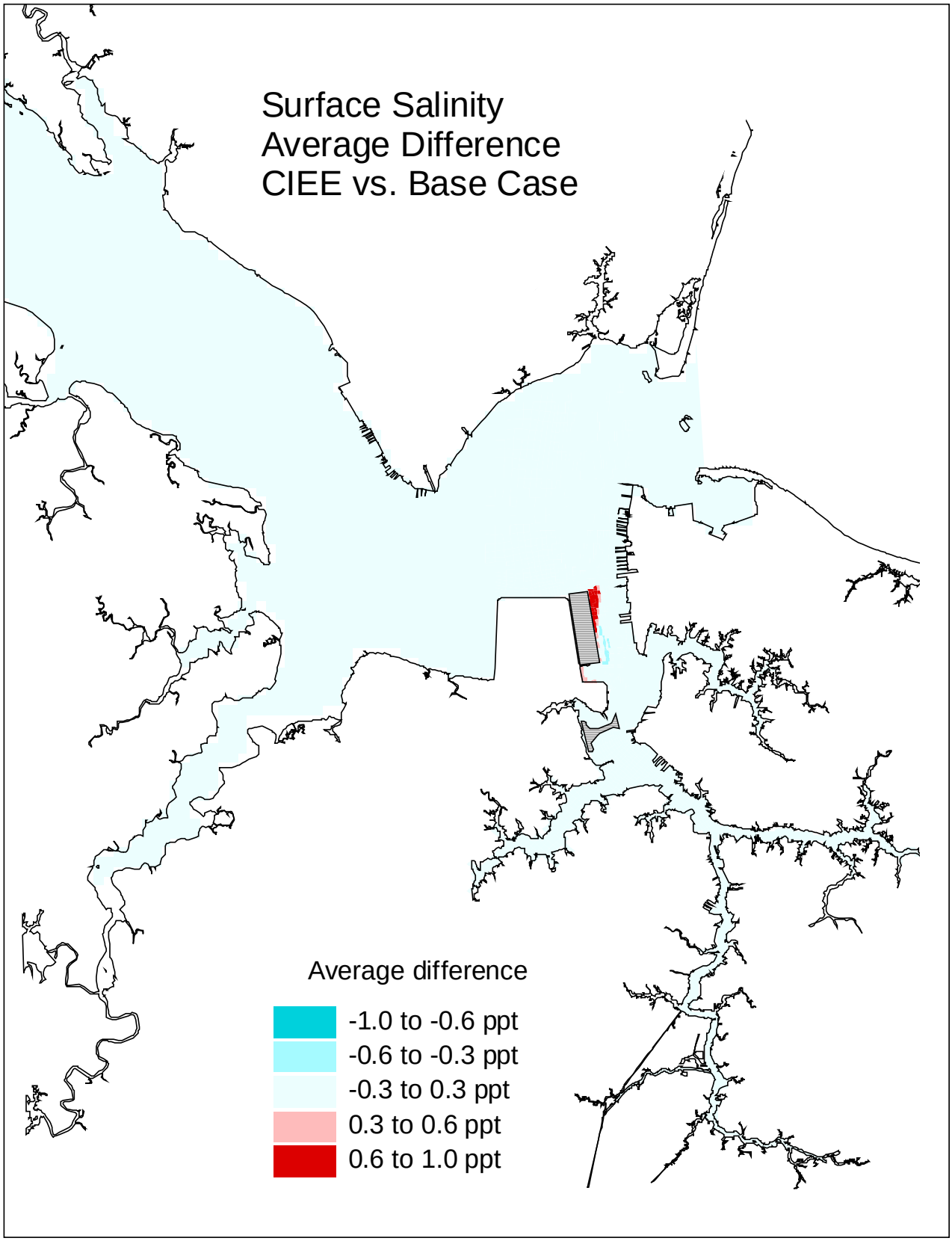

Figure C10. Single variable simulation comparison of the surface salinity average difference for the proposed Craney Island Eastward Expansion versus the Base Case.

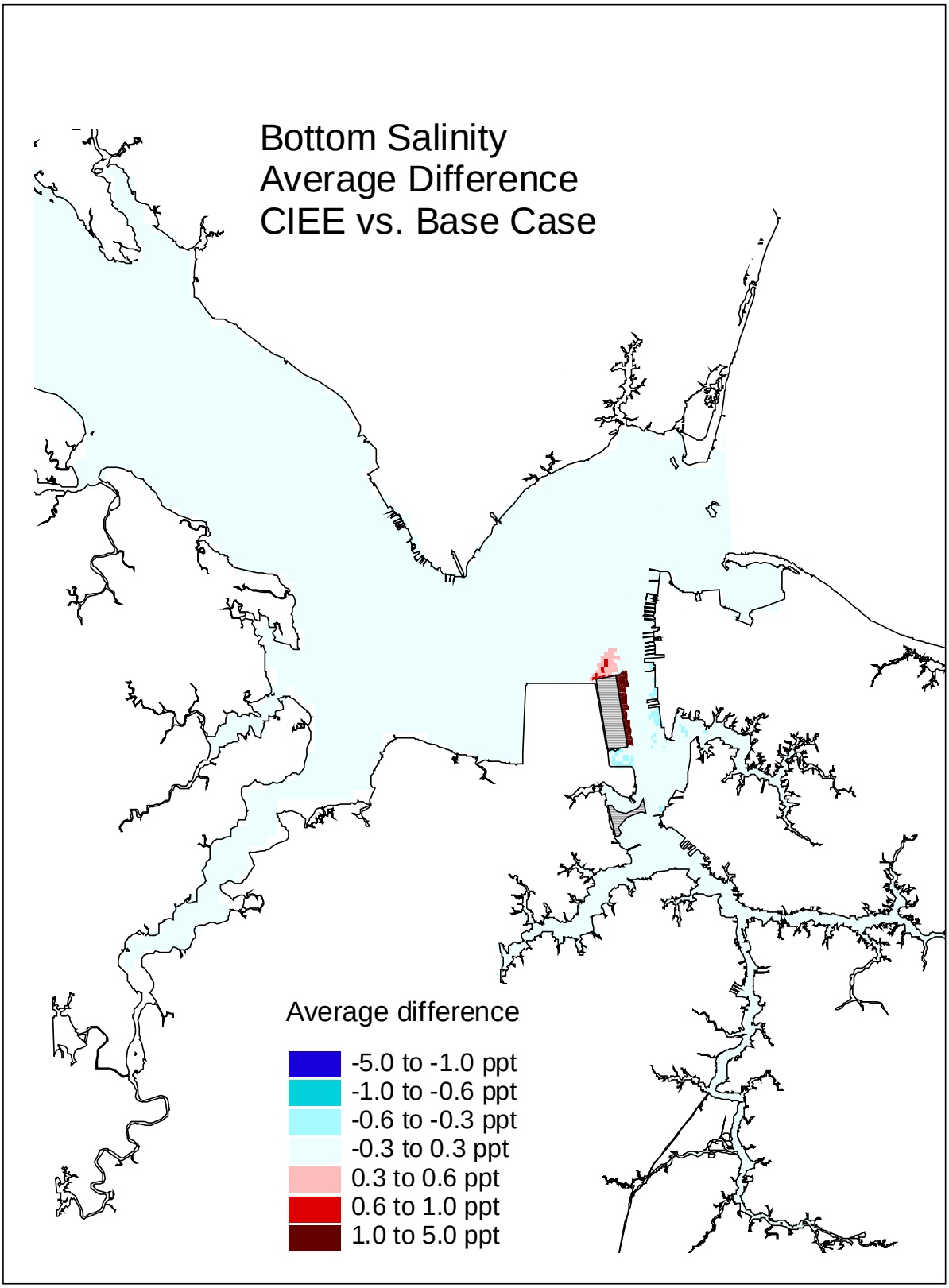

Figure C11. Single variable simulation comparison of the bottom salinity average difference for the proposed Craney Island Eastward Expansion versus the Base Case.

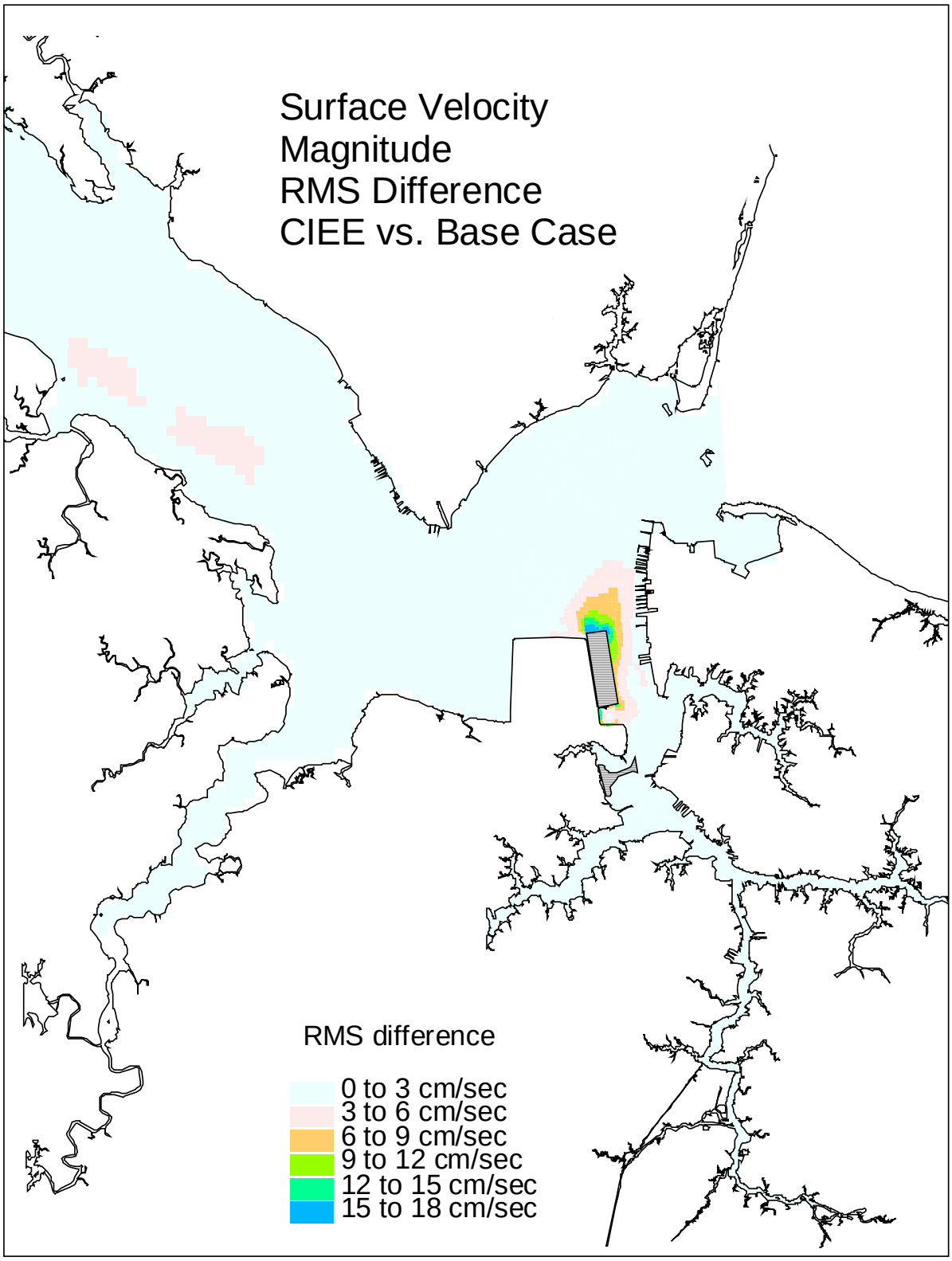

Figure C12. Single variable simulation comparison of the surface velocity RMS difference for the proposed Craney Island Eastward Expansion versus the Base Case.

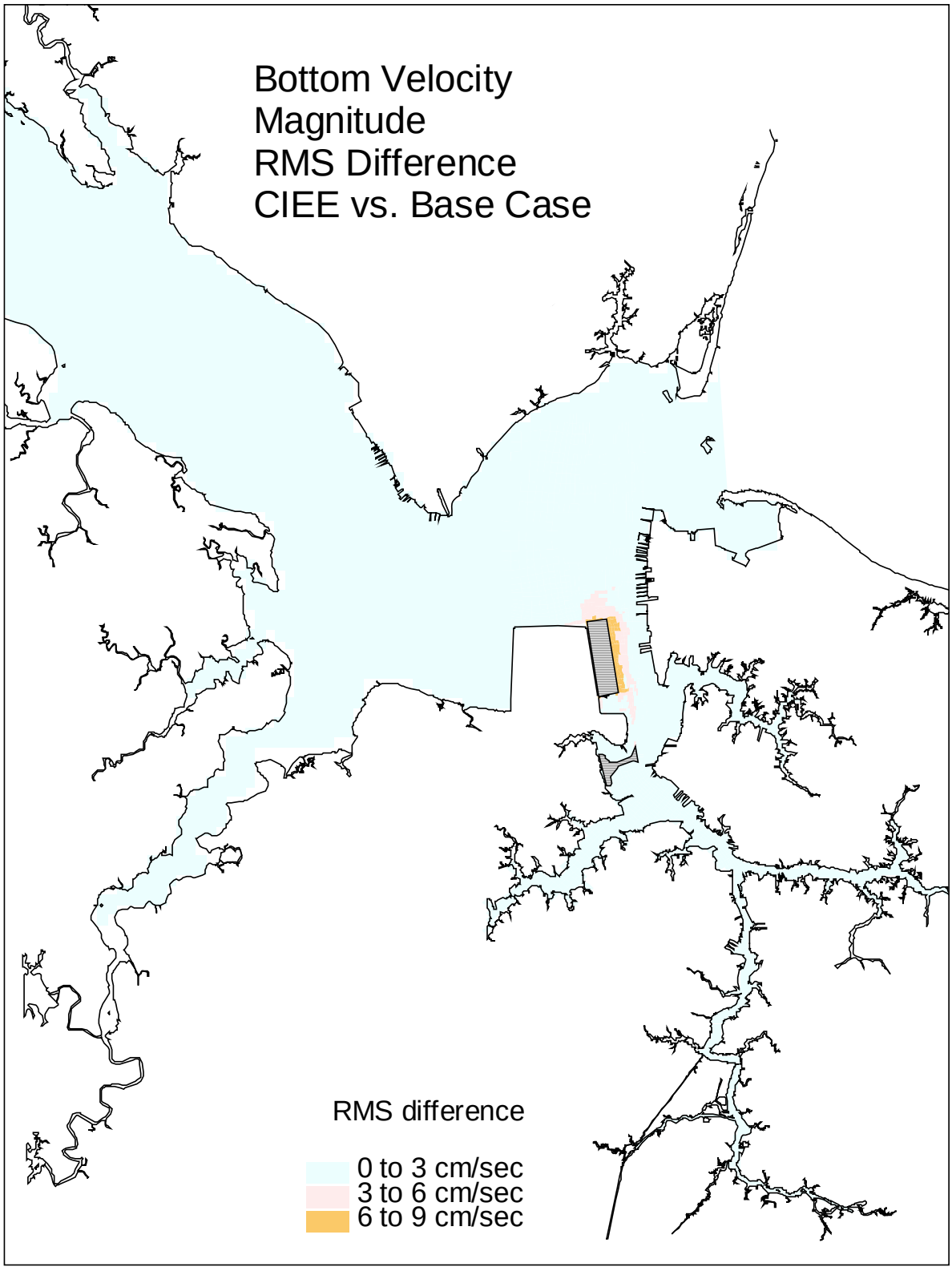

Figure C13. Single variable simulation comparison of the bottom velocity RMS difference for the proposed Craney Island Eastward Expansion versus the Base Case.

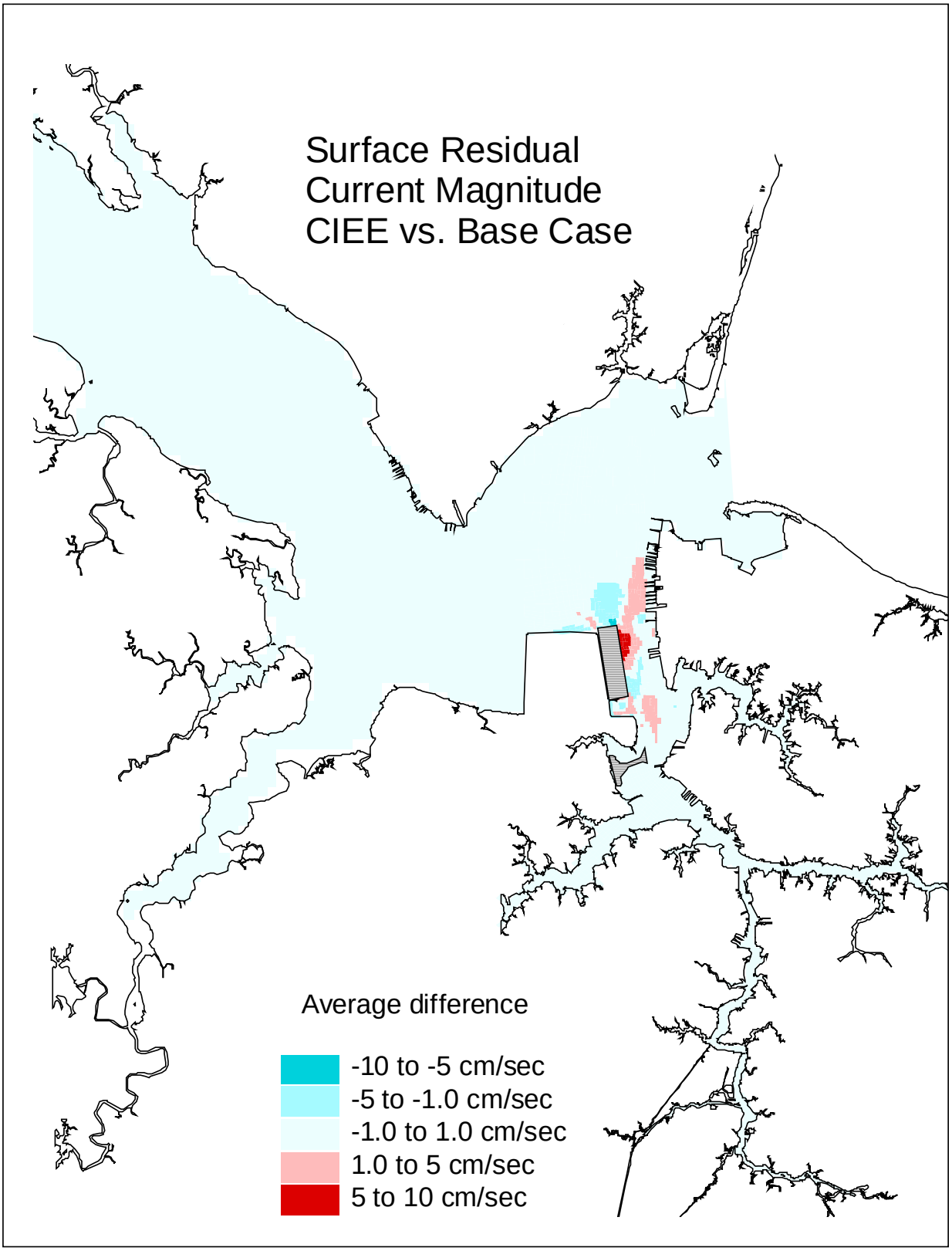

Figure C14. Single variable simulation comparison of the surface residual velocity average difference for the proposed Craney Island Eastward Expansion versus the Base Case.

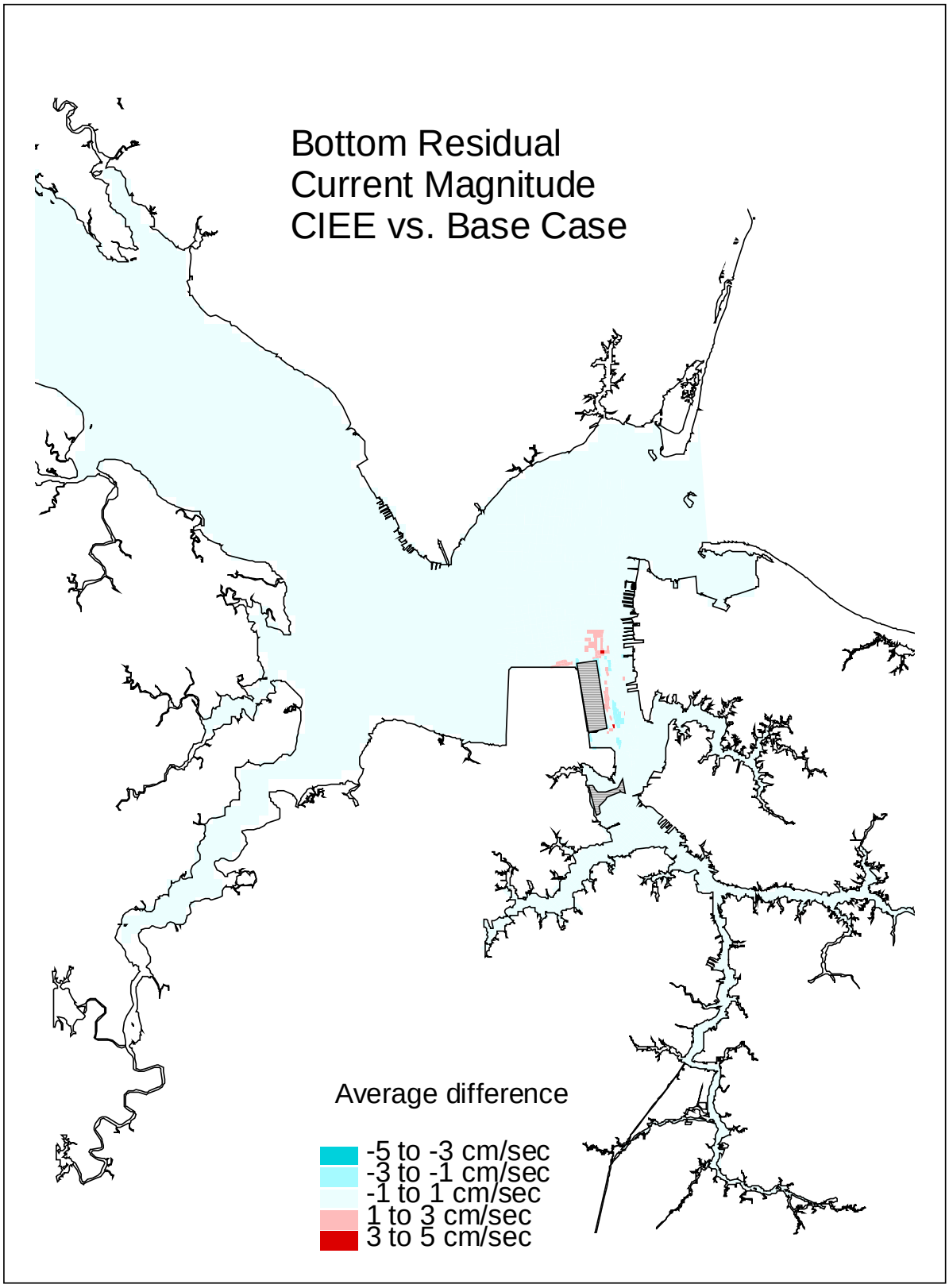

Figure C15. Single variable simulation comparison of the bottom residual velocity average difference for the proposed Craney Island Eastward Expansion versus the Base Case.

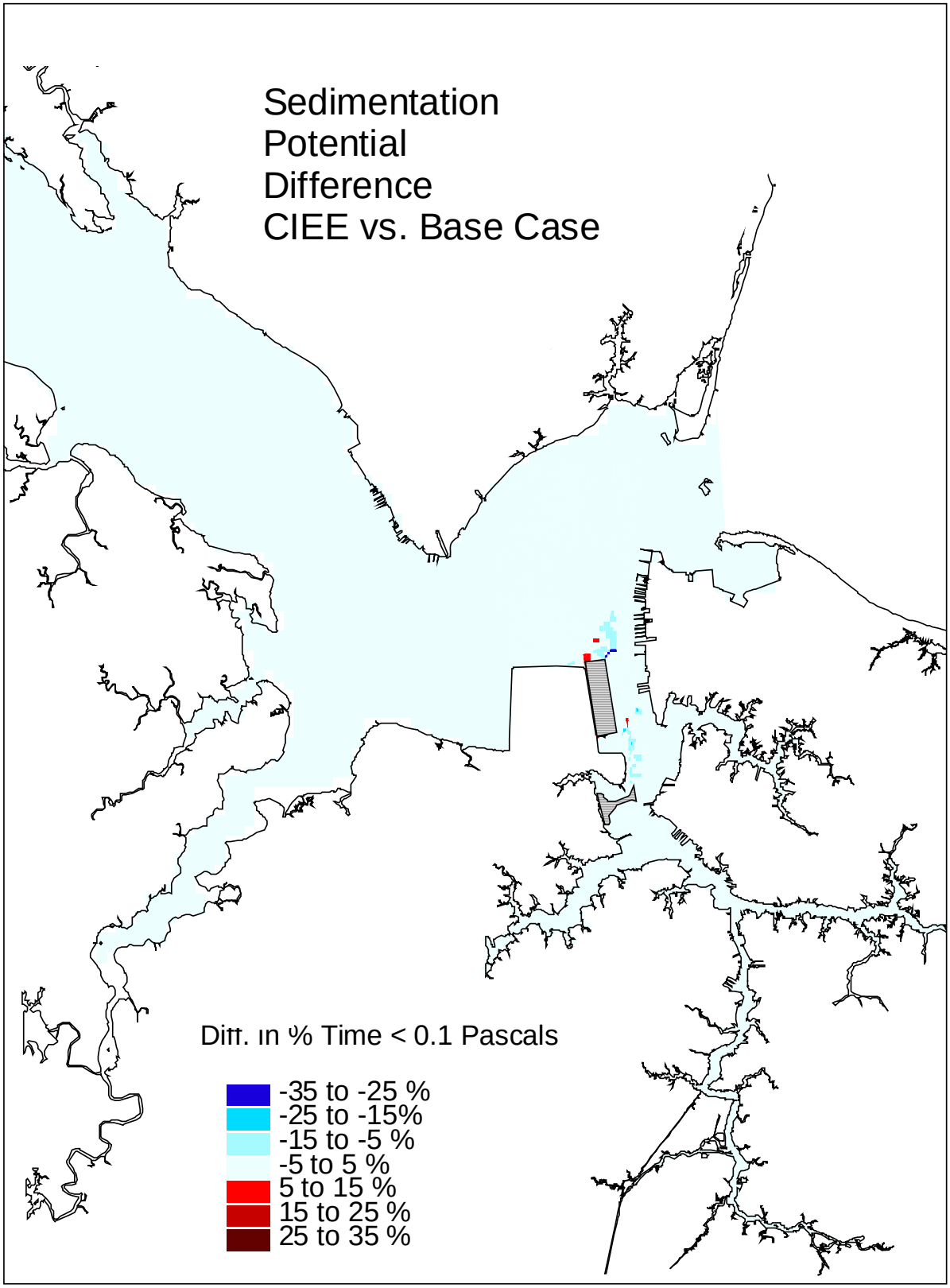

Figure C16. Single variable simulation comparison of the sedimentation potential difference for the proposed Craney Island Eastward Expansion versus the Base Case.

APPENDIX D

CIEE South Cell Expansion Scenario

Water Quality Model Results

at CBP Stations LE5.5, LE5.6, and ELI2 for 1999, 2000, and 2001

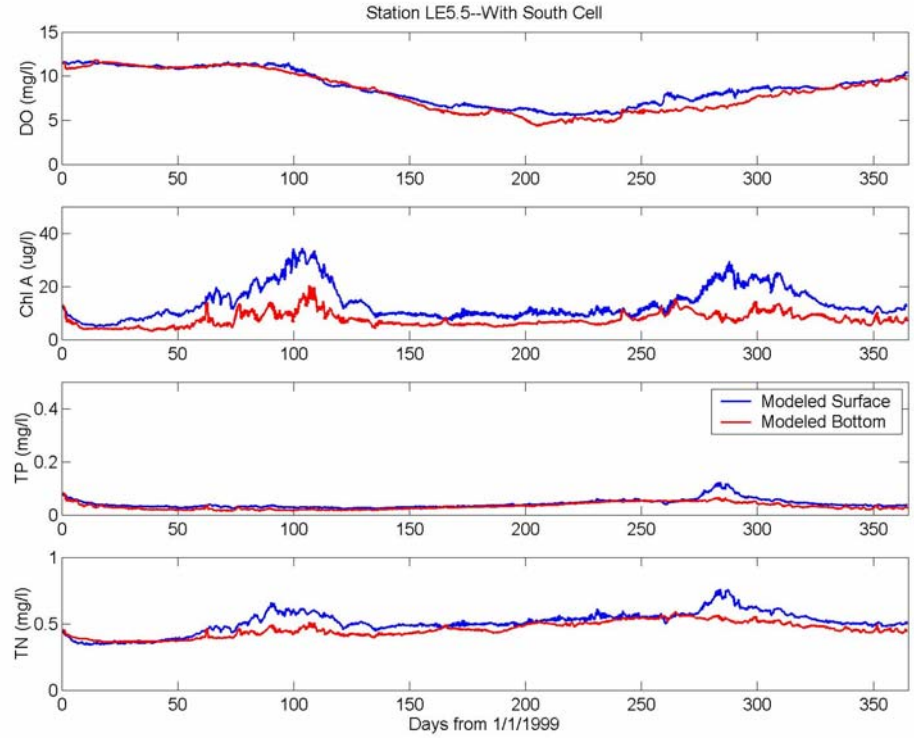

Figure D1. CIEE south cell expansion scenario model predictions for dissolved oxygen, chlorophyll-a, total phosphorus, and total nitrogen at CBP Station LE5.5 (surface and bottom layers) for 1999.

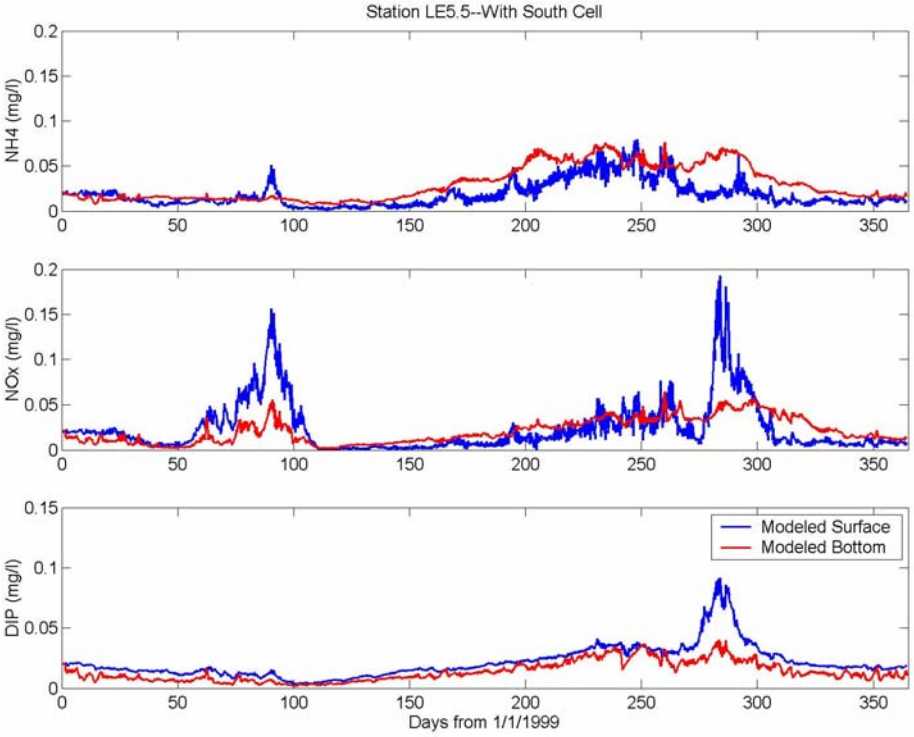

Figure D2. CIEE south cell expansion scenario model predictions for ammonium, nitrate-nitrite, and dissolved inorganic phosphorus at CBP Station LE5.5 (surface and bottom layers) for 1999.

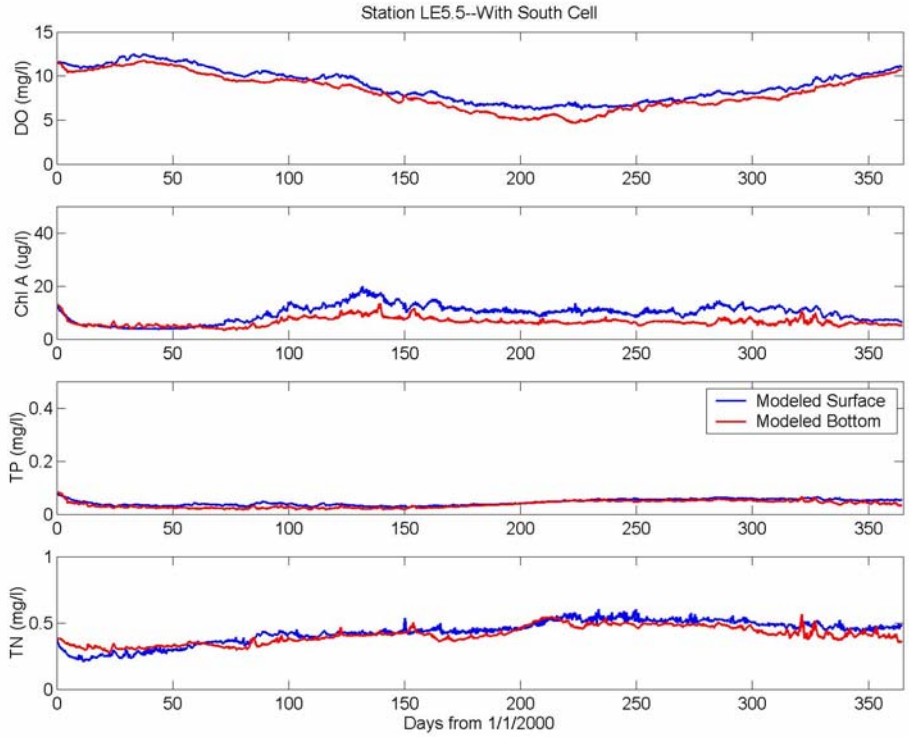

Figure D3. CIEE south cell expansion scenario model predictions for dissolved oxygen, chlorophyll-a, total phosphorus, and total nitrogen at CBP Station LE5.5 (surface and bottom layers) for 2000.

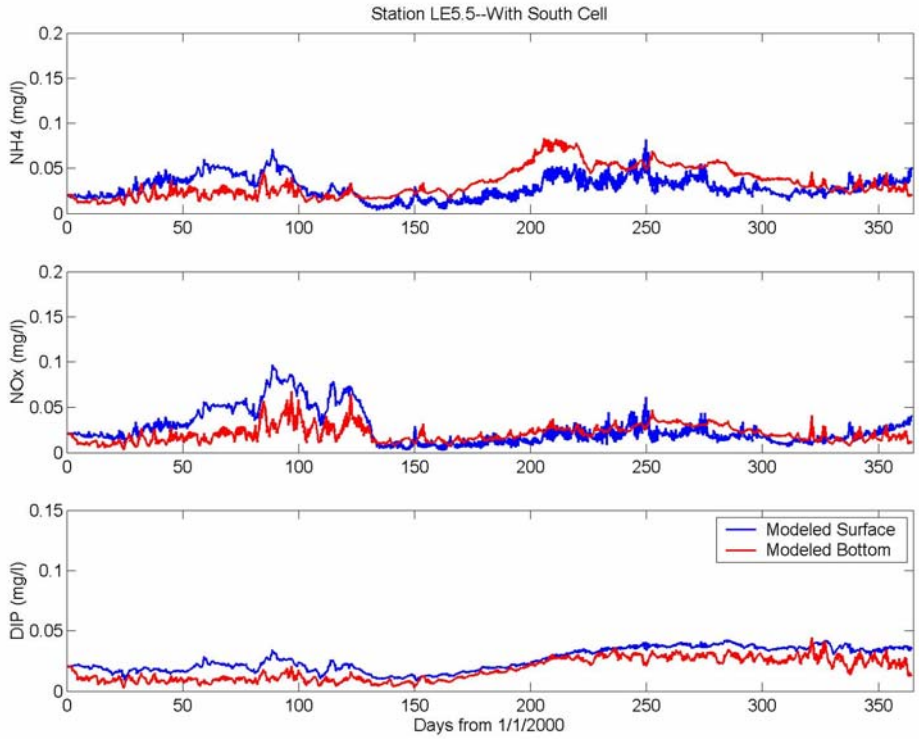

Figure D4. CIEE south cell expansion scenario model predictions for ammonium, nitrate-nitrite, and dissolved inorganic phosphorus at CBP Station LE5.5 (surface and bottom layers) for 2000.

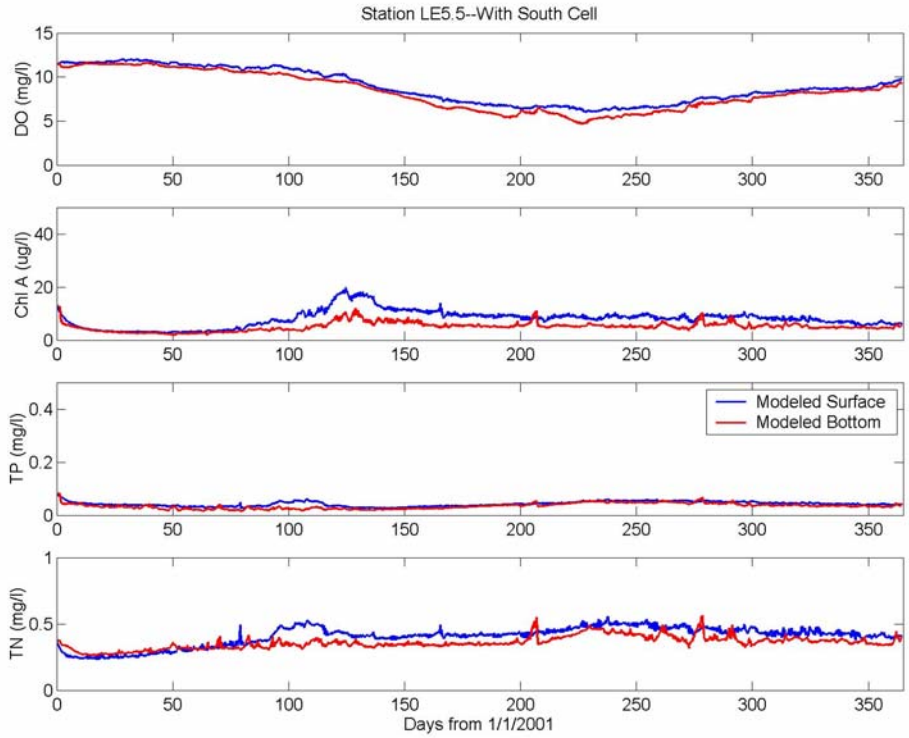

Figure D5. CIEE south cell expansion scenario model predictions for dissolved oxygen, chlorophyll-a, total phosphorus, and total nitrogen at CBP Station LE5.5 (surface and bottom layers) for 2001.

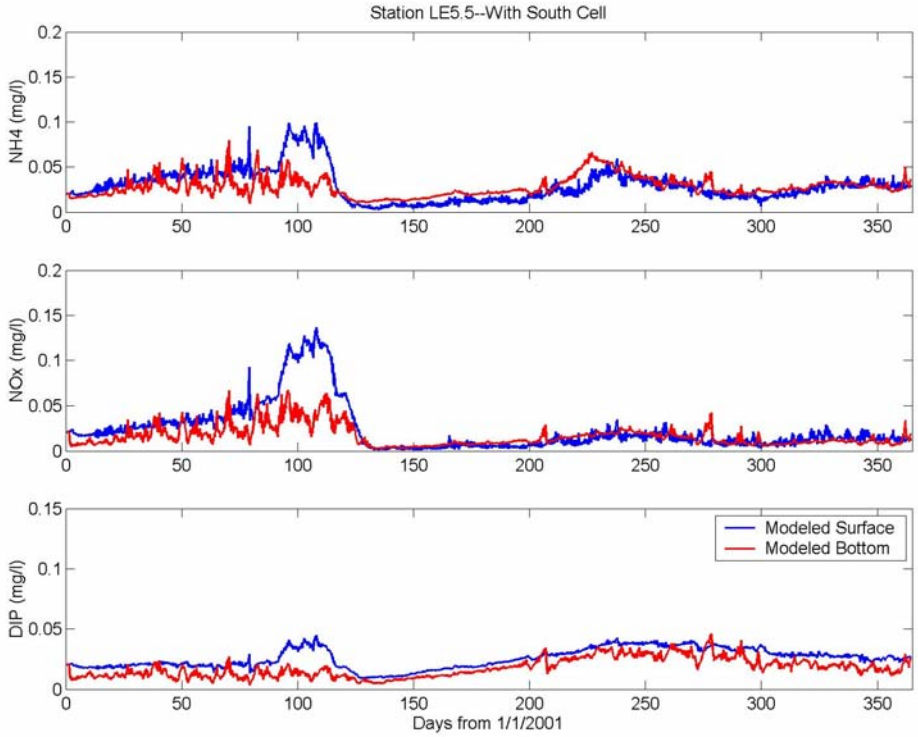

Figure D6. CIEE south cell expansion scenario model predictions for ammonium, nitrate-nitrite, and dissolved inorganic phosphorus at CBP Station LE5.5 (surface and bottom layers) for 2001.

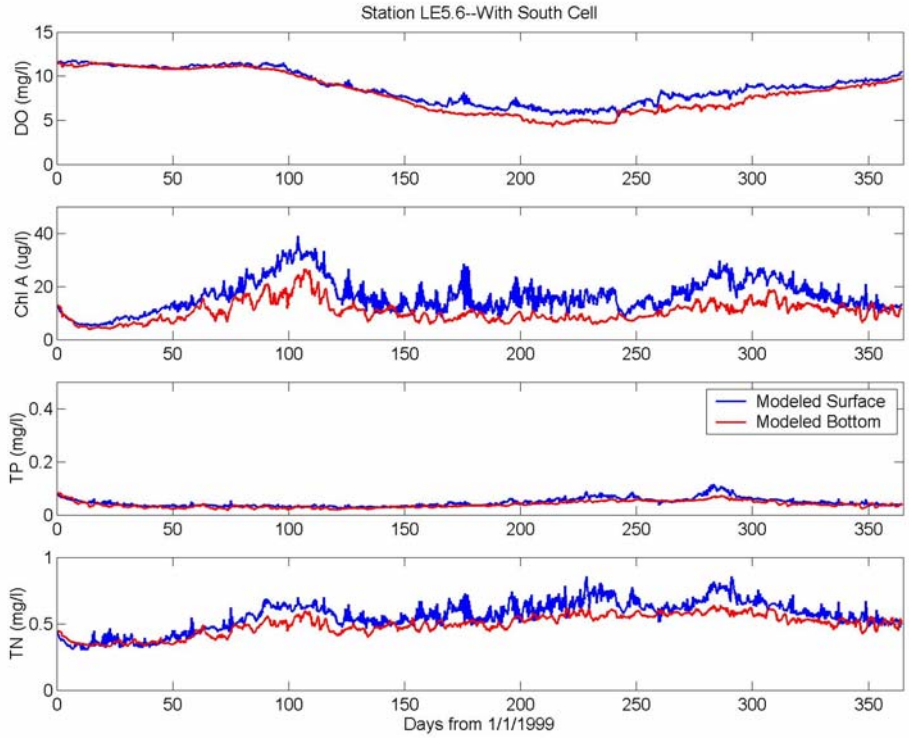

Figure D7. CIEE south cell expansion scenario model predictions for dissolved oxygen, chlorophyll-a, total phosphorus, and total nitrogen at CBP Station LE5.6 (surface and bottom layers) for 1999.

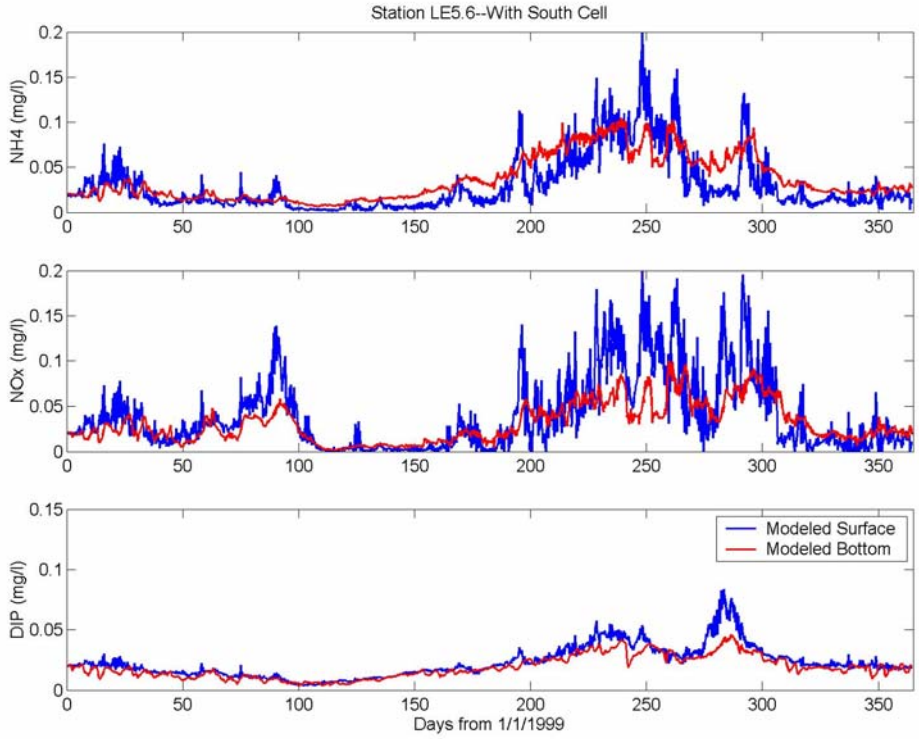

Figure D8. CIEE south cell expansion scenario model predictions for ammonium, nitrate-nitrite, and dissolved inorganic phosphorus at CBP Station LE5.6 (surface and bottom layers) for 1999.

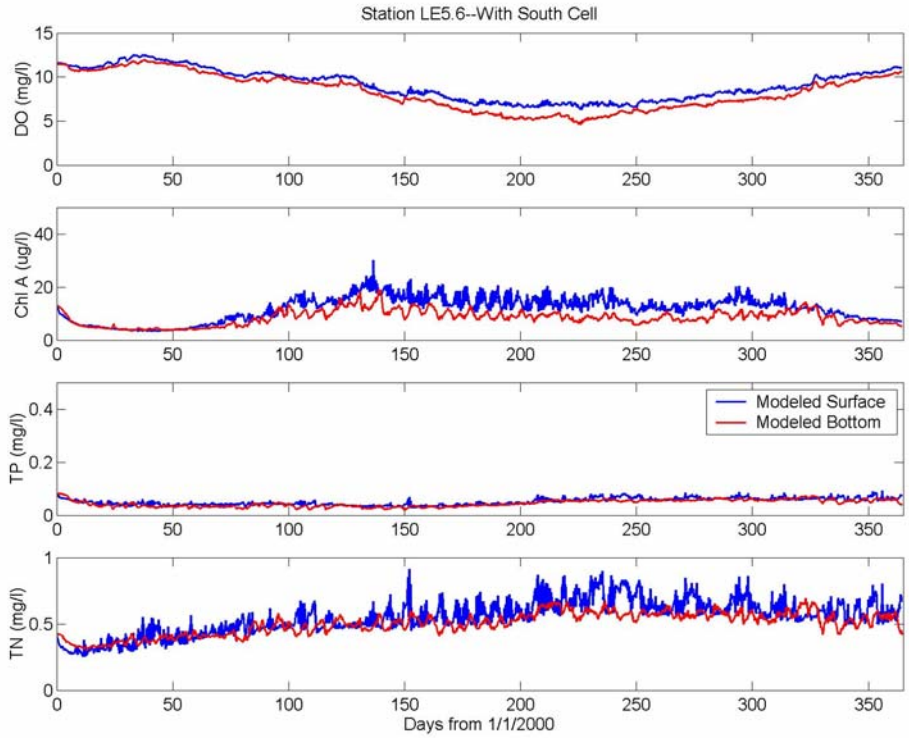

Figure D9. CIEE south cell expansion scenario model predictions for dissolved oxygen, chlorophyll-a, total phosphorus, and total nitrogen at CBP Station LE5.6 (surface and bottom layers) for 2000.

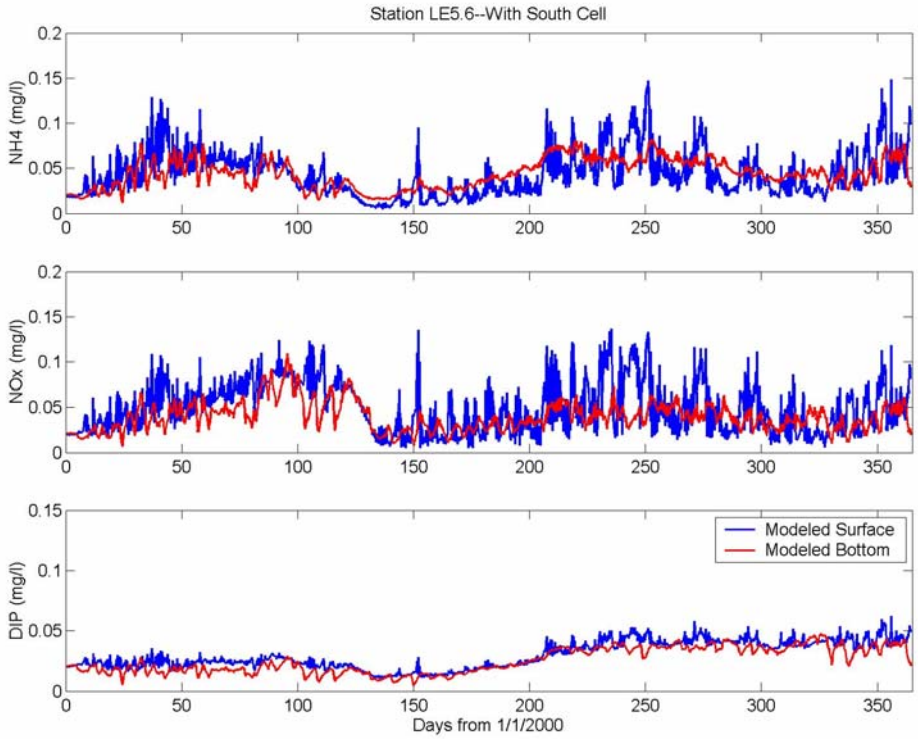

Figure D10. CIEE south cell expansion scenario model predictions for ammonium, nitrate-nitrite, and dissolved inorganic phosphorus at CBP Station LE5.6 (surface and bottom layers) for 2000.

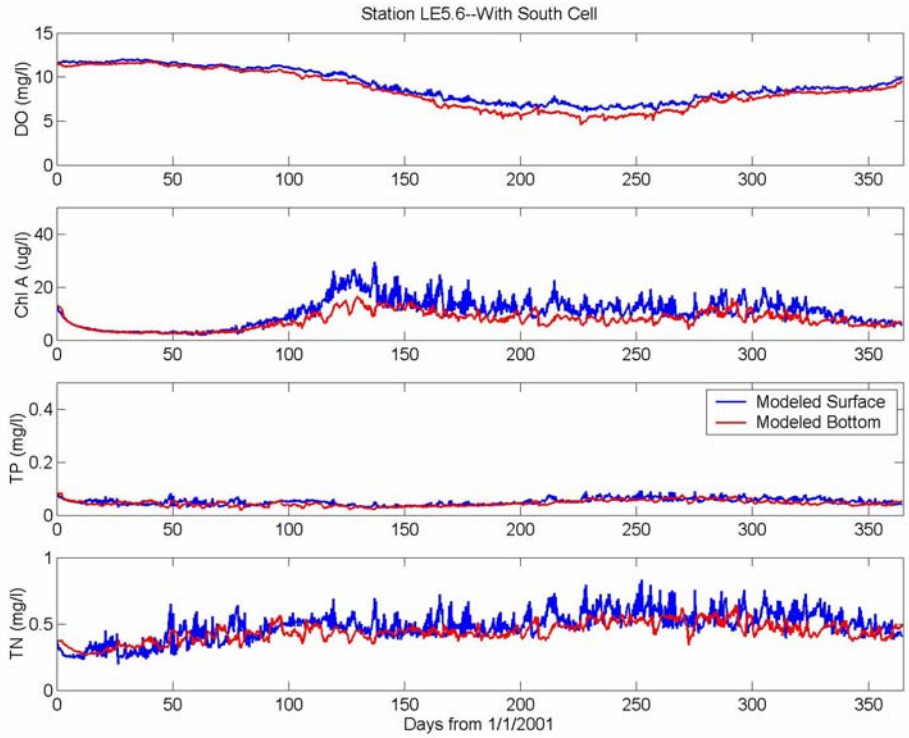

Figure D11. CIEE south cell expansion scenario model predictions for dissolved oxygen, chlorophyll-a, total phosphorus, and total nitrogen at CBP Station LE5.6 (surface and bottom layers) for 2001.

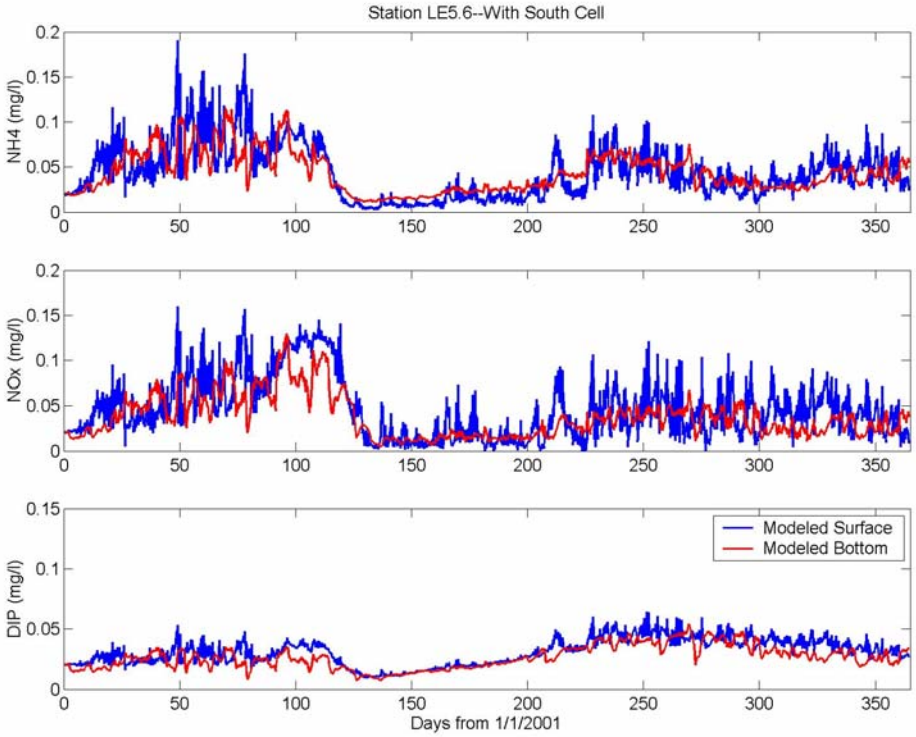

Figure D12. CIEE south cell expansion scenario model predictions for ammonium, nitrate-nitrite, and dissolved inorganic phosphorus at CBP Station LE5.6 (surface and bottom layers) for 2001.

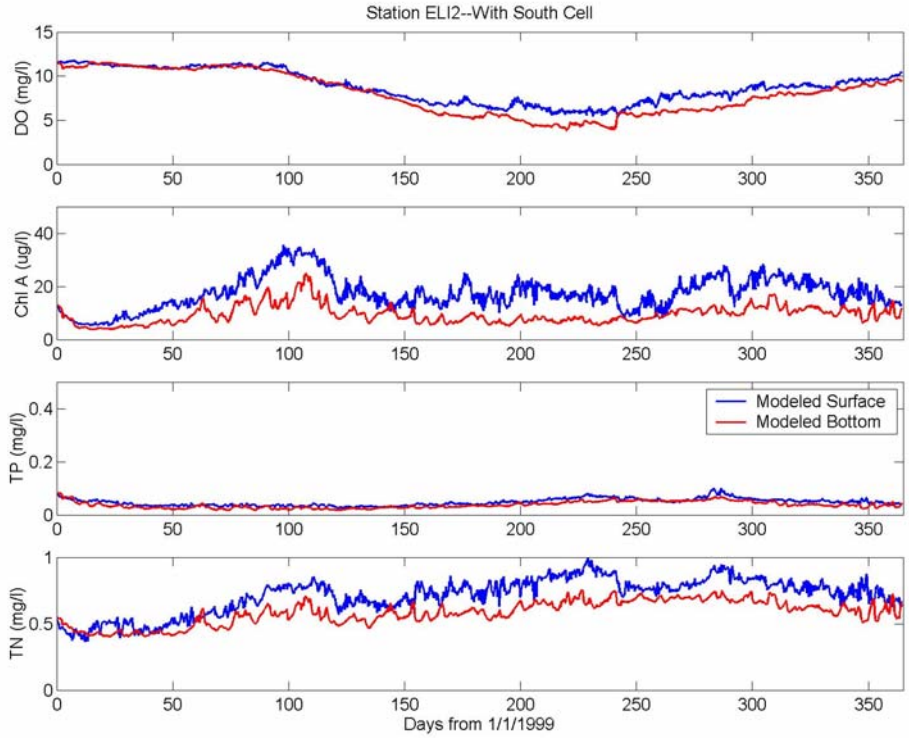

Figure D13. CIEE south cell expansion scenario model predictions for dissolved oxygen, chlorophyll-a, total phosphorus, and total nitrogen at CBP Station ELI2 (surface and bottom layers) for 1999.

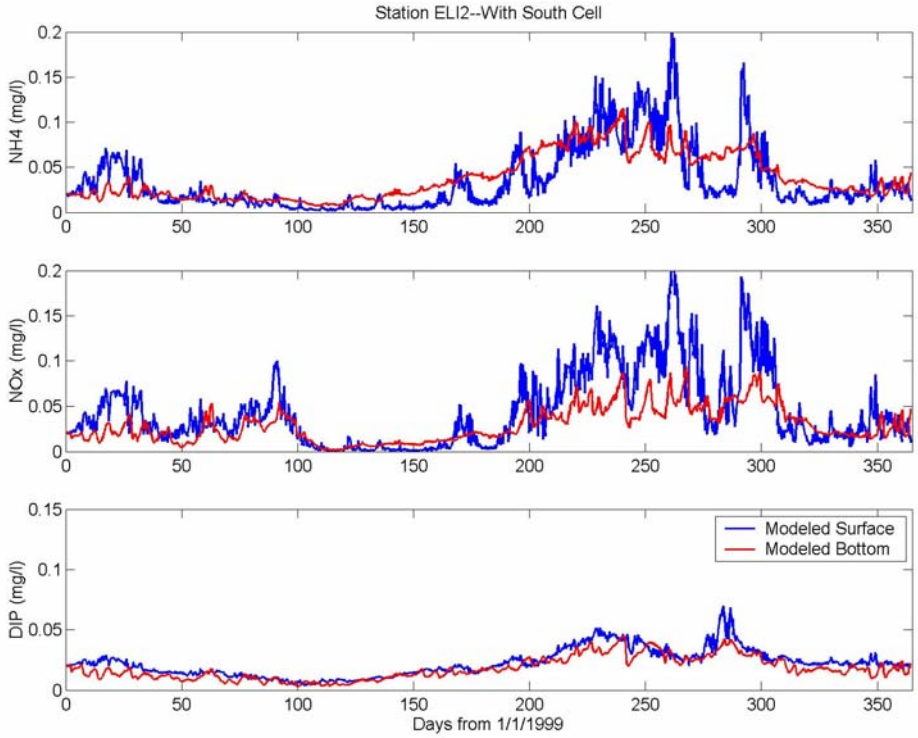

Figure D14. CIEE south cell expansion scenario model predictions for ammonium, nitrate-nitrite, and dissolved inorganic phosphorus at CBP Station ELI2 (surface and bottom layers) for 1999.

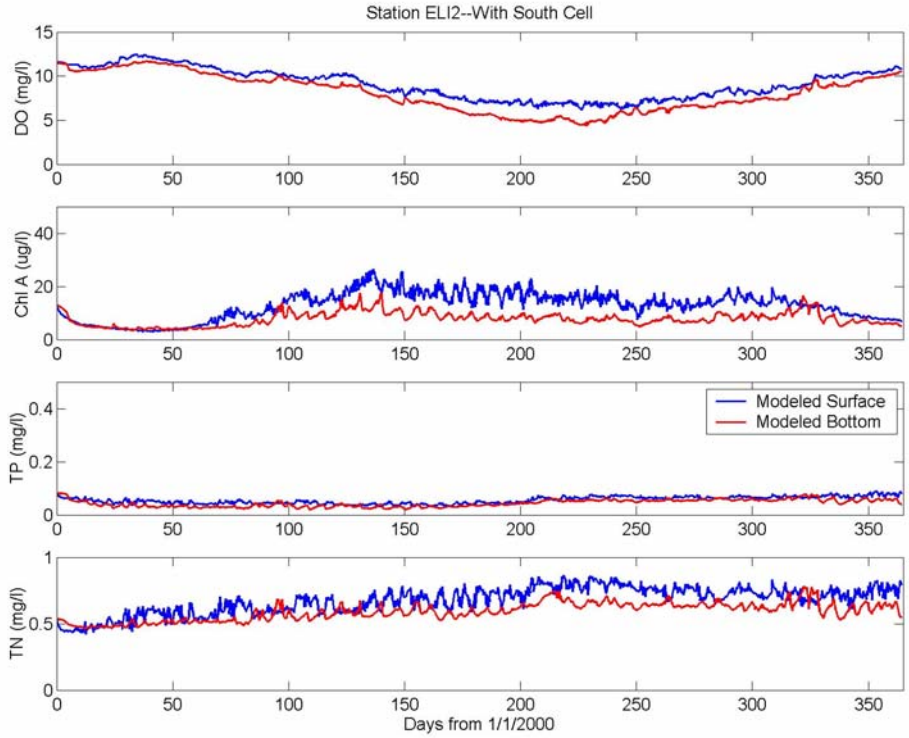

Figure D15. CIEE south cell expansion scenario model predictions for dissolved oxygen, chlorophyll-a, total phosphorus, and total nitrogen at CBP Station ELI2 (surface and bottom layers) for 2000.

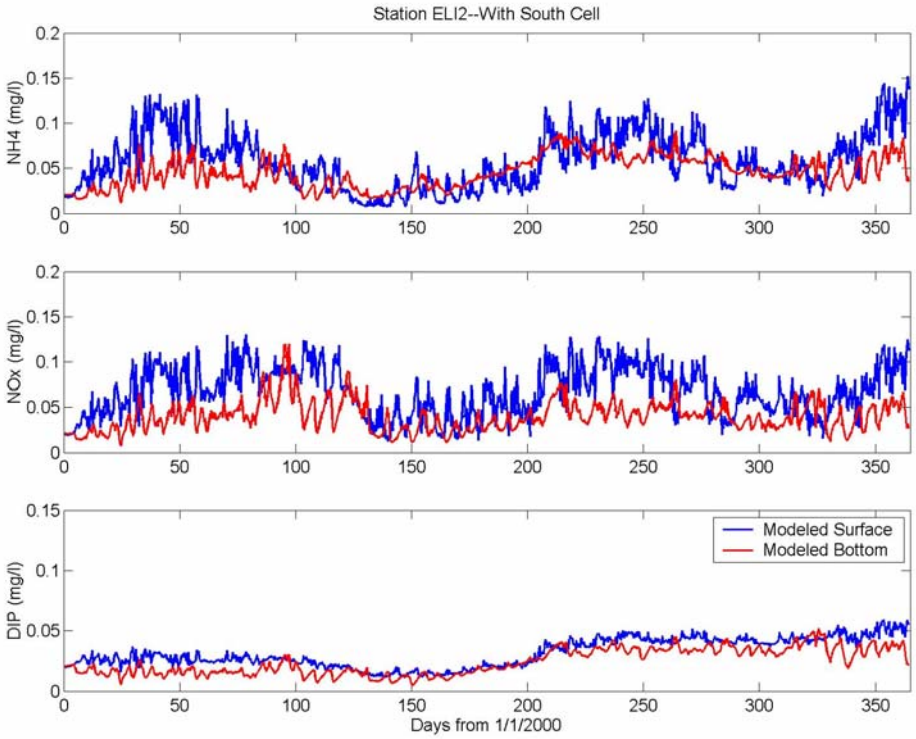

Figure D16. CIEE south cell expansion scenario model predictions for ammonium, nitrate-nitrite, and dissolved inorganic phosphorus at CBP Station ELI2 (surface and bottom layers) for 2000.

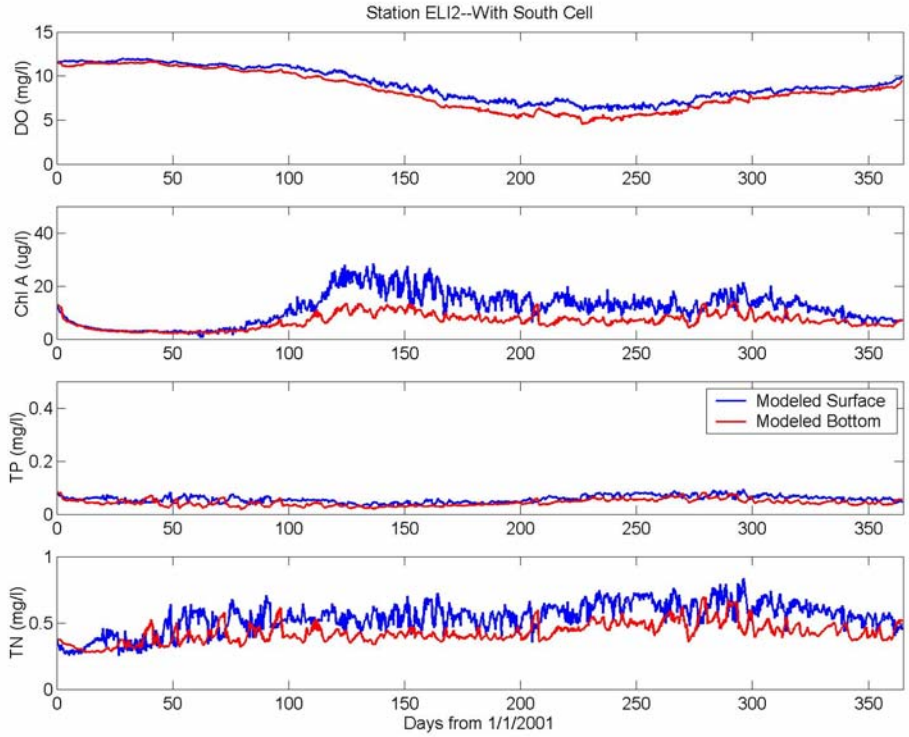

Figure D17. CIEE south cell expansion scenario model predictions for dissolved oxygen, chlorophyll-a, total phosphorus, and total nitrogen at CBP Station ELI2 (surface and bottom layers) for 2001.

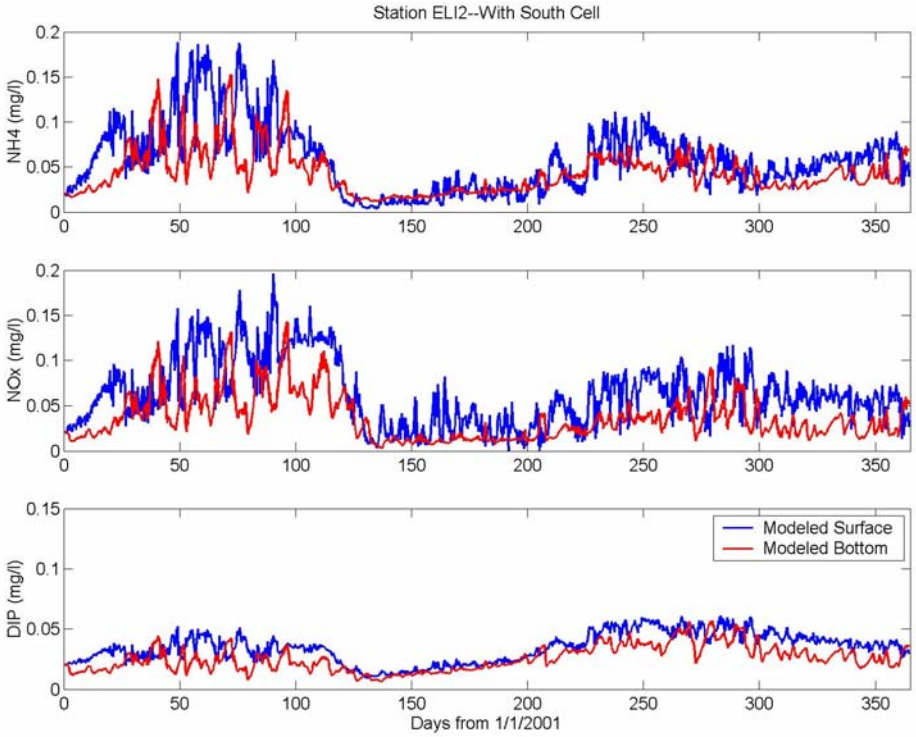

Figure D18. CIEE south cell expansion scenario model predictions for ammonium, nitrate-nitrite, and dissolved inorganic phosphorus at CBP Station ELI2 (surface and bottom layers) for 2001.

APPENDIX E

CIEE South Cell Expansion Scenario

Water Quality Model Analysis

Differences from Base Case (scenario minus base case)

CBP Stations LE5.5, LE5.6, and ELI2 for 1999, 2000, and 2001

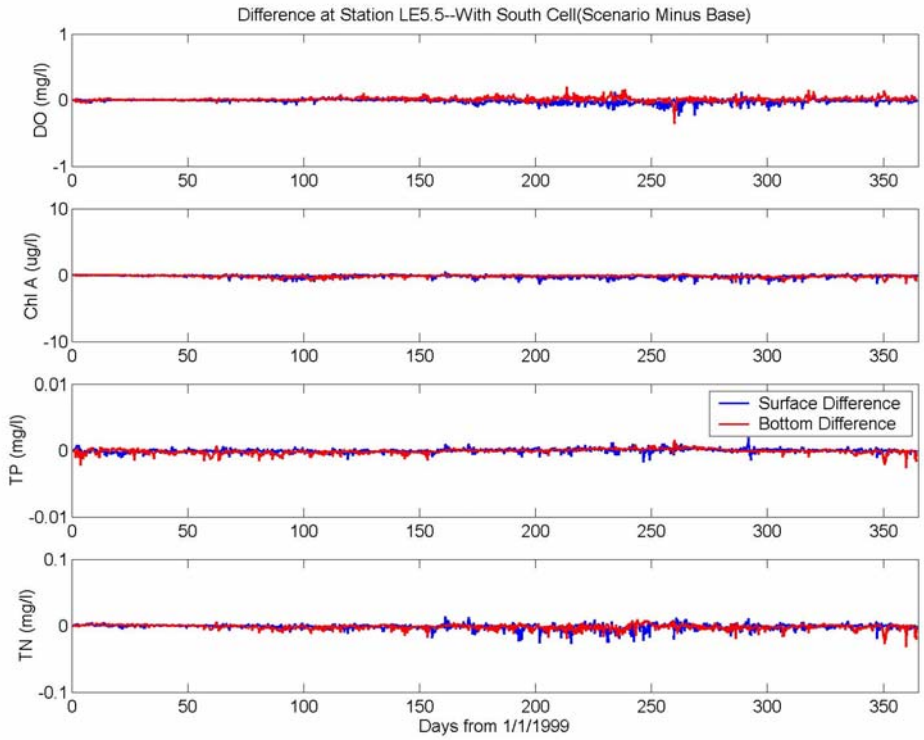

Figure E1. CIEE south cell expansion scenario minus base case differences of dissolved oxygen, chlorophyll-a, total phosphorus, and total nitrogen at CBP Station LE5.5 (surface and bottom layers) for 1999.

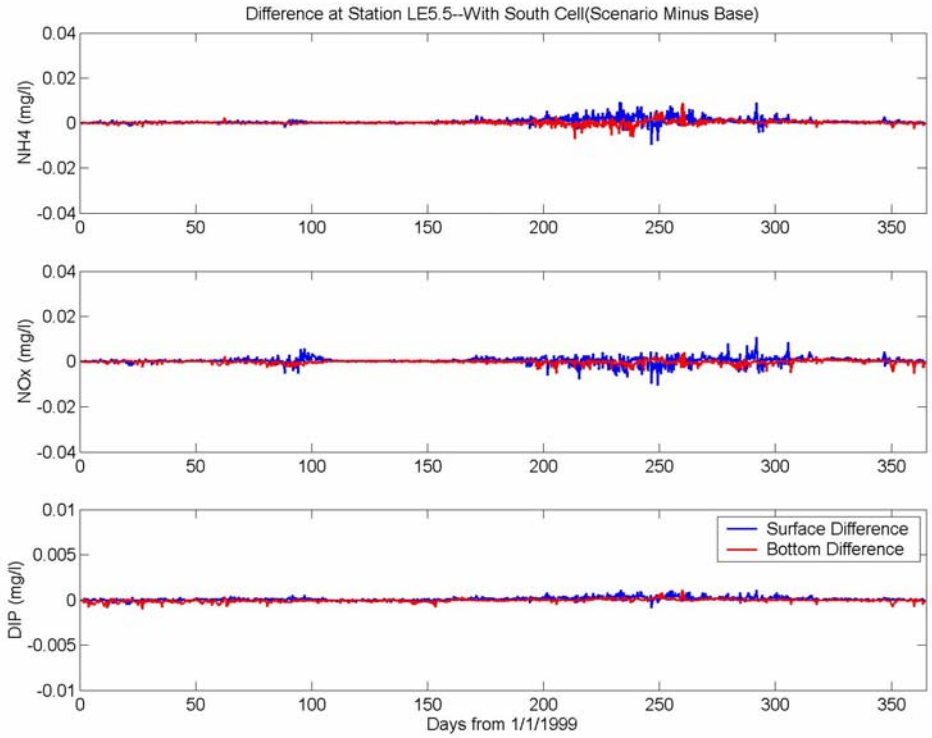

Figure E2. CIEE south cell expansion scenario minus base case differences of ammonium, nitrate-nitrite, and dissolved inorganic phosphorus at CBP Station LE5.5 (surface and bottom layers) for 1999.

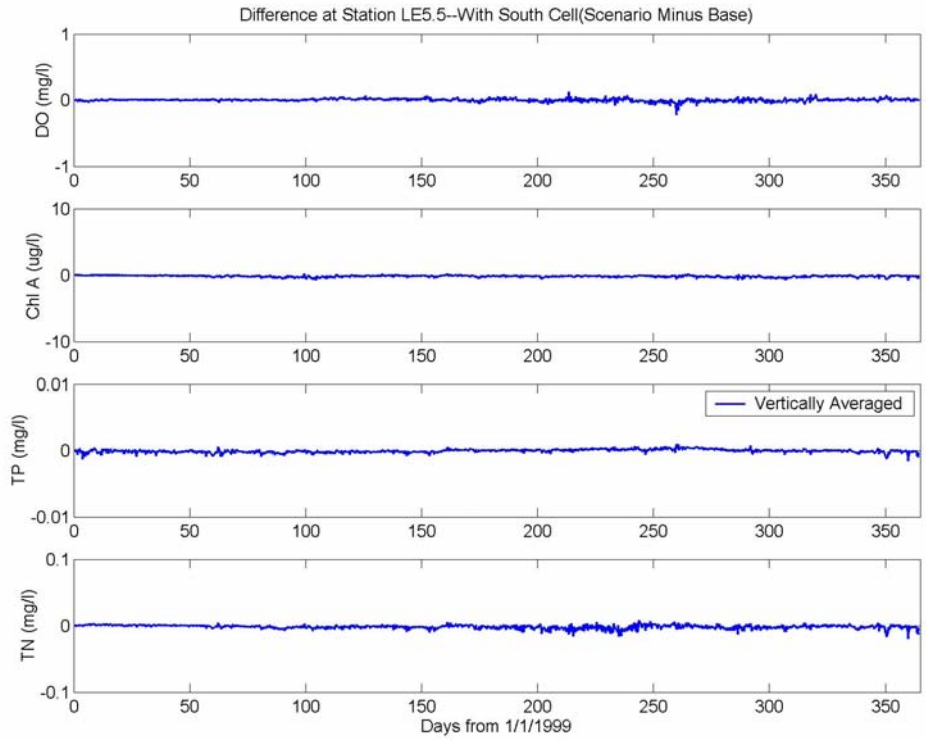

Figure E3. CIEE south cell expansion scenario minus base case differences of dissolved oxygen, chlorophyll-a, total phosphorus, and total nitrogen at CBP Station LE5.5 (vertically averaged) for 1999.

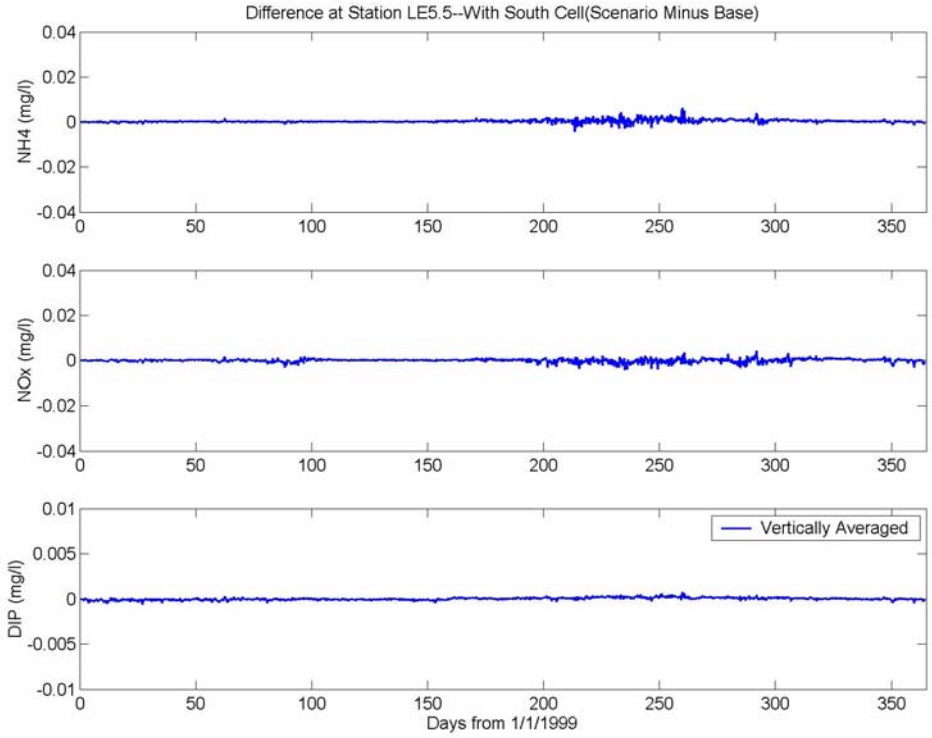

Figure E4. CIEE south cell expansion scenario minus base case differences of ammonium, nitrate-nitrite, and dissolved inorganic phosphorus at CBP Station LE5.5 (vertically averaged) for 1999.

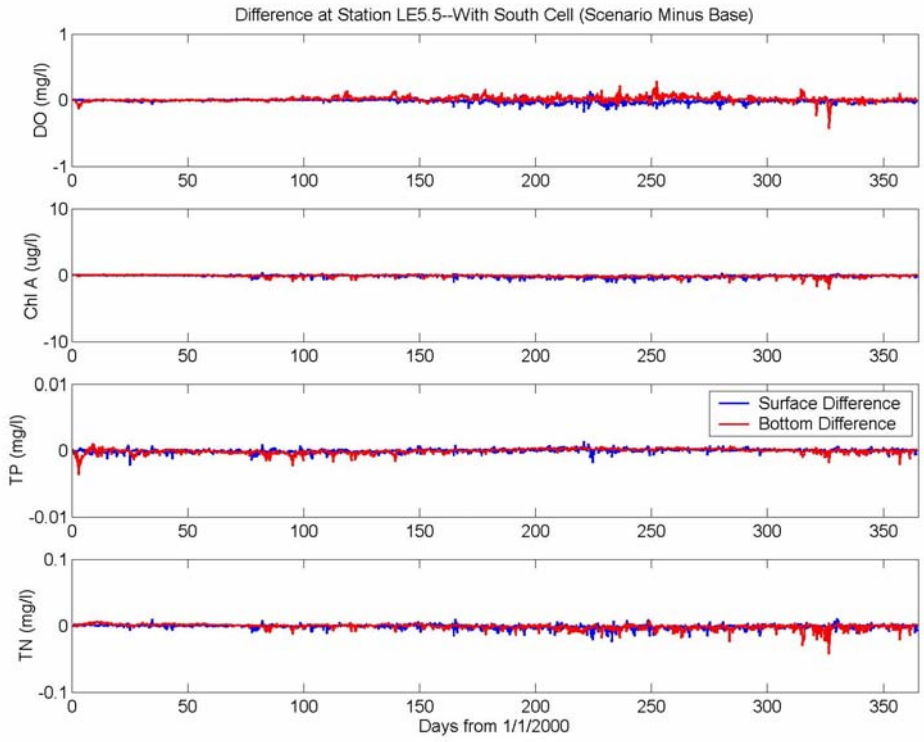

Figure E5. CIEE south cell expansion scenario minus base case differences of dissolved oxygen, chlorophyll-a, total phosphorus, and total nitrogen at CBP Station LE5.5 (surface and bottom layers) for 2000.

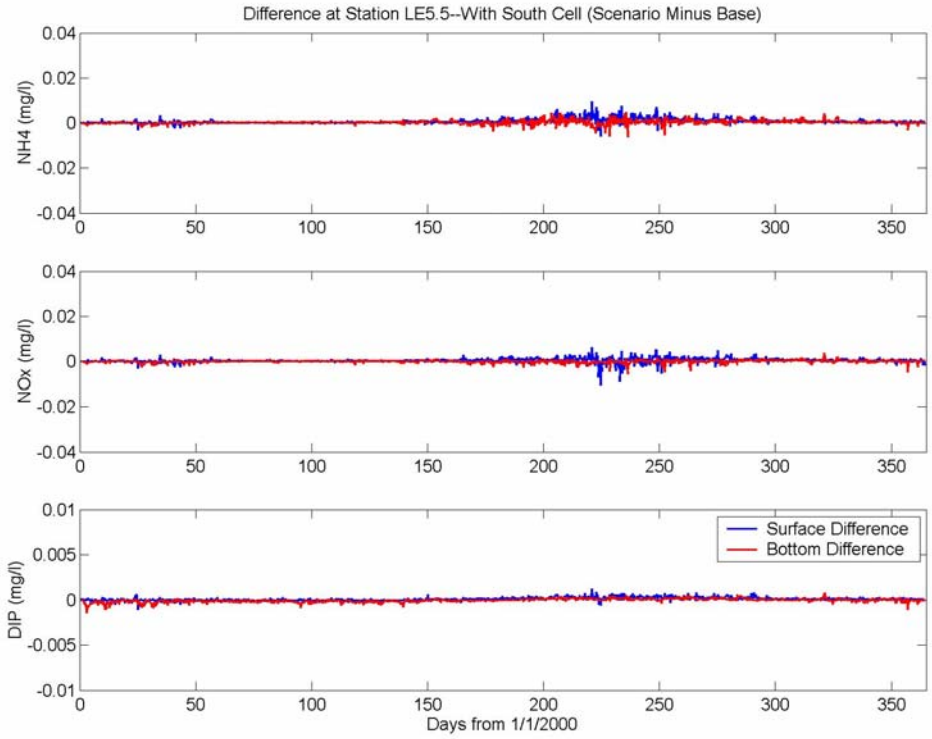

Figure E6. CIEE south cell expansion scenario minus base case differences of ammonium, nitrate-nitrite, and dissolved inorganic phosphorus at CBP Station LE5.5 (surface and bottom layers) for 2000.

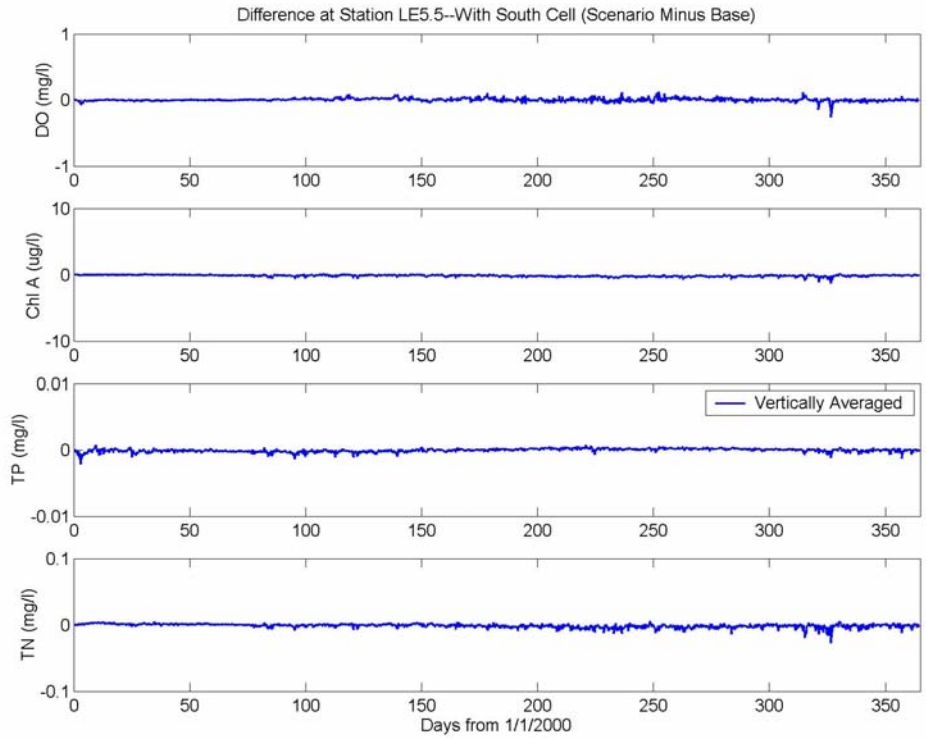

Figure E7. CIEE south cell expansion scenario minus base case differences of dissolved oxygen, chlorophyll-a, total phosphorus, and total nitrogen at CBP Station LE5.5 (vertically averaged) for 2000.

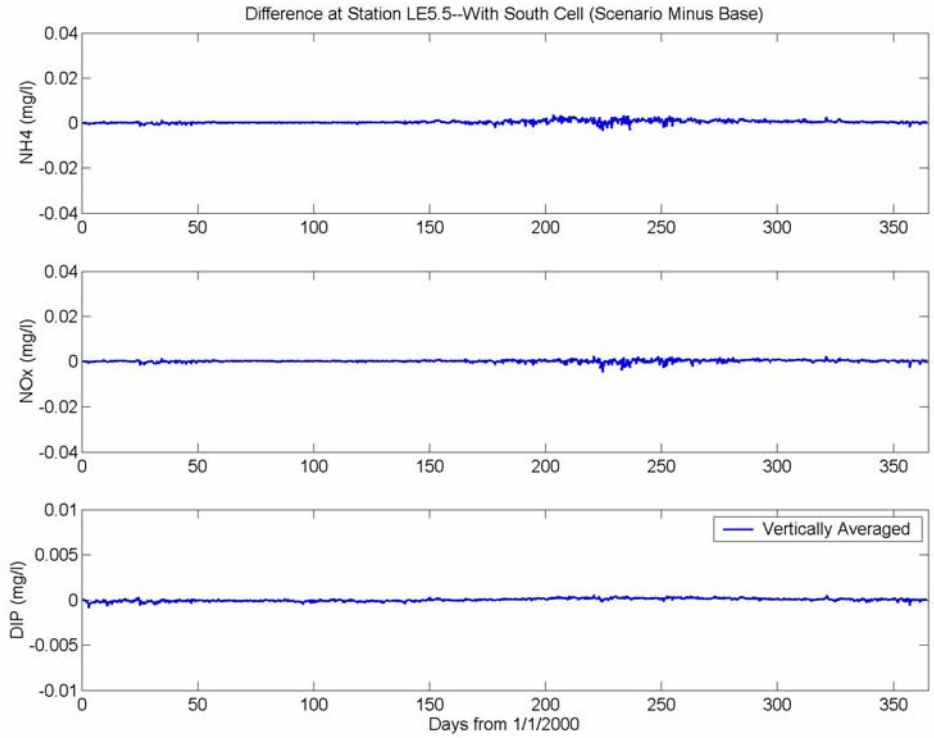

Figure E8. CIEE south cell expansion scenario minus base case differences of ammonium, nitrate-nitrite, and dissolved inorganic phosphorus at CBP Station LE5.5 (vertically averaged) for 2000.

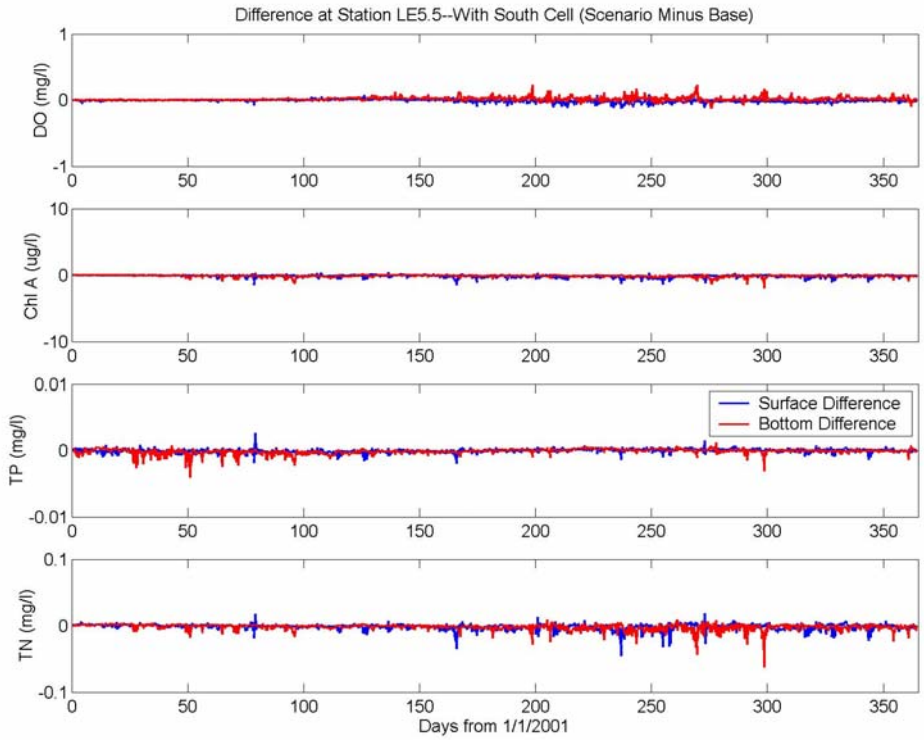

Figure E9. CIEE south cell expansion scenario minus base case differences of dissolved oxygen, chlorophyll-a, total phosphorus, and total nitrogen at CBP Station LE5.5 (surface and bottom layers) for 2001.

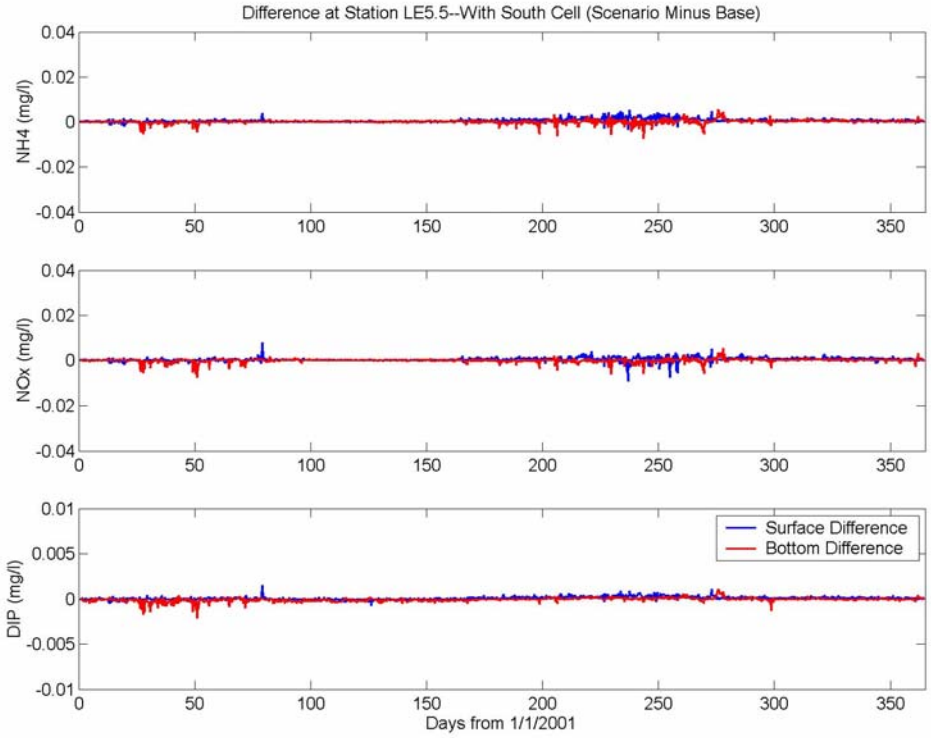

Figure E10. CIEE south cell expansion scenario minus base case differences of ammonium, nitrate-nitrite, and dissolved inorganic phosphorus at CBP Station LE5.5 (surface and bottom layers) for 2001.

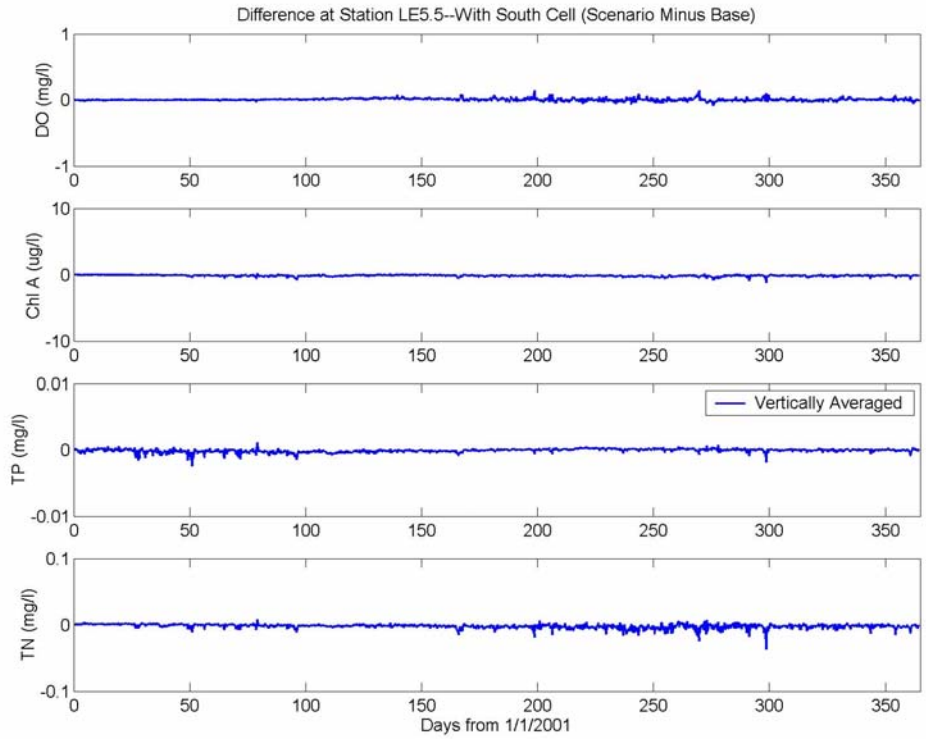

Figure E11. CIEE south cell expansion scenario minus base case differences of dissolved oxygen, chlorophyll-a, total phosphorus, and total nitrogen at CBP Station LE5.5 (vertically averaged) for 2001.

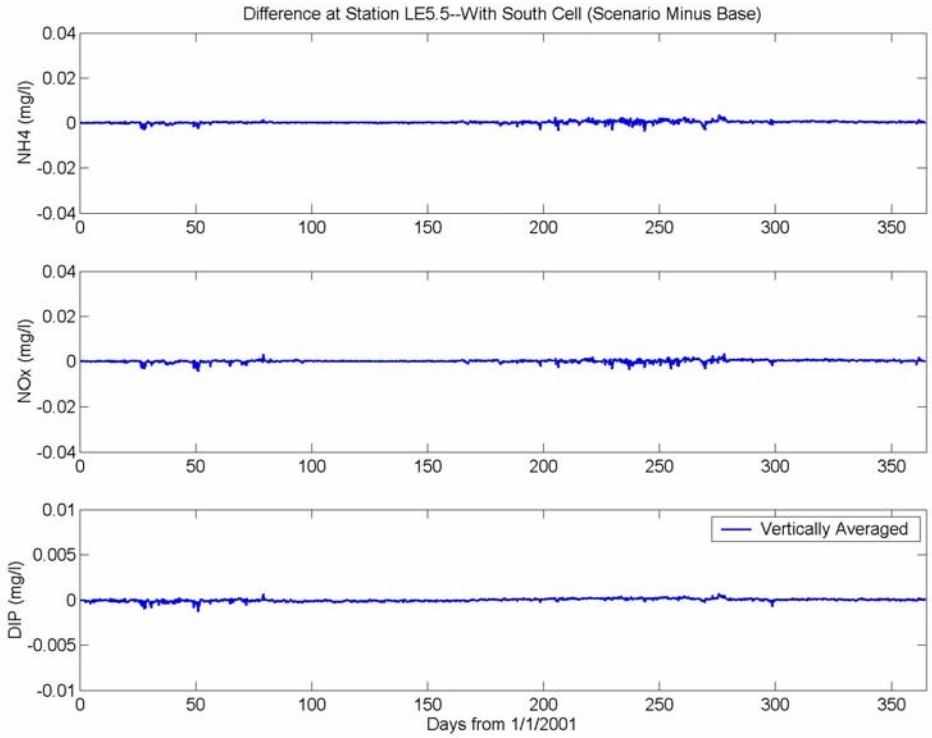

Figure E12. CIEE south cell expansion scenario minus base case differences of ammonium, nitrate-nitrite, and dissolved inorganic phosphorus at CBP Station LE5.5 (vertically averaged) for 2001.

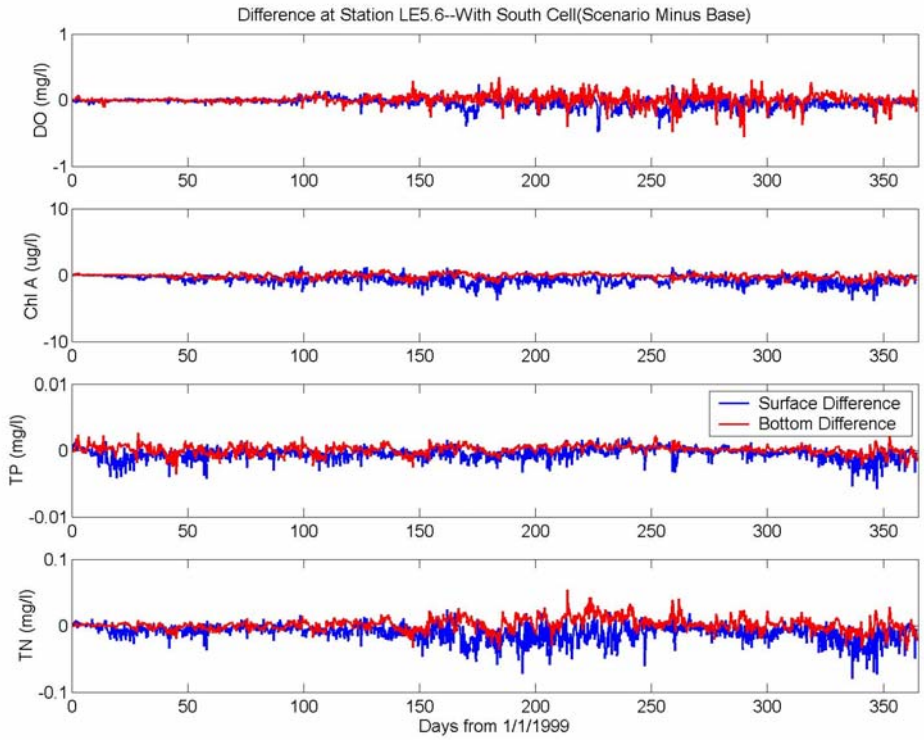

Figure E13. CIEE south cell expansion scenario minus base case differences of dissolved oxygen, chlorophyll-a, total phosphorus, and total nitrogen at CBP Station LE5.6 (surface and bottom layers) for 1999.

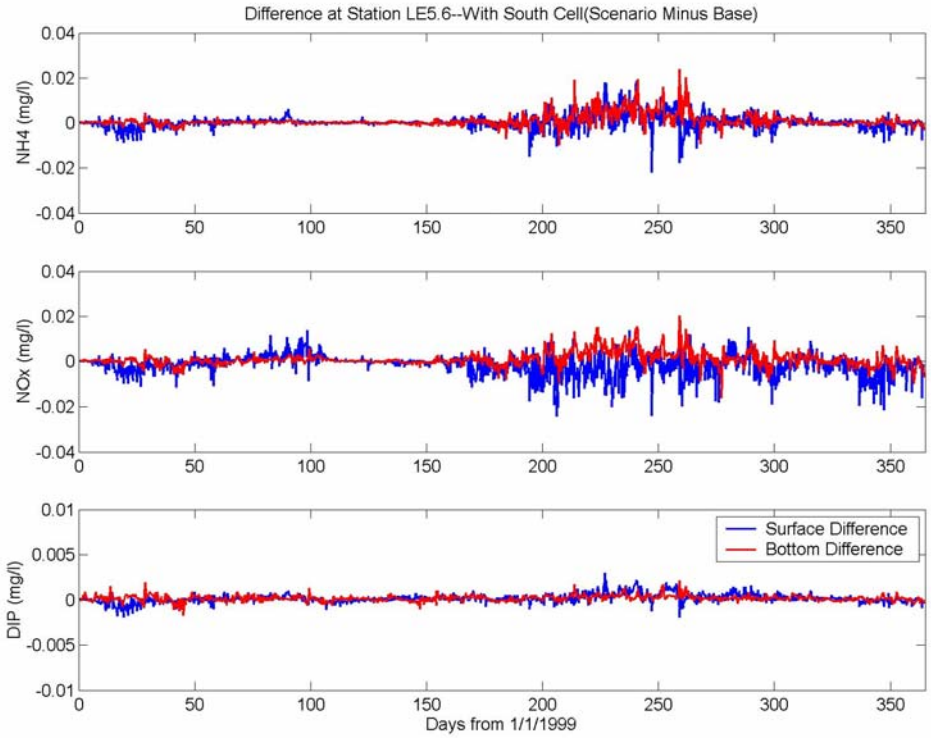

Figure E14. CIEE south cell expansion scenario minus base case differences of ammonium, nitrate-nitrite, and dissolved inorganic phosphorus at CBP Station LE5.6 (surface and bottom layers) for 1999.

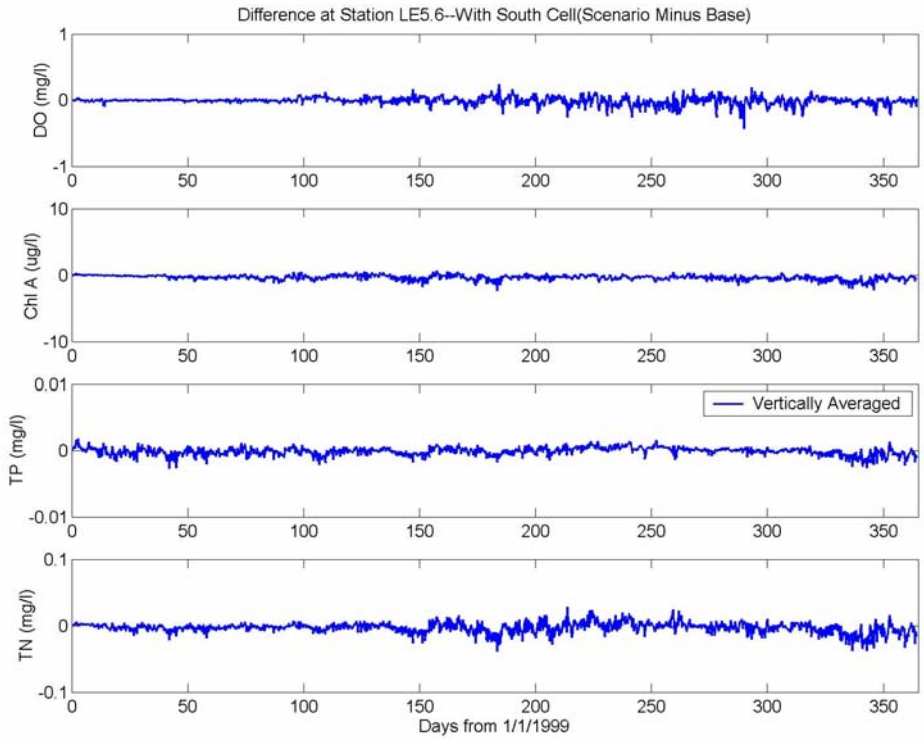

Figure E15. CIEE south cell expansion scenario minus base case differences of dissolved oxygen, chlorophyll-a, total phosphorus, and total nitrogen at CBP Station LE5.6 (vertically averaged) for 1999.

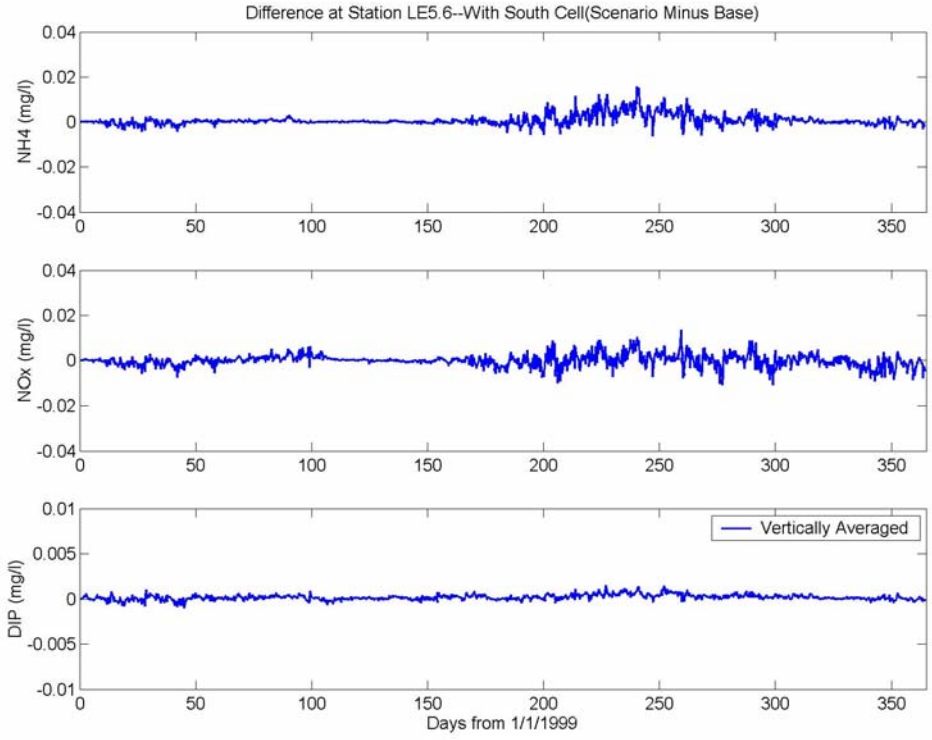

Figure E16. CIEE south cell expansion scenario minus base case differences of ammonium, nitrate-nitrite, and dissolved inorganic phosphorus at CBP Station LE5.6 (vertically averaged) for 1999.

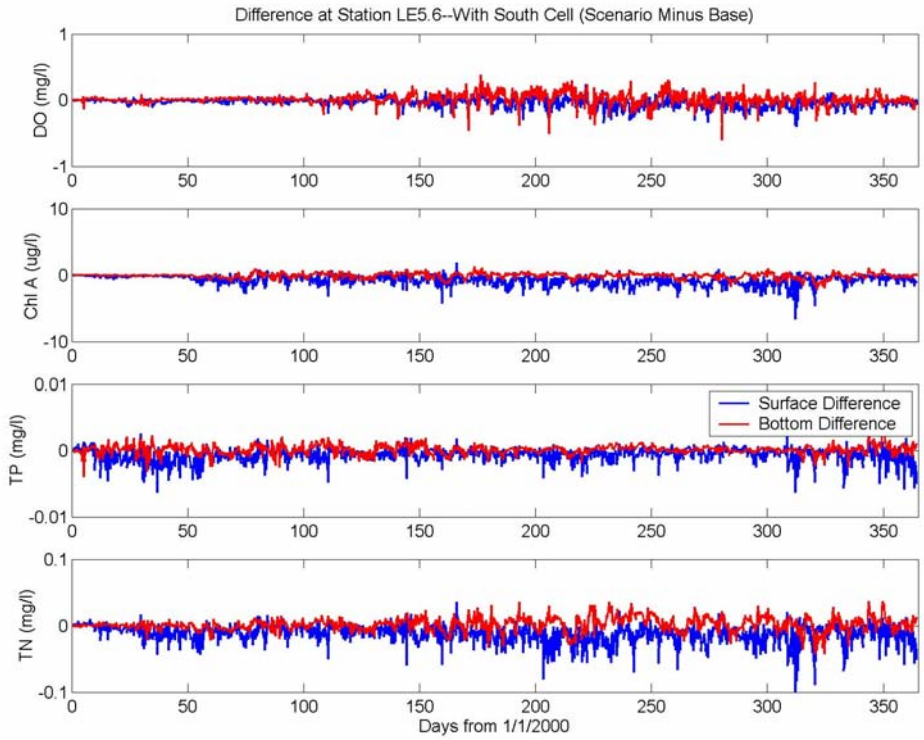

Figure E17. CIEE south cell expansion scenario minus base case differences of dissolved oxygen, chlorophyll-a, total phosphorus, and total nitrogen at CBP Station LE5.6 (surface and bottom layers) for 2000.

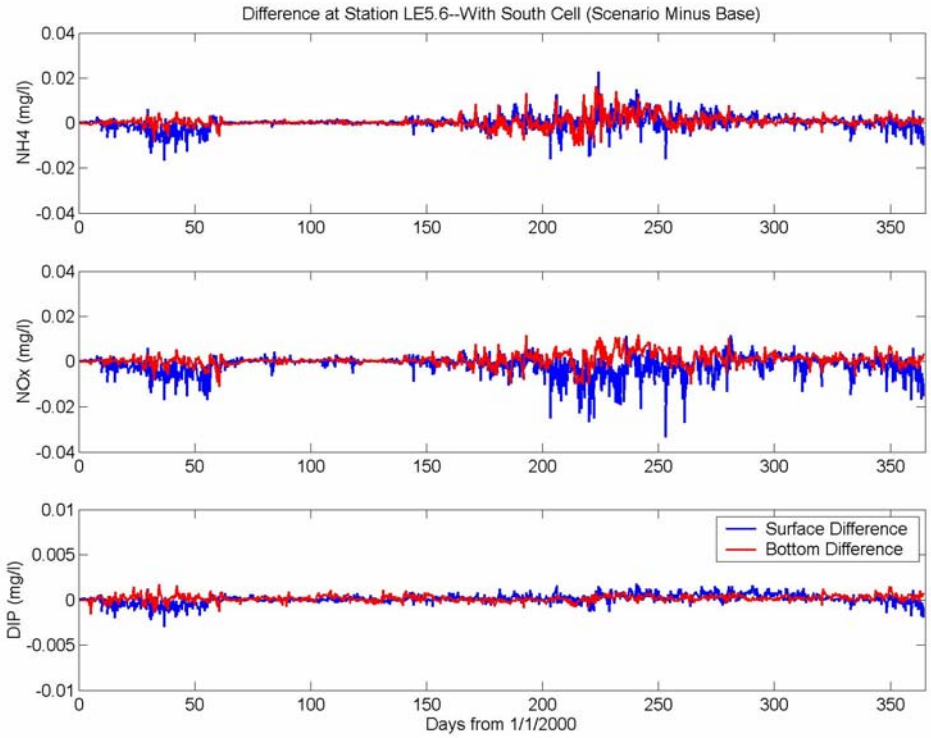

Figure E18. CIEE south cell expansion scenario minus base case differences of ammonium, nitrate-nitrite, and dissolved inorganic phosphorus at CBP Station LE5.6 (surface and bottom layers) for 2000.

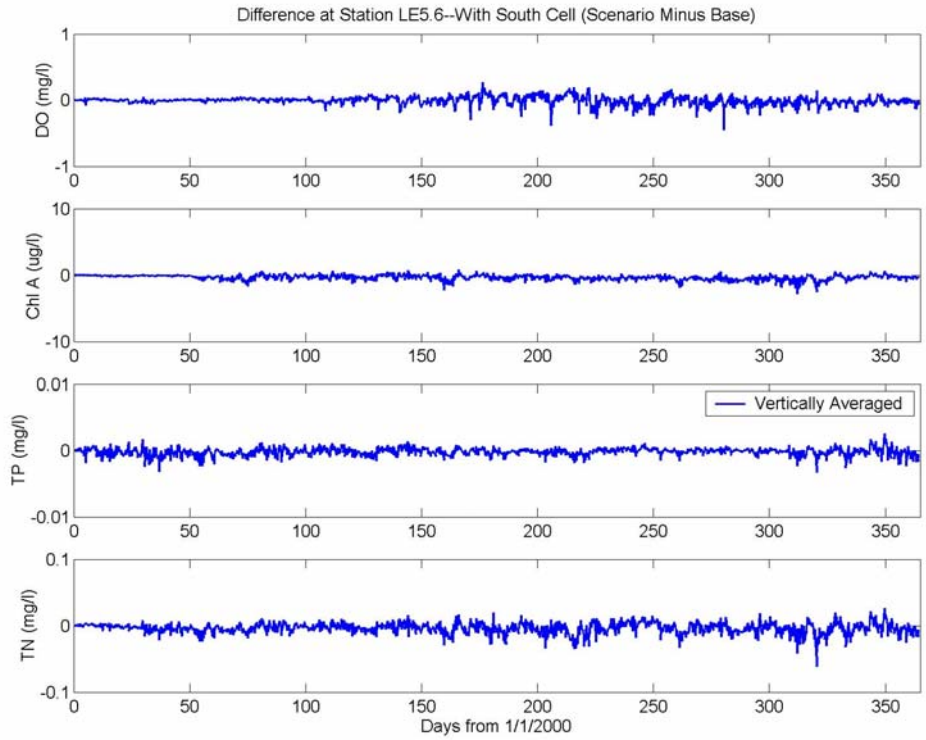

Figure E19. CIEE south cell expansion scenario minus base case differences of dissolved oxygen, chlorophyll-a, total phosphorus, and total nitrogen at CBP Station LE5.6 (vertically averaged) for 2000.

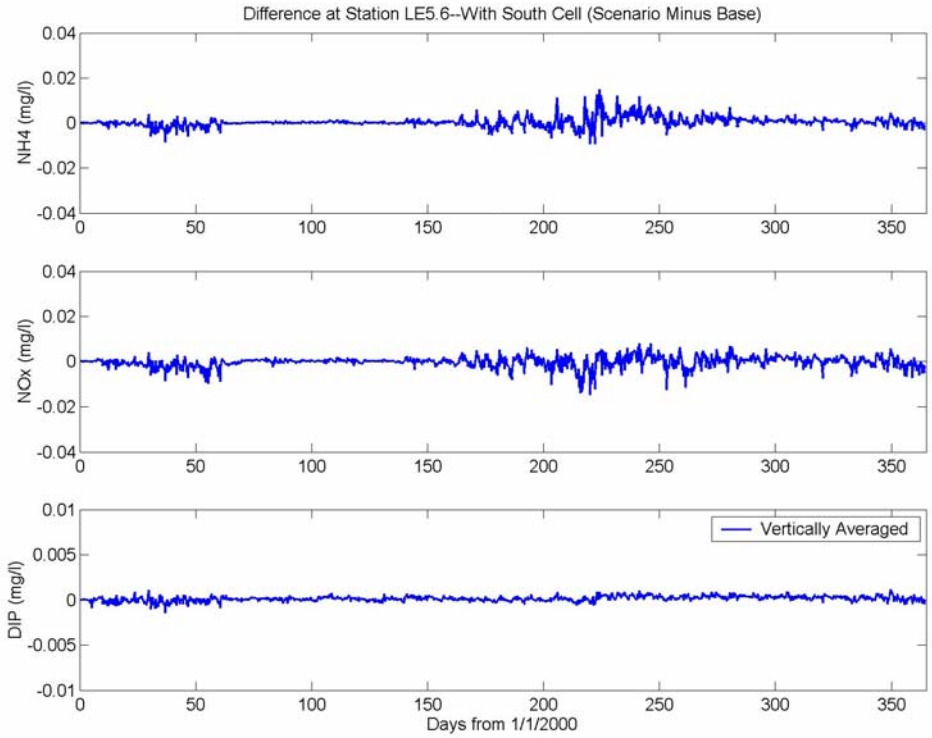

Figure E20. CIEE south cell expansion scenario minus base case differences of ammonium, nitrate-nitrite, and dissolved inorganic phosphorus at CBP Station LE5.6 (vertically averaged) for 2000.

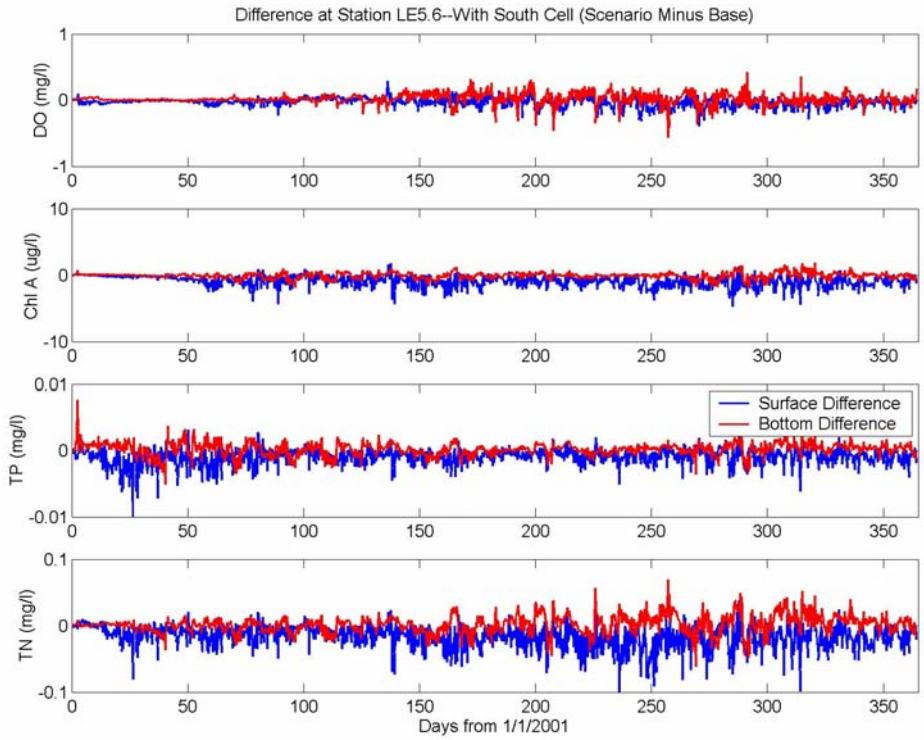

Figure E21. CIEE south cell expansion scenario minus base case differences of dissolved oxygen, chlorophyll-a, total phosphorus, and total nitrogen at CBP Station LE5.6 (surface and bottom layers) for 2001.

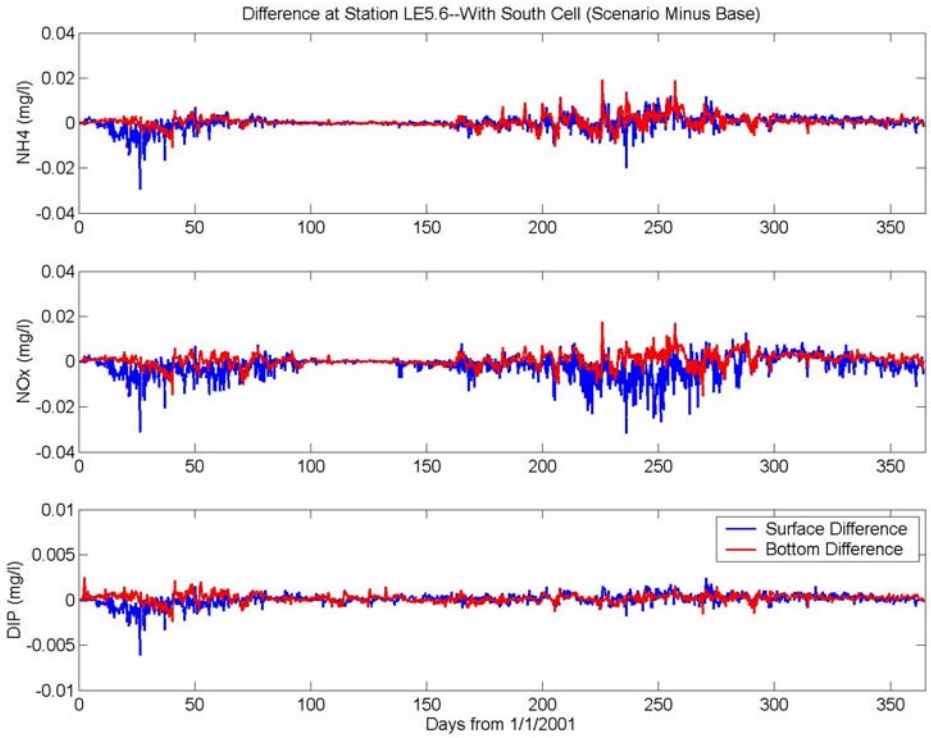

Figure E22. CIEE south cell expansion scenario minus base case differences of ammonium, nitrate-nitrite, and dissolved inorganic phosphorus at CBP Station LE5.6 (surface and bottom layers) for 2001.

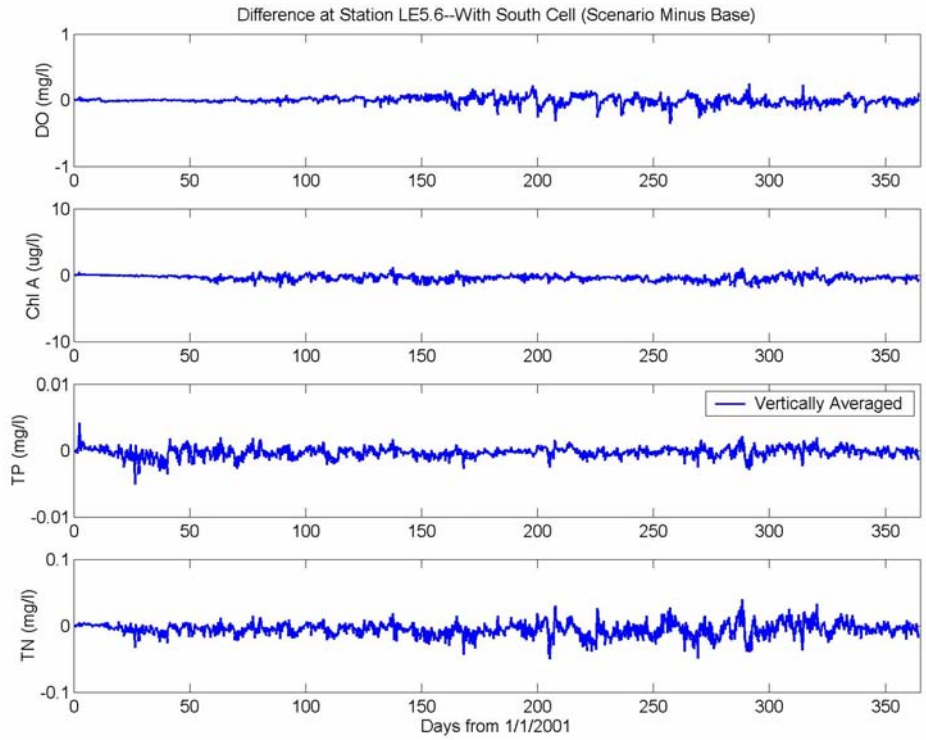

Figure E23. CIEE south cell expansion scenario minus base case differences of dissolved oxygen, chlorophyll-a, total phosphorus, and total nitrogen at CBP Station LE5.6 (vertically averaged) for 2001.

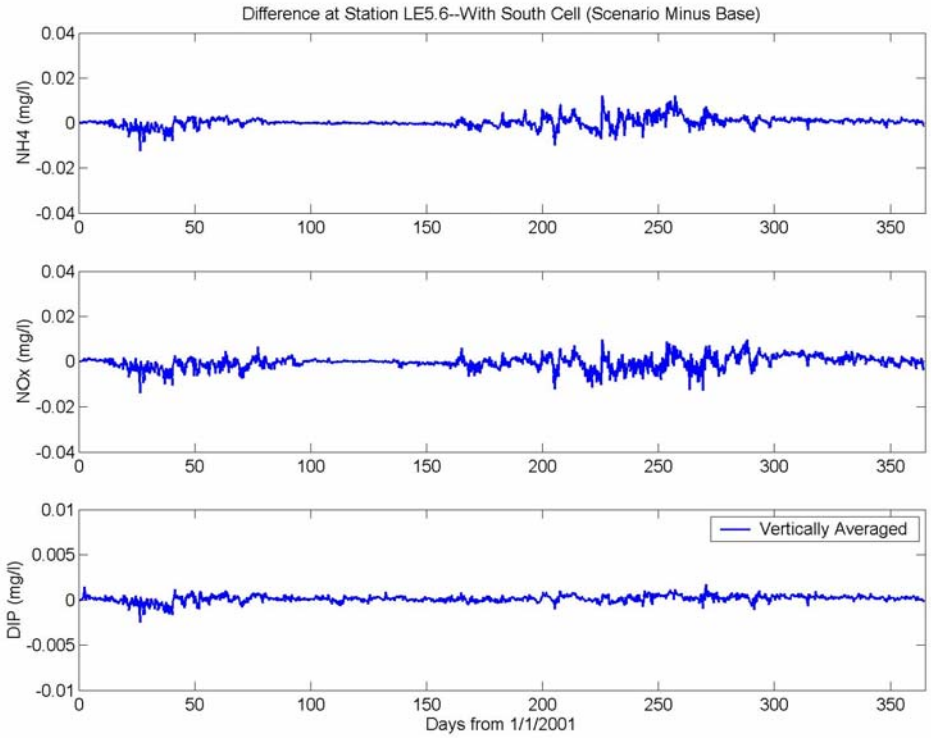

Figure E24. CIEE south cell expansion scenario minus base case differences of ammonium, nitrate-nitrite, and dissolved inorganic phosphorus at CBP Station LE5.6 (vertically averaged) for 2001.

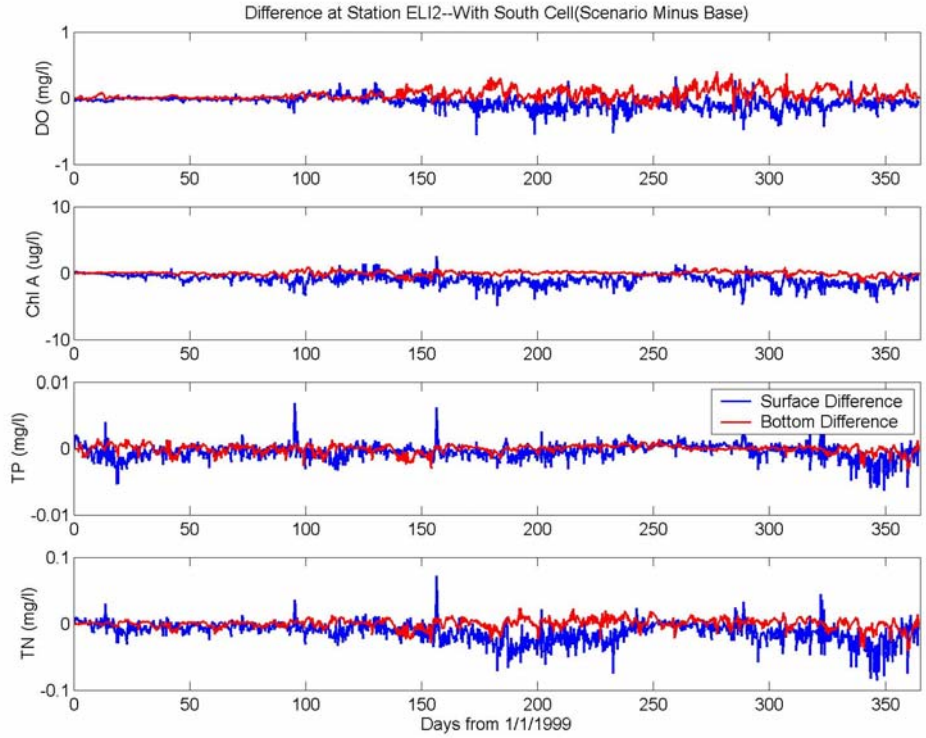

Figure E25. CIEE south cell expansion scenario minus base case differences of dissolved oxygen, chlorophyll-a, total phosphorus, and total nitrogen at CBP Station ELI2 (surface and bottom layers) for 1999.

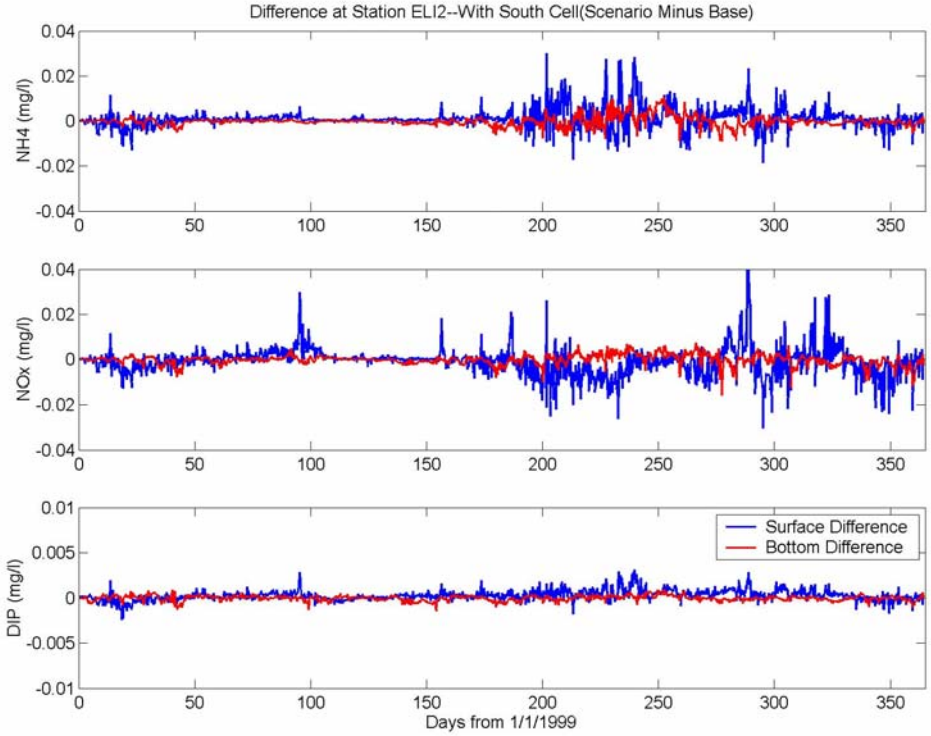

Figure E26. CIEE south cell expansion scenario minus base case differences of ammonium, nitrate-nitrite, and dissolved inorganic phosphorus at CBP Station ELI2 (surface and bottom layers) for 1999.

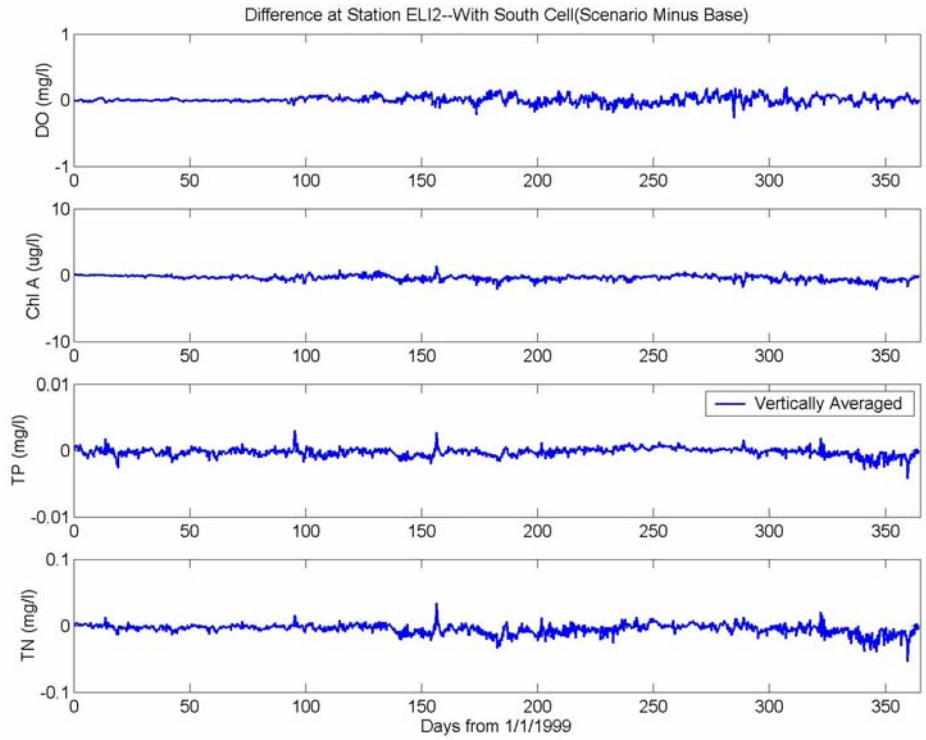

Figure E27. CIEE south cell expansion scenario minus base case differences of dissolved oxygen, chlorophyll-a, total phosphorus, and total nitrogen at CBP Station ELI2 (vertically averaged) for 1999.

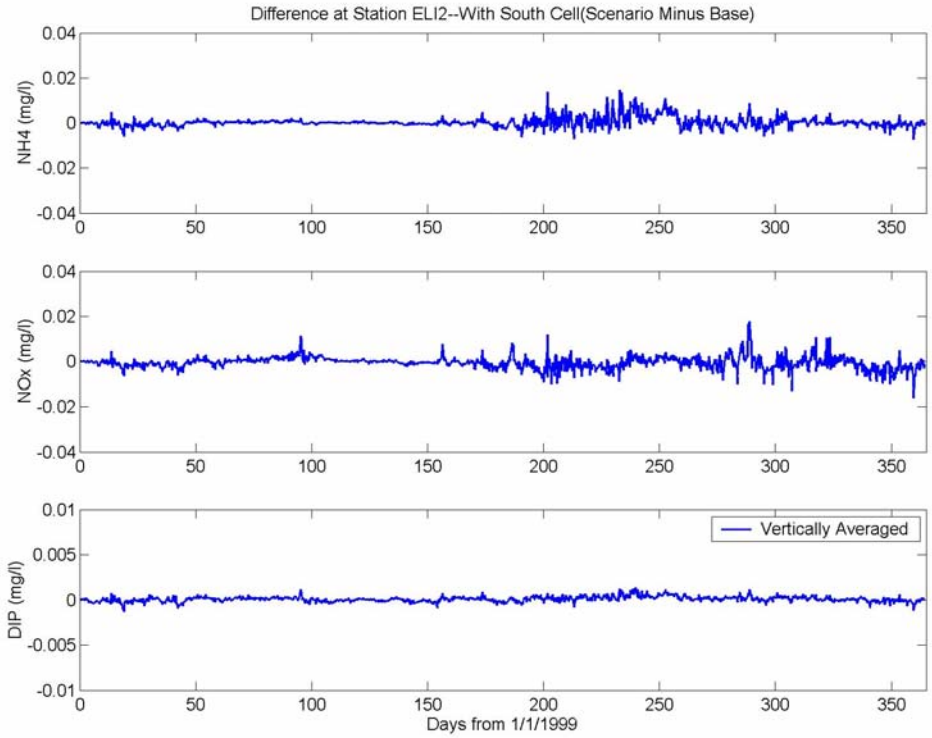

Figure E28. CIEE south cell expansion scenario minus base case differences of ammonium, nitrate-nitrite, and dissolved inorganic phosphorus at CBP Station ELI2 (vertically averaged) for 1999.

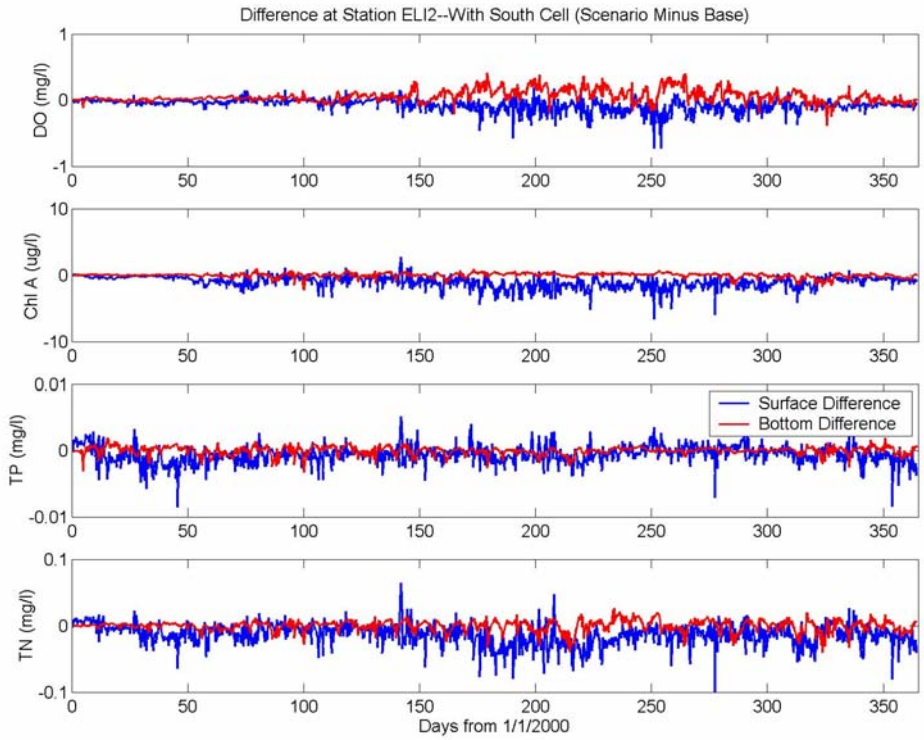

Figure E29. CIEE south cell expansion scenario minus base case differences of dissolved oxygen, chlorophyll-a, total phosphorus, and total nitrogen at CBP Station ELI2 (surface and bottom layers) for 2000.

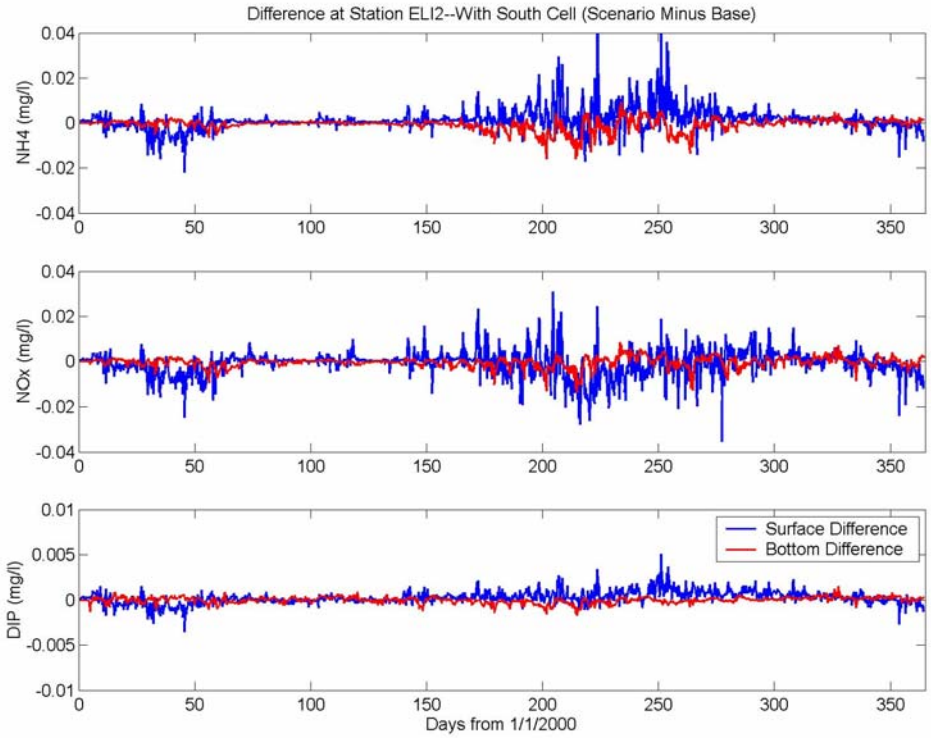

Figure E30. CIEE south cell expansion scenario minus base case differences of ammonium, nitrate-nitrite, and dissolved inorganic phosphorus at CBP Station ELI2 (surface and bottom layers) for 2000.

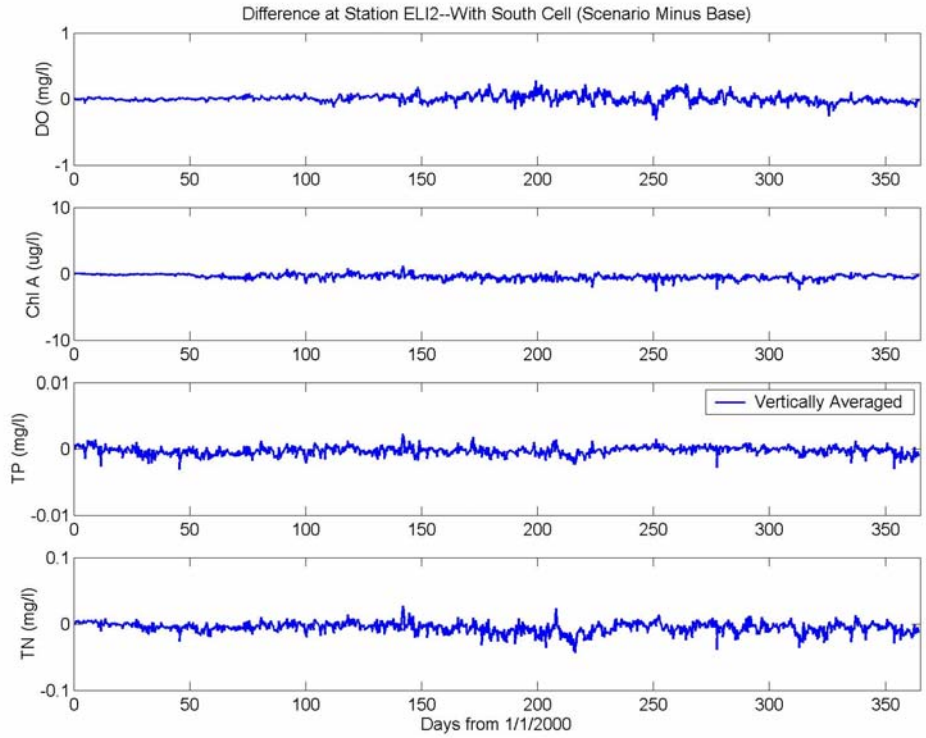

Figure E31. CIEE south cell expansion scenario minus base case differences of dissolved oxygen, chlorophyll-a, total phosphorus, and total nitrogen at CBP Station ELI2 (vertically averaged) for 2000.

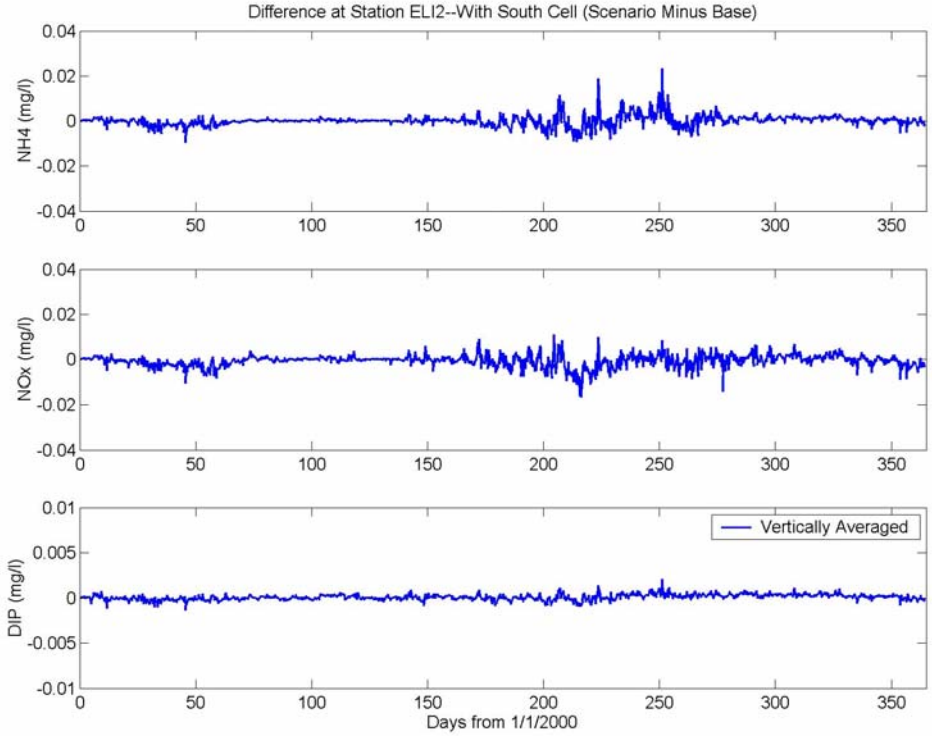

Figure E32. CIEE south cell expansion scenario minus base case differences of ammonium, nitrate-nitrite, and dissolved inorganic phosphorus at CBP Station ELI2 (vertically averaged) for 2000.

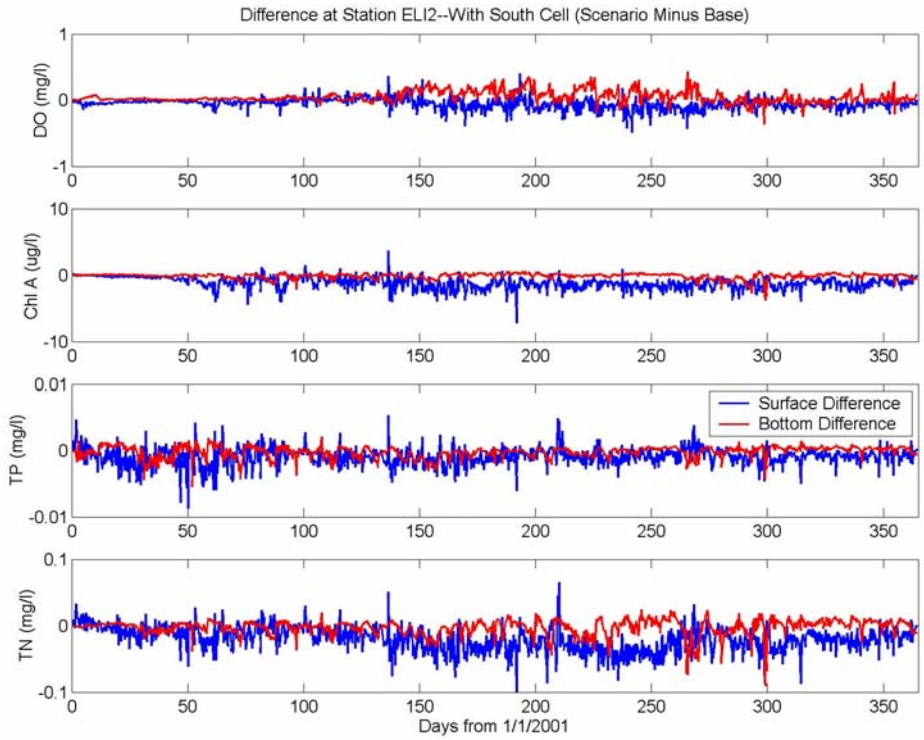

Figure E33. CIEE south cell expansion scenario minus base case differences of dissolved oxygen, chlorophyll-a, total phosphorus, and total nitrogen at CBP Station ELI2 (surface and bottom layers) for 2001.

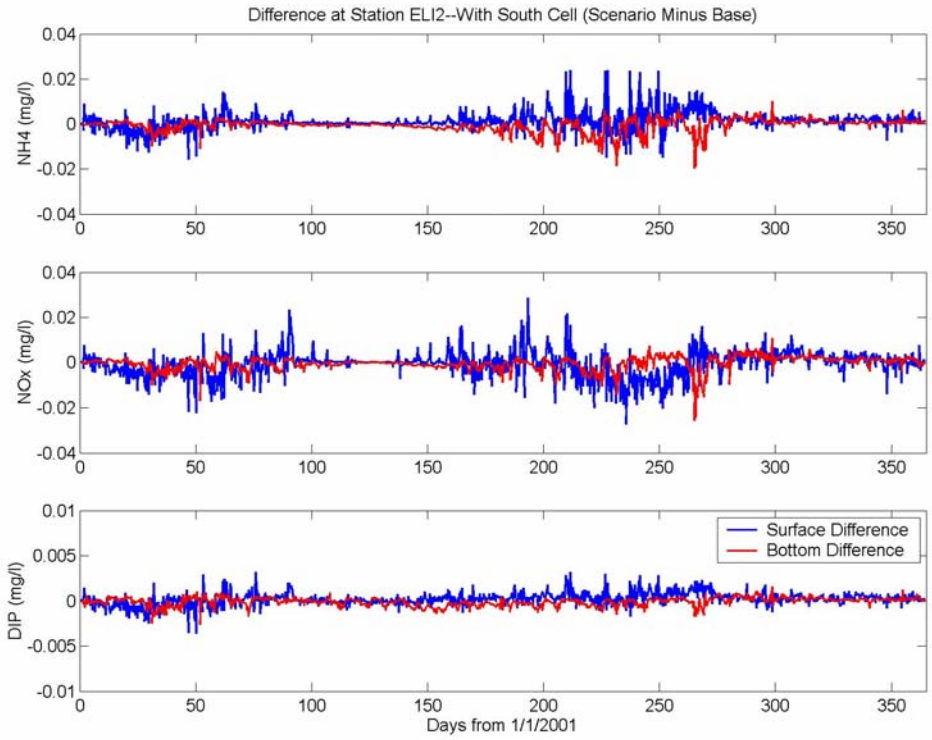

Figure E34. CIEE south cell expansion scenario minus base case differences of ammonium, nitrate-nitrite, and dissolved inorganic phosphorus at CBP Station ELI2 (surface and bottom layers) for 2001.

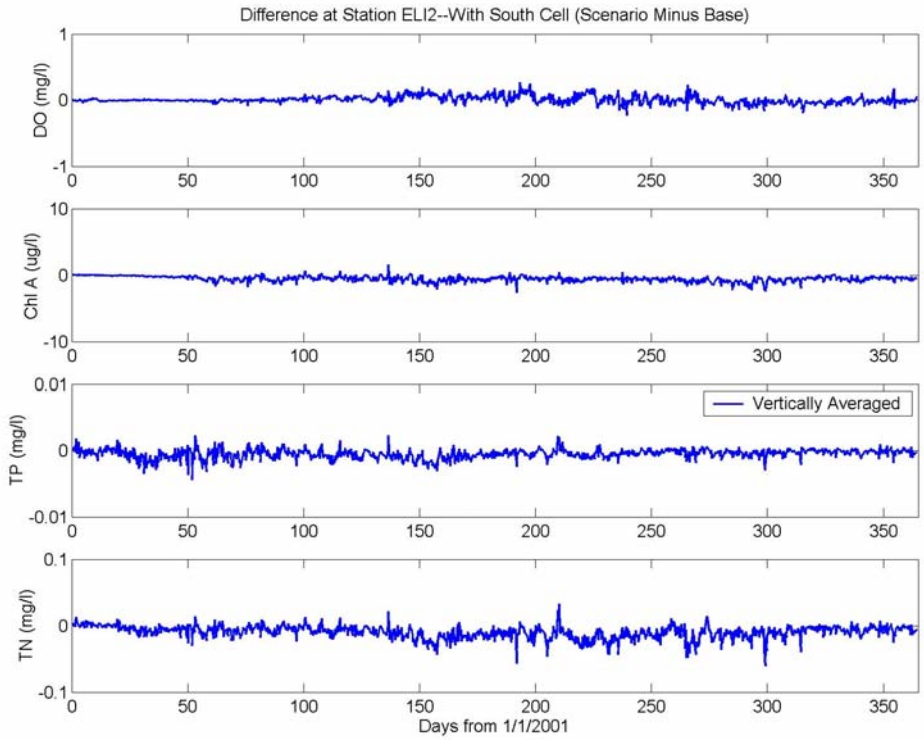

Figure E35. CIEE south cell expansion scenario minus base case differences of dissolved oxygen, chlorophyll-a, total phosphorus, and total nitrogen at CBP Station ELI2 (vertically averaged) for 2001.

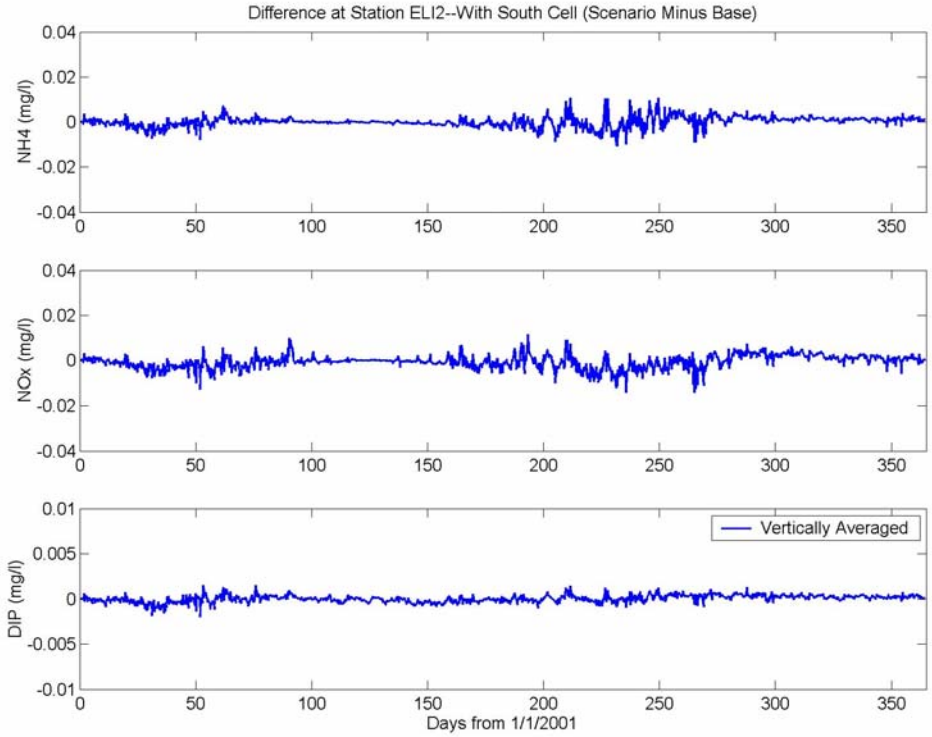

Figure E36. CIEE south cell expansion scenario minus base case differences of ammonium, nitrate-nitrite, and dissolved inorganic phosphorus at CBP Station ELI2 (vertically averaged) for 2001.

APPENDIX F

South Cell Expansion WQ Scenario Analysis

Temporal Plots of 30-day Average Differences from Base Case For Surface and Bottom Layers and Vertically Averaged

Tabulations of Vertically Averaged 30-day Average Differences

For 1999, 2000, and 2001 at CBP Stations LE5.5, LE5.6, and ELI2

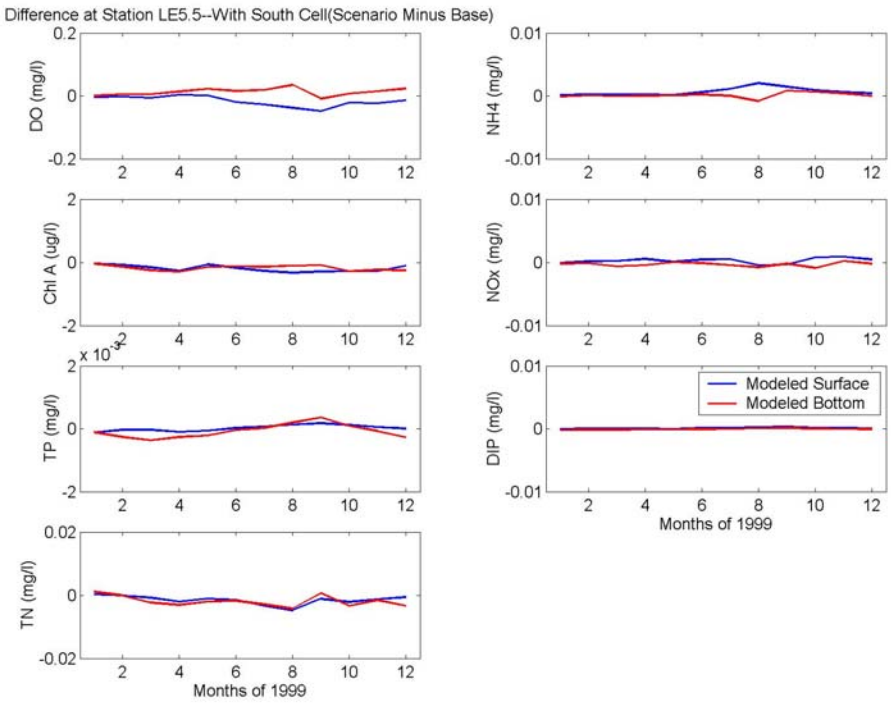

Figure F1. Differences in 30-day averages of dissolved oxygen, chlorophyll-a, total phosphorus, total nitrogen, ammonium, nitrate-nitrite, and dissolved inorganic phosphorus at CBP Station LE5.5 (surface and bottom layers) for 1999.

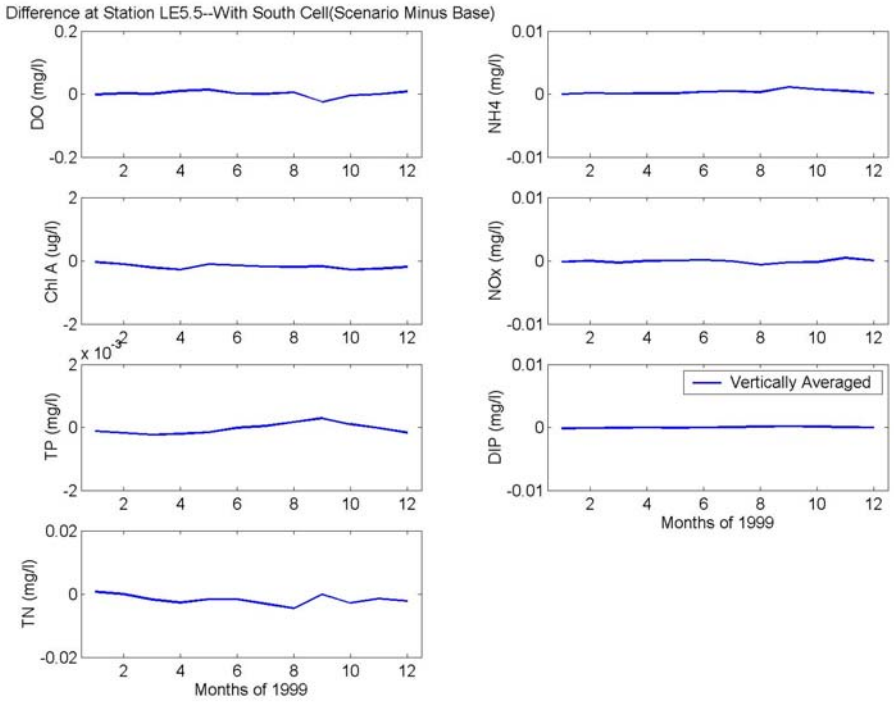

Figure F2. Differences in 30-day averages of dissolved oxygen, chlorophyll-a, total phosphorus, total nitrogen, ammonium, nitrate-nitrite, and dissolved inorganic phosphorus at CBP Station LE5.5 (vertically averaged) for 1999.

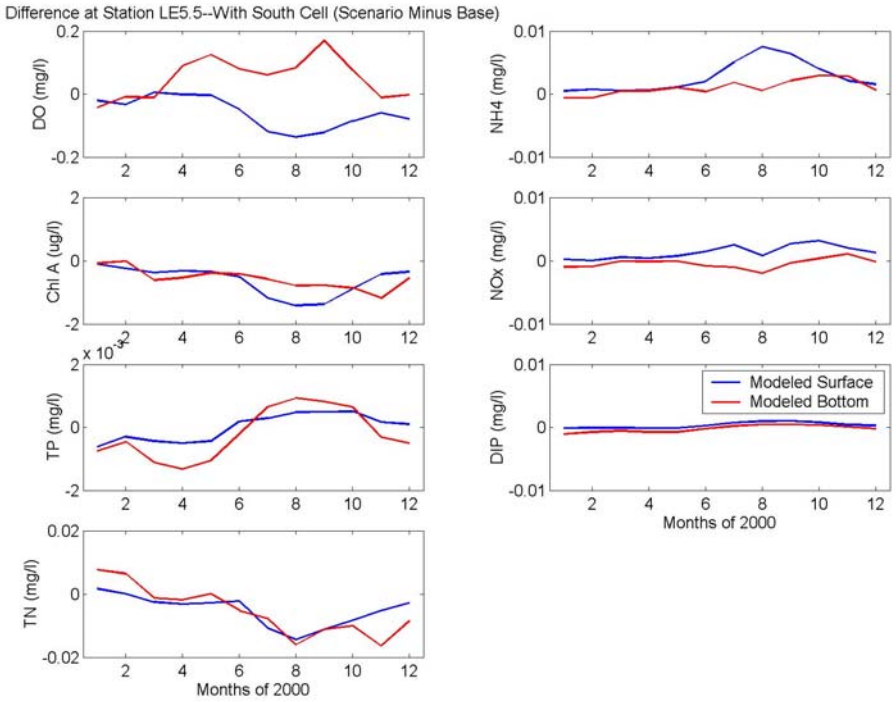

Figure F3. Differences in 30-day averages of dissolved oxygen, chlorophyll-a, total phosphorus, total nitrogen, ammonium, nitrate-nitrite, and dissolved inorganic phosphorus at CBP Station LE5.5 (surface and bottom layers) for 2000.

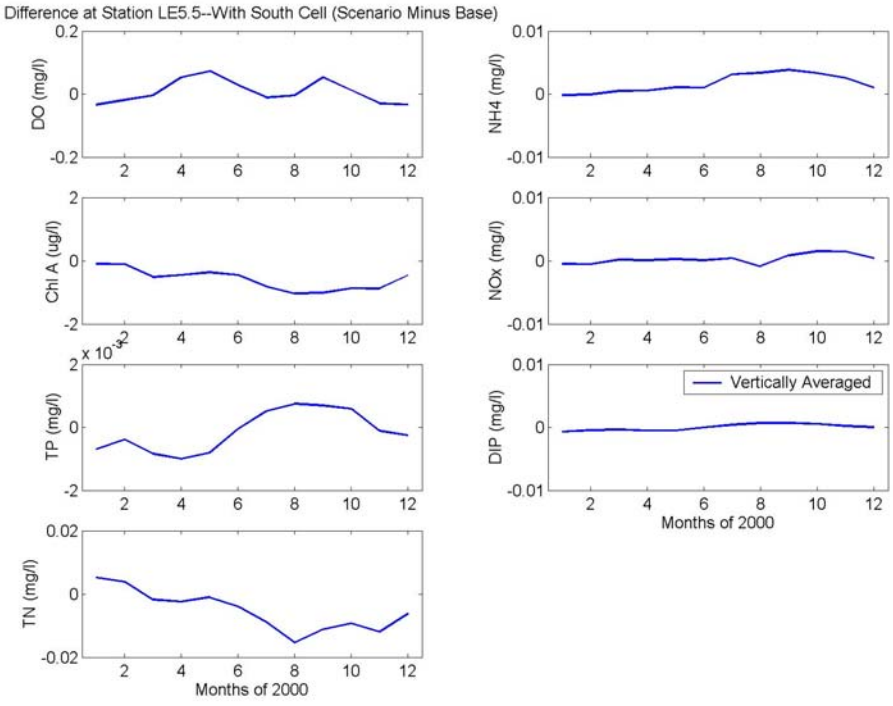

Figure F4. Differences in 30-day averages of dissolved oxygen, chlorophyll-a, total phosphorus, total nitrogen, ammonium, nitrate-nitrite, and dissolved inorganic phosphorus at CBP Station LE5.5 (vertically averaged) for 2000.

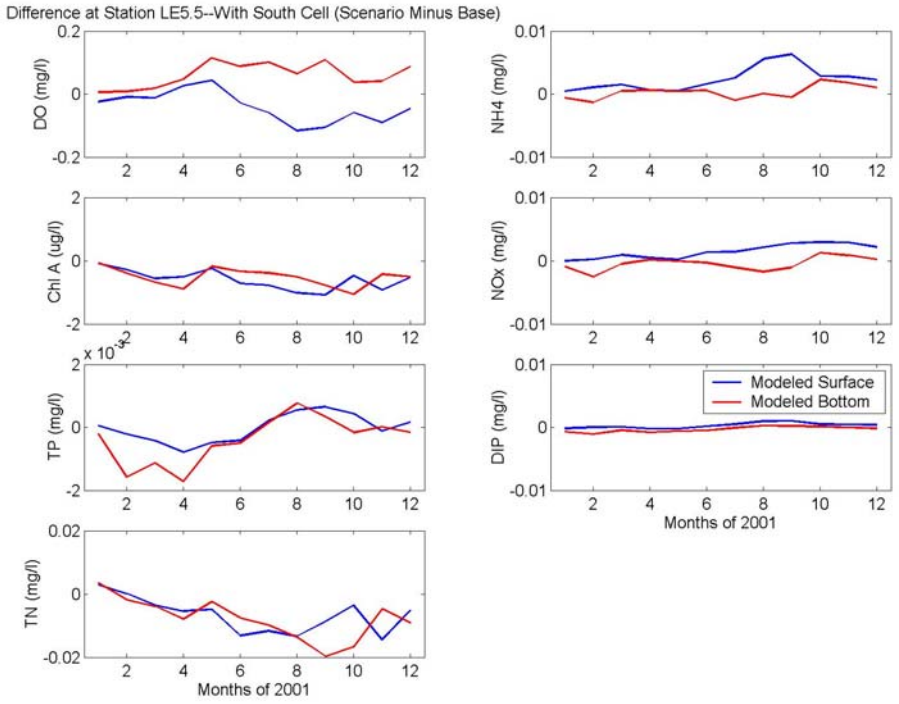

Figure F5. Differences in 30-day averages of dissolved oxygen, chlorophyll-a, total phosphorus, total nitrogen, ammonium, nitrate-nitrite, and dissolved inorganic phosphorus at CBP Station LE5.5 (surface and bottom layers) for 2001.

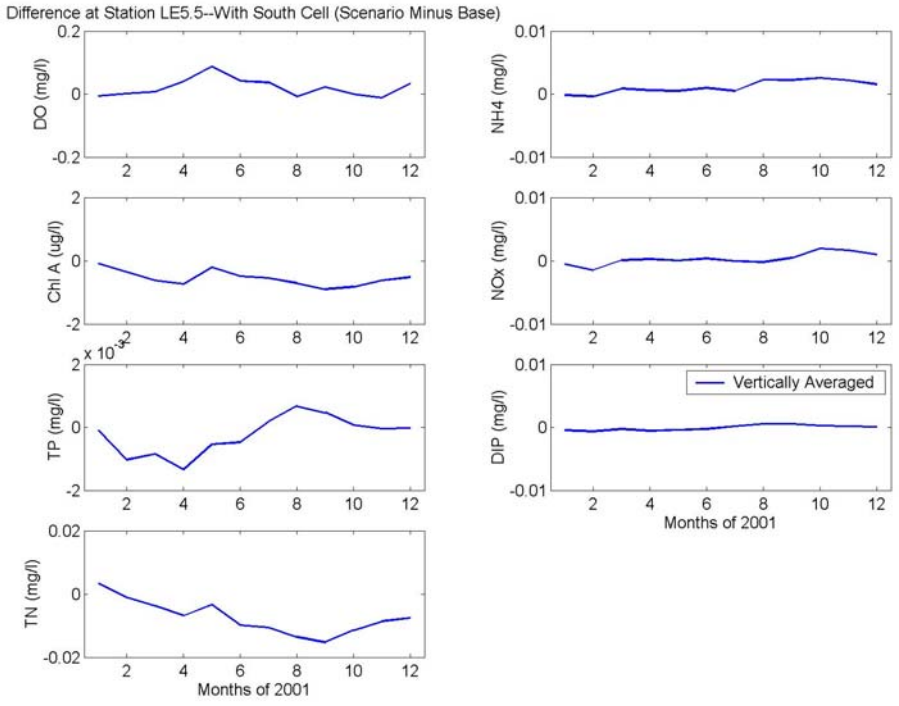

Figure F6. Differences in 30-day averages of dissolved oxygen, chlorophyll-a, total phosphorus, total nitrogen, ammonium, nitrate-nitrite, and dissolved inorganic phosphorus at CBP Station LE5.5 (vertically averaged) for 2001.

Table F1. Differences in 30-day averages of dissolved oxygen, chlorophyll-a, total phosphorus, total nitrogen, ammonium, nitrate-nitrite, and dissolved inorganic phosphorus at CBP Station LE5.5 (vertically averaged) for 1999, 2000, and 2001 (values plotted in Figures F2, F4, and F6).

	Month	**DO**	**Chl**	**TP**	**TN**	**NH_4**	**NO_X**	**DIP**
		mg/l	µg/l	mg/l	mg/l	mg/l	mg/l	mg/l
Station LE5.5 (1999)	Jan.	-0.00	-0.0	-0.0001	0.001	0.000	-0.0002	-0.0001
	Feb.	0.00	-0.1	-0.0002	-0.000	0.000	0.0000	-0.0001
	Mar.	0.00	-0.2	-0.0002	-0.002	0.000	-0.0003	-0.0001
	Apr.	0.01	-0.3	-0.0002	-0.003	0.000	0.0000	0.0000
	May	0.01	-0.1	-0.0002	-0.002	0.000	0.0000	-0.0001
	Jun.	0.00	-0.1	0.0000	-0.002	0.000	0.0001	0.0000
	Jul.	0.00	-0.2	0.0000	-0.003	0.001	-0.0001	0.0000
	Aug.	0.01	-0.2	0.0002	-0.005	0.000	-0.0007	0.0001
	Sep.	-0.02	-0.2	0.0003	-0.000	0.001	-0.0003	0.0002
	Oct.	-0.00	-0.3	0.0001	-0.003	0.001	-0.0002	0.0001
	Nov.	-0.00	-0.3	0.0000	-0.002	0.001	0.0005	0.0000
	Dec.	0.01	-0.2	-0.0002	-0.002	0.000	0.0000	0.0000
Detection limits:		**0.1**	**0.5**	**0.003**	**0.01**	**0.005**	**0.001**	**0.0015**

	Month	**DO**	**Chl**	**TP**	**TN**	**NH_4**	**NO_X**	**DIP**
		mg/l	µg/l	mg/l	mg/l	mg/l	mg/l	mg/l
Station LE5.5 (2000)	Jan.	-0.03	-0.1	-0.0007	0.005	-0.000	-0.0005	-0.0007
	Feb.	-0.02	-0.1	-0.0004	0.004	-0.000	-0.0006	-0.0005
	Mar.	-0.00	-0.5	-0.0008	-0.002	0.001	0.0002	-0.0004
	Apr.	0.05	-0.5	-0.0010	-0.002	0.001	0.0001	-0.0005
	May	0.07	-0.4	-0.0008	-0.001	0.001	0.0002	-0.0005
	Jun.	0.03	-0.5	0.0000	-0.004	0.001	0.0001	0.0000
	Jul.	-0.01	-0.8	0.0005	-0.009	0.003	0.0004	0.0004
	Aug.	-0.00	-1.0	0.0007	-0.015	0.003	-0.0009	0.0007
	Sep.	0.05	-1.0	0.0007	-0.011	0.004	0.0009	0.0007
	Oct.	0.01	-0.9	0.0006	-0.009	0.003	0.0015	0.0006
	Nov.	-0.03	-0.9	-0.0001	-0.012	0.003	0.0014	0.0002
	Dec.	-0.03	-0.5	-0.0003	-0.006	0.001	0.0004	0.0000
Detection limits:		**0.1**	**0.5**	**0.003**	**0.01**	**0.005**	**0.001**	**0.0015**

	Month	**DO**	**Chl**	**TP**	**TN**	**NH_4**	**NO_X**	**DIP**
		mg/l	µg/l	mg/l	mg/l	mg/l	mg/l	mg/l
Station LE5.5 (2001)	Jan.	-0.01	-0.1	-0.0001	0.003	-0.000	-0.0006	-0.0005
	Feb.	0.00	-0.3	-0.0010	-0.001	-0.000	-0.0015	-0.0007
	Mar.	0.01	-0.6	-0.0009	-0.004	0.001	0.0001	-0.0002
	Apr.	0.04	-0.7	-0.0013	-0.007	0.001	0.0003	-0.0006
	May	0.09	-0.2	-0.0005	-0.003	0.001	0.0000	-0.0004
	Jun.	0.04	-0.5	-0.0005	-0.010	0.001	0.0003	-0.0002
	Jul.	0.04	-0.5	0.0002	-0.011	0.001	-0.0001	0.0002
	Aug.	-0.01	-0.7	0.0007	-0.014	0.002	-0.0002	0.0005
	Sep.	0.02	-0.9	0.0005	-0.015	0.002	0.0005	0.0005
	Oct.	-0.00	-0.8	0.0001	-0.012	0.003	0.0019	0.0003
	Nov.	-0.01	-0.6	0.0000	-0.009	0.002	0.0017	0.0002
	Dec.	0.03	-0.5	0.0000	-0.008	0.002	0.0010	0.0001
Detection limits:		**0.1**	**0.5**	**0.003**	**0.01**	**0.005**	**0.001**	**0.0015**

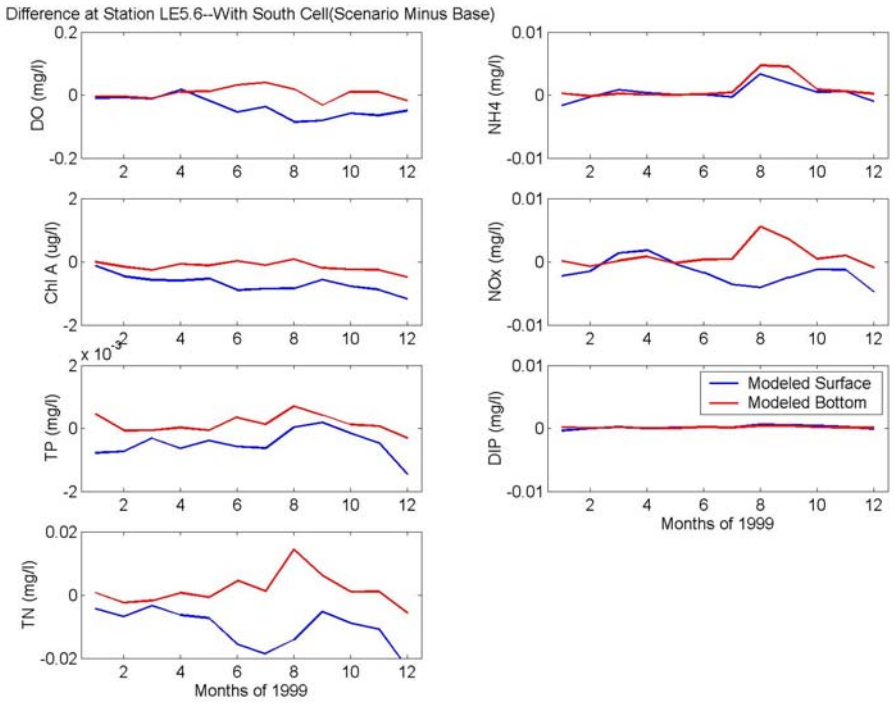

Figure F7. Differences in 30-day averages of dissolved oxygen, chlorophyll-a, total phosphorus, total nitrogen, ammonium, nitrate-nitrite, and dissolved inorganic phosphorus at CBP Station LE5.6 (surface and bottom layers) for 1999.

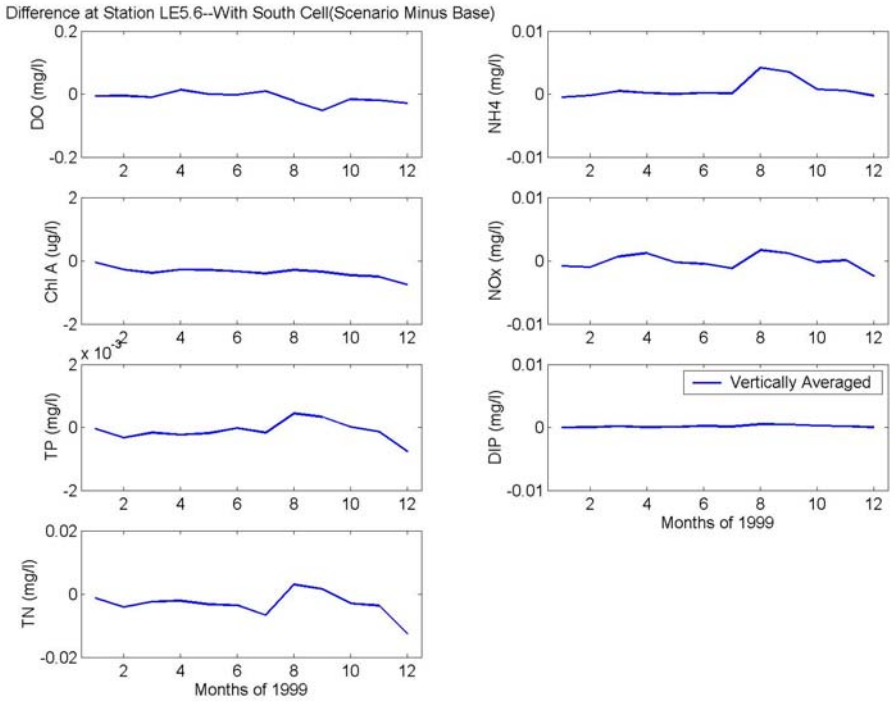

Figure F8. Differences in 30-day averages of dissolved oxygen, chlorophyll-a, total phosphorus, total nitrogen, ammonium, nitrate-nitrite, and dissolved inorganic phosphorus at CBP Station LE5.6 (vertically averaged) for 1999.

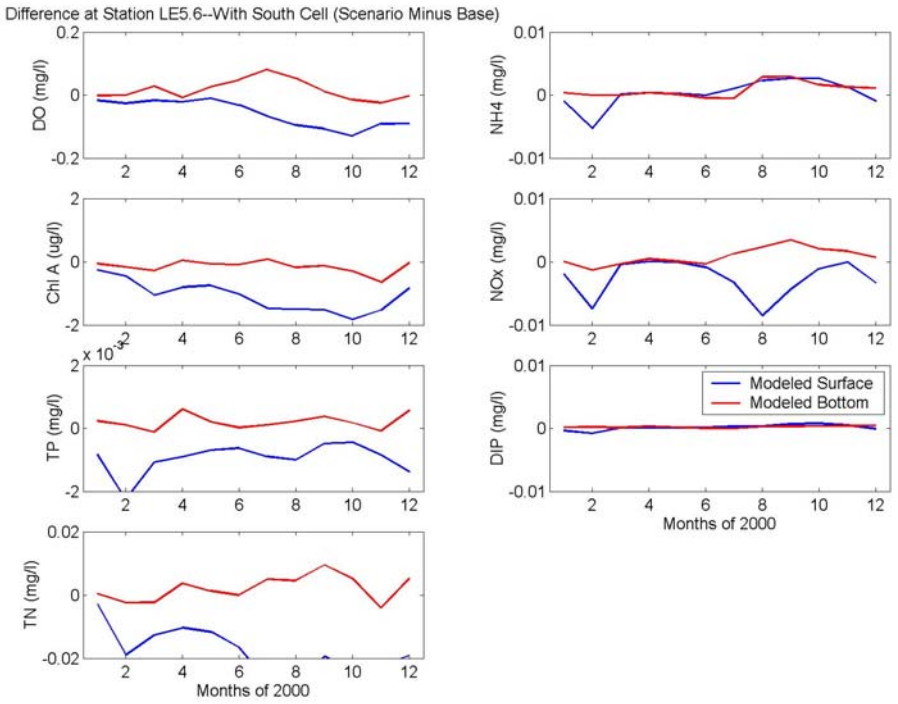

Figure F9. Differences in 30-day averages of dissolved oxygen, chlorophyll-a, total phosphorus, total nitrogen, ammonium, nitrate-nitrite, and dissolved inorganic phosphorus at CBP Station LE5.6 (surface and bottom layers) for 2000.

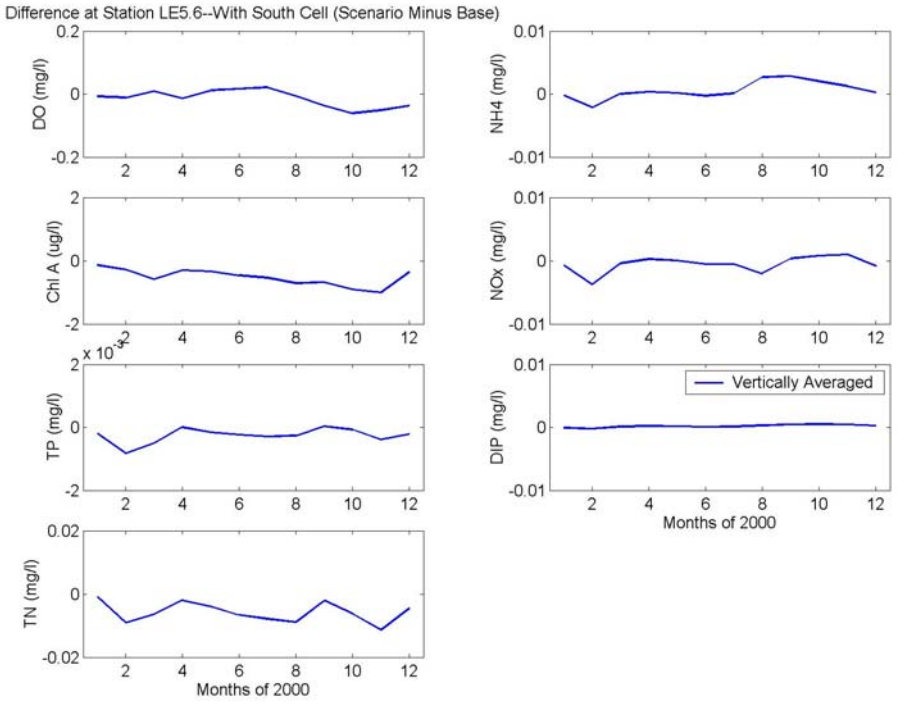

Figure F10. Differences in 30-day averages of dissolved oxygen, chlorophyll-a, total phosphorus, total nitrogen, ammonium, nitrate-nitrite, and dissolved inorganic phosphorus at CBP Station LE5.6 (vertically averaged) for 2000.

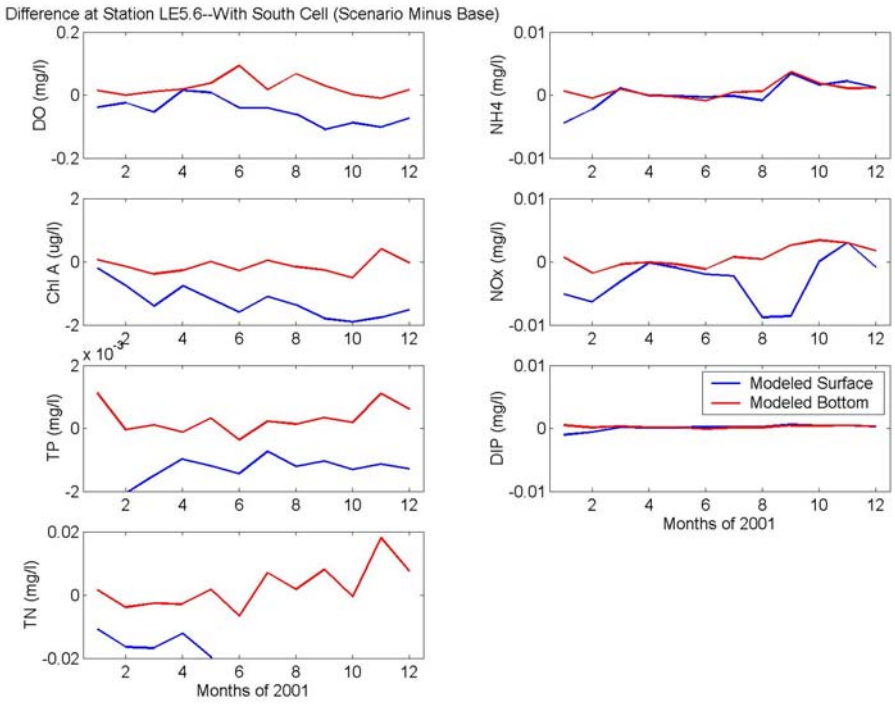

Figure F11. Differences in 30-day averages of dissolved oxygen, chlorophyll-a, total phosphorus, total nitrogen, ammonium, nitrate-nitrite, and dissolved inorganic phosphorus at CBP Station LE5.6 (surface and bottom layers) for 2001.

.

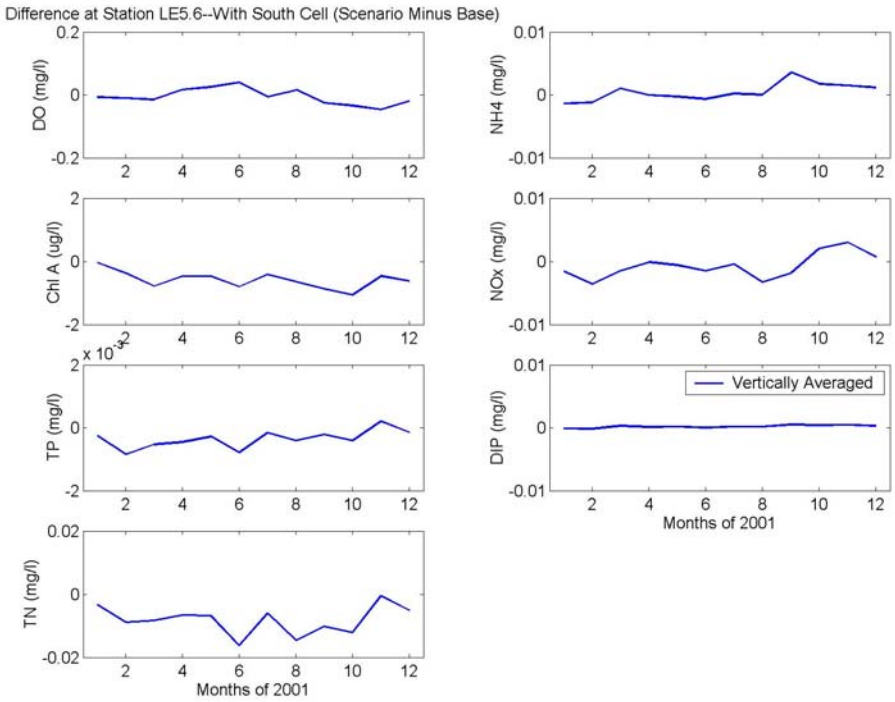

Figure F12. Differences in 30-day averages of dissolved oxygen, chlorophyll-a, total phosphorus, total nitrogen, ammonium, nitrate-nitrite, and dissolved inorganic phosphorus at CBP Station LE5.6 (vertically averaged) for 2001.

Table F2. Differences in 30-day averages of dissolved oxygen, chlorophyll-a, total phosphorus, total nitrogen, ammonium, nitrate-nitrite, and dissolved inorganic phosphorus at CBP Stations LE5.6 (vertically averaged) for 1999, 2000, and 2001 (values plotted in Figures F8, F10, and F12).

	Month	**DO**	**Chl**	**TP**	**TN**	**NH_4**	**NO_X**	**DIP**
		mg/l	µg/l	mg/l	mg/l	mg/l	mg/l	mg/l
Station LE5.6 (1999)	Jan.	-0.01	-0.1	0.0000	-0.001	-0.001	-0.0008	0.0000
	Feb.	-0.01	-0.3	-0.0003	-0.004	-0.000	-0.0010	0.0000
	Mar.	-0.01	-0.4	-0.0002	-0.002	0.001	0.0007	0.0002
	Apr.	0.01	-0.3	-0.0002	-0.002	0.000	0.0012	0.0000
	May	0.00	-0.3	-0.0002	-0.003	0.000	-0.0002	0.0001
	Jun.	-0.00	-0.3	0.0000	-0.004	0.000	-0.0005	0.0002
	Jul.	0.01	-0.4	-0.0002	-0.007	0.000	-0.0012	0.0001
	Aug.	-0.02	-0.3	0.0004	0.003	0.004	0.0017	0.0005
	Sep.	-0.05	-0.3	0.0003	0.002	0.004	0.0011	0.0005
	Oct.	-0.02	-0.4	0.0000	-0.003	0.001	-0.0002	0.0003
	Nov.	-0.02	-0.5	-0.0000	-0.004	0.001	0.0001	0.0002
	Dec.	-0.03	-0.8	-0.0008	-0.013	-0.000	-0.0025	0.0000
Detection limits:		**0.1**	**0.5**	**0.003**	**0.01**	**0.005**	**0.001**	**0.0015**

	Month	**DO**	**Chl**	**TP**	**TN**	**NH_4**	**NO_X**	**DIP**
		mg/l	µg/l	mg/l	mg/l	mg/l	mg/l	mg/l
Station LE5.6 (2000)	Jan.	-0.01	-0.1	-0.0002	-0.001	-0.000	-0.0007	-0.0001
	Feb.	-0.01	-0.3	-0.0008	-0.009	-0.002	-0.0037	-0.0002
	Mar.	0.01	-0.6	-0.0005	-0.007	0.000	-0.0004	0.0001
	Apr.	-0.01	-0.3	0.0000	-0.002	0.000	0.0003	0.0002
	May	0.01	-0.3	-0.0002	-0.004	0.000	0.0000	0.0001
	Jun.	0.02	-0.5	-0.0002	-0.007	-0.000	-0.0006	0.0001
	Jul.	0.02	-0.5	-0.0003	-0.008	0.000	-0.0005	0.0001
	Aug.	-0.01	-0.7	-0.0003	-0.009	0.003	-0.0020	0.0003
	Sep.	-0.04	-0.7	0.0000	-0.002	0.003	0.0003	0.0005
	Oct.	-0.06	-0.9	-0.0001	-0.006	0.002	0.0008	0.0005
	Nov.	-0.05	-1.0	-0.0004	-0.011	0.001	0.0010	0.0004
	Dec.	-0.04	-0.4	-0.0002	-0.005	0.000	-0.0009	0.0003
Detection limits:		**0.1**	**0.5**	**0.003**	**0.01**	**0.005**	**0.001**	**0.0015**

	Month	**DO**	**Chl**	**TP**	**TN**	**NH_4**	**NO_X**	**DIP**
		mg/l	µg/l	mg/l	mg/l	mg/l	mg/l	mg/l
Station LE5.6 (2001)	Jan.	-0.01	-0.0	-0.0003	-0.003	-0.001	-0.0016	-0.0001
	Feb.	-0.01	-0.4	-0.0009	-0.009	-0.001	-0.0036	-0.0002
	Mar.	-0.02	-0.8	-0.0005	-0.008	0.001	-0.0015	0.0003
	Apr.	0.02	-0.5	-0.0005	-0.007	0.000	-0.0001	0.0001
	May	0.03	-0.5	-0.0003	-0.007	-0.000	-0.0006	0.0001
	Jun.	0.04	-0.8	-0.0008	-0.016	-0.001	-0.0015	0.0000
	Jul.	-0.01	-0.4	-0.0002	-0.006	0.000	-0.0005	0.0002
	Aug.	0.02	-0.6	-0.0004	-0.015	0.000	-0.0033	0.0002
	Sep.	-0.03	-0.9	-0.0002	-0.010	0.004	-0.0019	0.0005
	Oct.	-0.03	-1.1	-0.0004	-0.012	0.002	0.0020	0.0004
	Nov.	-0.05	-0.5	0.0002	-0.001	0.002	0.0030	0.0005
	Dec.	-0.02	-0.6	-0.0002	-0.005	0.001	0.0007	0.0003
Detection limits:		**0.1**	**0.5**	**0.003**	**0.01**	**0.005**	**0.001**	**0.0015**

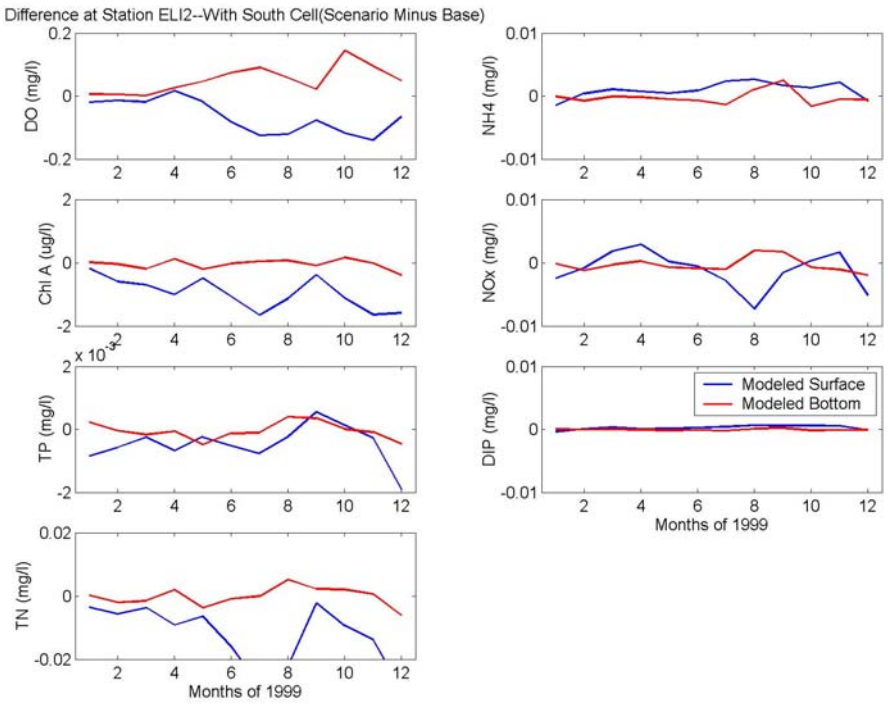

Figure F13. Differences in 30-day averages of dissolved oxygen, chlorophyll-a, total phosphorus, total nitrogen, ammonium, nitrate-nitrite, and dissolved inorganic phosphorus at CBP Station ELI2 (surface and bottom layers) for 1999.

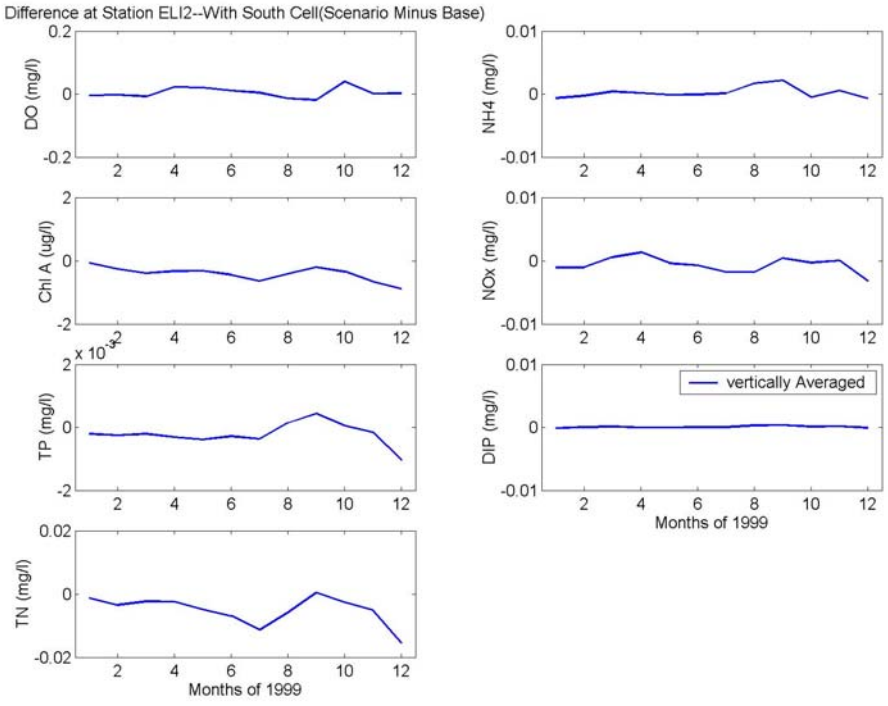

Figure F14. Differences in 30-day averages of dissolved oxygen, chlorophyll-a, total phosphorus, total nitrogen, ammonium, nitrate-nitrite, and dissolved inorganic phosphorus at CBP Station ELI2 (vertically averaged) for 1999.

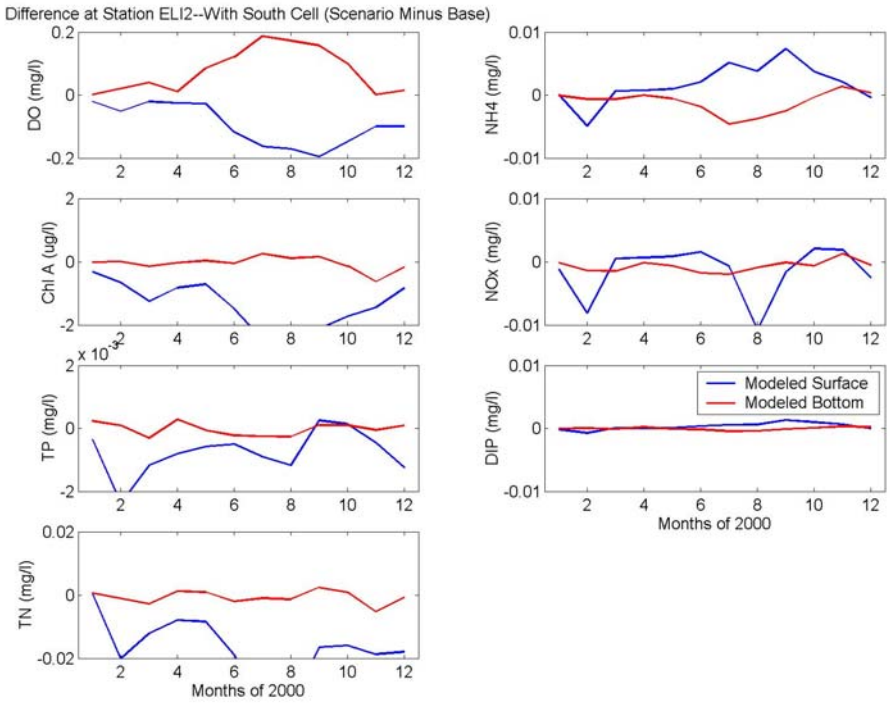

Figure F15. Differences in 30-day averages of dissolved oxygen, chlorophyll-a, total phosphorus, total nitrogen, ammonium, nitrate-nitrite, and dissolved inorganic phosphorus at CBP Station ELI2 (surface and bottom layers) for 2000.

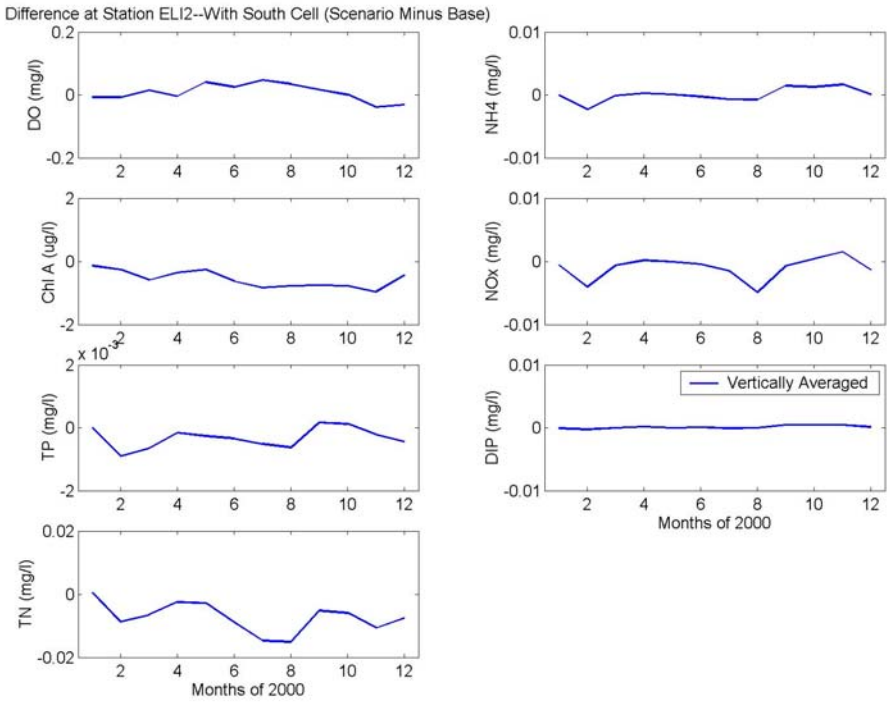

Figure F16. Differences in 30-day averages of dissolved oxygen, chlorophyll-a, total phosphorus, total nitrogen, ammonium, nitrate-nitrite, and dissolved inorganic phosphorus at CBP Station ELI2 (vertically averaged) for 2000.

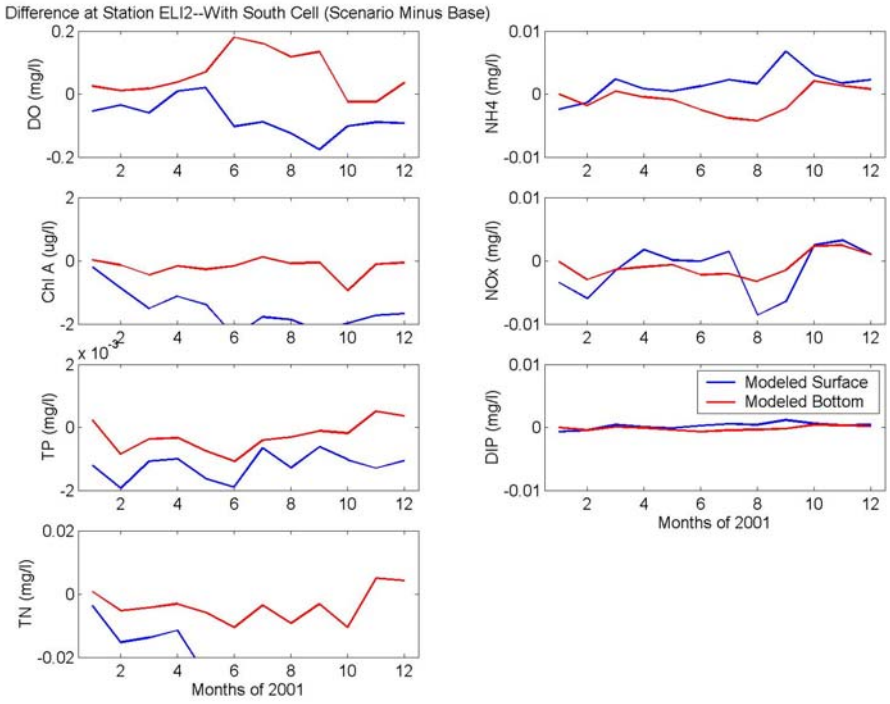

Figure F17. Differences in 30-day averages of dissolved oxygen, chlorophyll-a, total phosphorus, total nitrogen, ammonium, nitrate-nitrite, and dissolved inorganic phosphorus at CBP Station LE5.6 (vertically averaged) for 2001.

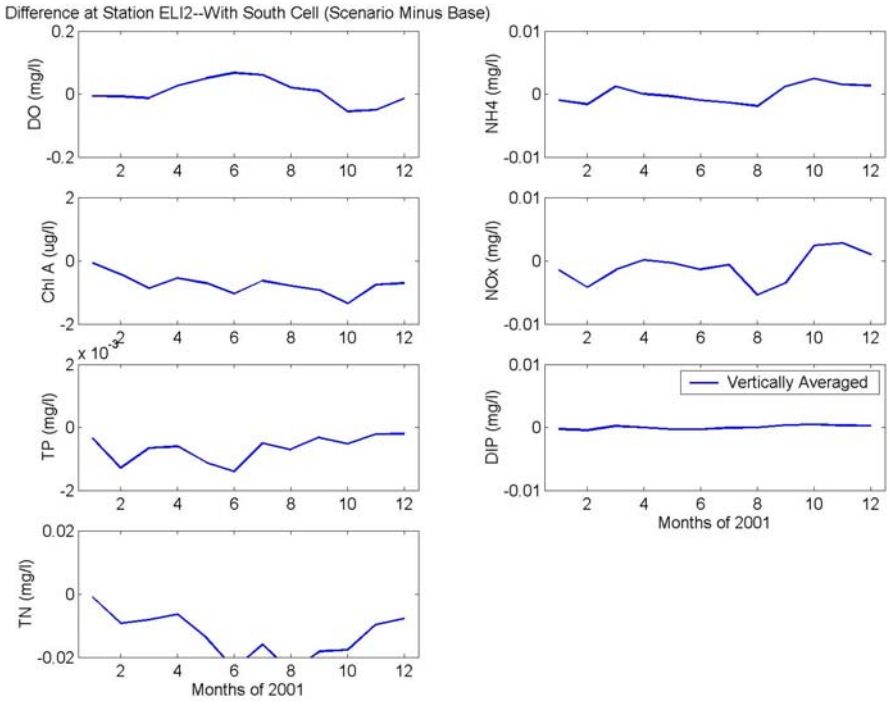

Figure F18. Differences in 30-day averages of dissolved oxygen, chlorophyll-a, total phosphorus, total nitrogen, ammonium, nitrate-nitrite, and dissolved inorganic phosphorus at CBP Station ELI2 (vertically averaged) for 2001.

Table F3. Differences in 30-day averages of dissolved oxygen, chlorophyll-a, total phosphorus, total nitrogen, ammonium, nitrate-nitrite, and dissolved inorganic phosphorus at CBP Station ELI2 (vertically averaged) for 1999, 2000, and 2001 (values plotted in Figures F14, F16, and F18).

	Month	DO	Chl	TP	TN	NH_4	NO_X	DIP
		mg/l	µg/l	mg/l	mg/l	mg/l	mg/l	mg/l
Station ELI2 (1999)	Jan.	-0.00	-0.1	-0.0002	-0.001	-0.001	-0.0011	-0.0001
	Feb.	-0.00	-0.3	-0.0003	-0.004	-0.000	-0.0011	0.0000
	Mar.	-0.01	-0.4	-0.0002	-0.002	0.000	0.0006	0.0001
	Apr.	0.02	-0.3	-0.0003	-0.003	0.000	0.0013	0.0000
	May	0.02	-0.3	-0.0004	-0.005	-0.000	-0.0004	0.0000
	Jun.	0.01	-0.4	-0.0003	-0.007	-0.000	-0.0007	0.0000
	Jul.	0.00	-0.6	-0.0004	-0.011	0.000	-0.0018	0.0000
	Aug.	-0.01	-0.4	0.0001	-0.006	0.002	-0.0018	0.0003
	Sep.	-0.02	-0.2	0.0004	0.000	0.002	0.0004	0.0004
	Oct.	0.04	-0.3	0.0001	-0.003	-0.001	-0.0003	0.0001
	Nov.	0.00	-0.7	-0.0002	-0.005	0.001	0.0000	0.0001
	Dec.	0.00	-0.9	-0.0010	-0.016	-0.001	-0.0032	-0.0001
Detection limits:		**0.1**	**0.5**	**0.003**	**0.01**	**0.005**	**0.001**	**0.0015**

	Month	DO	Chl	TP	TN	NH_4	NO_X	DIP
		mg/l	µg/l	mg/l	mg/l	mg/l	mg/l	mg/l
Station ELI2 (2000)	Jan.	-0.01	-0.1	0.0000	0.001	0.000	-0.0006	-0.0001
	Feb.	-0.01	-0.3	-0.0009	-0.009	-0.002	-0.0041	-0.0003
	Mar.	0.02	-0.6	-0.0007	-0.007	-0.000	-0.0007	0.0000
	Apr.	-0.00	-0.4	-0.0002	-0.003	0.000	0.0001	0.0001
	May	0.04	-0.3	-0.0003	-0.003	0.000	-0.0001	0.0000
	Jun.	0.03	-0.6	-0.0003	-0.009	-0.000	-0.0004	0.0001
	Jul.	0.05	-0.8	-0.0005	-0.015	-0.001	-0.0015	-0.0001
	Aug.	0.04	-0.8	-0.0006	-0.015	-0.001	-0.0049	0.0000
	Sep.	0.02	-0.8	0.0002	-0.005	0.001	-0.0007	0.0005
	Oct.	0.00	-0.8	0.0001	-0.006	0.001	0.0005	0.0004
	Nov.	-0.04	-1.0	-0.0002	-0.011	0.002	0.0015	0.0004
	Dec.	-0.03	-0.4	-0.0004	-0.008	0.000	-0.0013	0.0001
Detection limits:		**0.1**	**0.5**	**0.003**	**0.01**	**0.005**	**0.001**	**0.0015**

	Month	DO	Chl	TP	TN	NH_4	NO_X	DIP
		mg/l	µg/l	mg/l	mg/l	mg/l	mg/l	mg/l
Station ELI2 (2001)	Jan.	-0.01	-0.1	-0.0003	-0.001	-0.001	-0.0015	-0.0003
	Feb.	-0.01	-0.4	-0.0013	-0.009	-0.002	-0.0042	-0.0005
	Mar.	-0.01	-0.9	-0.0007	-0.008	0.001	-0.0015	0.0002
	Apr.	0.03	-0.5	-0.0006	-0.006	0.000	0.0001	0.0000
	May	0.05	-0.7	-0.0011	-0.014	-0.000	-0.0003	-0.0003
	Jun.	0.07	-1.1	-0.0014	-0.024	-0.001	-0.0014	-0.0003
	Jul.	0.06	-0.6	-0.0005	-0.016	-0.001	-0.0007	-0.0001
	Aug.	0.02	-0.8	-0.0007	-0.025	-0.002	-0.0054	0.0000
	Sep.	0.01	-0.9	-0.0003	-0.018	0.001	-0.0035	0.0003
	Oct.	-0.06	-1.4	-0.0005	-0.018	0.003	0.0024	0.0005
	Nov.	-0.05	-0.8	-0.0002	-0.010	0.002	0.0028	0.0003
	Dec.	-0.01	-0.7	-0.0002	-0.008	0.001	0.0010	0.0003
Detection limits:		**0.1**	**0.5**	**0.003**	**0.01**	**0.005**	**0.001**	**0.0015**

APPENDIX G

Spatial Plots of

Dissolved Oxygen Differences

Between CIEE South Cell Expansion and Base Case

For 30-Day Averages in June, July, August, and September

for 1999, 2000, and 2001

Vertical Average and Surface and Bottom Layers

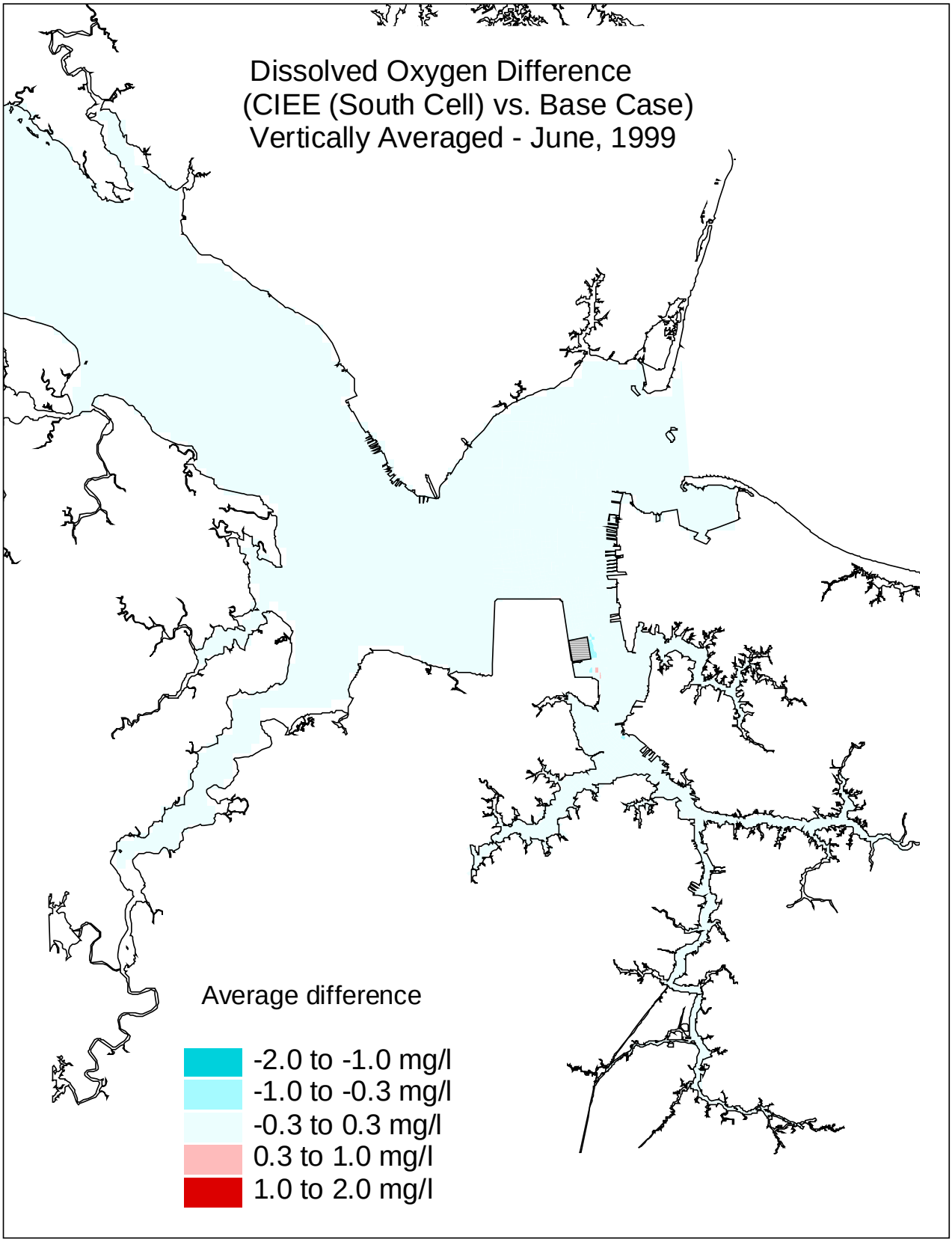

Figure G1. Dissolved oxygen (30-day average, vertically averaged) difference between the CIEE south cell expansion and the base case for June, 1999.

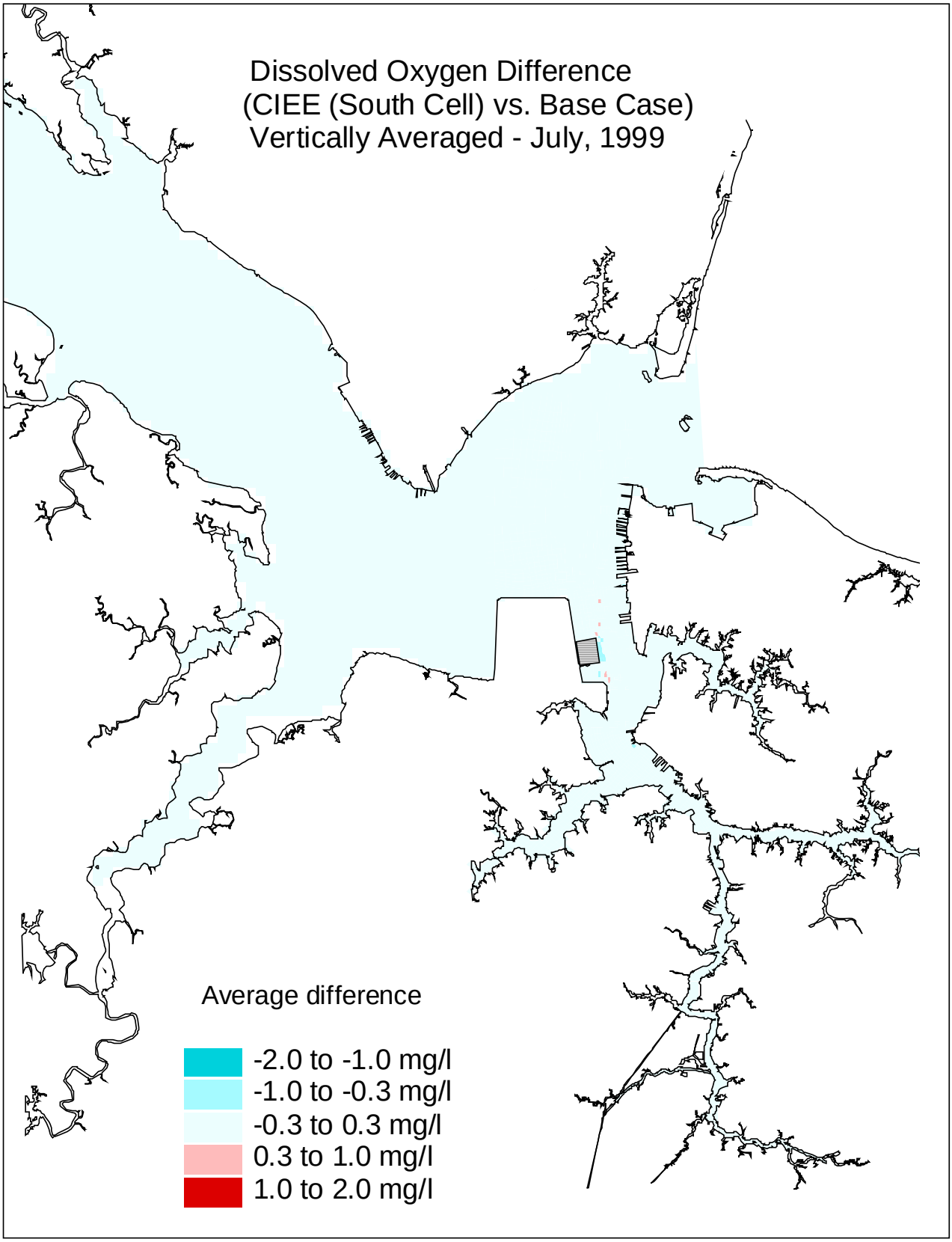

Figure G2. Dissolved oxygen (30-day average, vertically averaged) difference between the CIEE south cell expansion and the base case for July, 1999.

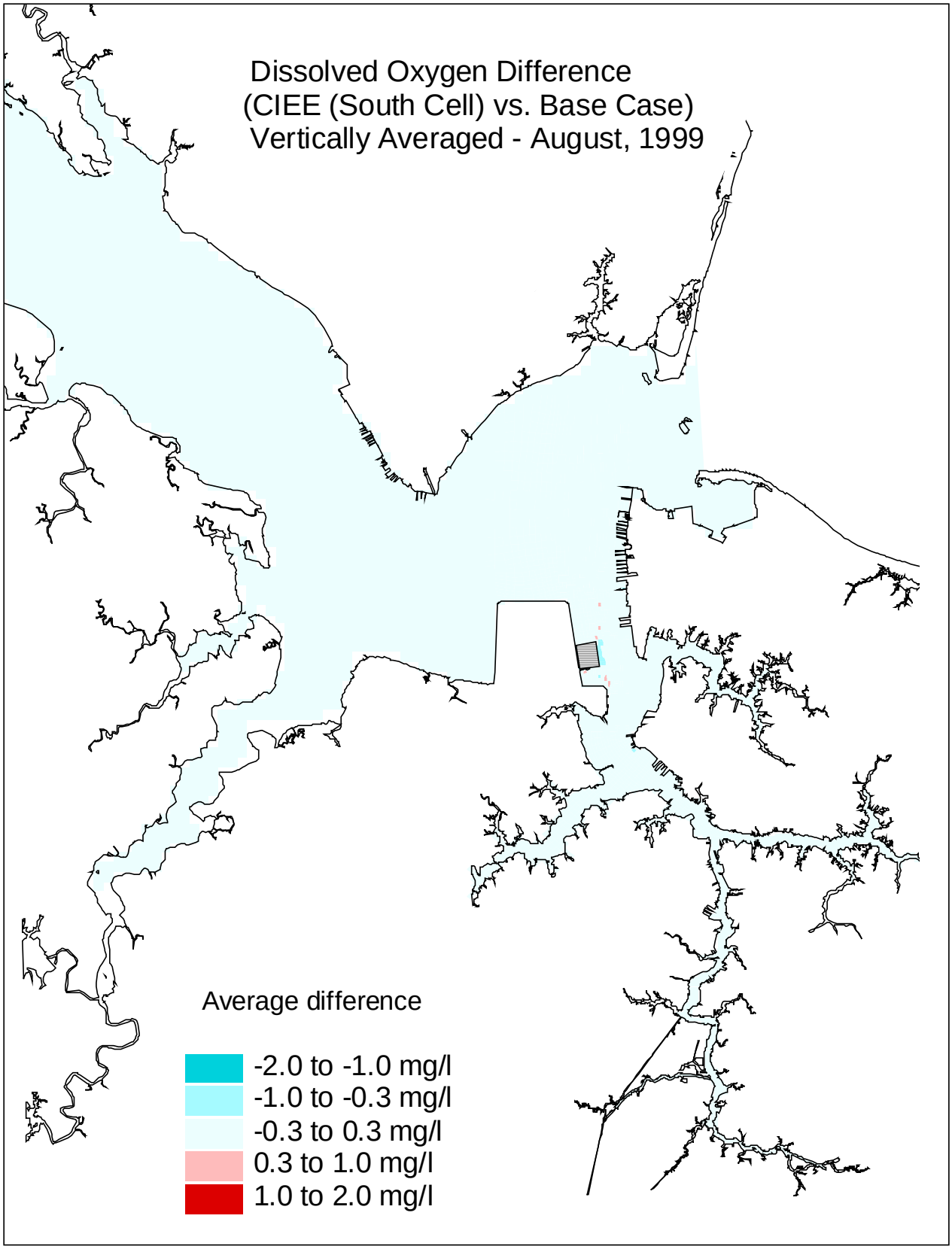

Figure G3. Dissolved oxygen (30-day average, vertically averaged) difference between the CIEE south cell expansion and the base case for August, 1999.

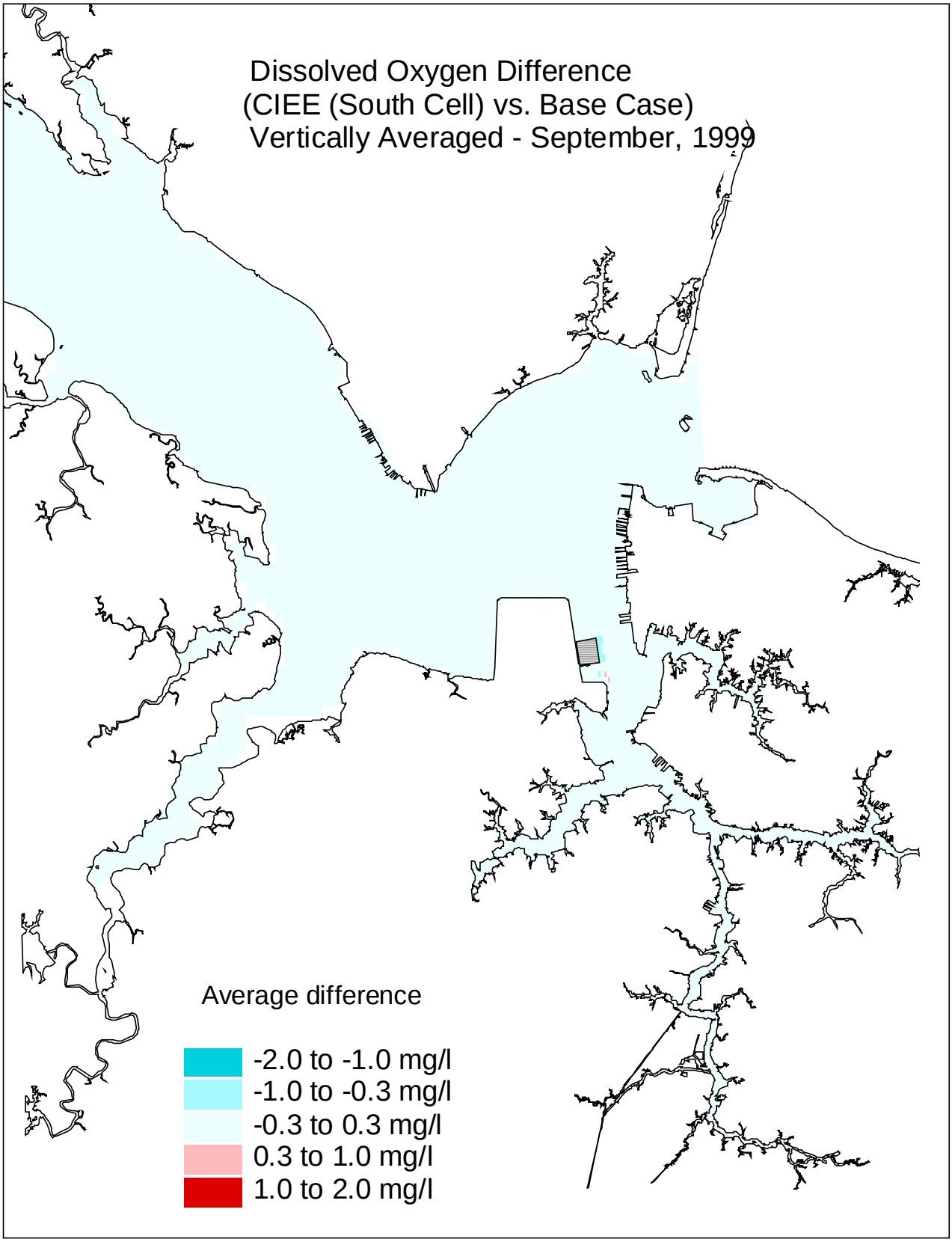

Figure G4. Dissolved oxygen (30-day average, vertically averaged) difference between the CIEE south cell expansion and the base case for September, 1999.

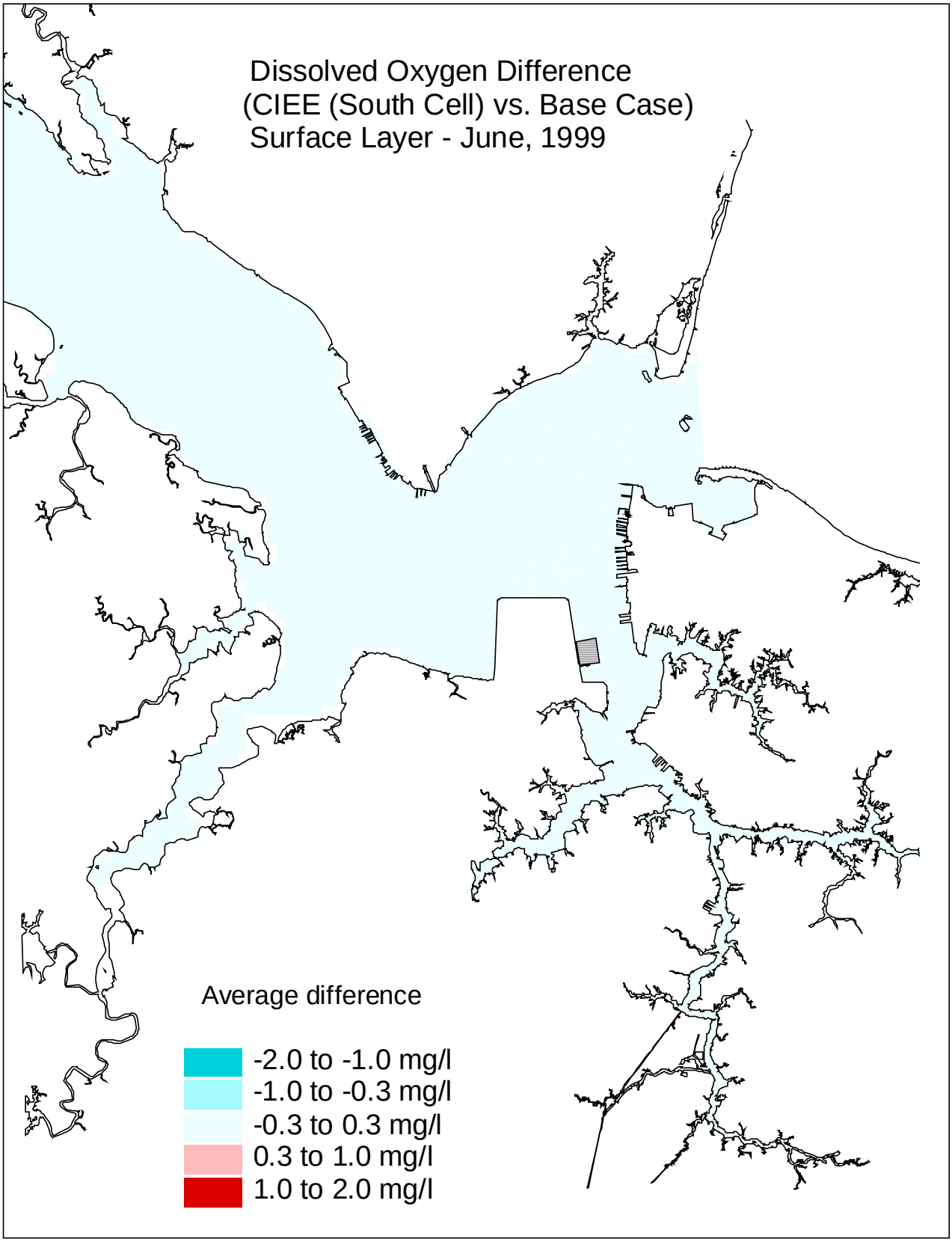

Figure G5. Dissolved oxygen (30-day average, at the surface layer) difference between the CIEE south cell expansion and the base case for June, 1999.

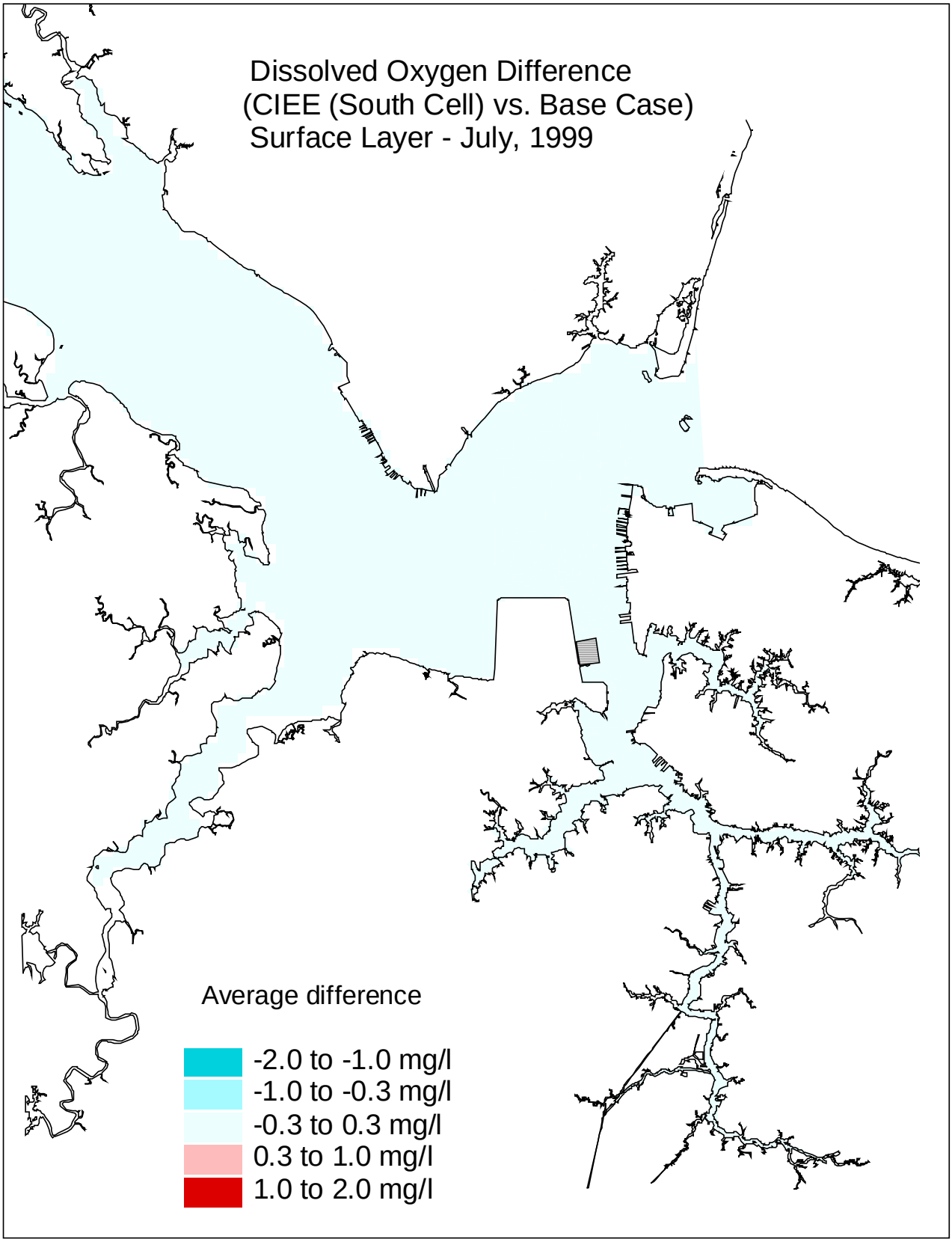

Figure G6. Dissolved oxygen (30-day average, at the surface layer) difference between the CIEE south cell expansion and the base case for July, 1999.

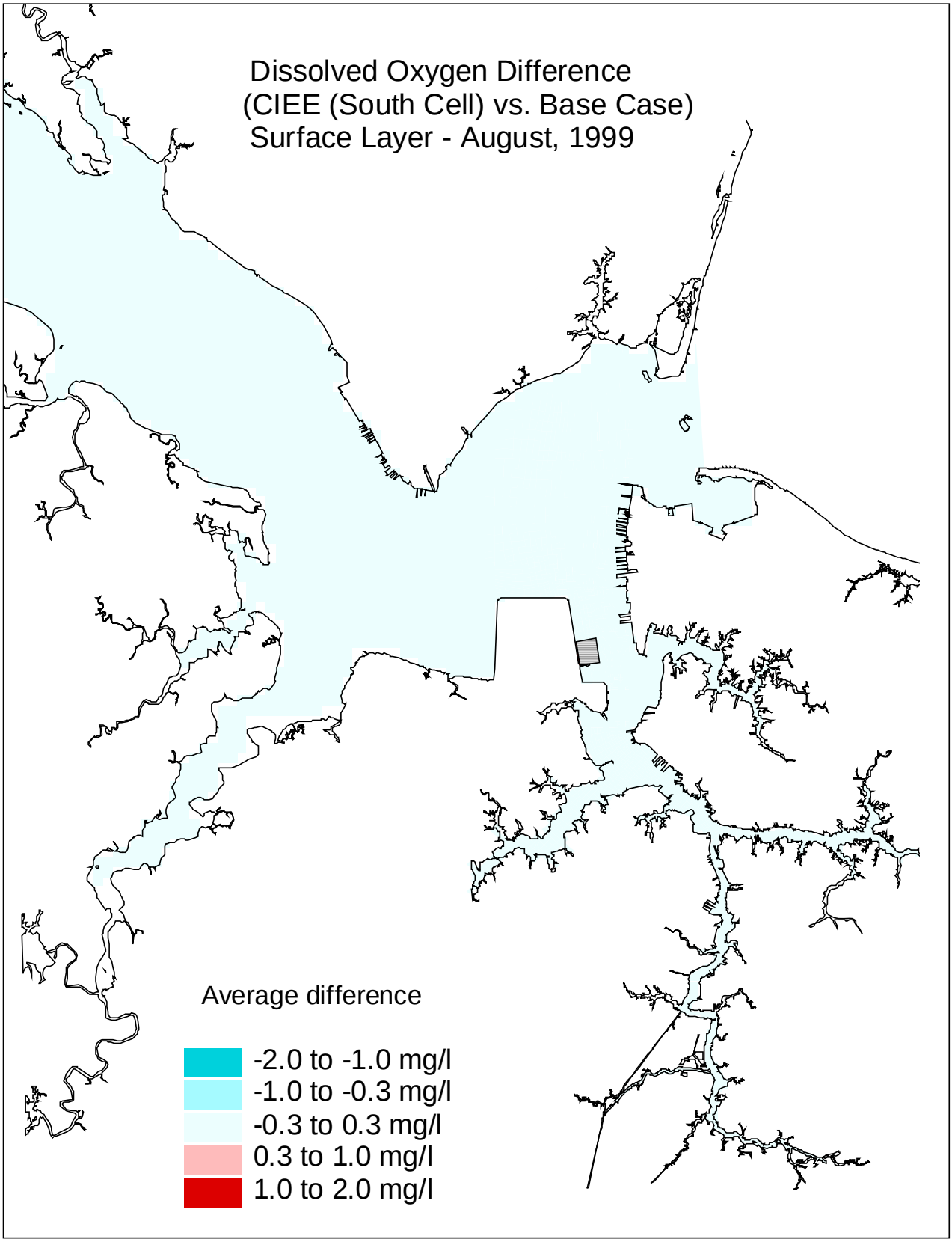

Figure G7. Dissolved oxygen (30-day average, at the surface layer) difference between the CIEE south cell expansion and the base case for August, 1999.

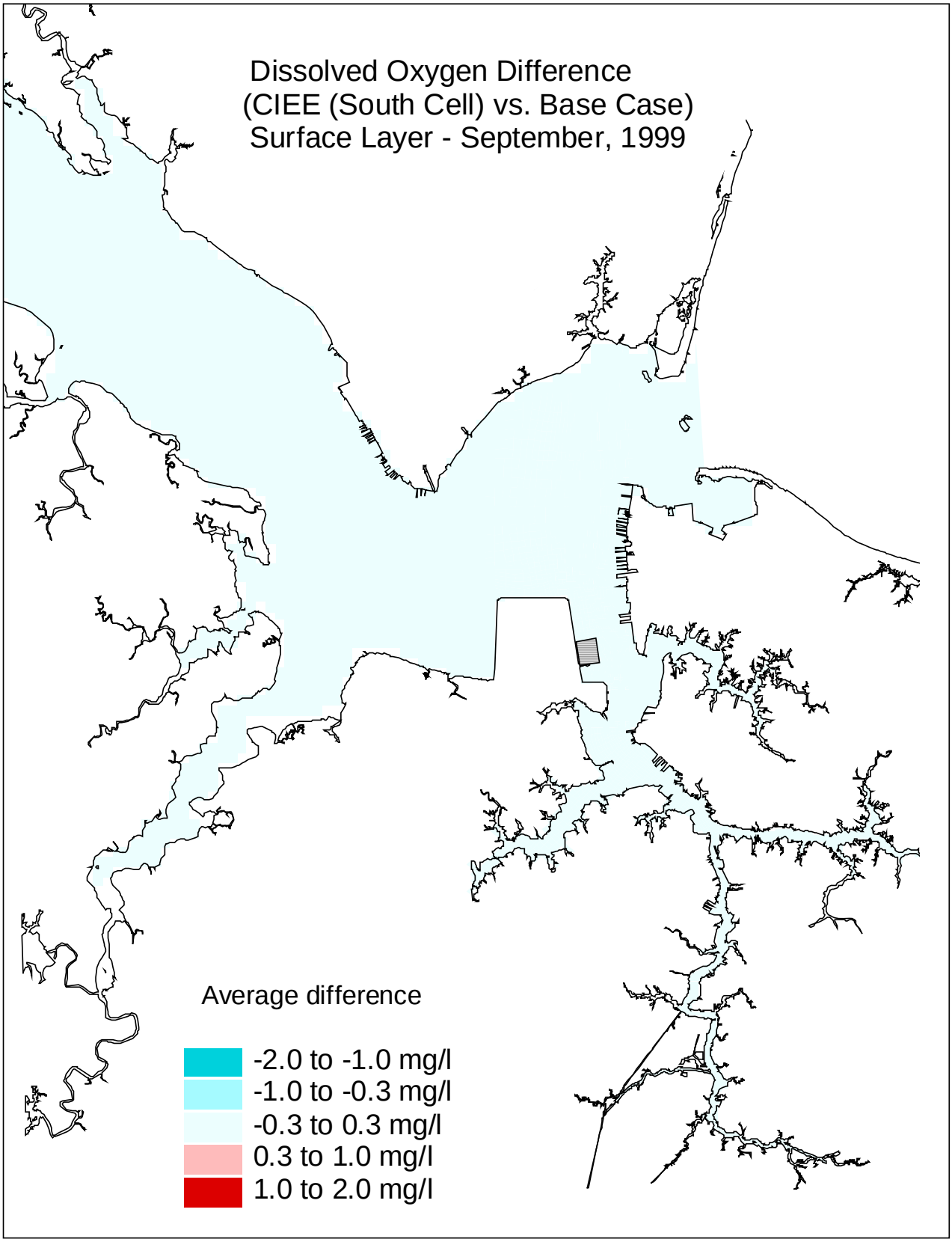

Figure G8. Dissolved oxygen (30-day average, at the surface layer) difference between the CIEE south cell expansion and the base case for September, 1999.

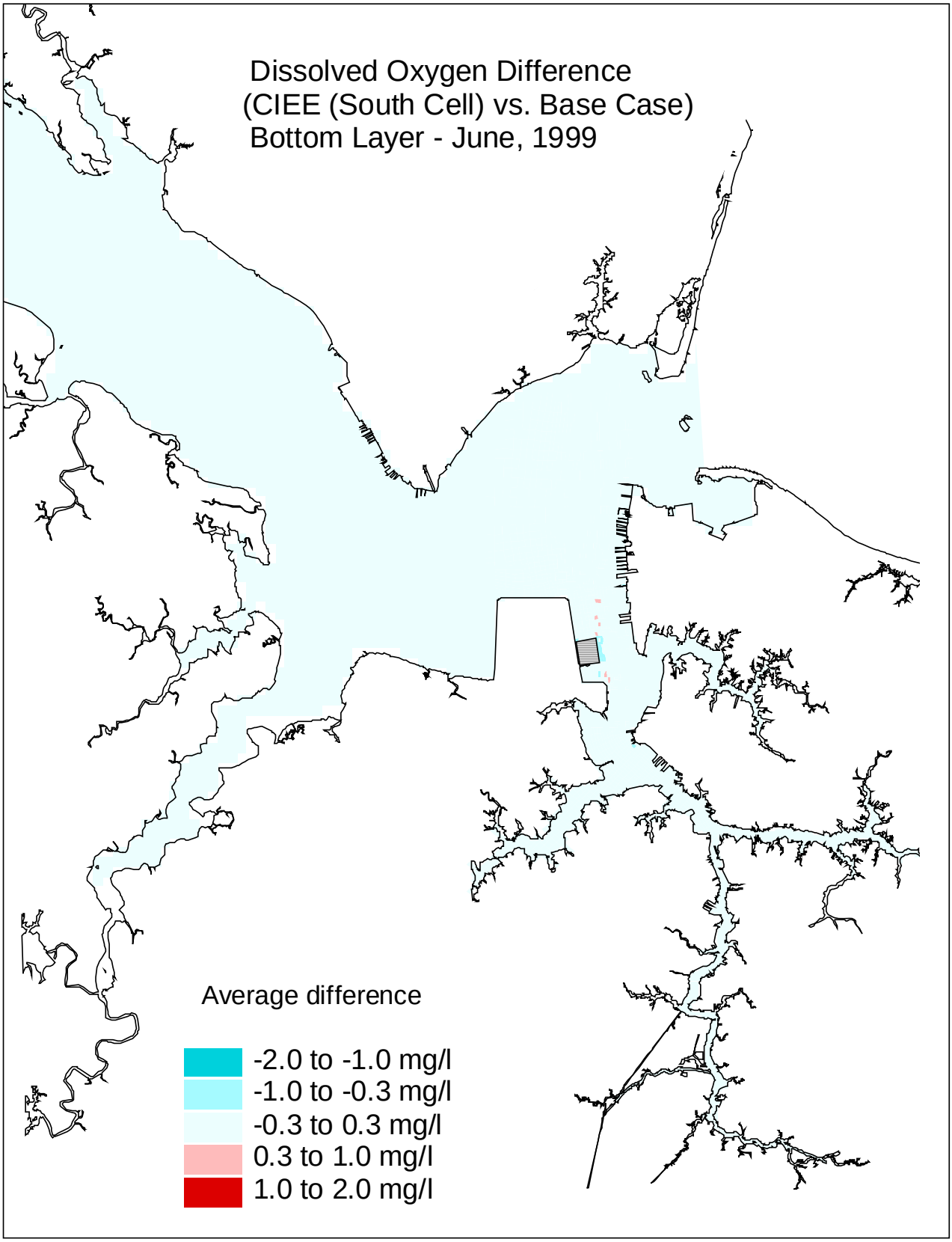

Figure G9. Dissolved oxygen (30-day average, at the bottom layer) difference between the CIEE south cell expansion and the base case for June, 1999.

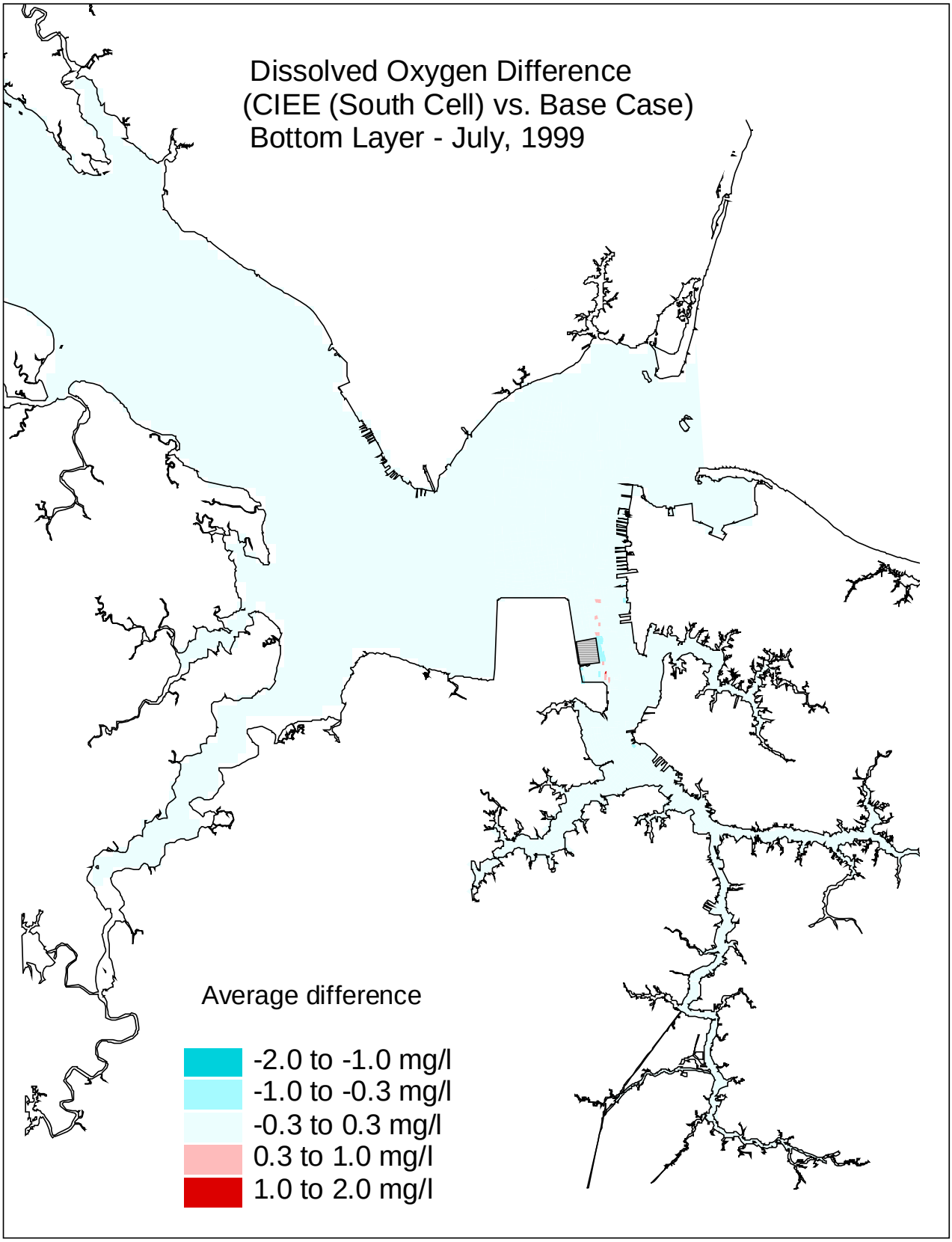

Figure G10. Dissolved oxygen (30-day average, at the bottom layer) difference between the CIEE south cell expansion and the base case for July, 1999.

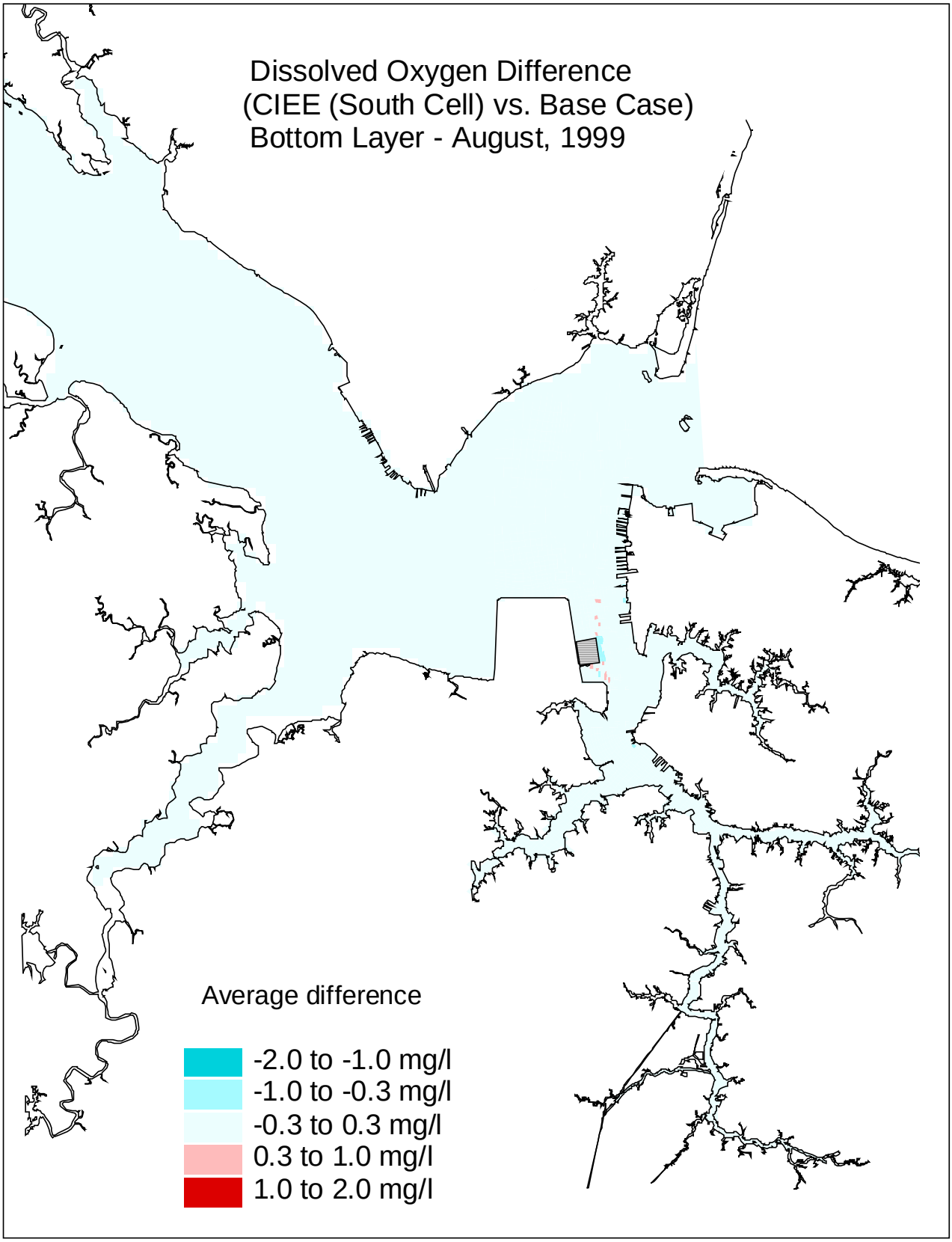

Figure G11. Dissolved oxygen (30-day average, at the bottom layer) difference between the CIEE south cell expansion and the base case for August, 1999.

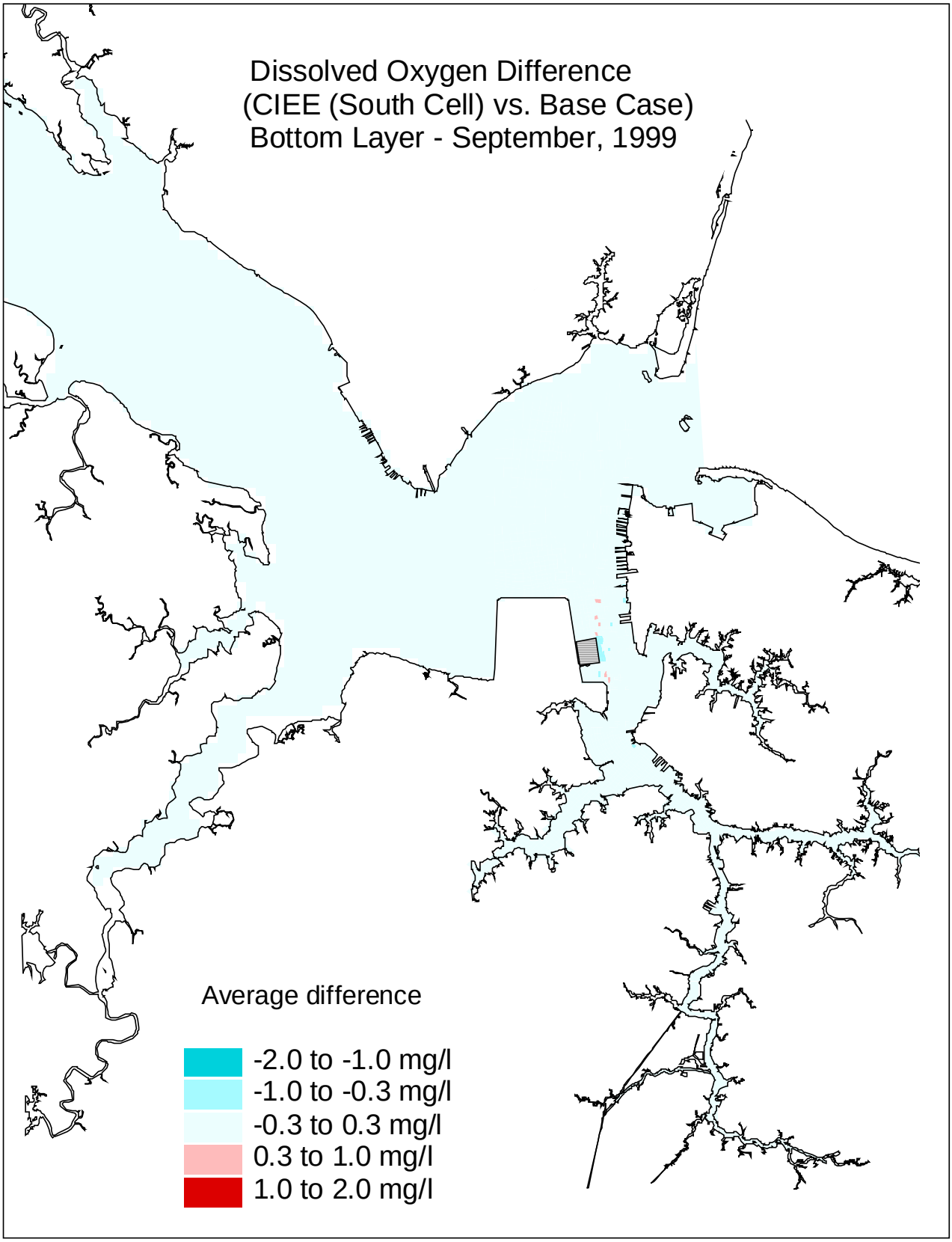

Figure G12. Dissolved oxygen (30-day average, at the bottom layer) difference between the CIEE south cell expansion and the base case for September, 1999.

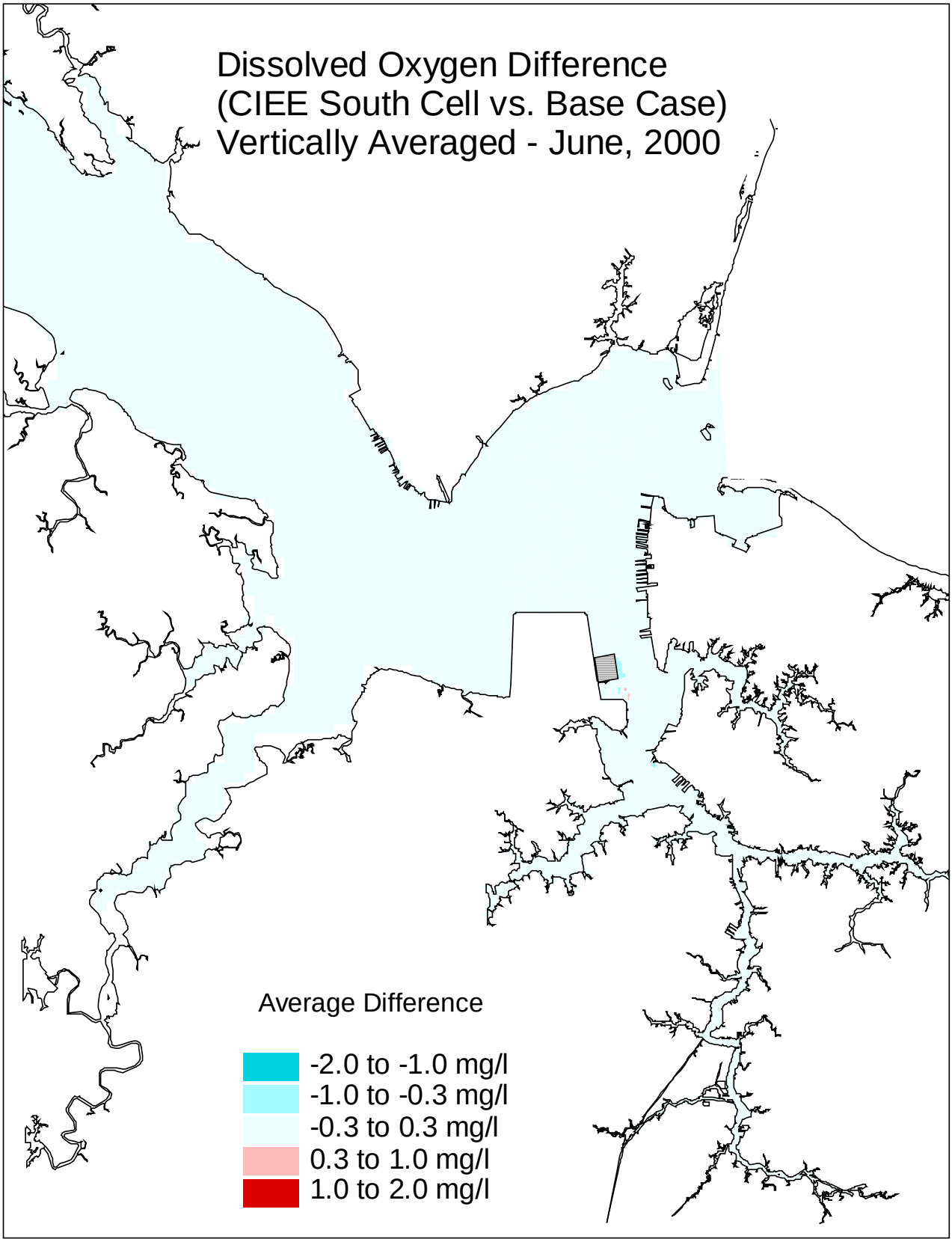

Figure G13. Dissolved oxygen (30-day average, vertically averaged) difference between the CIEE south cell expansion and the base case for June, 2000.

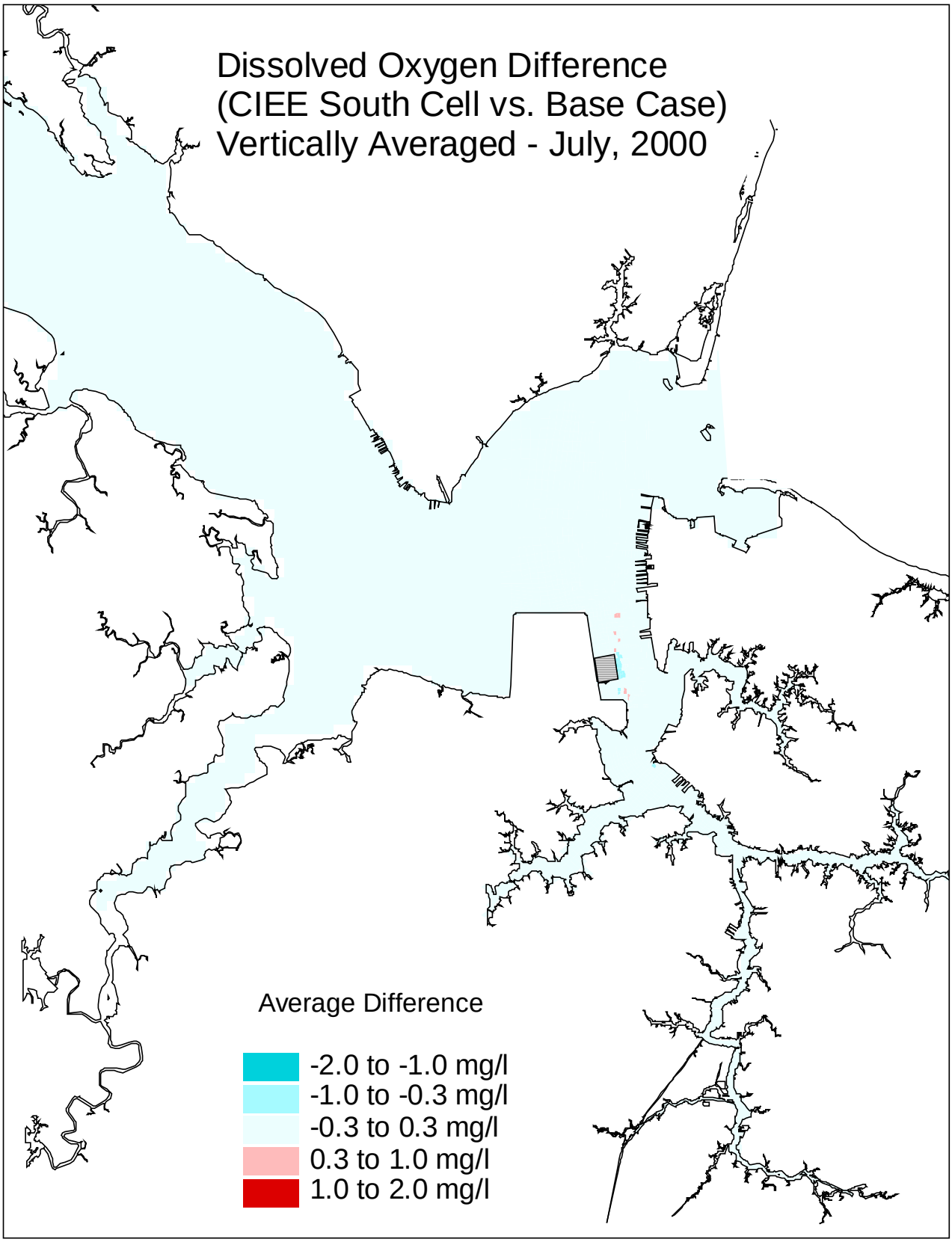

Figure G14. Dissolved oxygen (30-day average, vertically averaged) difference between the CIEE south cell expansion and the base case for July, 2000.

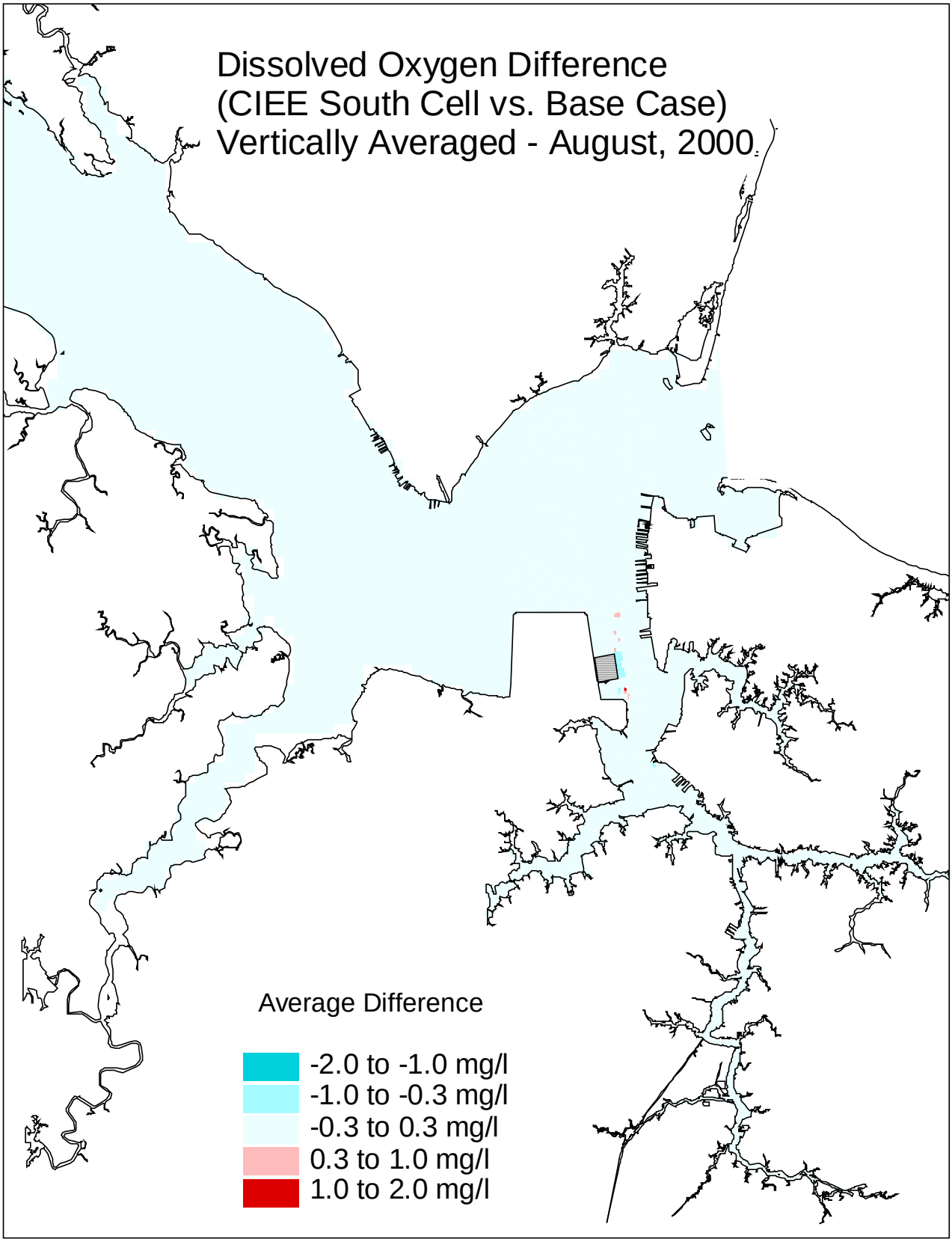

Figure G15. Dissolved oxygen (30-day average, vertically averaged) difference between the CIEE south cell expansion and the base case for August, 2000.

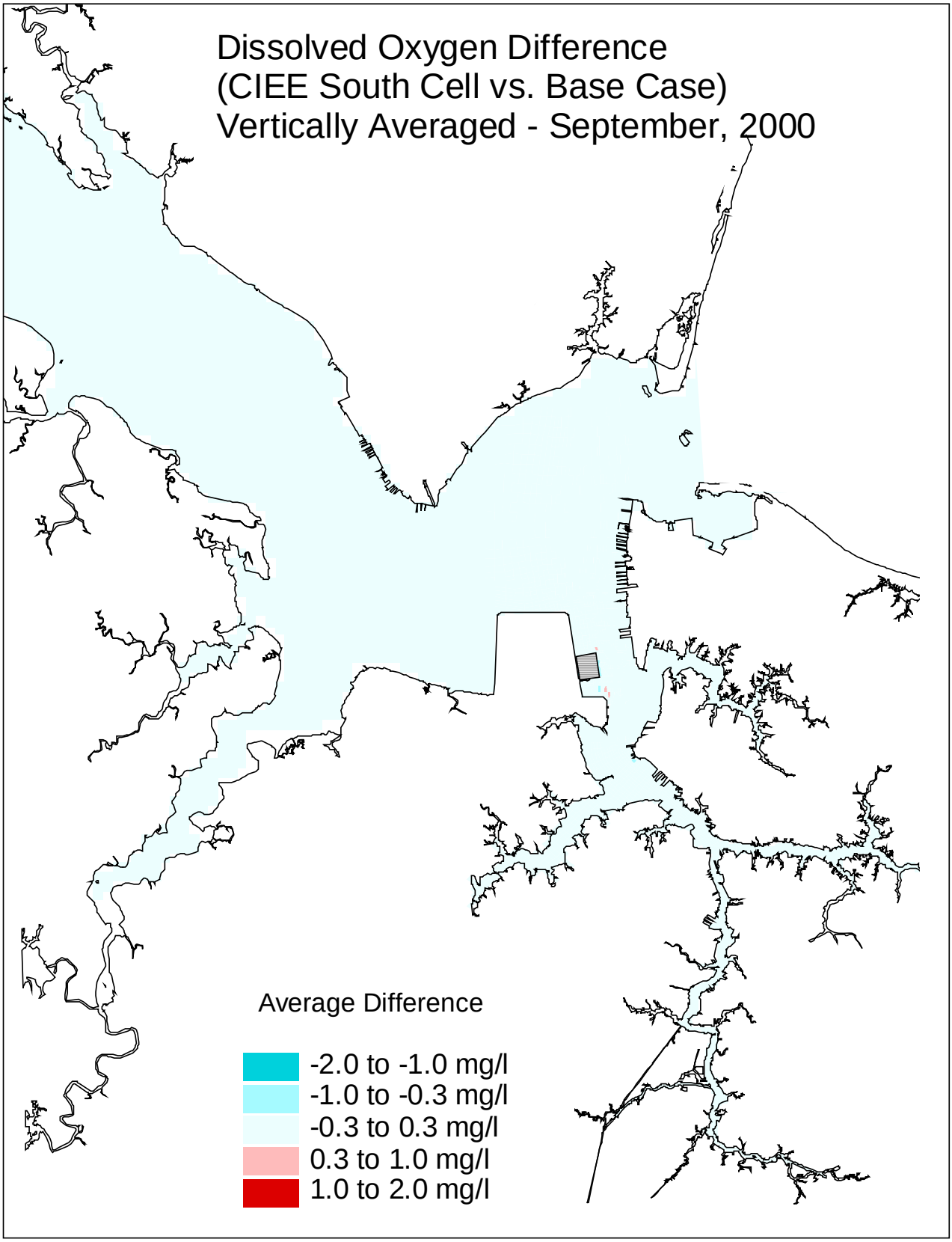

Figure G16. Dissolved oxygen (30-day average, vertically averaged) difference between the CIEE south cell expansion and the base case for September, 2000.

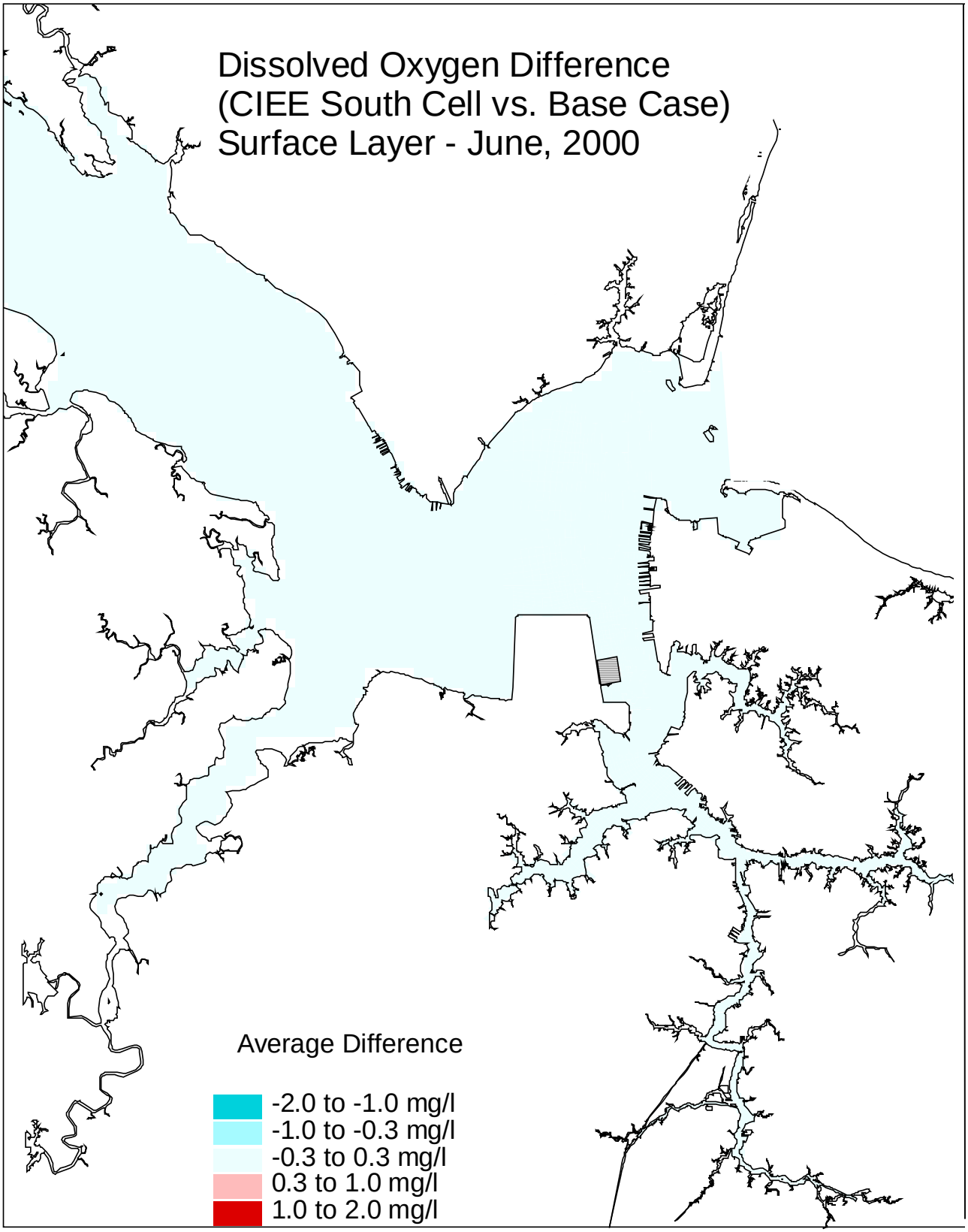

Figure G17. Dissolved oxygen (30-day average, at the surface layer) difference between the CIEE south cell expansion and the base case for June, 2000.

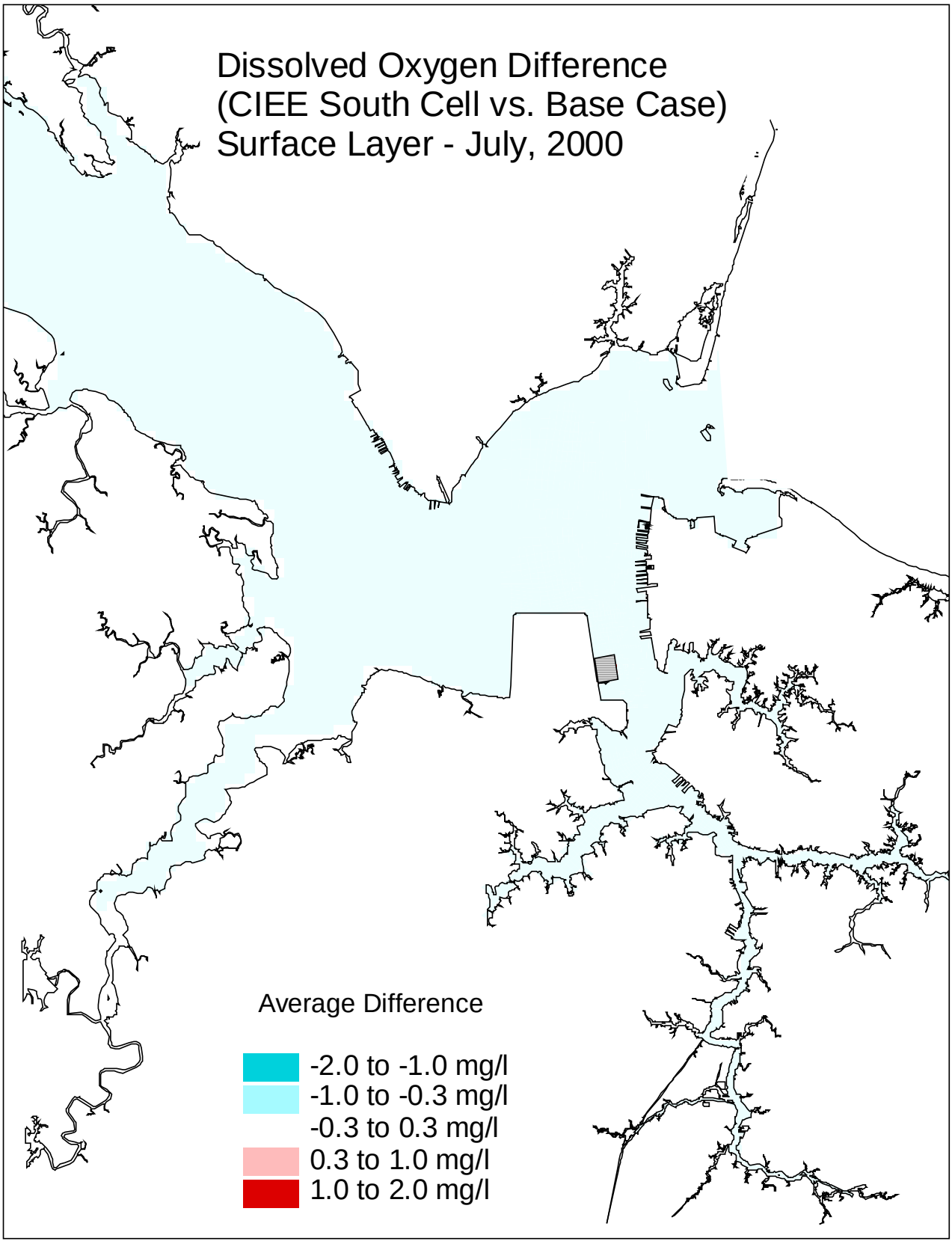

Figure G18. Dissolved oxygen (30-day average, at the surface layer) difference between the CIEE south cell expansion and the base case for July, 2000.

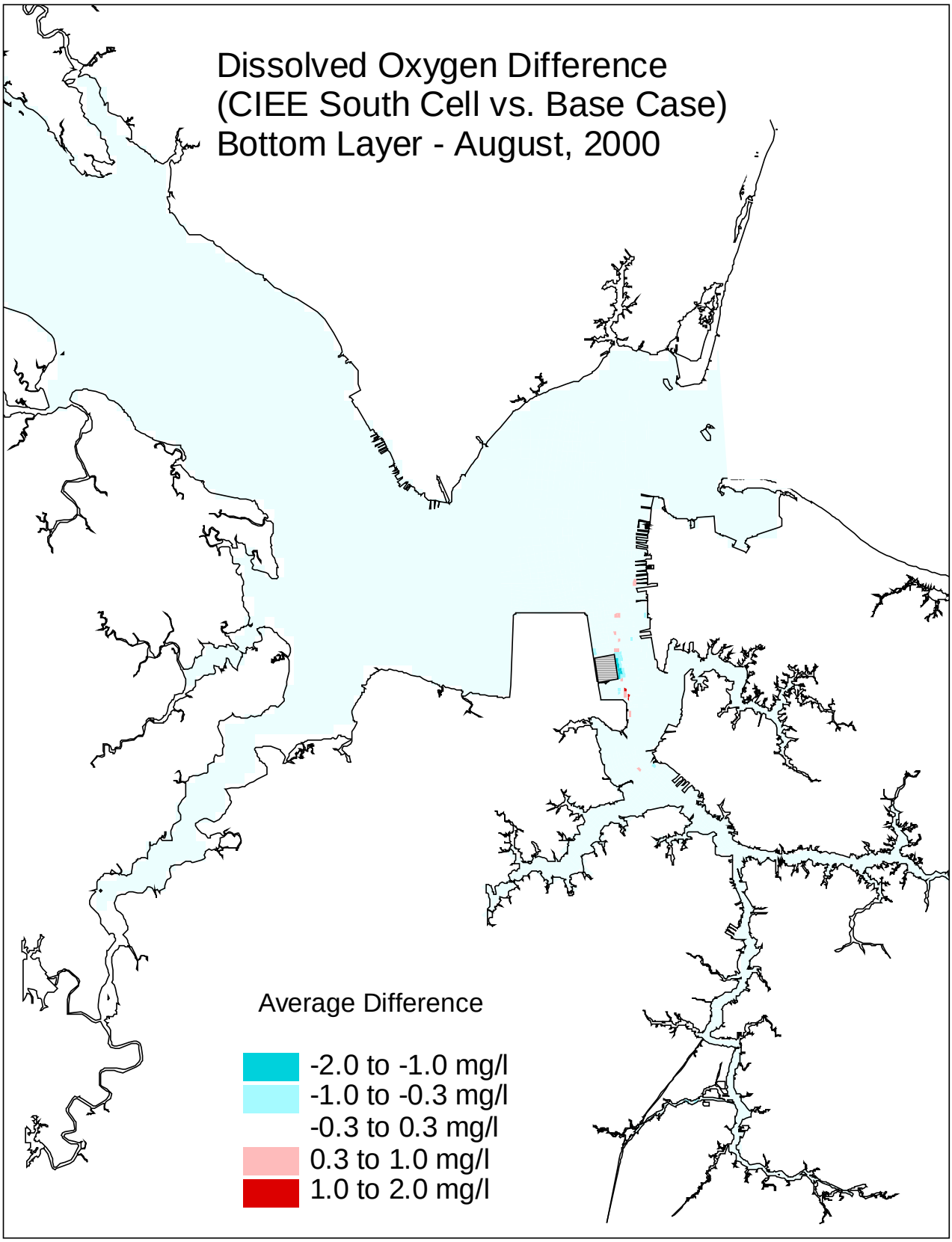

Figure G19. Dissolved oxygen (30-day average, at the surface layer) difference between the CIEE south cell expansion and the base case for August, 2000.

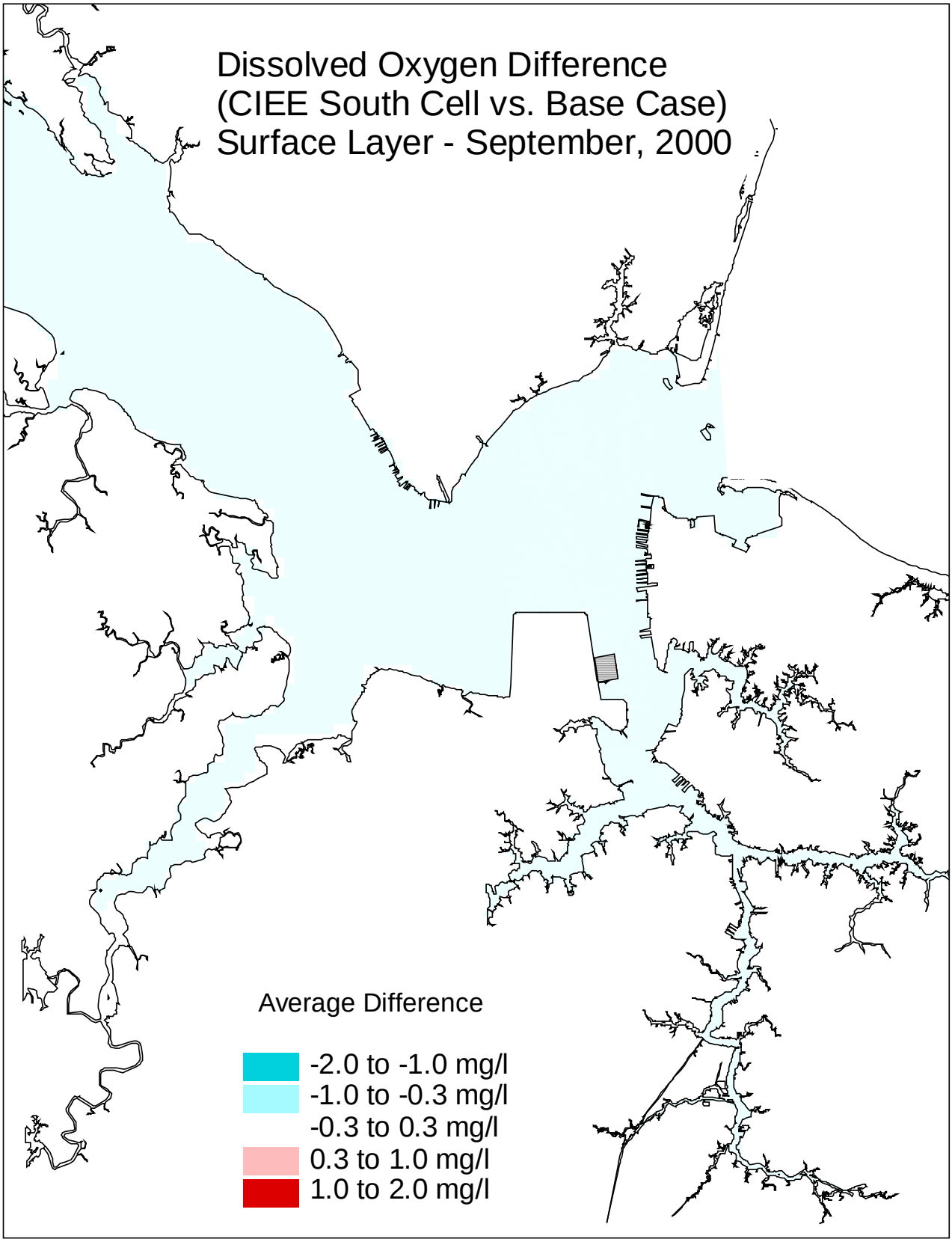

Figure G20. Dissolved oxygen (30-day average, at the surface layer) difference between the CIEE south cell expansion and the base case for September, 2000.

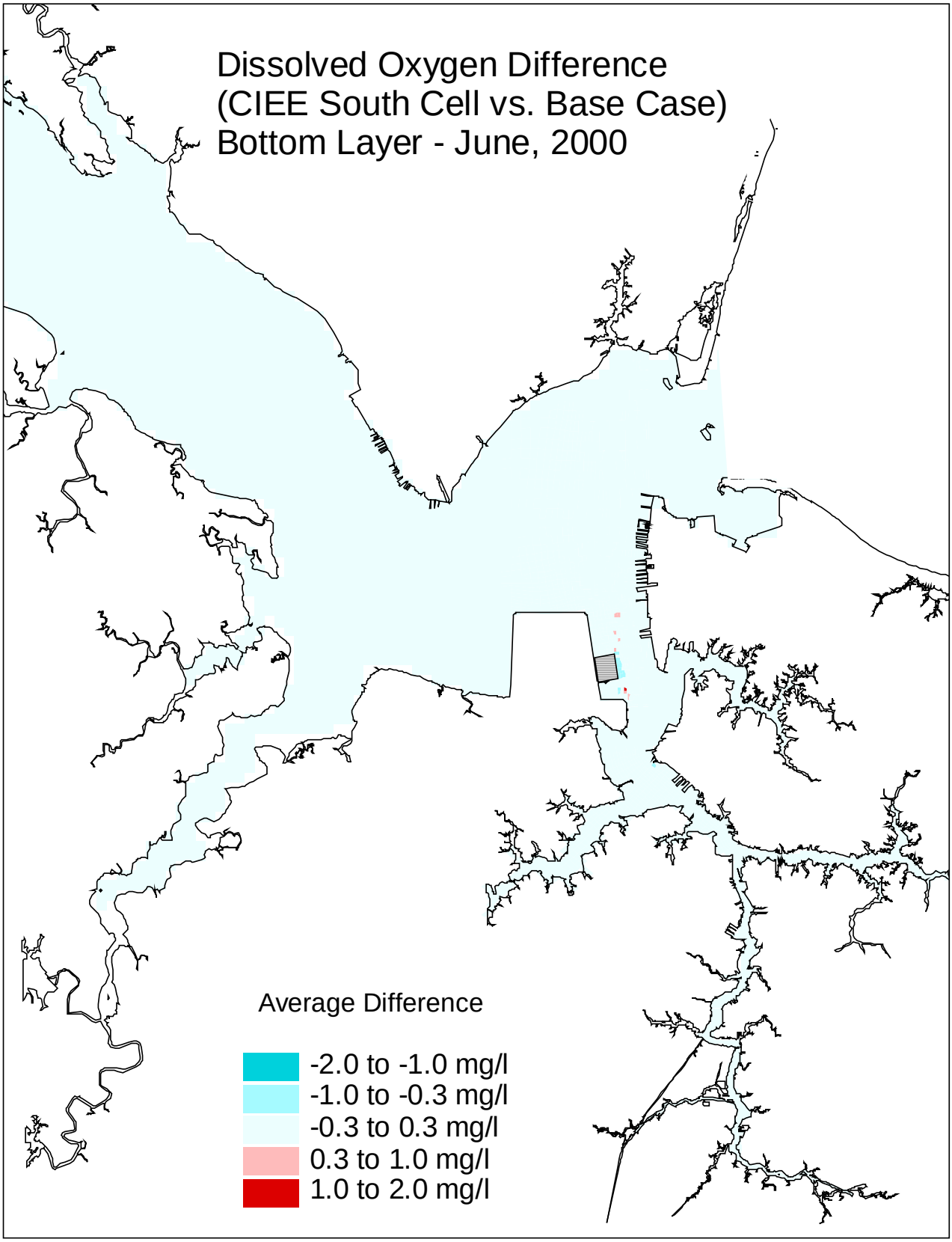

Figure G21. Dissolved oxygen (30-day average, at the bottom layer) difference between the CIEE south cell expansion and the base case for June, 2000.

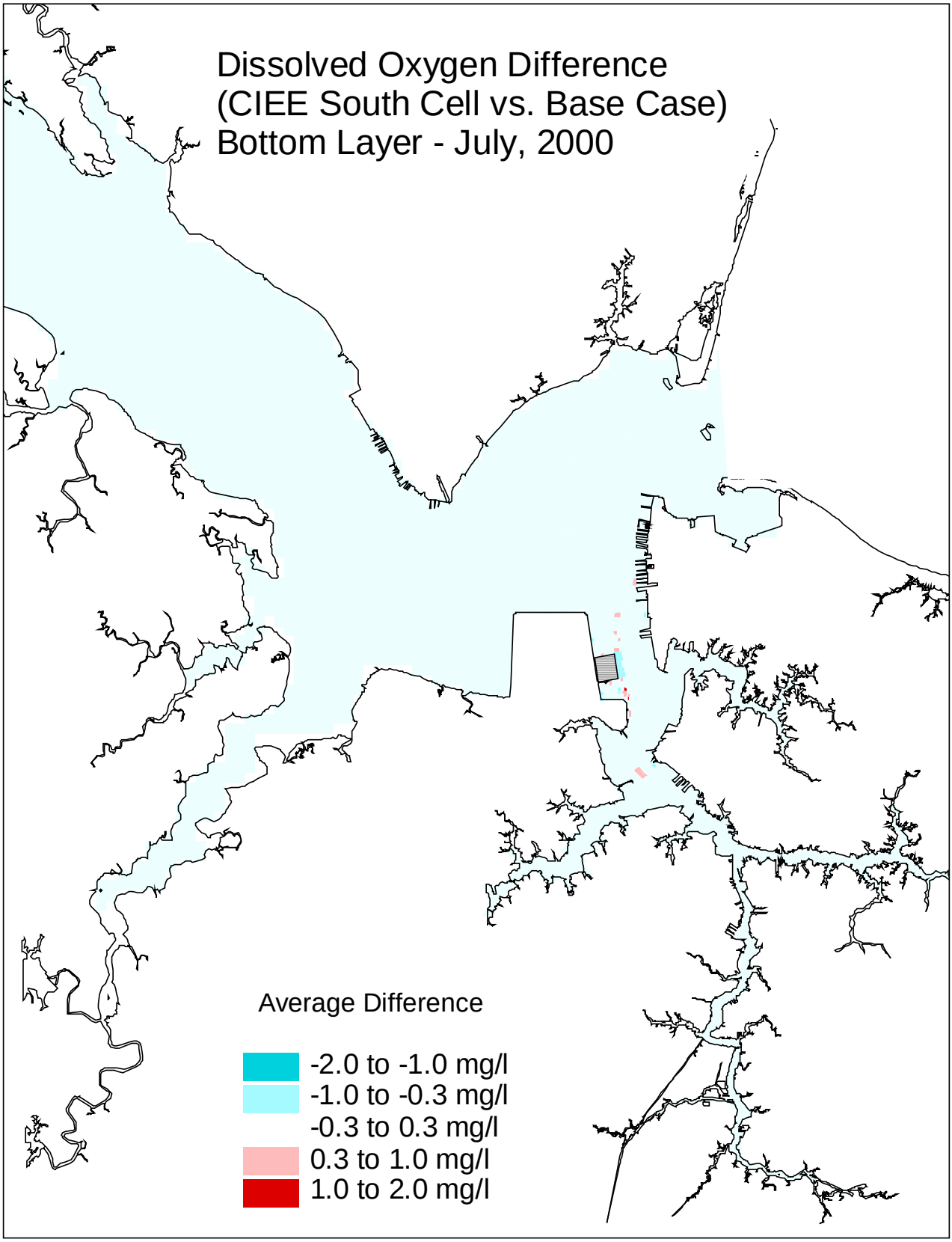

Figure G22. Dissolved oxygen (30-day average, at the bottom layer) difference between the CIEE south cell expansion and the base case for July, 2000.

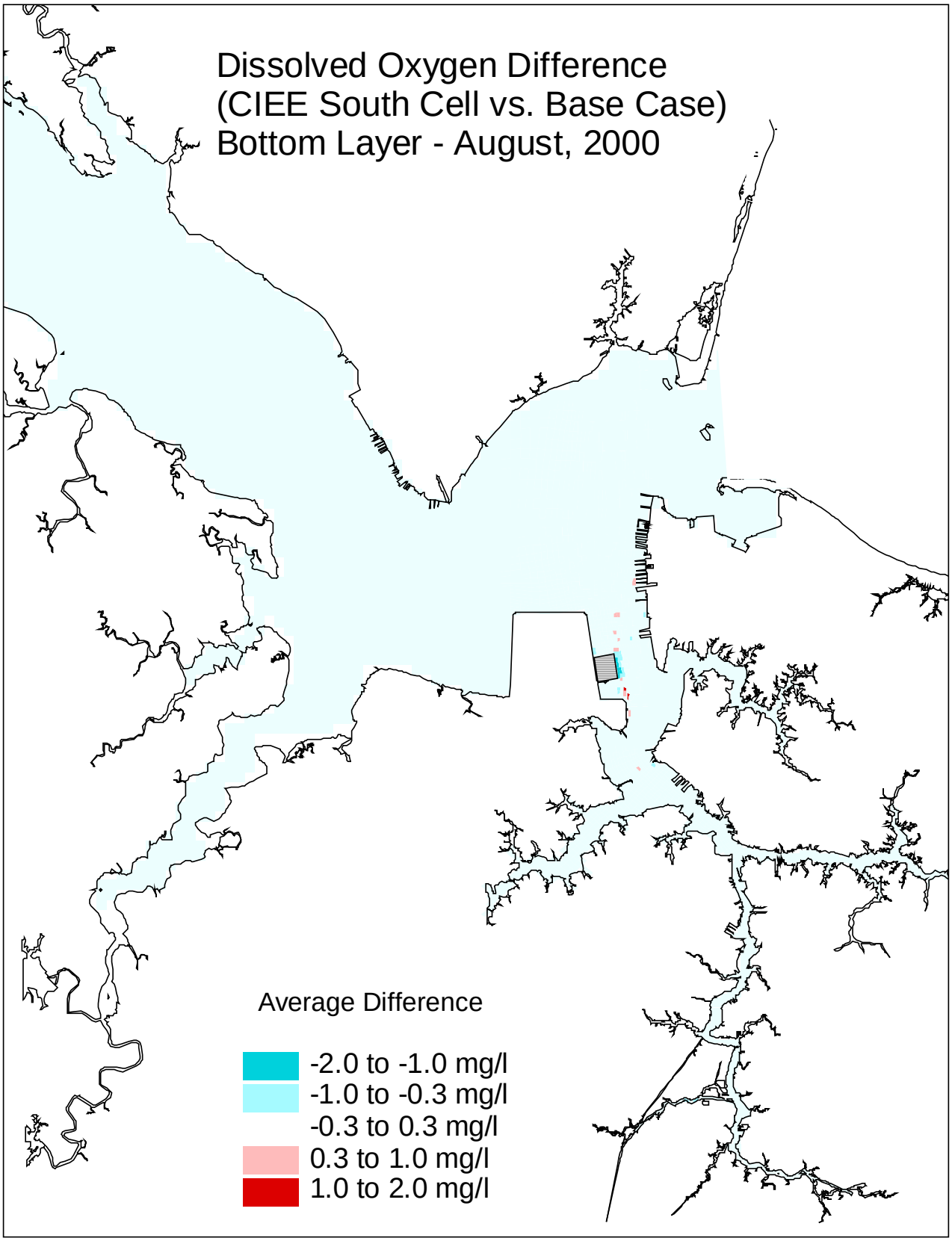

Figure G23. Dissolved oxygen (30-day average, at the bottom layer) difference between the CIEE south cell expansion and the base case for August, 2000.

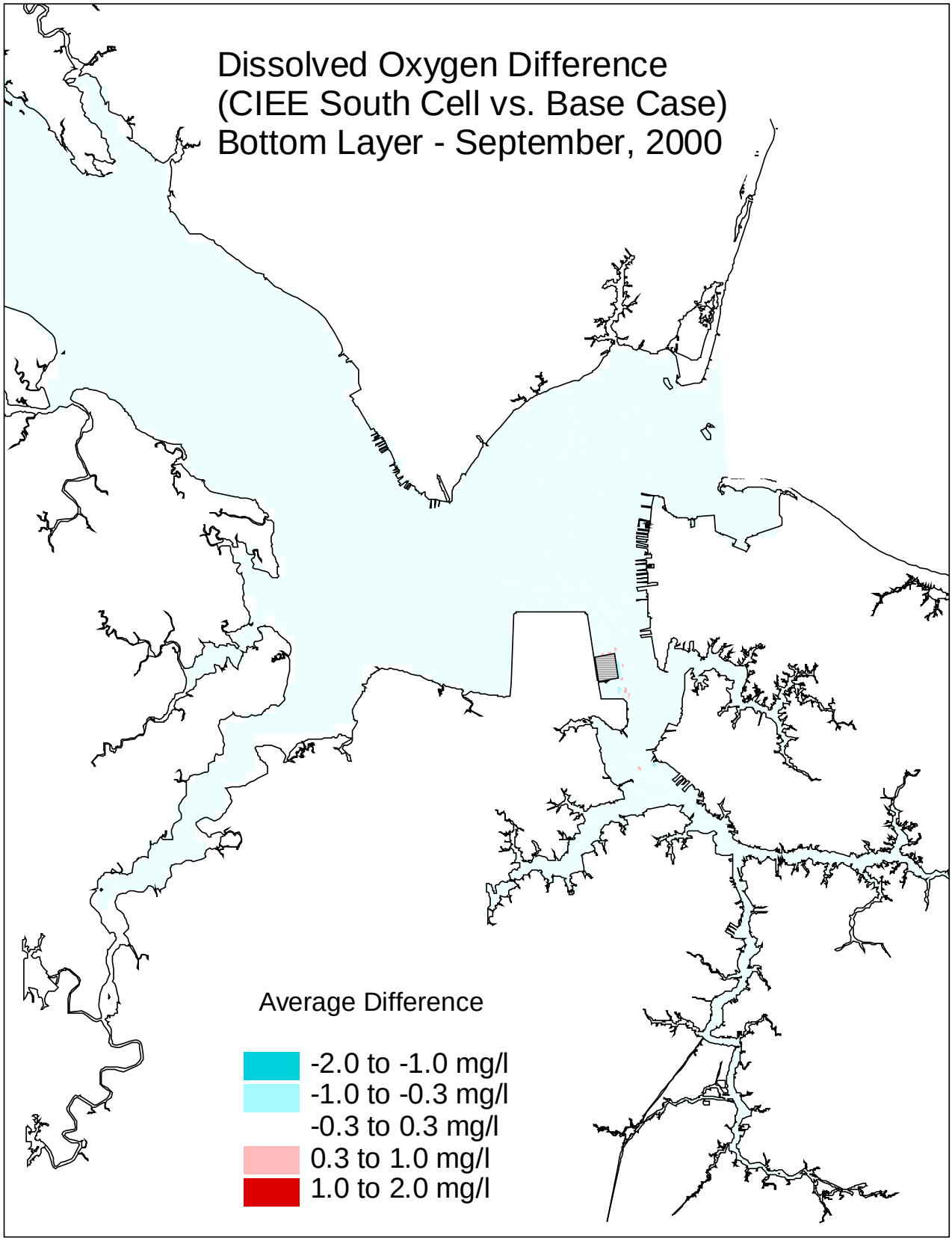

Figure G24. Dissolved oxygen (30-day average, at the bottom layer) difference between the CIEE south cell expansion and the base case for September, 2000.

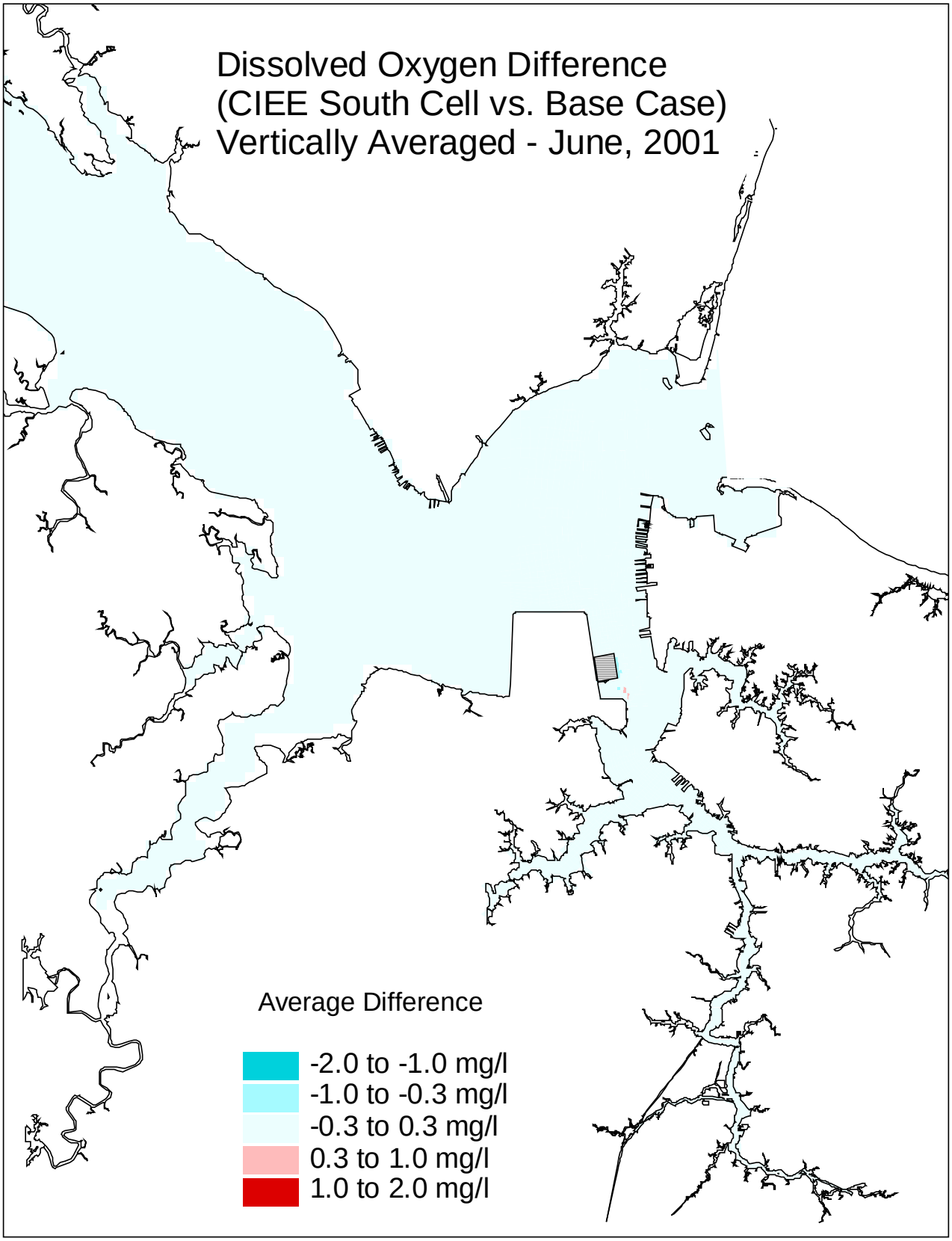

Figure G25. Dissolved oxygen (30-day average, vertically averaged) difference between the CIEE south cell expansion and the base case for June, 2001.

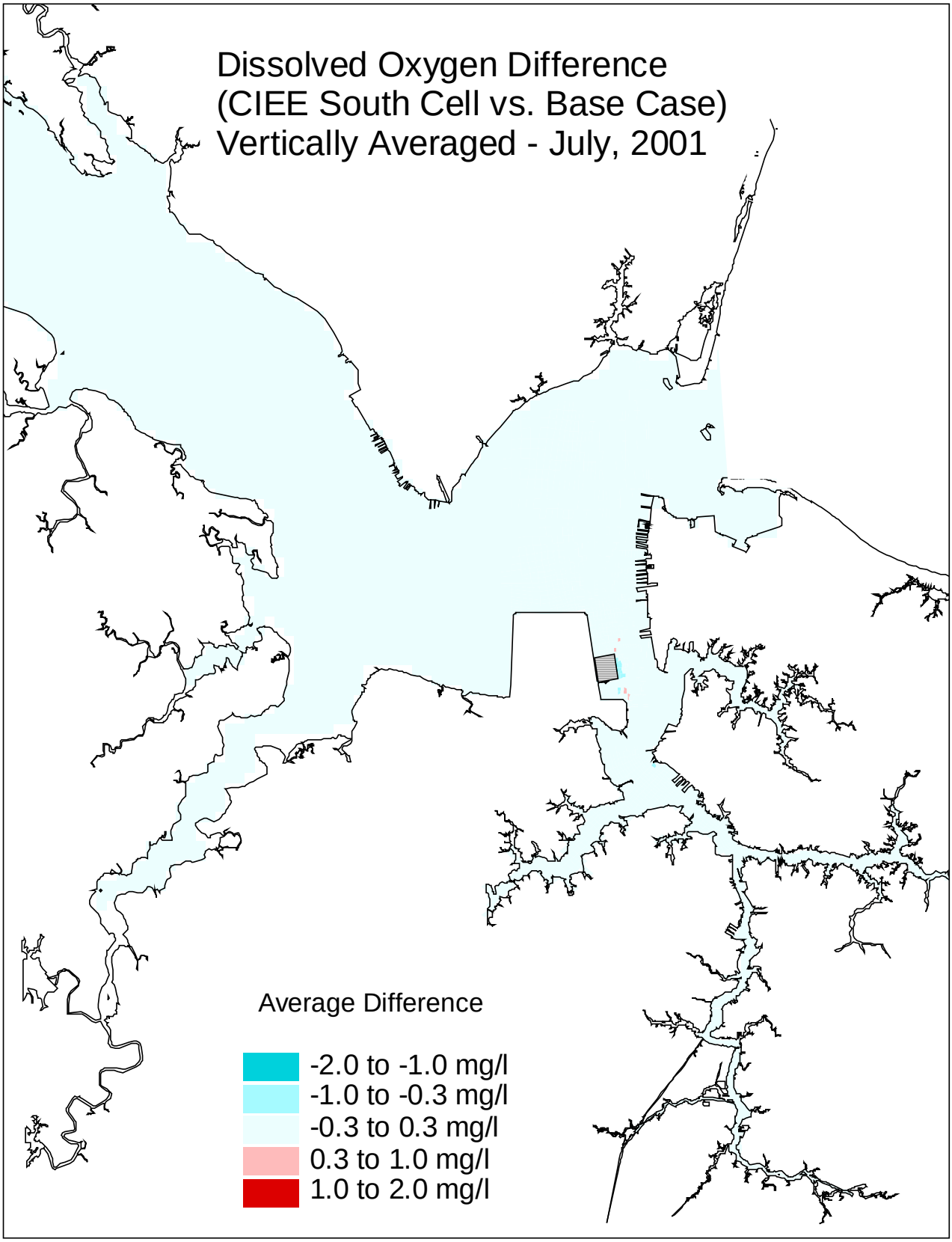

Figure G26. Dissolved oxygen (30-day average, vertically averaged) difference between the CIEE south cell expansion and the base case for July, 2001.

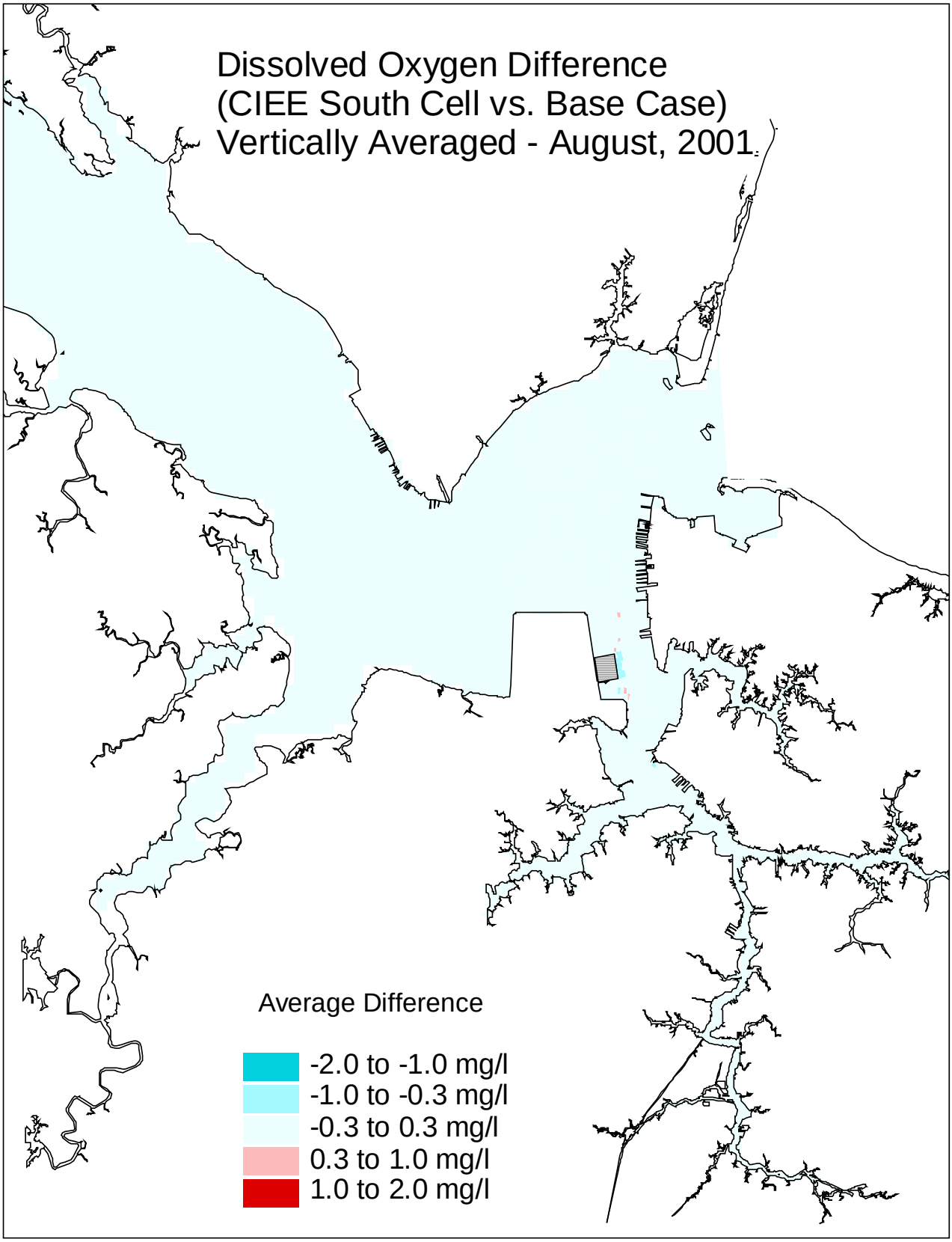

Figure G27. Dissolved oxygen (30-day average, vertically averaged) difference between the CIEE south cell expansion and the base case for August, 2001.

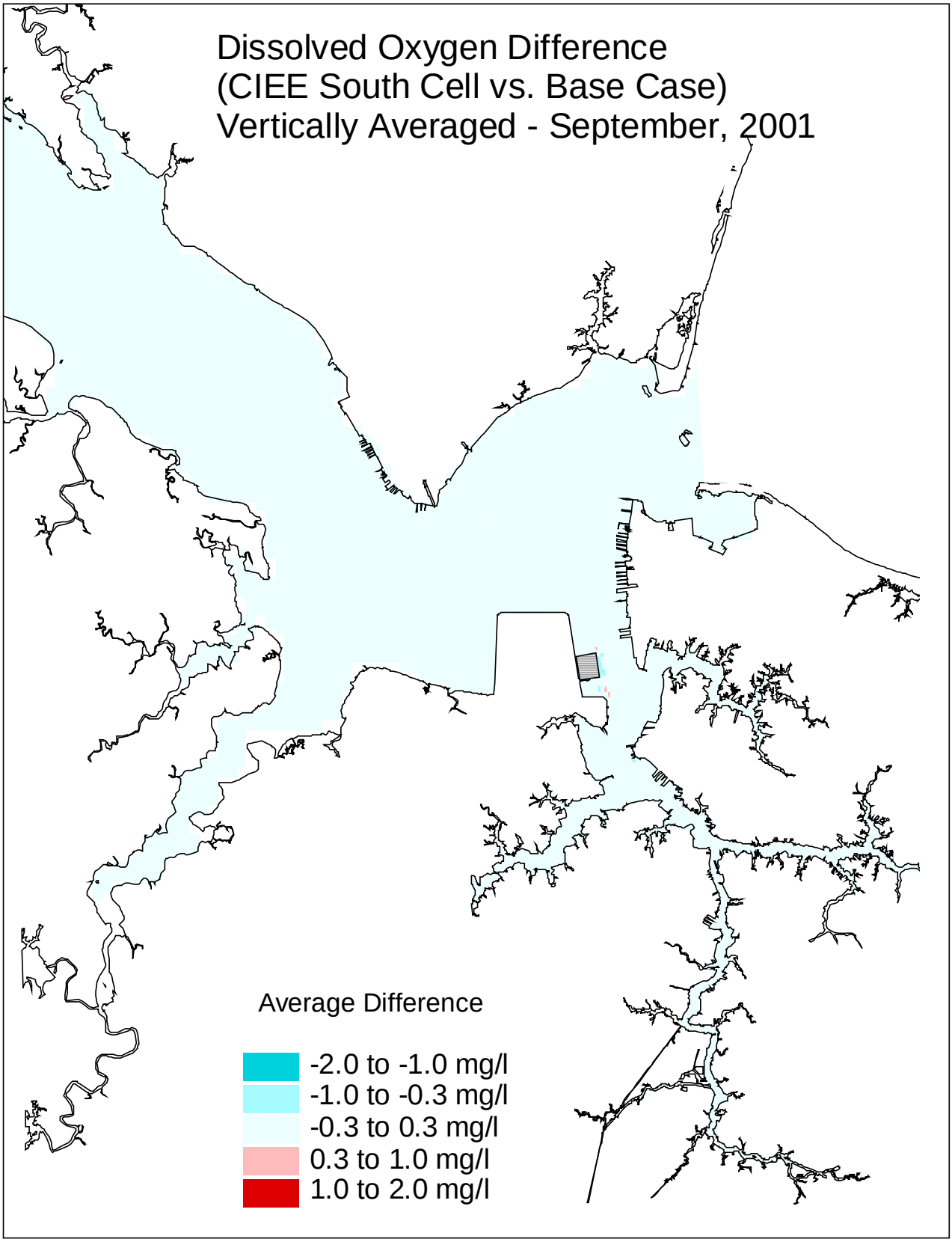

Figure G28. Dissolved oxygen (30-day average, vertically averaged) difference between the CIEE south cell expansion and the base case for September, 2001.

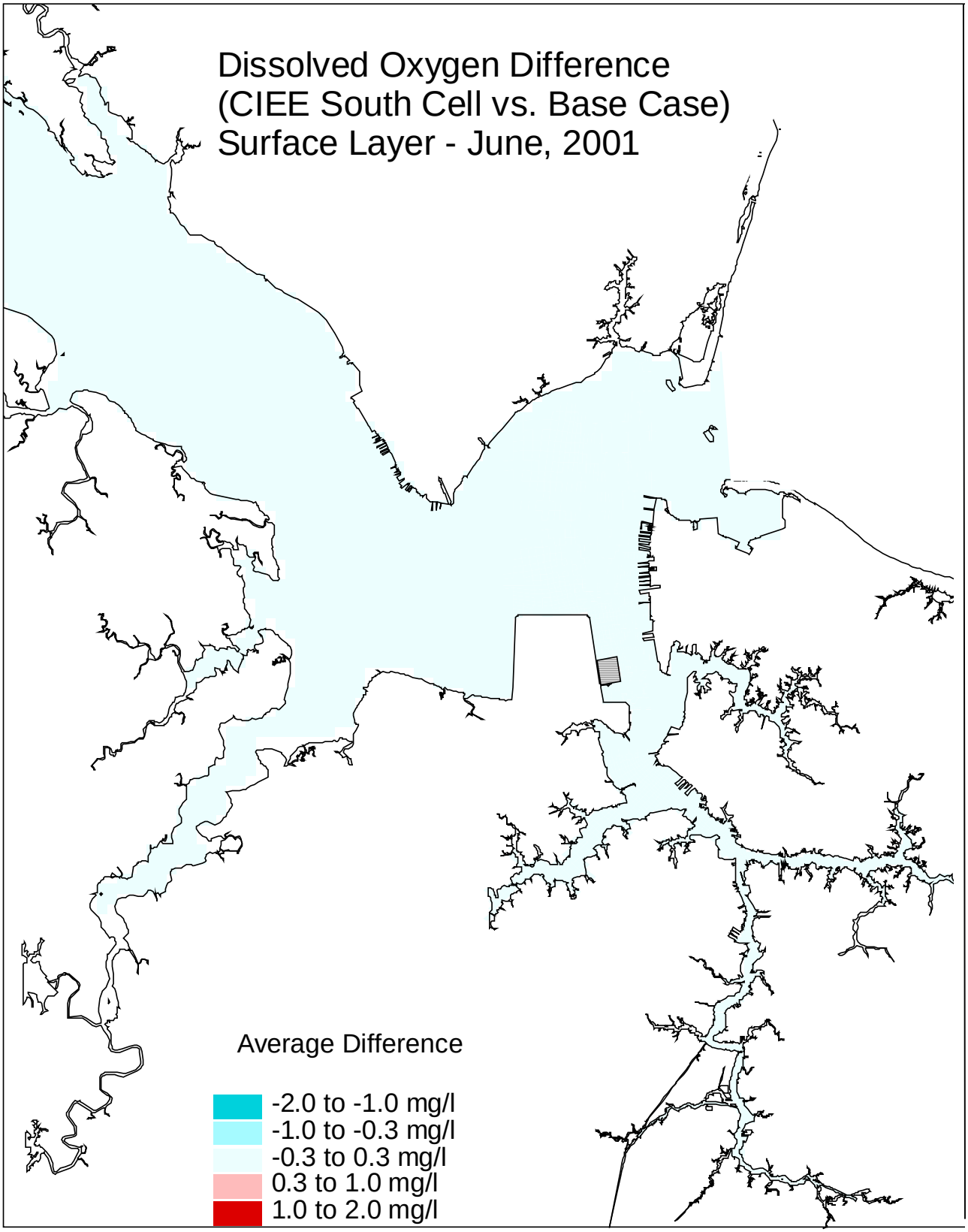

Figure G29. Dissolved oxygen (30-day average, at the surface layer) difference between the CIEE south cell expansion and the base case for June, 2001.

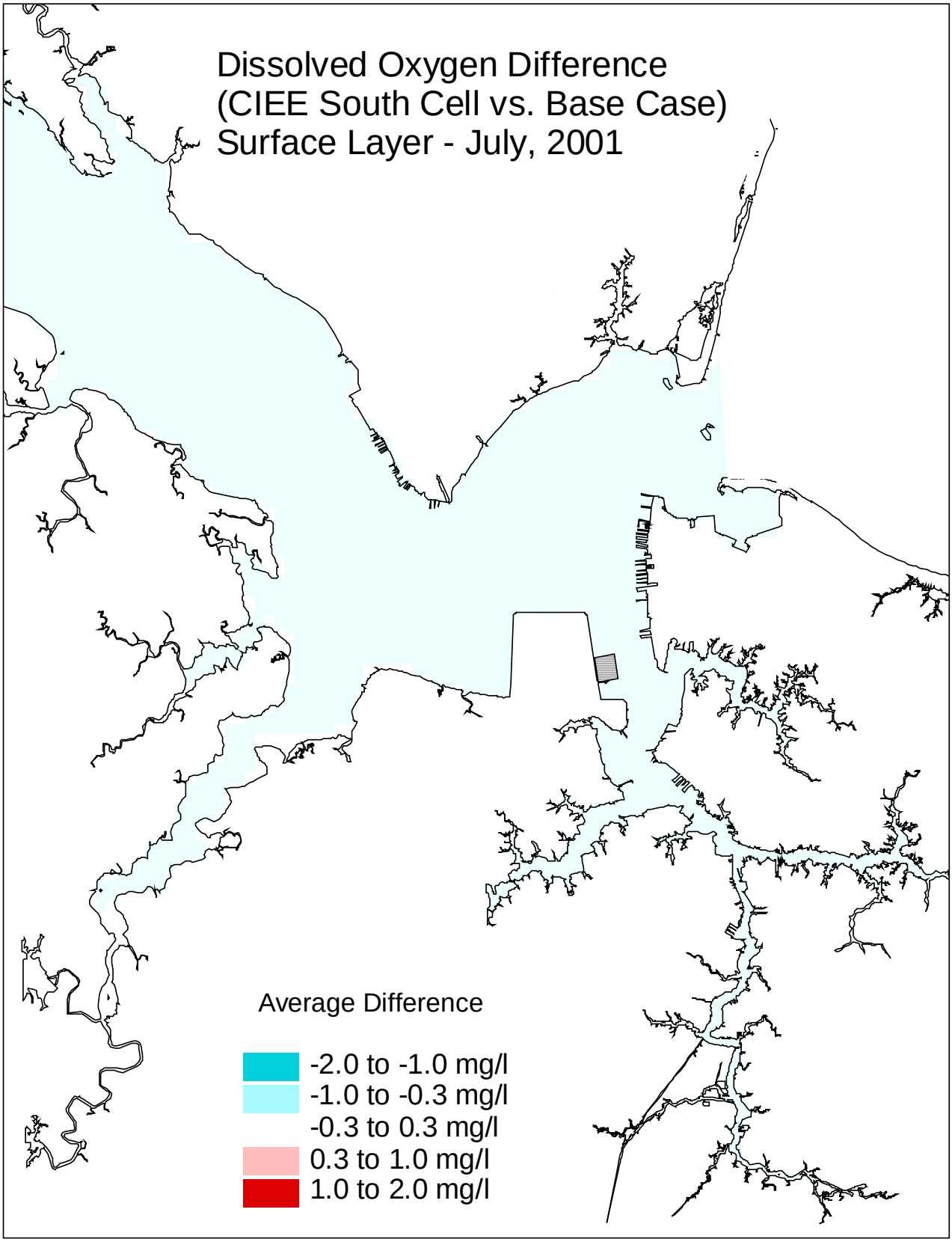

Figure G30. Dissolved oxygen (30-day average, at the surface layer) difference between the CIEE south cell expansion and the base case for July, 2001.

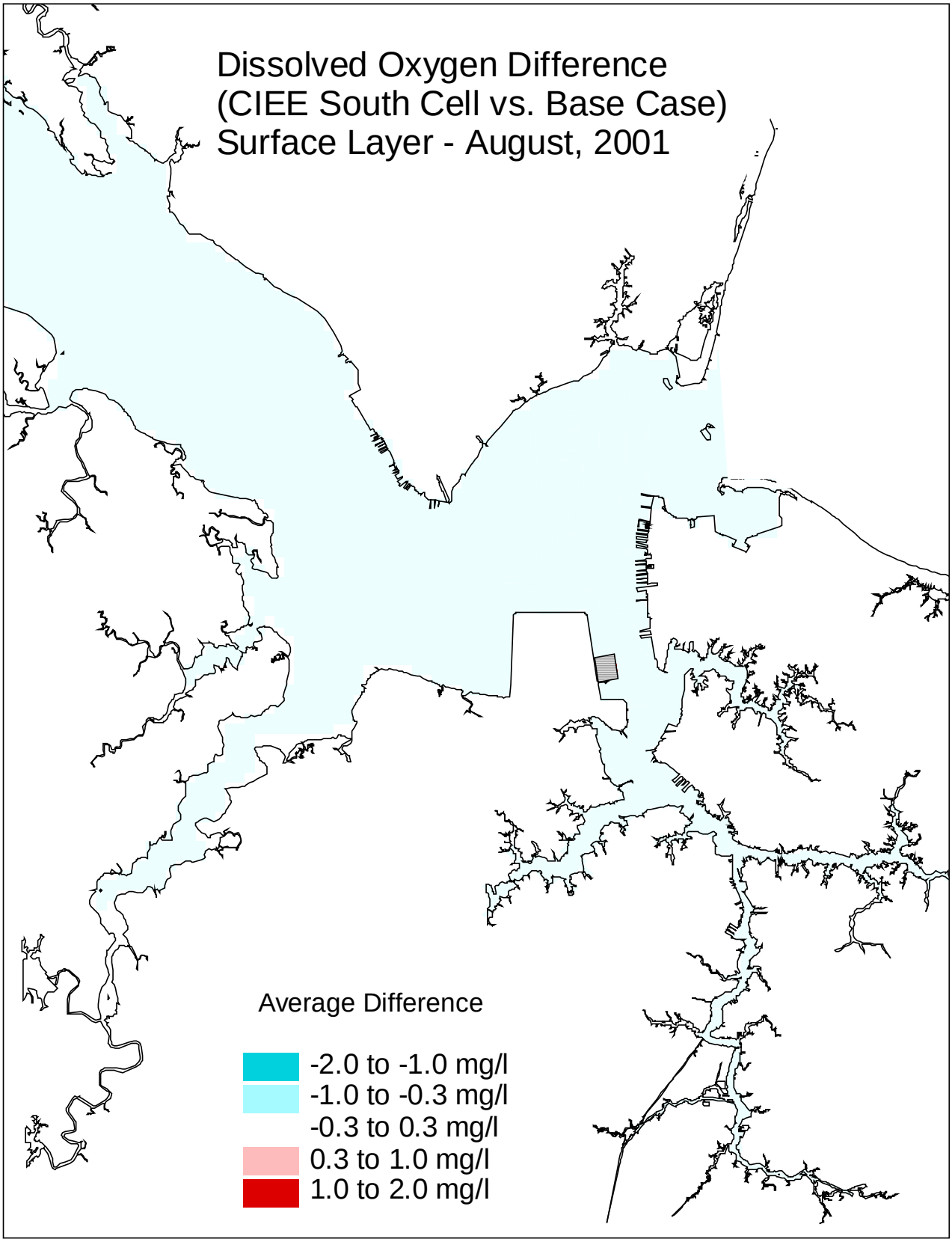

Figure G31. Dissolved oxygen (30-day average, at the surface layer) difference between the CIEE south cell expansion and the base case for August, 2001.

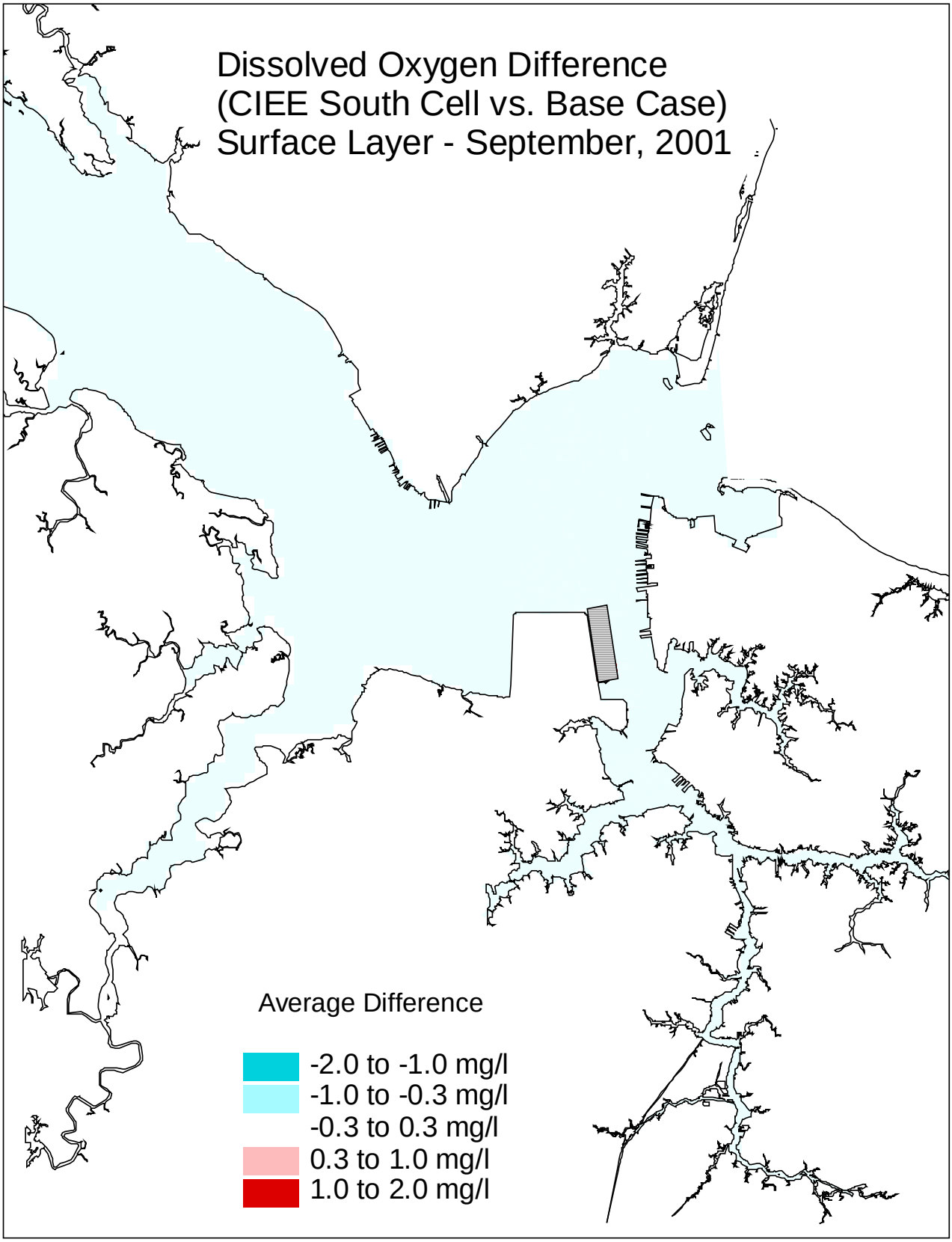

Figure G32. Dissolved oxygen (30-day average, at the surface layer) difference between the CIEE south cell expansion and the base case for September, 2001.

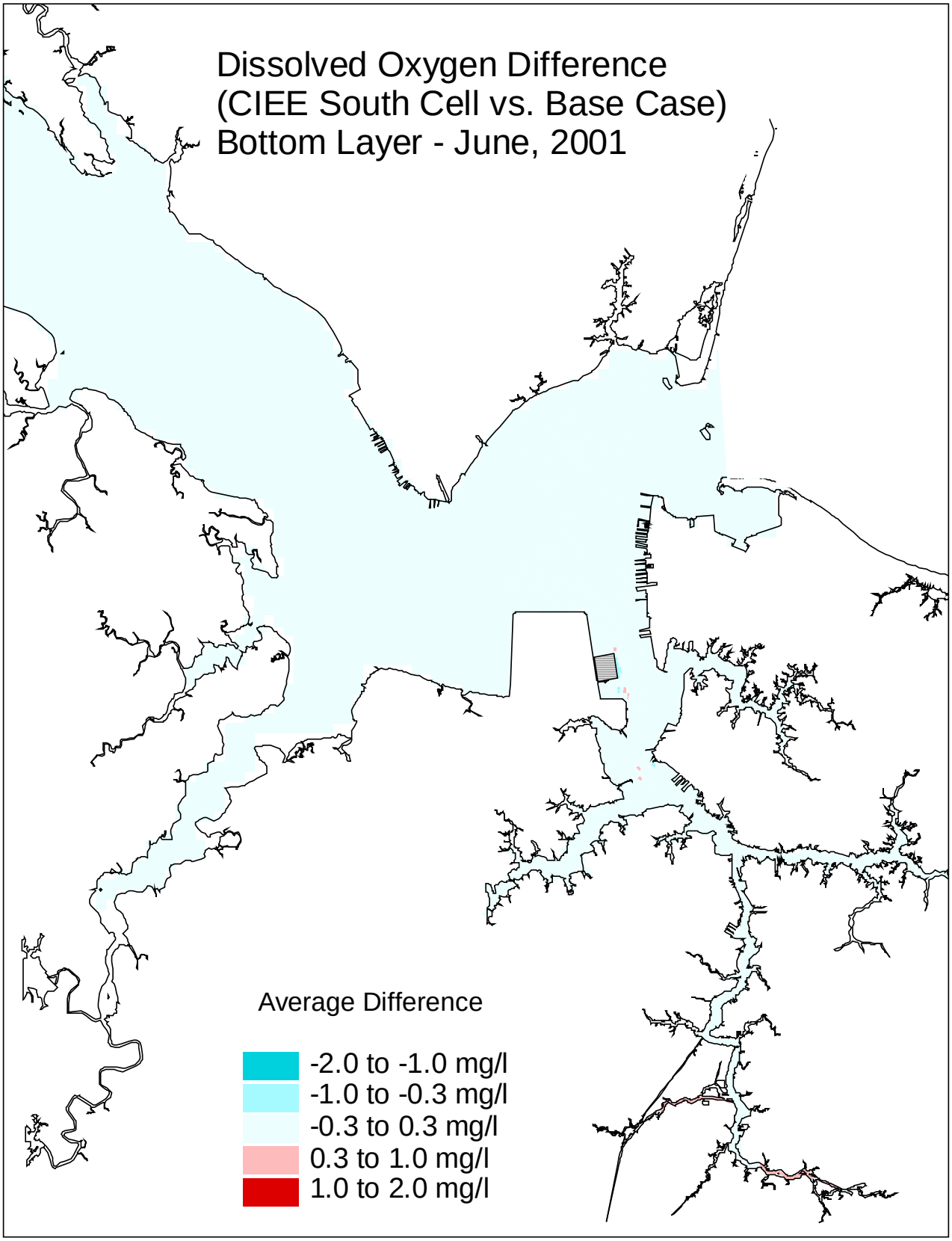

Figure G33. Dissolved oxygen (30-day average, at the bottom layer) difference between the CIEE south cell expansion and the base case for June, 2001.

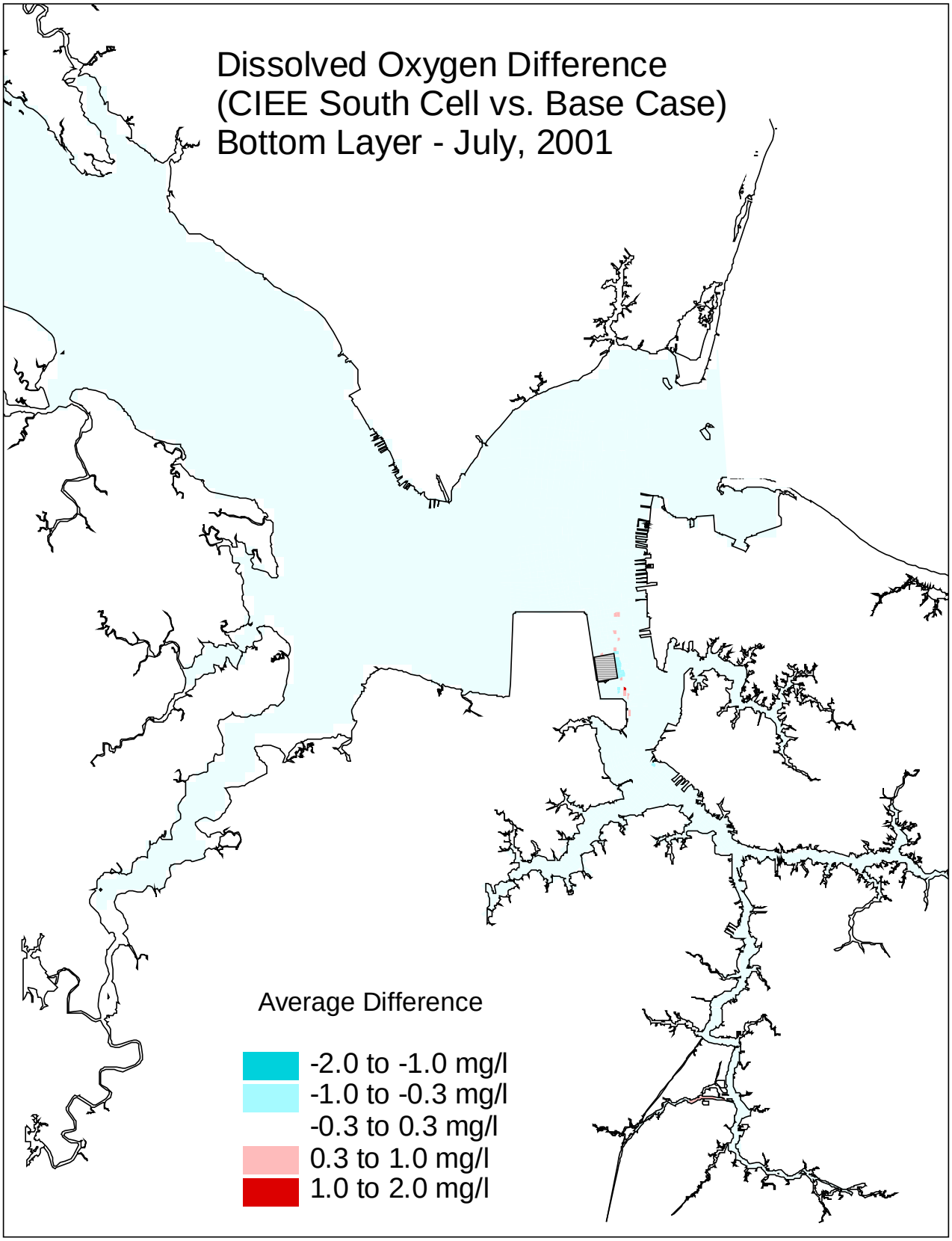

Figure G34. Dissolved oxygen (30-day average, at the bottom layer) difference between the CIEE south cell expansion and the base case for July, 2001.

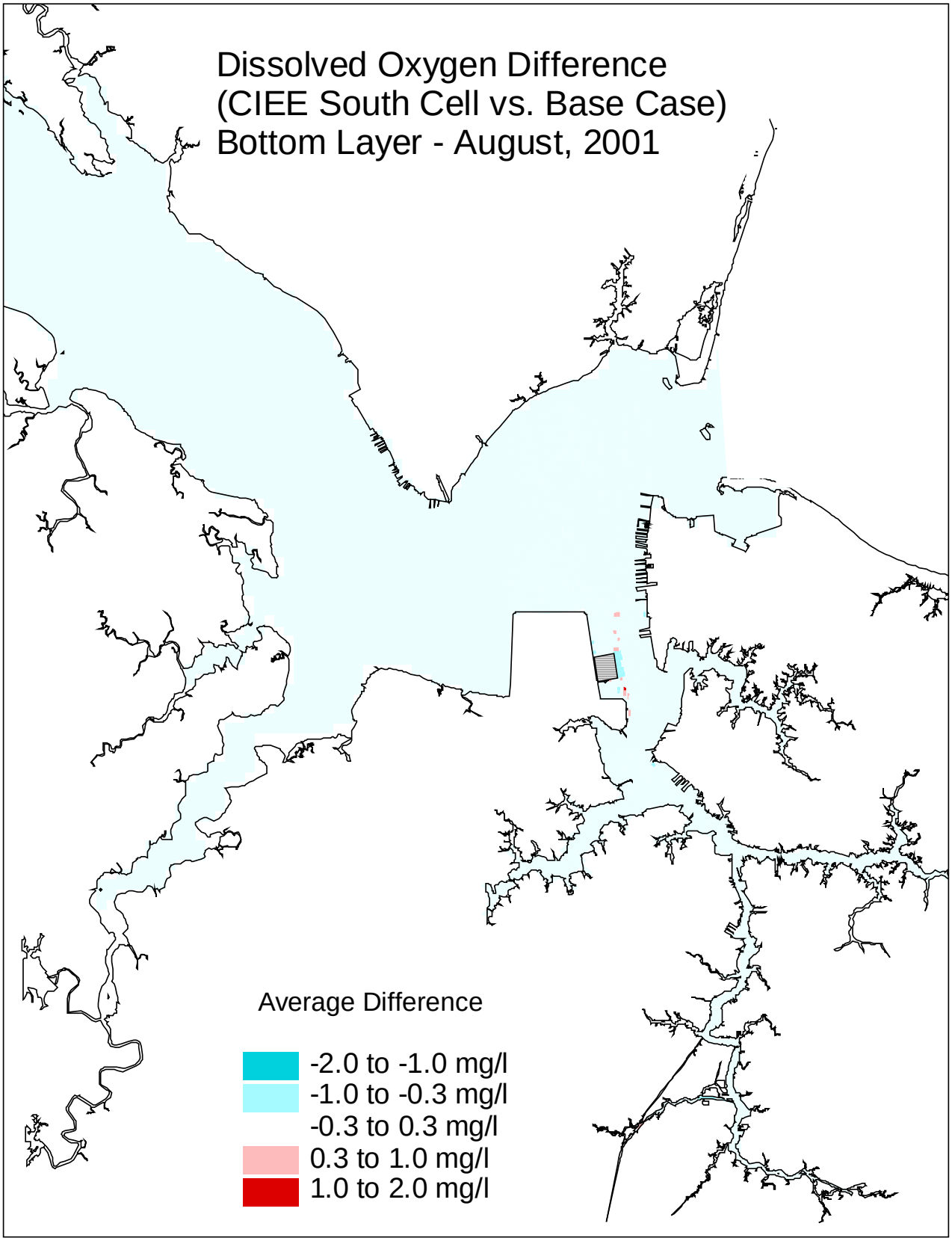

Figure G35. Dissolved oxygen (30-day average, at the bottom layer) difference between the CIEE south cell expansion and the base case for August, 2001.

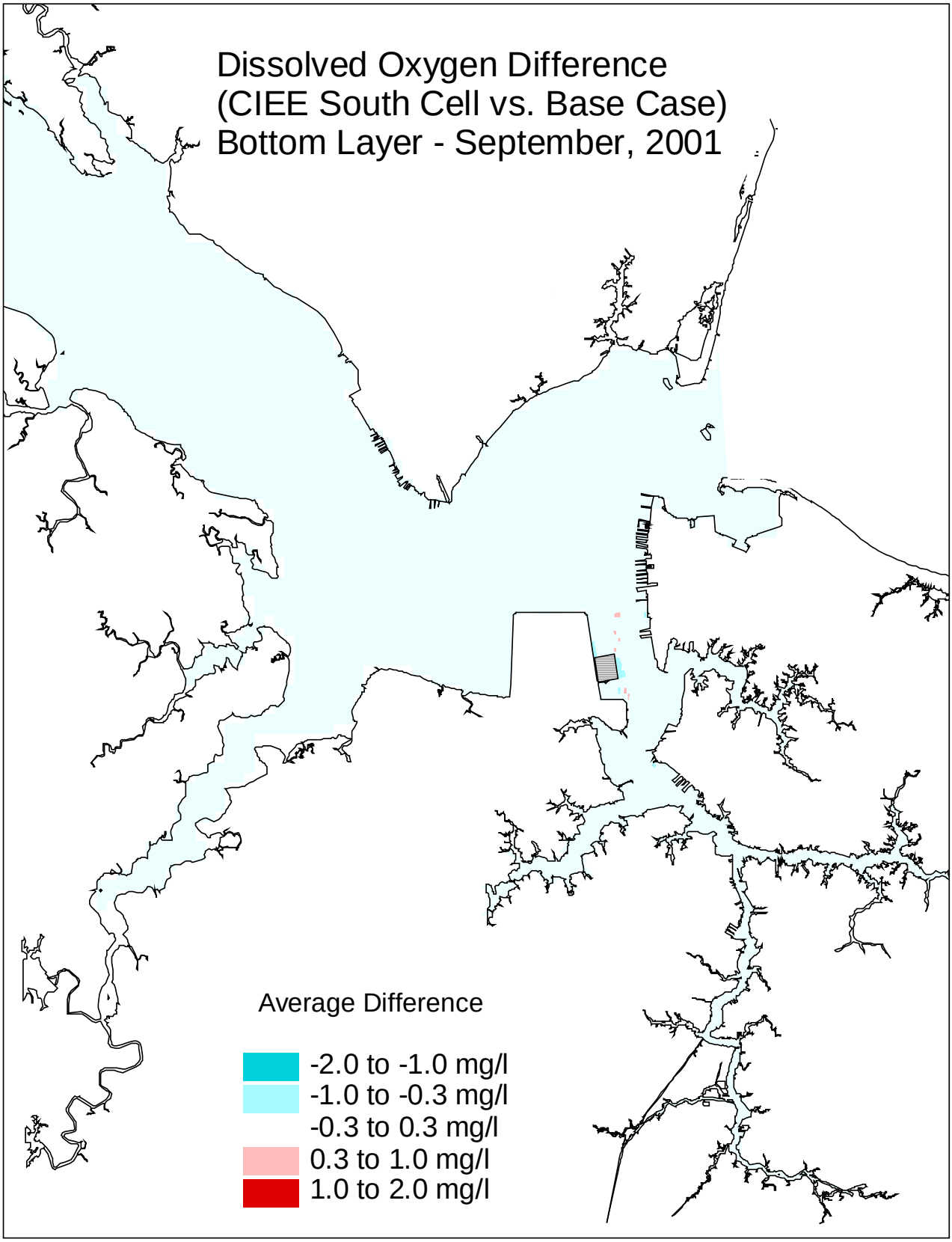

Figure G36. Dissolved oxygen (30-day average, at the bottom layer) difference between the CIEE south cell expansion and the base case for September, 2001.

APPENDIX G1

Spatial Plots of

Dissolved Oxygen Differences

Between CIEE South Cell Expansion and Base Case

For 30-Day Averages in June, July, August, and September

for 1999, 2000, and 2001

Comparison at Present Bottom Depth (pre-construction depth)

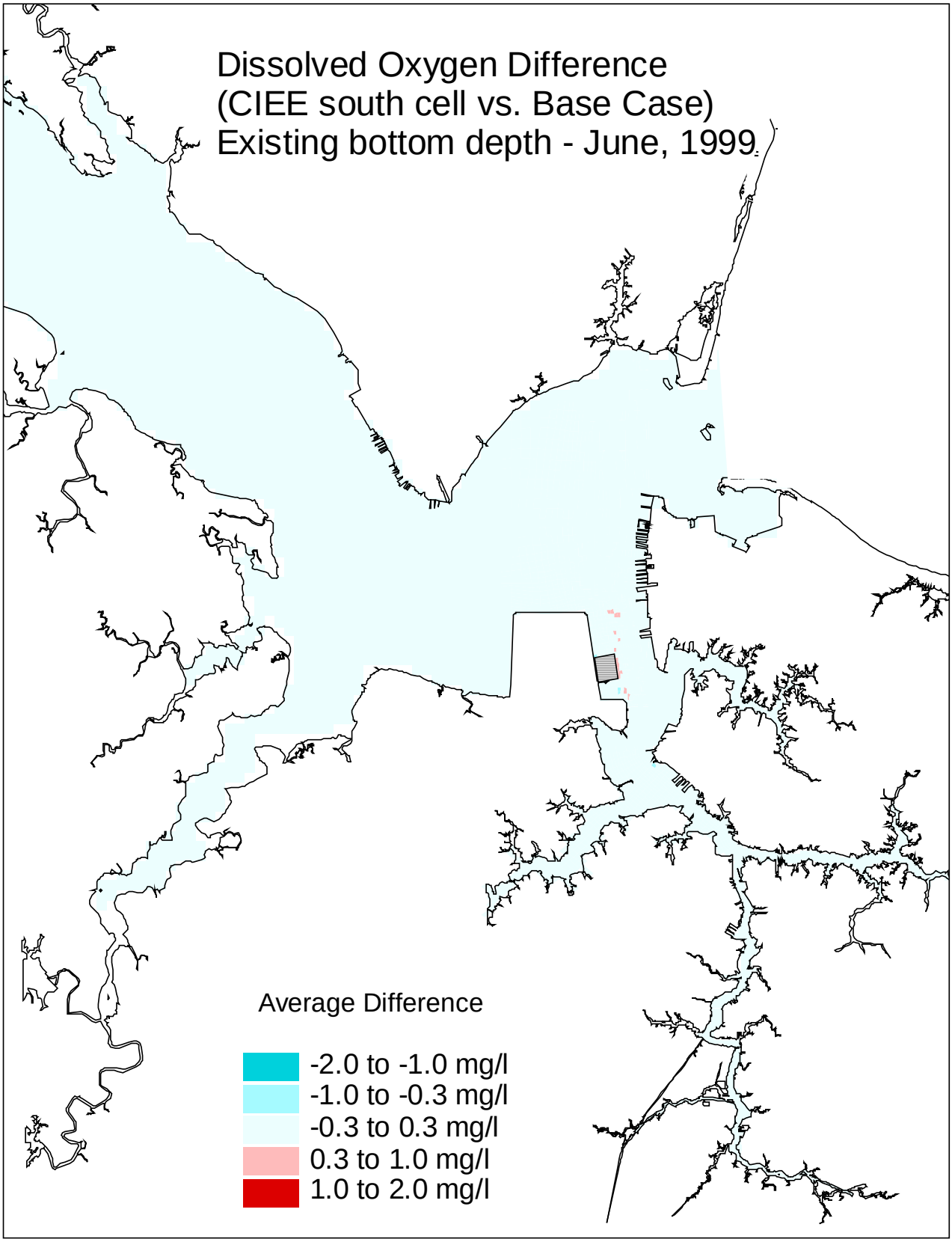

Figure G1-1. Dissolved oxygen (30-day average, at present bottom depth) difference between the CIEE south cell expansion and the base case for June, 1999.

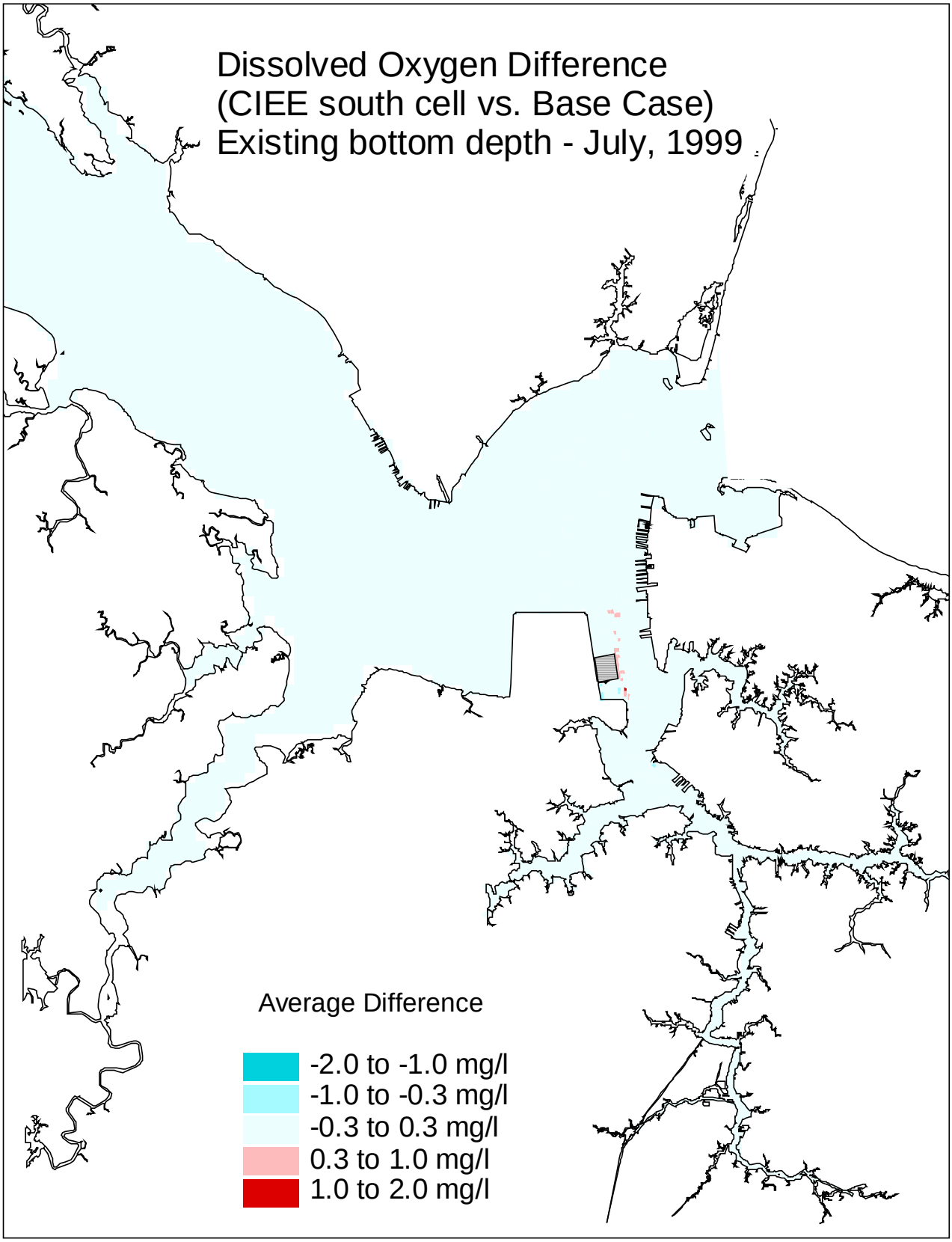

Figure G1-2. Dissolved oxygen (30-day average, at present bottom depth) difference between the CIEE south cell expansion and the base case for July, 1999.

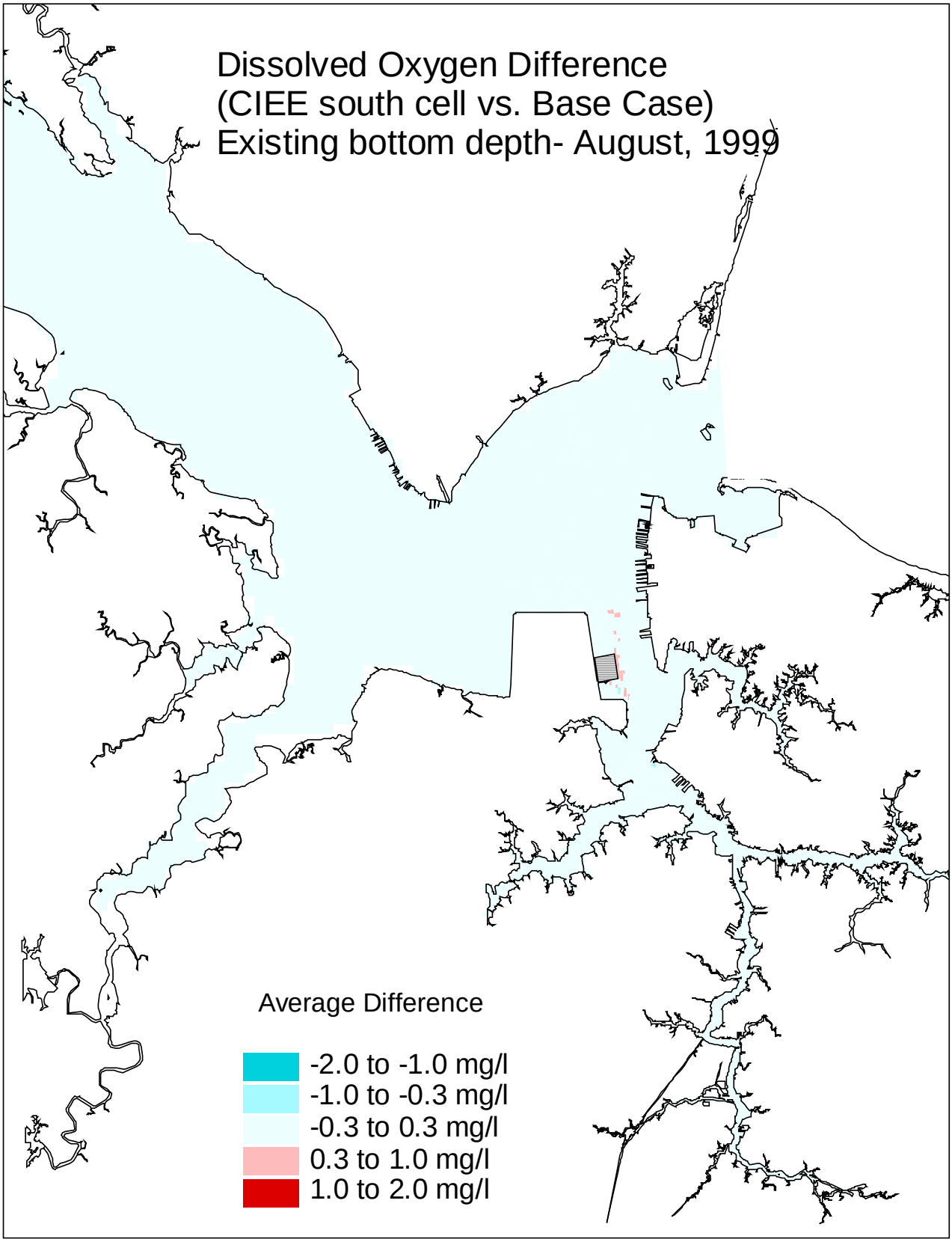

Figure G1-3. Dissolved oxygen (30-day average, at present bottom depth) difference between the CIEE south cell expansion and the base case for August, 1999.

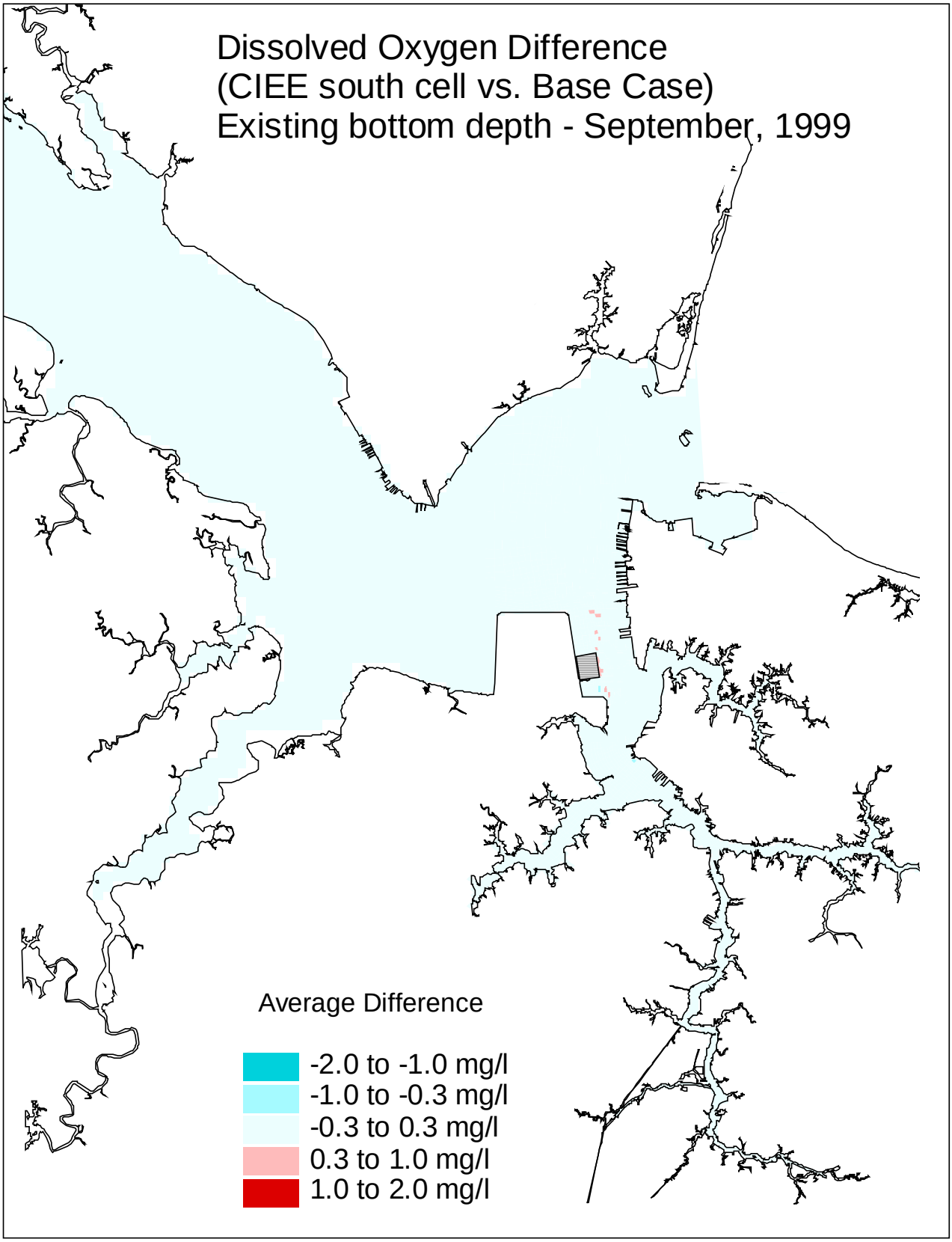

Figure G1-4. Dissolved oxygen (30-day average, at present bottom depth) difference between the CIEE south cell expansion and the base case for September, 1999.

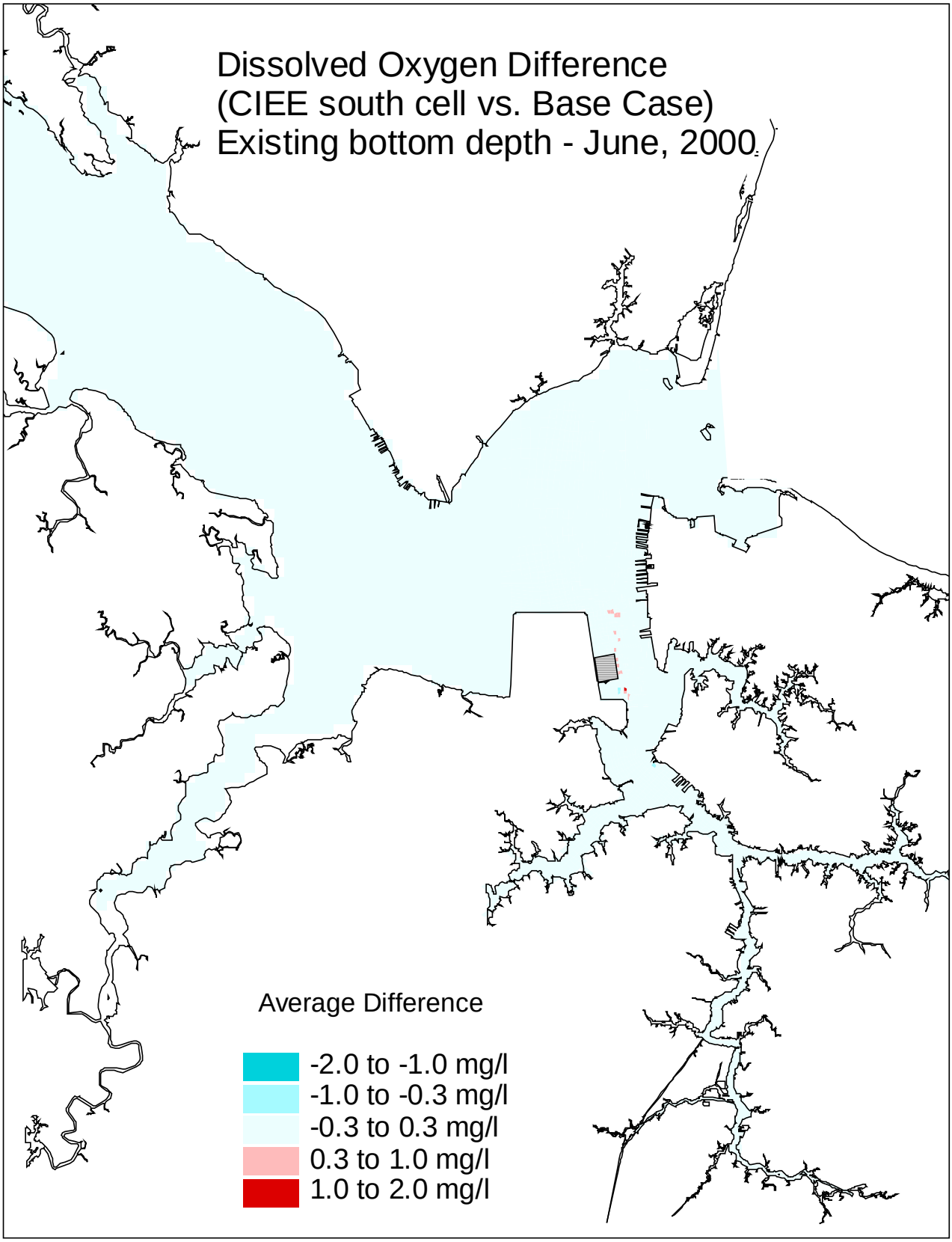

Figure G1-5. Dissolved oxygen (30-day average, at present bottom depth) difference between the CIEE south cell expansion and the base case for June, 2000.

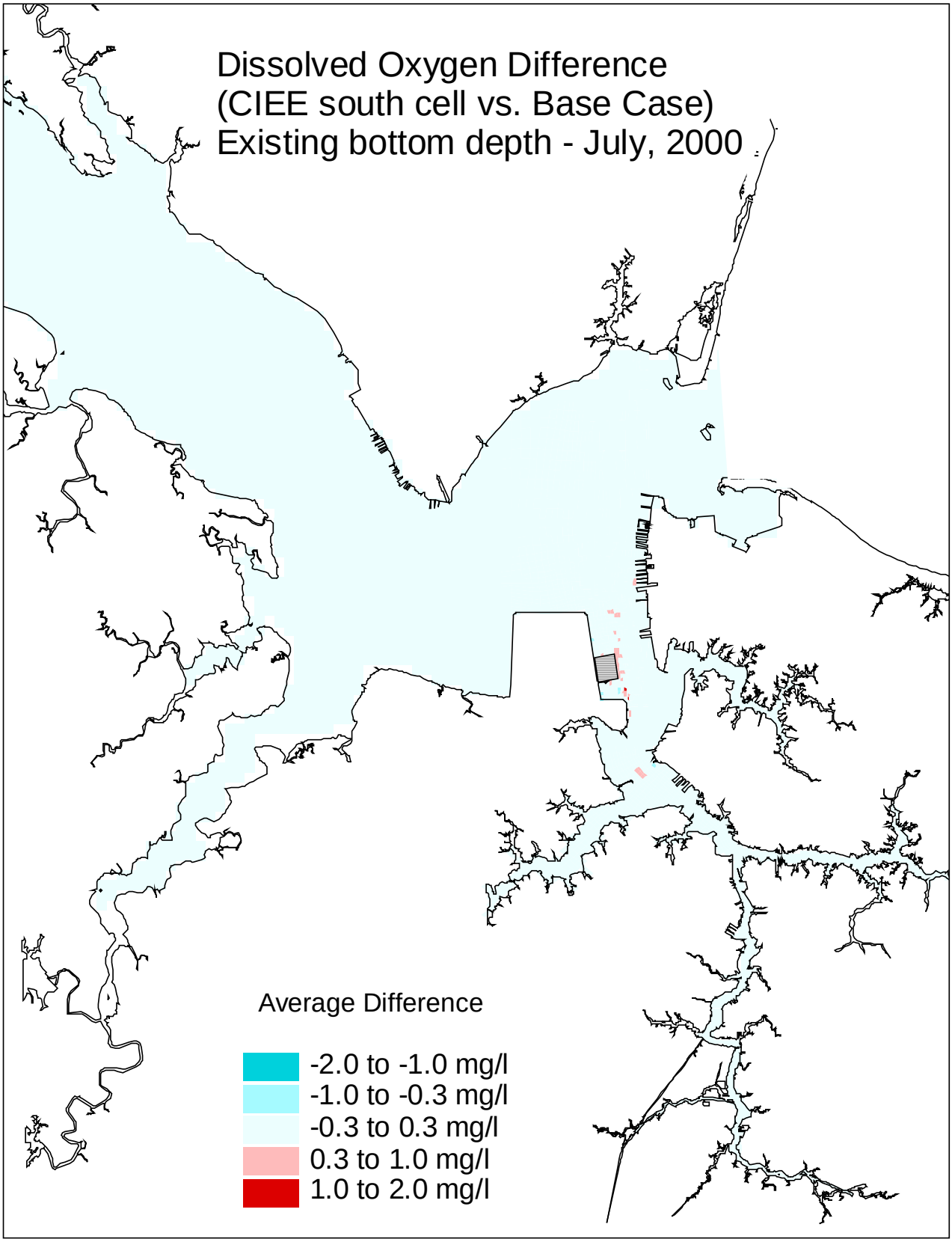

Figure G1-6. Dissolved oxygen (30-day average, at present bottom depth) difference between the CIEE south cell expansion and the base case for July, 2000.

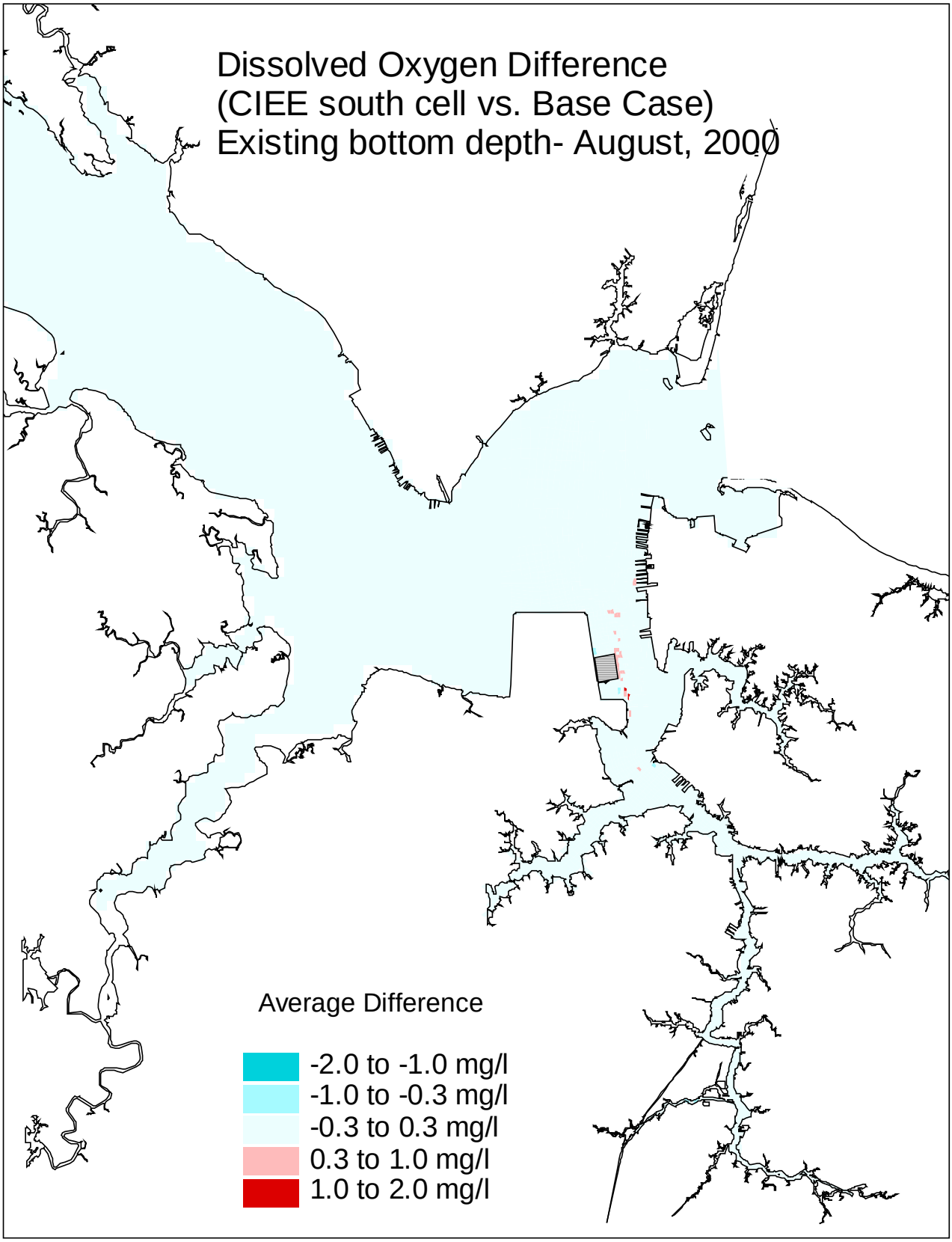

Figure G1-7. Dissolved oxygen (30-day average, at present bottom depth) difference between the CIEE south cell expansion and the base case for August, 2000.

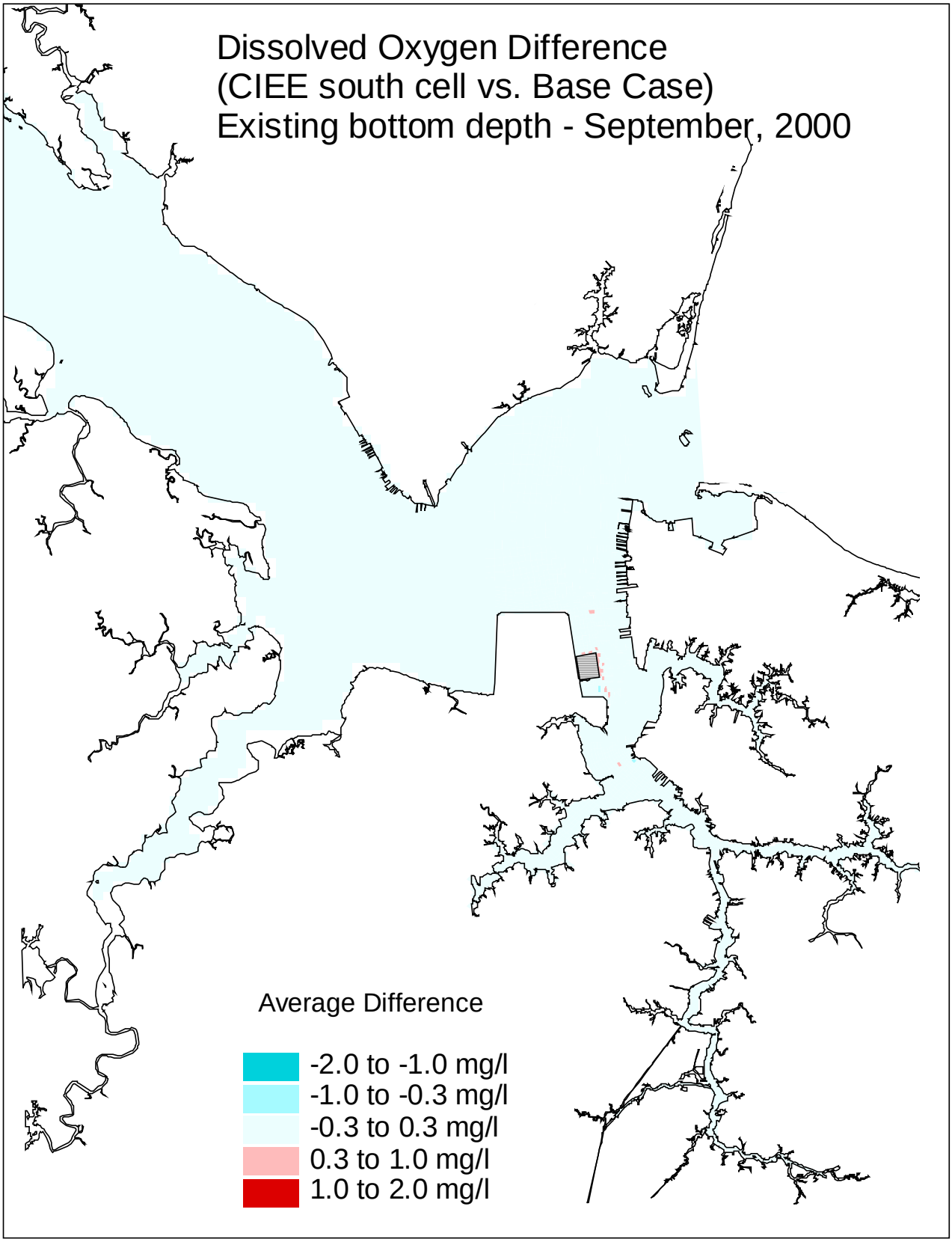

Figure G1-8. Dissolved oxygen (30-day average, at present bottom depth) difference between the CIEE south cell expansion and the base case for September, 2000.

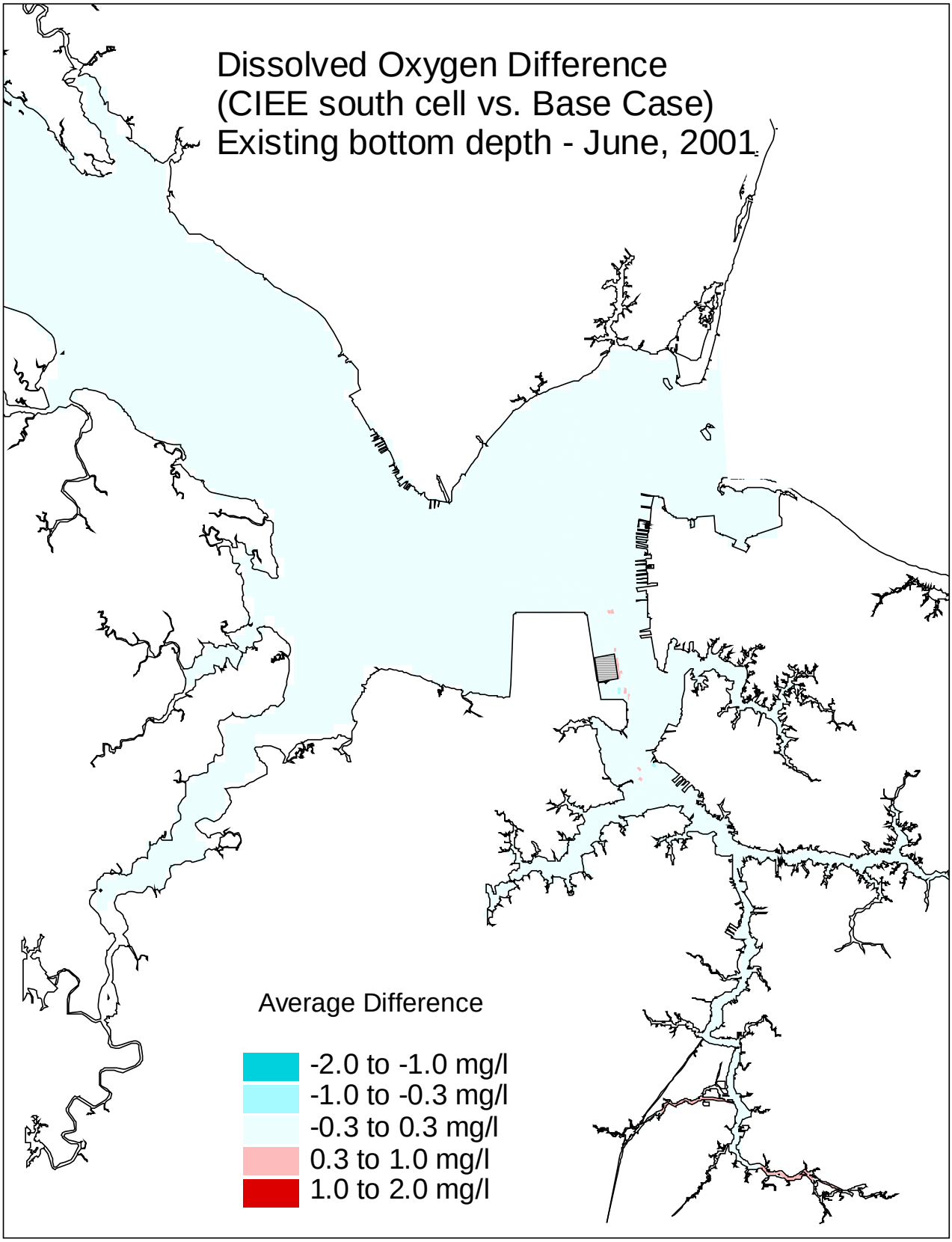

Figure G1-9. Dissolved oxygen (30-day average, at present bottom depth) difference between the CIEE south cell expansion and the base case for June, 2001.

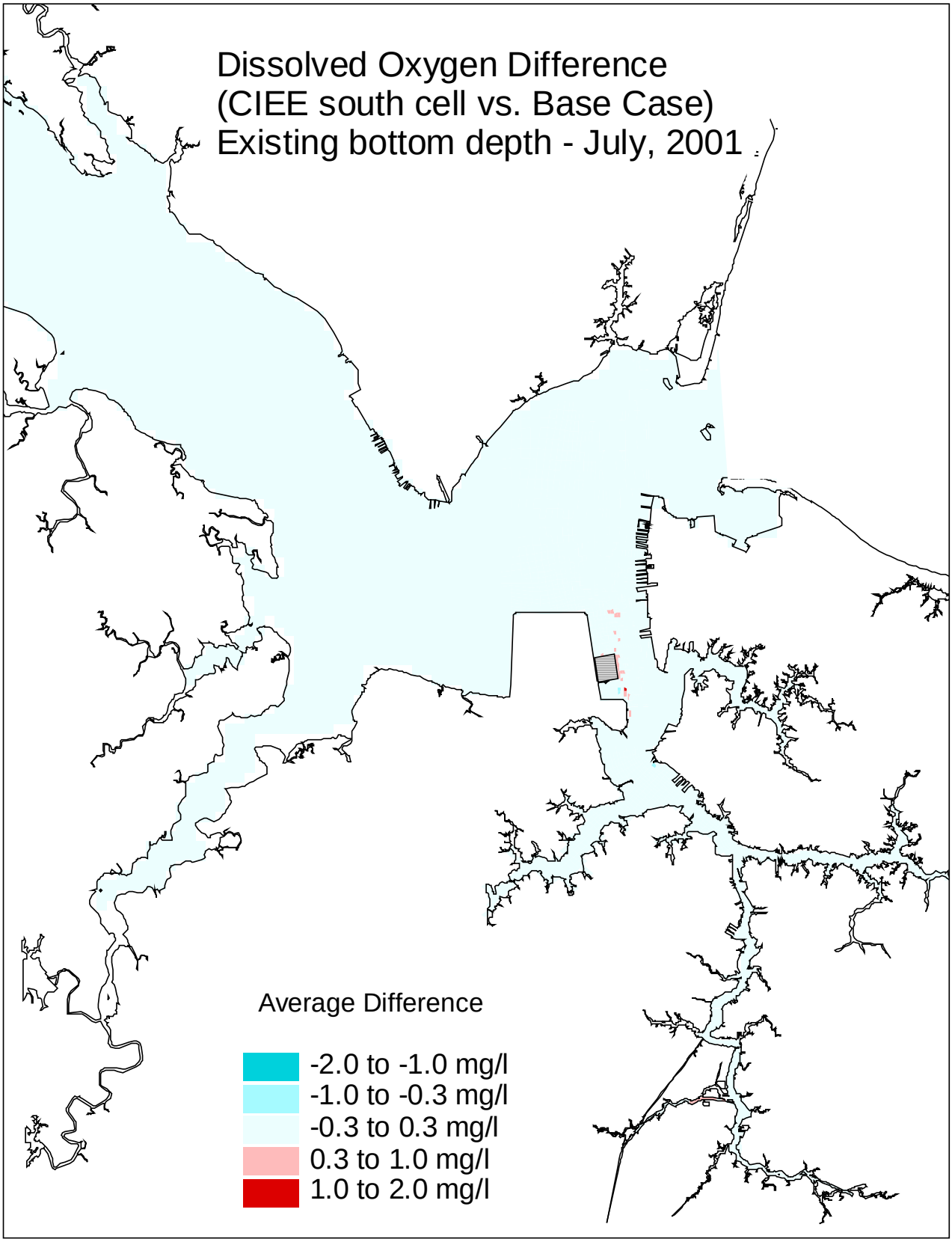

Figure G1-10. Dissolved oxygen (30-day average, at present bottom depth) difference between the CIEE south cell expansion and the base case for July, 2001.

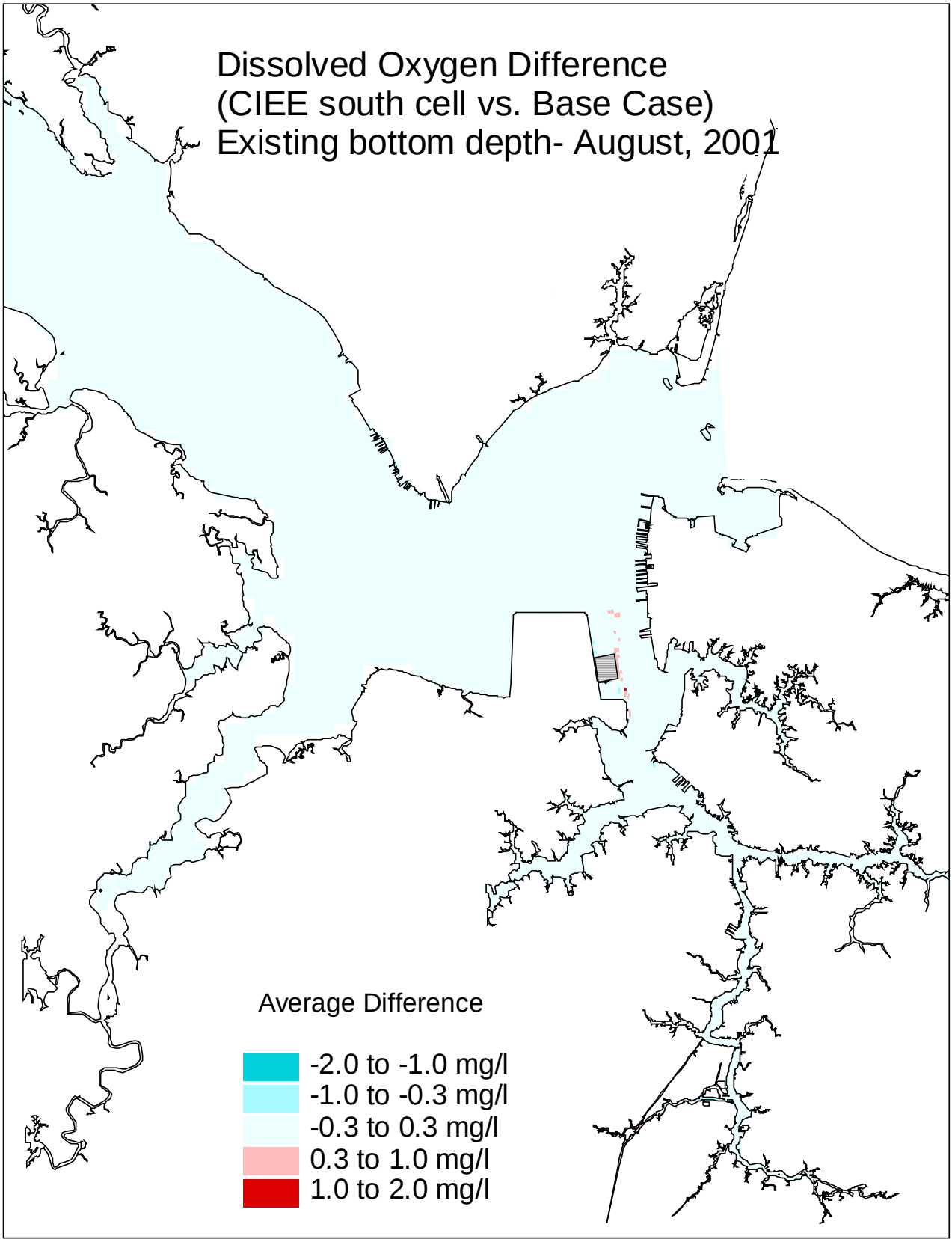

Figure G1-11. Dissolved oxygen (30-day average, at present bottom depth) difference between the CIEE south cell expansion and the base case for August, 2001.

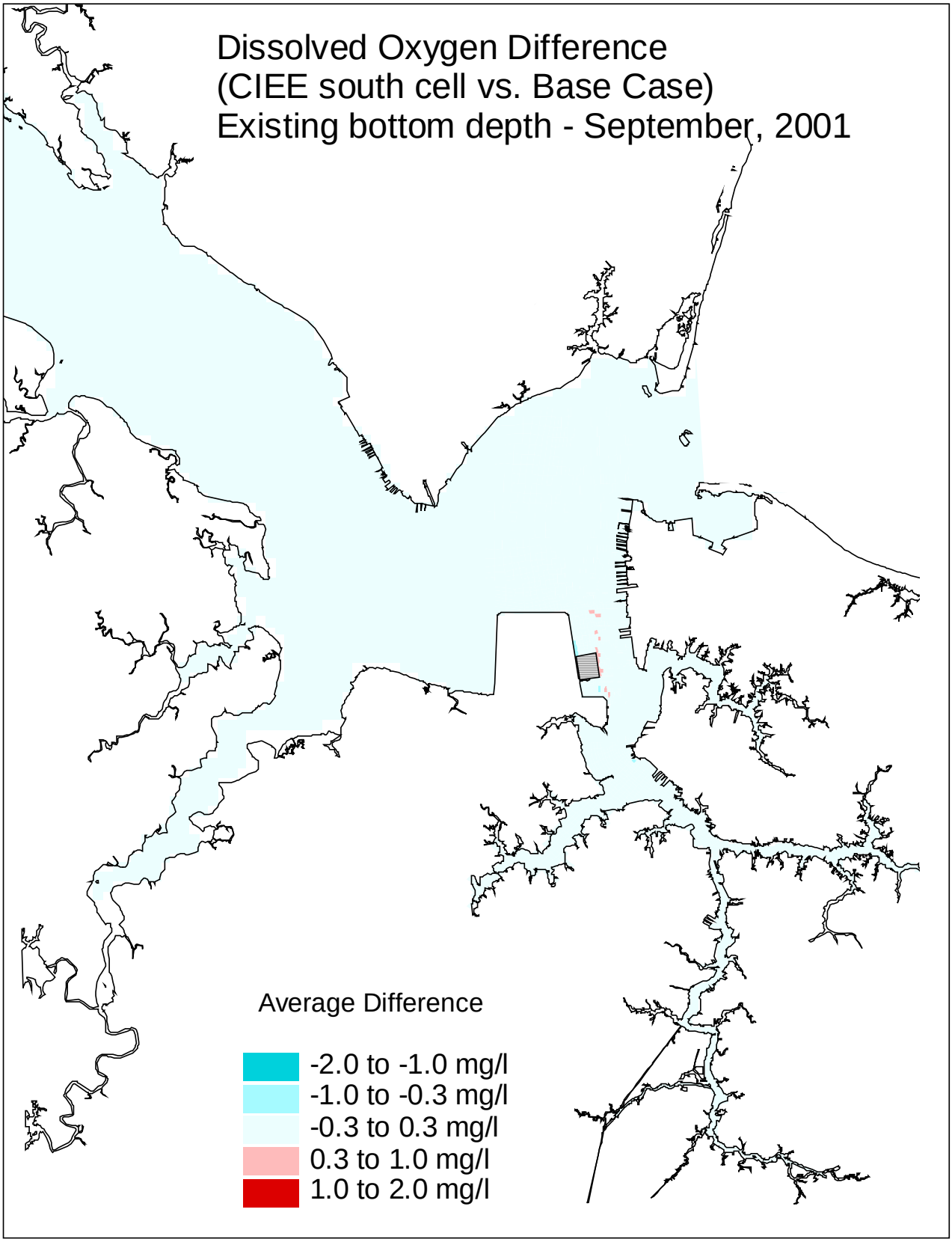

Figure G1-12. Dissolved oxygen (30-day average, at present bottom depth) difference between the CIEE south cell expansion and the base case for September, 2001.

APPENDIX H

CIEE Full Expansion Scenario

Water Quality Model Results

at CBP Stations LE5.5, LE5.6, and ELI2 for 1999, 2000, and 2001

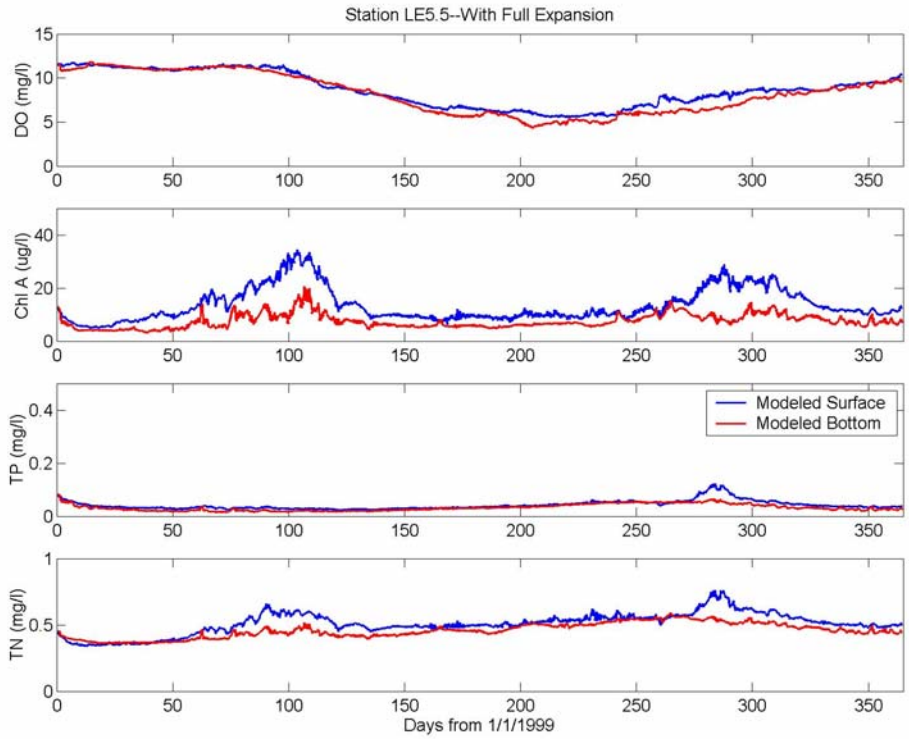

Figure H1. CIEE full expansion scenario model predictions for dissolved oxygen, chlorophyll-a, total phosphorus, and total nitrogen at CBP Station LE5.5 (surface and bottom layers) for 1999.

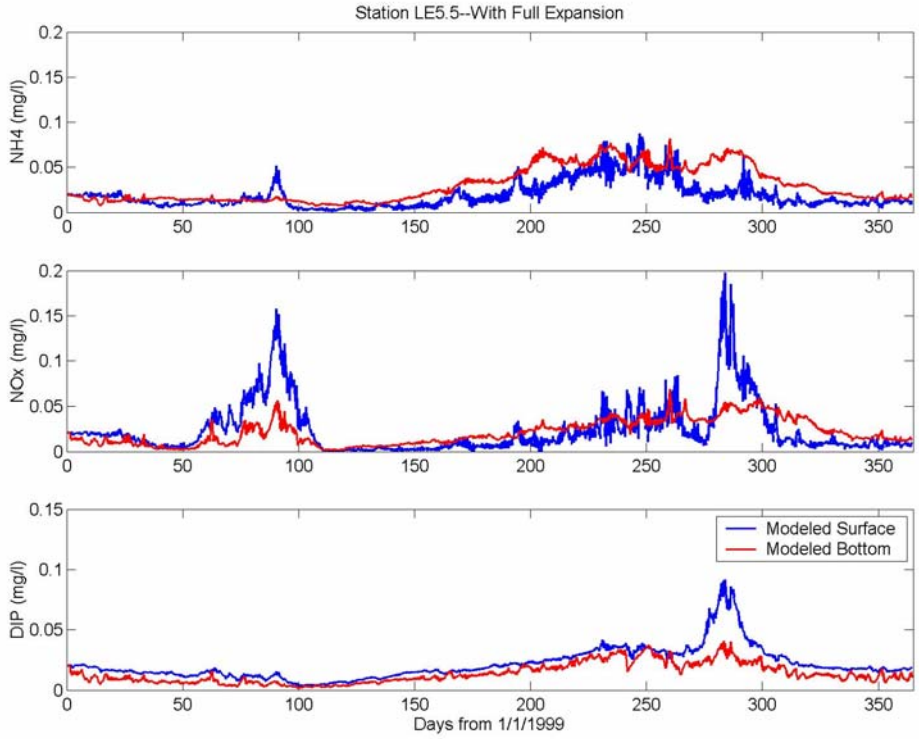

Figure H2. CIEE full expansion scenario model predictions for ammonium, nitrate-nitrite, and dissolved inorganic phosphorus at CBP Station LE5.5 (surface and bottom layers) for 1999.

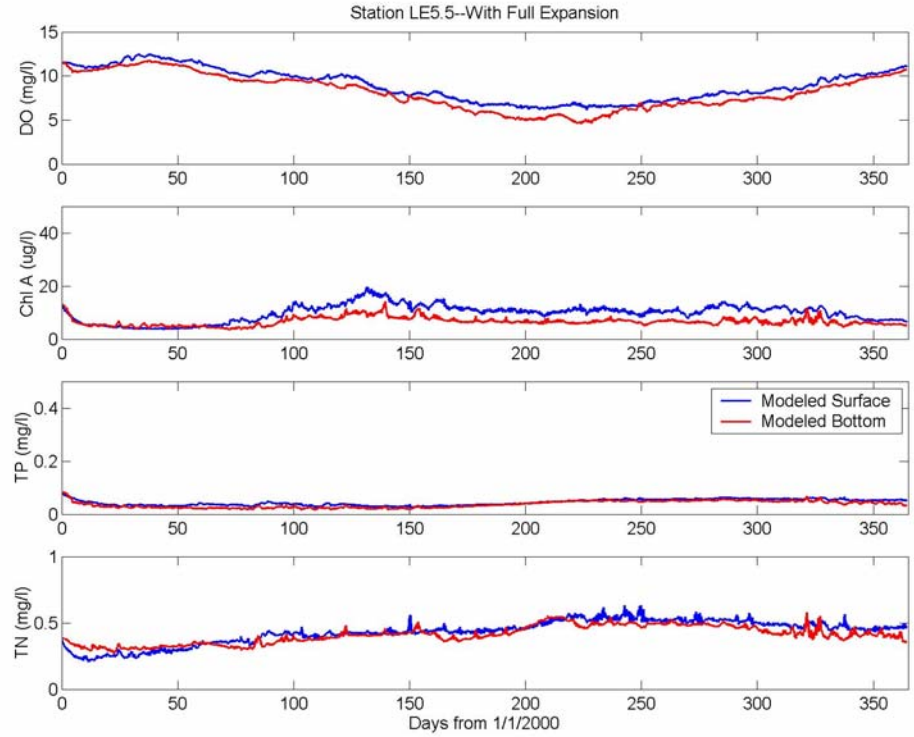

Figure H3. CIEE full expansion scenario model predictions for dissolved oxygen, chlorophyll-a, total phosphorus, and total nitrogen at CBP Station LE5.5 (surface and bottom layers) for 2000.

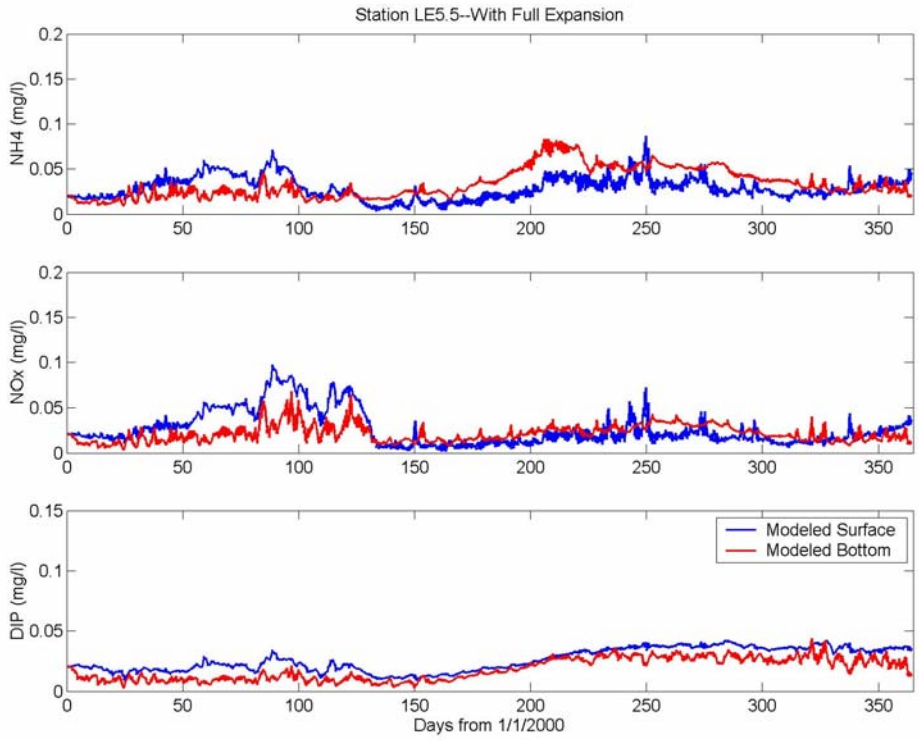

Figure H4. CIEE full expansion scenario model predictions for ammonium, nitrate-nitrite, and dissolved inorganic phosphorus at CBP Station LE5.5 (surface and bottom layers) for 2000.

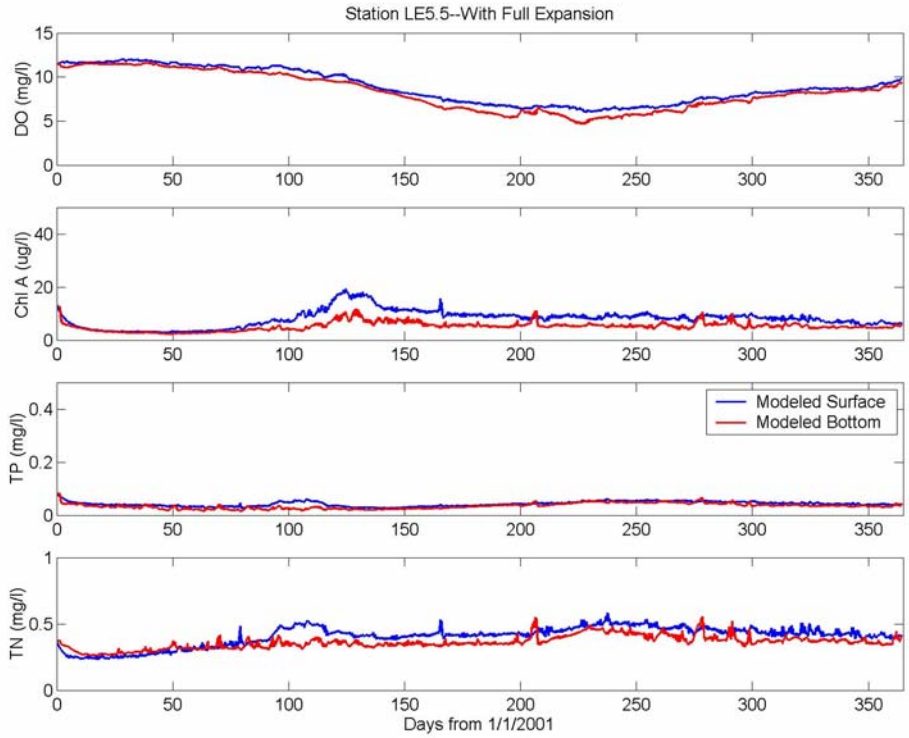

Figure H5. CIEE full expansion scenario model predictions for dissolved oxygen, chlorophyll-a, total phosphorus, and total nitrogen at CBP Station LE5.5 (surface and bottom layers) for 2001.

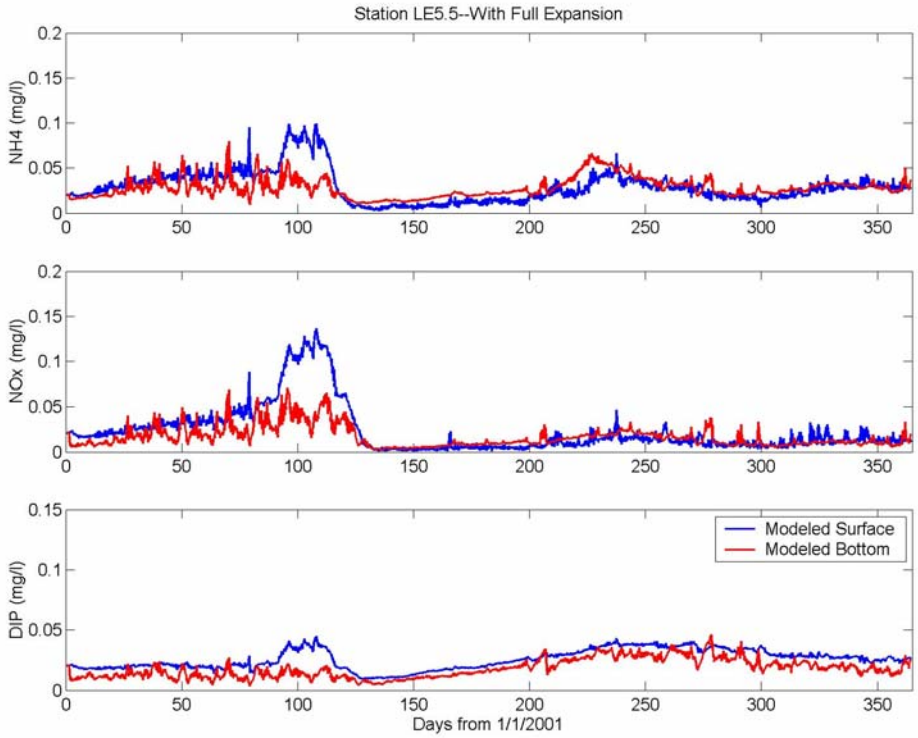

Figure H6. CIEE full expansion scenario model predictions for ammonium, nitrate-nitrite, and dissolved inorganic phosphorus at CBP Station LE5.5 (surface and bottom layers) for 2001.

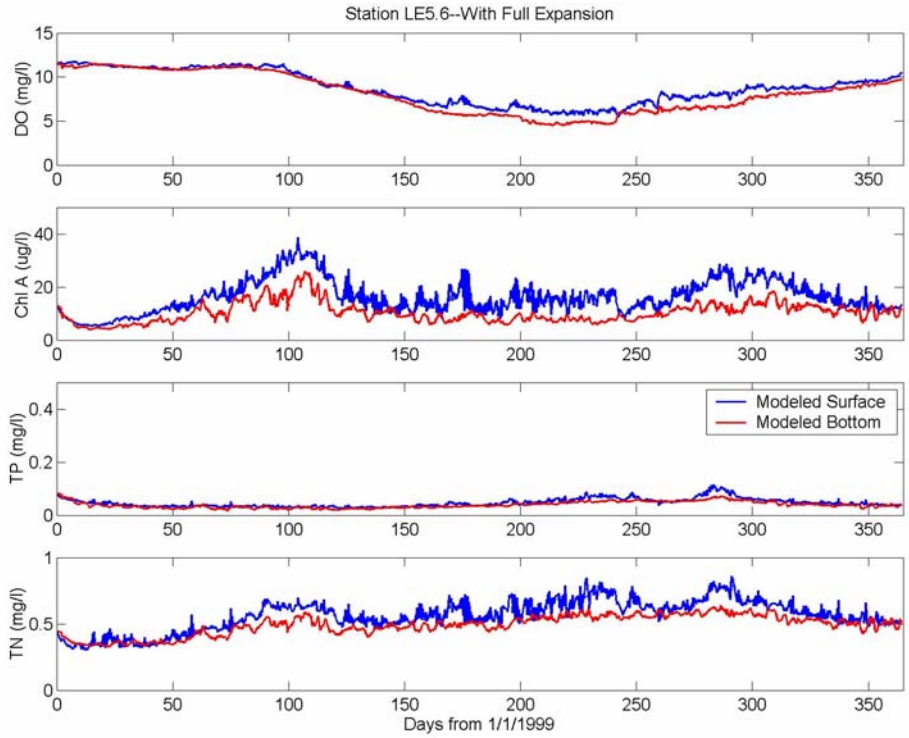

Figure H7. CIEE full expansion scenario model predictions for dissolved oxygen, chlorophyll-a, total phosphorus, and total nitrogen at CBP Station LE5.6 (surface and bottom layers) for 1999.

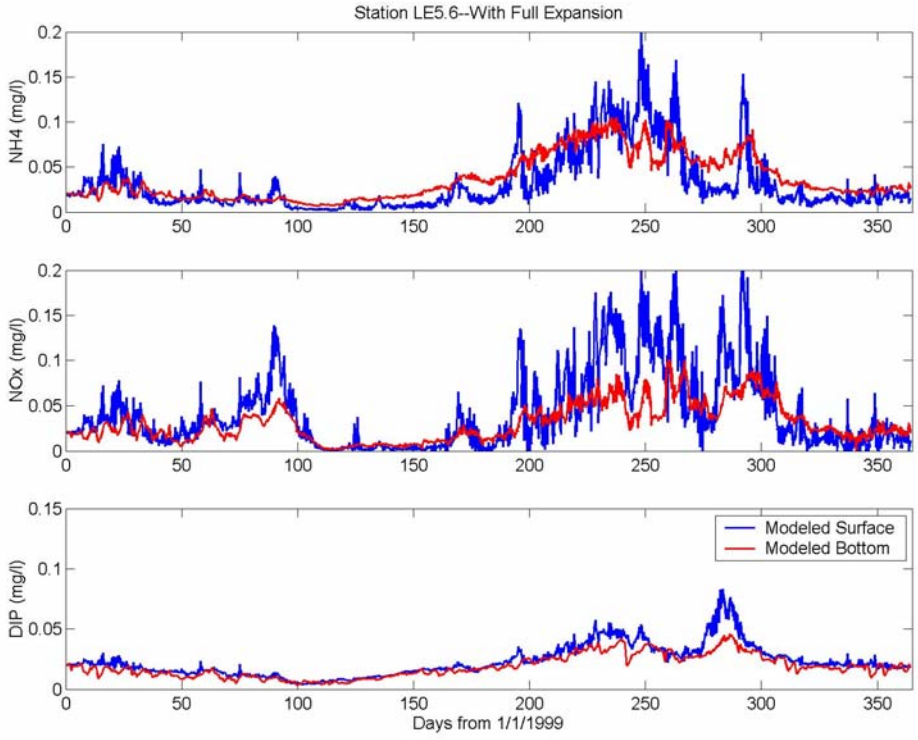

Figure H8. CIEE full expansion scenario model predictions for ammonium, nitrate-nitrite, and dissolved inorganic phosphorus at CBP Station LE5.6 (surface and bottom layers) for 1999.

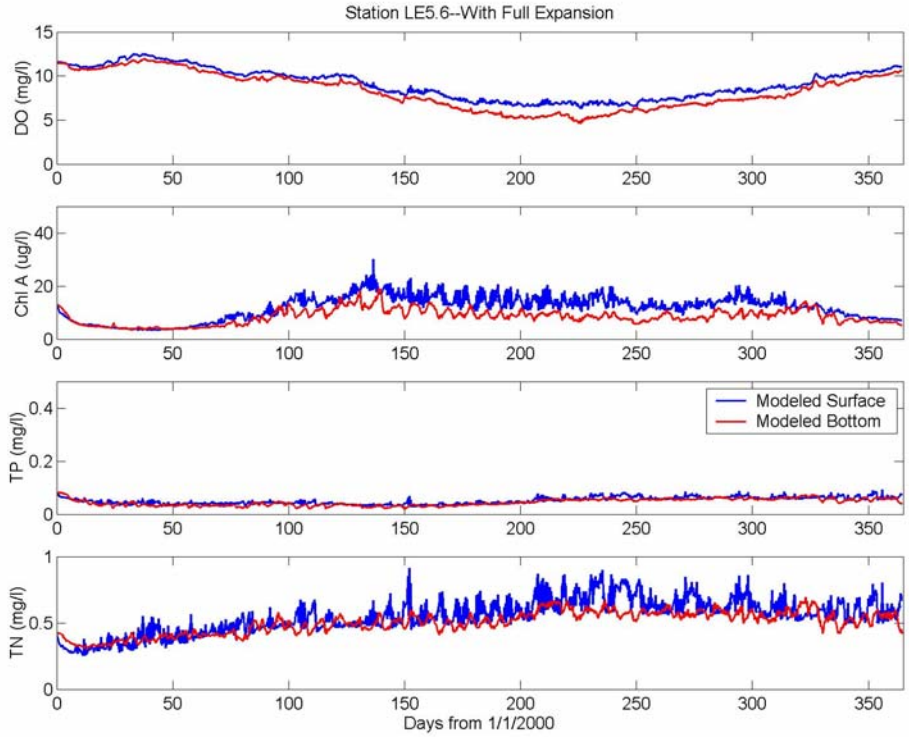

Figure H9. CIEE full expansion scenario model predictions for dissolved oxygen, chlorophyll-a, total phosphorus, and total nitrogen at CBP Station LE5.6 (surface and bottom layers) for 2000.

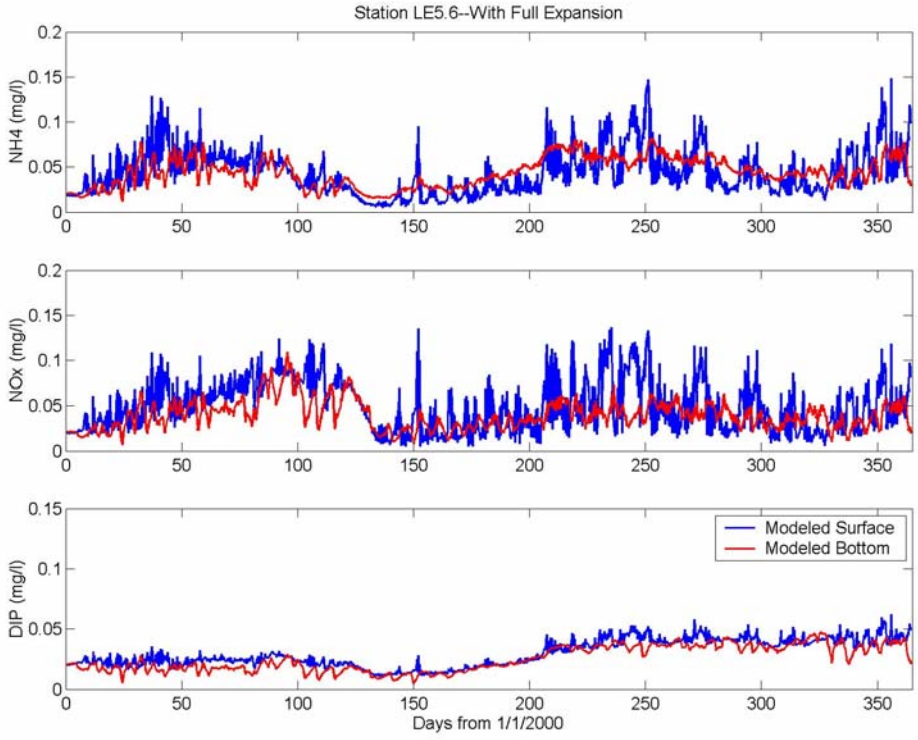

Figure H10. CIEE full expansion scenario model predictions for ammonium, nitrate-nitrite, and dissolved inorganic phosphorus at CBP Station LE5.6 (surface and bottom layers) for 2000.

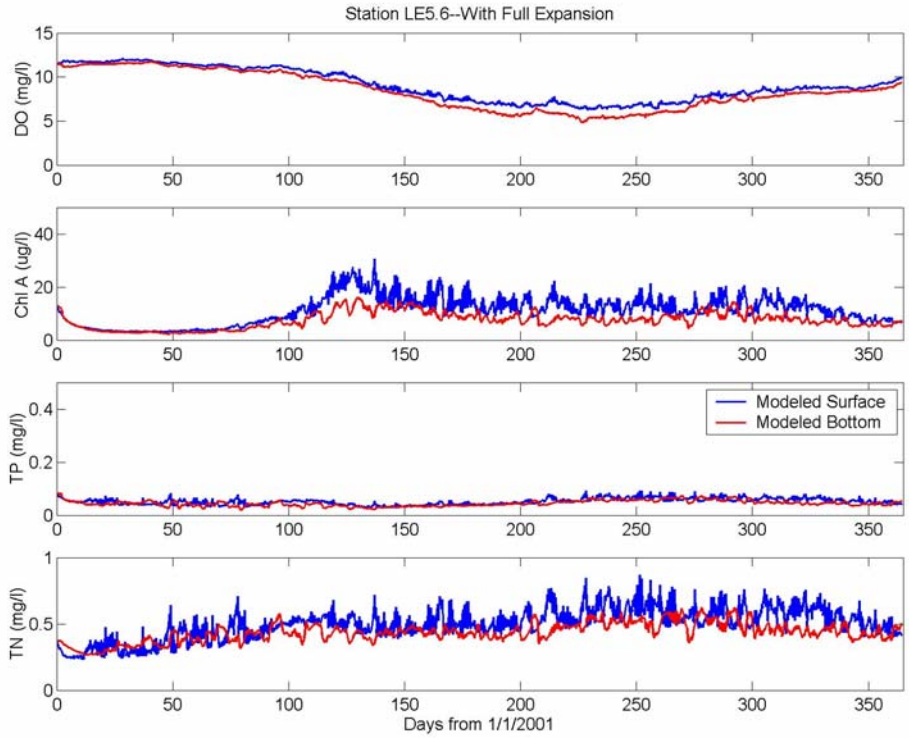

Figure H11. CIEE full expansion scenario model predictions for dissolved oxygen, chlorophyll-a, total phosphorus, and total nitrogen at CBP Station LE5.6 (surface and bottom layers) for 2001.

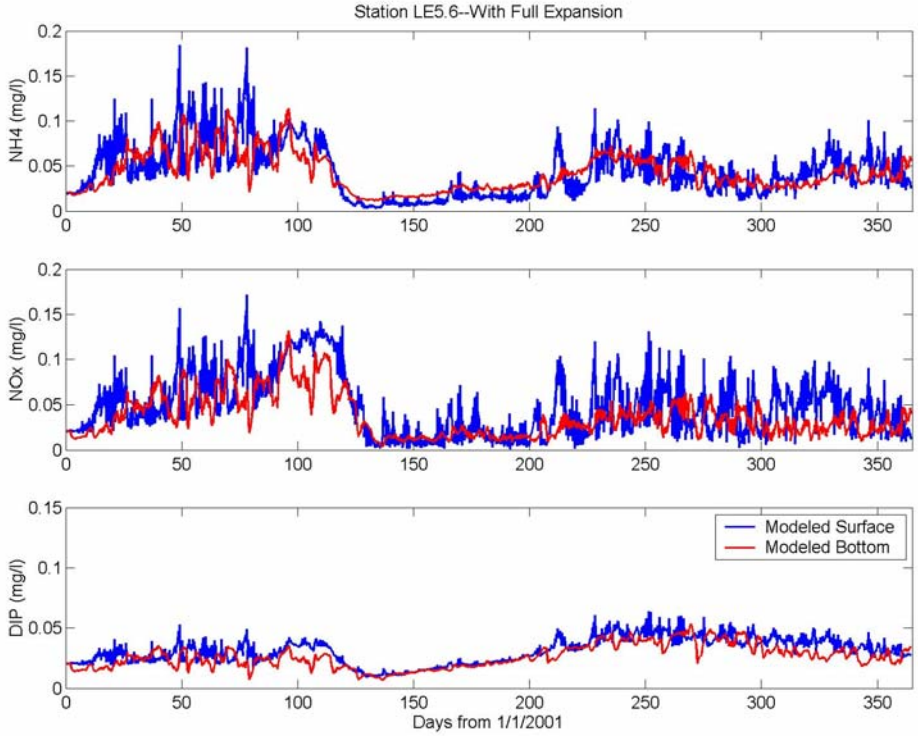

Figure H12. CIEE full expansion scenario model predictions for ammonium, nitrate-nitrite, and dissolved inorganic phosphorus at CBP Station LE5.6 (surface and bottom layers) for 2001.

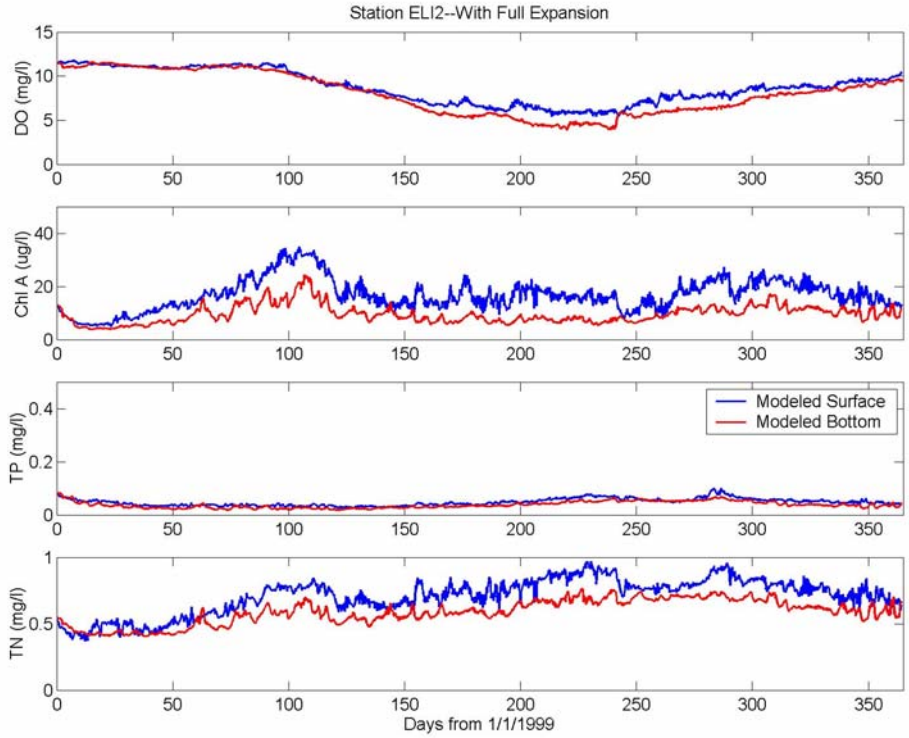

Figure H13. CIEE full expansion scenario model predictions for dissolved oxygen, chlorophyll-a, total phosphorus, and total nitrogen at CBP Station ELI2 (surface and bottom layers) for 1999.

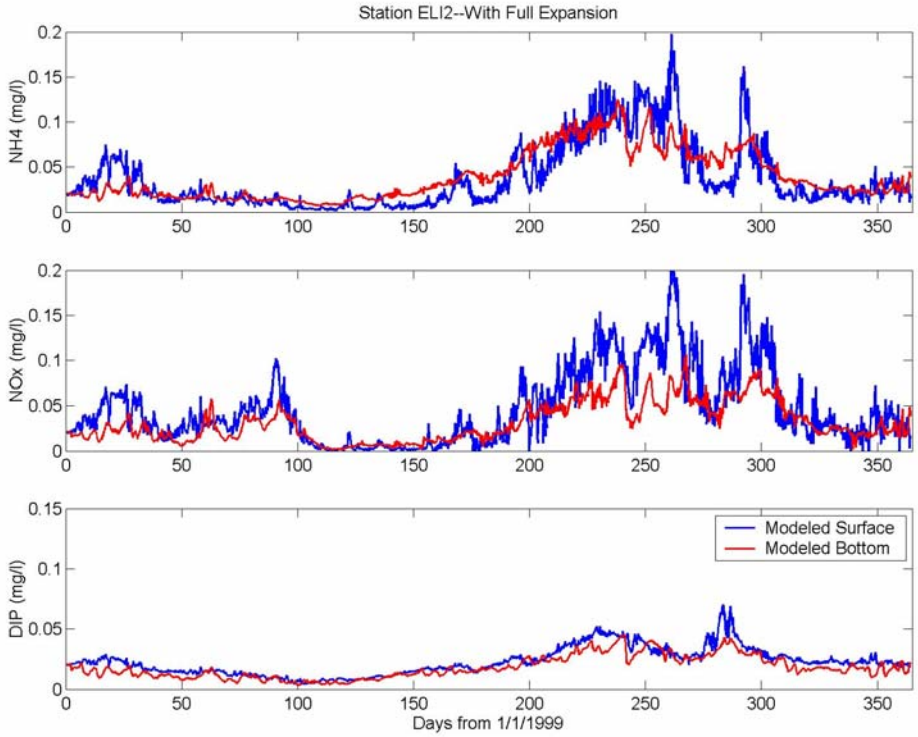

Figure H14. CIEE full expansion scenario model predictions for ammonium, nitrate, nitrite, and dissolved inorganic phosphorus at CBP Station ELI2 (surface and bottom layers) for 1999.

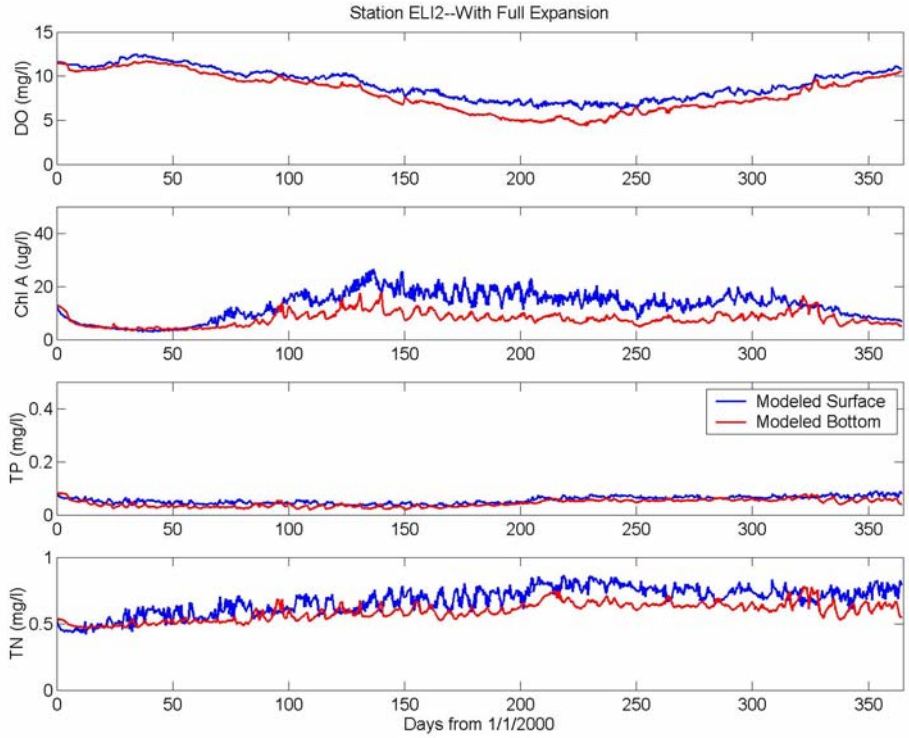

Figure H15. CIEE full expansion scenario model predictions for dissolved oxygen, chlorophyll-a, total phosphorus, and total nitrogen at CBP Station ELI2 (surface and bottom layers) for 2000.

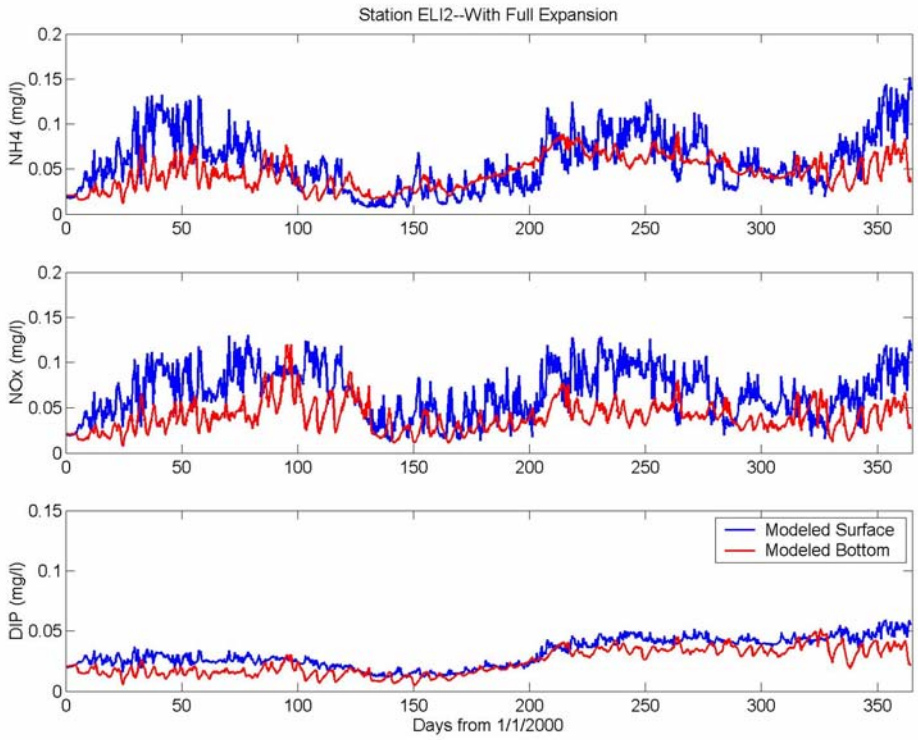

Figure H16. CIEE full expansion scenario model predictions for ammonium, nitrate, nitrite, and dissolved inorganic phosphorus at CBP Station ELI2 (surface and bottom layers) for 2000.

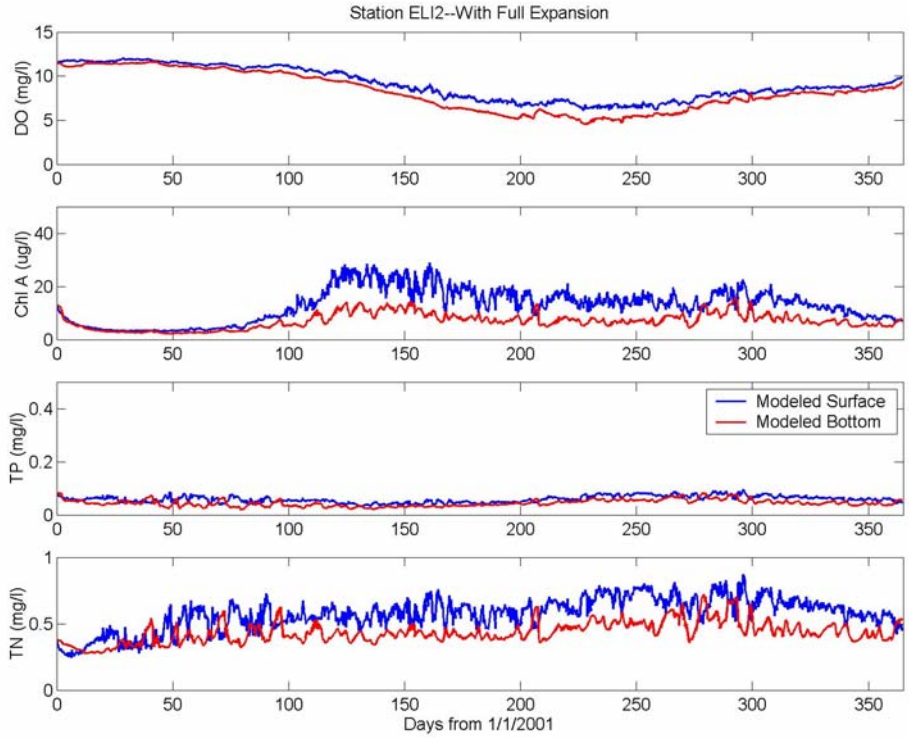

Figure H17. CIEE full expansion scenario model predictions for dissolved oxygen, chlorophyll-a, total phosphorus, and total nitrogen at CBP Station ELI2 (surface and bottom layers) for 2001.

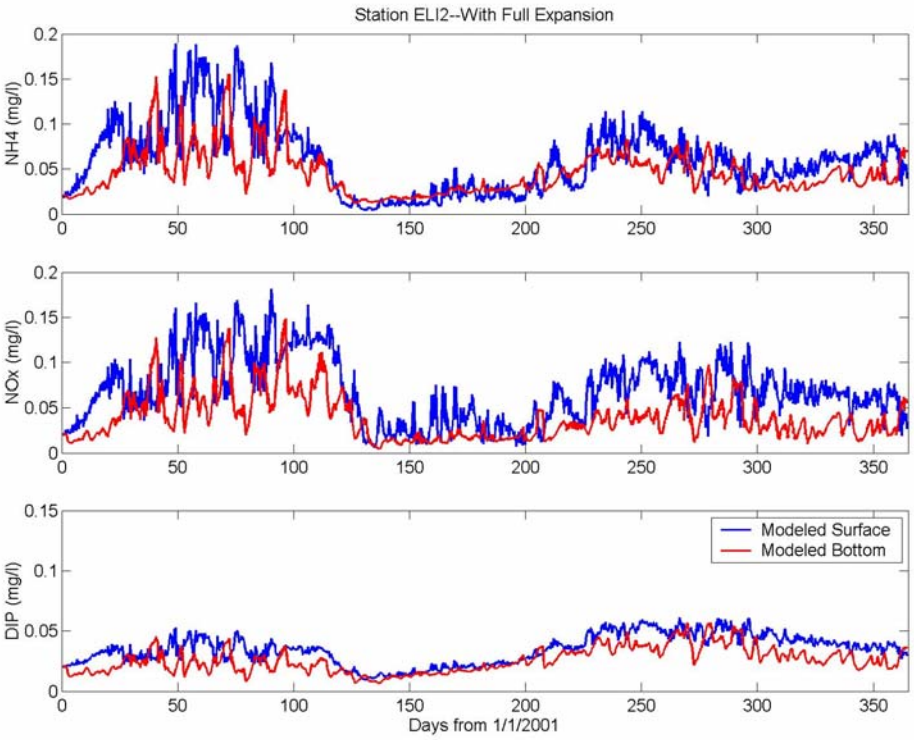

Figure H18. CIEE full expansion scenario model predictions for ammonium, nitrate, nitrite, and dissolved inorganic phosphorus at CBP Station ELI2 (surface and bottom layers) for 2001.

APPENDIX I

CIEE Full Expansion Scenario

Water Quality Model Analysis

Differences from Base Case (scenario minus base case)

CBP Stations LE5.5, LE5.6, and ELI2 for 1999, 2000, and 2001

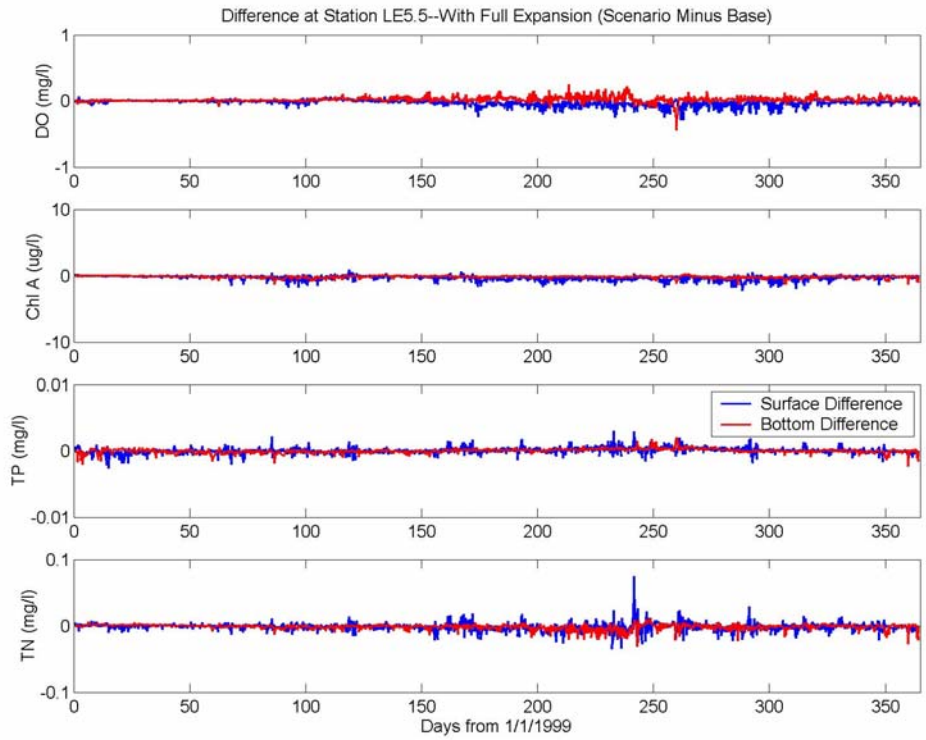

Figure I1. CIEE full expansion scenario minus base case differences of dissolved oxygen, chlorophyll-a, total phosphorus, and total nitrogen at CBP Station LE5.5 (surface and bottom layers) for 1999.

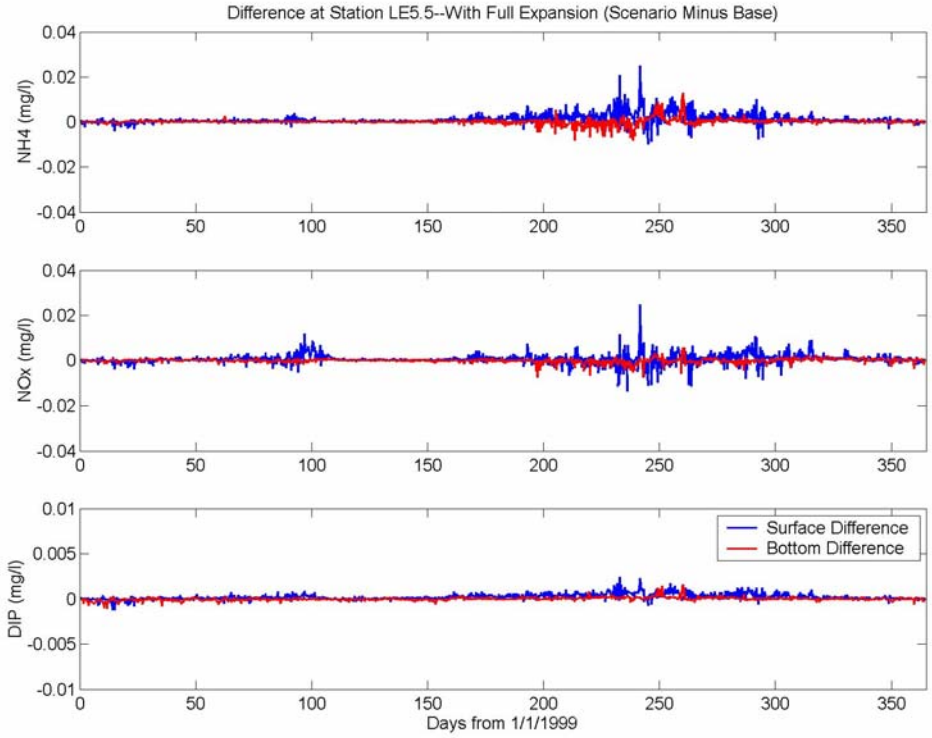

Figure I2. CIEE full expansion scenario minus base case differences of of ammonium, nitrate-nitrite, and dissolved inorganic phosphorus at CBP Station LE5.5 (surface and bottom layers) for 1999.

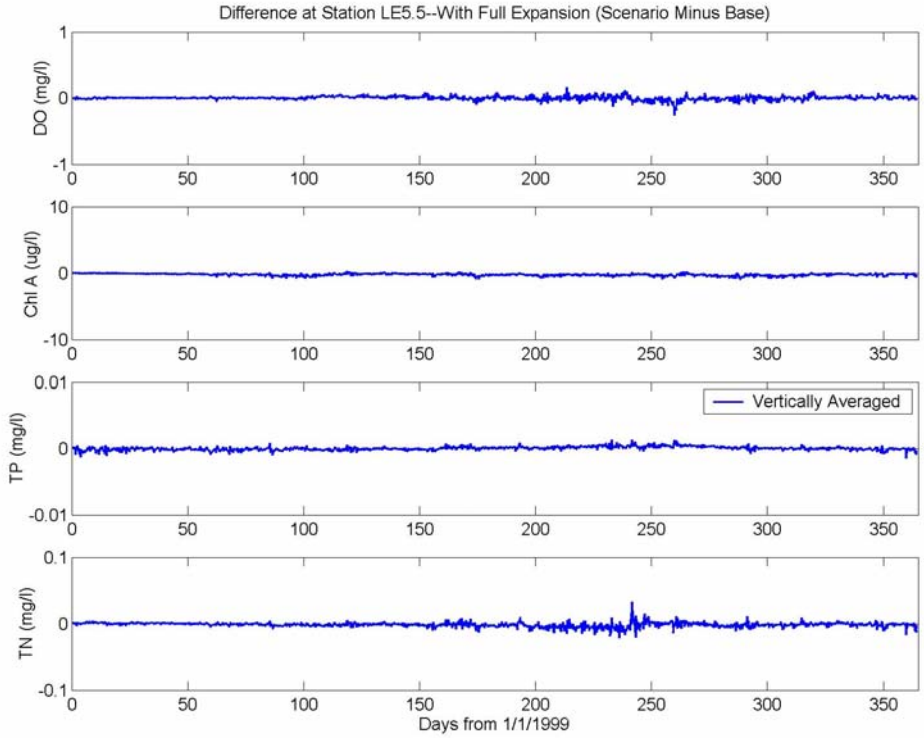

Figure I3. CIEE full expansion scenario minus base case differences of dissolved oxygen, chlorophyll-a, total phosphorus, and total nitrogen at CBP Station LE5.5 (vertically averaged) for 1999.

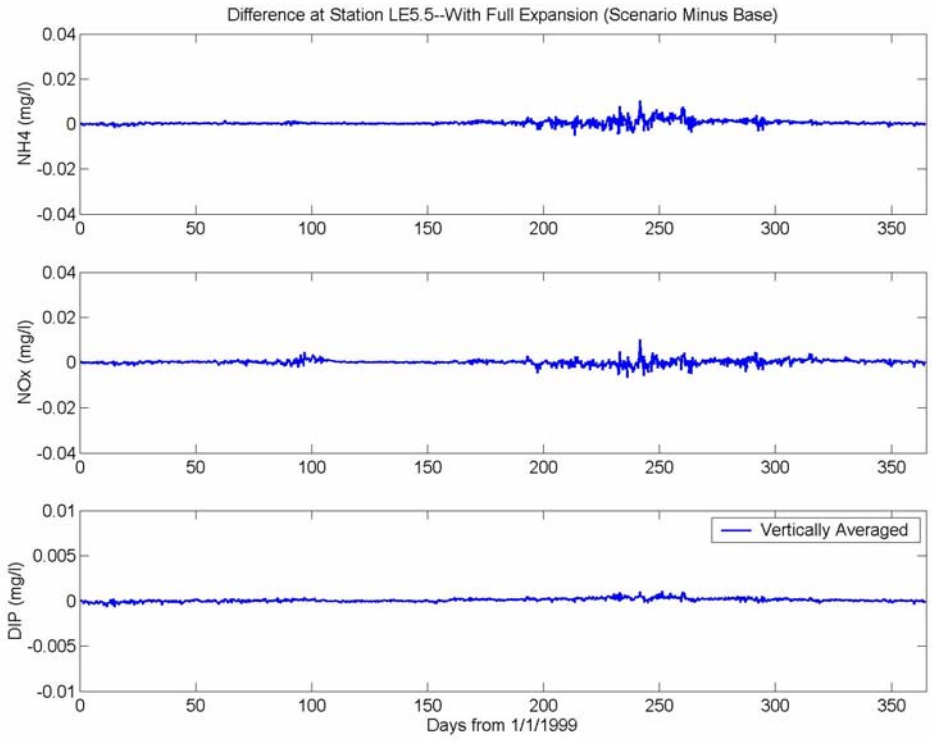

Figure I4. CIEE full expansion scenario minus base case differences of ammonium, nitrate-nitrite, and dissolved inorganic phosphorus at CBP Station LE5.5 (vertically averaged) for 1999.

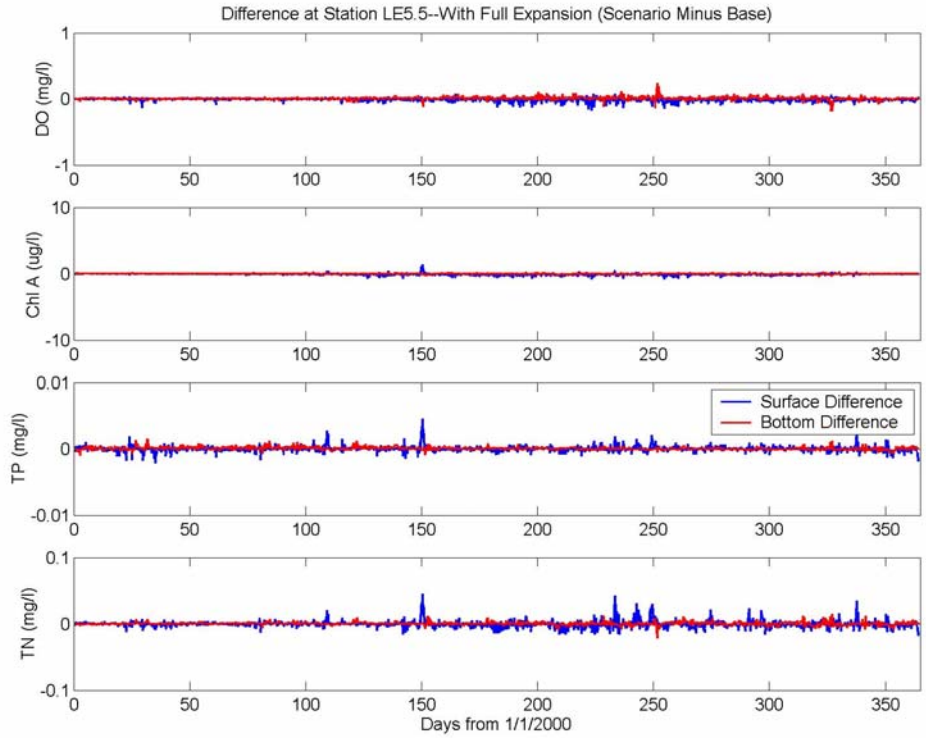

Figure I5. CIEE full expansion scenario minus base case differences of dissolved oxygen, chlorophyll-a, total phosphorus, and total nitrogen at CBP Station LE5.5 (surface and bottom layers) for 2000.

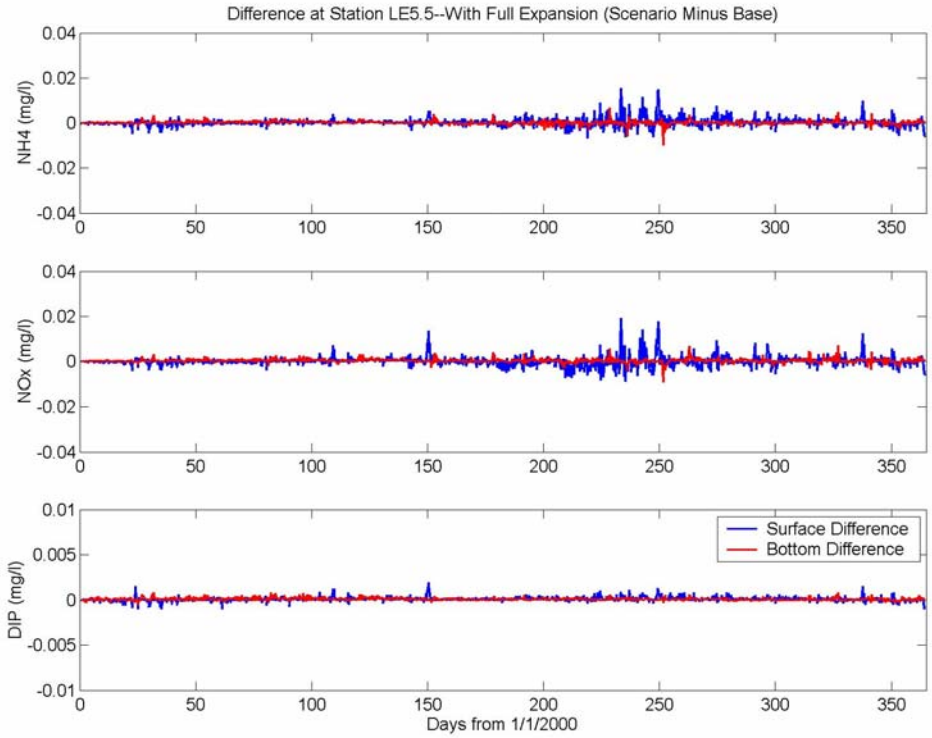

Figure I6. CIEE full expansion scenario minus base case differences of ammonium, nitrate-nitrite, and dissolved inorganic phosphorus at CBP Station LE5.5 (surface and bottom layers) for 2000.

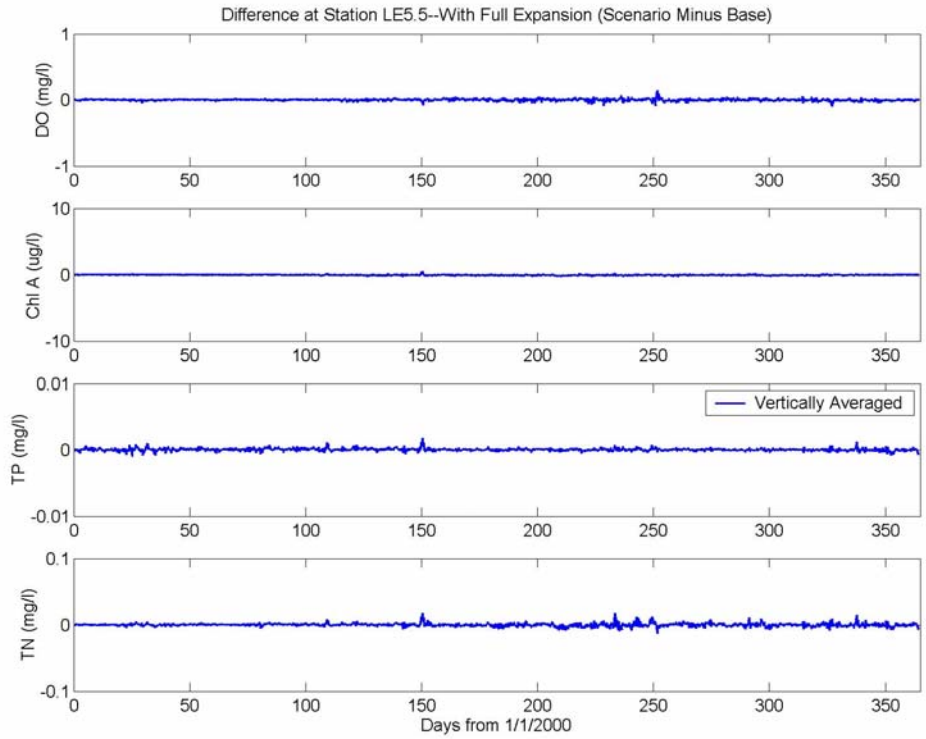

Figure I7. CIEE full expansion scenario minus base case differences of dissolved oxygen, chlorophyll-a, total phosphorus, and total nitrogen at CBP Station LE5.5 (vertically averaged) for 2000.

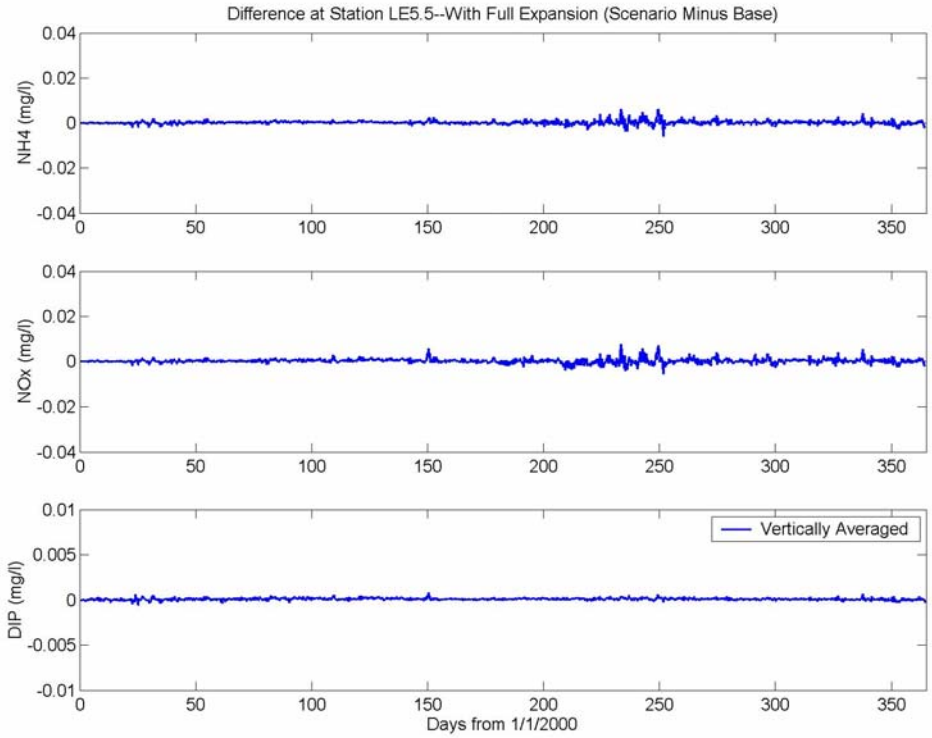

Figure I8. CIEE full expansion scenario minus base case differences of ammonium, nitrate-nitrite, and dissolved inorganic phosphorus at CBP Station LE5.5 (vertically averaged) for 2000.

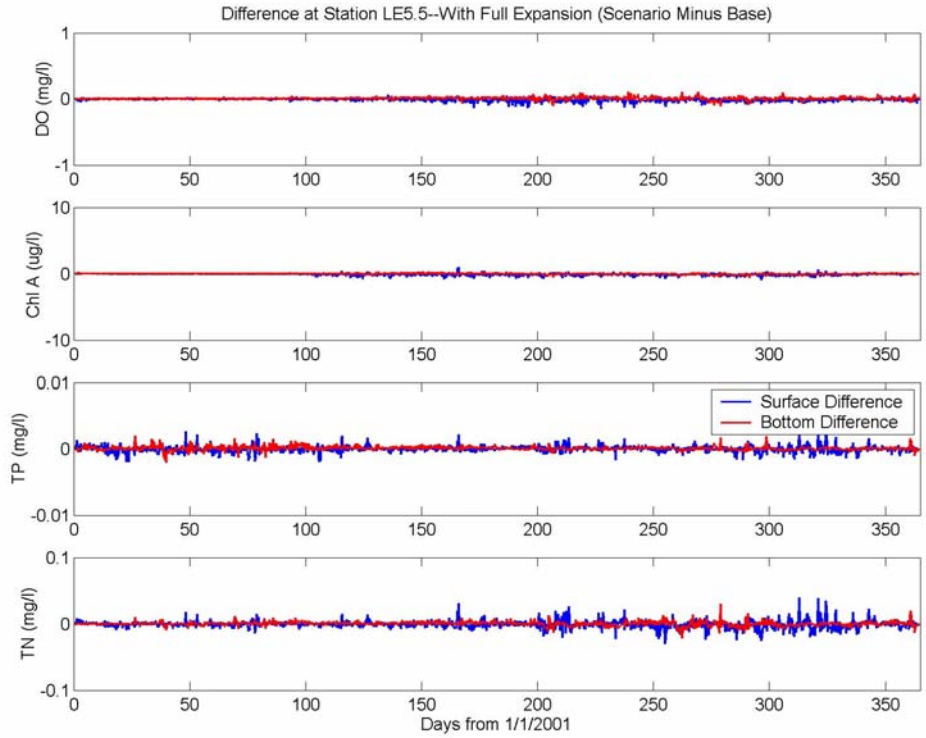

Figure I9. CIEE full expansion scenario minus base case differences of dissolved oxygen, chlorophyll-a, total phosphorus, and total nitrogen at CBP Station LE5.5 (surface and bottom layers) for 2001.

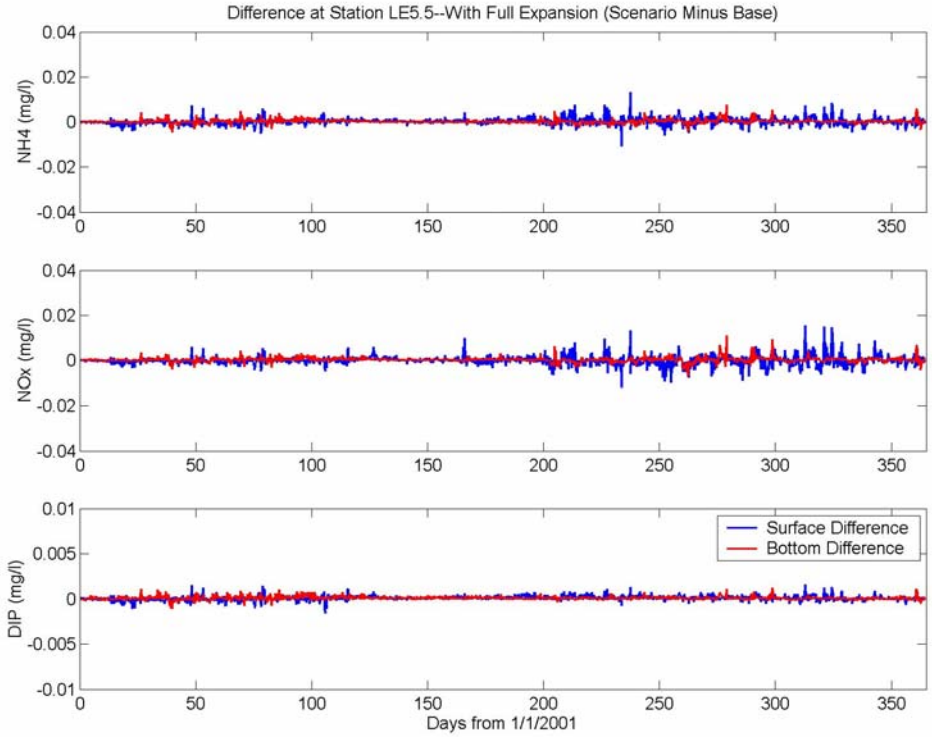

Figure I10. CIEE full expansion scenario minus base case differences of ammonium, nitrate-nitrite, and dissolved inorganic phosphorus at CBP Station LE5.5 (surface and bottom layers) for 2001.

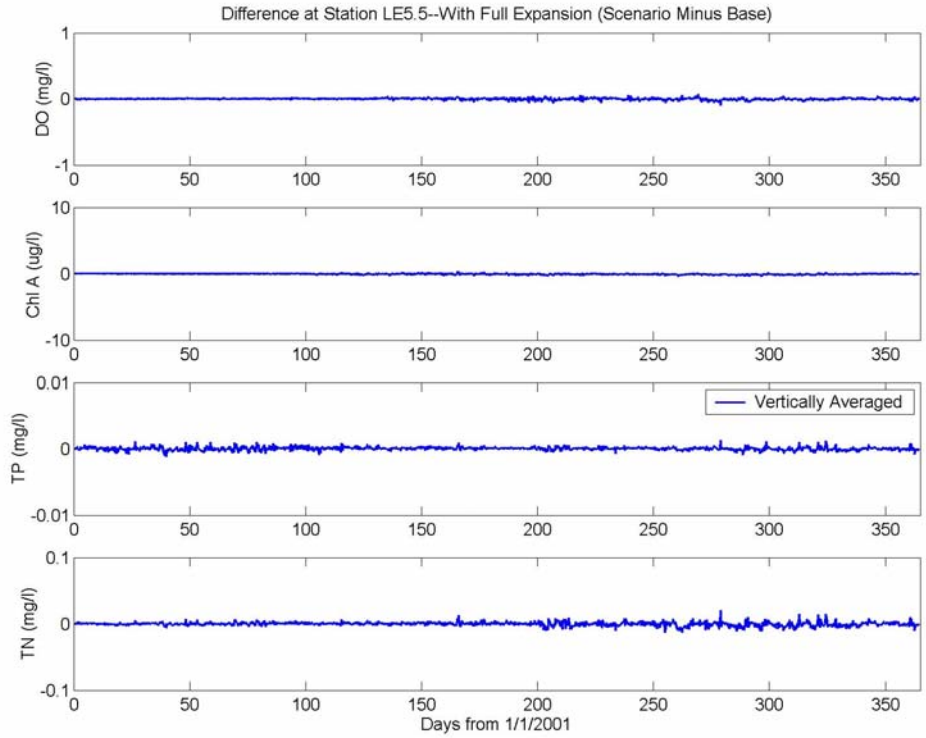

Figure I11. CIEE full expansion scenario minus base case differences of dissolved oxygen, chlorophyll-a, total phosphorus, and total nitrogen at CBP Station LE5.5 (vertically averaged) for 2001.

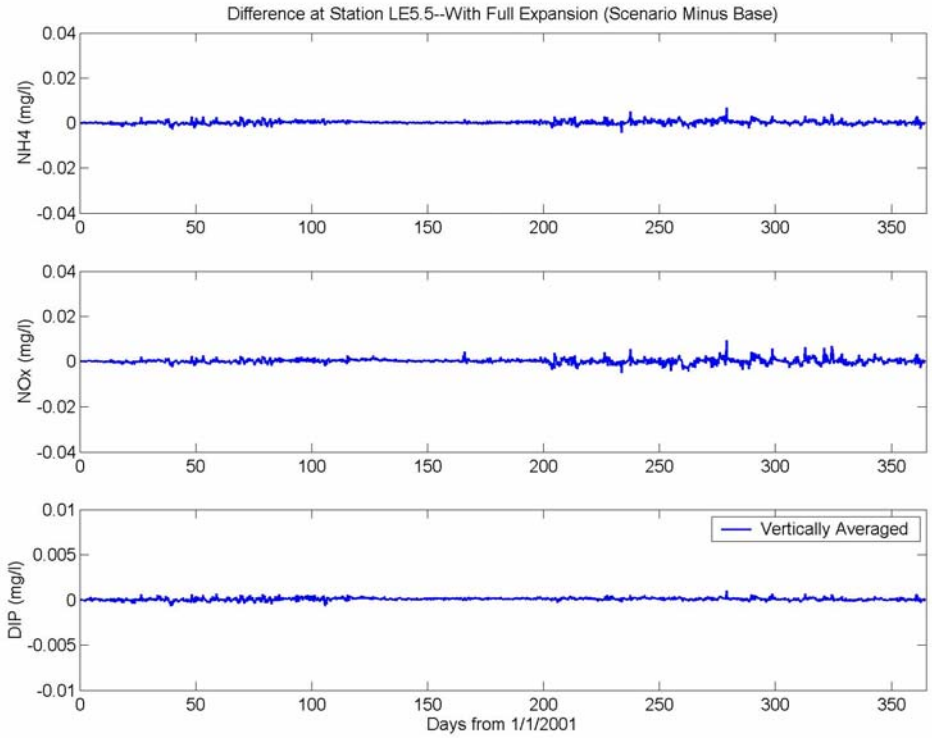

Figure I12. CIEE full expansion scenario minus base case differences of ammonium, nitrate-nitrite, and dissolved inorganic phosphorus at CBP Station LE5.5 (vertically averaged) for 2001.

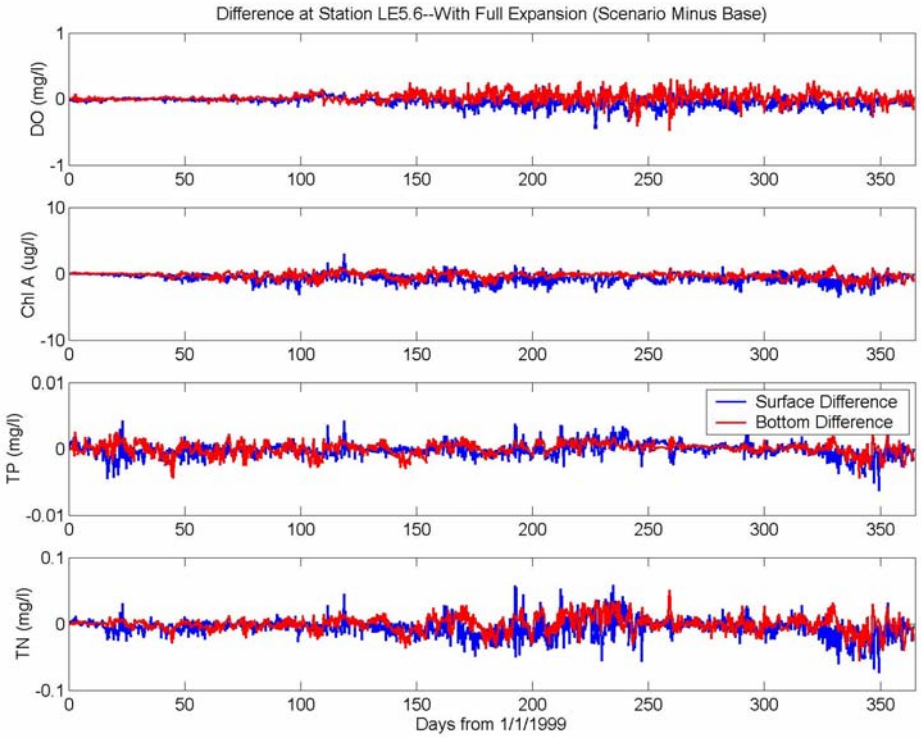

Figure I13. CIEE full expansion scenario minus base case differences of dissolved oxygen, chlorophyll-a, total phosphorus, and total nitrogen at CBP Station LE5.6 (surface and bottom layers) for 1999.

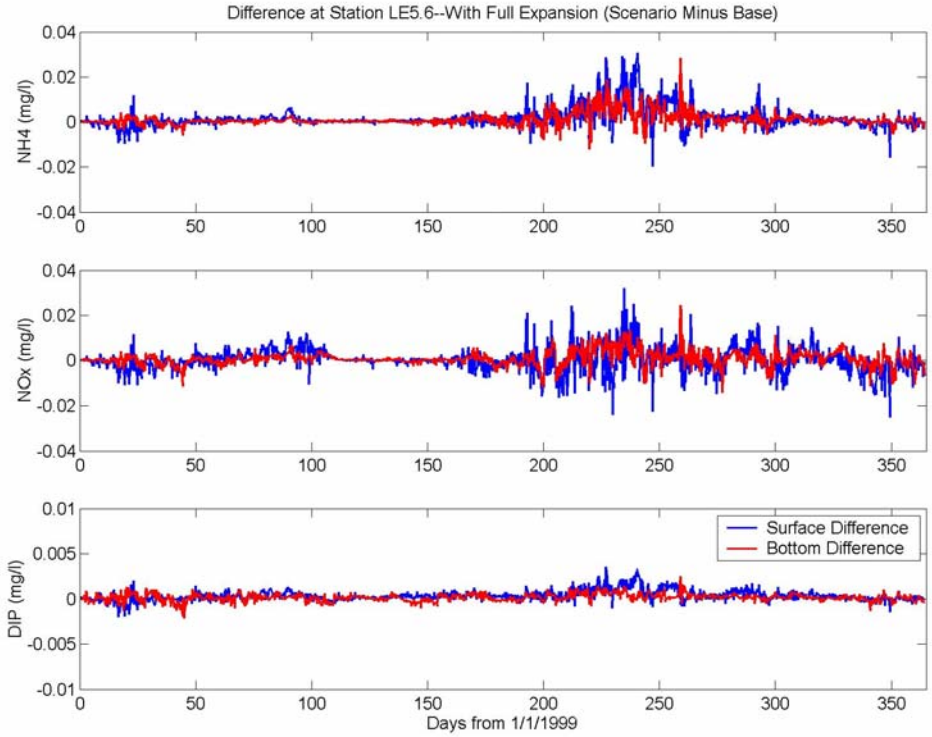

Figure I14. CIEE full expansion scenario minus base case differences of ammonium, nitrate-nitrite, and dissolved inorganic phosphorus at CBP Station LE5.6 (surface and bottom layers) for 1999.

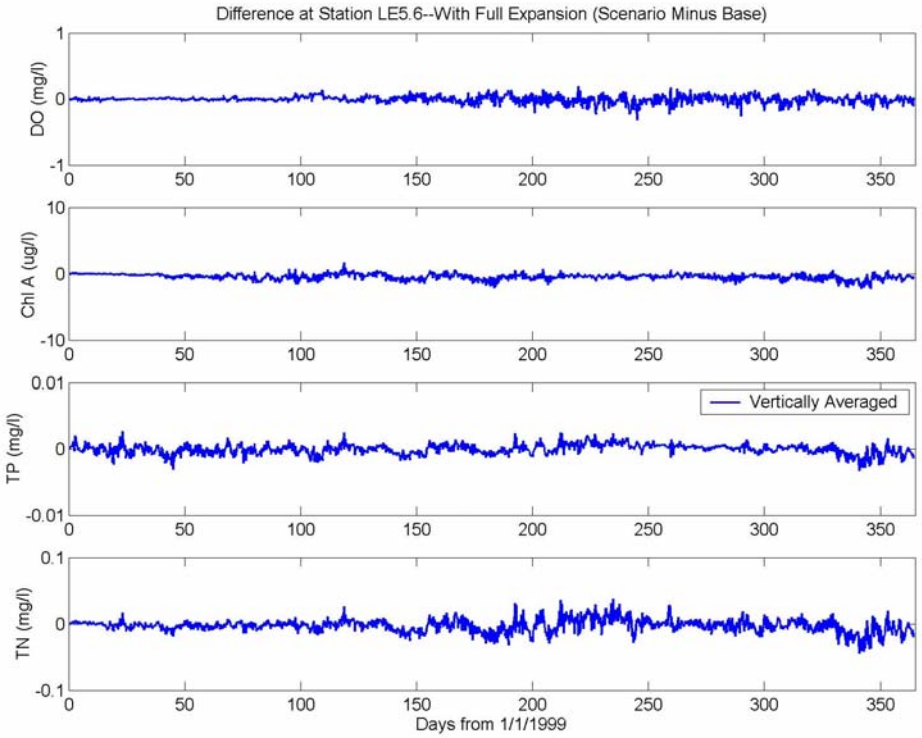

Figure I15. CIEE full expansion scenario minus base case differences of dissolved oxygen, chlorophyll-a, total phosphorus, and total nitrogen at CBP Station LE5.6 (vertically averaged) for 1999.

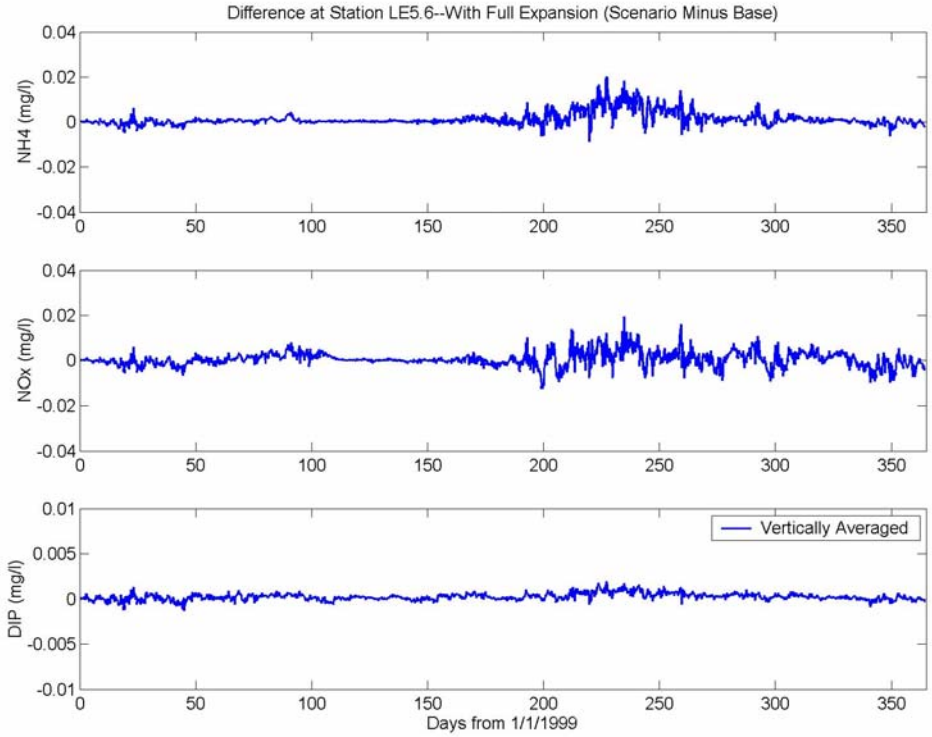

Figure I16. CIEE full expansion scenario minus base case differences of ammonium, nitrate-nitrite, and dissolved inorganic phosphorus at CBP Station LE5.6 (vertically averaged) for 1999.

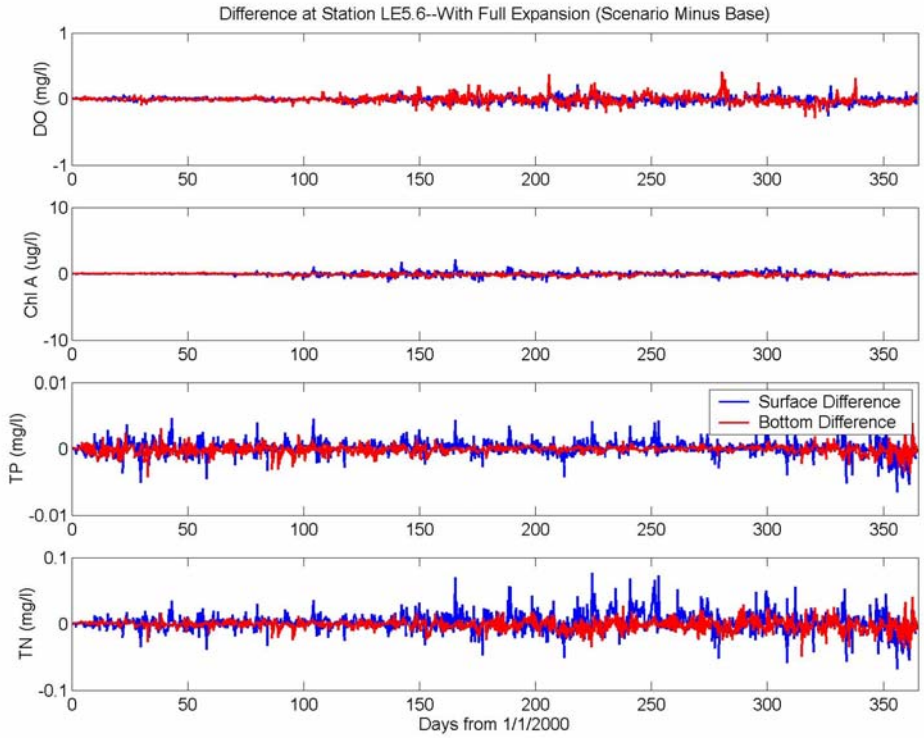

Figure I17. CIEE full expansion scenario minus base case differences of dissolved oxygen, chlorophyll-a, total phosphorus, and total nitrogen at CBP Station LE5.6 (surface and bottom layers) for 2000.

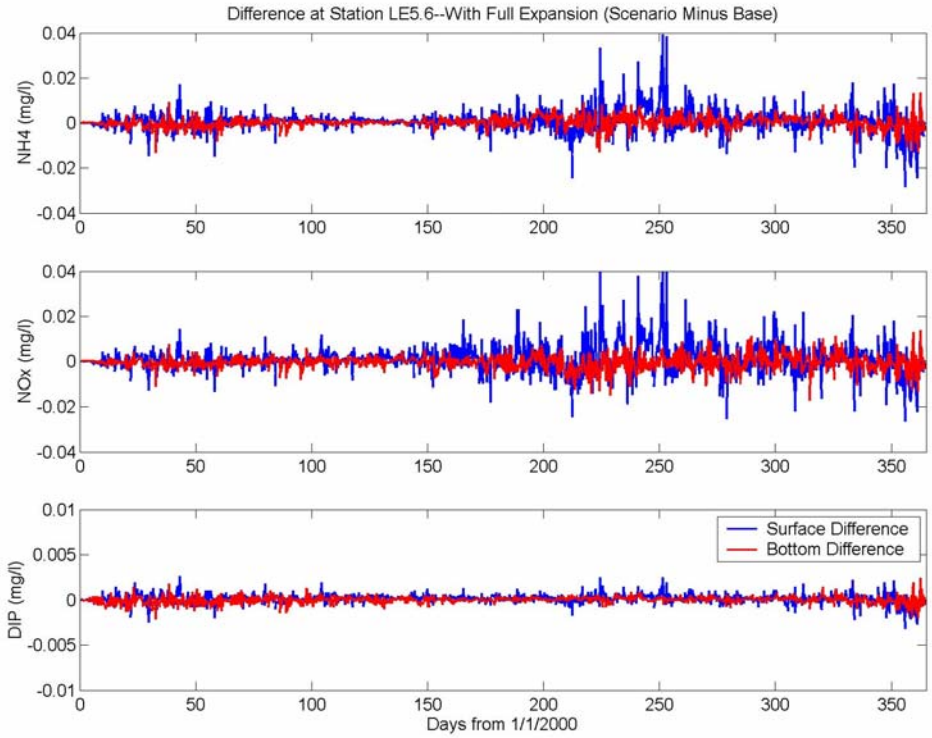

Figure I18. CIEE full expansion scenario minus base case differences of ammonium, nitrate-nitrite, and dissolved inorganic phosphorus at CBP Station LE5.6 (surface and bottom layers) for 2000.

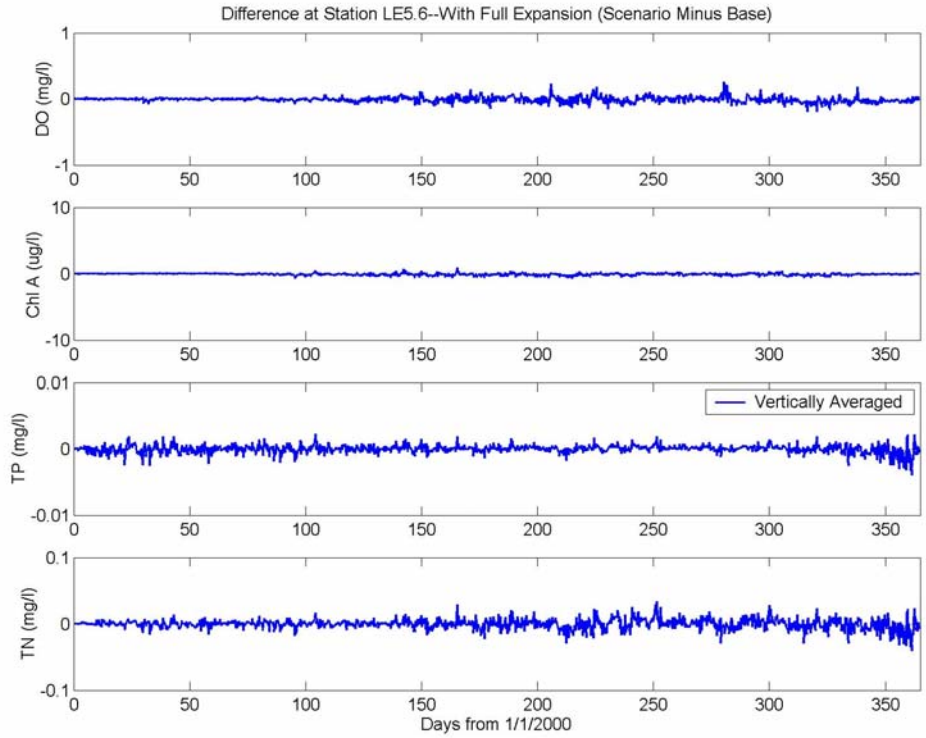

Figure I19. CIEE full expansion scenario minus base case differences of dissolved oxygen, chlorophyll-a, total phosphorus, and total nitrogen at CBP Station LE5.6 (vertically averaged) for 2000.

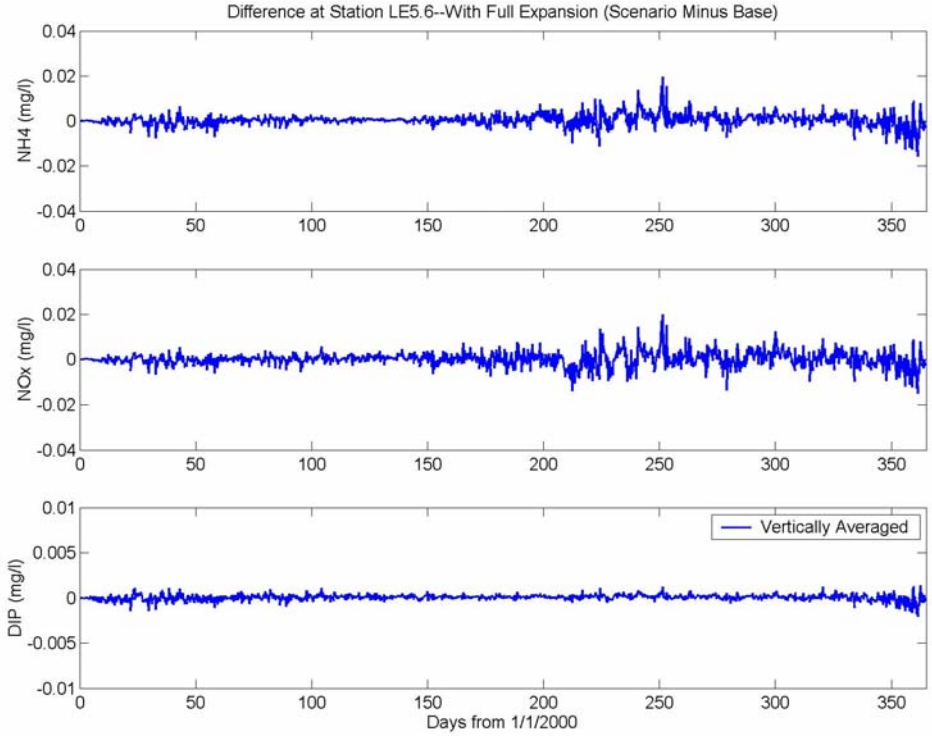

Figure I20. CIEE full expansion scenario minus base case differences of ammonium, nitrate-nitrite, and dissolved inorganic phosphorus at CBP Station LE5.6 (vertically averaged) for 2000.

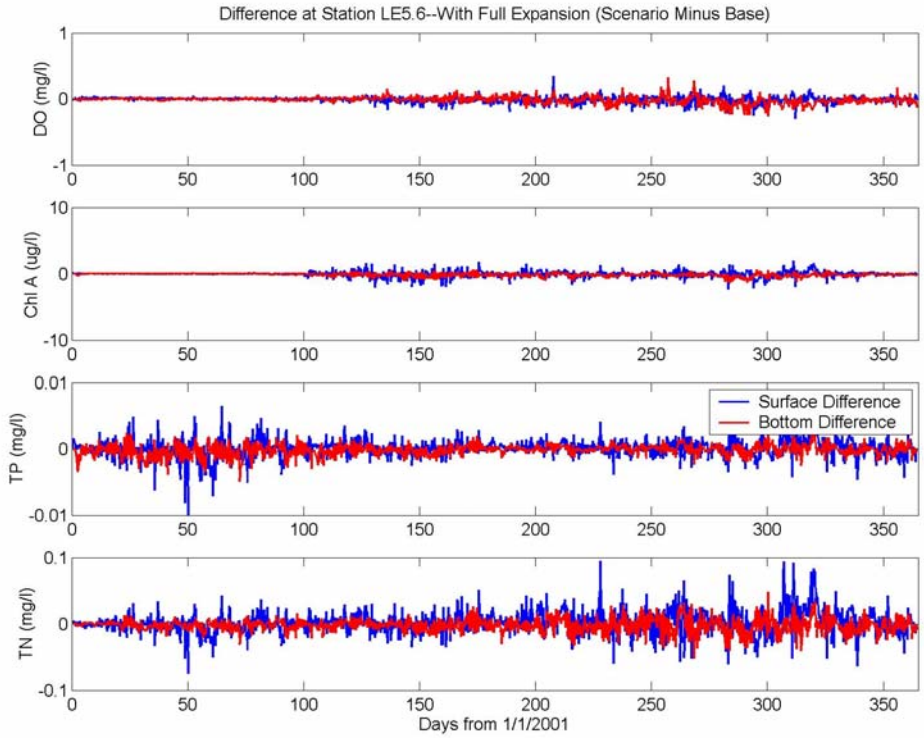

Figure I21. CIEE full expansion scenario minus base case differences of dissolved oxygen, chlorophyll-a, total phosphorus, and total nitrogen at CBP Station LE5.6 (surface and bottom layers) for 2001.

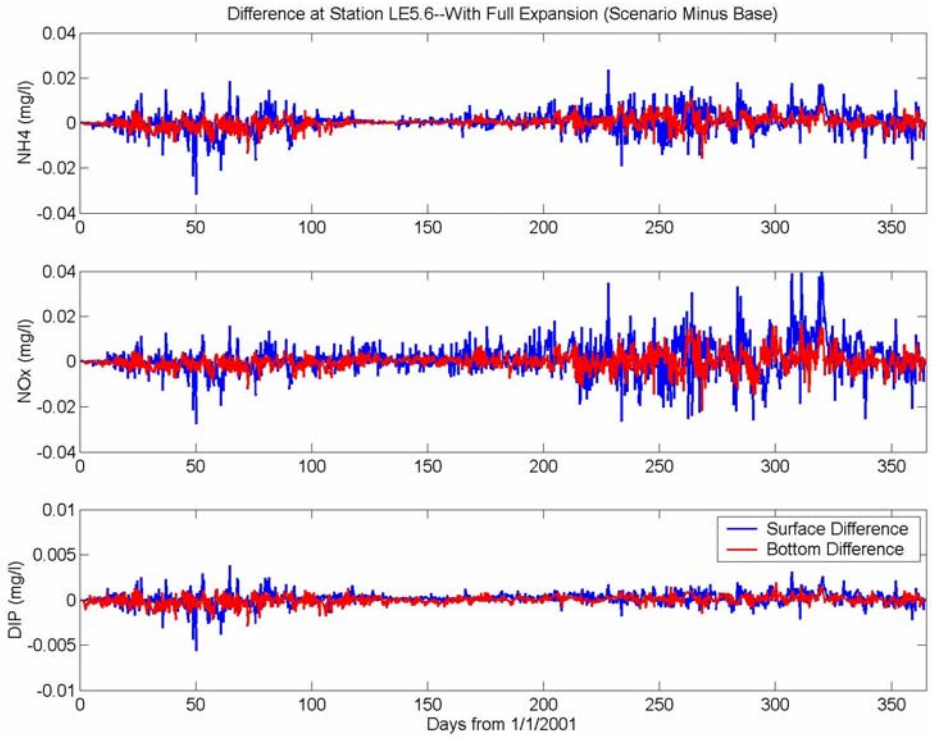

Figure I22. CIEE full expansion scenario minus base case differences of ammonium, nitrate-nitrite, and dissolved inorganic phosphorus at CBP Station LE5.6 (surface and bottom layers) for 2001.

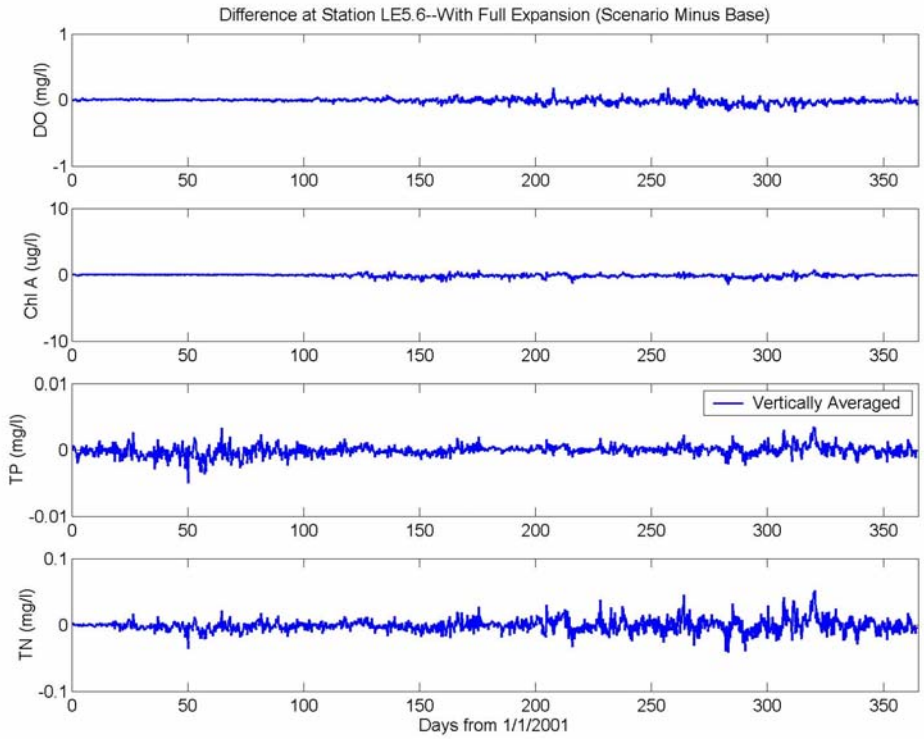

Figure I23. CIEE full expansion scenario minus base case differences of dissolved oxygen, chlorophyll-a, total phosphorus, and total nitrogen at CBP Station LE5.6 (vertically averaged) for 2001.

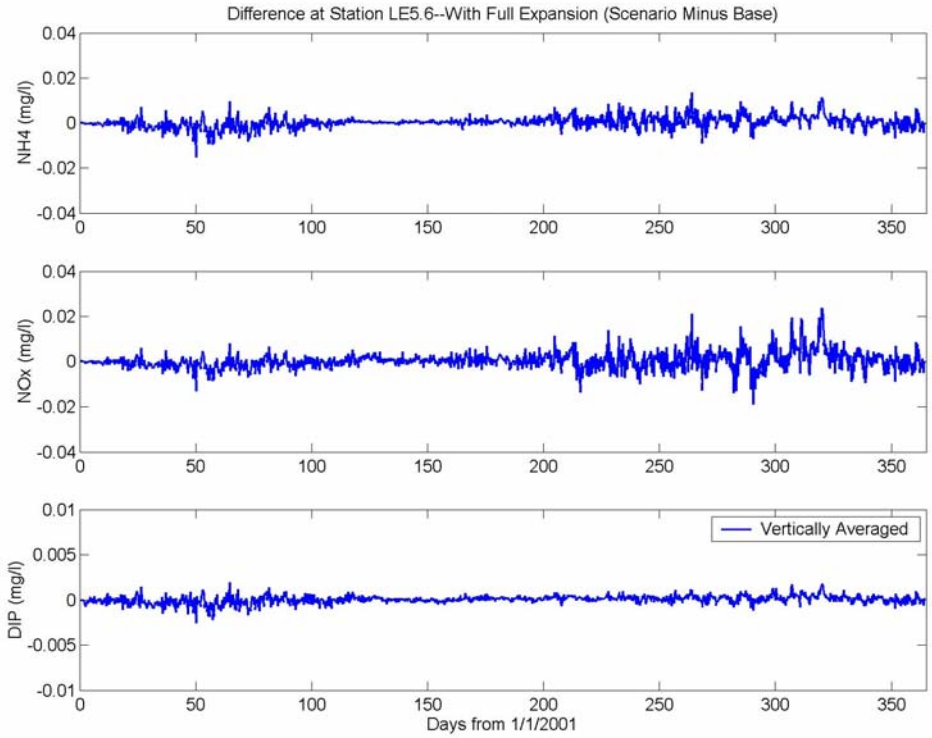

Figure I24. CIEE full expansion scenario minus base case differences of ammonium, nitrate-nitrite, and dissolved inorganic phosphorus at CBP Station LE5.6 (vertically averaged) for 2001.

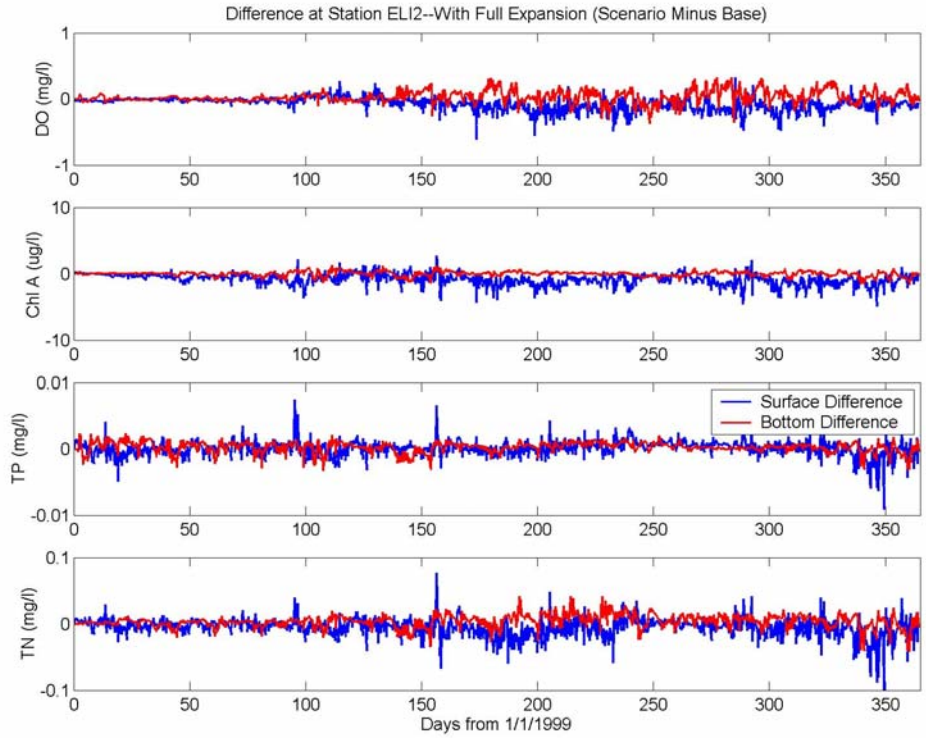

Figure I25. CIEE full expansion scenario minus base case differences of dissolved oxygen, chlorophyll-a, total phosphorus, and total nitrogen at CBP Station ELI2 (surface and bottom layers) for 1999.

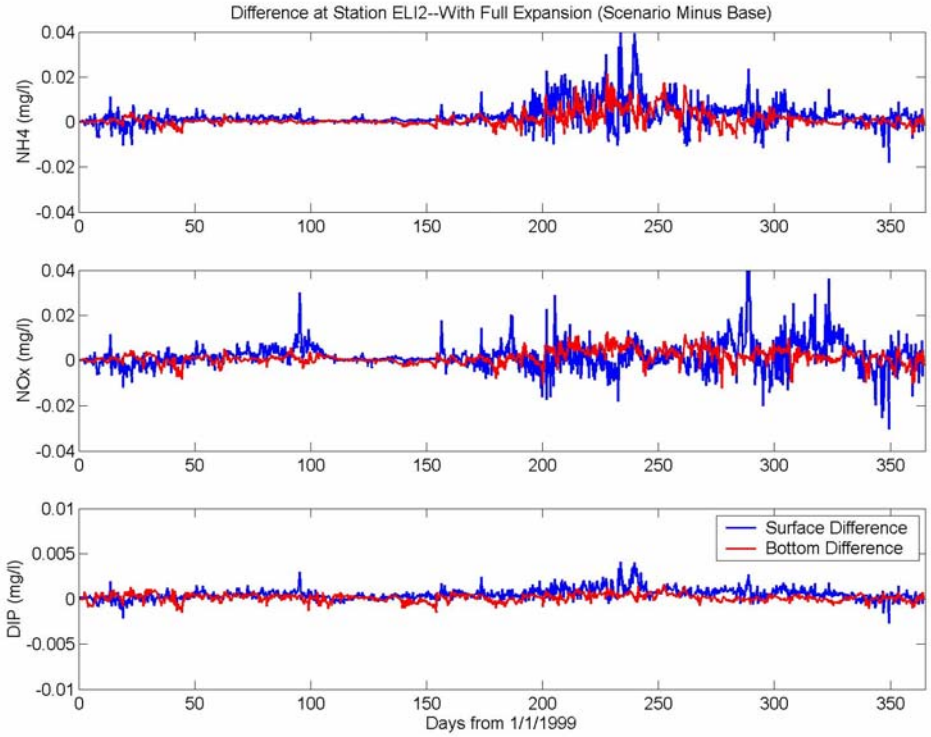

Figure I26. CIEE full expansion scenario minus base case differences of ammonium, nitrate-nitrite, and dissolved inorganic phosphorus at CBP Station ELI2 (surface and bottom layers) for 1999.

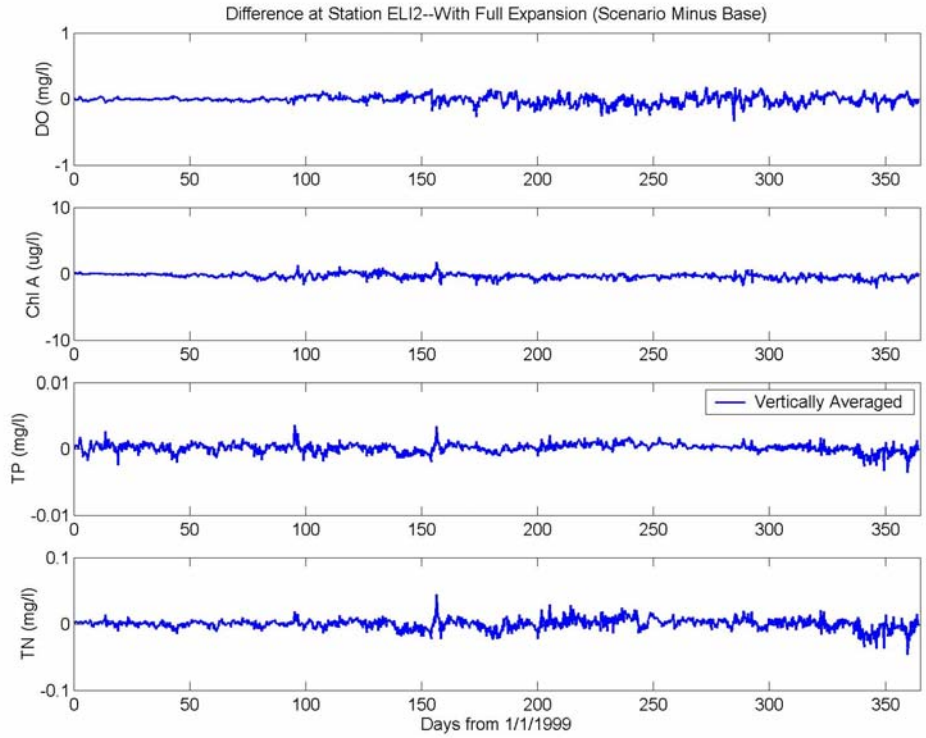

Figure I27. CIEE full expansion scenario minus base case differences of dissolved oxygen, chlorophyll-a, total phosphorus, and total nitrogen at CBP Station ELI2 (vertically averaged) for 1999.

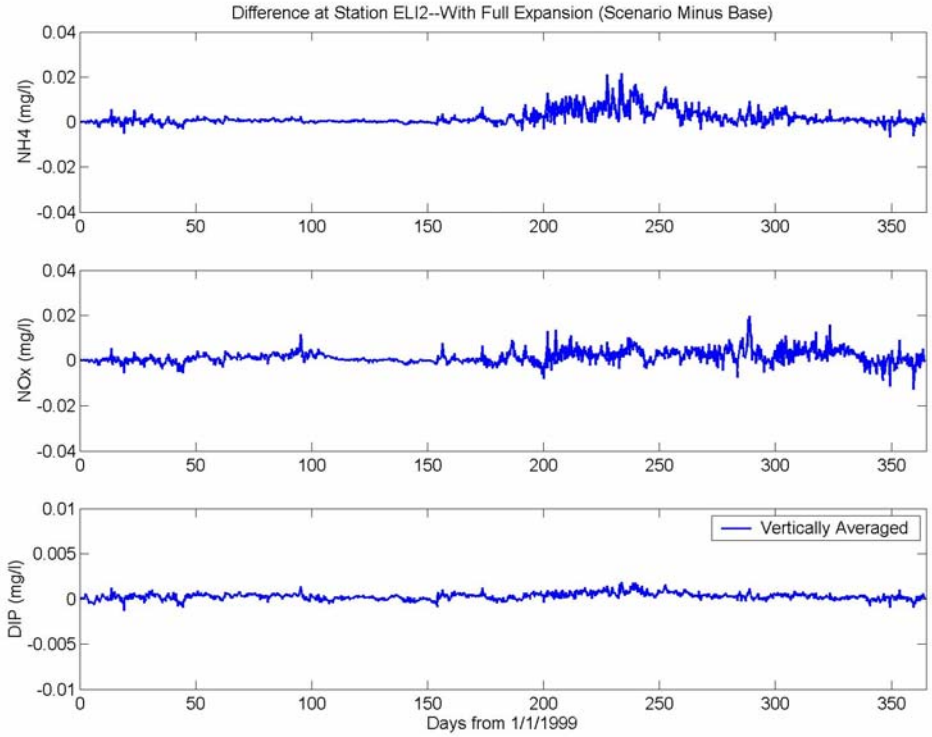

Figure I28. CIEE full expansion scenario minus base case differences of ammonium, nitrate-nitrite, and dissolved inorganic phosphorus at CBP Station ELI2 (vertically averaged) for 1999.

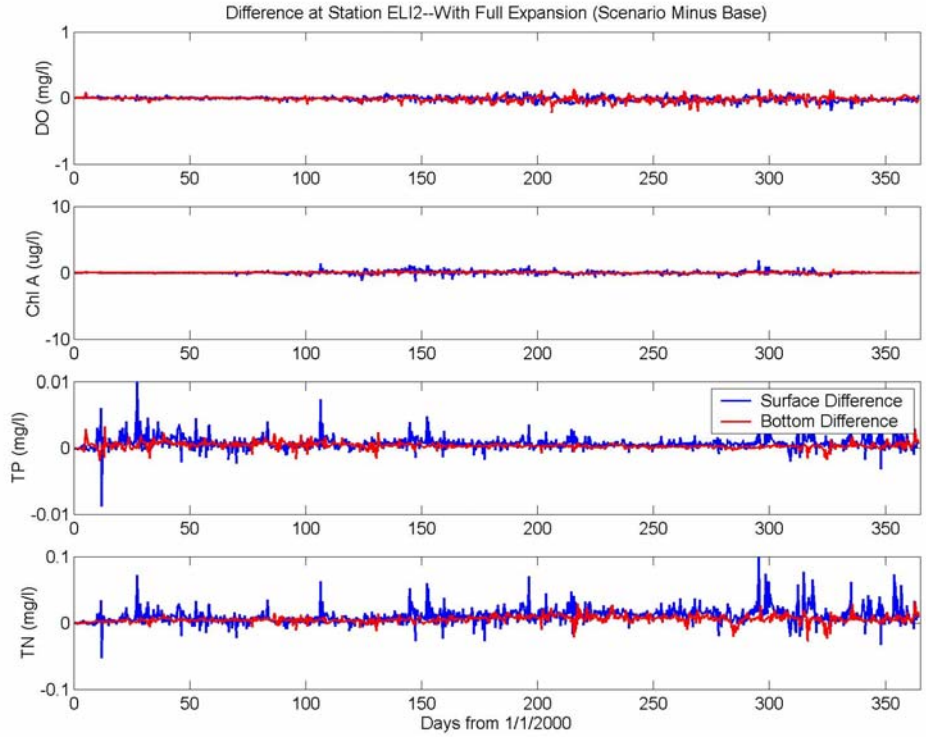

Figure I29. CIEE full expansion scenario minus base case differences of dissolved oxygen, chlorophyll-a, total phosphorus, and total nitrogen at CBP Station ELI2 (surface and bottom layers) for 2000.

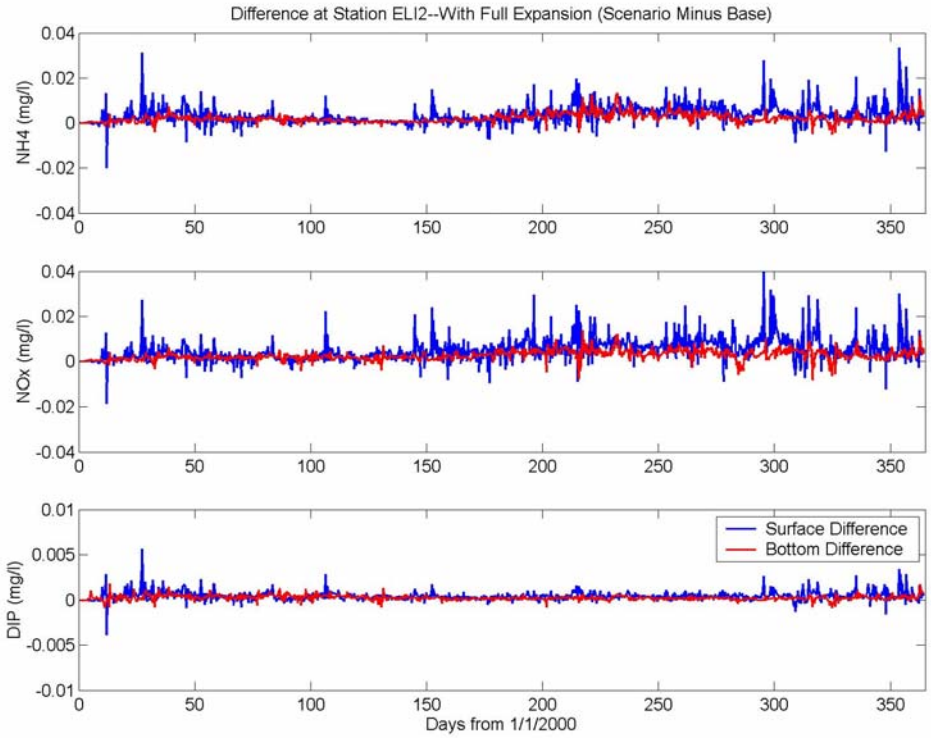

Figure I30. CIEE full expansion scenario minus base case differences of ammonium, nitrate-nitrite, and dissolved inorganic phosphorus at CBP Station ELI2 (surface and bottom layers) for 2000.

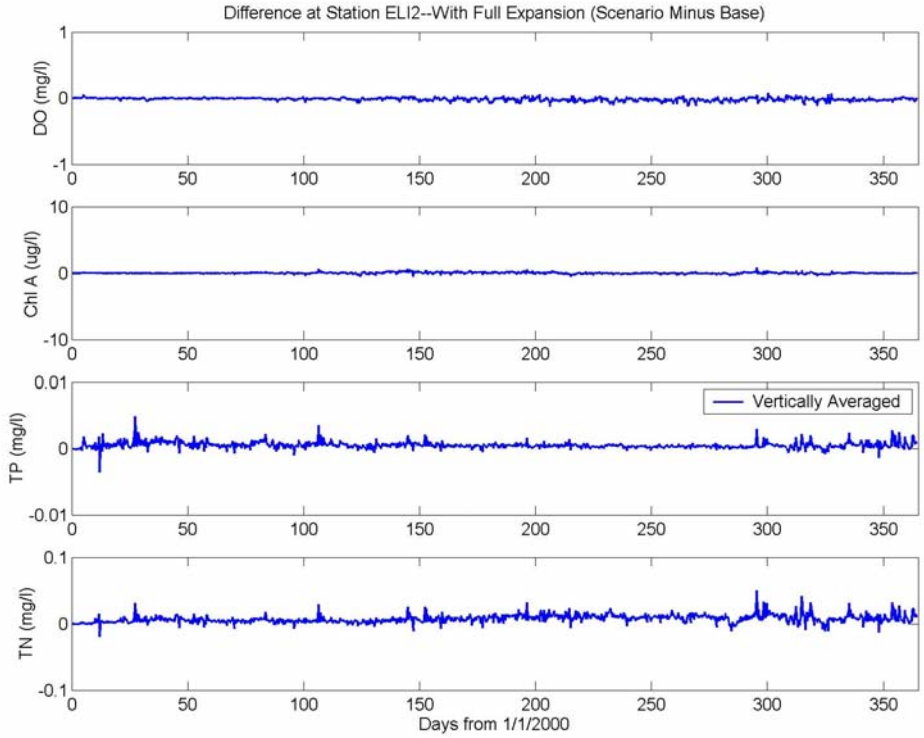

Figure I31. CIEE full expansion scenario minus base case differences of dissolved oxygen, chlorophyll-a, total phosphorus, and total nitrogen at CBP Station ELI2 (vertically averaged) for 2000.

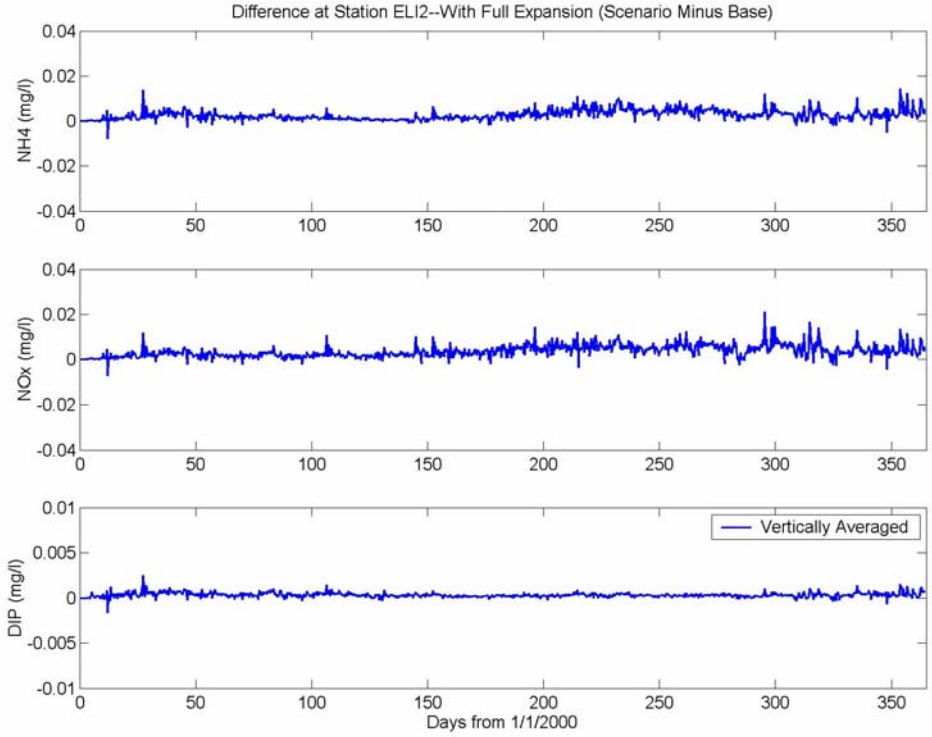

Figure I32. CIEE full expansion scenario minus base case differences of ammonium, nitrate-nitrite, and dissolved inorganic phosphorus at CBP Station ELI2 (vertically averaged) for 2000.

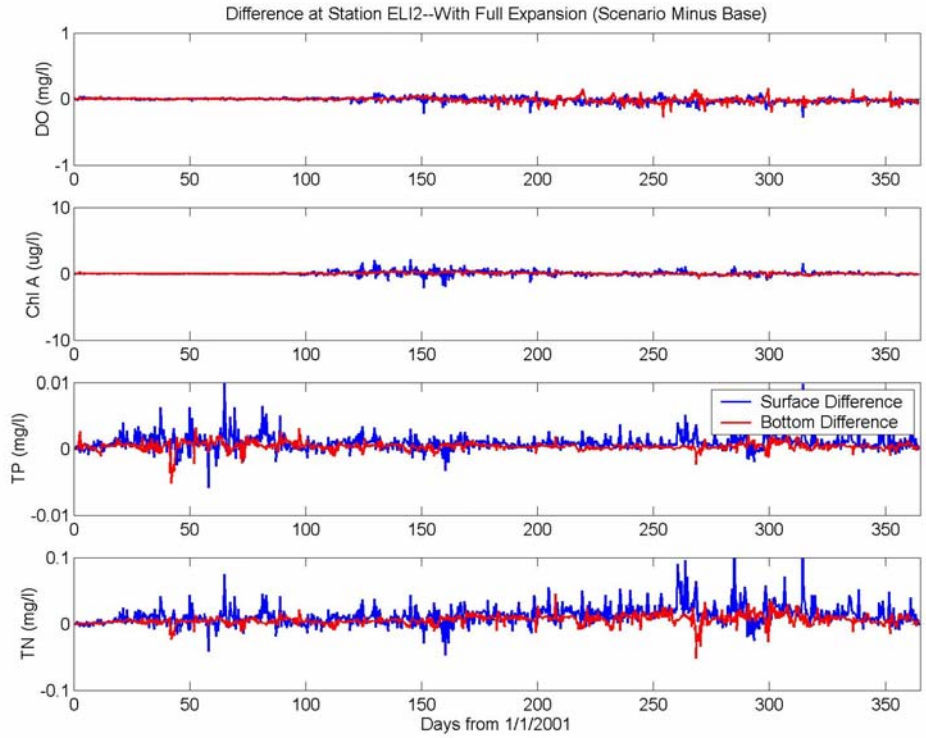

Figure I33. CIEE full expansion scenario minus base case differences of dissolved oxygen, chlorophyll-a, total phosphorus, and total nitrogen at CBP Station ELI2 (surface and bottom layers) for 2001.

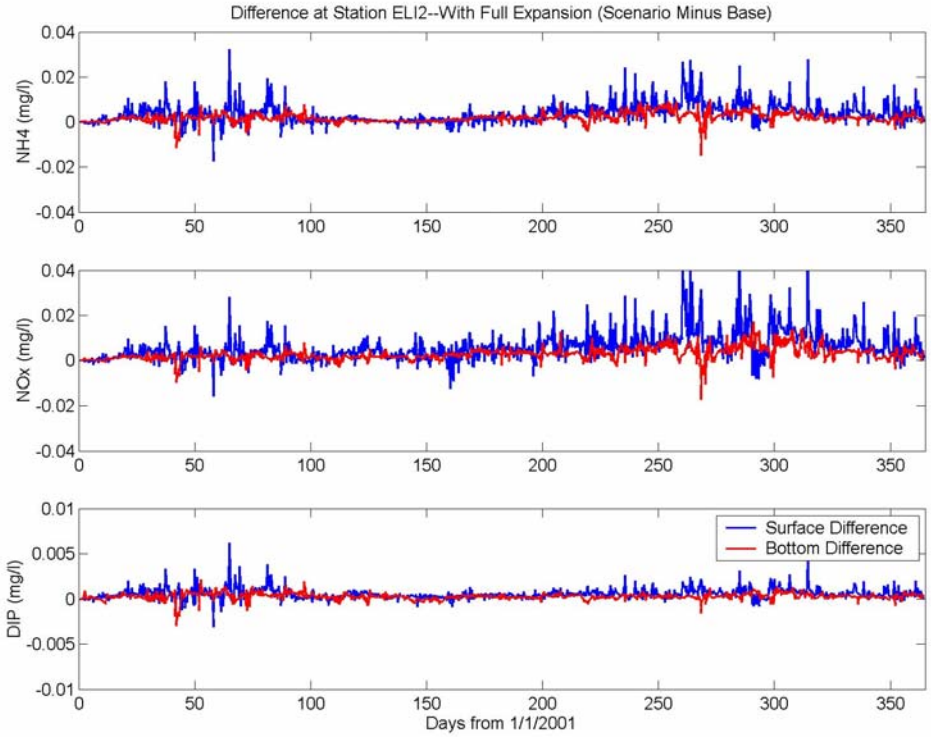

Figure I34. CIEE full expansion scenario minus base case differences of ammonium, nitrate-nitrite, and dissolved inorganic phosphorus at CBP Station ELI2 (surface and bottom layers) for 2001.

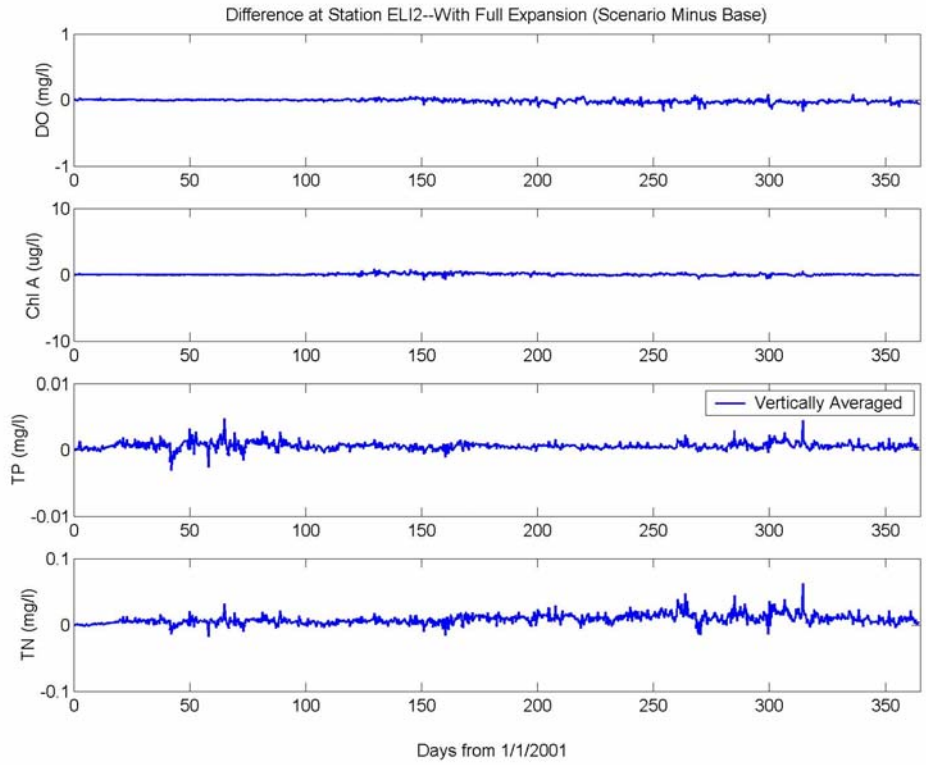

Figure I35. CIEE full expansion scenario minus base case differences of dissolved oxygen, chlorophyll-a, total phosphorus, and total nitrogen at CBP Station ELI2 (vertically averaged) for 2001.

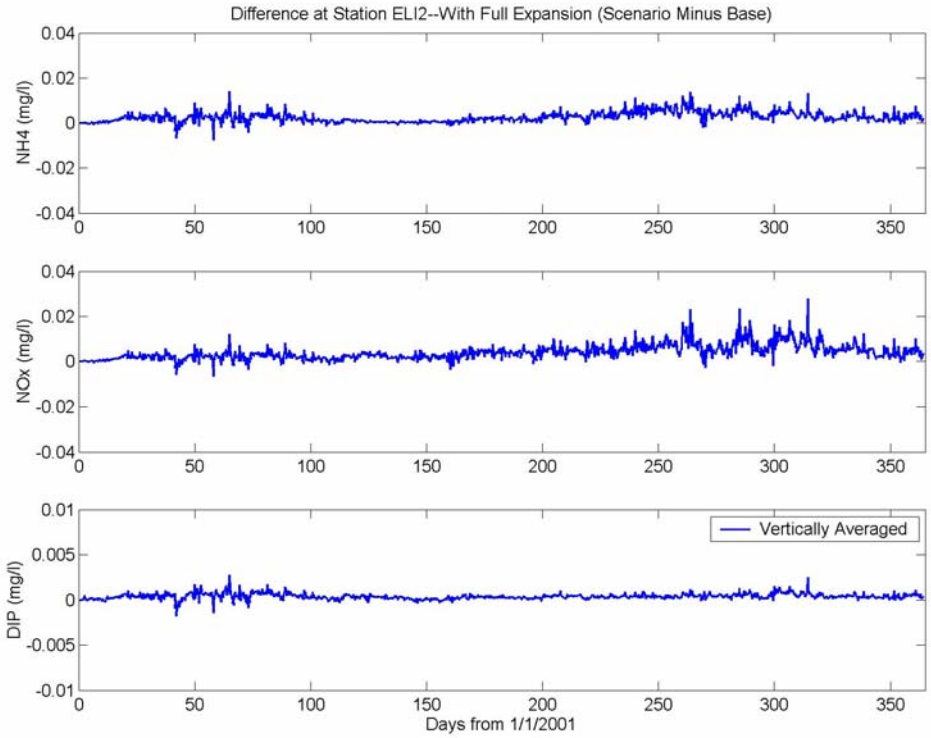

Figure I36. CIEE full expansion scenario minus base case differences of ammonium, nitrate-nitrite, and dissolved inorganic phosphorus at CBP Station ELI2 (vertically averaged) for 2001.

APPENDIX J

Full Expansion WQ Scenario Analysis

Temporal Plots of 30-day Average Differences from Base Case For Surface and Bottom Layers and Vertically Averaged

Tabulations of Vertically Averaged 30-day Average Differences

For 1999, 2000, and 2001 at CBP Stations LE5.5, LE5.6, and ELI2

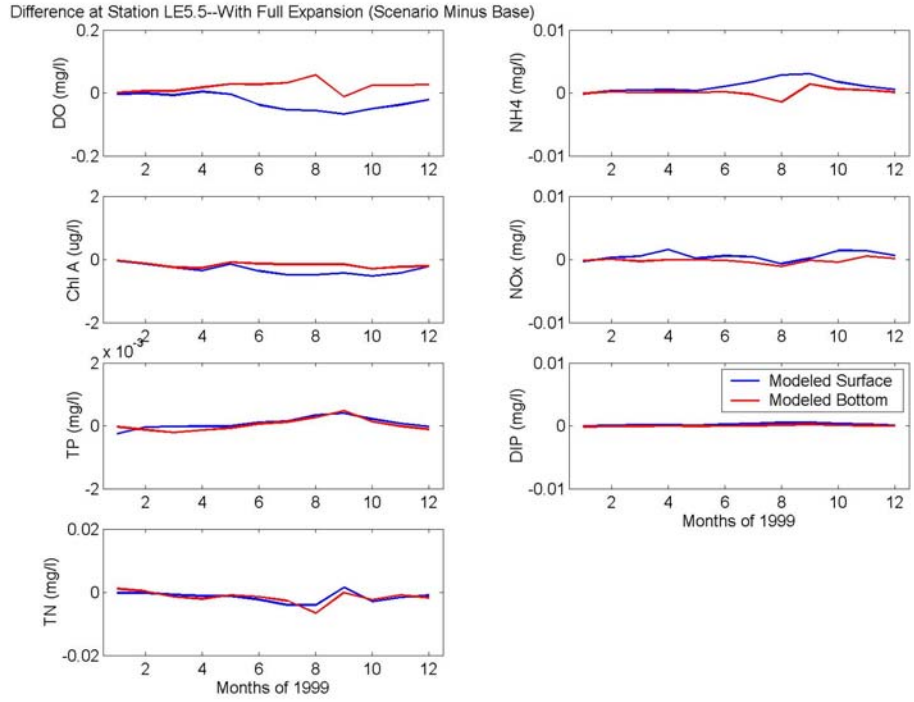

Figure J1. Differences in 30-day averages of dissolved oxygen, chlorophyll-a, total phosphorus, total nitrogen, ammonium, nitrate-nitrite, and dissolved inorganic phosphorus at CBP Station LE5.5 (surface and bottom layers) for 1999.

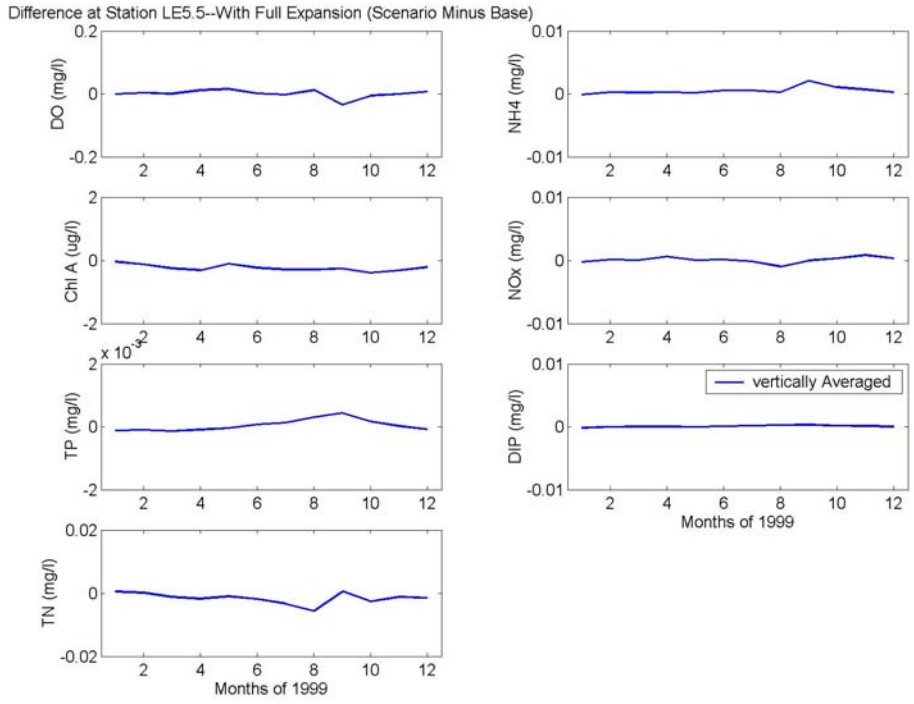

Figure J2. Differences in 30-day averages of dissolved oxygen, chlorophyll-a, total phosphorus, total nitrogen, ammonium, nitrate-nitrite, and dissolved inorganic phosphorus at CBP Station LE5.5 (vertically averaged) for 1999.

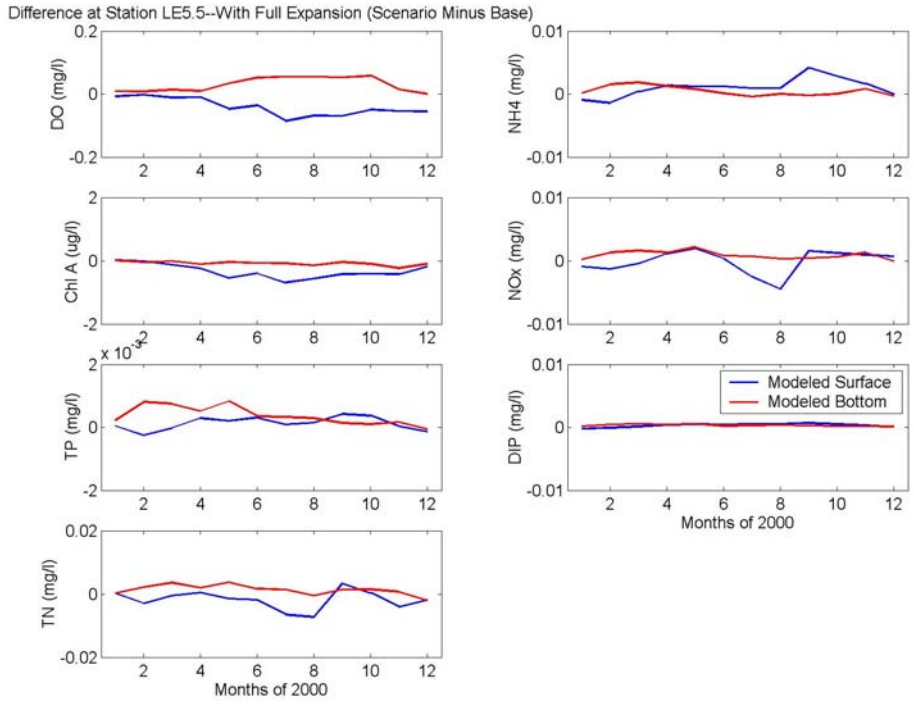

Figure J3. Differences in 30-day averages of dissolved oxygen, chlorophyll-a, total phosphorus, total nitrogen, ammonium, nitrate-nitrite, and dissolved inorganic phosphorus at CBP Station LE5.5 (surface and bottom layers) for 2000.

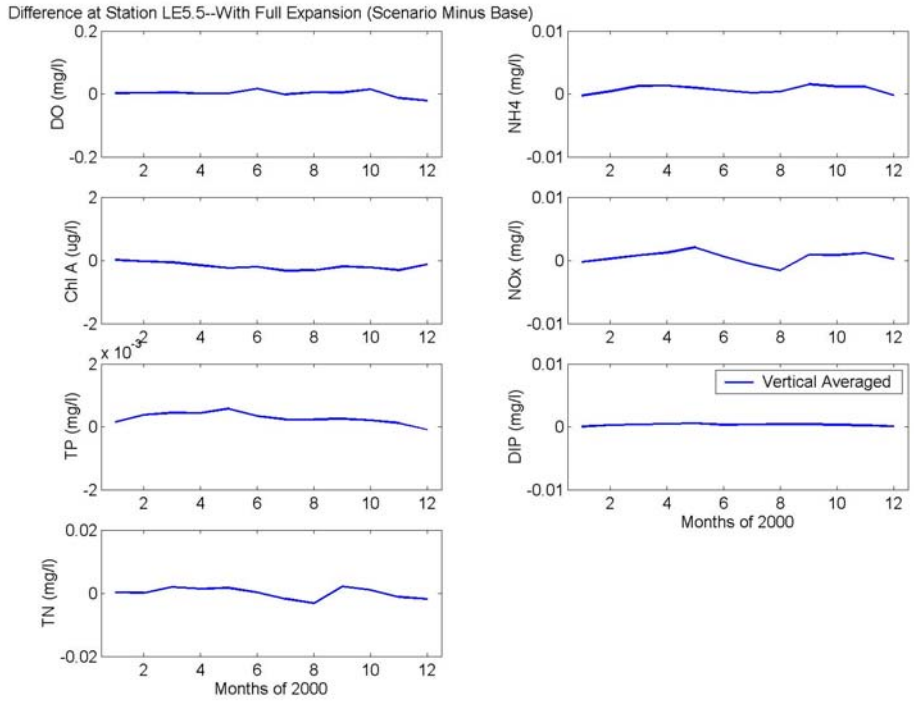

Figure J4. Differences in 30-day averages of dissolved oxygen, chlorophyll-a, total phosphorus, total nitrogen, ammonium, nitrate-nitrite, and dissolved inorganic phosphorus at CBP Station LE5.5 (vertically averaged) for 2000.

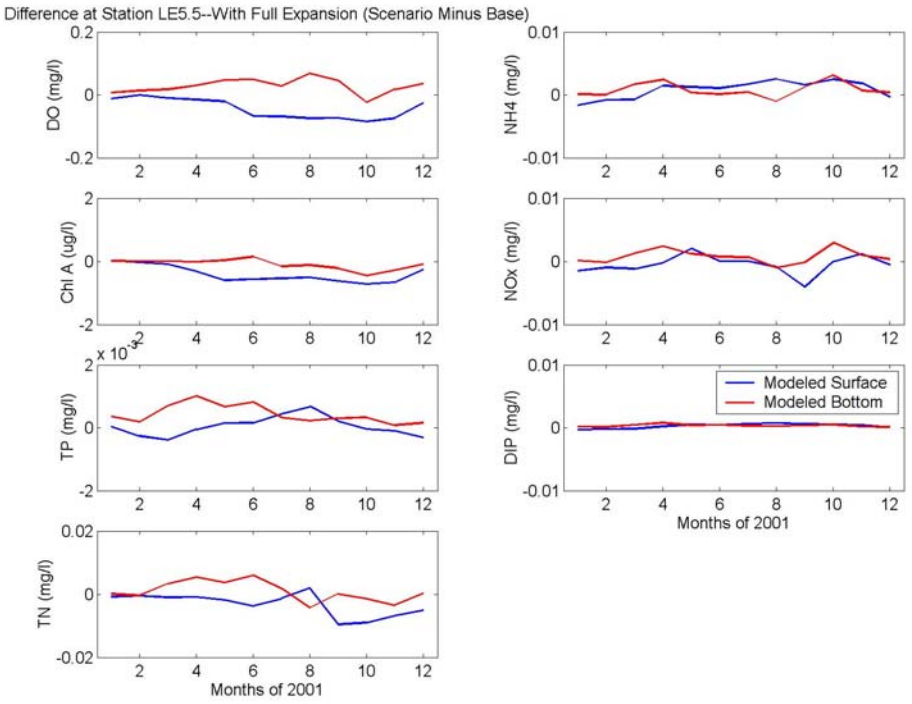

Figure J5. Differences in 30-day averages of dissolved oxygen, chlorophyll-a, total phosphorus, total nitrogen, ammonium, nitrate-nitrite, and dissolved inorganic phosphorus at CBP Station LE5.5 (surface and bottom layers) for 2001.

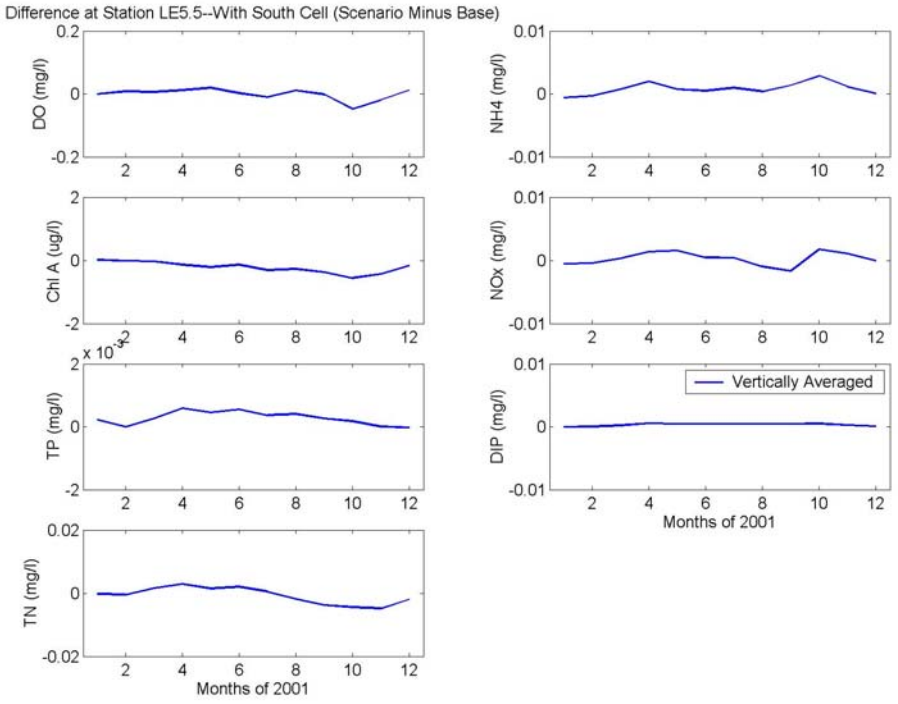

Figure J6. Differences in 30-day averages of dissolved oxygen, chlorophyll-a, total phosphorus, total nitrogen, ammonium, nitrate-nitrite, and dissolved inorganic phosphorus at CBP Station LE5.5 (vertically averaged) for 2001.

Table J1. Differences in 30-day averages of dissolved oxygen, chlorophyll-a, total phosphorus, total nitrogen, ammonium, nitrate-nitrite, and dissolved inorganic phosphorus at CBP Station LE5.5 (vertically averaged) for 1999, 2000, and 2001 (values plotted in Figures J2, J4, and J6).

	Month	**DO**	**Chl**	**TP**	**TN**	**NH_4**	**NO_X**	**DIP**
		mg/l	µg/l	mg/l	mg/l	mg/l	mg/l	mg/l
Station LE5.5 (1999)	Jan.	-0.00	-0.0	-0.0001	0.001	-0.000	-0.0003	-0.0001
	Feb.	0.00	-0.1	-0.0001	0.000	0.000	0.0001	0.0000
	Mar.	0.00	-0.2	-0.0001	-0.001	0.000	0.0000	0.0000
	Apr.	0.01	-0.3	-0.0001	-0.002	0.000	0.0006	0.0000
	May	0.02	-0.1	0.0000	-0.001	0.000	0.0000	0.0000
	Jun.	0.00	-0.2	0.0001	-0.002	0.001	0.0001	0.0001
	Jul.	-0.00	-0.3	0.0001	-0.003	0.001	-0.0002	0.0002
	Aug.	0.01	-0.3	0.0003	-0.006	0.000	-0.0010	0.0003
	Sep.	-0.03	-0.3	0.0004	0.001	0.002	0.0000	0.0003
	Oct.	-0.01	-0.4	0.0002	-0.003	0.001	0.0003	0.0002
	Nov.	-0.00	-0.3	0.0000	-0.001	0.001	0.0008	0.0001
	Dec.	0.01	-0.2	-0.0001	-0.002	0.000	0.0003	0.0000
Detection limits:		**0.1**	**0.5**	**0.003**	**0.01**	**0.005**	**0.001**	**0.0015**

	Month	**DO**	**Chl**	**TP**	**TN**	**NH_4**	**NO_X**	**DIP**
		mg/l	µg/l	mg/l	mg/l	mg/l	mg/l	mg/l
Station LE5.5 (2000)	Jan.	0.00	0.0	0.0002	0.000	-0.000	-0.0003	0.0000
	Feb.	0.00	-0.0	0.0004	0.000	0.000	0.0003	0.0002
	Mar.	0.00	-0.1	0.0004	0.002	0.001	0.0008	0.0004
	Apr.	0.00	-0.2	0.0004	0.001	0.001	0.0012	0.0004
	May	0.00	-0.2	0.0006	0.002	0.001	0.0021	0.0005
	Jun.	0.02	-0.2	0.0003	0.000	0.001	0.0006	0.0003
	Jul.	-0.00	-0.3	0.0002	-0.002	0.000	-0.0006	0.0004
	Aug.	0.01	-0.3	0.0002	-0.003	0.000	-0.0016	0.0004
	Sep.	0.00	-0.2	0.0003	0.002	0.002	0.0009	0.0004
	Oct.	0.02	-0.2	0.0002	0.001	0.001	0.0008	0.0003
	Nov.	-0.01	-0.3	0.0001	-0.001	0.001	0.0012	0.0002
	Dec.	-0.02	-0.1	-0.0001	-0.002	-0.000	0.0003	0.0001
Detection limits:		**0.1**	**0.5**	**0.003**	**0.01**	**0.005**	**0.001**	**0.0015**

	Month	**DO**	**Chl**	**TP**	**TN**	**NH_4**	**NO_X**	**DIP**
		mg/l	µg/l	mg/l	mg/l	mg/l	mg/l	mg/l
Station LE5.5 (2001)	Jan.	-0.00	0.0	0.0002	-0.000	-0.001	-0.0005	0.0000
	Feb.	0.01	-0.0	0.0000	-0.000	-0.000	-0.0005	0.0000
	Mar.	0.01	-0.0	0.0003	0.002	0.001	0.0003	0.0002
	Apr.	0.01	-0.1	0.0006	0.003	0.002	0.0014	0.0006
	May	0.02	-0.2	0.0005	0.002	0.001	0.0015	0.0004
	Jun.	0.00	-0.1	0.0006	0.002	0.001	0.0004	0.0005
	Jul.	-0.01	-0.3	0.0004	0.001	0.001	0.0004	0.0004
	Aug.	0.01	-0.3	0.0004	-0.002	0.000	-0.0010	0.0005
	Sep.	-0.00	-0.4	0.0003	-0.004	0.001	-0.0017	0.0005
	Oct.	-0.05	-0.6	0.0002	-0.005	0.003	0.0017	0.0005
	Nov.	-0.02	-0.4	0.0000	-0.005	0.001	0.0011	0.0003
	Dec.	0.01	-0.2	0.0000	-0.002	0.000	0.0000	0.0001
Detection limits:		**0.1**	**0.5**	**0.003**	**0.01**	**0.005**	**0.001**	**0.0015**

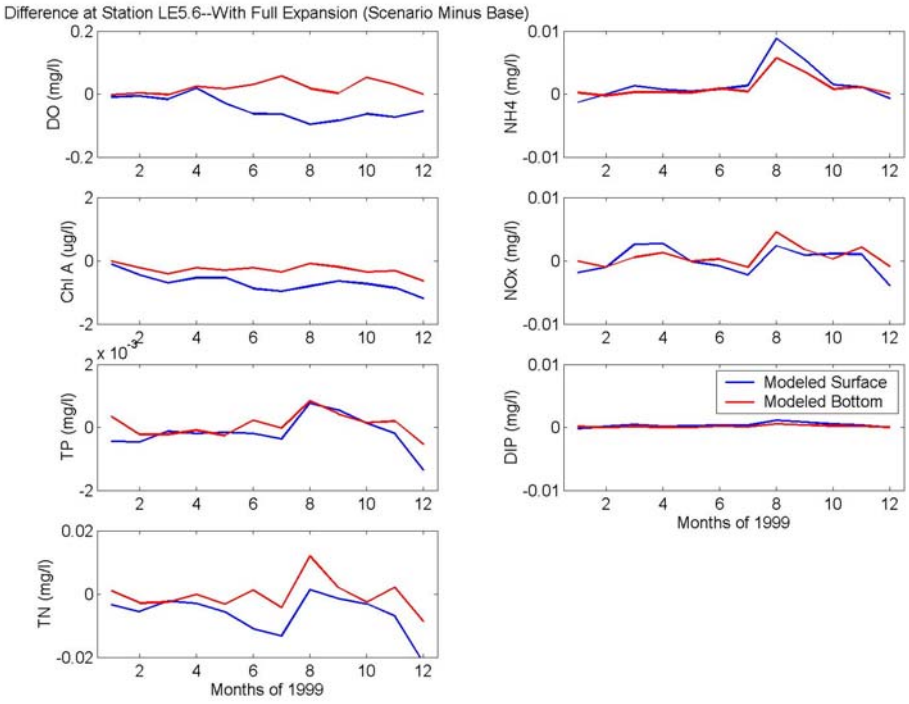

Figure J7. Differences in 30-day averages of dissolved oxygen, chlorophyll-a, total phosphorus, total nitrogen, ammonium, nitrate-nitrite, and dissolved inorganic phosphorus at CBP Station LE5.6 (surface and bottom layers) for 1999.

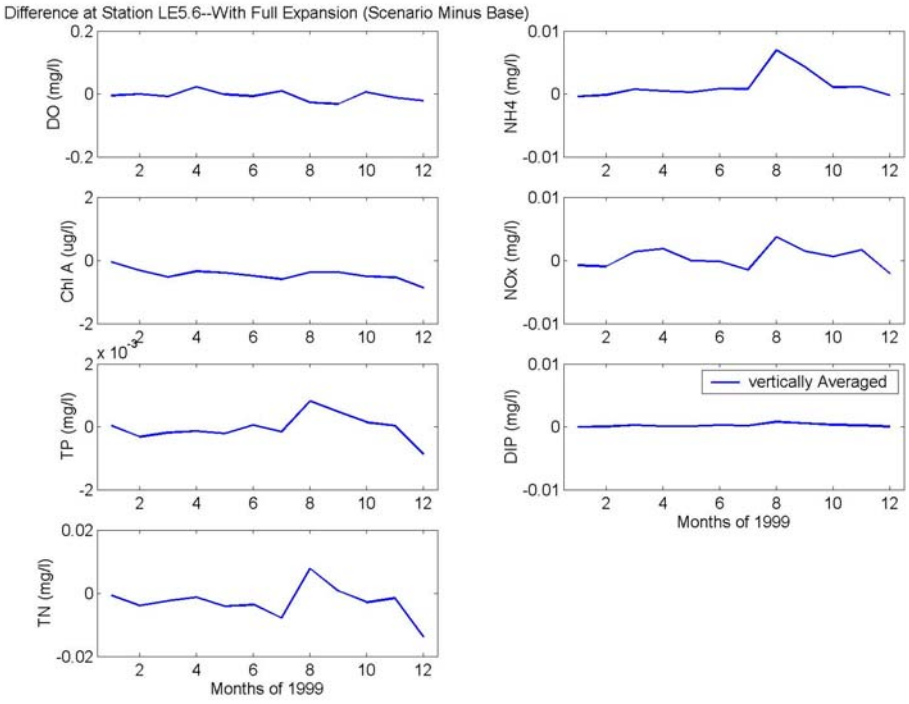

Figure J8. Differences in 30-day averages of dissolved oxygen, chlorophyll-a, total phosphorus, total nitrogen, ammonium, nitrate-nitrite, and dissolved inorganic phosphorus at CBP Station LE5.6 (vertically averaged) for 1999.

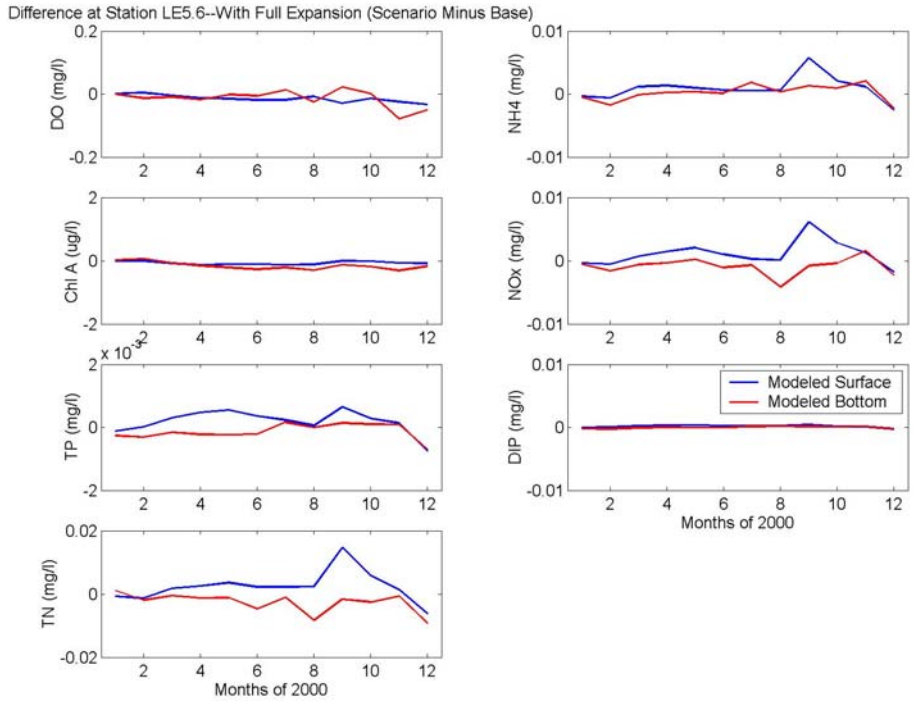

Figure J9. Differences in 30-day averages of dissolved oxygen, chlorophyll-a, total phosphorus, total nitrogen, ammonium, nitrate-nitrite, and dissolved inorganic phosphorus at CBP Station LE5.6 (surface and bottom layers) for 2000.

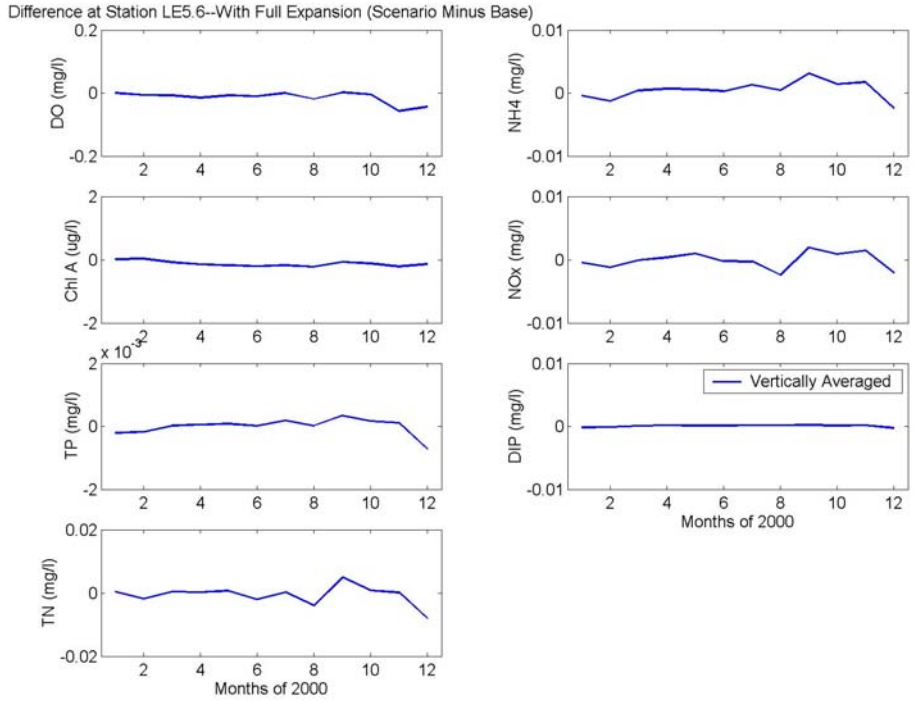

Figure J10. Differences in 30-day averages of dissolved oxygen, chlorophyll-a, total phosphorus, total nitrogen, ammonium, nitrate-nitrite, and dissolved inorganic phosphorus at CBP Station LE5.6 (vertically averaged) for 2000.

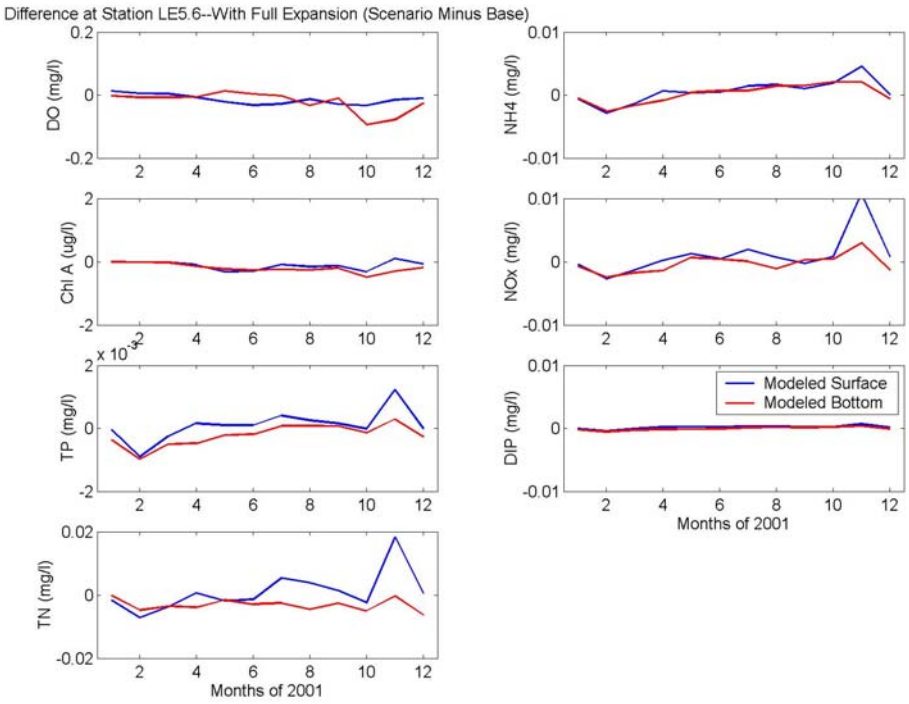

Figure J11. Differences in 30-day averages of dissolved oxygen, chlorophyll-a, total phosphorus, total nitrogen, ammonium, nitrate-nitrite, and dissolved inorganic phosphorus at CBP Station LE5.6 (surface and bottom layers) for 2001.

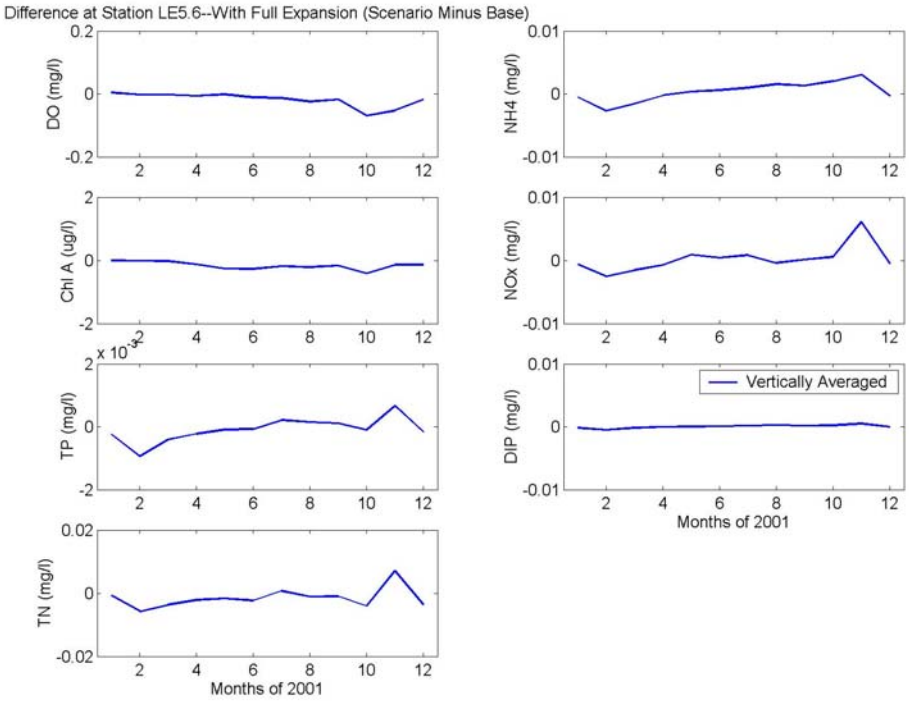

Figure J12. Differences in 30-day averages of dissolved oxygen, chlorophyll-a, total phosphorus, total nitrogen, ammonium, nitrate-nitrite, and dissolved inorganic phosphorus at CBP Station LE5.6 (vertically averaged) for 2001.

Table J2. Differences in 30-day averages of dissolved oxygen, chlorophyll-a, total phosphorus, total nitrogen, ammonium, nitrate-nitrite, and dissolved inorganic phosphorus at CBP Station LE5.6 (vertically averaged) for 1999, 2000, and 2001 (values plotted in Figures J8, J10, and J12).

	Month	**DO**	**Chl**	**TP**	**TN**	**NH_4**	**NO_X**	**DIP**
		mg/l	µg/l	mg/l	mg/l	mg/l	mg/l	mg/l
Station LE5.6 (1999)	Jan.	-0.01	-0.1	0.0000	-0.001	-0.000	-0.0008	0.0000
	Feb.	-0.00	-0.3	-0.0003	-0.004	-0.000	-0.0010	0.0000
	Mar.	-0.01	-0.5	-0.0002	-0.002	0.001	0.0014	0.0002
	Apr.	0.02	-0.4	-0.0001	-0.001	0.001	0.0018	0.0001
	May	-0.00	-0.4	-0.0002	-0.004	0.000	-0.0001	0.0001
	Jun.	-0.01	-0.5	0.0001	-0.004	0.001	-0.0002	0.0003
	Jul.	0.01	-0.6	-0.0002	-0.008	0.001	-0.0015	0.0002
	Aug.	-0.03	-0.4	0.0008	0.008	0.007	0.0037	0.0008
	Sep.	-0.03	-0.4	0.0005	0.001	0.004	0.0014	0.0006
	Oct.	0.01	-0.5	0.0001	-0.003	0.001	0.0006	0.0003
	Nov.	-0.01	-0.5	0.0000	-0.002	0.001	0.0017	0.0002
	Dec.	-0.02	-0.9	-0.0009	-0.014	-0.000	-0.0021	0.0000
Detection limits:		**0.1**	**0.5**	**0.003**	**0.01**	**0.005**	**0.001**	**0.0015**

	Month	**DO**	**Chl**	**TP**	**TN**	**NH_4**	**NO_X**	**DIP**
		mg/l	µg/l	mg/l	mg/l	mg/l	mg/l	mg/l
Station LE5.6 (2000)	Jan.	0.00	0.0	-0.0002	0.000	-0.000	-0.0005	-0.0002
	Feb.	-0.01	0.0	-0.0002	-0.002	-0.001	-0.0012	-0.0001
	Mar.	-0.01	-0.1	0.0000	0.000	0.000	-0.0001	0.0001
	Apr.	-0.01	-0.2	0.0001	0.000	0.001	0.0004	0.0002
	May	-0.01	-0.2	0.0001	0.001	0.001	0.0010	0.0001
	Jun.	-0.01	-0.2	0.0000	-0.002	0.000	-0.0002	0.0001
	Jul.	0.00	-0.2	0.0002	0.000	0.001	-0.0003	0.0002
	Aug.	-0.02	-0.2	0.0000	-0.004	0.001	-0.0024	0.0002
	Sep.	0.00	-0.1	0.0003	0.005	0.003	0.0020	0.0002
	Oct.	-0.00	-0.1	0.0002	0.001	0.001	0.0009	0.0001
	Nov.	-0.06	-0.2	0.0001	0.000	0.002	0.0014	0.0002
	Dec.	-0.04	-0.1	-0.0007	-0.008	-0.002	-0.0021	-0.0003
Detection limits:		**0.1**	**0.5**	**0.003**	**0.01**	**0.005**	**0.001**	**0.0015**

	Month	**DO**	**Chl**	**TP**	**TN**	**NH_4**	**NO_X**	**DIP**
		mg/l	µg/l	mg/l	mg/l	mg/l	mg/l	mg/l
Station LE5.6 (2001)	Jan.	0.00	-0.0	-0.0002	-0.001	-0.001	-0.0007	-0.0001
	Feb.	-0.00	-0.0	-0.0009	-0.006	-0.003	-0.0025	-0.0005
	Mar.	-0.00	-0.0	-0.0004	-0.004	-0.002	-0.0015	-0.0002
	Apr.	-0.01	-0.1	-0.0002	-0.002	-0.000	-0.0008	0.0000
	May	-0.00	-0.3	-0.0001	-0.002	0.000	0.0009	0.0000
	Jun.	-0.01	-0.3	-0.0001	-0.002	0.001	0.0004	0.0001
	Jul.	-0.01	-0.2	0.0002	0.001	0.001	0.0008	0.0002
	Aug.	-0.02	-0.2	0.0001	-0.001	0.002	-0.0004	0.0002
	Sep.	-0.02	-0.2	0.0001	-0.001	0.001	0.0001	0.0002
	Oct.	-0.07	-0.4	-0.0001	-0.004	0.002	0.0005	0.0002
	Nov.	-0.05	-0.1	0.0007	0.007	0.003	0.0061	0.0005
	Dec.	-0.02	-0.1	-0.0002	-0.004	-0.000	-0.0005	0.0000
Detection limits:		**0.1**	**0.5**	**0.003**	**0.01**	**0.005**	**0.001**	**0.0015**

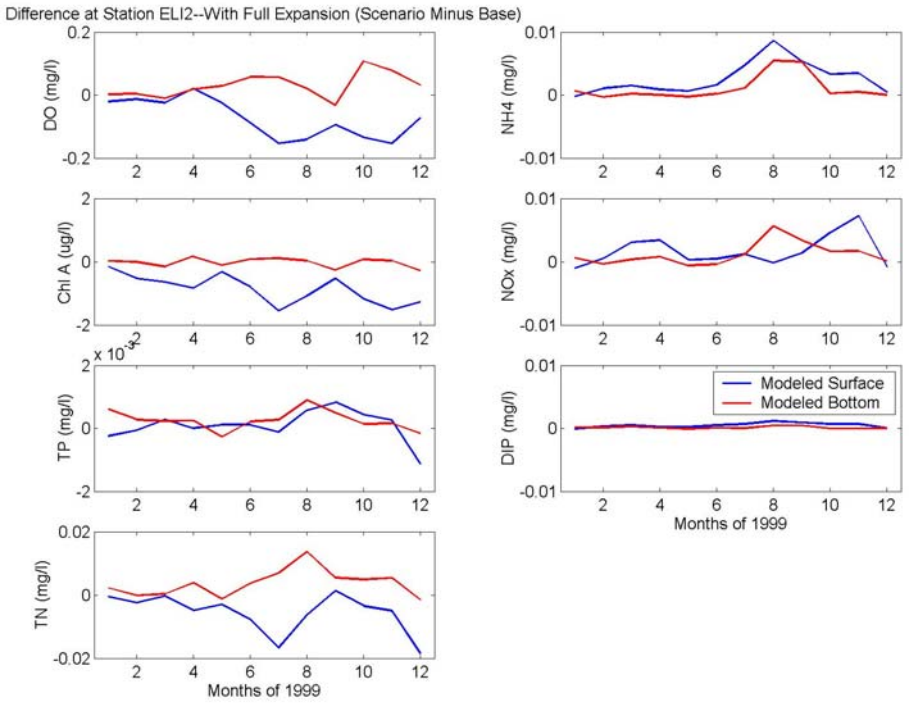

Figure J13. Differences in 30-day averages of dissolved oxygen, chlorophyll-a, total phosphorus, total nitrogen, ammonium, nitrate-nitrite, and dissolved inorganic phosphorus at CBP Station ELI2 (surface and bottom layers) for 1999.

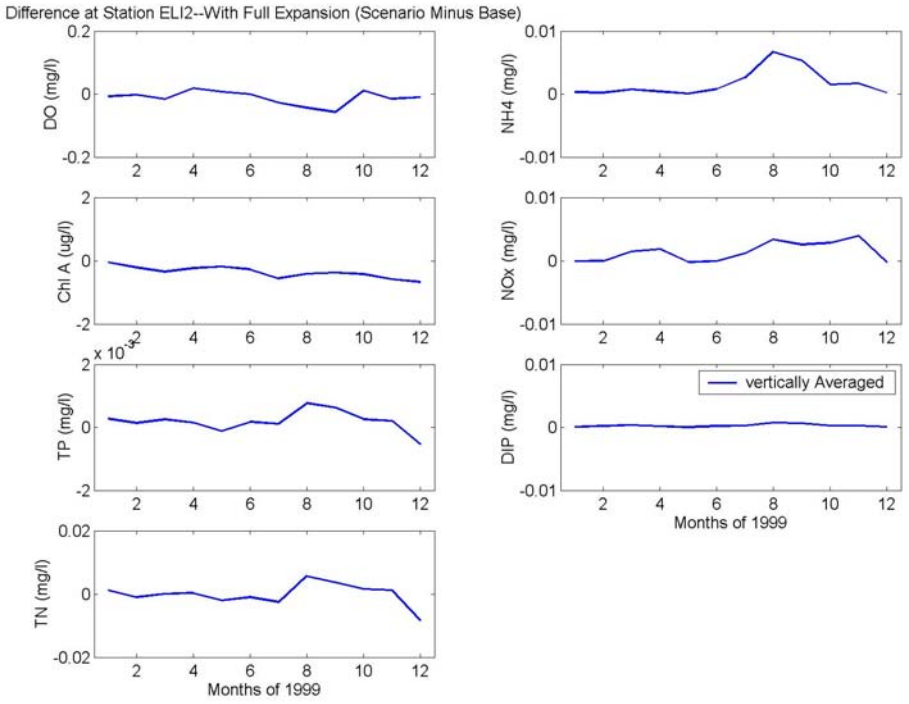

Figure J14. Differences in 30-day averages of dissolved oxygen, chlorophyll-a, total phosphorus, total nitrogen, ammonium, nitrate-nitrite, and dissolved inorganic phosphorus at CBP Station ELI2 (vertically averaged) for 1999.

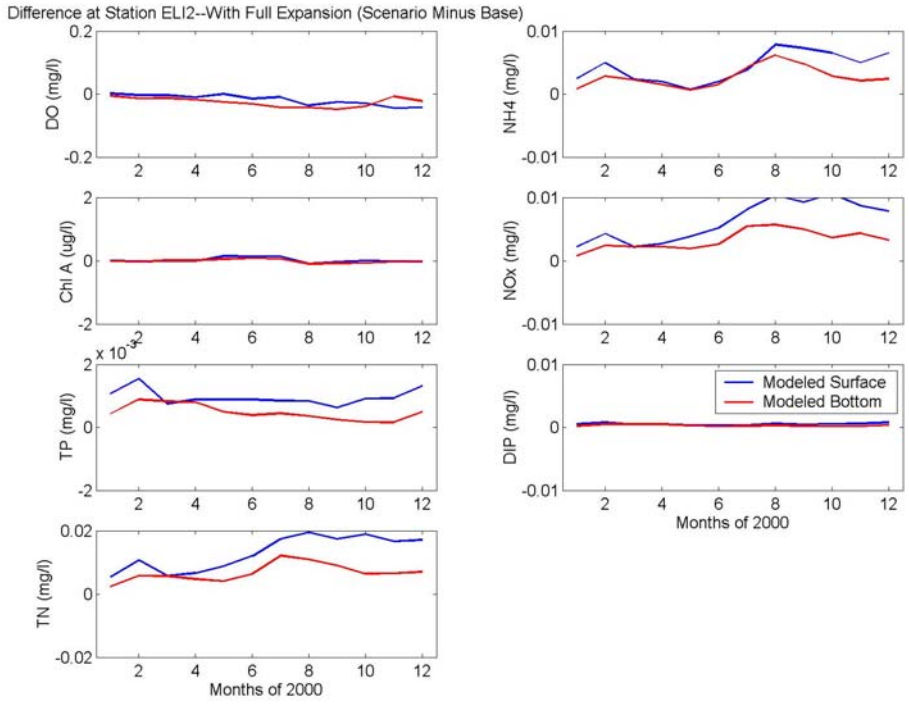

Figure J15. Differences in 30-day averages of dissolved oxygen, chlorophyll-a, total phosphorus, total nitrogen, ammonium, nitrate-nitrite, and dissolved inorganic phosphorus at CBP Station ELI2 (surface and bottom layers) for 2000.

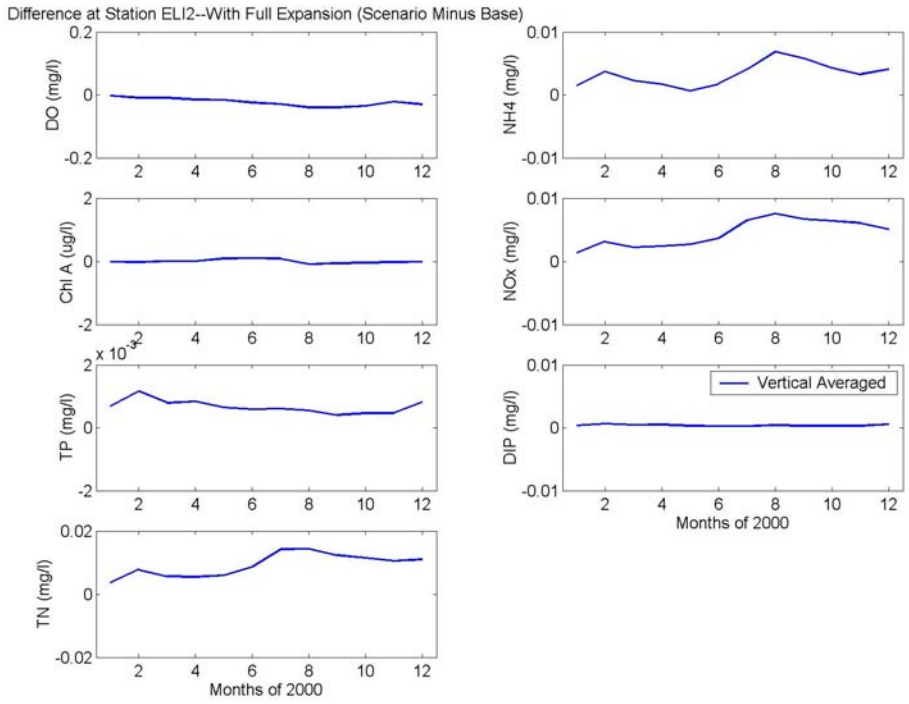

Figure J16. Differences in 30-day averages of dissolved oxygen, chlorophyll-a, total phosphorus, total nitrogen, ammonium, nitrate-nitrite, and dissolved inorganic phosphorus at CBP Station ELI2 (vertically averaged) for 2000.

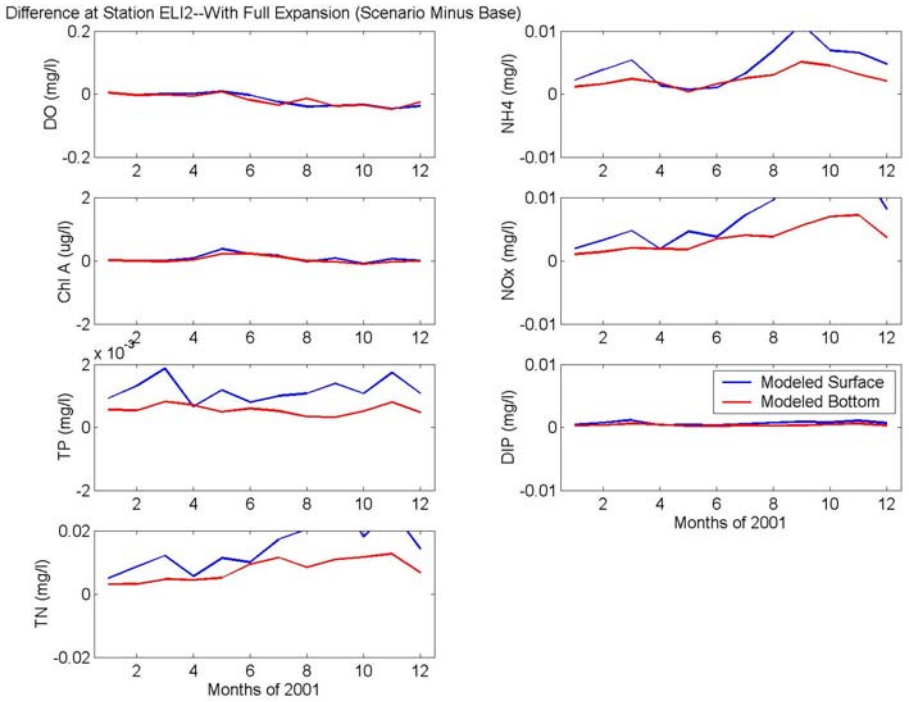

Figure J17. Differences in 30-day averages of dissolved oxygen, chlorophyll-a, total phosphorus, total nitrogen, ammonium, nitrate-nitrite, and dissolved inorganic phosphorus at CBP Station ELI2 (surface and bottom layers) for 2001.

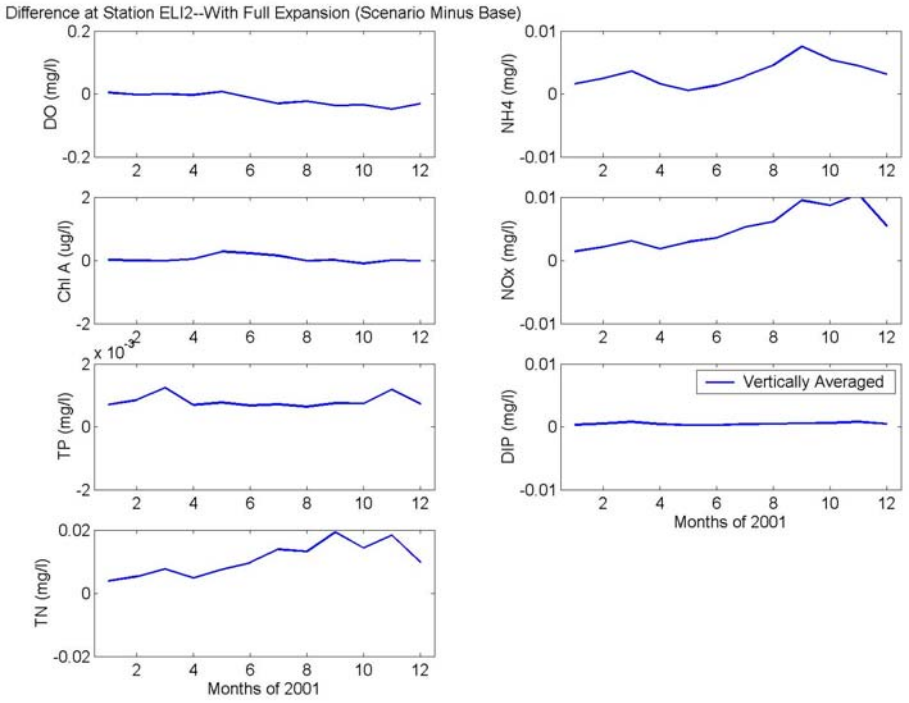

Figure J18. Differences in 30-day averages of dissolved oxygen, chlorophyll-a, total phosphorus, total nitrogen, ammonium, nitrate-nitrite, and dissolved inorganic phosphorus at CBP Station ELI2 (vertically averaged) for 2001.

Table J3. Differences in 30-day averages of dissolved oxygen, chlorophyll-a, total phosphorus, total nitrogen, ammonium, nitrate-nitrite, and dissolved inorganic phosphorus at CBP Station ELI2 (vertically averaged) for 1999, 2000, and 2001 (values plotted in Figures J14, J16, and J18).

	Month	**DO**	**Chl**	**TP**	**TN**	**NH_4**	**NO_X**	**DIP**
		mg/l	µg/l	mg/l	mg/l	mg/l	mg/l	mg/l
Station ELI2 (1999)	Jan.	-0.01	-0.1	0.0003	0.001	0.000	-0.0001	0.0001
	Feb.	-0.00	-0.2	0.0001	-0.001	0.000	0.0000	0.0002
	Mar.	-0.02	-0.4	0.0003	0.000	0.001	0.0015	0.0004
	Apr.	0.02	-0.2	0.0001	0.000	0.000	0.0018	0.0001
	May	0.01	-0.2	-0.0001	-0.002	0.000	-0.0002	0.0000
	Jun.	-0.00	-0.3	0.0002	-0.001	0.001	-0.0001	0.0002
	Jul.	-0.03	-0.6	0.0001	-0.003	0.003	0.0012	0.0003
	Aug.	-0.04	-0.4	0.0008	0.006	0.007	0.0033	0.0007
	Sep.	-0.06	-0.4	0.0006	0.004	0.005	0.0026	0.0006
	Oct.	0.01	-0.4	0.0003	0.002	0.002	0.0028	0.0003
	Nov.	-0.02	-0.6	0.0002	0.001	0.002	0.0039	0.0003
	Dec.	-0.01	-0.7	-0.0005	-0.008	0.000	-0.0002	0.0000
Detection limits:		**0.1**	**0.5**	**0.003**	**0.01**	**0.005**	**0.001**	**0.0015**

	Month	**DO**	**Chl**	**TP**	**TN**	**NH_4**	**NO_X**	**DIP**
		mg/l	µg/l	mg/l	mg/l	mg/l	mg/l	mg/l
Station ELI2 (2000)	Jan.	-0.00	-0.0	0.0007	0.004	0.002	0.0014	0.0003
	Feb.	-0.01	-0.0	0.0012	0.008	0.004	0.0031	0.0007
	Mar.	-0.01	0.0	0.0008	0.006	0.002	0.0022	0.0005
	Apr.	-0.01	0.0	0.0008	0.006	0.002	0.0024	0.0005
	May	-0.02	0.1	0.0006	0.006	0.001	0.0027	0.0003
	Jun.	-0.02	0.1	0.0006	0.009	0.002	0.0036	0.0003
	Jul.	-0.03	0.1	0.0006	0.014	0.004	0.0065	0.0003
	Aug.	-0.04	-0.1	0.0006	0.014	0.007	0.0075	0.0004
	Sep.	-0.04	-0.1	0.0004	0.012	0.006	0.0067	0.0003
	Oct.	-0.03	-0.0	0.0005	0.011	0.004	0.0064	0.0003
	Nov.	-0.02	-0.0	0.0005	0.011	0.003	0.0061	0.0003
	Dec.	-0.03	-0.0	0.0008	0.011	0.004	0.0051	0.0005
Detection limits:		**0.1**	**0.5**	**0.003**	**0.01**	**0.005**	**0.001**	**0.0015**

	Month	**DO**	**Chl**	**TP**	**TN**	**NH_4**	**NO_X**	**DIP**
		mg/l	µg/l	mg/l	mg/l	mg/l	mg/l	mg/l
Station ELI2 (2001)	Jan.	0.00	0.0	0.0007	0.004	0.002	0.0014	0.0003
	Feb.	-0.00	-0.0	0.0009	0.005	0.003	0.0021	0.0005
	Mar.	-0.00	-0.0	0.0012	0.008	0.004	0.0031	0.0008
	Apr.	-0.00	0.0	0.0007	0.005	0.002	0.0019	0.0004
	May	0.01	0.3	0.0008	0.008	0.001	0.0029	0.0003
	Jun.	-0.01	0.2	0.0007	0.010	0.001	0.0036	0.0003
	Jul.	-0.03	0.1	0.0007	0.014	0.003	0.0053	0.0004
	Aug.	-0.02	-0.0	0.0006	0.013	0.005	0.0061	0.0005
	Sep.	-0.04	0.0	0.0008	0.019	0.008	0.0095	0.0005
	Oct.	-0.03	-0.1	0.0007	0.014	0.006	0.0087	0.0006
	Nov.	-0.05	0.0	0.0012	0.018	0.005	0.0104	0.0008
	Dec.	-0.03	-0.0	0.0007	0.010	0.003	0.0055	0.0005
Detection limits:		**0.1**	**0.5**	**0.003**	**0.01**	**0.005**	**0.001**	**0.0015**

APPENDIX K

Spatial Plots of

Dissolved Oxygen Differences

Between CIEE Full Expansion and Base Case

For 30-Day Averages in June, July, August, and September

for 1999, 2000, and 2001

Vertical Average and Surface and Bottom Layers

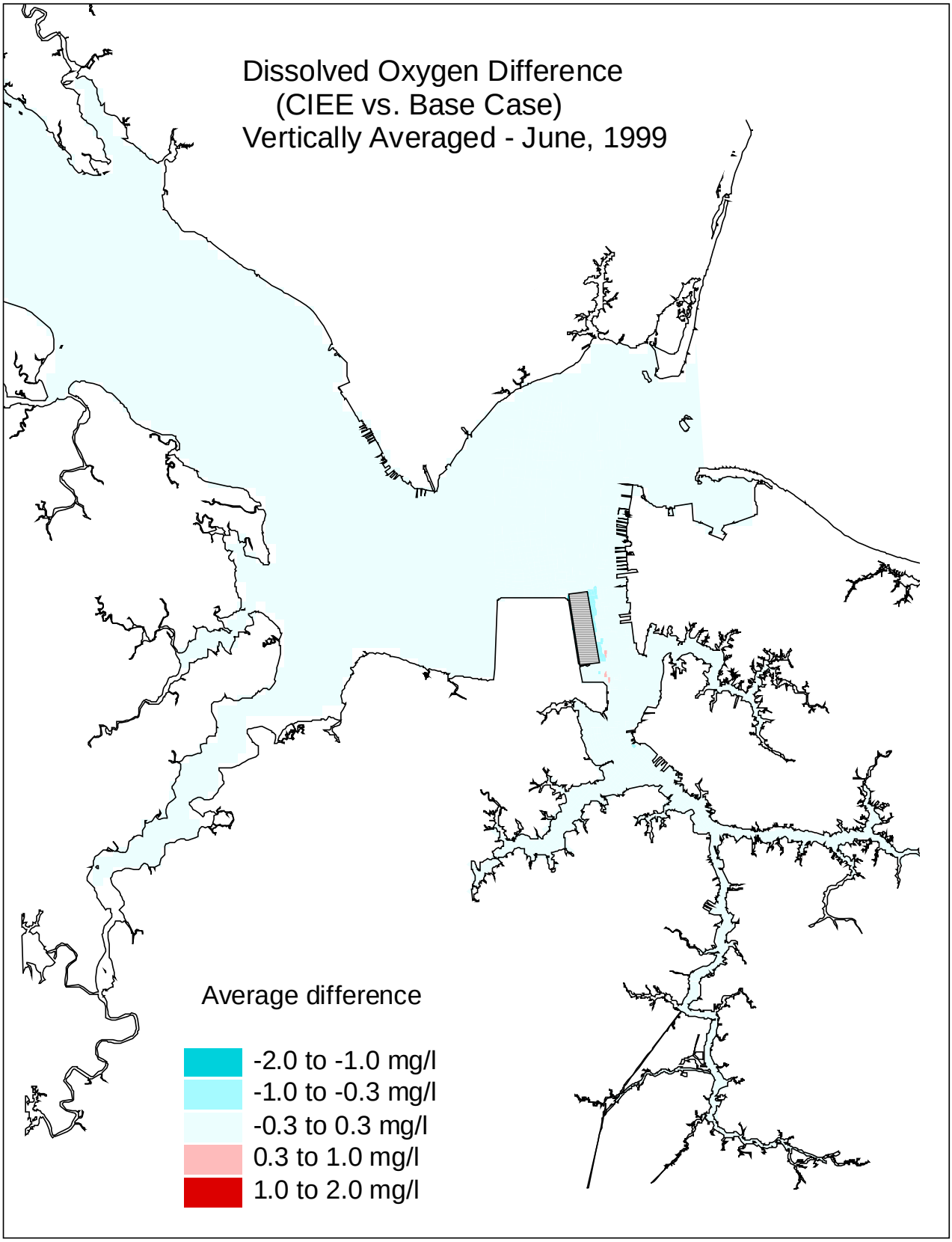

Figure K1. Dissolved oxygen (30-day average, vertically averaged) difference between the CIEE full expansion and the base case for June, 1999.

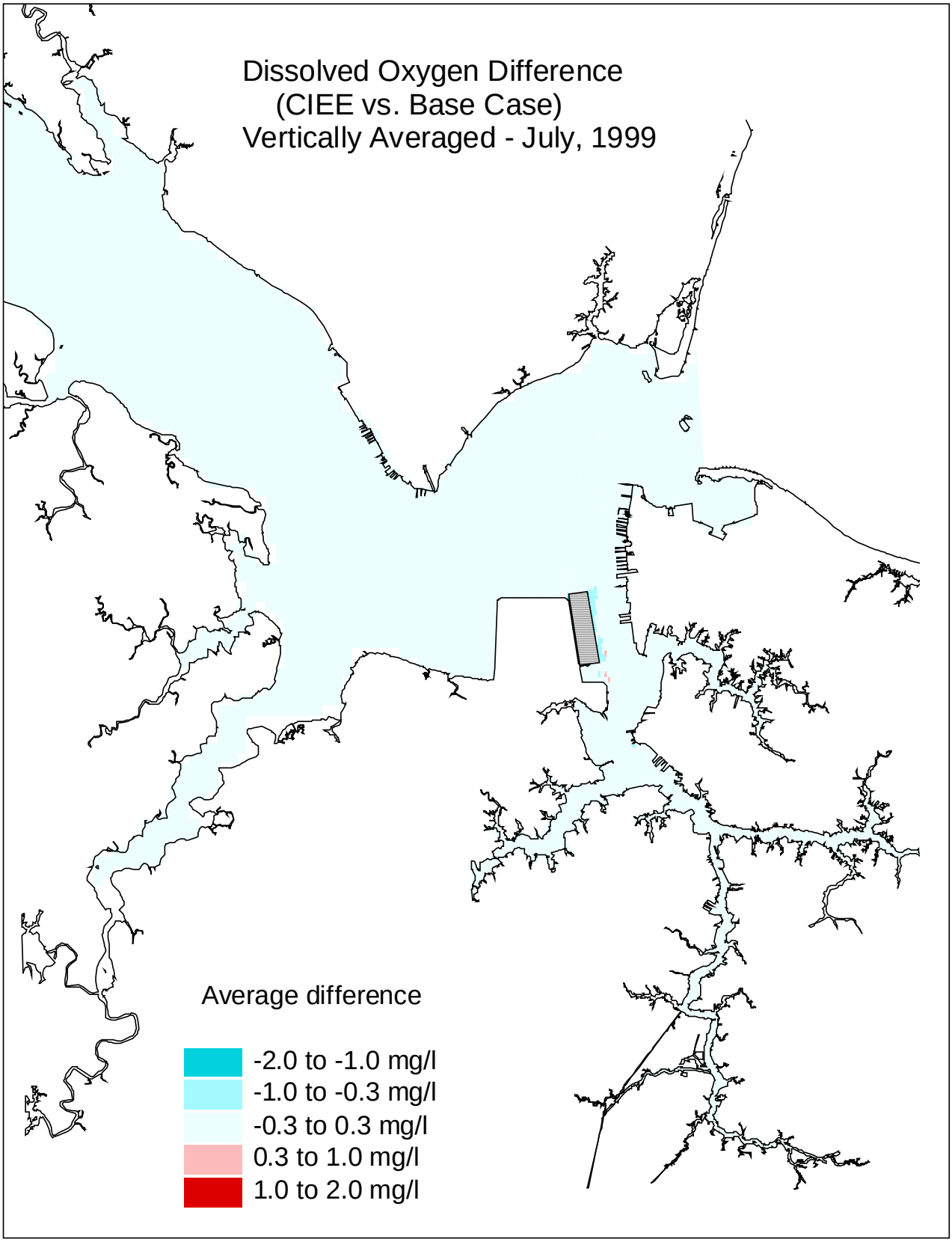

Figure K2. Dissolved oxygen (30-day average, vertically averaged) difference between the CIEE full expansion and the base case for July, 1999.

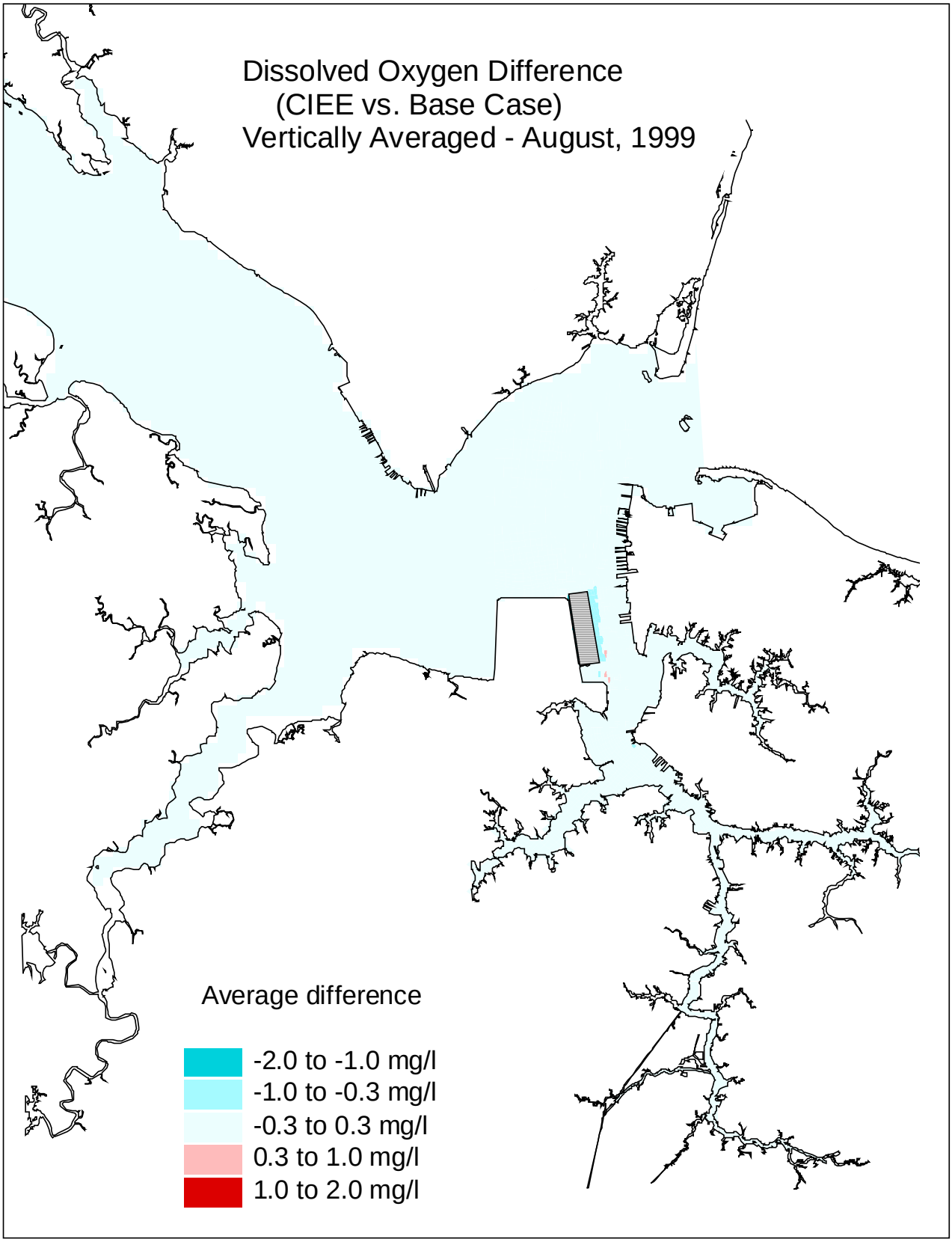

Figure K3. Dissolved oxygen (30-day average, vertically averaged) difference between the CIEE full expansion and the base case for August, 1999.

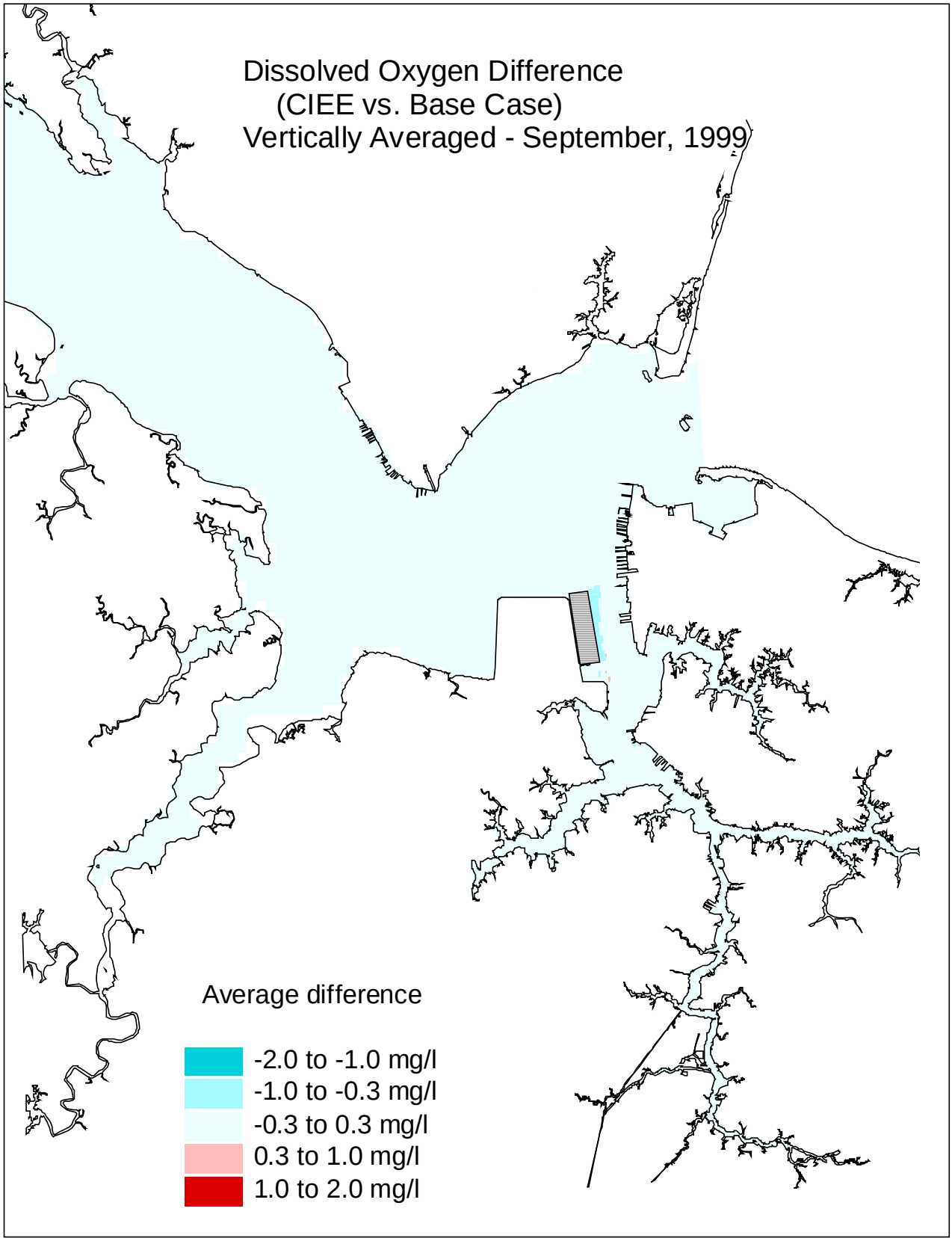

Figure K4. Dissolved oxygen (30-day average, vertically averaged) difference between the CIEE full expansion and the base case for September, 1999.

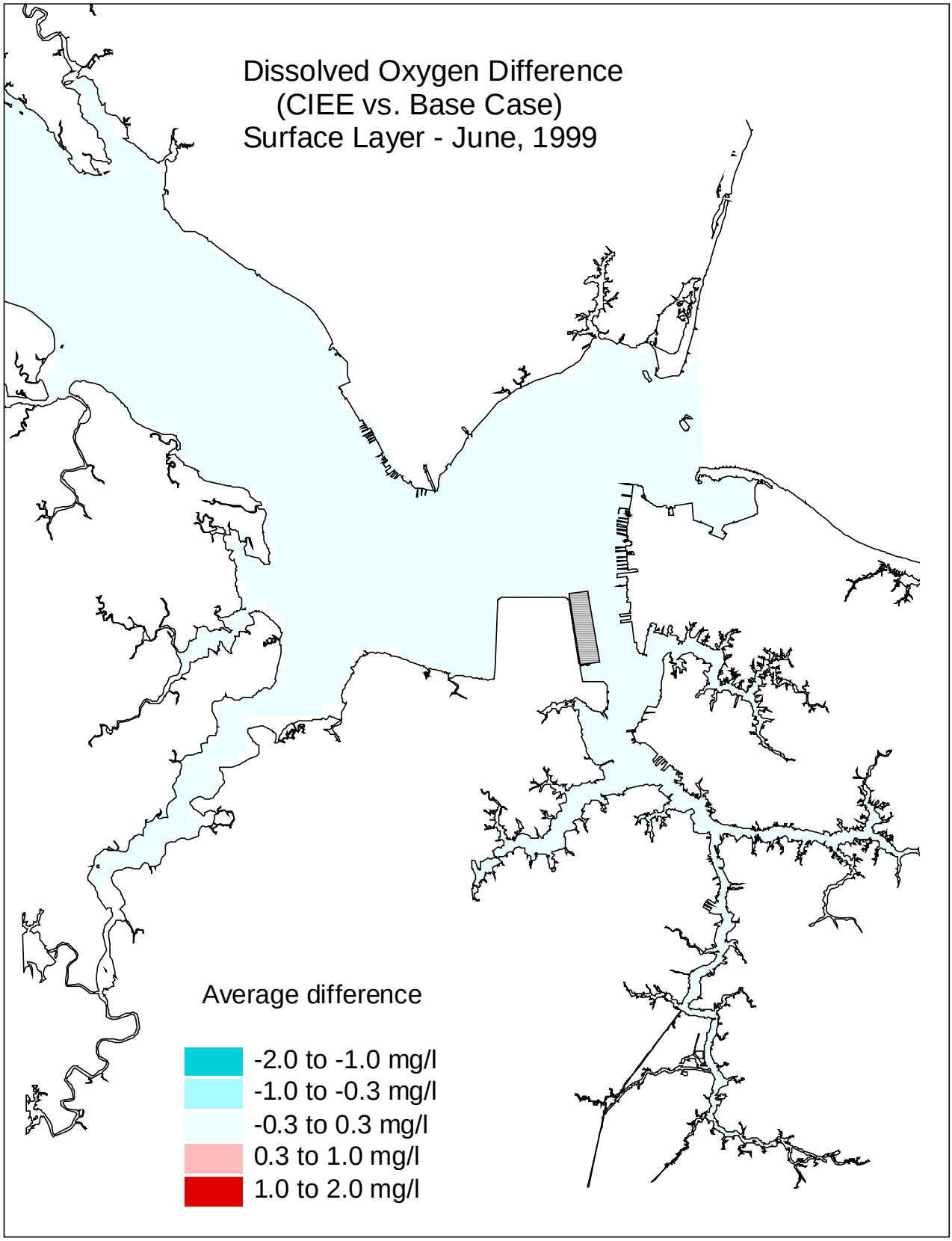

Figure K5. Dissolved oxygen (30-day average, at the surface layer) difference between the CIEE full expansion and the base case for June, 1999.

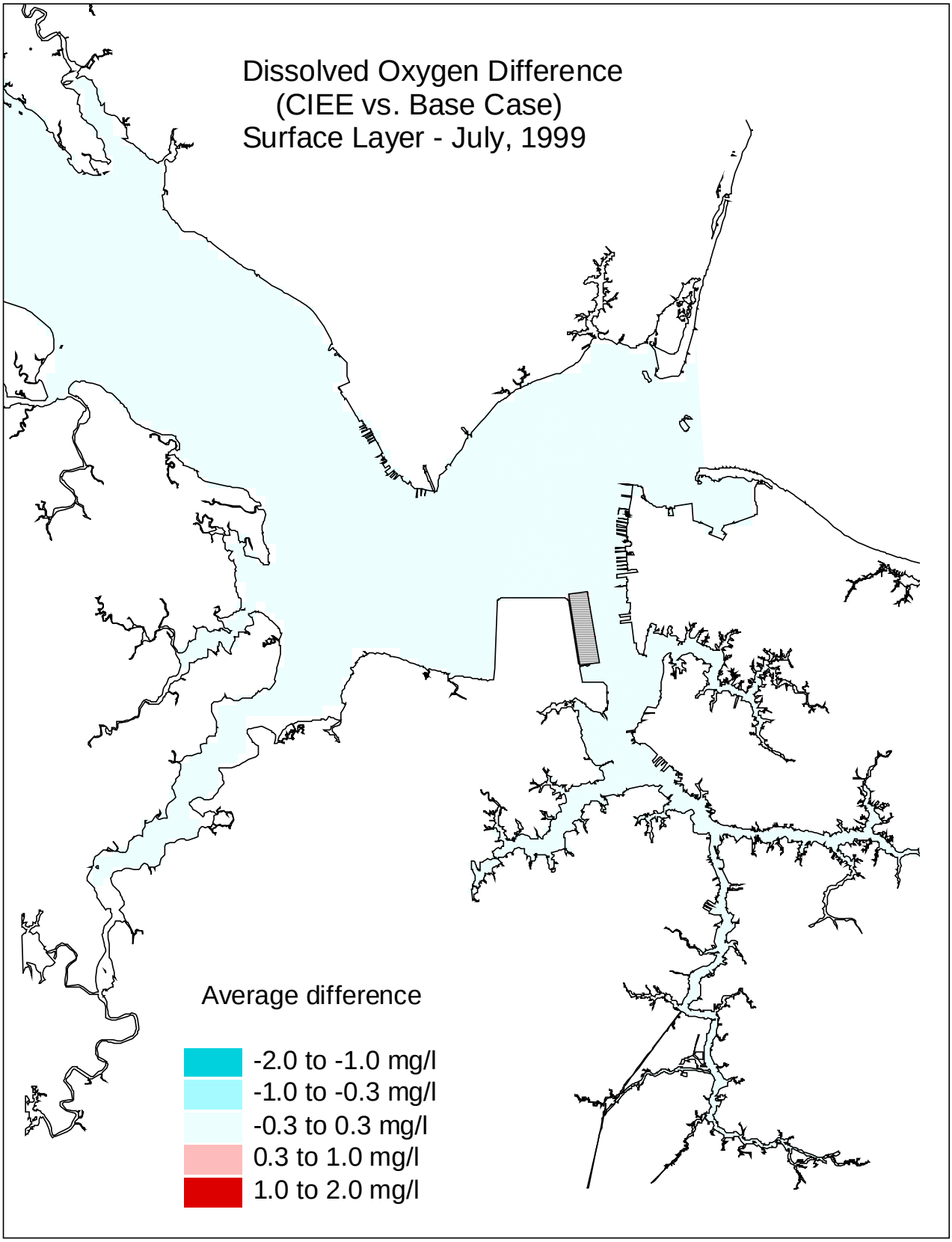

Figure K6. Dissolved oxygen (30-day average, at the surface layer) difference between the CIEE full expansion and the base case for July, 1999.

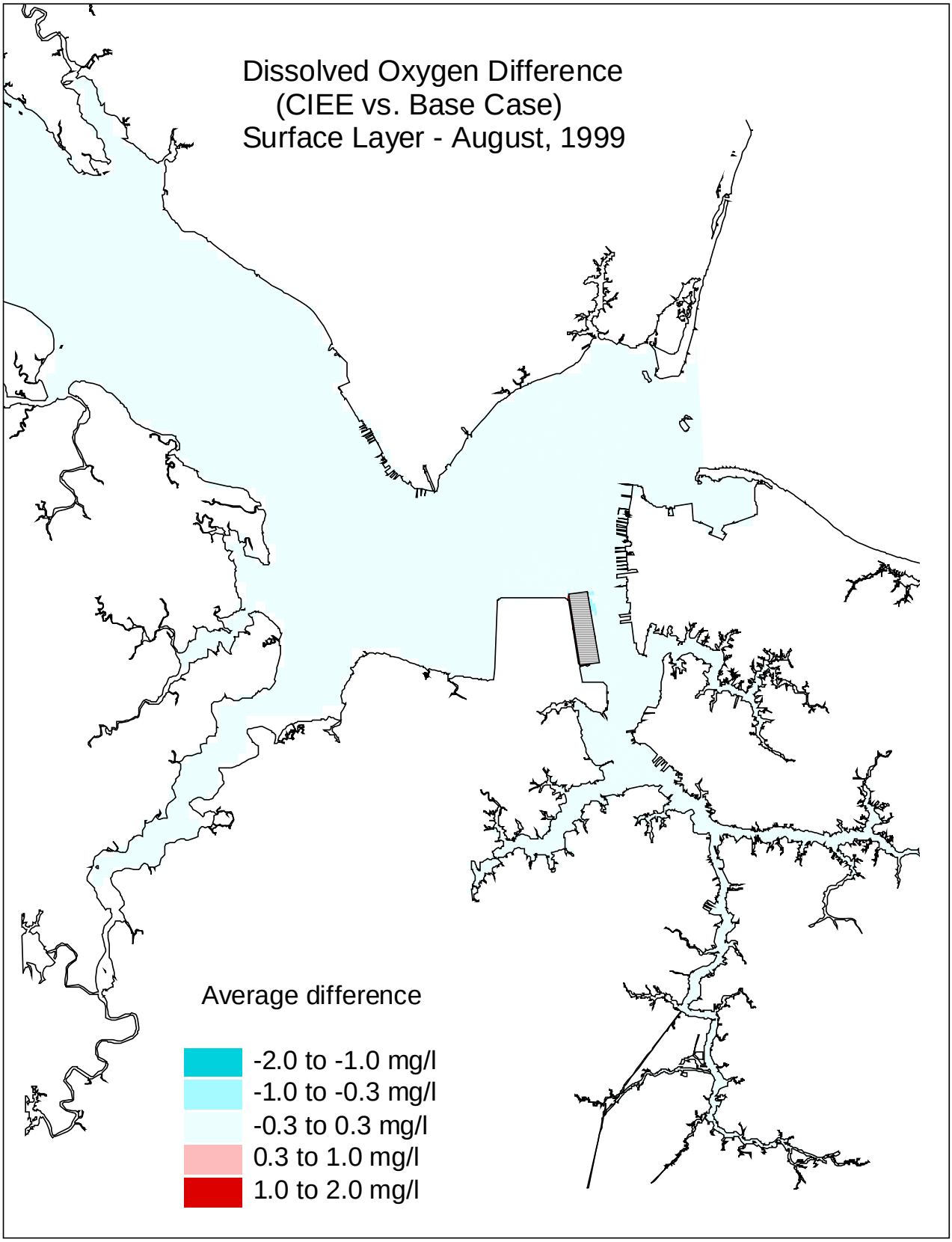

Figure K7. Dissolved oxygen (30-day average, at the surface layer) difference between the CIEE full expansion and the base case for August, 1999.

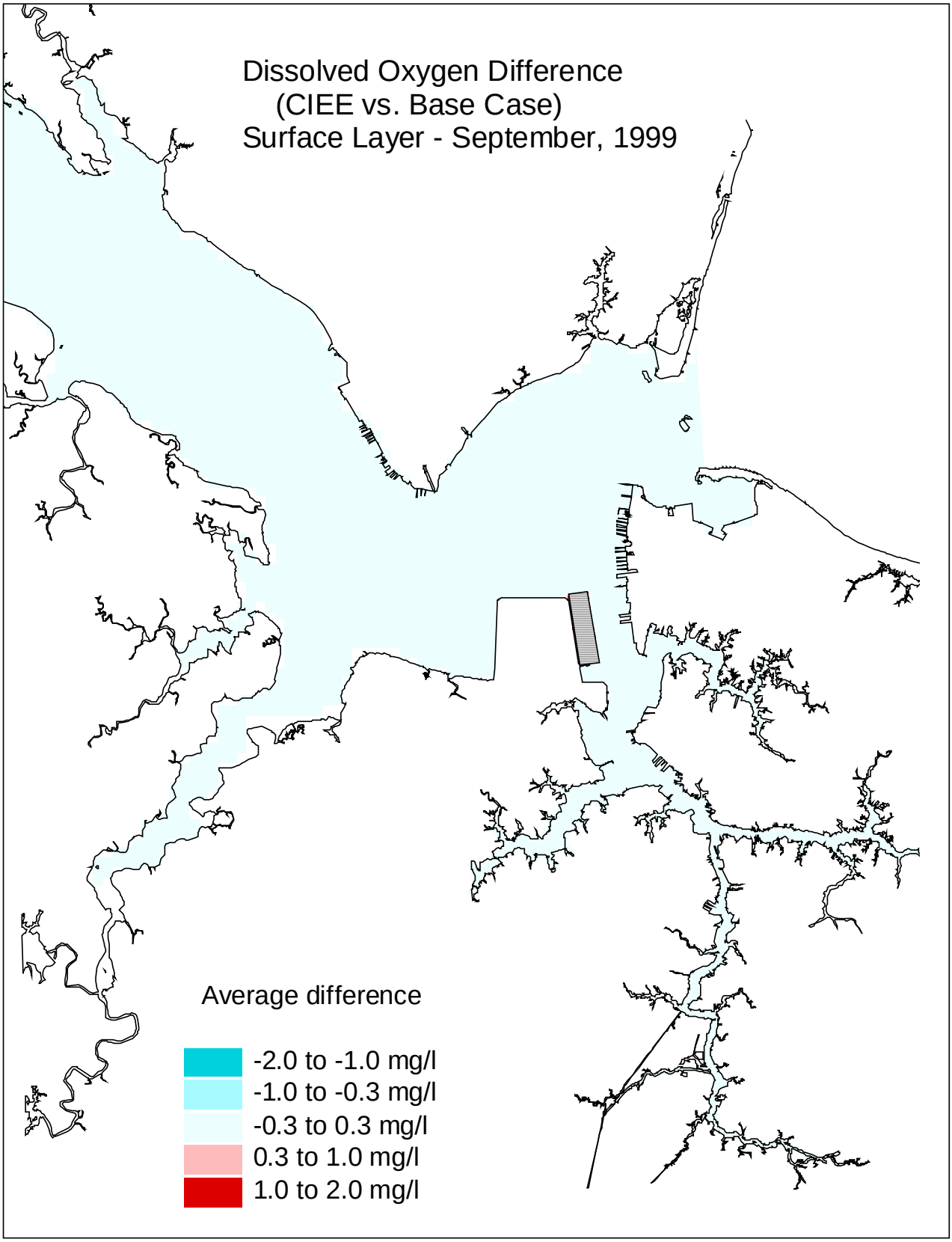

Figure K8. Dissolved oxygen (30-day average, at the surface layer) difference between the CIEE full expansion and the base case for September, 1999.

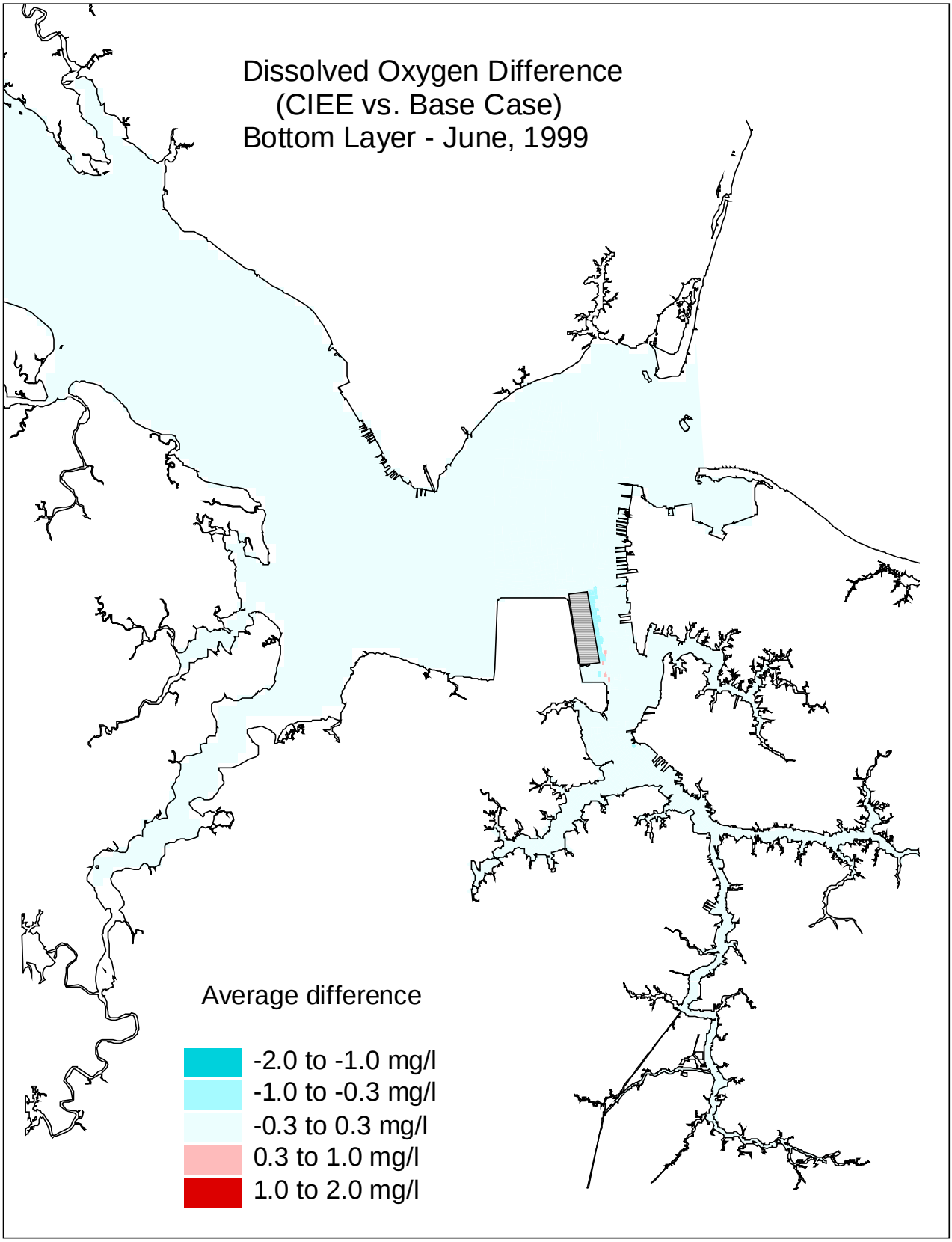

Figure K9. Dissolved oxygen (30-day average, at the bottom layer) difference between the CIEE full expansion and the base case for June, 1999.

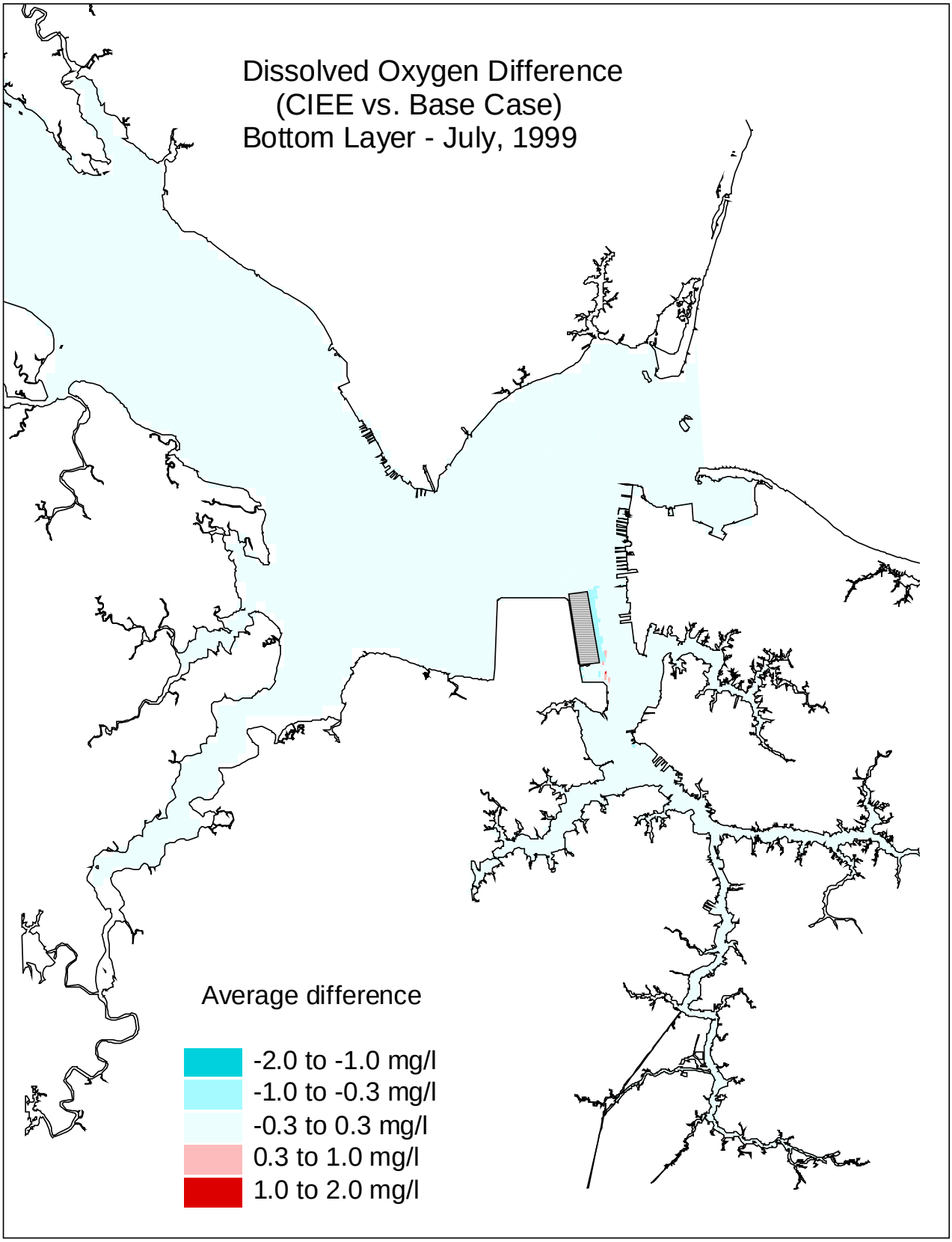

Figure K10. Dissolved oxygen (30-day average, at the bottom layer) difference between the CIEE full expansion and the base case for July, 1999.

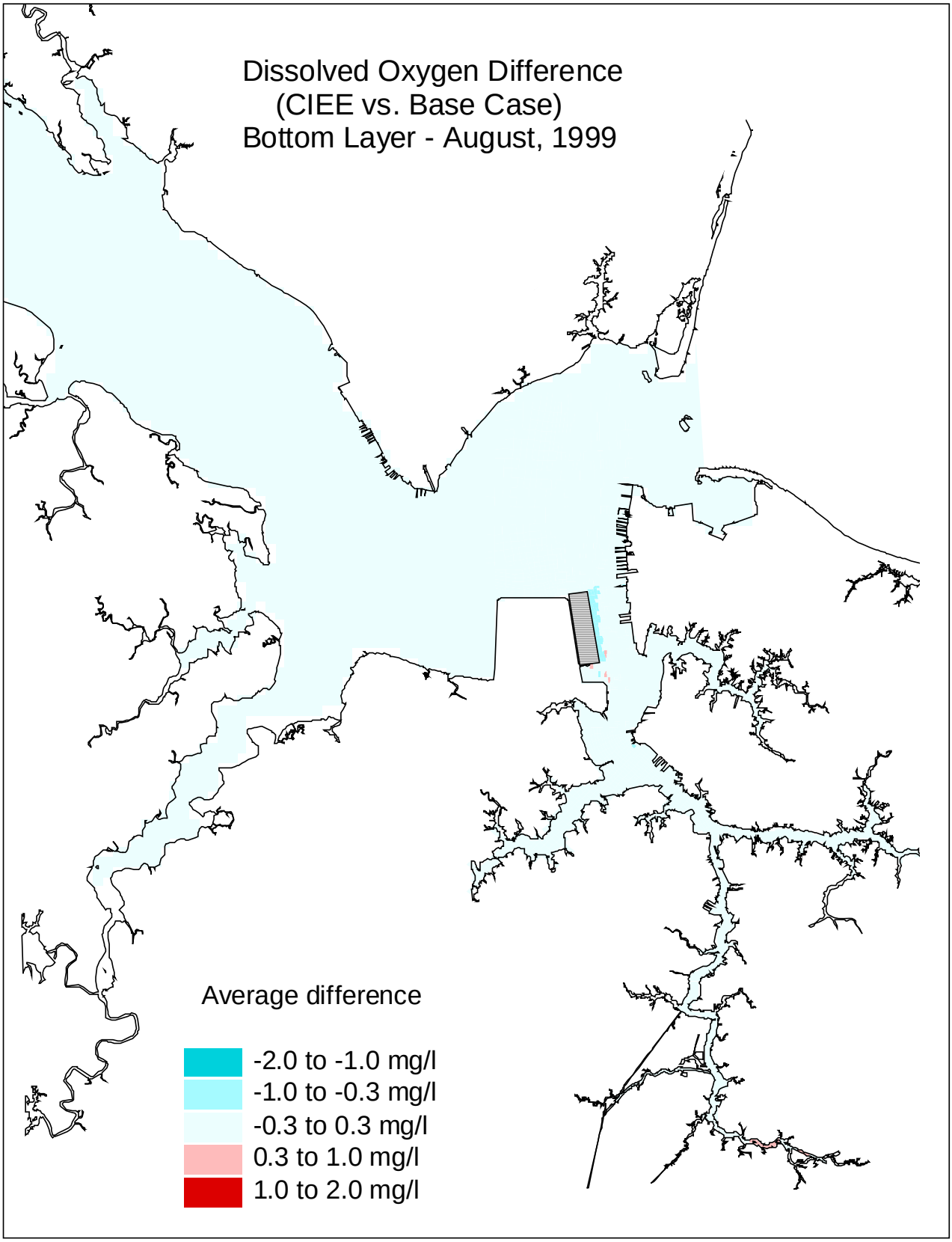

Figure K11. Dissolved oxygen (30-day average, at the bottom layer) difference between the CIEE full expansion and the base case for August, 1999.

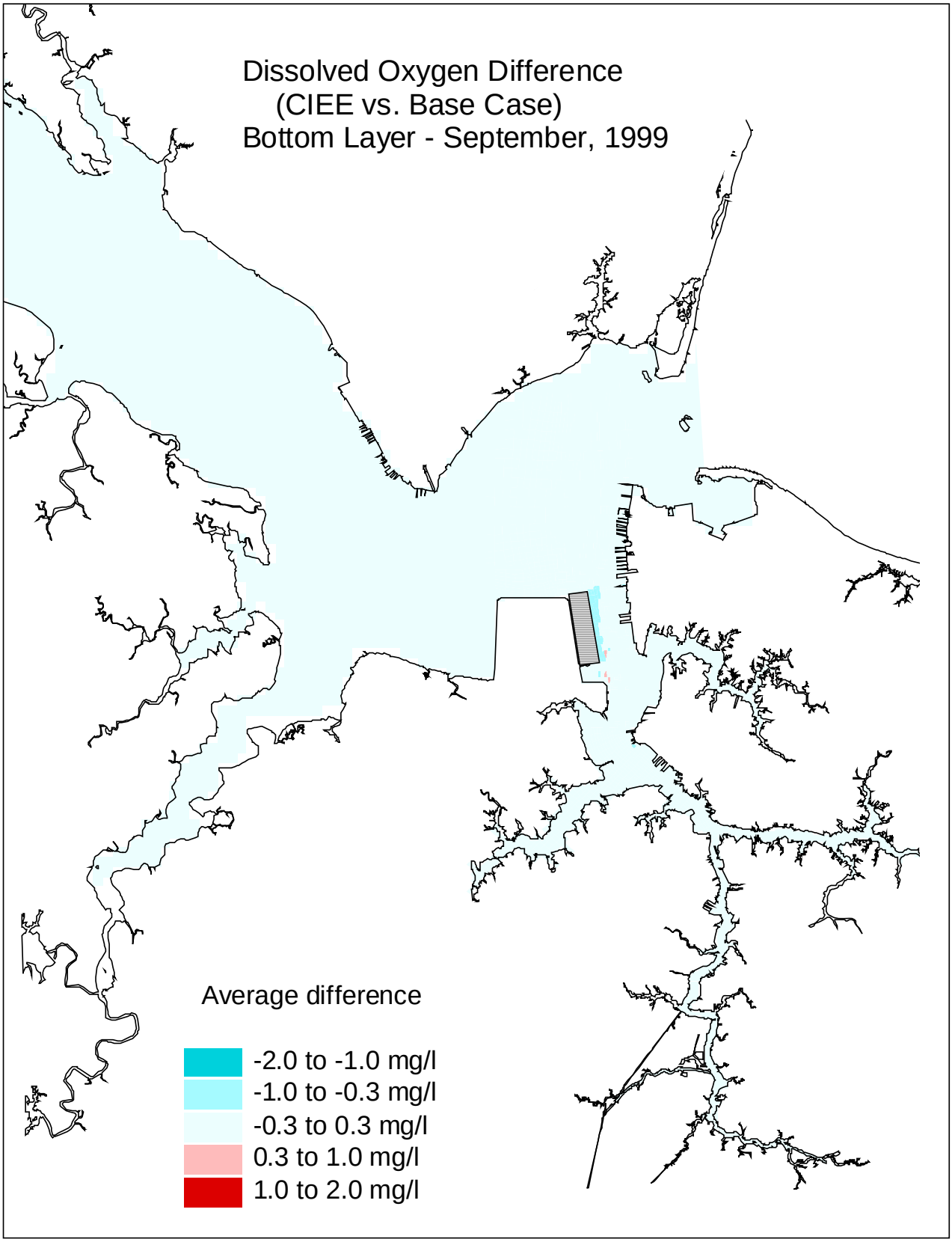

Figure K12. Dissolved oxygen (30-day average, at the bottom layer) difference between the CIEE full expansion and the base case for September, 1999.

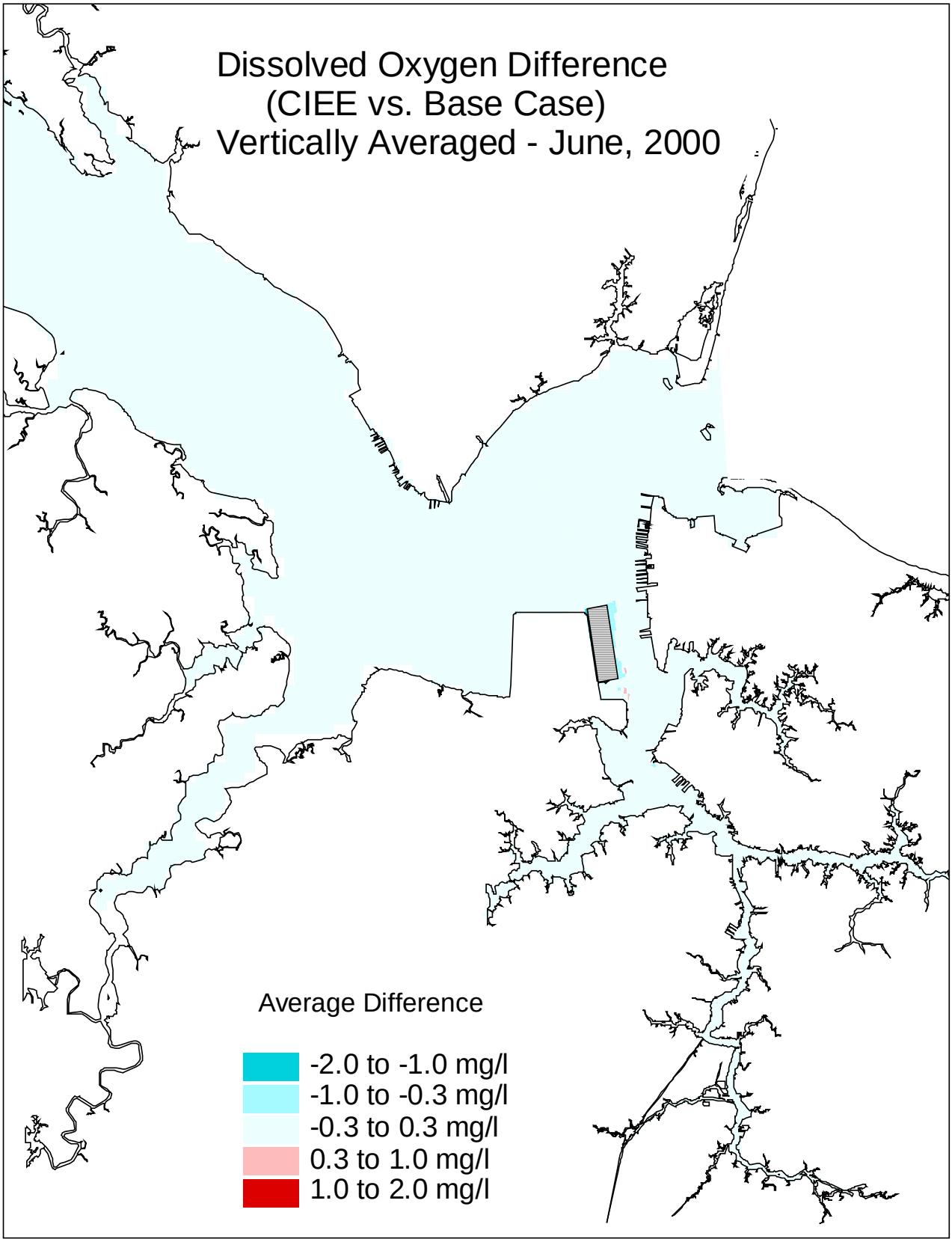

Figure K13. Dissolved oxygen (30-day average, vertically averaged) difference between the CIEE full expansion and the base case for June, 2000.

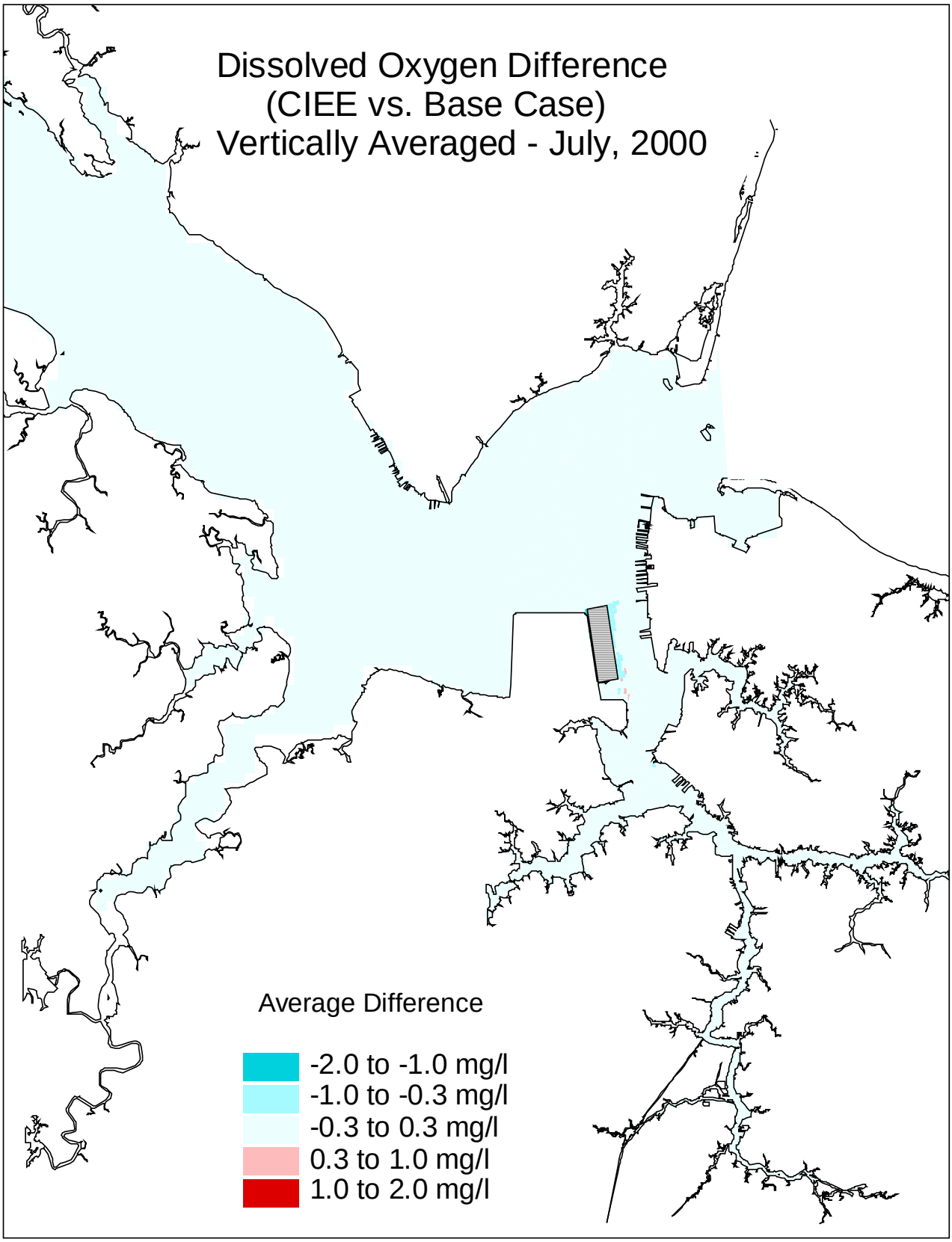

Figure K14. Dissolved oxygen (30-day average, vertically averaged) difference between the CIEE full expansion and the base case for July, 2000.

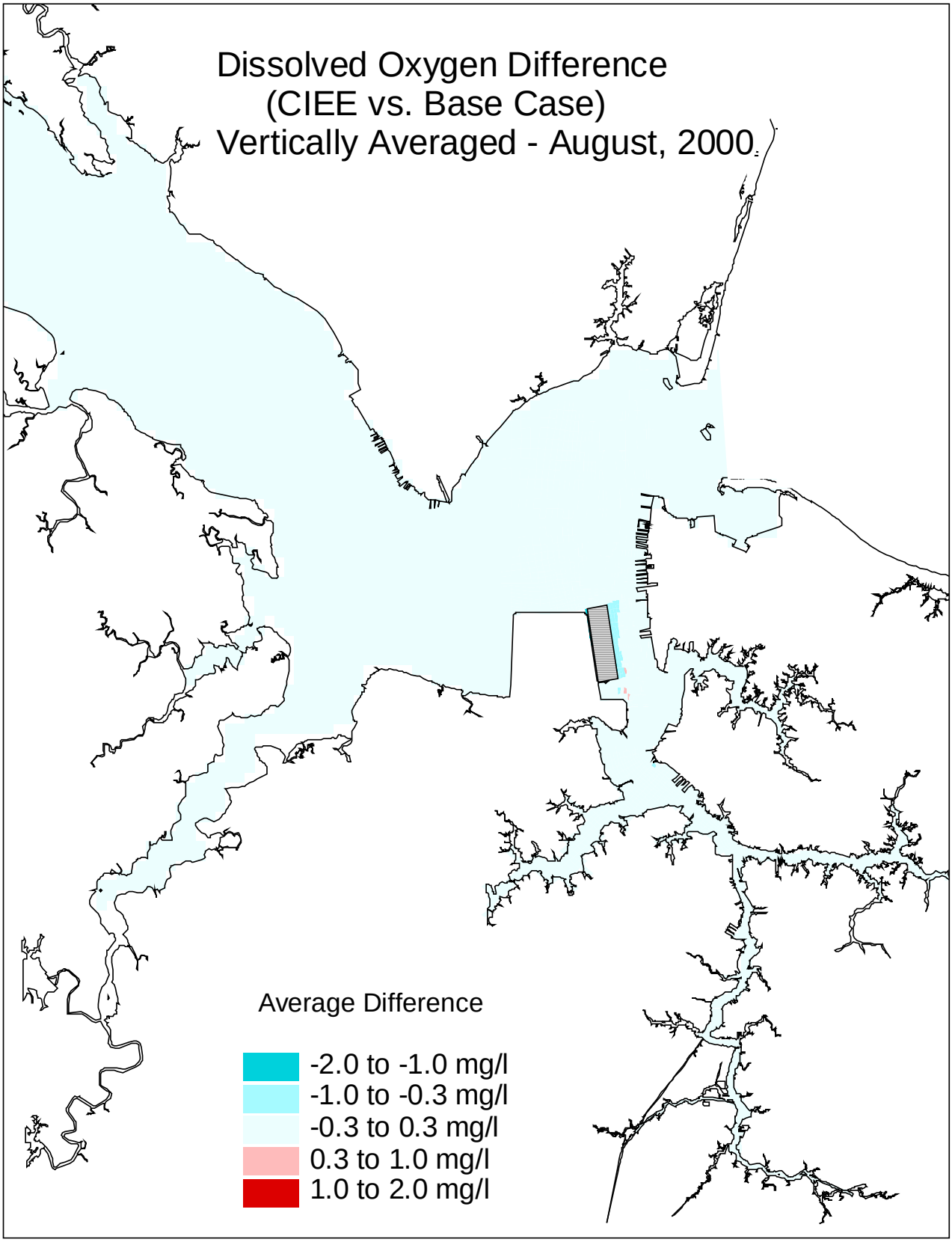

Figure K15. Dissolved oxygen (30-day average, vertically averaged) difference between the CIEE full expansion and the base case for August, 2000.

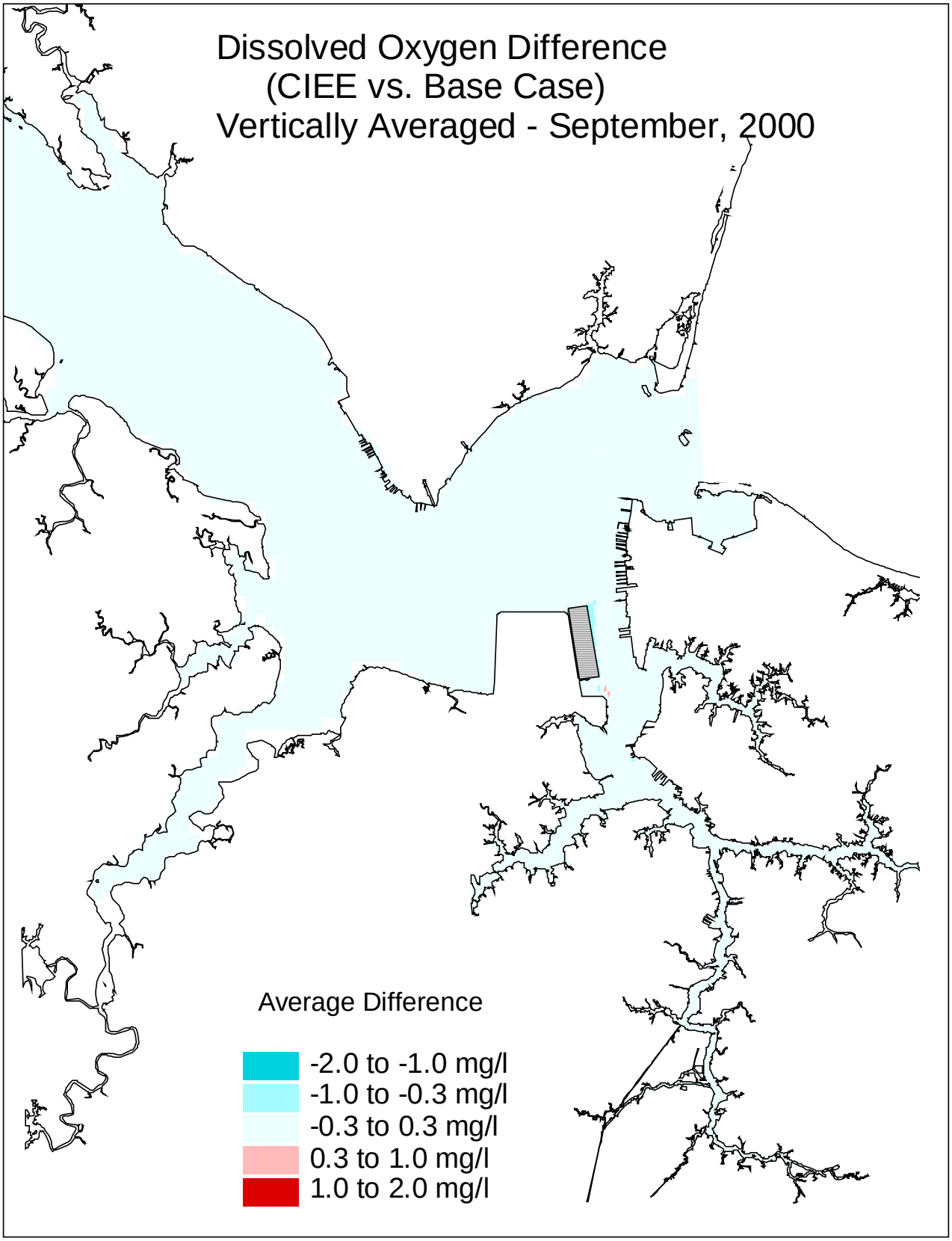

Figure K16. Dissolved oxygen (30-day average, vertically averaged) difference between the CIEE full expansion and the base case for September, 2000.

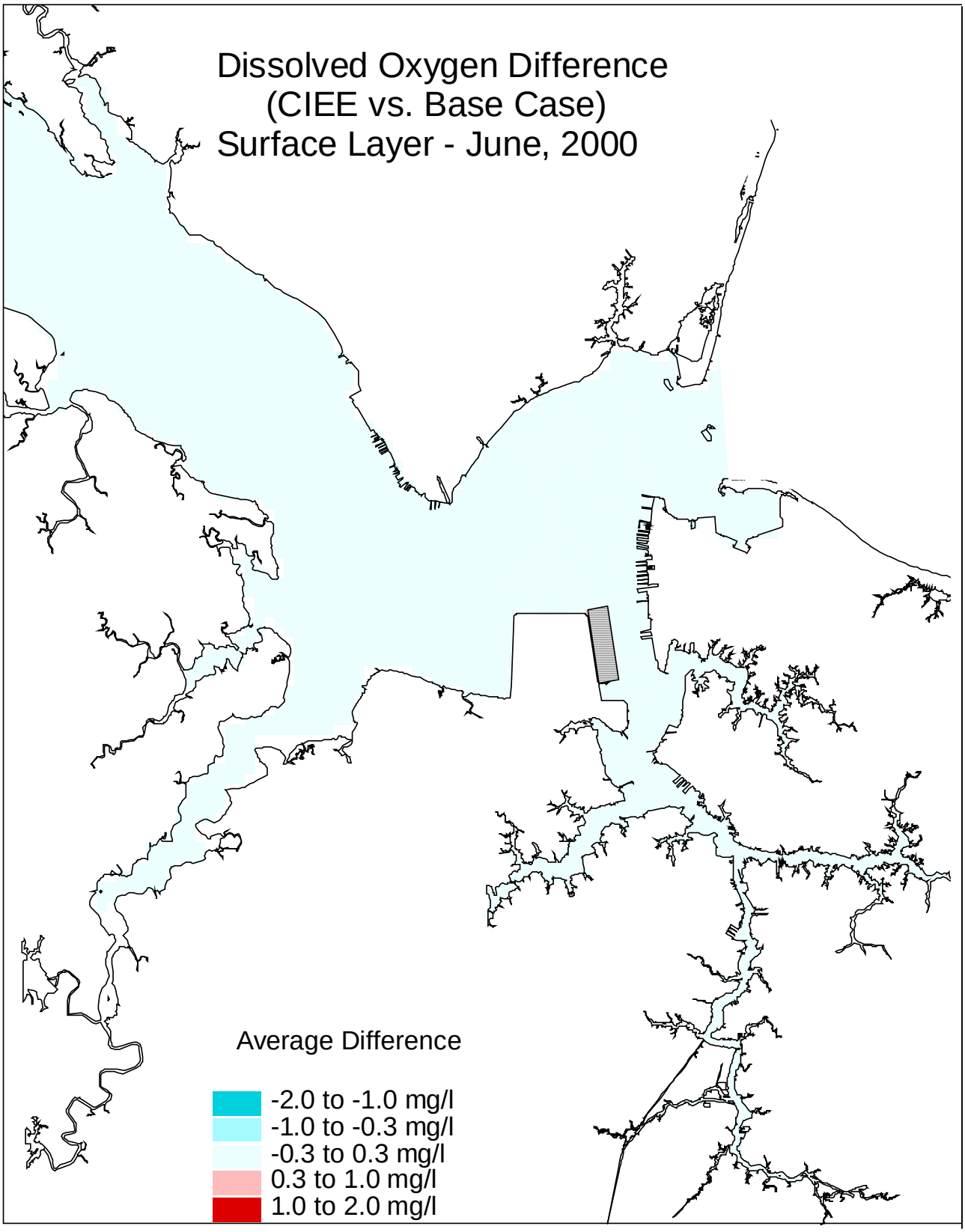

Figure K17. Dissolved oxygen (30-day average, at the surface layer) difference between the CIEE full expansion and the base case for June, 2000.

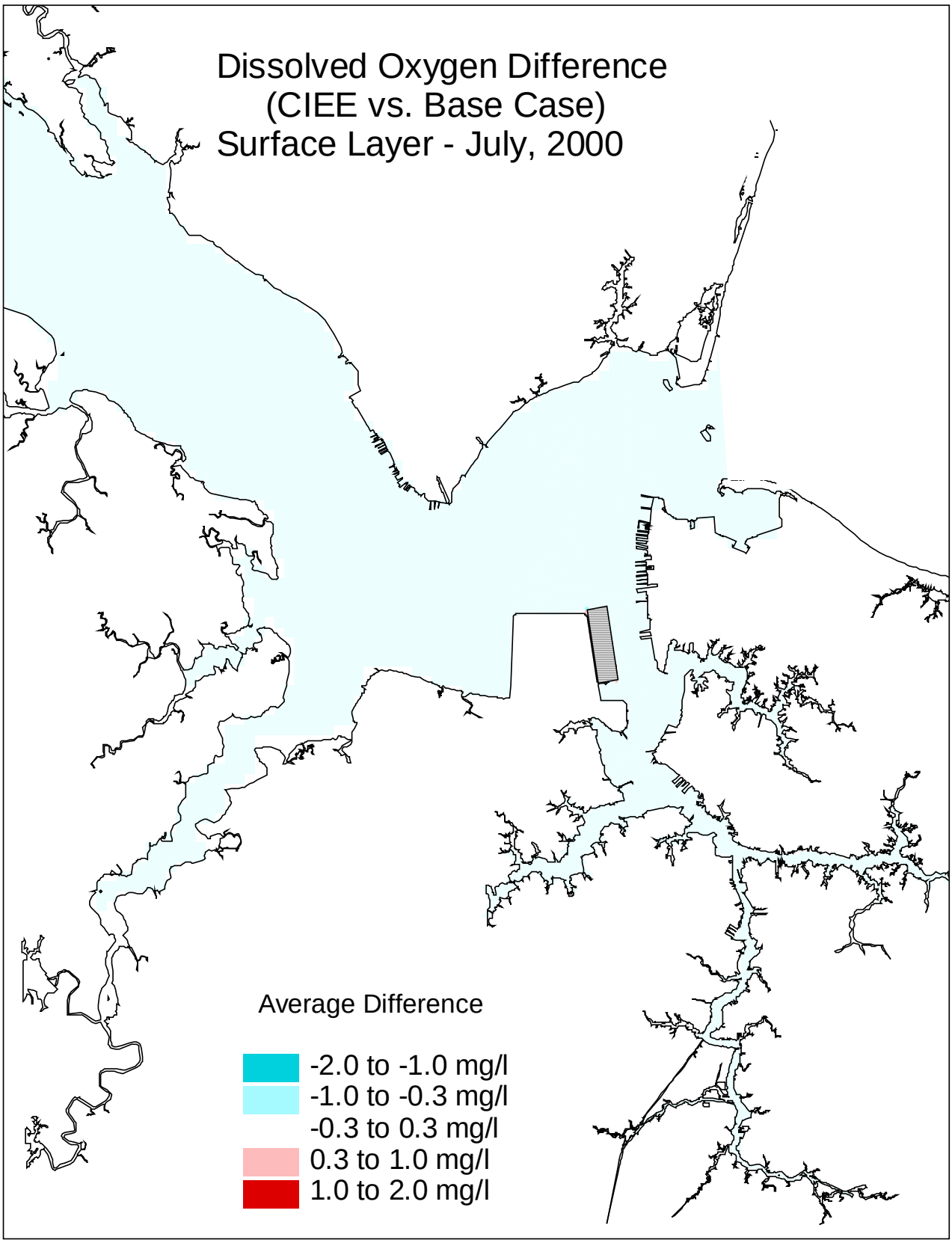

Figure K18. Dissolved oxygen (30-day average, at the surface layer) difference between the CIEE full expansion and the base case for July, 2000.

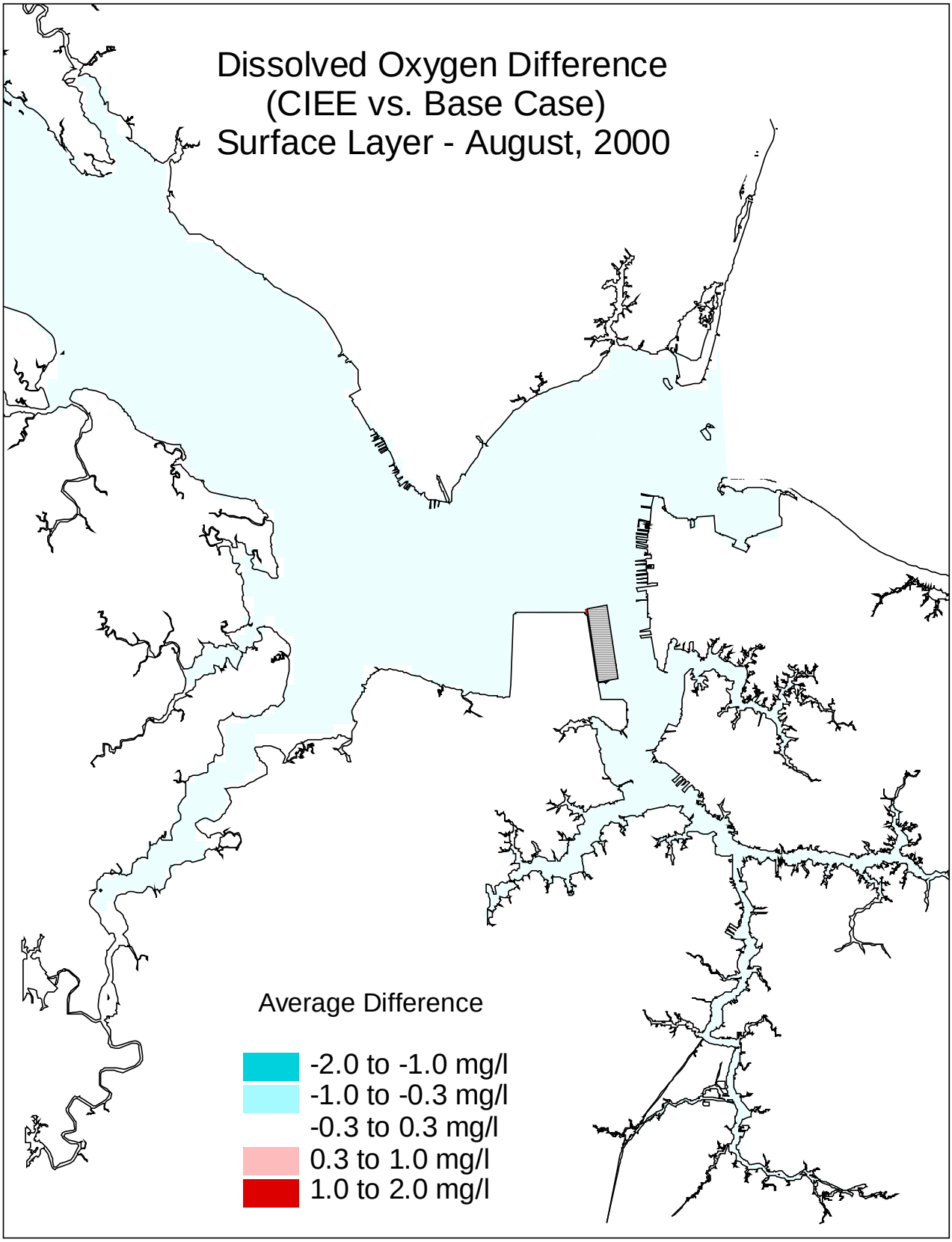

Figure K19. Dissolved oxygen (30-day average, at the surface layer) difference between the CIEE full expansion and the base case for August, 2000.

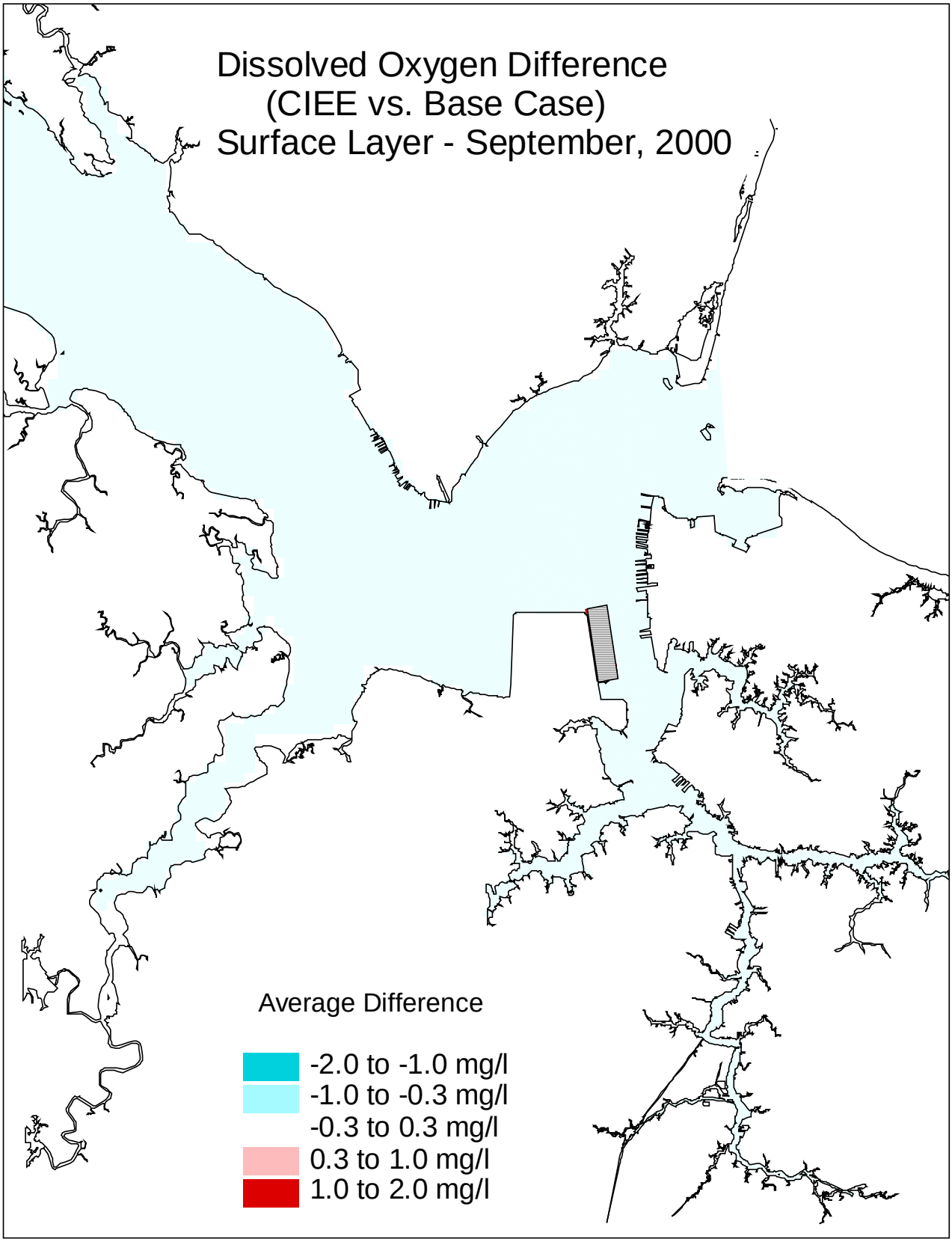

Figure K20. Dissolved oxygen (30-day average, at the surface layer) difference between the CIEE full expansion and the base case for September, 2000.

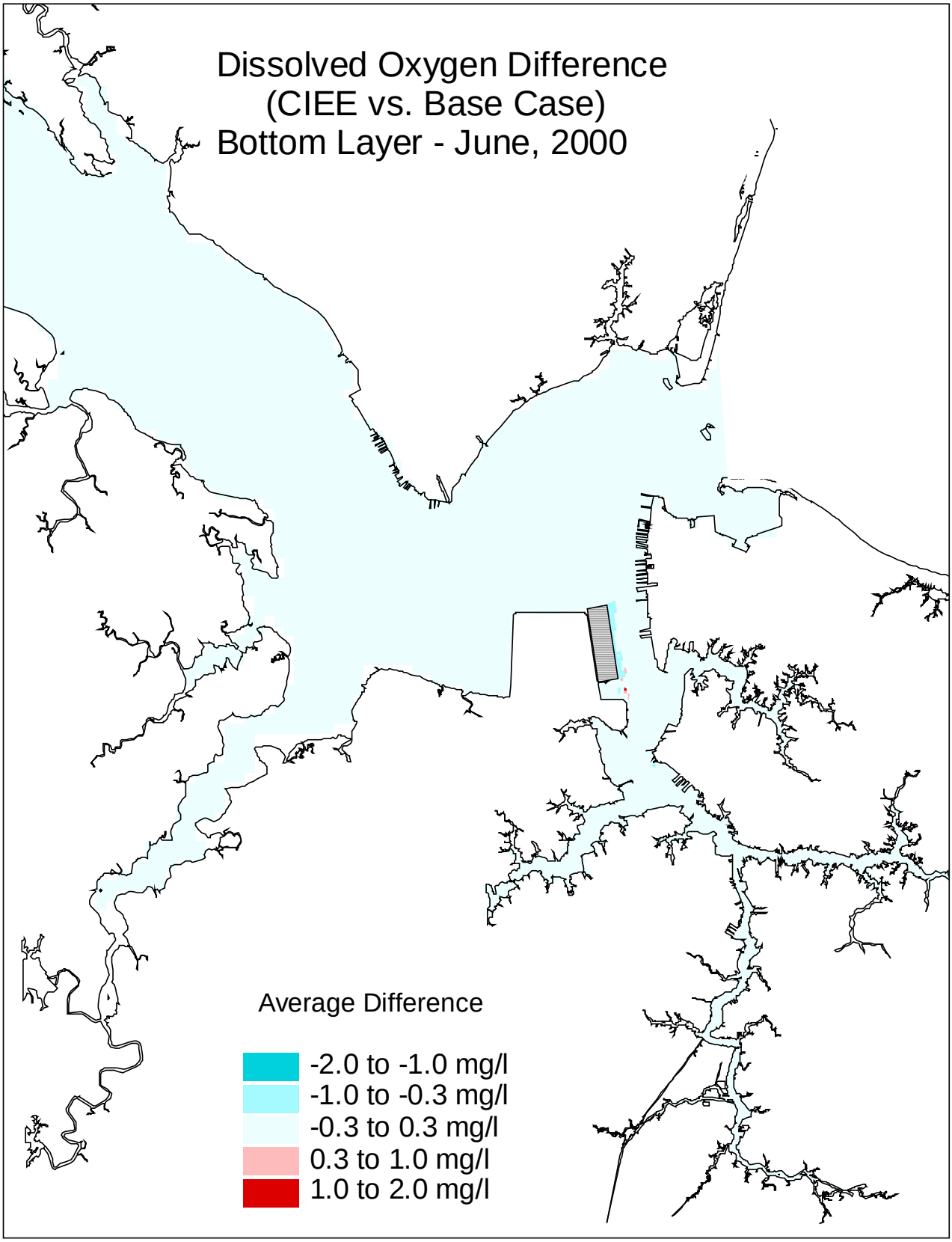

Figure K21. Dissolved oxygen (30-day average, at the bottom layer) difference between the CIEE full expansion and the base case for June, 2000.

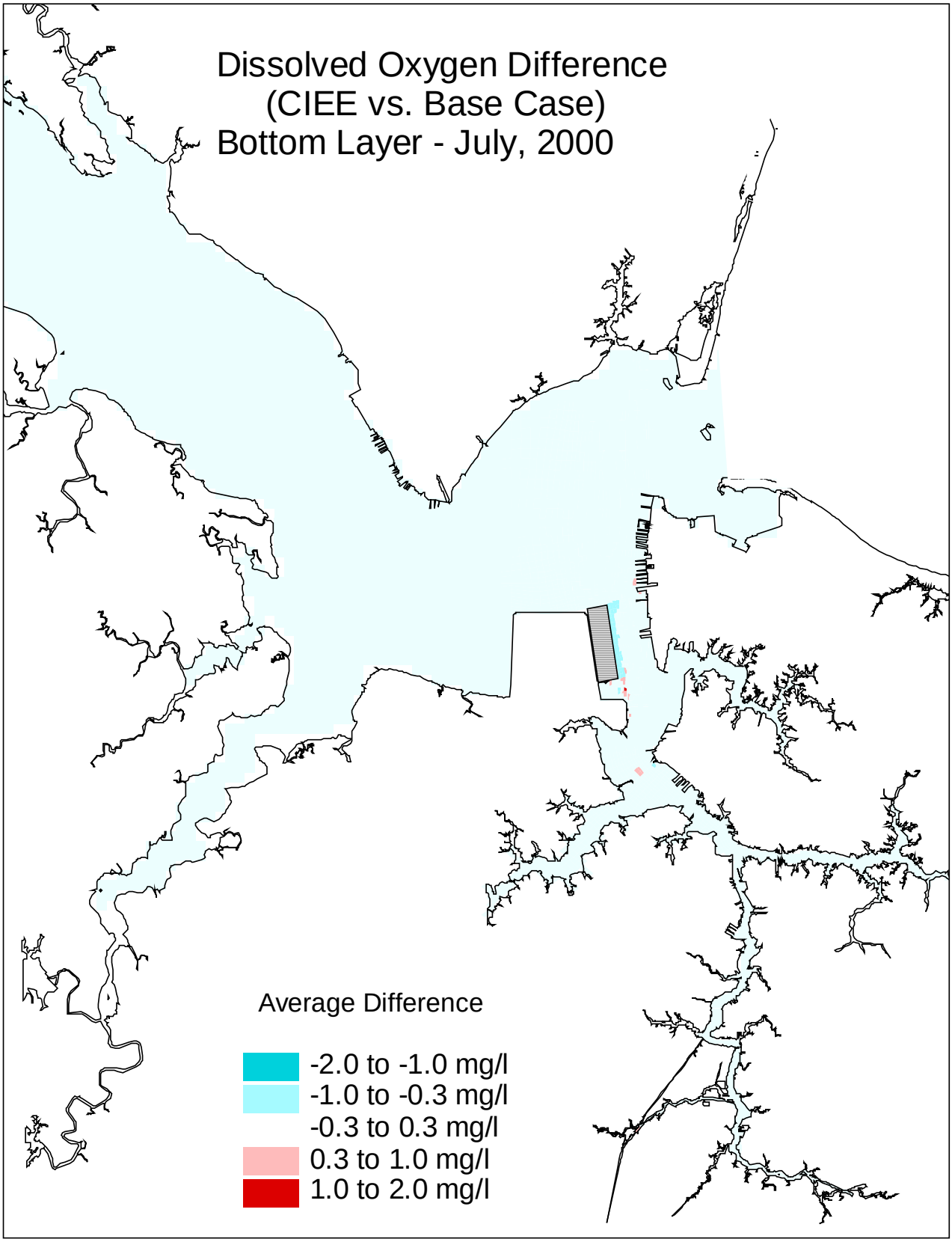

Figure K22. Dissolved oxygen (30-day average, at the bottom layer) difference between the CIEE full expansion and the base case for July, 2000.

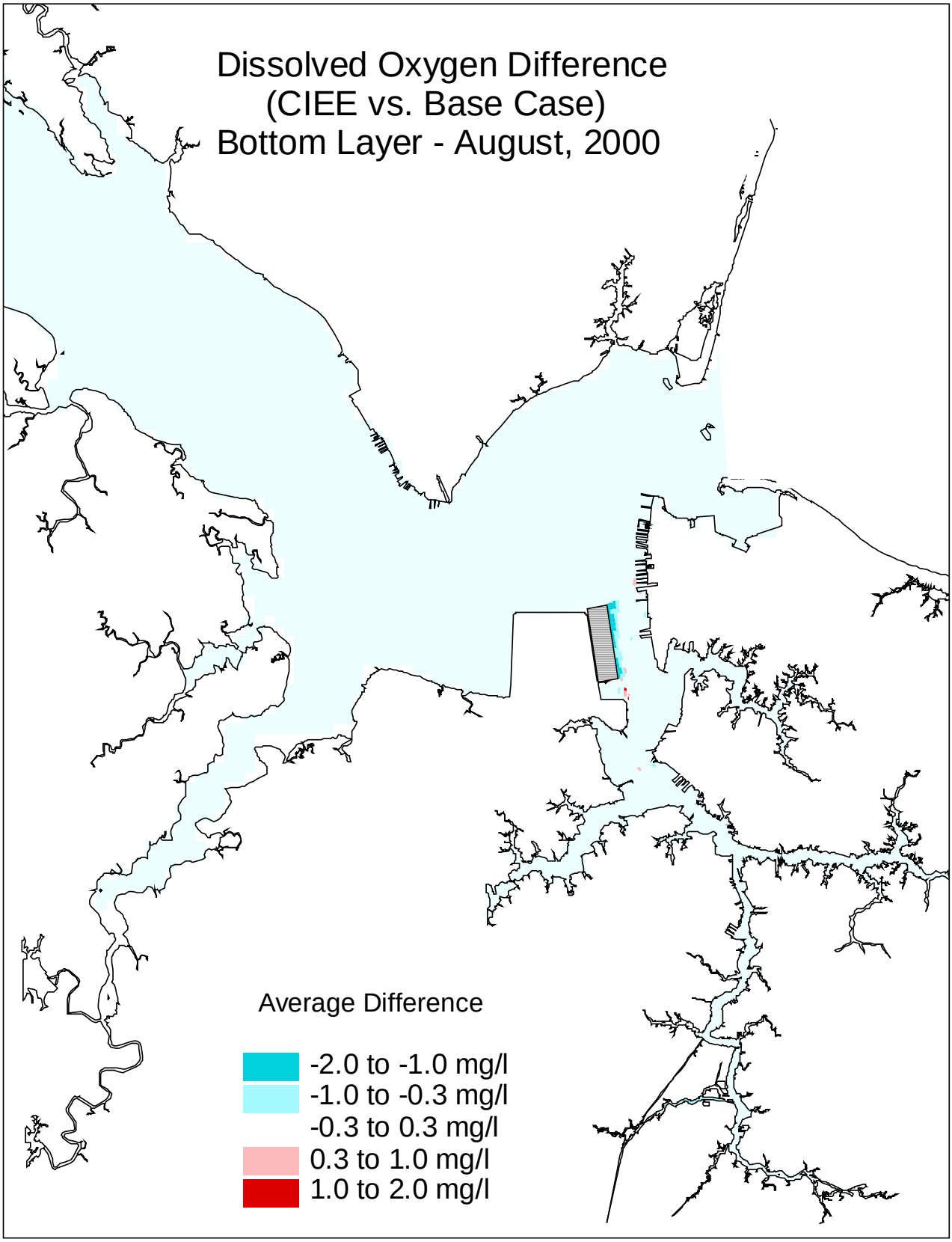

Figure K23. Dissolved oxygen (30-day average, at the bottom layer) difference between the CIEE full expansion and the base case for August, 2000.

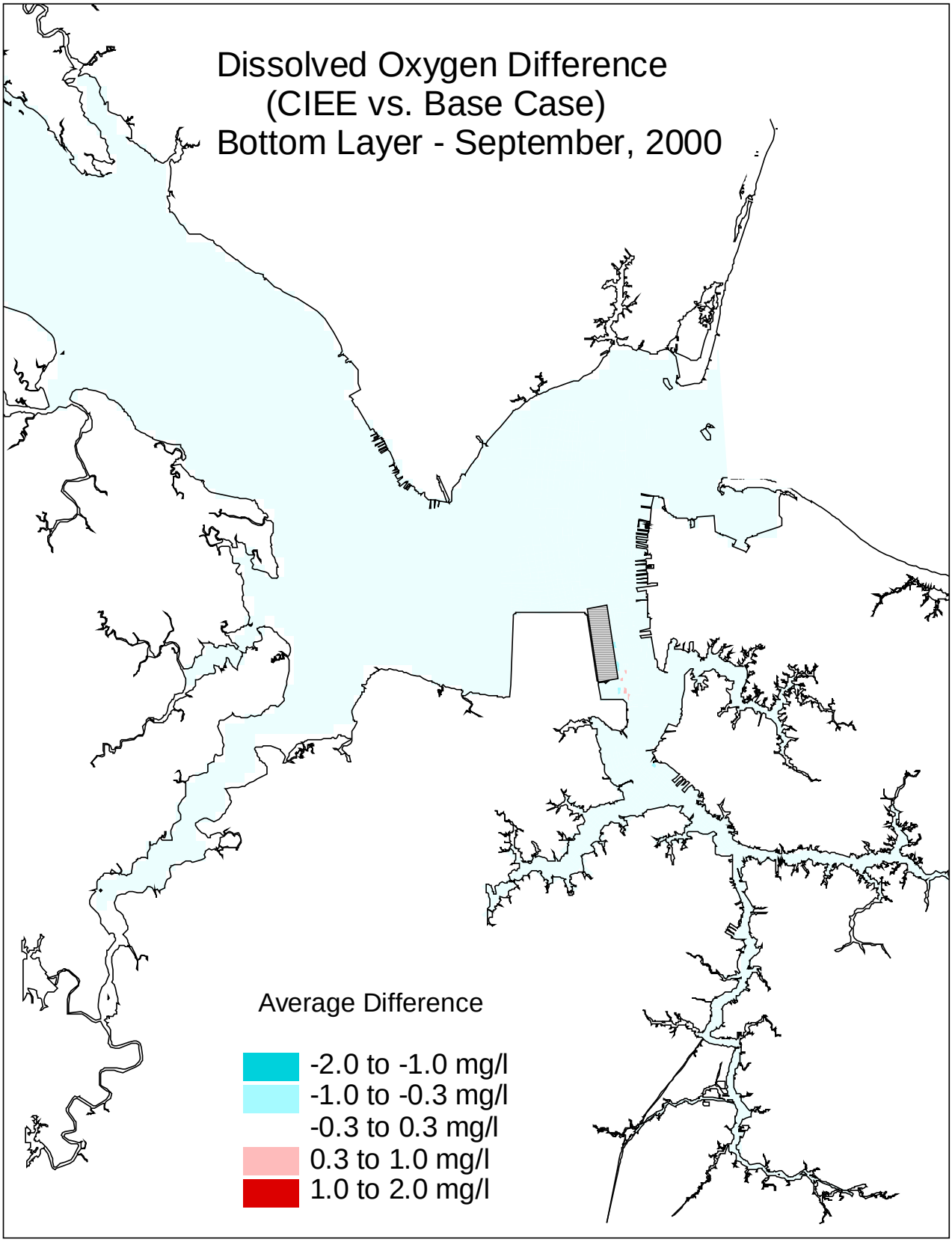

Figure K24. Dissolved oxygen (30-day average, at the bottom layer) difference between the CIEE full expansion and the base case for September, 2000.

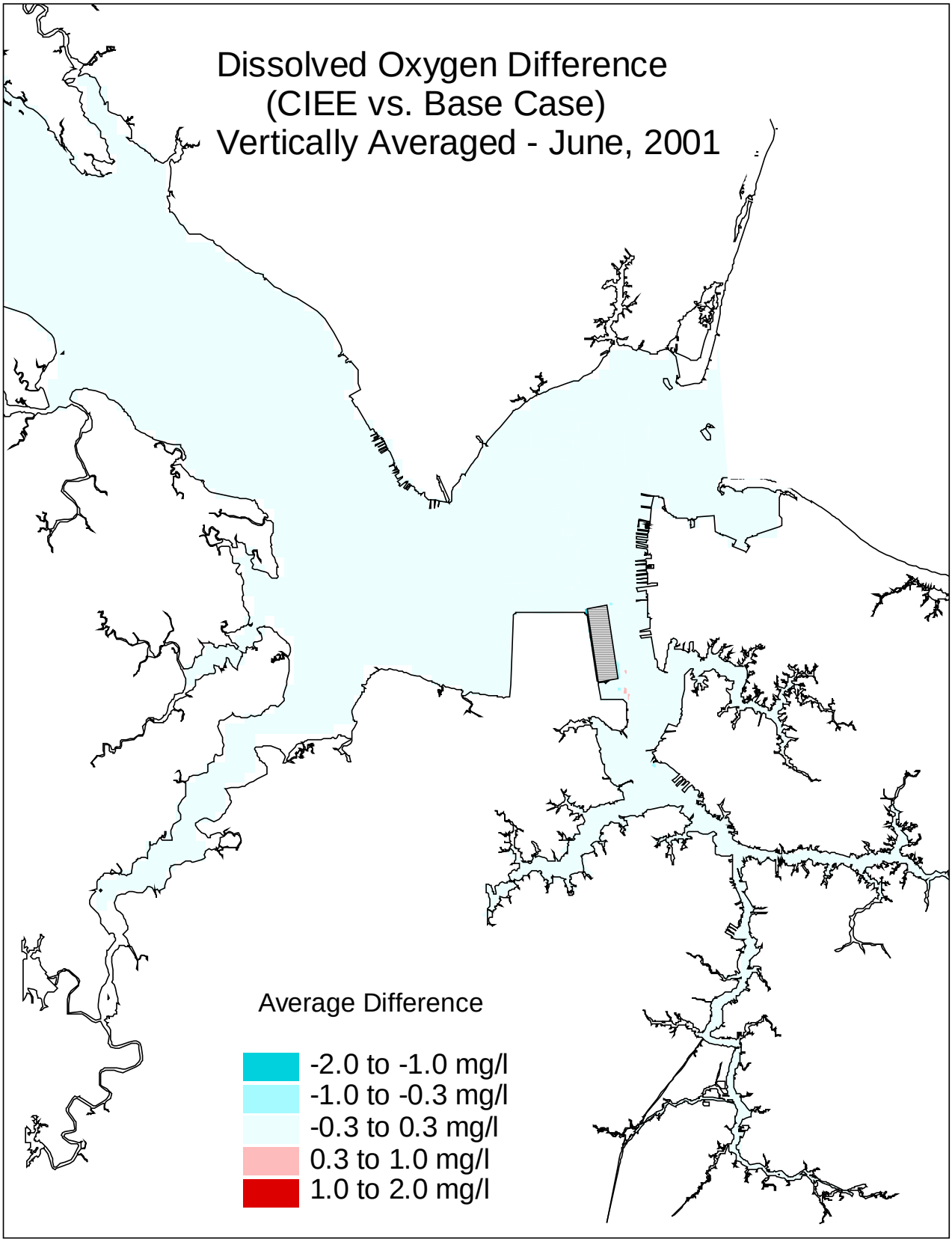

Figure K25. Dissolved oxygen (30-day average, vertically averaged) difference between the CIEE full expansion and the base case for June, 2001.

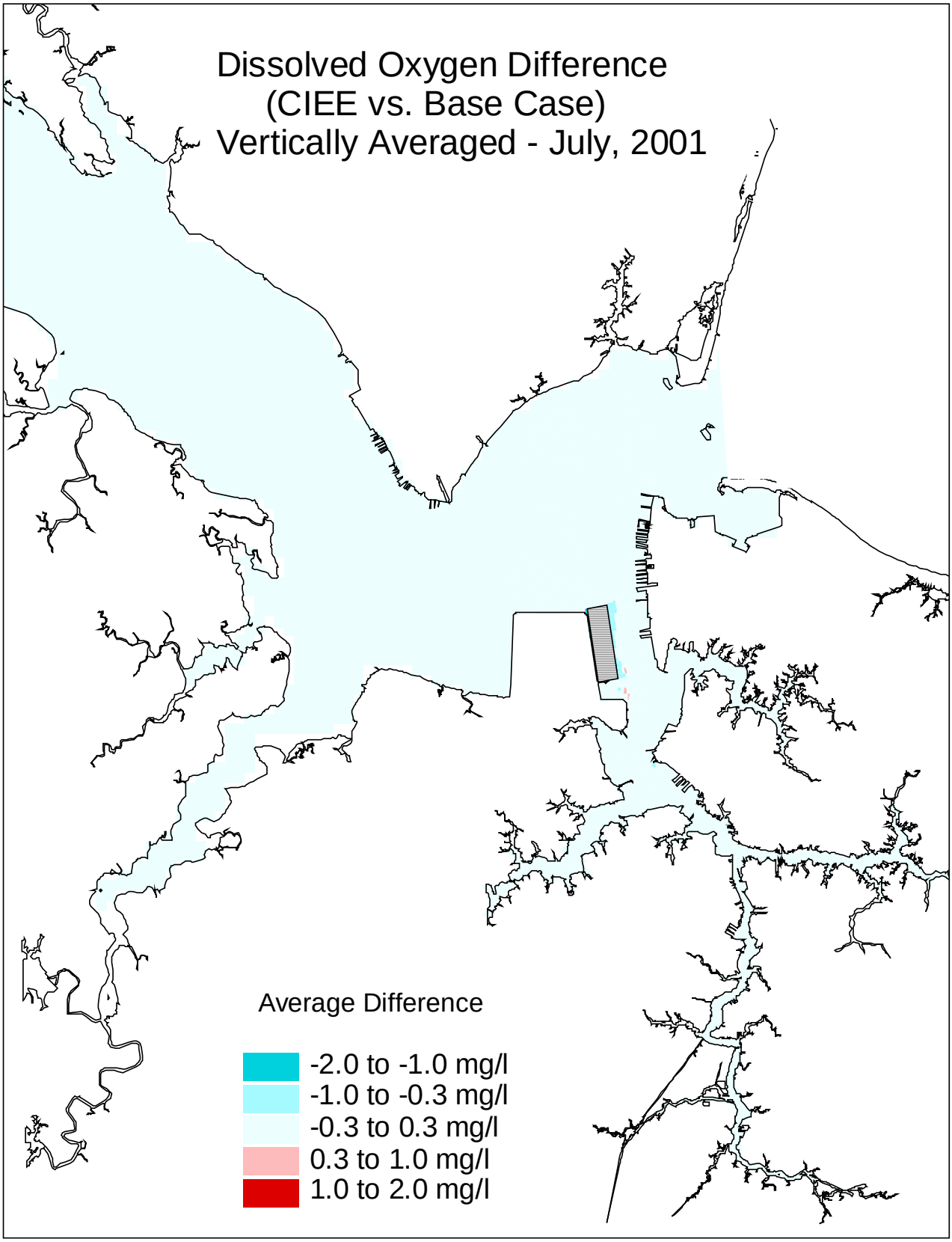

Figure K26. Dissolved oxygen (30-day average, vertically averaged) difference between the CIEE full expansion and the base case for July, 2001.

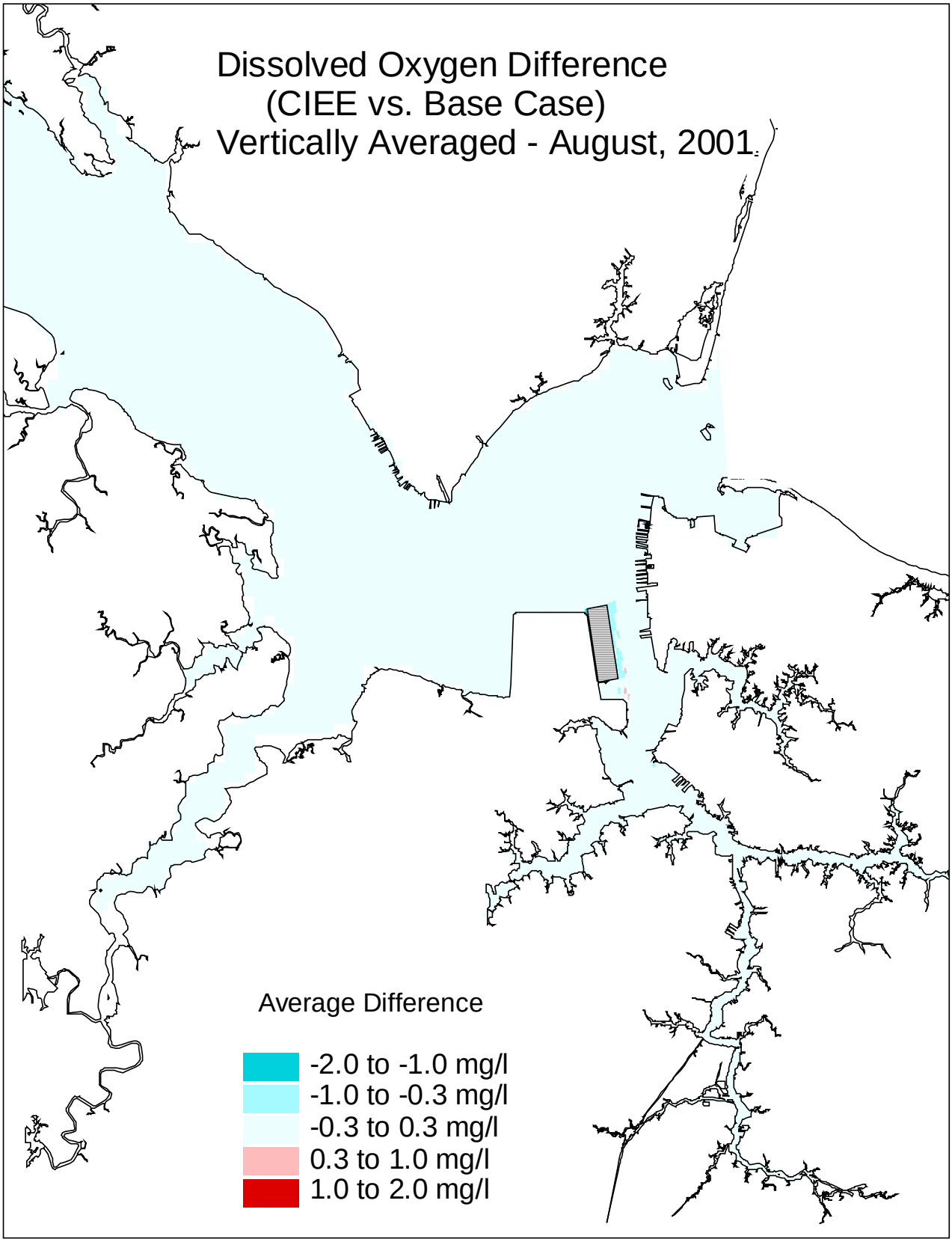

Figure K27. Dissolved oxygen (30-day average, vertically averaged) difference between the CIEE full expansion and the base case for August, 2001.

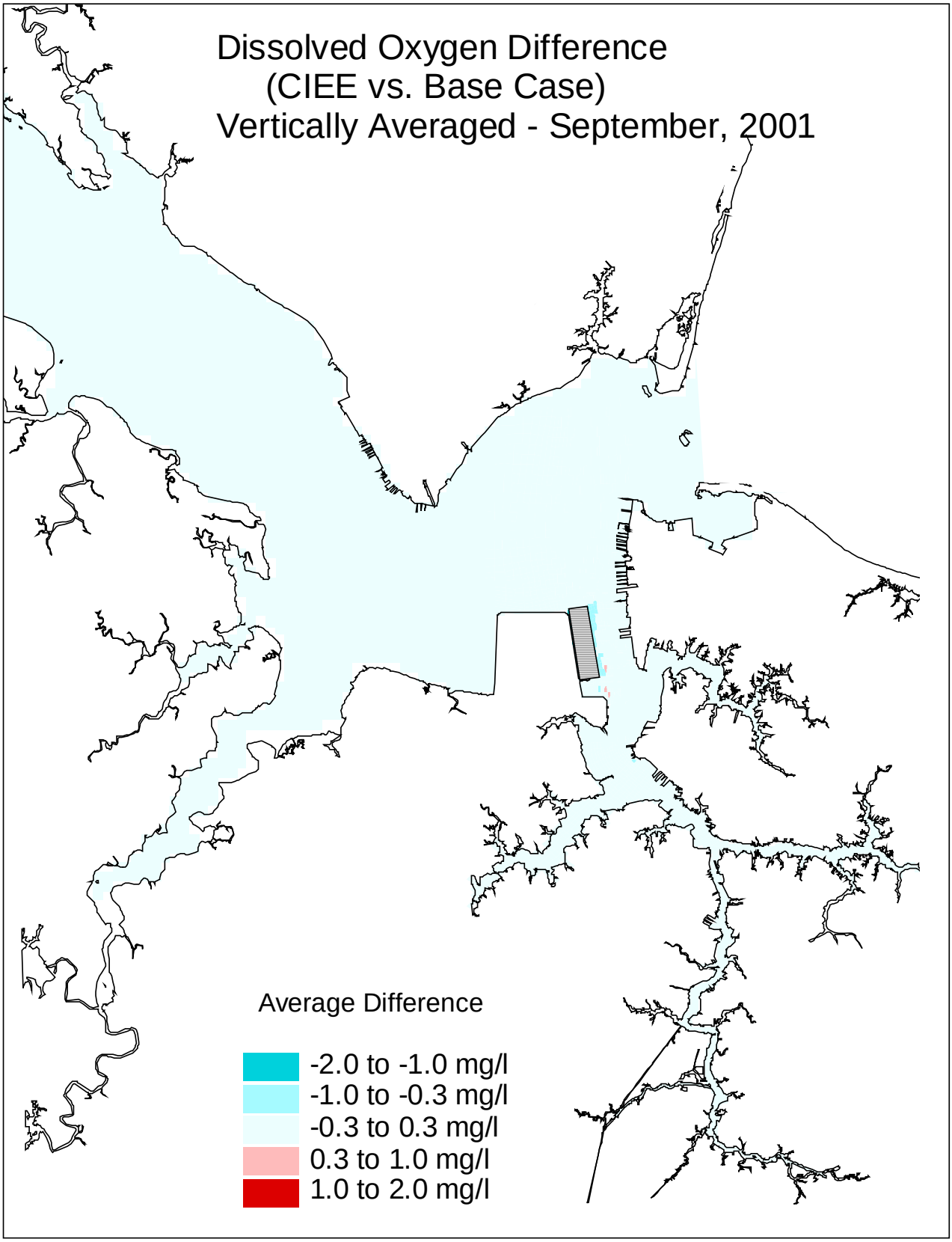

Figure K28. Dissolved oxygen (30-day average, vertically averaged) difference between the CIEE full expansion and the base case for September, 2001.

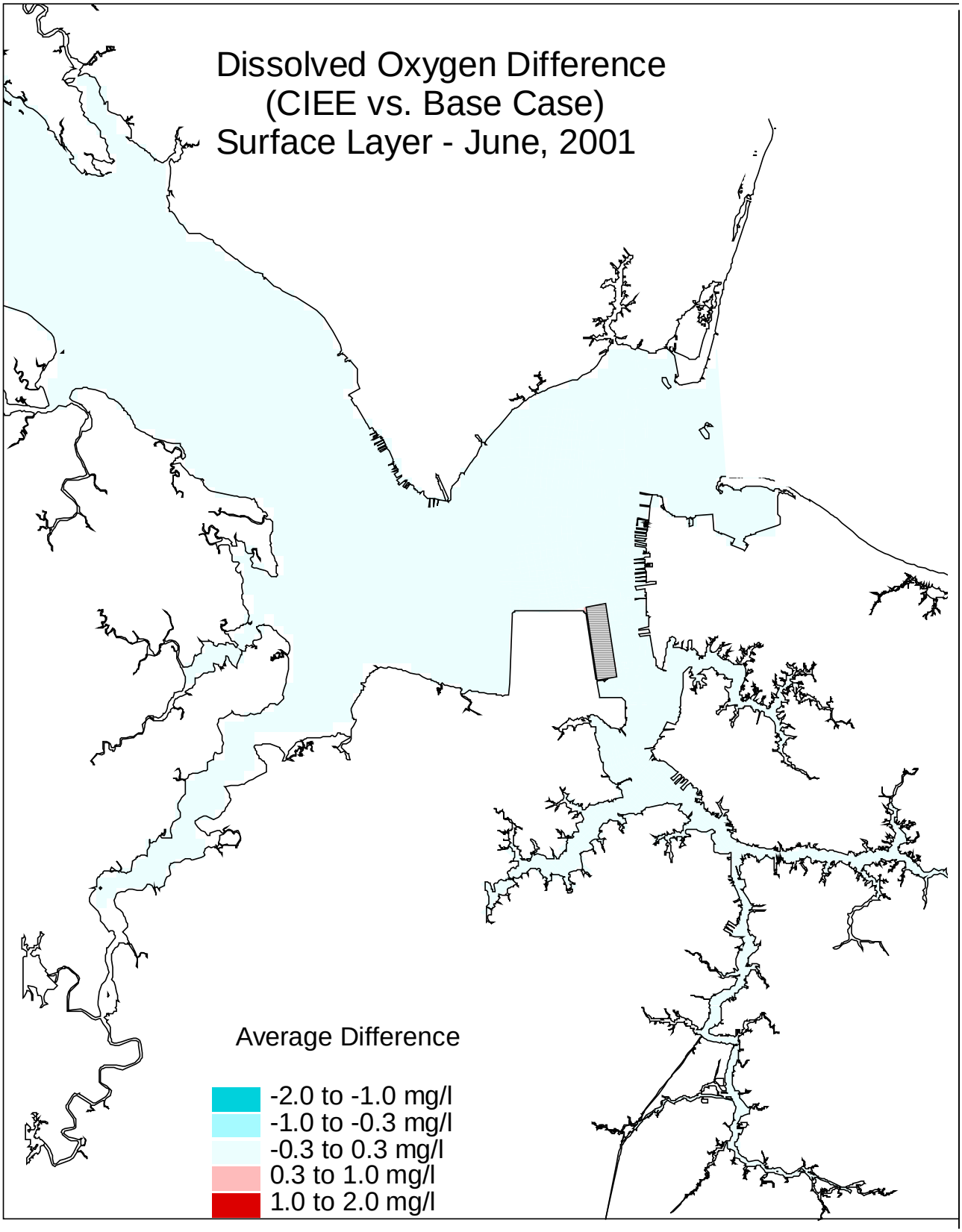

Figure K29. Dissolved oxygen (30-day average, at the surface layer) difference between the CIEE full expansion and the base case for June, 2001.

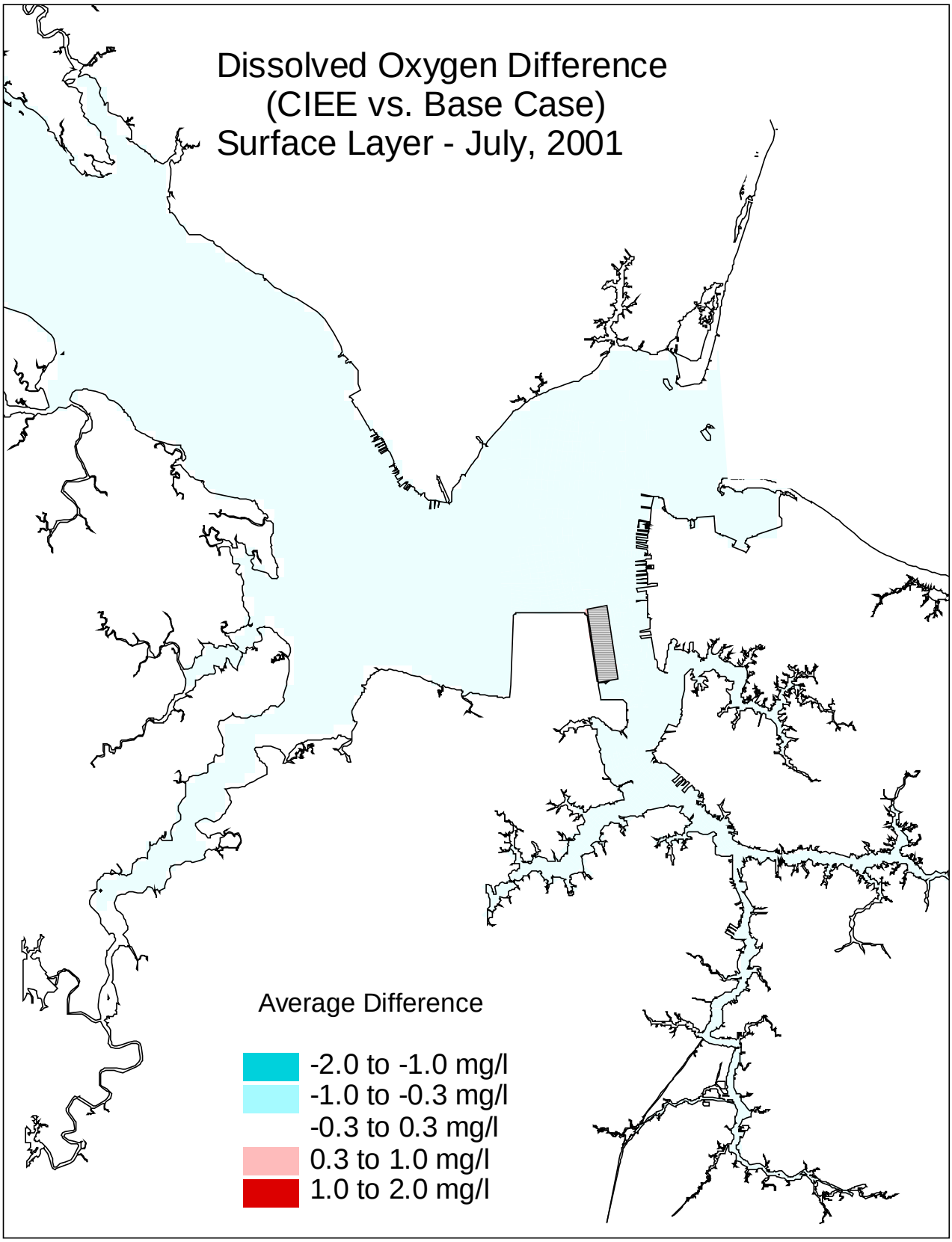

Figure K30. Dissolved oxygen (30-day average, at the surface layer) difference between the CIEE full expansion and the base case for July, 2001.

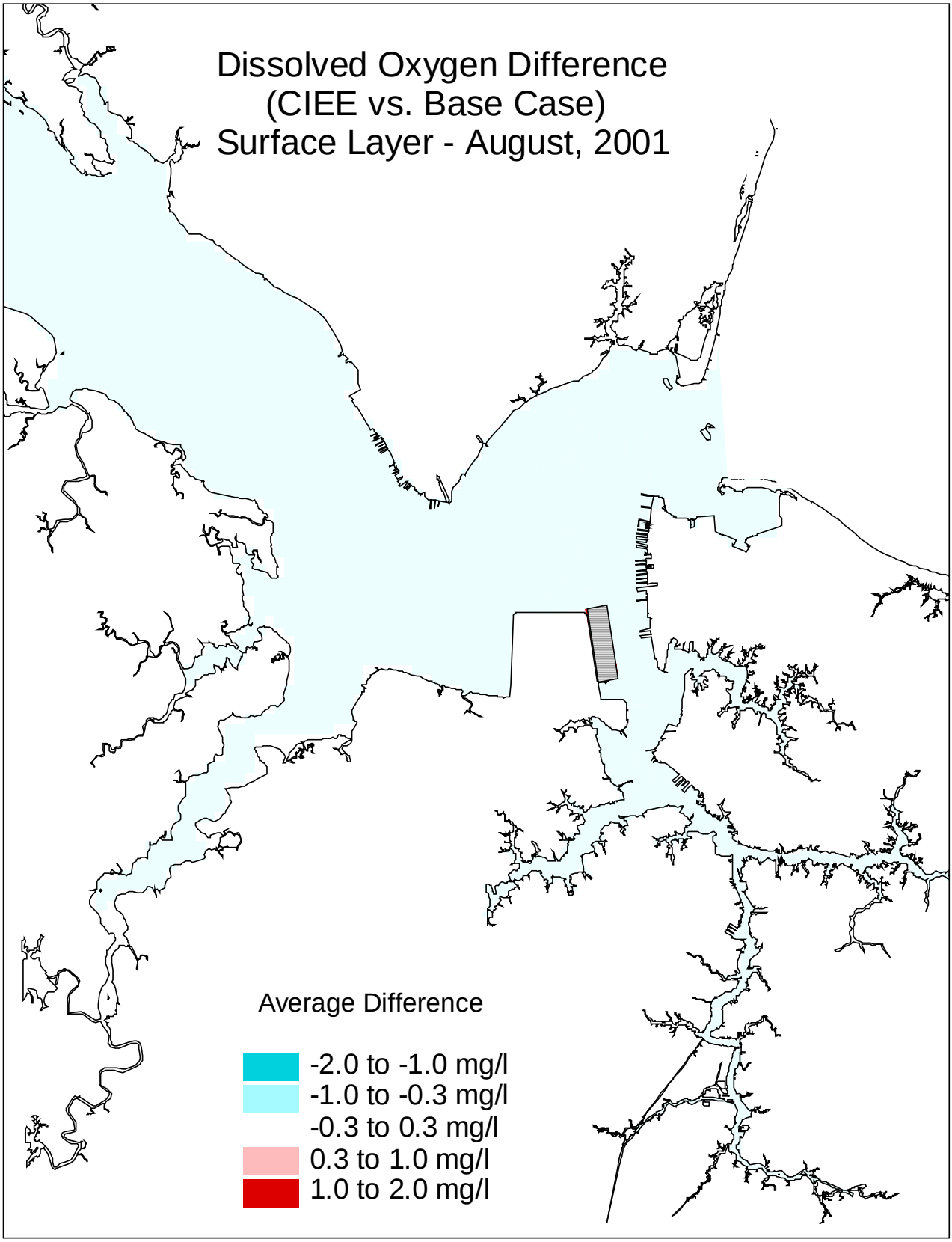

Figure K31. Dissolved oxygen (30-day average, at the surface layer) difference between the CIEE full expansion and the base case for August, 2001.

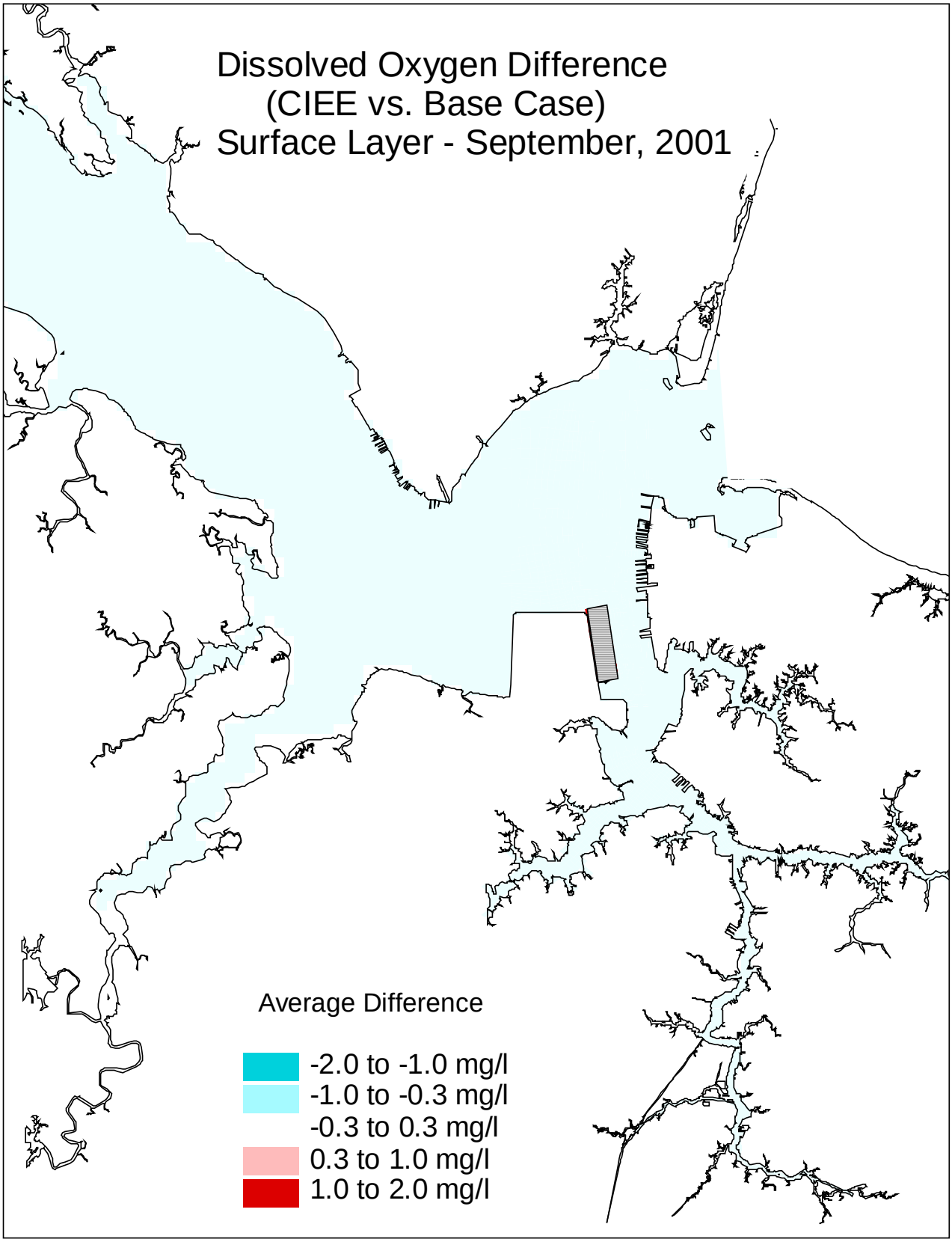

Figure K32. Dissolved oxygen (30-day average, at the surface layer) difference between the CIEE full expansion and the base case for September, 2001.

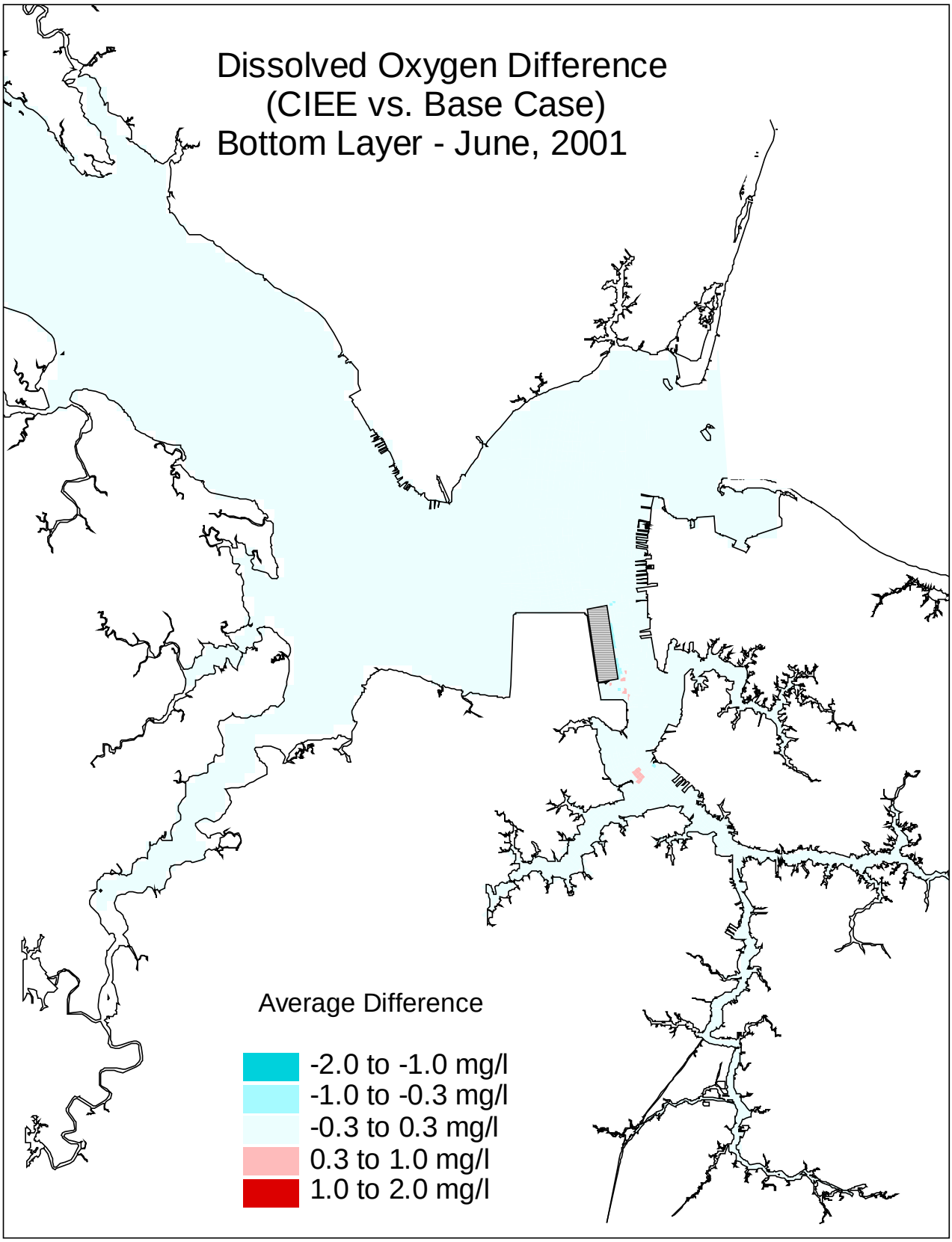

Figure K33. Dissolved oxygen (30-day average, at the bottom layer) difference between the CIEE full expansion and the base case for June, 2001.

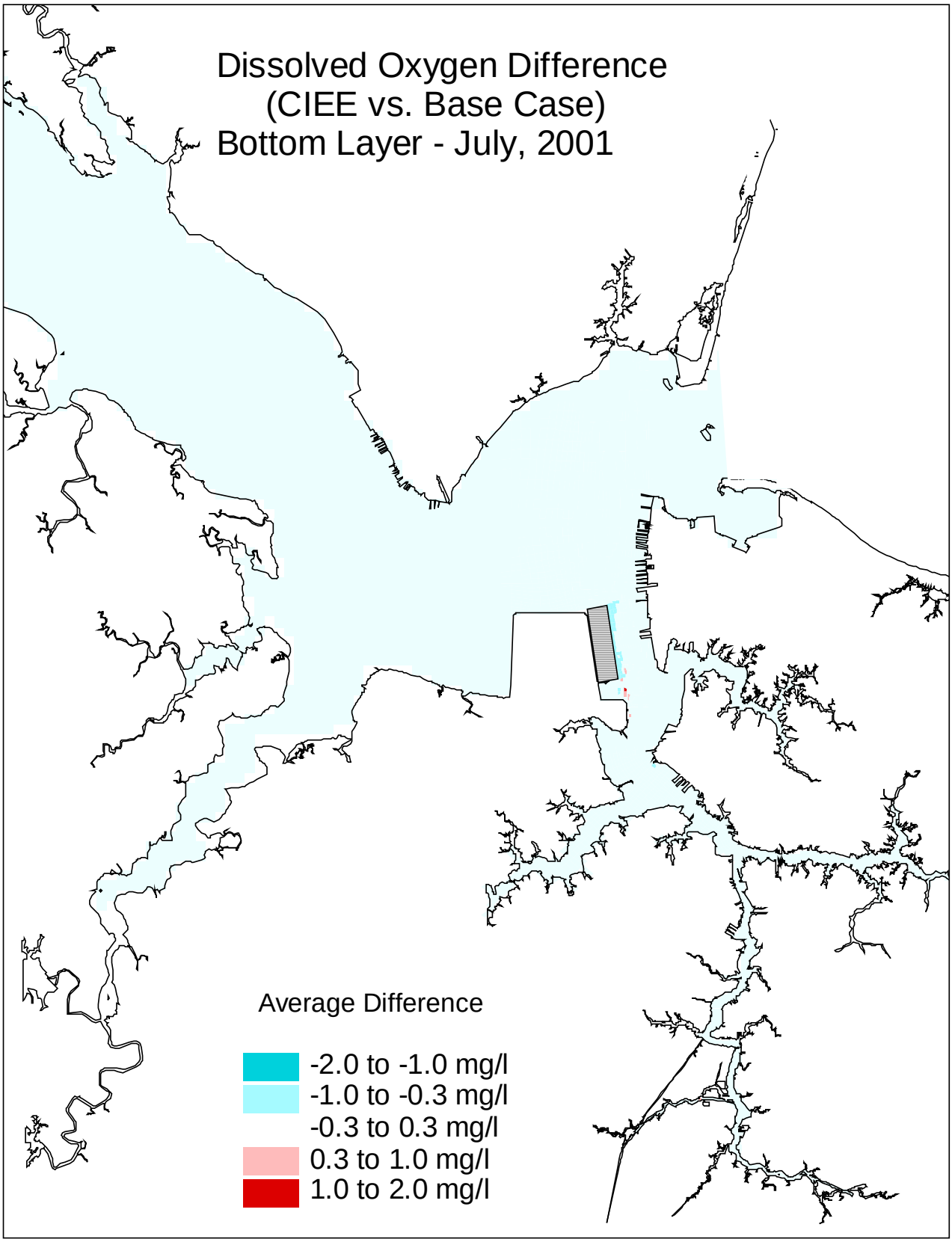

Figure K34. Dissolved oxygen (30-day average, at the bottom layer) difference between the CIEE full expansion and the base case for July, 2001.

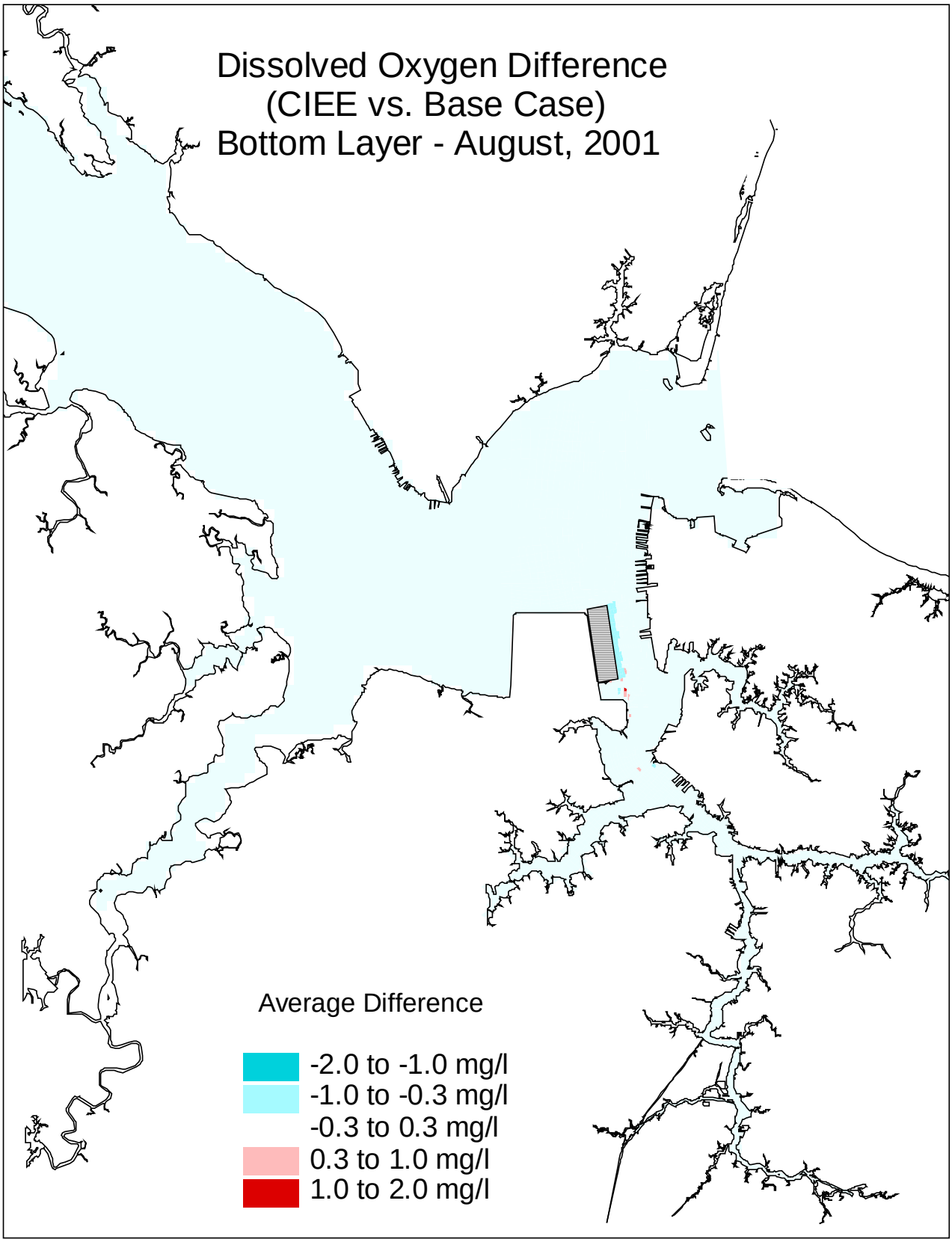

Figure K35. Dissolved oxygen (30-day average, at the bottom layer) difference between the CIEE full expansion and the base case for August, 2001.

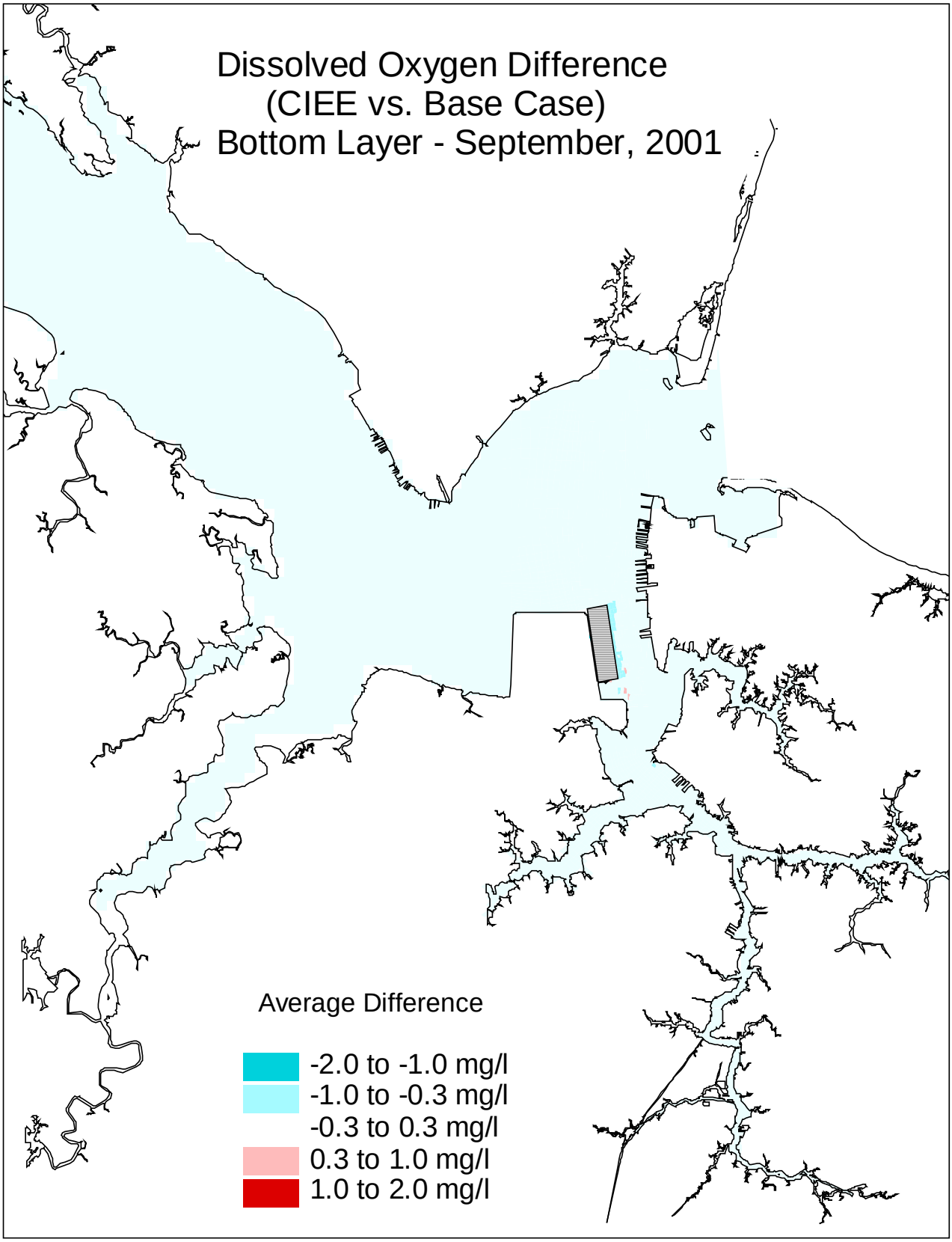

Figure K36. Dissolved oxygen (30-day average, at the bottom layer) difference between the CIEE full expansion and the base case for September, 2001.

APPENDIX K1

Spatial Plots of

Dissolved Oxygen Differences

Between CIEE Full Expansion and Base Case

For 30-Day Averages in June, July, August, and September

for 1999, 2000, and 2001

Comparison at Present Bottom Depth (pre-construction depth)

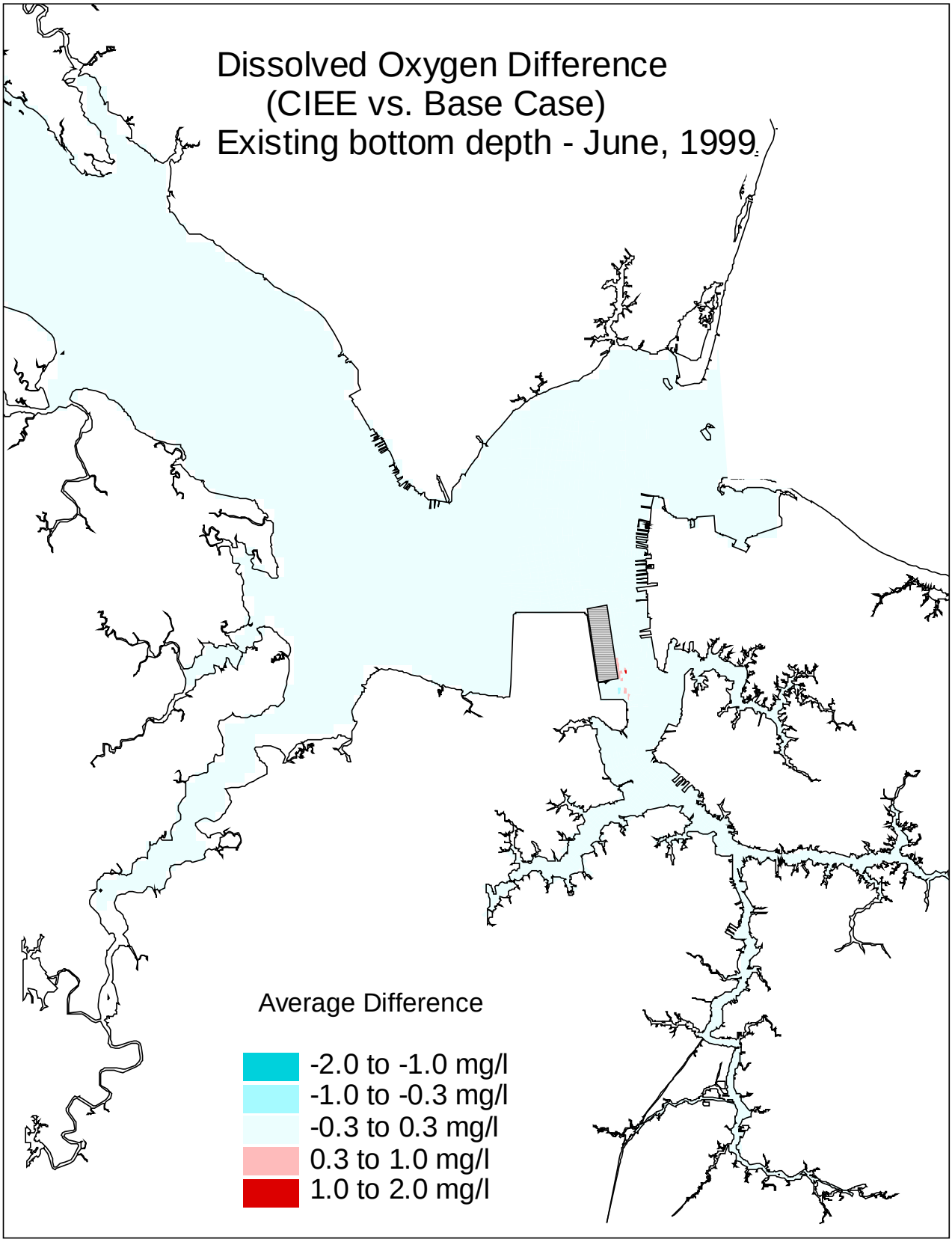

Figure K1-1. Dissolved oxygen (30-day average, at present bottom depth) difference between the CIEE full expansion and the base case for June, 1999.

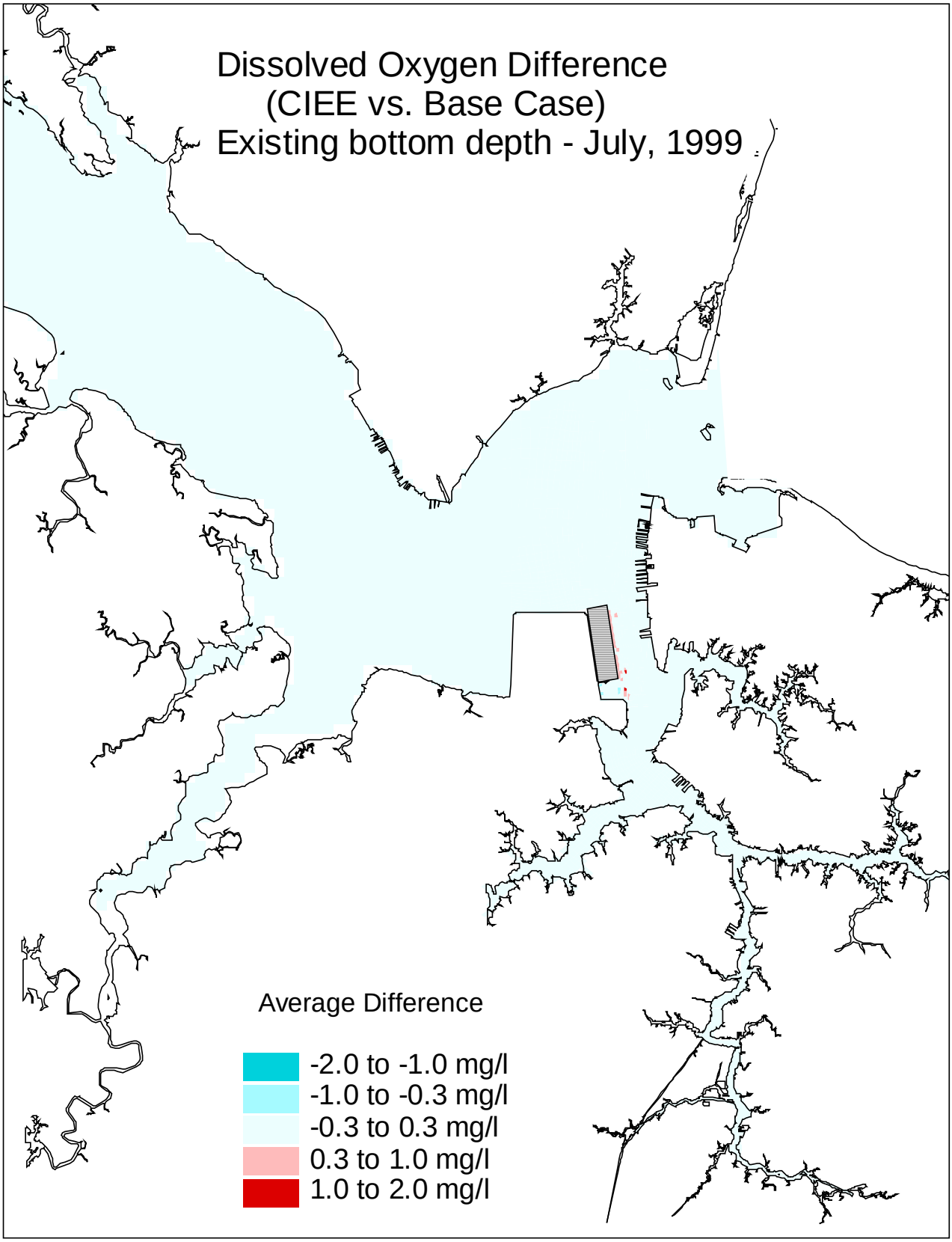

Figure K1-2. Dissolved oxygen (30-day average, at present bottom depth) difference between the CIEE full expansion and the base case for July, 1999.

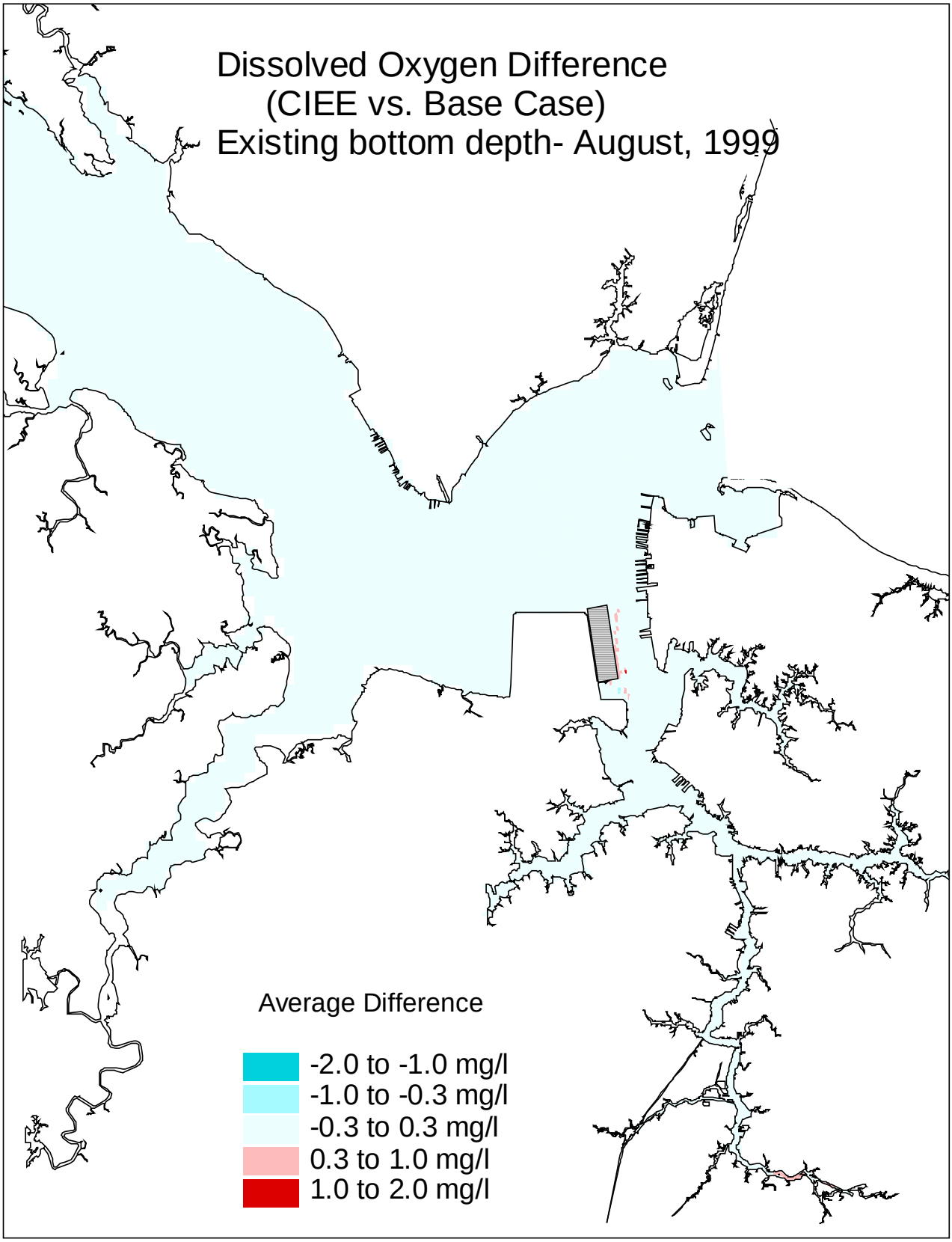

Figure K1-3. Dissolved oxygen (30-day average, at present bottom depth) difference between the CIEE full expansion and the base case for August, 1999.

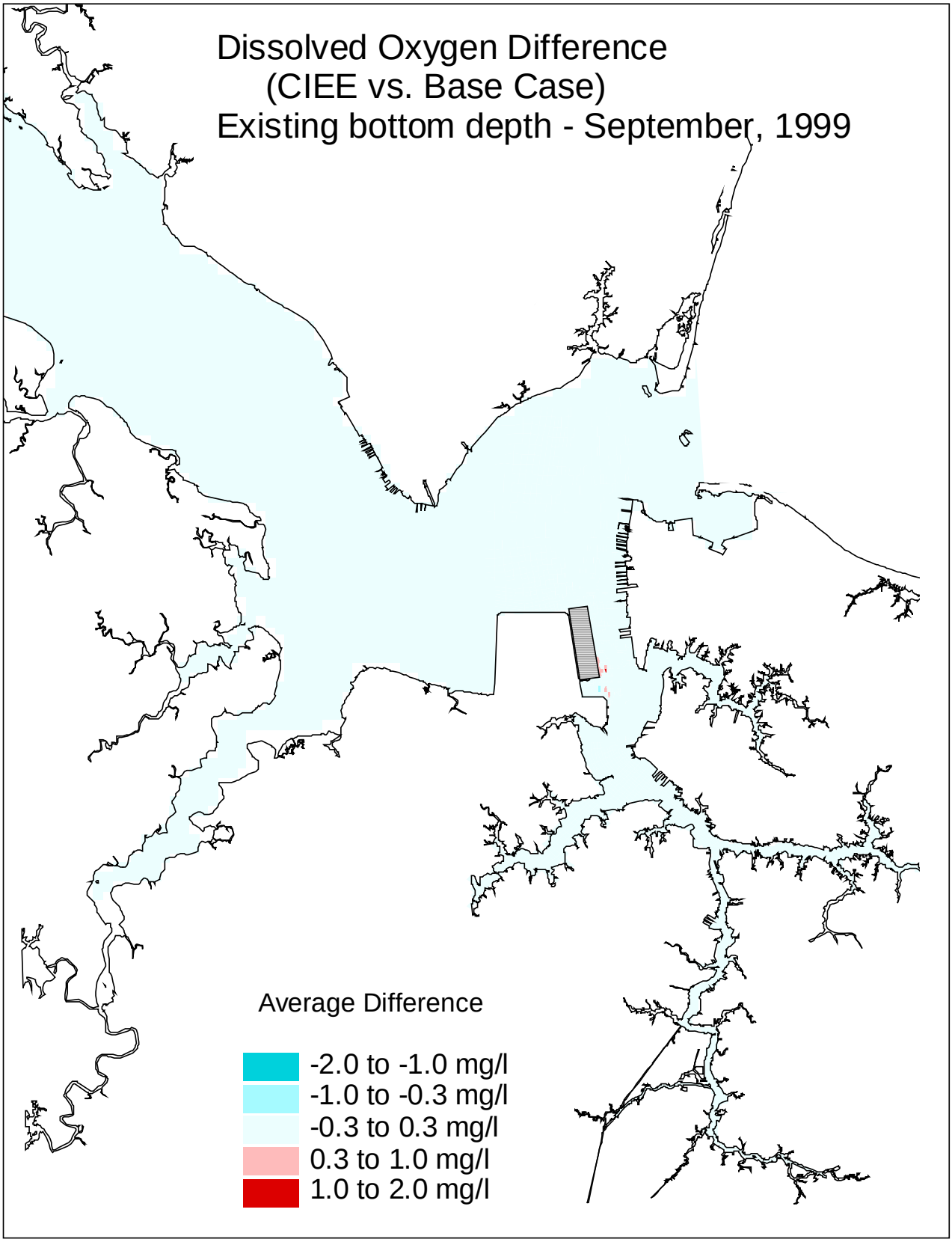

Figure K1-4. Dissolved oxygen (30-day average, at present bottom depth) difference between the CIEE full expansion and the base case for September, 1999.

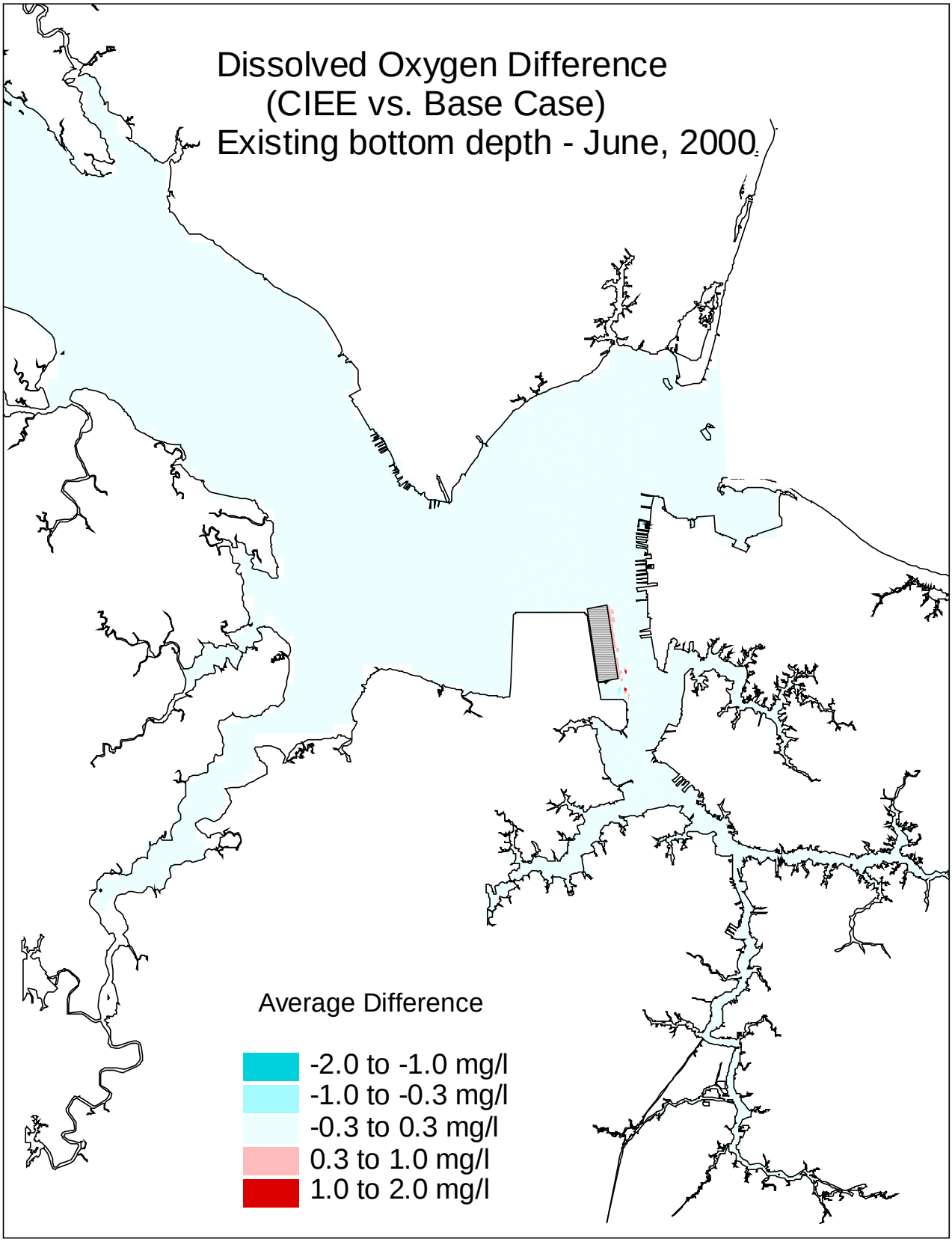

Figure K1-5. Dissolved oxygen (30-day average, at present bottom depth) difference between the CIEE full expansion and the base case for June, 2000.

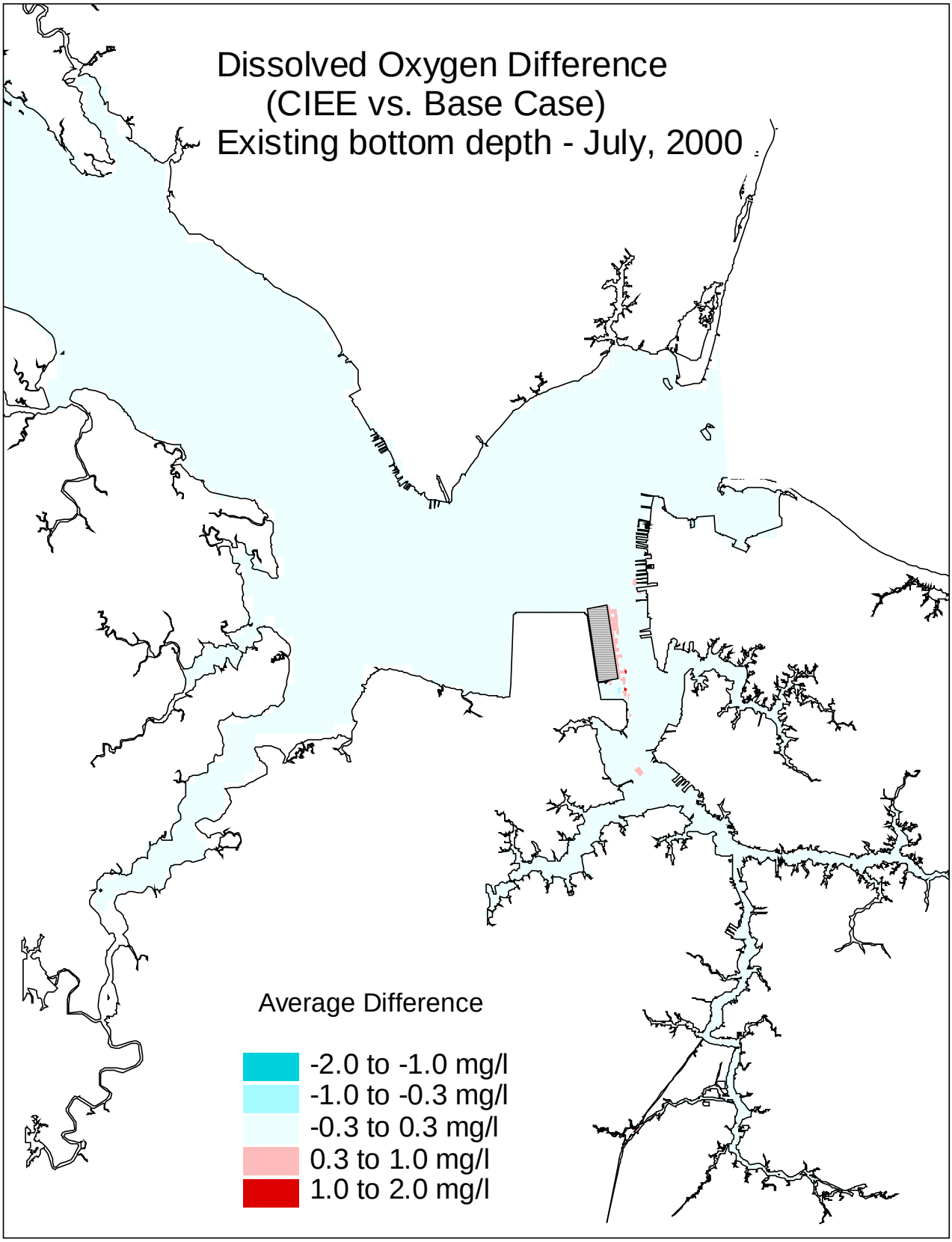

Figure K1-6. Dissolved oxygen (30-day average, at present bottom depth) difference between the CIEE full expansion and the base case for July, 2000.

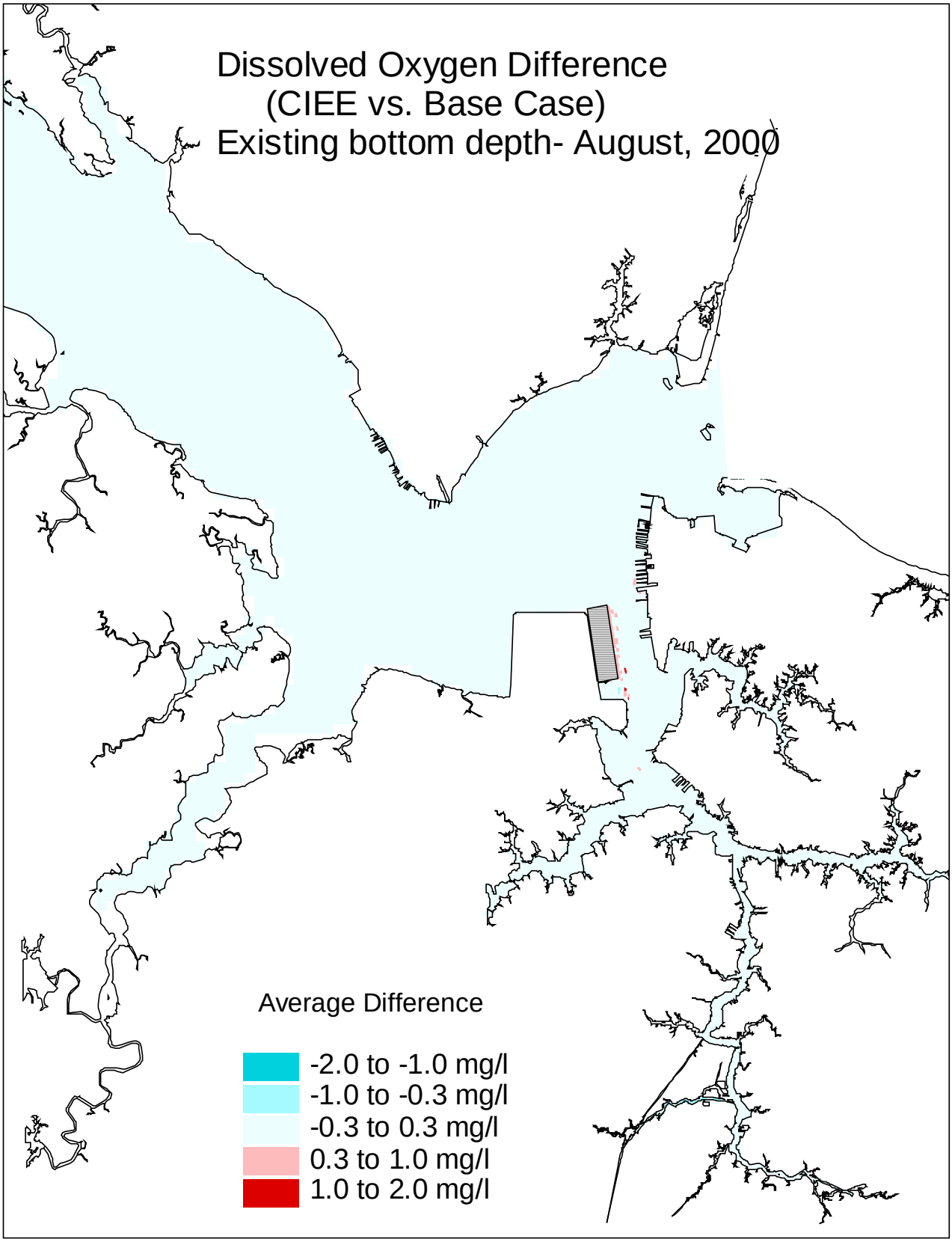

Figure K1-7. Dissolved oxygen (30-day average, at present bottom depth) difference between the CIEE full expansion and the base case for August, 2000.

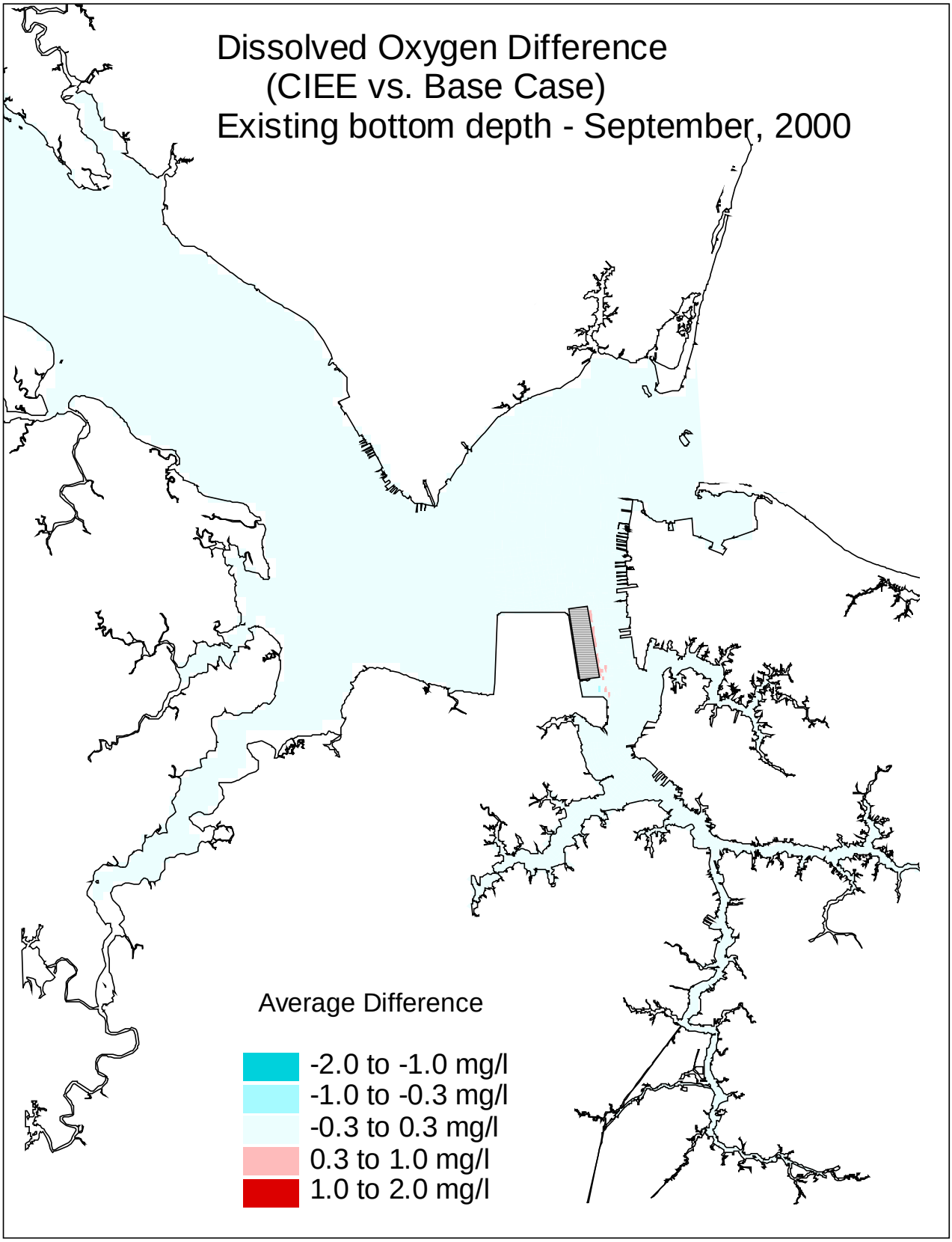

Figure K1-8. Dissolved oxygen (30-day average, at present bottom depth) difference between the CIEE full expansion and the base case for September, 2000.

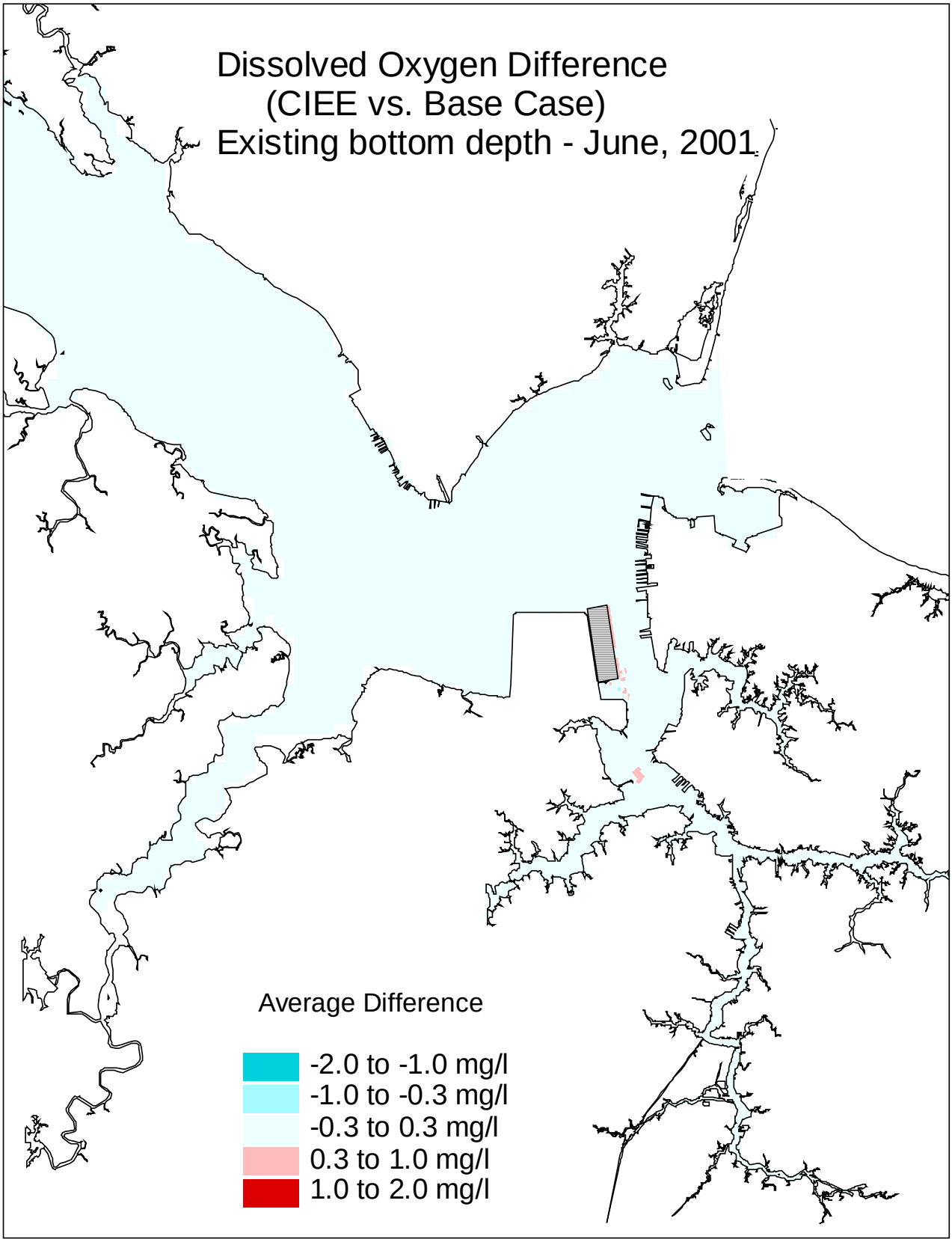

Figure K1-9. Dissolved oxygen (30-day average, at present bottom depth) difference between the CIEE full expansion and the base case for June, 2001.

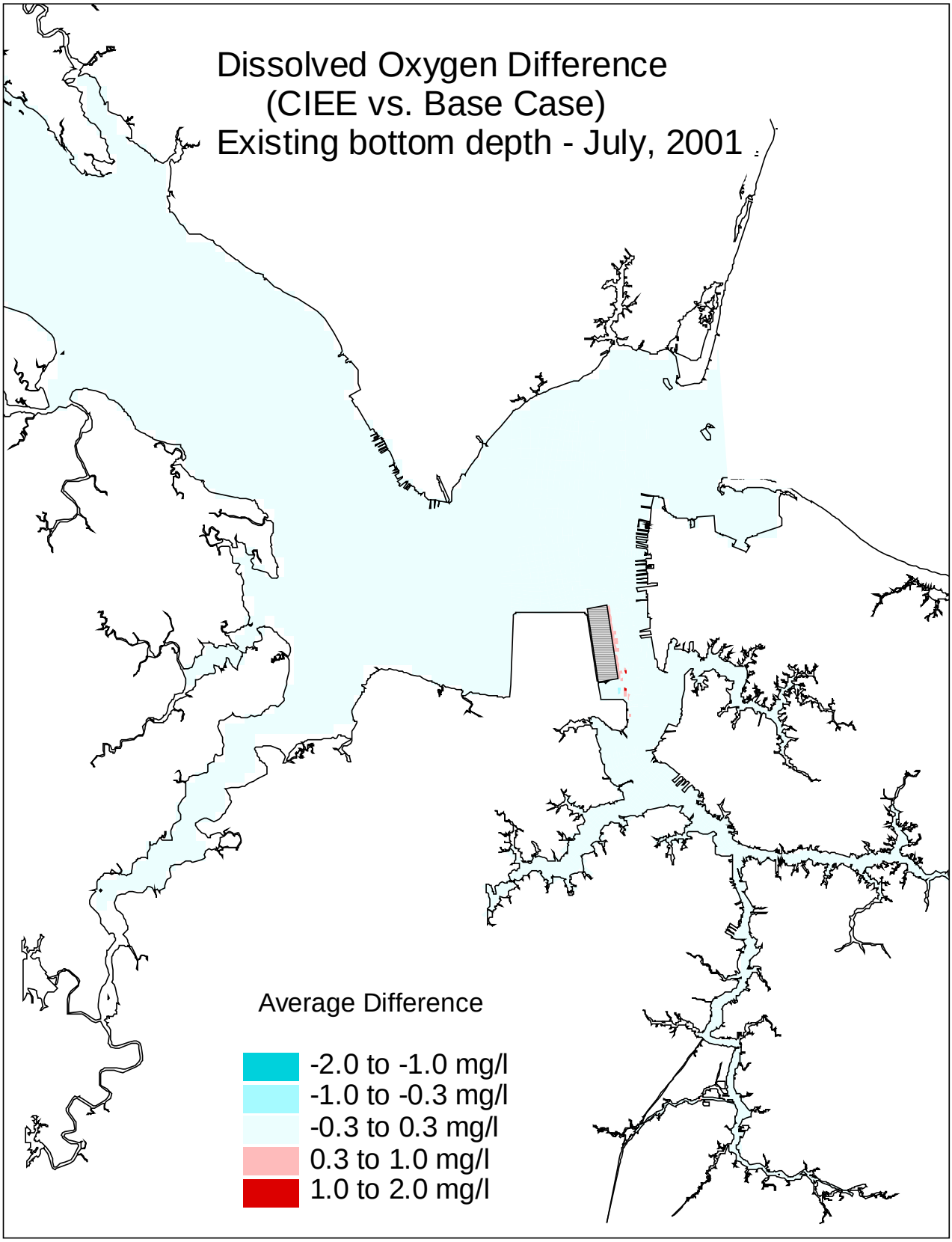

Figure K1-10. Dissolved oxygen (30-day average, at present bottom depth) difference between the CIEE full expansion and the base case for July, 2001.

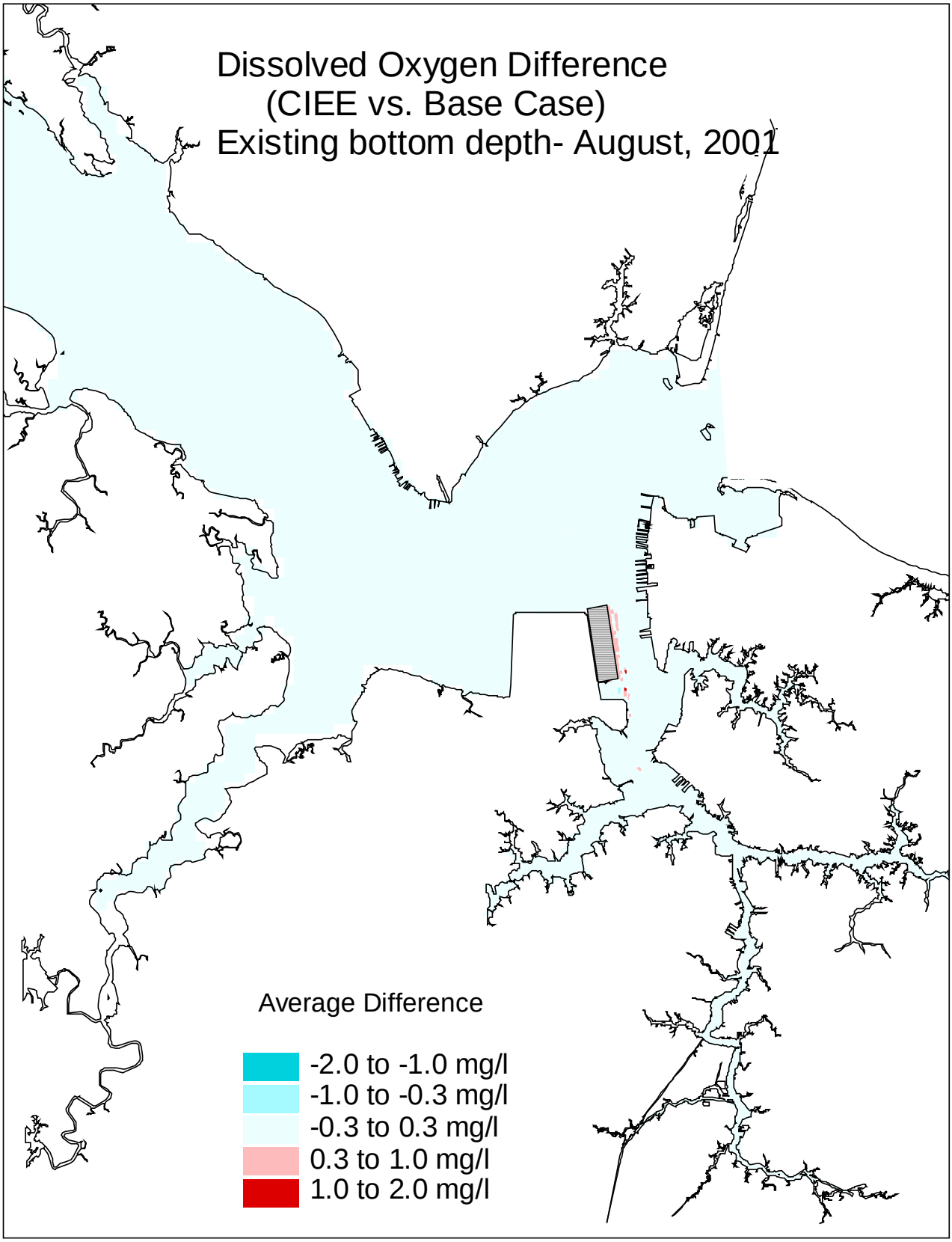

Figure K1-11. Dissolved oxygen (30-day average, at present bottom depth) difference between the CIEE full expansion and the base case for August, 2001.

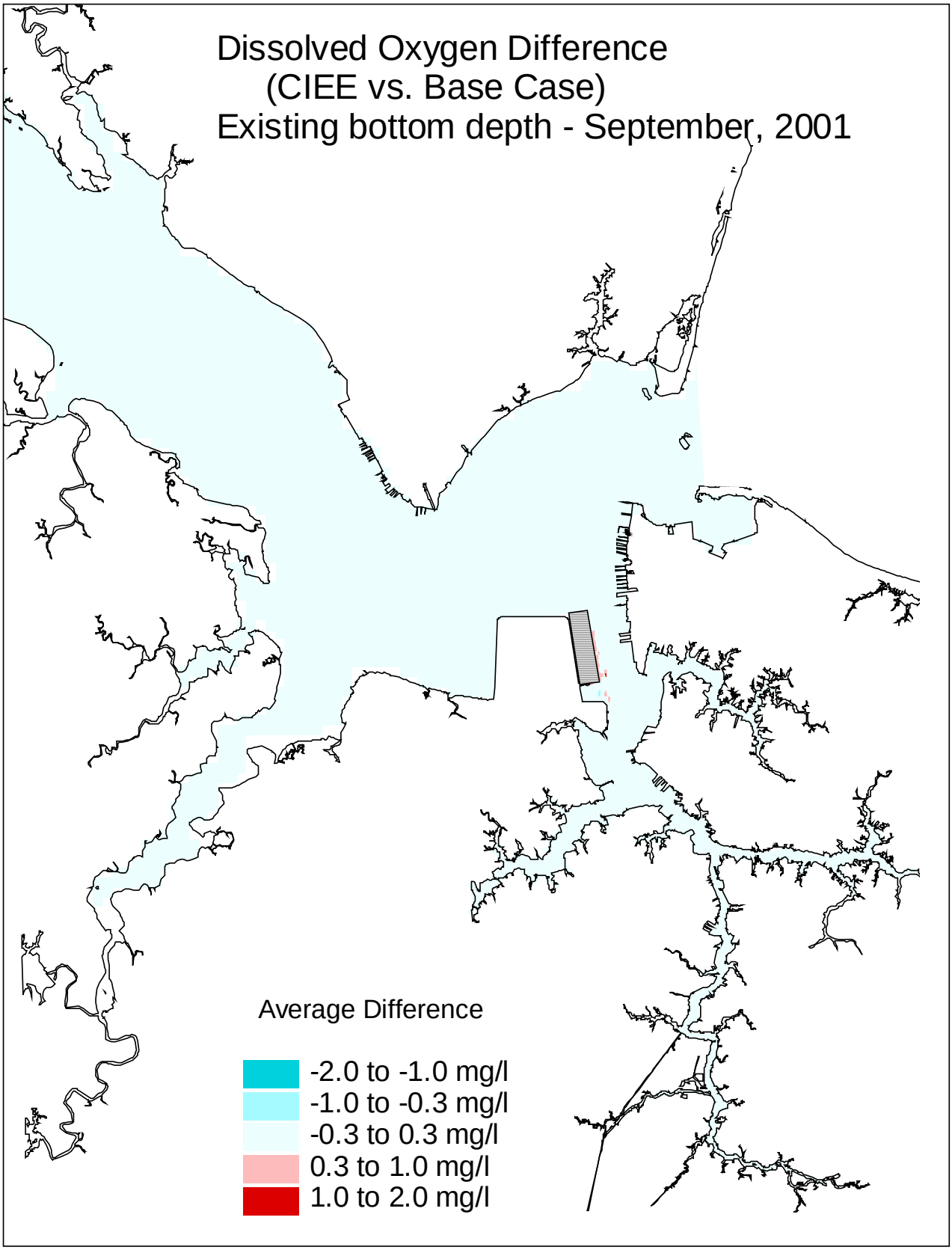

Figure K1-12. Dissolved oxygen (30-day average, at present bottom depth) difference between the CIEE full expansion and the base case for September, 2001.

APPENDIX L

Model Sensitivity to:

1) watershed loading
2) phytoplankton maximum growth rate
3) vertical stratification and mixing

at CBP Stations LE5.5, LE5.6, and ELI2 for 1999

(See discussion – Chapter VI)

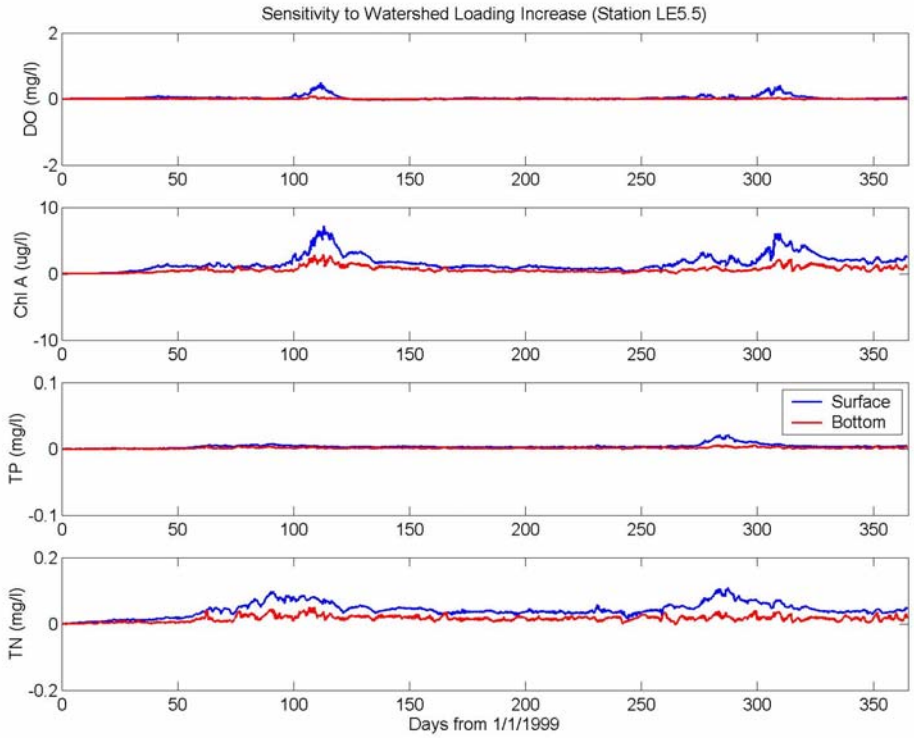

Figure L.1. Differences of model predictions for dissolved oxygen, chlorophyll-a, total phosphorus, and total nitrogen at CBP Station LE5.5 (surface and bottom layers) for 1999 due to an increase in all watershed nonpoint source loadings by 10% (ST-1).

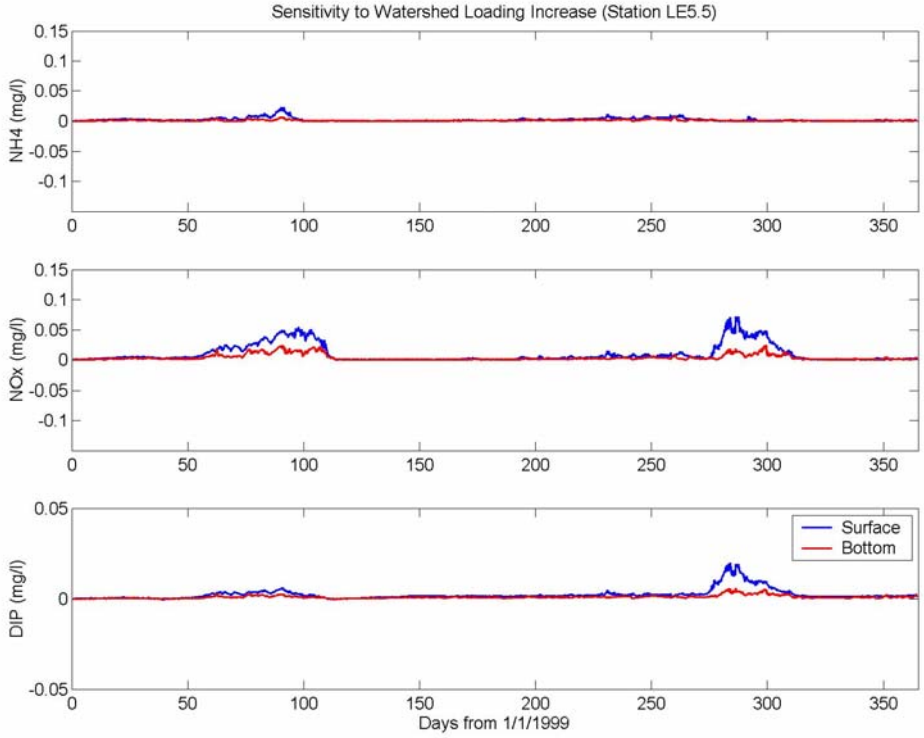

Figure L.2. Differences of model predictions for ammonium, nitrate-nitrite, and dissolved inorganic phosphorus at CBP Station LE5.5 (surface and bottom layers) for 1999 due to an increase in all watershed nonpoint source loadings by 10% (ST-1).

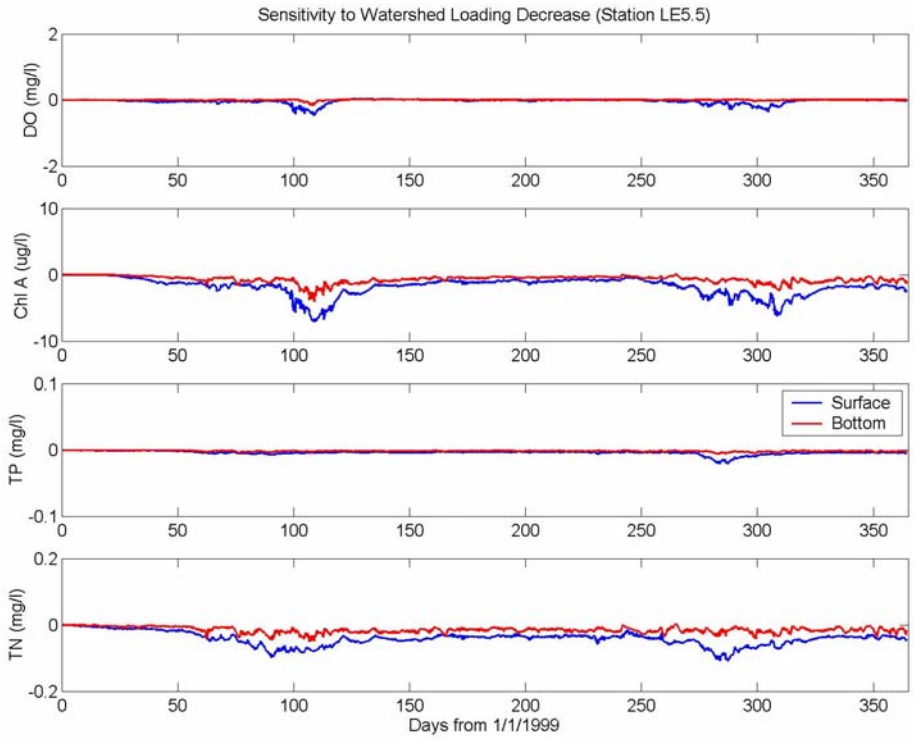

Figure L.3. Differences of model predictions for dissolved oxygen, chlorophyll-a, total phosphorus, and total nitrogen at CBP Station LE5.5 (surface and bottom layers) for 1999 due to a decrease in all watershed nonpoint source loadings by 10% (ST-2).

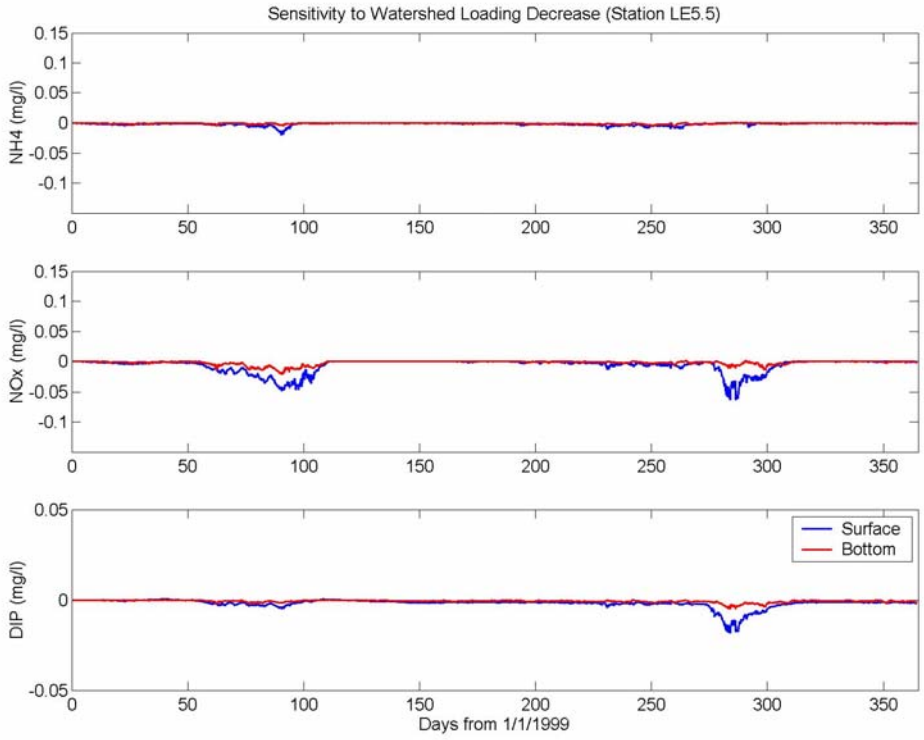

Figure L.4. Differences of model predictions for ammonium, nitrate-nitrite, and dissolved inorganic phosphorus at CBP Station LE5.5 (surface and bottom layers) for 1999 due to a decrease in all watershed nonpoint source loadings by 10% (ST-2).

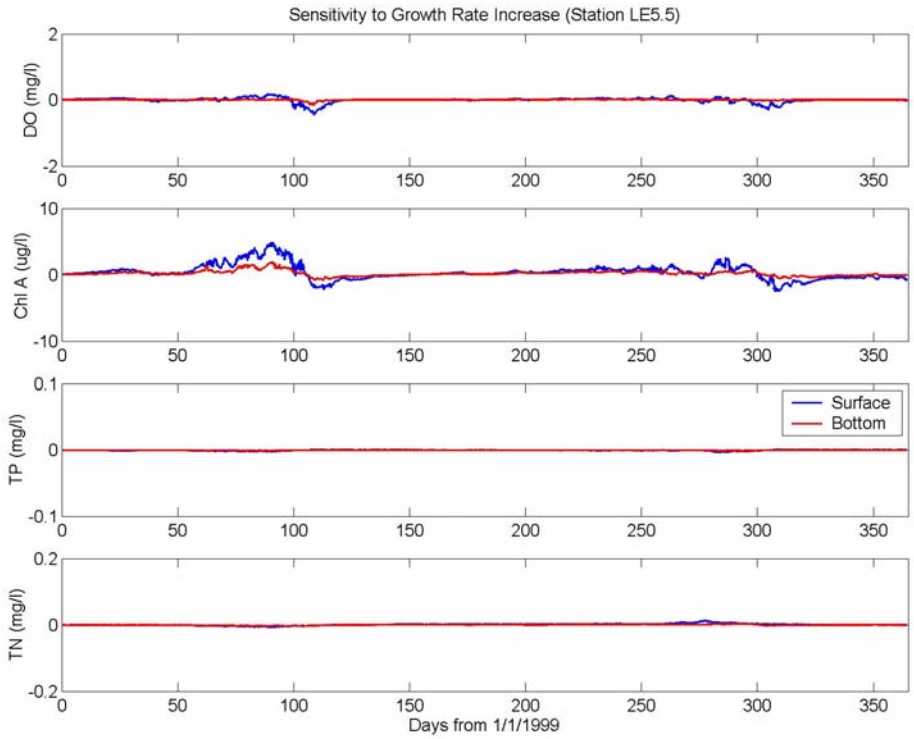

Figure L.5. Differences of model predictions for dissolved oxygen, chlorophyll-a, total phosphorus, and total nitrogen at CBP Station LE5.5 (surface and bottom layers) for 1999 due to a increase in the maximum growth rate from 2.0/day to 2.25/day (ST-3).

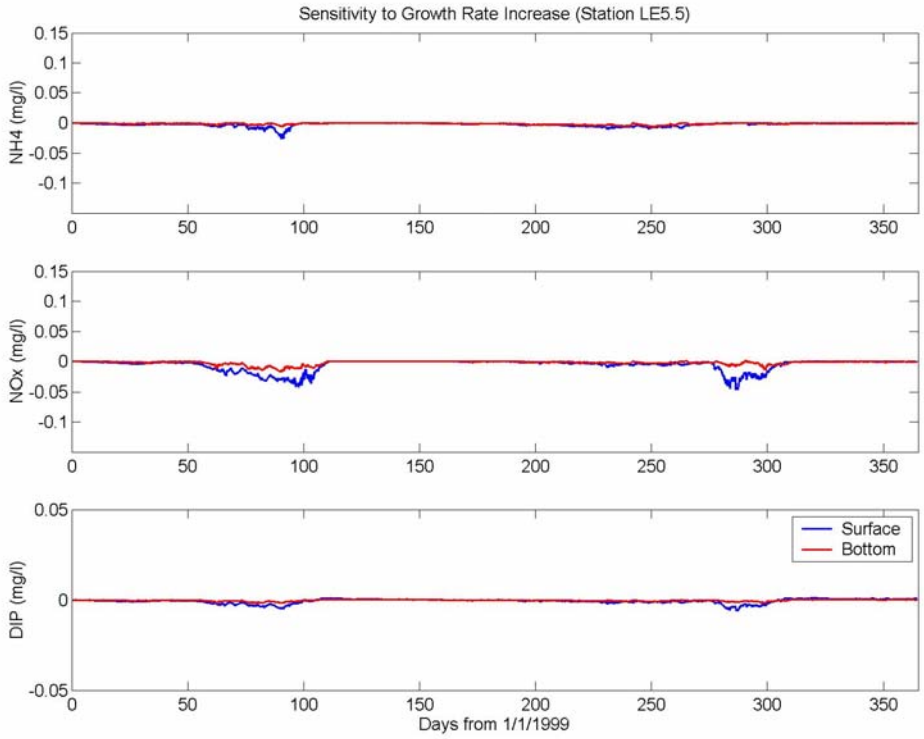

Figure L.6. Differences of model predictions for ammonium, nitrate-nitrite, and dissolved inorganic phosphorus at CBP Station LE5.5 (surface and bottom layers) for 1999 due to a increase in the maximum growth rate from 2.0/day to 2.25/day (ST-3).

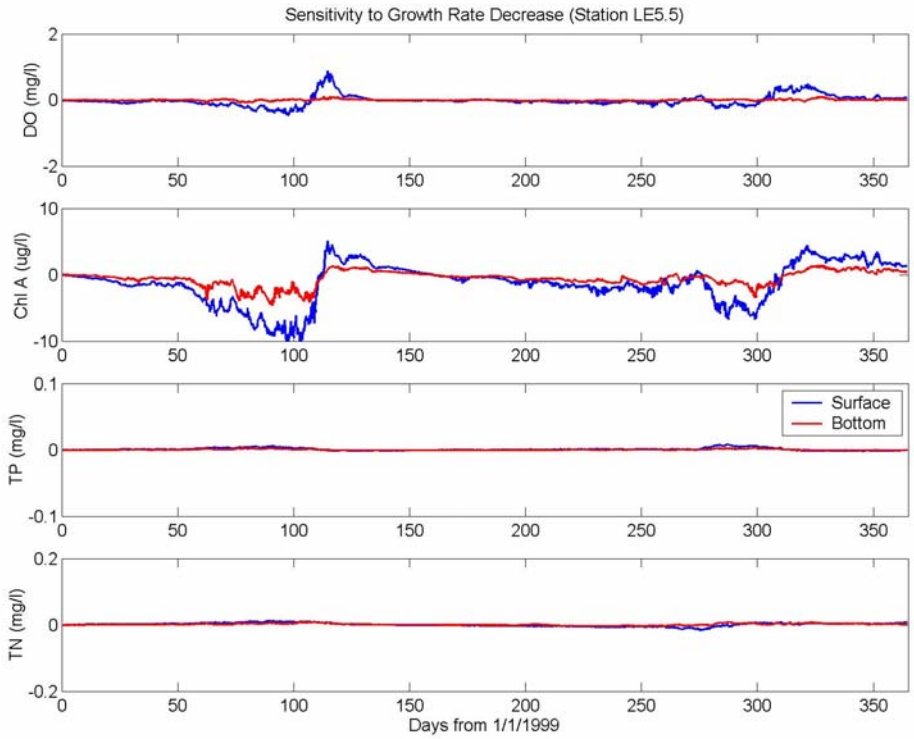

Figure L.7. Differences of model predictions for dissolved oxygen, chlorophyll-a, total phosphorus, and total nitrogen at CBP Station LE5.5 (surface and bottom layers) for 1999 due to a decrease in the growth rate from 2 to 1.75 (ST-4).

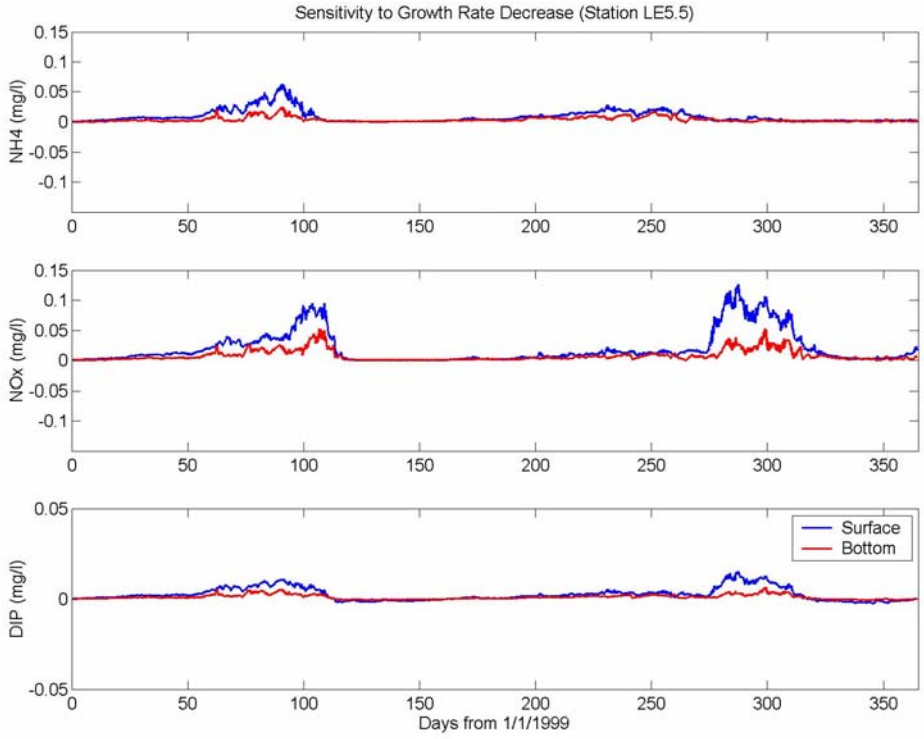

Figure L.8. Differences of model predictions for ammonium, nitrate-nitrite, and dissolved inorganic phosphorus at CBP Station LE5.5 (surface and bottom layers) for 1999 due to a decrease in the maximum growth rate from 2.0/day to 1.75/day (ST-4).

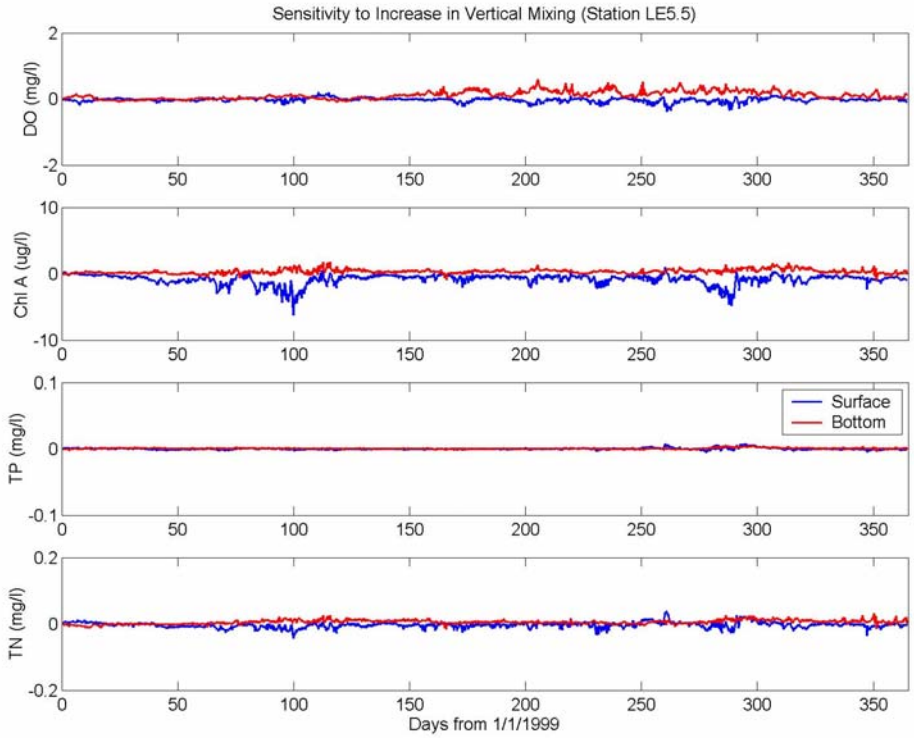

Figure L.9. Differences of model predictions for dissolved oxygen, chlorophyll-a, total phosphorus, and total nitrogen at CBP Station LE5.5 (surface and bottom layers) for 1999 due to an increase in the background eddy diffusivity from 10^{-6} m^2/s to 10^{-5} m^2/s (ST-5).

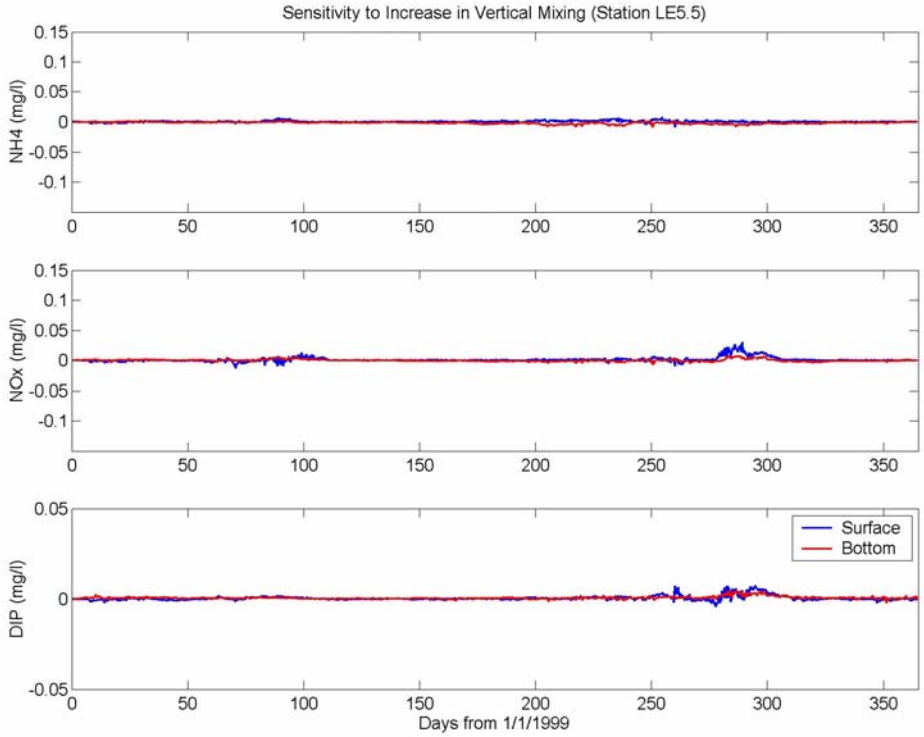

Figure L.10. Differences of model predictions for ammonium, nitrate-nitrite, and dissolved inorganic phosphorus at CBP Station LE5.5 (surface and bottom layers) for 1999 due to an increase in the background eddy diffusivity from 10^{-6} m^2/s to 10^{-5} m^2/s (ST-5).

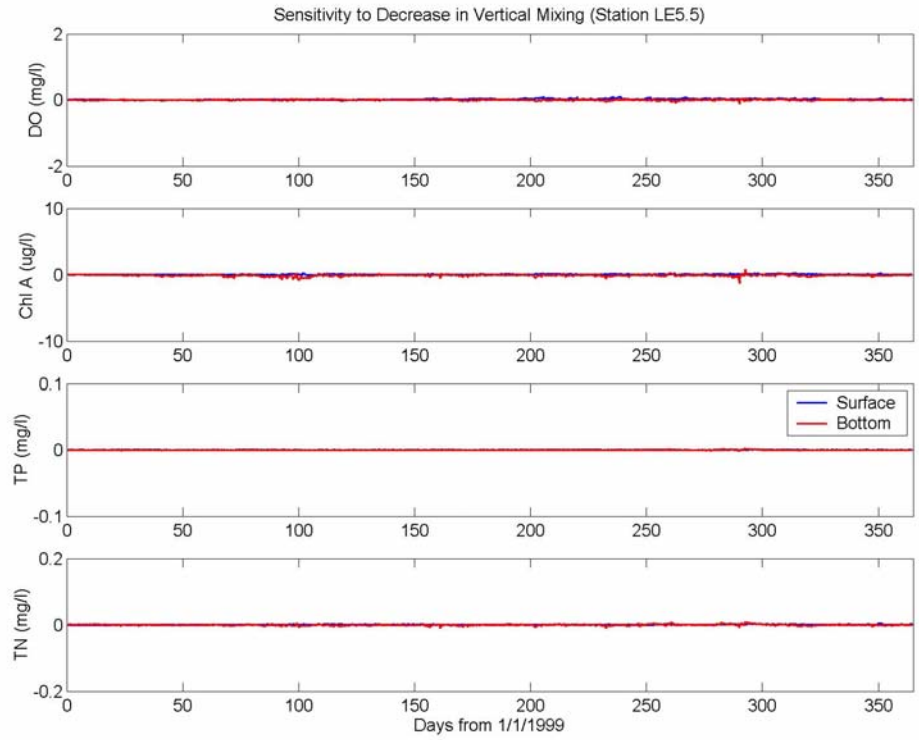

Figure L.11. Differences of model predictions for dissolved oxygen, chlorophyll-a, total phosphorus, and total nitrogen at CBP Station LE5.5 (surface and bottom layers) for 1999 due to a decrease in the background eddy diffusivity from 10^{-6} m^2/s to 10^{-7} m^2/s (ST-6).

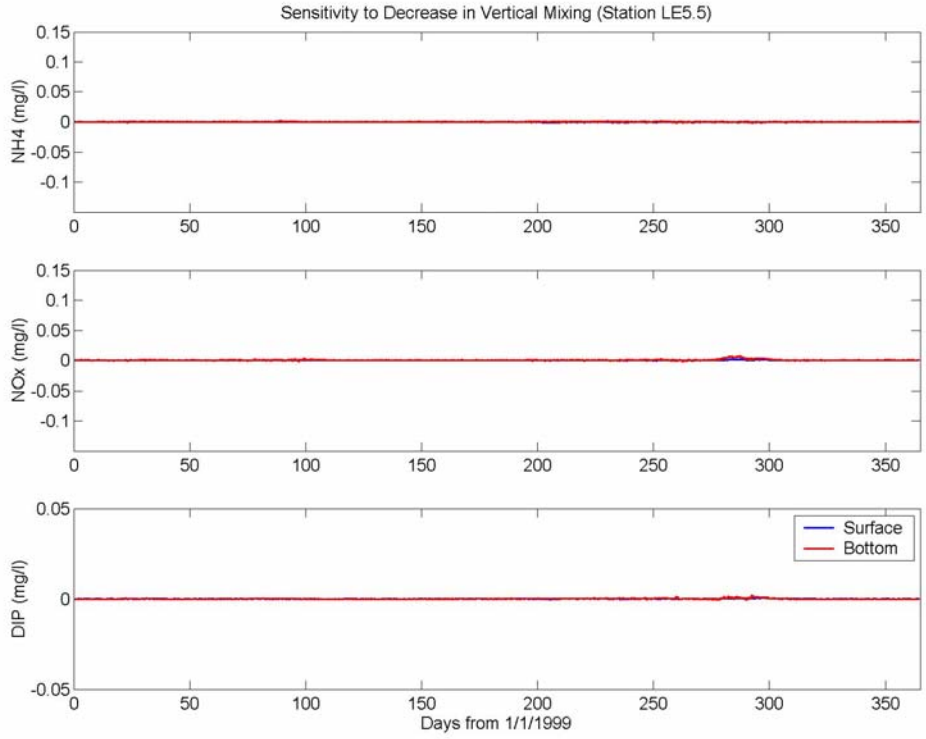

Figure L.12. Differences of model predictions for ammonium, nitrate-nitrite, and dissolved inorganic phosphorus at CBP Station LE5.5 (surface and bottom layers) for 1999 due to a decrease in the background eddy diffusivity from 10^{-6} m^2/s to 10^{-7} m^2/s (ST-6).

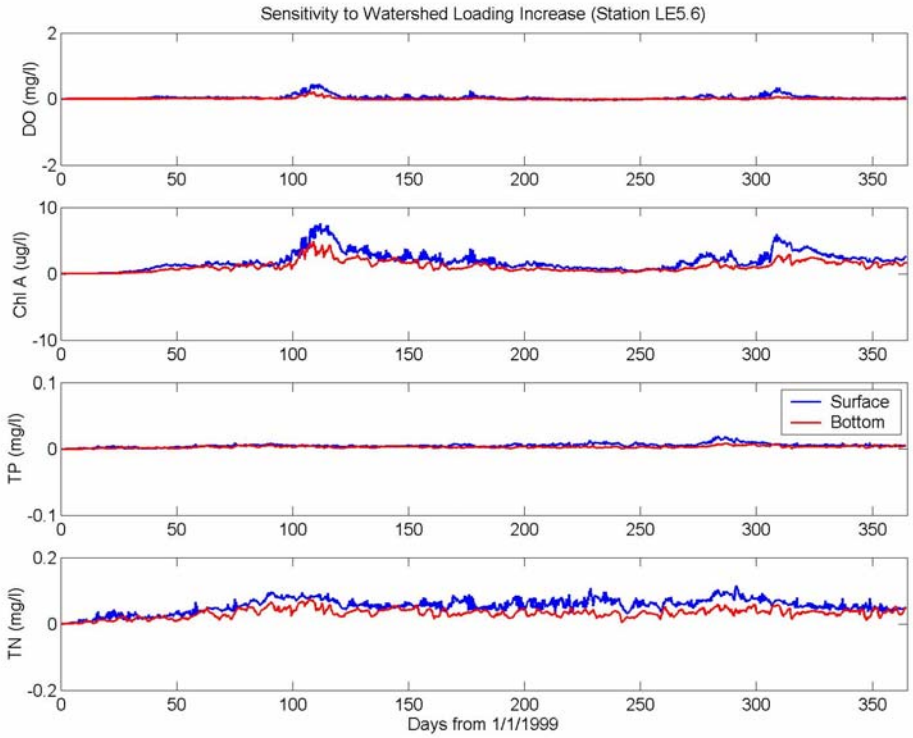

Figure L.13. Differences of model predictions for dissolved oxygen, chlorophyll-a, total phosphorus, and total nitrogen at CBP Station LE5.6 (surface and bottom layers) for 1999 due to an increase in all watershed nonpoint source loadings by 10% (ST-1).

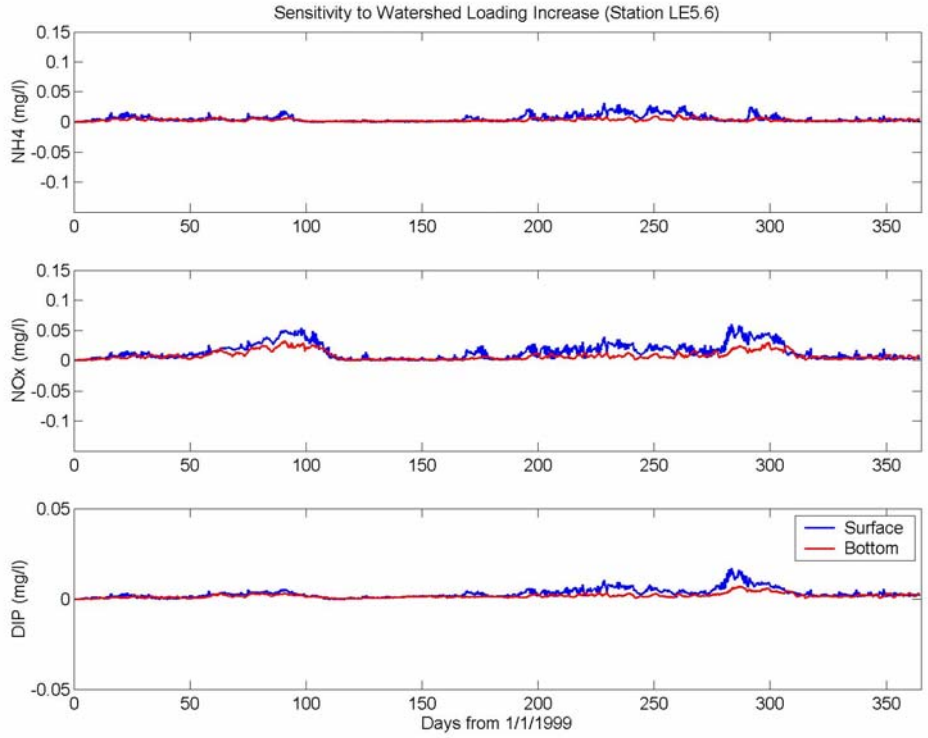

Figure L.14. Differences of model predictions for ammonium, nitrate-nitrite, and dissolved inorganic phosphorus at CBP Station LE5.6 (surface and bottom layers) for 1999 due to an increase in all watershed nonpoint source loadings by 10% (ST-1).

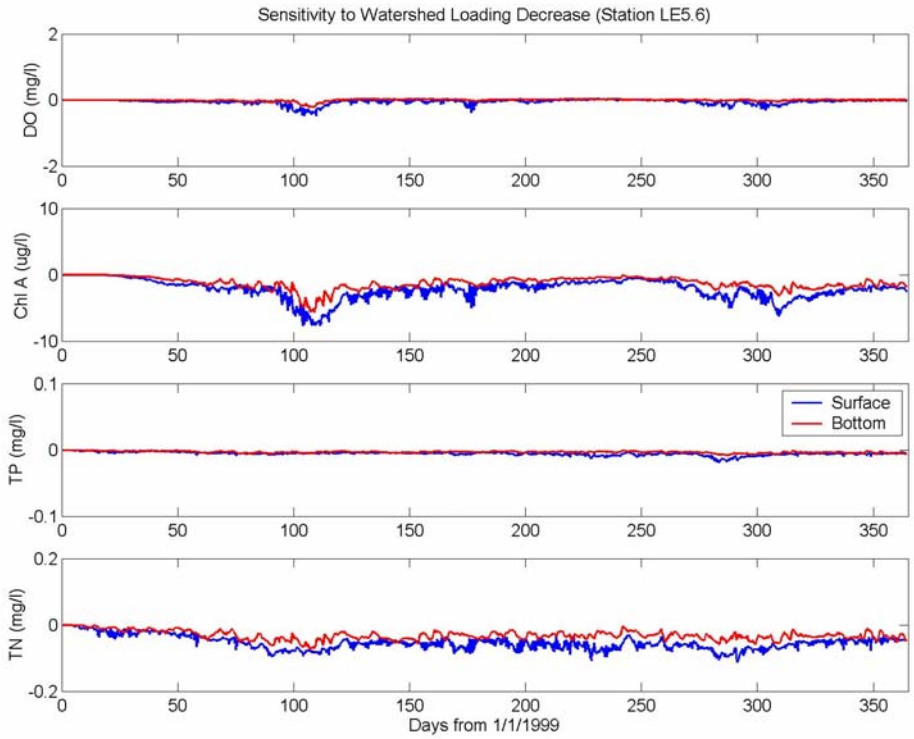

Figure L.15. Differences of model predictions for dissolved oxygen, chlorophyll-a, total phosphorus, and total nitrogen at CBP Station LE5.6 (surface and bottom layers) for 1999 due to a decrease in all watershed nonpoint source loadings by 10% (ST-2).

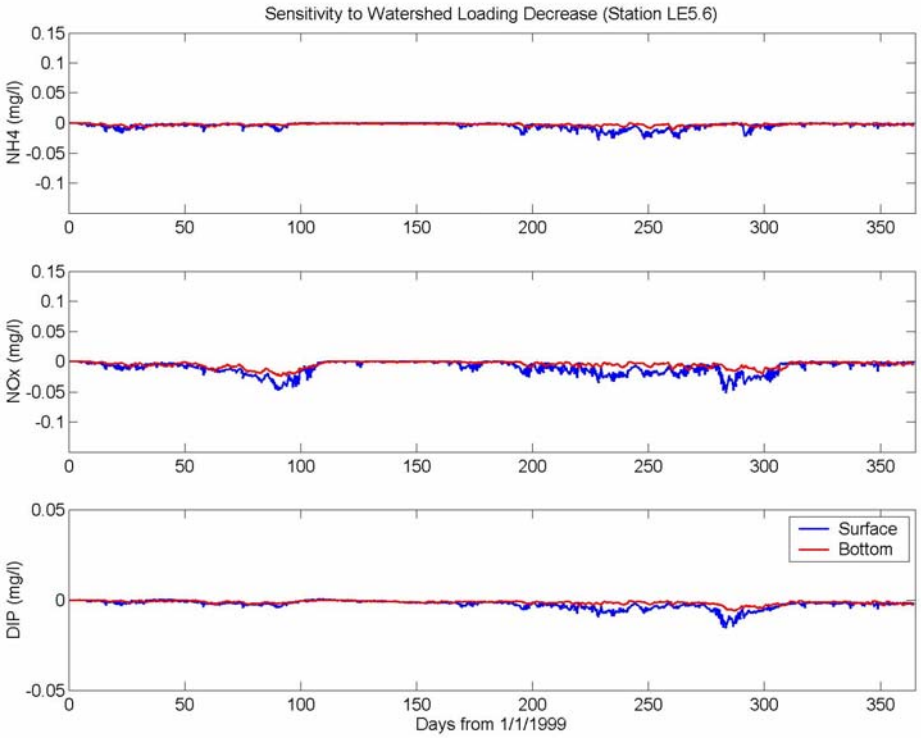

Figure L.16. Differences of model predictions for ammonium, nitrate-nitrite, and dissolved inorganic phosphorus at CBP Station LE5.6 (surface and bottom layers) for 1999 due to a decrease in all watershed nonpoint source loadings by 10% (ST-2).

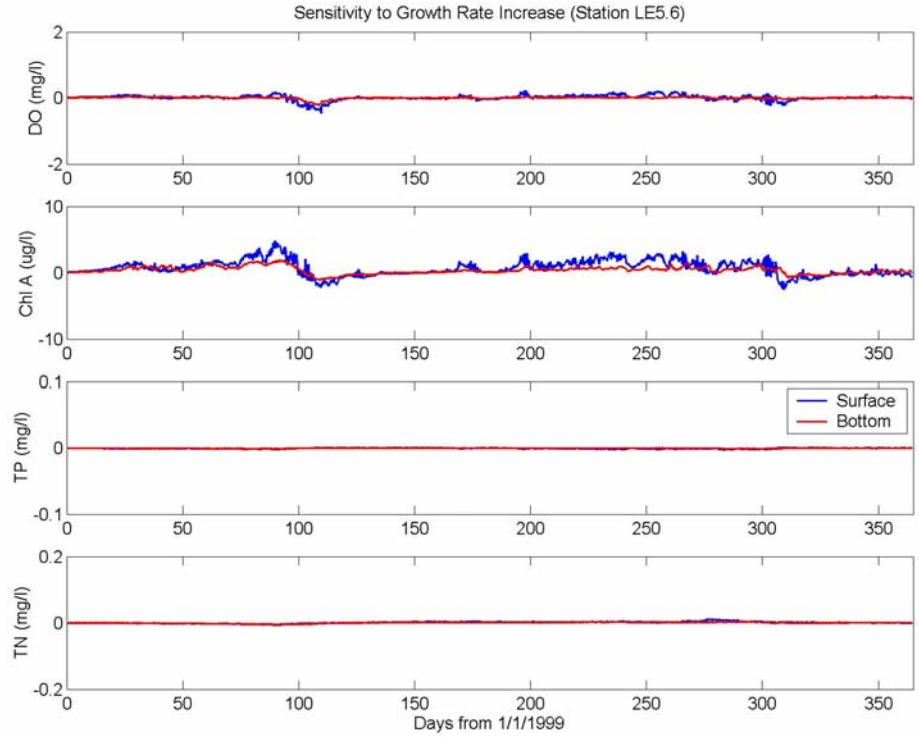

Figure L.17. Differences of model predictions for dissolved oxygen, chlorophyll-a, total phosphorus, and total nitrogen at CBP Station LE5.6 (surface and bottom layers) for 1999 due to a increase in the maximum growth rate from 2.0/day to 2.25/day (ST-3).

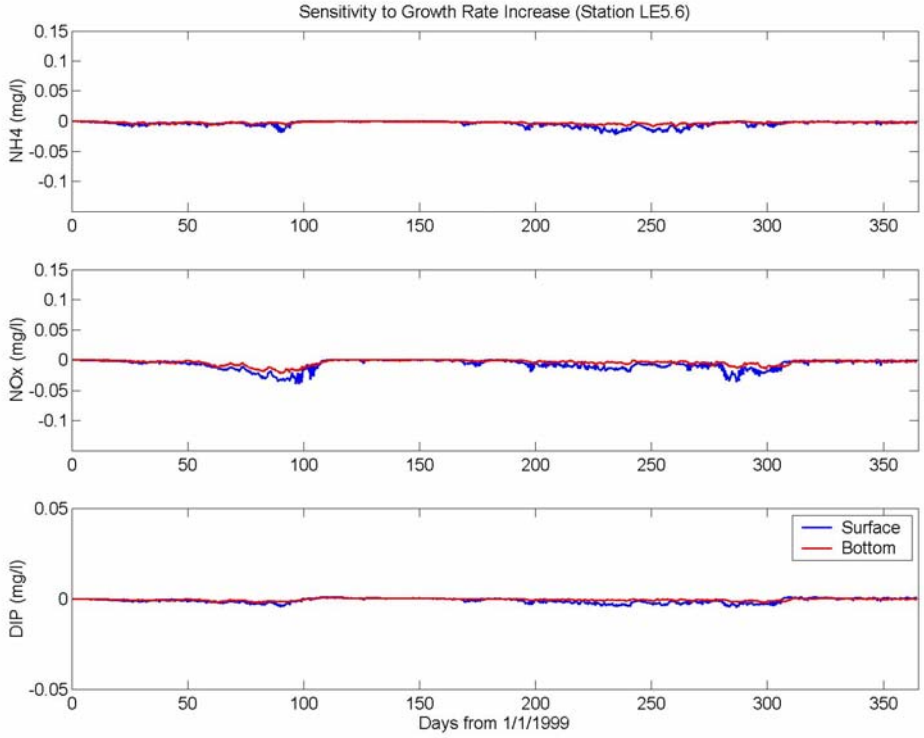

Figure L.18. Differences of model predictions for ammonium, nitrate-nitrite, and dissolved inorganic phosphorus at CBP Station LE5.6 (surface and bottom layers) for 1999 due to a increase in the maximum growth rate from 2.0/day to 2.25/day (ST-3).

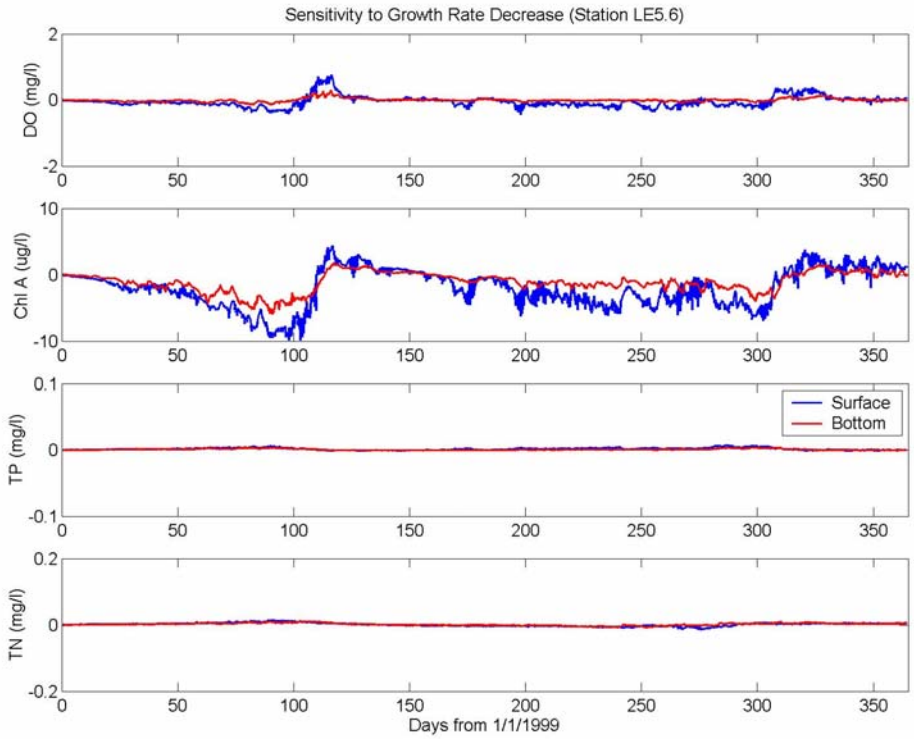

Figure L.19. Differences of model predictions for dissolved oxygen, chlorophyll-a, total phosphorus, and total nitrogen at CBP Station LE5.6 (surface and bottom layers) for 1999 due to a decrease in the maximum growth rate from 2.0/day to 1.75/day (ST-4).

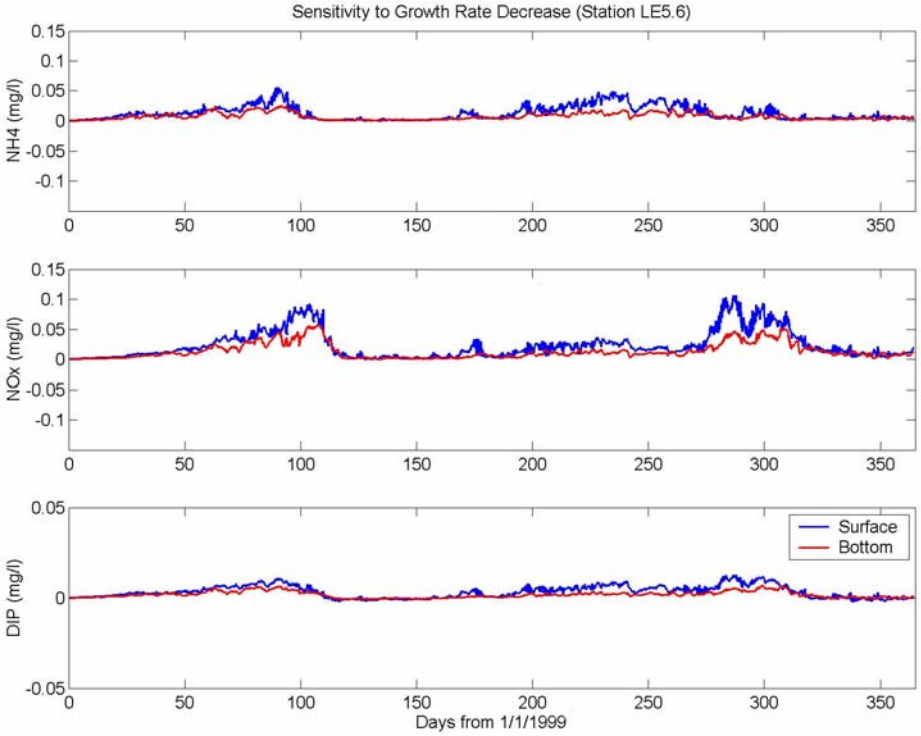

Figure L.20. Differences of model predictions for ammonium, nitrate-nitrite, and dissolved inorganic phosphorus at CBP Station LE5.6 (surface and bottom layers) for 1999 due to a decrease in the maximum growth rate from 2.0/day to 1.75/day (ST-4).

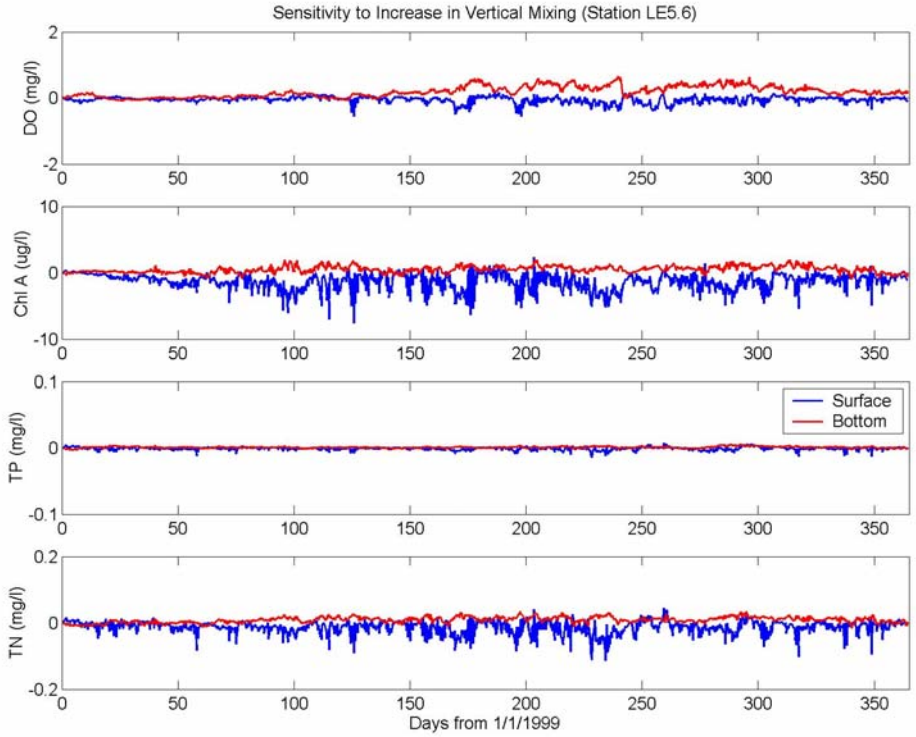

Figure L.21. Differences of model predictions for dissolved oxygen, chlorophyll-a, total phosphorus, and total nitrogen at CBP Station LE5.6 (surface and bottom layers) for 1999 due to an increase in the eddy diffusivity from 10^{-6} m^2/s to 10^{-5} m^2/s (ST-5).

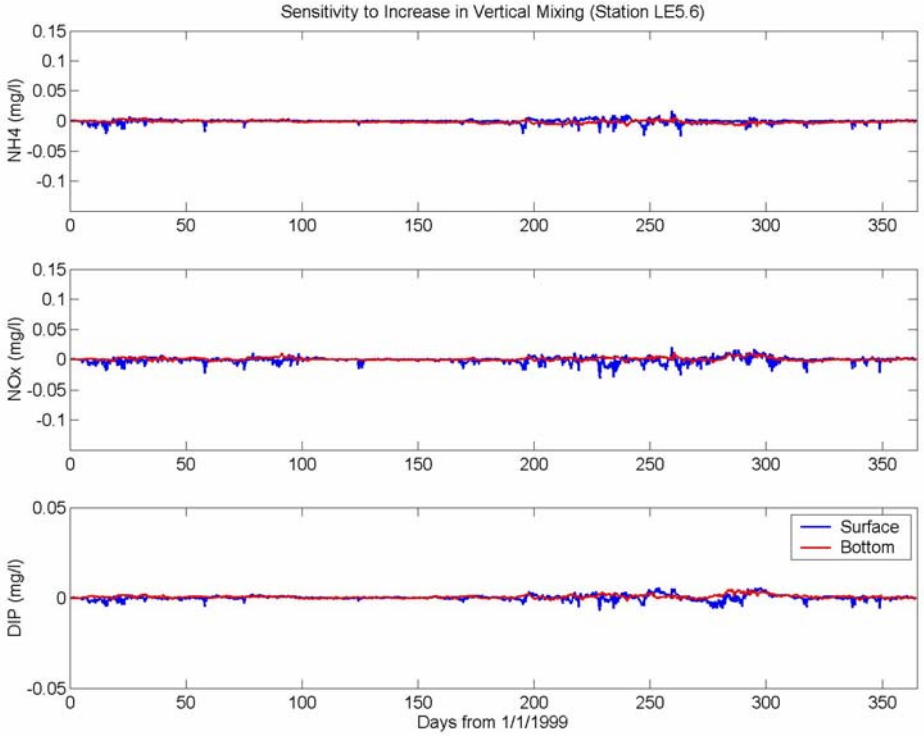

Figure L.22. Differences of model predictions for ammonium, nitrate-nitrite, and dissolved inorganic phosphorus at CBP Station LE5.6 (surface and bottom layers) for 1999 due to an increase in the eddy diffusivity from 10^{-6} m^2/s to 10^{-5} m^2/s (ST-5).

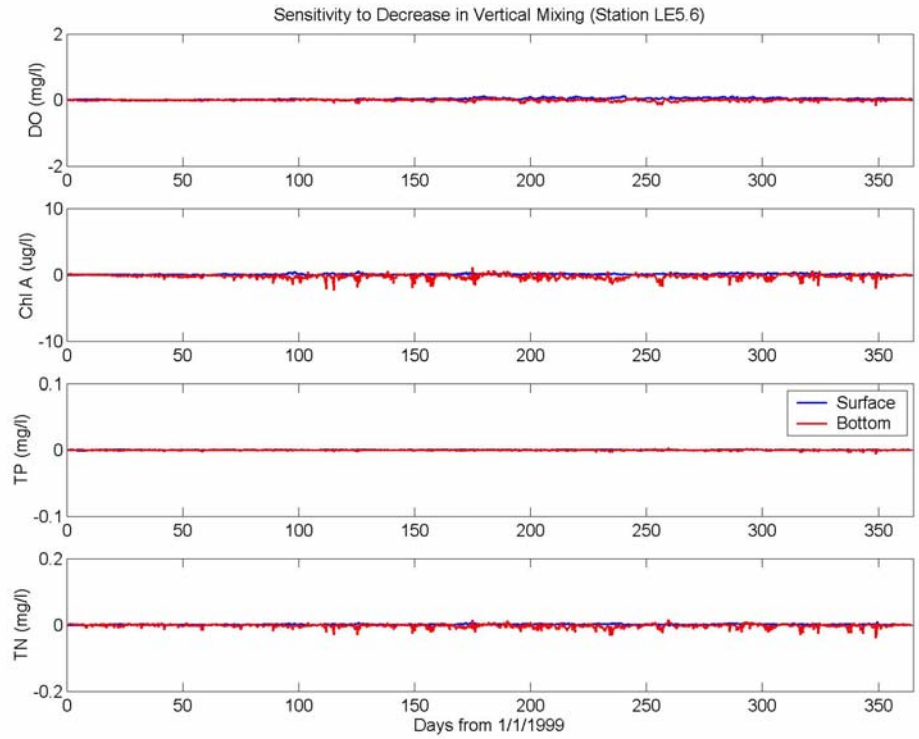

Figure L.23. Differences of model predictions for dissolved oxygen, chlorophyll-a, total phosphorus, and total nitrogen at CBP Station LE5.6 (surface and bottom layers) for 1999 due to a decrease in the background eddy diffusivity from 10^{-6} m^2/s to 10^{-7} m^2/s (ST-6).

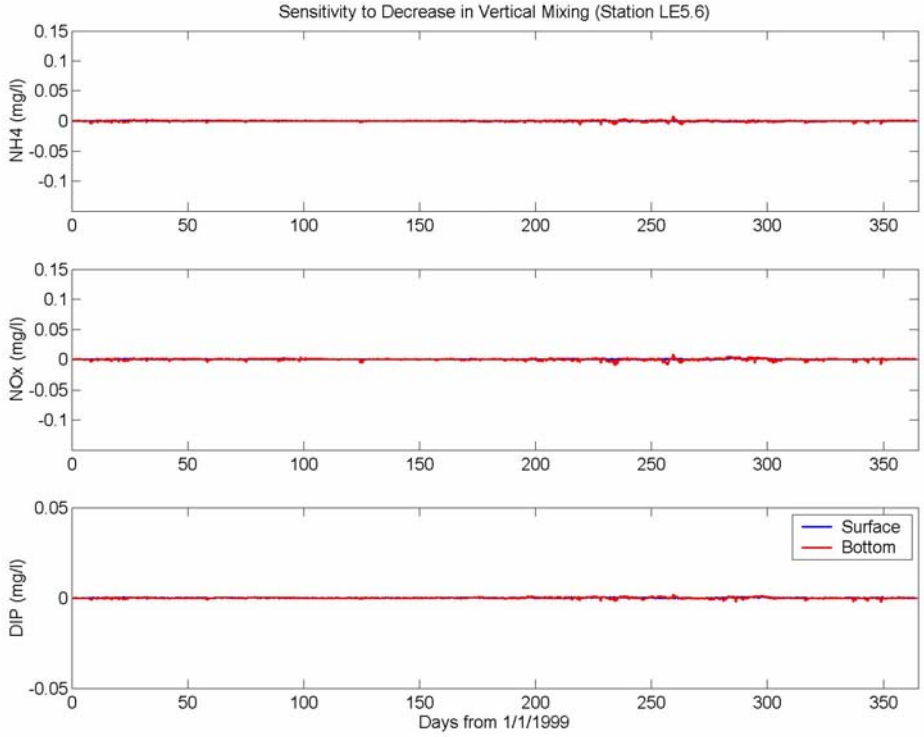

Figure L.24. Differences of model predictions for ammonium, nitrate-nitrite, and dissolved inorganic phosphorus at CBP Station LE5.6 (surface and bottom layers) for 1999 due to a decrease in the background eddy diffusivity from 10^{-6} m^2/s to 10^{-7} m^2/s (ST-6).

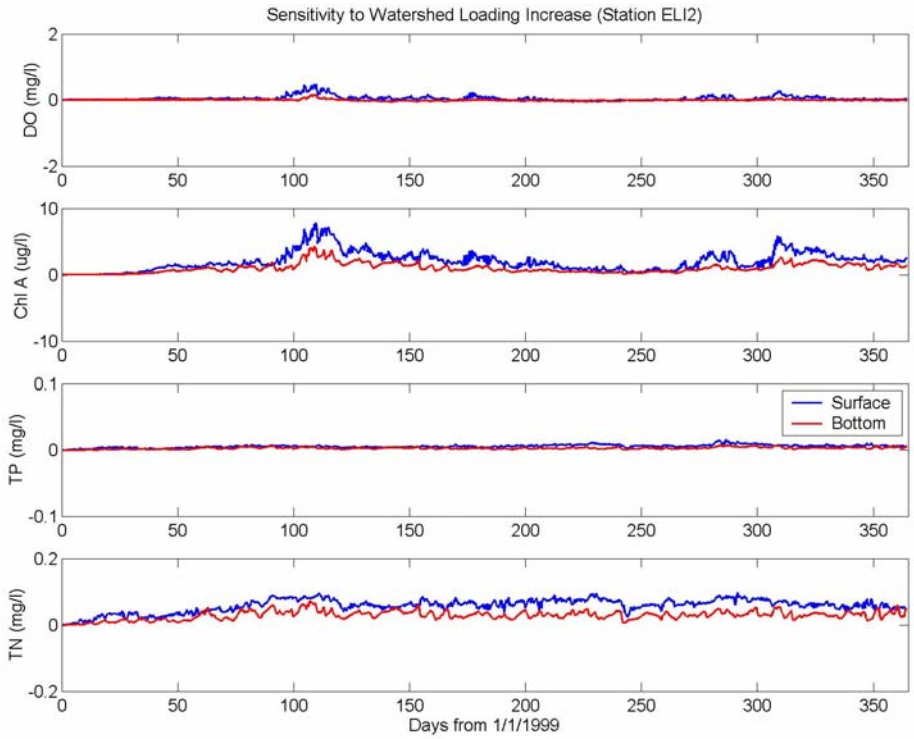

Figure L.25. Differences of model predictions for dissolved oxygen, chlorophyll-a, total phosphorus, and total nitrogen at CBP Station ELI2 (surface and bottom layers) for 1999 due to an increase in all watershed nonpoint source loadings by 10% (ST-1).

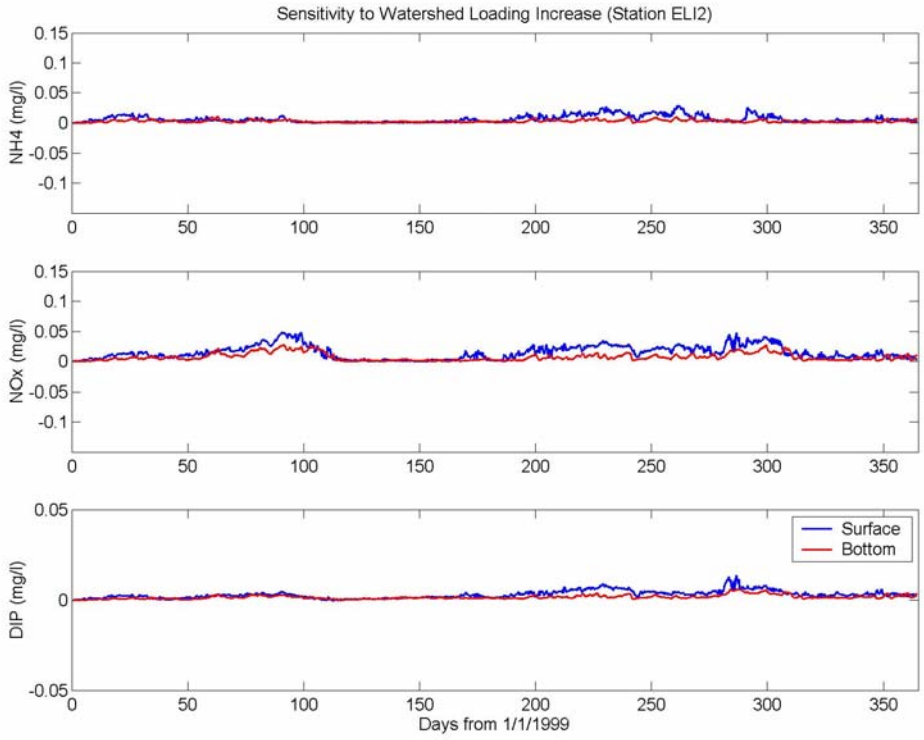

Figure L.26. Differences of model predictions for ammonium, nitrate-nitrite, and dissolved inorganic phosphorus at CBP Station ELI2 (surface and bottom layers) for 1999 due to an increase in all watershed nonpoint source loadings by 10% (ST-1).

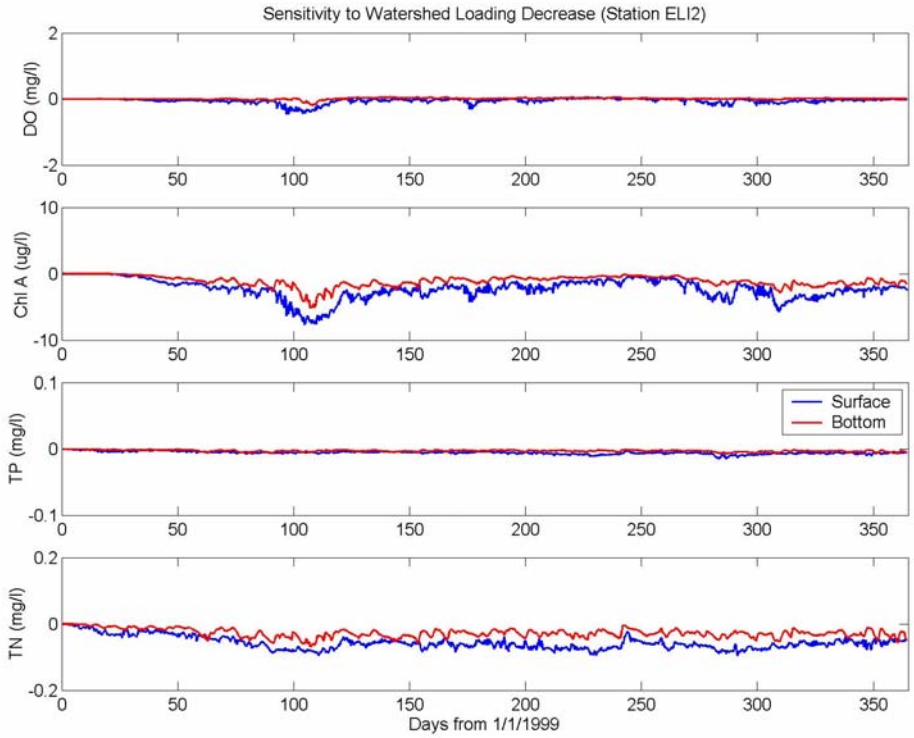

Figure L.27. Differences of model predictions for dissolved oxygen, chlorophyll-a, total phosphorus, and total nitrogen at CBP Station ELI2 (surface and bottom layers) for 1999 due to a decrease in all watershed nonpoint source loadings by 10% (ST-2).

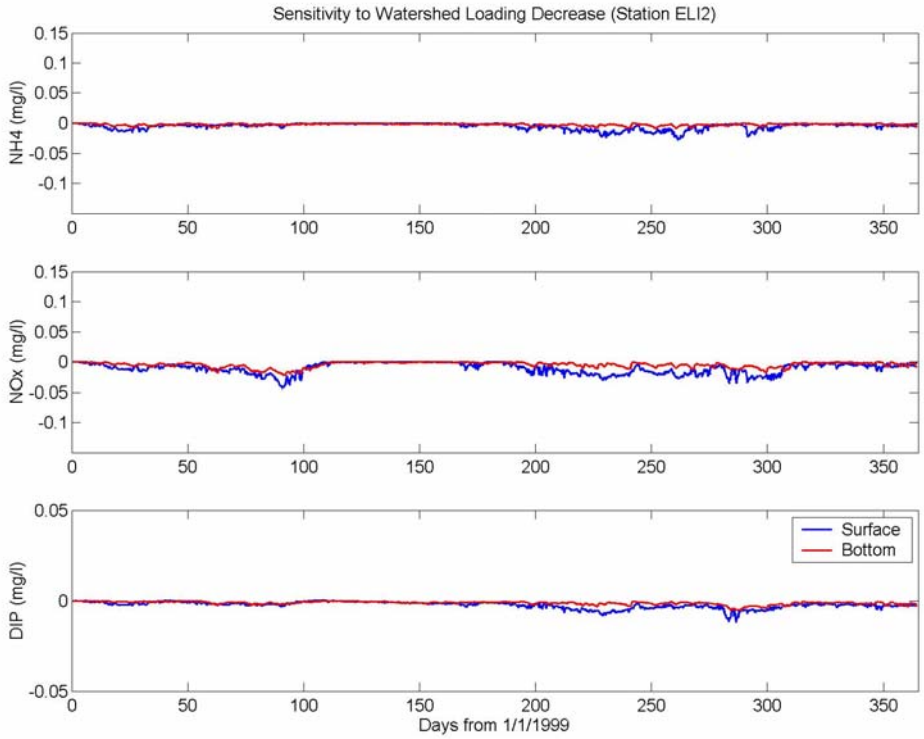

Figure L.28. Differences of model predictions for ammonium, nitrate-nitrite, and dissolved inorganic phosphorus at CBP Station ELI2 (surface and bottom layers) for 1999 due to a decrease in all watershed nonpoint source loadings by 10% (ST-2).

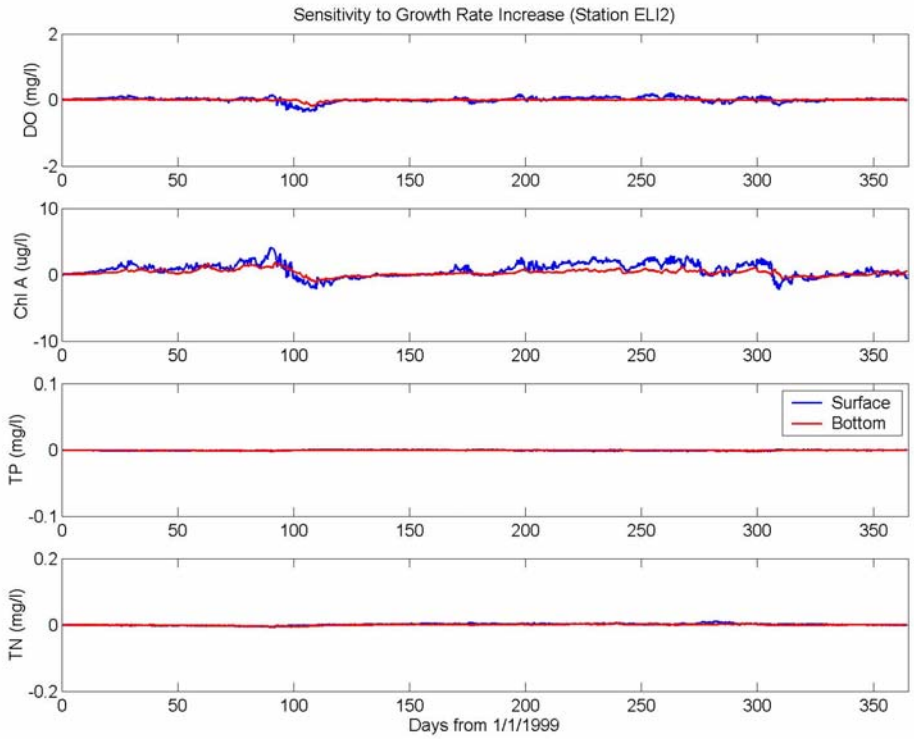

Figure L.29. Differences of model predictions for dissolved oxygen, chlorophyll-a, total phosphorus, and total nitrogen at CBP Station ELI2 (surface and bottom layers) for 1999 due to an increase in the maximum growth rate from 2.0/day to 2.25/day (ST-3).

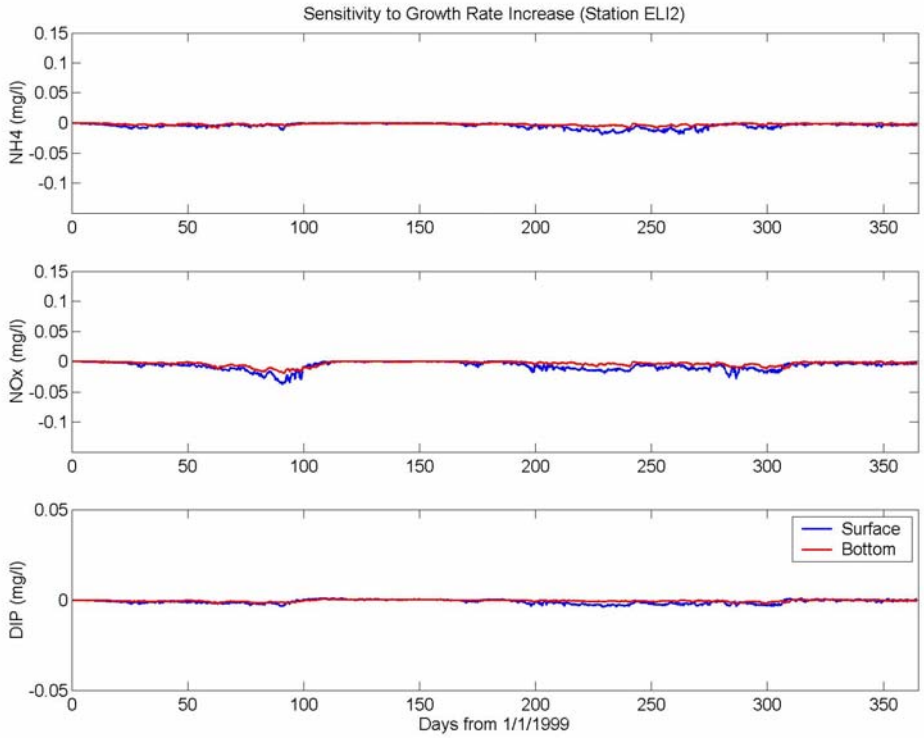

Figure L.30. Differences of model predictions for ammonium, nitrate-nitrite, and dissolved inorganic phosphorus at CBP Station ELI2 (surface and bottom layers) for 1999 due to an increase in the maximum growth rate from 2.0/day to 2.25/day (ST-3).

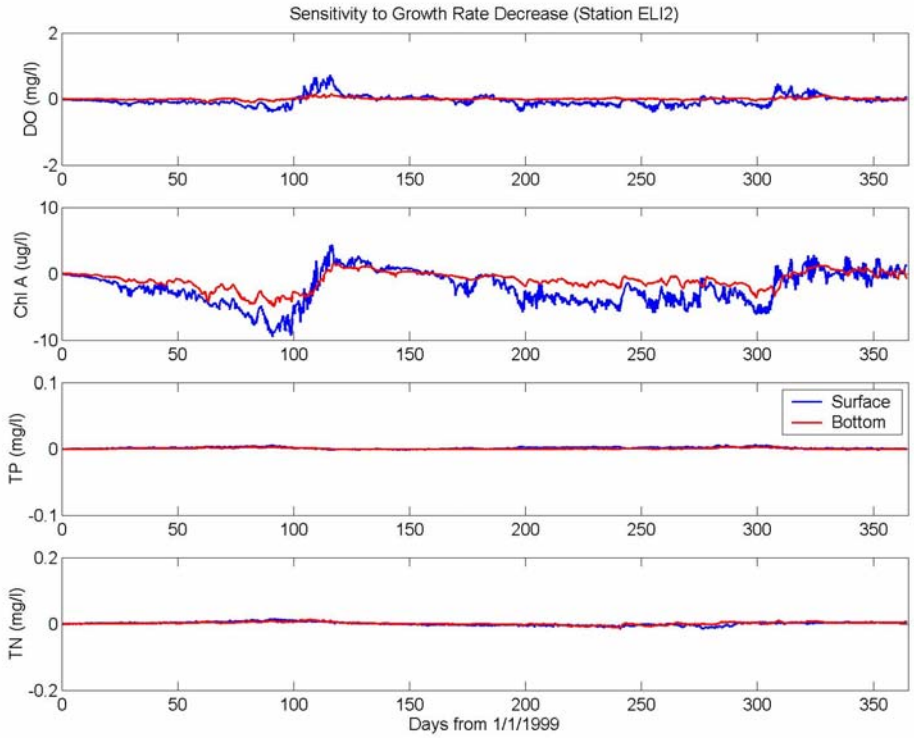

Figure L.31. Differences of model predictions for dissolved oxygen, chlorophyll-a, total phosphorus, and total nitrogen at CBP Station ELI2 (surface and bottom layers) for 1999 due to a decrease in the maximum growth rate from 2.0/day to 1.75/day (ST-4).

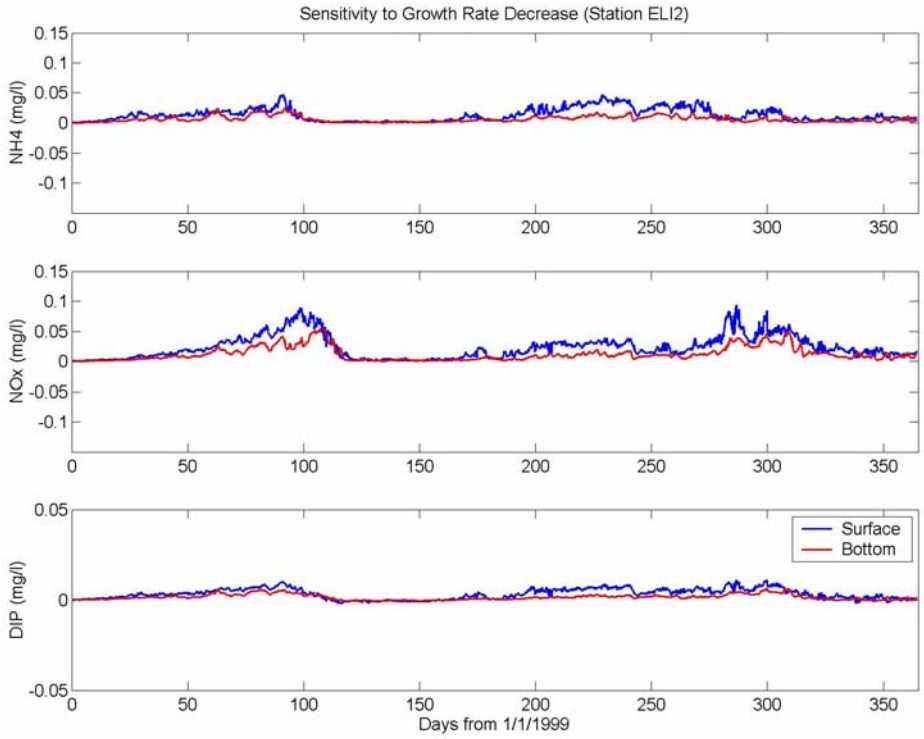

Figure L.32. Differences of model predictions for ammonium, nitrate-nitrite, and dissolved inorganic phosphorus at CBP Station ELI2 (surface and bottom layers) for 1999 due to a decrease in the maximum growth rate from 2.0/day to 1.75/day (ST-4).

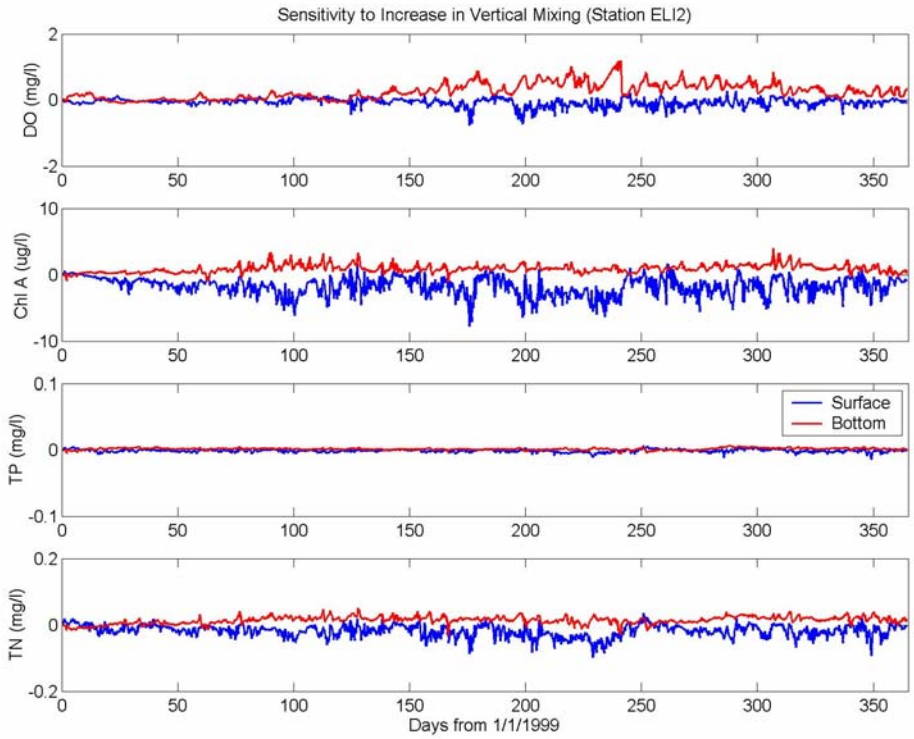

Figure L.33. Differences of model predictions for dissolved oxygen, chlorophyll-a, total phosphorus, and total nitrogen at CBP Station ELI2 (surface and bottom layers) for 1999 due to an increase in the background eddy diffusivity from 10^{-6} m^2/s to 10^{-5} m^2/s (ST-5).

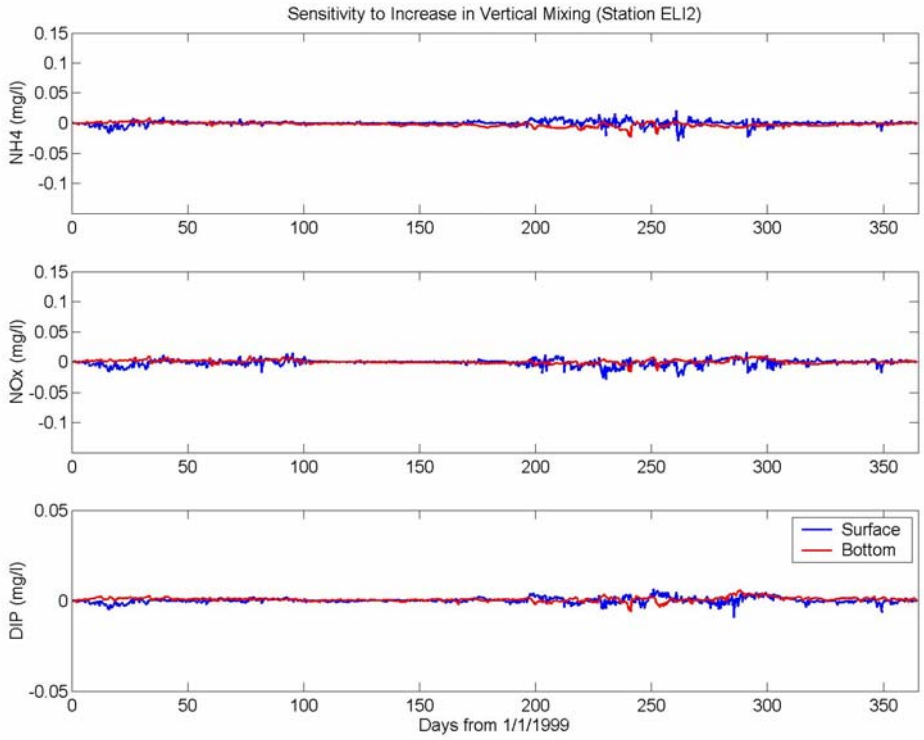

Figure L.34. Differences of model predictions for ammonium, nitrate-nitrite, and dissolved inorganic phosphorus at CBP Station ELI2 (surface and bottom layers) for 1999 due to an increase in the background eddy diffusivity from 10^{-6} m^2/s to 10^{-5} m^2/s (ST-5).

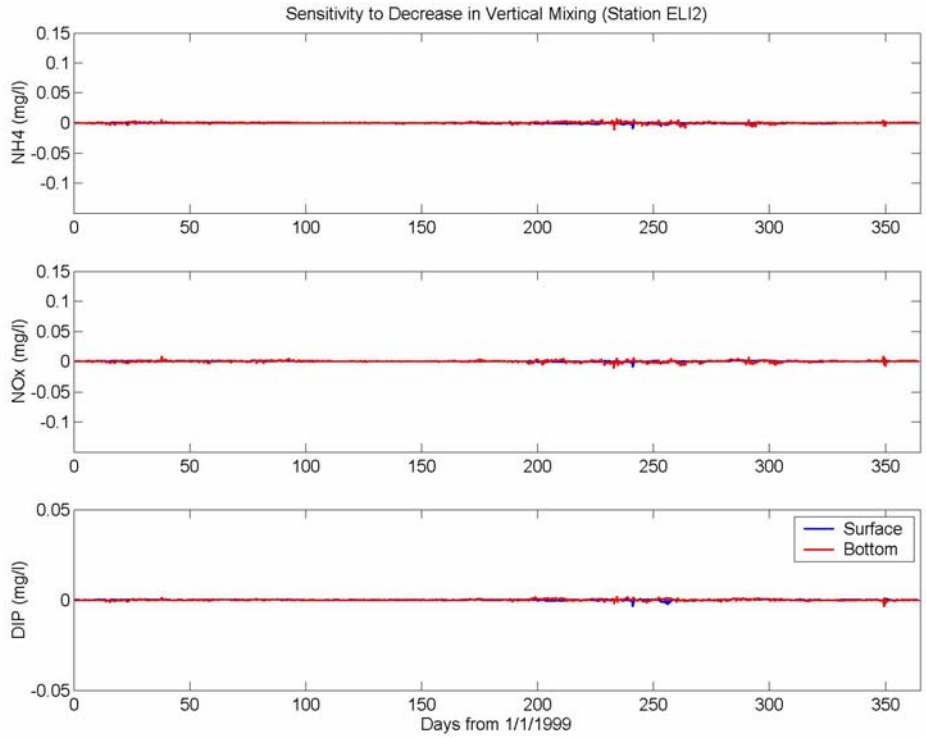

Figure L.35. Differences of model predictions for dissolved oxygen, chlorophyll-a, total phosphorus, and total nitrogen at CBP Station ELI2 (surface and bottom layers) for 1999 due to a decrease in the background eddy diffusivity from 10^{-6} m^2/s to 10^{-7} m^2/s (ST-6).

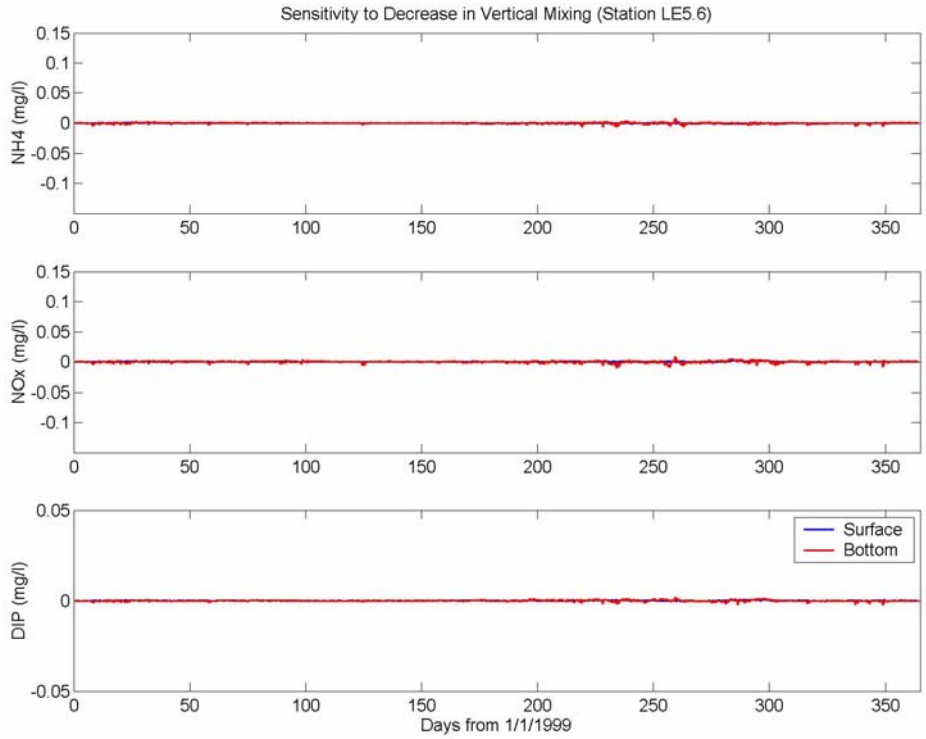

Figure L.36. Differences of model predictions for ammonium, nitrate-nitrite, and dissolved inorganic phosphorus at CBP Station ELI2 (surface and bottom layers) for 1999 due to a decrease in the background eddy diffusivity from 10^{-6} m^2/s to 10^{-7} m^2/s (ST-6).